

*power systems*

Rik De Doncker  
Duco W.J. Pulle  
André Veltman

# Advanced Electrical Drives

Analysis, Modeling, Control



Springer



# Power Systems

For further volumes:  
[www.springer.com/series/4622](http://www.springer.com/series/4622)

Rik De Doncker • Duco W.J. Pulle •  
André Veltman

# Advanced Electrical Drives

Analysis, Modeling, Control



Springer

Prof. Dr. Rik De Doncker  
RWTH Aachen University  
Inst. for Power Electronics  
and Electrical Drives (ISEA)  
Jägerstr. 17-19  
52066 Aachen  
Germany  
[aed@isea.rwth-aachen.de](mailto:aed@isea.rwth-aachen.de)

Dr. André Veltman  
TU Eindhoven  
Den Dolech 2  
5612 AZ Eindhoven  
The Netherlands  
[a.veltman@piak.nl](mailto:a.veltman@piak.nl)

Dr. Duco W.J. Pulle  
Zener Electric Pty Ltd.  
Horsley Road 366  
2214 Milperra, Sydney  
New South Wales  
Australia

Additional material to this book can be downloaded from <http://extras.springer.com>.

ISSN 1612-1287

e-ISSN 1860-4676

ISBN 978-94-007-0179-3

e-ISBN 978-94-007-0181-6

DOI 10.1007/978-94-007-0181-6

Springer Dordrecht Heidelberg London New York

© Springer Science+Business Media B.V. 2011

No part of this work may be reproduced, stored in a retrieval system, or transmitted in any form or by any means, electronic, mechanical, photocopying, microfilming, recording or otherwise, without written permission from the Publisher, with the exception of any material supplied specifically for the purpose of being entered and executed on a computer system, for exclusive use by the purchaser of the work.

*Cover design:* VTEX, Vilnius

Printed on acid-free paper

Springer is part of Springer Science+Business Media ([www.springer.com](http://www.springer.com))



*In memory of Prof. A. J. A. Vandenput  
who has inspired the authors.*

# Foreword

The value of a textbook is largely determined by how well its structure supports the reader in mastering the depth and breadth of the intended subject. This textbook provides a structure that can achieve that goal for engineers seeking to master key technologies for a wide range of advanced electrical drives.

To achieve that goal it wisely places very significant, but common background material in the early chapters, where it introduces the core topologies of power converters and the key issues needed to understand and apply practical power electronic converters. It also lays a sound foundation for understanding the two fundamental approaches for current regulators: hysteresis control and model-based control. By providing a sound and detailed background on power converters and current regulators, the rest of the text is able to focus on the advanced electrical drive concepts that are unique to the major classes of machines: DC, AC synchronous machines, AC induction machines, and switched reluctance machines.

Common structures are used to great advantage. To develop a common basis for modeling and control, the machines that are predominately Lorentz force machines, i.e. the DC, AC synchronous, and AC induction (asynchronous) machines are all modeled using an ideal rotating transformer. By first applying it to the DC machine, the link to AC machines is very clear. Common modules are used to provide uniformity in the discussion between the various machine types and to be directly compatible with a simulation modeling environment. A similar structure is extensively used for the controls modules that follow the machine modules.

The text's separation of machine modeling from drive control is very helpful. Machine modeling lays a foundation such the controls can logically sequence from classical to advanced drive methodologies. The inclusion of both surface and interior permanent magnet synchronous machines is particularly relevant since those machines are beginning to dominate many applications. The significant treatment of field weakening operation is also critical. The inclusion of limits such as maximum current, maximum flux, maximum torque

per flux, and maximum torque per ampere make the range of operation of the machine drives very transparent. The universal field-oriented control structure is aptly used to unify the subsequent presentation of indirect and direct field orientation control methods.

A very clear transition is made from predominately Lorentz force-based machines to purely reluctance torque-based machines. The detailed modeling and evaluation of switched reluctance machines allows drives engineers to correctly model the inherently pulsating torque that each phase provides. The treatment of saturation and its affect on power conversion leads nicely into evaluation of drives with these properties. By including a rigorous discussion of classical hysteresis current control and multi-phase direct instantaneous torque control, the reader can appreciate the structure needed for high performance control of torque in switched reluctance drives.

Throughout the text, extensive tutorials tie modules that codify key concepts in the theory, to their implementation in a simulation environment. This makes it possible for the reader to quickly explore details and develop confidence in their mastery of major concepts for advanced electrical drives.

By following the approach of this book, I believe that advanced drive engineers will be able to develop depth and breadth that is not normally easy to achieve.

Madison, Wisconsin, U.S.A.

*Robert D. Lorenz*



# Preface

Mastering the synergy of electromagnetics, control, power electronics and mechanical concepts remains an intellectual challenge. Nevertheless, this barrier must be overcome by engineers and senior students who have a need or desire to comprehend the theoretical and practical aspects of modern electrical drives. In this context, the term *drive* represents a plethora of motion control systems as present in industry.

This book *Advanced Electrical Drives* builds on basic concepts outlined in the book *Fundamentals of Electrical Drives* by the same authors. Hence, it is prudent for the uninitiated reader to consider this material prior to tackling the more advanced material presented in this text. Others well versed in the basic concepts of electrical drives should be able to readily assimilate the material presented as every effort has been made to ensure that the material presented can be mastered without the need to continually switch between the books.

In our previous work, the unique concept of an *ideal rotating transformer* (IRTF), as developed by the authors, was introduced to facilitate the basic understanding of torque production in electrical machines. The application of the IRTF module to modern electrical machines as introduced in *Fundamentals of Electrical Drives* is fully explored in this volume and as such allows the user to examine a range of unique dynamic and steady-state machine models which covers brushed DC, non-salient/salient synchronous and induction machines.

In addition, this volume explains the *universal field oriented* (UFO) concept which demonstrates the concepts of modern vector control and exemplifies the seamless transition between so-called *stator flux* and *rotor flux* oriented control techniques. This powerful tool is used for the development of flux oriented machine models of rotating field machines. These models form the basis of UFO vector control techniques which are covered extensively together with traditional drive concepts. In the last sections of this book, attention is given to the dynamic modeling of *switched reluctance* (SR)

drives, where a comprehensive set of modeling tools and control techniques are presented which are complemented by a set of *build and play* modules.

As with the previous book, the interactive learning process using *build and play* modules is continued. Again the simulation tool CASPOC is used which contains a tailored set of modules which bring to life the circuit and generic models introduced in the text. This approach provides the reader with the opportunity to interactively explore and fully comprehend and visualize the concepts presented in this text. For this purpose, realtime modules which allow the reader to view the simulations without further software licensing needs are provided on the Springer website (<http://extras.springer.com>).

The text *Advanced Electrical Drives* should appeal to the readers in industry and universities who have a desire or need to understand the intricacies of modern electrical drives without loosing sight of the fundamental principles. The book brings together the concepts of IRTF and UFO which allows a comprehensive and insightful analysis of AC electrical drives in terms of modeling and control. Particular attention is also given to switched reluctance drives modeling methods and modern control techniques. Extensive use is made of *build and play modules* in this book which for the first time provides the user with the ability to interactively examine and understand the topics present in this book.

Aachen, Germany  
Aachen, Germany  
Culemborg, Netherlands

*Rik De Doncker*  
*Duco W. J. Pulle*  
*André Veltman*

# Acknowledgements

That this work has come to fruition stems from a deep belief that the material presented in this book will be of profound value to the educational institutions and the engineering community as a whole. In particular, the fast but accurate simulations that accompany the tutorials provide a new way of learning that is highly interactive, so that they may stimulate creativity of students and experts alike by virtue of virtual experiments.

The content of this book reflects on the collective academic and industrial experience of the authors and co-workers. In this context, the inputs of students and research associates cannot be overestimated. The authors wish to acknowledge the staff at the Institute for Power Electronics and Electrical Drives (ISEA) of RWTH Aachen University. In particular, the authors would like to thank (in alphabetical order) Matthias Bösing, Christian Carstensen, Martin Hennen, Knut Kasper, Markus Kunter, Christoph Neuhaus, and Daniel van Treek for their contribution over the last three years. We would also like to thank Paul van der Hulst of Piak Electronic Design b.v., Culemborg, Netherlands, for supporting the final editing work and providing many good suggestions. Furthermore, the simulation tools that support the tutorials would not have been possible without the generous support of Peter van Duijsen of Simulation-Research, Alphen aan den Rijn, Netherlands, to support and make available to the readers of this book all CASPOC simulations. The experimental setup used to validate and demonstrate the algorithms was supported by AixControl GmbH, Aachen, Germany. The authors are grateful to the American University of Sharjah, United Arab Emirates, for supporting a working visit to RWTH Aachen University.



# Contents

<b>1</b>	<b>Modern Electrical Drives: An Overview .....</b>	<b>1</b>
1.1	Introduction .....	1
1.2	Drive Technology Trends .....	3
1.2.1	Electrical Machines .....	3
1.2.2	Power Converters.....	6
1.2.3	Embedded Control and Communication Links.....	8
1.3	Drive Design Methodology.....	11
1.4	Experimental Setup.....	13
<b>2</b>	<b>Modulation Techniques for Power Electronic Converters ..</b>	<b>17</b>
2.1	Introduction .....	17
2.2	Single-Phase Half-Bridge Converter .....	19
2.3	Single-Phase Full-Bridge Converter .....	23
2.4	Three-Phase Converter .....	28
2.4.1	Space Vector Modulation .....	33
2.5	Dead-Time Effects .....	38
2.6	Tutorials .....	41
2.6.1	Tutorial 1: Half-Bridge Converter with Pulse Width Modulation .....	41
2.6.2	Tutorial 2: Half-Bridge Converter with PWM and Dead-Time Effects .....	43
2.6.3	Tutorial 3: Full-Bridge Converter with Pulse Width Modulation .....	45
2.6.4	Tutorial 4: Three-Phase Pulse Width Modulator with Pulse Centering .....	47
2.6.5	Tutorial 5: Three-Phase Converter with Pulse Width Modulator .....	49
2.6.6	Tutorial 6: Three-Phase Simplified Converter without PWM .....	51

<b>3 Current Control of Generalized Load .....</b>	<b>55</b>
3.1 Current Control of Single-Phase Load .....	55
3.1.1 Hysteresis Current Control .....	55
3.1.2 Model Based Current Control .....	58
3.1.3 Augmented Model Based Current Control .....	63
3.2 Current Control of a Three-Phase Load .....	64
3.2.1 Three-Phase Hysteresis Current Control .....	67
3.2.2 Model Based Three-Phase Current Control .....	73
3.2.3 Augmented Three-Phase Model Based Current Control	80
3.2.4 Frequency Spectrum of Hysteresis and Model Based Current Controllers .....	81
3.3 Tutorials .....	83
3.3.1 Tutorial 1: Single-Phase Hysteresis Current Control...	83
3.3.2 Tutorial 2: Single-Phase Model Based Current Control	84
3.3.3 Tutorial 3: Three-Phase <i>Box Method</i> Type Hysteresis Current Control .....	86
3.3.4 Tutorial 4: Three-Phase Model Based Current Control	89
3.3.5 Tutorial 5: Three-Phase Model Based Current Control without PWM, Using Simplified Approach .....	92
<b>4 Drive Principles .....</b>	<b>95</b>
4.1 ITF and IRTF Concepts .....	95
4.2 Electromagnetic Torque Control Principles .....	100
4.2.1 DC Machine .....	101
4.2.2 Synchronous Machine .....	103
4.2.3 Induction Machine .....	106
4.3 Drive Dynamics .....	108
4.3.1 Linear and Rotational Motion .....	109
4.3.2 Rotational to Translational Transmission .....	111
4.3.3 Gear Transmission .....	113
4.3.4 Dynamic Model of a Drive Train .....	115
4.4 Shaft Speed Control Loop Design Principles .....	117
4.5 Tutorials .....	122
4.5.1 Tutorial 1: Elementary Synchronous Drive .....	122
4.5.2 Tutorial 2: Elementary Asynchronous (Induction) Drive .....	123
4.5.3 Tutorial 3: Elementary DC Drive .....	125
4.5.4 Tutorial 4: Drive Dynamics Example .....	126
4.5.5 Tutorial 5: Speed Control Loop Design Example .....	127
<b>5 Modeling and Control of DC Machines .....</b>	<b>131</b>
5.1 Separately Excited, Current-Controlled DC Machine .....	132
5.1.1 Symbolic Model of the DC Machine .....	133
5.1.2 Generic Model DC Machine .....	135
5.2 Field-Oriented Machine Model .....	135

5.3	Control of Separately Excited DC Machines . . . . .	138
5.3.1	Controller Concept . . . . .	138
5.3.2	Operational Drive Boundaries . . . . .	139
5.3.3	Use of Current Source IRTF Based Model . . . . .	146
5.3.4	Use of a Voltage Source with a Model Based Current Control . . . . .	147
5.4	Tutorials . . . . .	150
5.4.1	Tutorial 1: Current Source Model of a Brushed DC Machine with Segmented Commutation Module . . . . .	150
5.4.2	Tutorial 2: Modeling of a Current and Voltage Source Connected Brushed DC Motor . . . . .	152
5.4.3	Tutorial 3: Current Source Connected Brushed DC Motor with Field Weakening Controller . . . . .	154
5.4.4	Tutorial 4: DC Drive Operating under Model Based Current Control and a Field Weakening Controller . . . . .	157
5.4.5	Tutorial 5: DC Drive with Model Based Current Control and Shaft Speed Control Loop . . . . .	159
5.4.6	Tutorial 6: Experimental Results of DC Machine . . . . .	161
<b>6</b>	<b>Synchronous Machine Modeling Concepts . . . . .</b>	<b>165</b>
6.1	Non-salient Machine . . . . .	165
6.1.1	Symbolic Model of a Non-salient Machine . . . . .	166
6.1.2	Generic Model . . . . .	167
6.1.3	Rotor-Oriented Model: Non-salient Synchronous Machine . . . . .	169
6.1.4	Steady-State Analysis . . . . .	171
6.2	Salient Synchronous Machine . . . . .	175
6.2.1	Generic Model . . . . .	177
6.2.2	Rotor-Oriented Model of the Salient Synchronous Machine . . . . .	178
6.2.3	Steady-State Analysis . . . . .	180
6.3	Tutorials . . . . .	184
6.3.1	Tutorial 1: Dynamic Model of a Non-salient Synchronous Machine . . . . .	184
6.3.2	Tutorial 2: Steady-State Analysis of a Non-salient Synchronous Machine . . . . .	186
6.3.3	Tutorial 3: Stator Flux Linkage Excited Dynamic Model of a Synchronous Machine to Demonstrate the Rotor Flux Oriented Concept . . . . .	187
6.3.4	Tutorial 4: Dynamic Model of a Synchronous Machine with Adjustable Saliency . . . . .	189
6.3.5	Tutorial 5: Steady-State Analysis of a Salient Synchronous Machine . . . . .	191

<b>7 Control of Synchronous Machine Drives .....</b>	193
7.1 Controller Principles .....	193
7.2 Control of Non-salient Synchronous Machines .....	195
7.2.1 Operation under Drive Limitations .....	196
7.2.2 Field Weakening Operation for PM Non-salient Drives	200
7.2.3 Field Weakening for PM Non-salient Drives, with Constant Stator Flux Linkage Control .....	206
7.2.4 Field Weakening for Electrically Excited Non-salient Drive, with Constant Stator Flux and Unity Power Factor Control .....	209
7.3 Control of Salient Synchronous Machines .....	213
7.4 Field-Oriented Control of a Current-Controlled Synchronous Machine .....	217
7.5 Field-Oriented control of a Voltage-Source Connected Synchronous Machine .....	219
7.6 Tutorials .....	222
7.6.1 Tutorial 1: Non-salient Synchronous Drive .....	222
7.6.2 Tutorial 2: Non-salient Synchronous Drive, Constant Stator Flux Operation .....	224
7.6.3 Tutorial 3: Non-salient Synchronous Drive, Unity Power Factor Operation .....	226
7.6.4 Tutorial 4: Salient Synchronous Drive .....	228
7.6.5 Tutorial 5: PM Salient Synchronous Drive with Model Based Current Control .....	230
7.6.6 Tutorial 6: Experimental Results of a PM Non-salient Synchronous Drive .....	234
<b>8 Induction Machine Modeling Concepts .....</b>	239
8.1 Induction Machine with Squirrel-Cage Rotor .....	239
8.2 Zero Leakage Inductance Models of Induction Machines .....	241
8.2.1 IRTF Based Model of the Induction Machine .....	241
8.2.2 Field-Oriented Model .....	243
8.3 Machine Models with Leakage Inductances .....	247
8.3.1 Fundamental IRTF Based Model .....	247
8.3.2 Universal IRTF Based Model .....	248
8.3.2.1 Rotor Flux Based IRTF Model .....	254
8.3.2.2 Stator Flux Based IRTF Model .....	256
8.3.3 Universal Stationary Frame Oriented Model .....	257
8.3.4 Universal Field-Oriented (UFO) Model .....	258
8.3.4.1 Rotor Flux Oriented Model .....	261
8.3.4.2 Stator Flux Oriented Model .....	264
8.3.5 Synchronous Frame Oriented Heyland diagram .....	267
8.3.6 Steady-State Analysis .....	268
8.4 Parameter Identification and Estimates .....	270
8.5 Single-Phase Induction Machines .....	273

8.5.1	Steady-State Analysis of Capacitor-Run Single-Phase Induction Machines .....	277
8.6	Tutorials .....	285
8.6.1	Tutorial 1: Simplified Induction Machine Model .....	285
8.6.2	Tutorial 2: Universal Induction Machine Model .....	286
8.6.3	Tutorial 3: Universal Stationary Oriented Induction Machine Model .....	288
8.6.4	Tutorial 4: Current Controlled Zero Leakage Flux Oriented Machine Model .....	289
8.6.5	Tutorial 5: Current Controlled Universal Field Oriented (UFO) Model.....	291
8.6.6	Tutorial 6: Parameter Estimation Using Name Plate Data and Known Stator Resistance .....	292
8.6.7	Tutorial 7: Grid Connected Induction Machine .....	294
8.6.8	Tutorial 8: Steady State Characteristics, Grid Connected Induction Machine.....	296
8.6.9	Tutorial 9: Grid Connected Single-Phase Induction Machine.....	297
<b>9</b>	<b>Control of Induction Machine Drives .....</b>	<b>303</b>
9.1	Voltage-to-Frequency (V/f) Control .....	303
9.1.1	Simple V/f Speed Controller .....	305
9.1.2	V/f Torque Controller with Shaft Speed Sensor .....	309
9.2	Field-Oriented Control .....	311
9.2.1	Controller Principle.....	312
9.2.2	Controller Structure .....	314
9.2.3	UFO Module Structure .....	315
9.2.4	IFO Using Measured Shaft Speed or Shaft Angle .....	316
9.2.5	DFO with Air-Gap Flux Sensors .....	318
9.2.6	DFO with Sensor Coils .....	319
9.2.7	DFO with Voltage and Current Transducers .....	320
9.2.8	DFO with Current and Shaft Speed Transducers .....	321
9.3	Operational Drive Boundaries for Rotor Flux Oriented Control .....	323
9.4	Field Weakening for Rotor Flux Oriented IM Drives .....	327
9.5	Interfacing FOC with Current-Controlled IM.....	331
9.6	Interfacing FOC with Voltage-Source-Connected IM .....	333
9.7	Tutorials .....	337
9.7.1	Tutorial 1: Simplified V/f Drive .....	337
9.7.2	Tutorial 2: V/f Drive with Shaft Speed Sensor .....	340
9.7.3	Tutorial 3: Universal Field-Oriented (UFO) Control with a Current Source Based Machine Model and Known Shaft Angle.....	342
9.7.4	Tutorial 4: Induction Machine Drive with UFO Controller and Model-Based Current Control .....	348

9.7.5	Tutorial 5: Rotor Flux Oriented Induction Machine Drive with UFO Controller and Field Weakening Controller .....	352
9.7.6	Tutorial 6: Experimental Results of an Induction Machine with UFO Controller.....	357
<b>10</b>	<b>Switched Reluctance Drive Systems .....</b>	<b>361</b>
10.1	Basic Machine Concepts .....	363
10.2	Operating Principles .....	365
10.2.1	Single-Phase Motor Concept .....	365
10.2.2	Torque Production and Energy Conversion Principles ..	367
10.2.3	Single-Phase Switched Reluctance Machine: A Linear Example .....	371
10.2.4	Switched Reluctance Modeling Concepts .....	380
10.2.5	Representation of the Magnetization Characteristics ..	383
10.2.6	Converter and Control Concepts .....	384
10.2.7	Example of Low and High Speed Drive Operation ..	387
10.3	Multi-Phase Machines.....	392
10.3.1	Converter Concepts .....	394
10.4	Control of Switched Reluctance Drives .....	396
10.4.1	Drive Characteristics and Operating Range .....	396
10.4.2	Drive Operational Aspects .....	398
10.4.3	Direct Instantaneous Torque Control (DITC) .....	409
10.5	Switched Reluctance Demonstration Machine .....	416
10.6	Tutorials .....	421
10.6.1	Tutorial 1: Analysis of a Linear SR Machine, with Current Excitation .....	421
10.6.2	Tutorial 2: Non-linear SR Machine, with Voltage Excitation and Hysteresis Current Controller .....	424
10.6.3	Tutorial 3: Non-linear SR Machine, with Voltage Excitation and PWM Controller .....	427
10.6.4	Tutorial 4: Four-Phase Non-linear SR Model, with Voltage Excitation and Hysteresis Control .....	430
10.6.5	Tutorial 5: Four-Phase Non-linear SR Model, with Voltage Excitation and Direct Instantaneous Torque Control (DITC) .....	433
<b>References .....</b>	<b>439</b>	
<b>Abbreviations .....</b>	<b>445</b>	
<b>List of symbols .....</b>	<b>447</b>	
<b>List of indices .....</b>	<b>449</b>	
<b>Index .....</b>	<b>453</b>	



# Chapter 1

## Modern Electrical Drives: An Overview

### 1.1 Introduction

An electrical drive, as shown in Fig. 1.1 can be defined in terms of its ability to efficiently convert energy from an electrical *power source* to a *mechanical load*. The main purpose of the drive is to control a mechanical load or process. The direction of energy flow is generally from electrical to mechanical, i.e., motoring mode with power flow from the *power source* to the *mechanical load* via the *converter* and *machine* as shown in Fig. 1.1. However, the energy flow can in some cases be reversed, in which case the drive often is configured bi-directional to also allow energy flow from the *mechanical load* to the *power source*. Modern electrical drives, as considered in this book, utilize power electronic devices to (digitally) control this power conversion process, a feature which is highlighted in Fig. 1.1 by the presence of the *modulator* and *control* unit. Note that in some cases the *modulator* is simply removed in which the power electronic devices in the *converter* are controlled directly via the *controller* module. In addition to the above the controller module

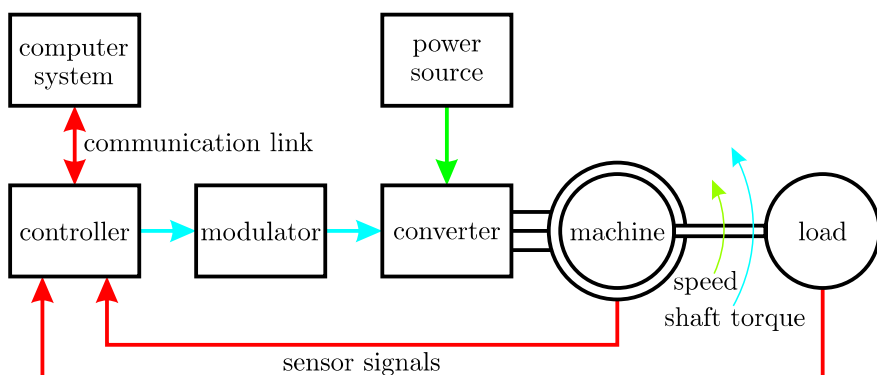


**Fig. 1.1** Typical drive set-up

shown in Fig. 1.1 must be able to communicate with higher level computer systems because drives are progressively networked. Communication links to high level computer networks are required to support a range of functions, such as commissioning, initialization, diagnostics and higher level process control. The embedded digital controller shown in Fig. 1.1 houses the high-speed logic devices, processors and electronic circuitry needed to accommodate the *sensor signals* derived from mechanical and electrical sensors. Furthermore, and most importantly, suitable control algorithms must be developed to facilitate the power conversion processes within the drive. From this perspective, drive technology can be considered as a relative “newcomer”. This statement maybe put in perspective by considering that electrical machine development commenced approximately one hundred and fifty years ago. However, with the advent of new materials and new design tools, novel machine concepts such as linear machines, PM magnet, switched reluctance and transversal flux machines, to name only a few, have been developed over the past twenty years. Power electronic devices have on the other hand been around for about forty five years, while high-speed digital devices have only been available over the past twenty five years. Furthermore, suitable control algorithms such as *field-oriented control* have been developed over the past thirty years. Ongoing drive development is fueled by the continuous emergence of new drive related drive products such as new processors, sensors and most importantly new control algorithms aimed at, for example, the elimination of expensive position sensors in electrical drives. Such developments enhance drive robustness, improve reliability, and expand the use of electrical drives to other industrial applications, hitherto considered to be unfeasible. The power range associated with these industrial applications is impressive and typically ranges from a few milliwatts to hundreds of megawatt, which underlines the flexibility and broad application base of modern drive technology. Figure 1.2 shows two examples which are positioned at opposite ends of the drive power range.

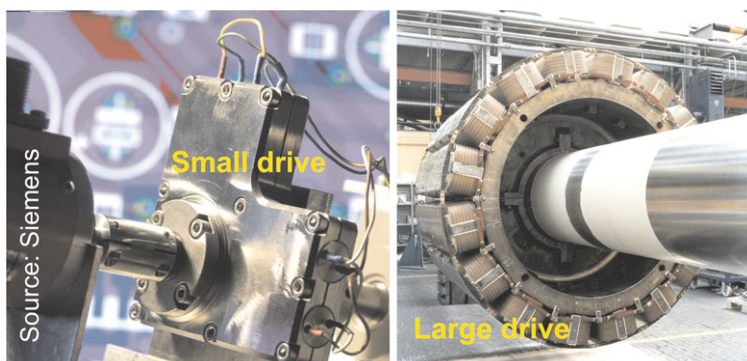


**Fig. 1.2** Two examples of drive technology at opposite ends of the power range. Left picture, a very small (less than 1 W) drive, right picture, a high power (in excess of 10 MW) example [59]

## 1.2 Drive Technology Trends

This section aims to provide the reader with an overview of technology trends associated with key components of the electrical drive as shown in Fig. 1.1. Most importantly the objective in each of the ensuing subsections is to identify important developments and trends of key drive elements such as the machine, converter and controller.

### 1.2.1 Electrical Machines

The primary electro-mechanical energy converter of the drive is the electrical machine, which must be controlled in accordance with the industrial processes in which the unit is deployed. Modern electrical drives typically use one of the three electrical machine types shown in Fig. 1.3. These machine types are referred to as the *induction* (*asynchronous*), *PM synchronous* and *switched reluctance* machine and are shown in Fig. 1.3 consecutively from top to bottom and will be discussed extensively in this book. Both asynchronous and synchronous machine configurations depicted in Fig. 1.3 are shown with the typical three-phase winding, which is located in the stator slots of the machine. Note that other machine types including the *brushed DC machine* are also still in use. Of the three configurations shown in Fig. 1.3, the induction machine is most commonly found in industrial drives. This can be attributed to the inherent robustness of the machine itself and the presence of tried and proven drive components which form the basis of a reliable drive. Above all, the emergence of fast, low-cost digital processors and micro-controllers has been instrumental in achieving this market position, given that these units are able to accommodate well established control algorithms such as *field-oriented control*. The end result is a brushless and in many cases (position) sensorless induction machine drive with dynamic performance that outperforms that of the classical brushed DC machine.

An important performance parameter of the machine is the *power density*, i.e., the output power to weight ratio in (kW/kg). The power density over the past century has steadily increased from  $0.02\text{ kW/kg}$  at the beginning of the 20<sup>th</sup> century to  $0.15\text{ kW/kg}$  by 1970, according to an ‘S’ curve as typically found in maturing technologies. The expectation at that time was that further substantial increases in power density were unlikely. Consequently, power density values were expected to level off around the  $0.16\text{ kW/kg}$  value, given the need to keep operating temperatures within acceptable levels. The importance of this statement follows from Fig. 1.4, which shows the relationship between operating temperature and lifetime. Hence, according to this figure, a life-time of, for example, 80 000 h can be expected provided operat-

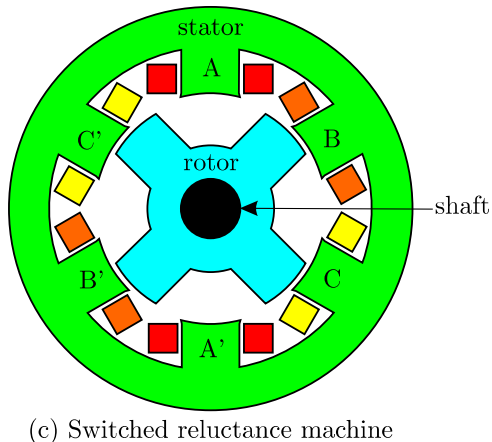
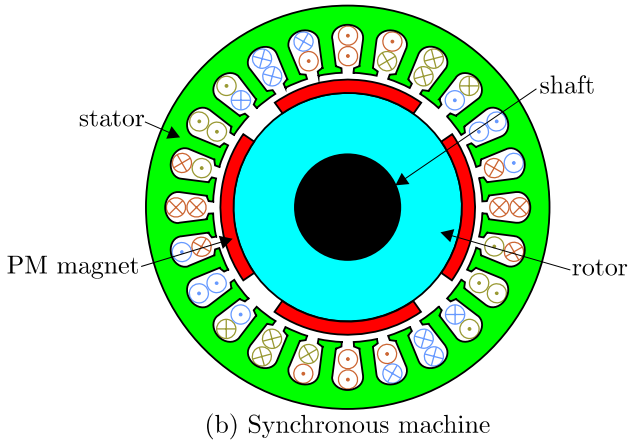
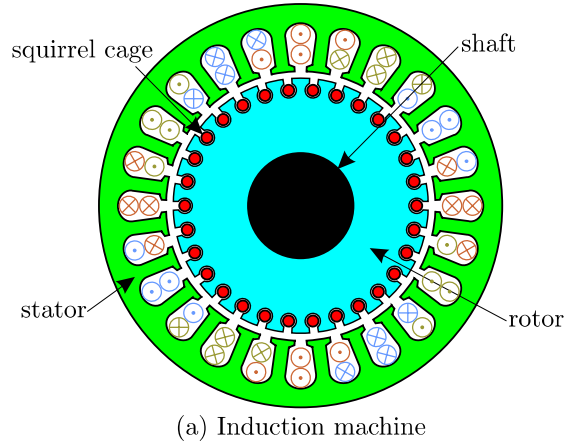


**Fig. 1.3** Example of commonly used machine configurations

ing temperatures are constrained to 200 °C whereby the latter is primarily dependent on the power density level.

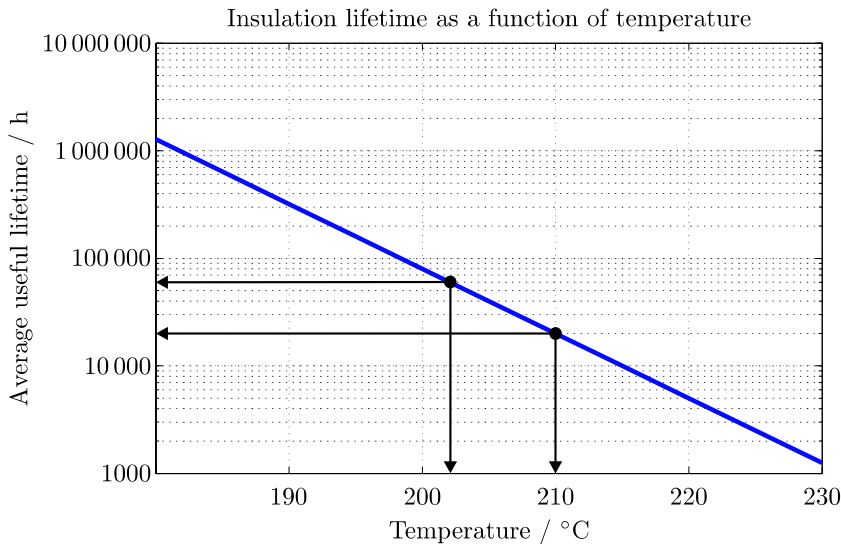


**Fig. 1.4** Useful life time of insulation material versus temperature

Subsequently, improvements in power density could, according to thinking in the past century, only be realized by the development of more efficient magnetic materials, i.e., with lower eddy current and hysteresis losses, and/or improvements in insulation materials as to allow extended operation at higher temperatures, without compromising machine life time. Given these arguments, the reader may well be surprised to hear that machines with power densities between 1.2 kW/kg and 3.5 kW/kg are now emerging despite the fact that the magnetic and insulation material have virtually remained unchanged. A set of factors have contributed to this substantial increase in power density namely:

- Improvements in bearing and gear technology have been primarily instrumental in achieving high power densities. In this context it is noted that output power is the product of shaft torque and shaft speed. Rated shaft torque is primarily determined by rotor volume and maximum flux density of 2 T, (which has not substantially changed over the past century). This implies that power density improvements have been achieved by substantially raising operating speeds from typically 3000 rpm (as commonly used around the turn of the last century) to 6000 rpm for traction machine and 16 000 rpm in hybrid and electrical vehicles. Machines with speeds reaching 100 000 rpm are now manufactured with inherent excellent cooling capabilities and power density values up to 3.5 kW/kg. Such machines operate

under low torque conditions which implies that the design can be made light and compact.

- Improvements in quality control and automated production reduces losses and allows design with higher precision. A prime example is the use of copper injection techniques for manufacturing squirrel-cage rotors of induction machines [3].
- Availability of improved design tools (to be discussed in Sect. 1.3) for machines which allow the user to examine and fine tune magnetic, thermal (to identify hot spots) and acoustical behavior. In addition, extensive simulation tool are now available which allow the user to examine dynamic drive operation with different load and control scenarios.
- Improved cooling techniques to avoid hot spots, which leads to a better utilization of available insulation materials. Consequently, better thermal conductivity is achievable in machines.
- Reduced derating of converter connected machines. Traditionally a 15% derating figure was imposed to counter the temperature rise due to higher harmonics generated by the converter. Modern converter are able to operate with higher (than used in the previous century) operating frequencies without compromising cost and efficiency of the converter, as will become apparent in the ensuing subsection.

### **1.2.2 Power Converters**

The development of power electronic converter has over the past twenty five years been substantial as may be gauged from the volumetric power density parameter, i.e., the ratio of converter apparent power to volume  $\text{kVA}/\text{m}^3$ . For industrial air-cooled *ac* to *ac* converters the volumetric power density has increased from  $30 \text{ kVA}/\text{m}^3$  (at the end of the last century) to present day values up to  $500 \text{ kVA}/\text{m}^3$ . These substantial improvements to the volumetric power density can be attributed to a number of factors namely:

- Availability of power semiconductors able to switch more efficiently, i.e., with lower power dissipation in comparison with values found in devices present at the turn of the century.
- Improvements to heat-sink technology which means that smaller modules can be developed.
- Use of topologies and control techniques to minimize power device losses, such as for example soft-switching techniques.
- Use of better design tools as will become apparent in Sect. 1.3.
- Availability of compact high-performance digital processors with extensive I/O capabilities that can be readily interfaced with the equally compact power electronic drive circuitry required to control the switching devices.

- Design and manufacturing improvements in passive devices most notably in capacitors which play a key role in terms of overall voltage source converter sizing and costs.

The culmination of the improvements indicated above is exemplified by the availability of building blocks as shown in Fig. 1.5, to construct a complete inverter and ‘off-the-shelf’ commercial inverters, as shown in Fig. 1.6, which can be readily interfaced to electrical machines. Note that the term *inverter* refers to a dc to ac converter, as shown in Fig. 1.1.

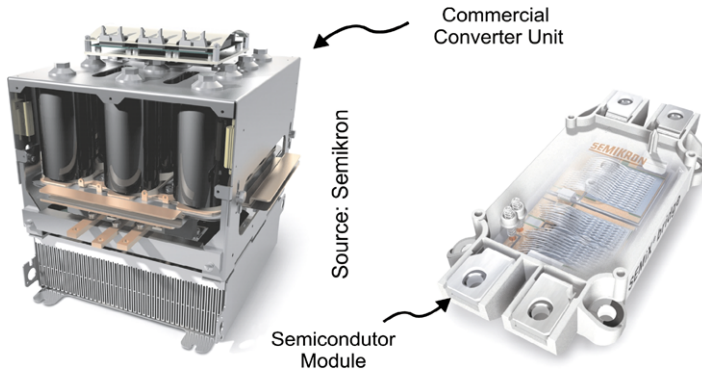


**Fig. 1.5** Example of commercial converter unit and integrated semiconductor module which can be used to build an inverter [58]



**Fig. 1.6** Example of modern inverter technology with standard communication interfaces [72]

In this section, the emphasis has been predominantly placed on improvements in volumetric power density. However, improvements in converter technology leading to the ability to operate at much higher electrical fundamental frequencies have also been instrumental in realizing high-speed drives.

The primary design constraint on the volumetric power density of the converter is thermal, i.e., the need to limit operating temperatures and guarantee sufficient thermal cycles of the semiconductor devices and corresponding packages. This implies that the volumetric power density is to a large extend governed by the specific losses of the devices in use, method of cooling and drive operating conditions. In electric and hybrid vehicles high power-density values for machine and converter are essential. An example of such as drive, as shown in Fig. 1.7, utilizes a liquid cooled DC to AC converter with a volumetric power density of  $6000 \text{ kVA/m}^3$  and a 55 kW switched reluctance machine with a power density of approximately  $1.2 \text{ kW/kg}$ .

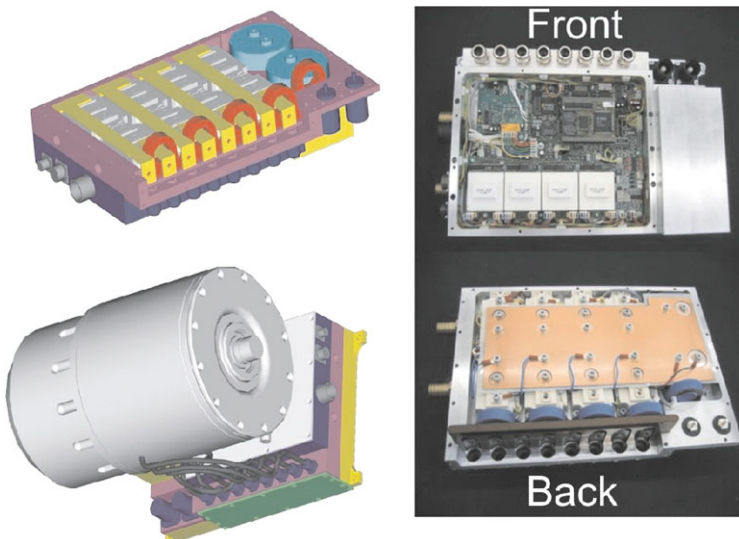


**Fig. 1.7** Example of an electrical vehicle propulsion unit which utilizes a liquid cooled AC–DC converter and 55 kW switched reluctance machine [15, 10]

### 1.2.3 Embedded Control and Communication Links

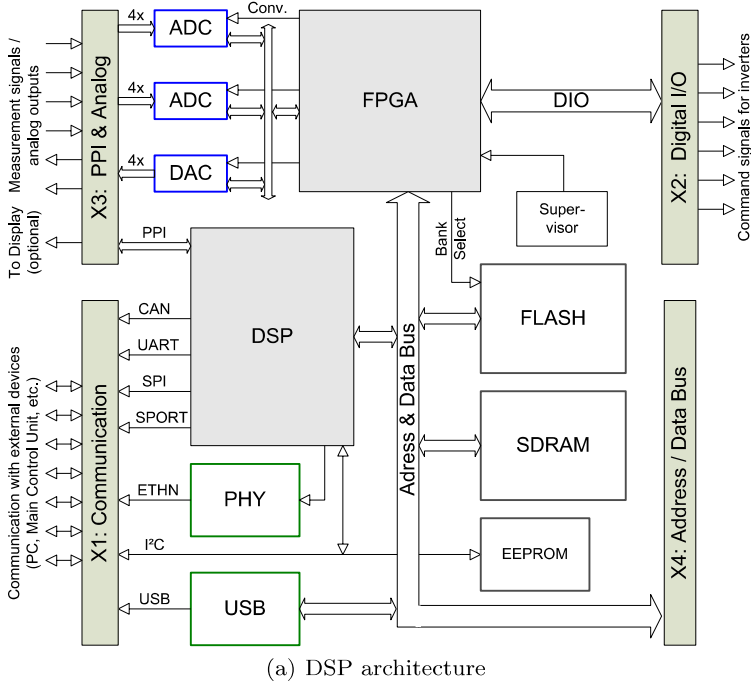
The *controller* and *modulator* (if used), as shown in Fig. 1.1, are part of an embedded system which is interfaced with the switching device drivers, and sensors (voltage and/or current and position/speed measurements). In

addition, these specialized computer systems in the form of digital signal processors or micro-controllers are specifically tailored for electrical drive applications. As such they are provided with extensive interface (digital/analog inputs and outputs) capabilities including networking capabilities for communication with other higher level computer systems. Both fixed and floating point processors are available with able computing power to accommodate the real time processing requirements of the drive. An example of a DSP unit as given in Fig. 1.8(a) clearly shows the multiple I/O *command* signals and other interface capabilities as required for an electrical drive.

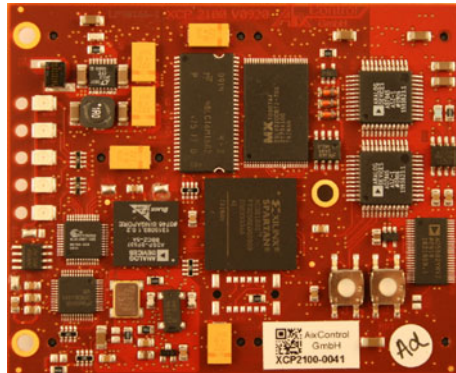
The advancements in drive development could not have been realized without innovations over the past thirty years in the field of control algorithms, software tools and hardware related to the controller. A brief overview of key innovations related to the controller can be summarized as follows:

- Development of *Field oriented control* (FOC) algorithms for AC machines. This control technique has led to the complete decoupling of the flux linkage and current. As such control of an AC machine is akin with the brushed DC machine, in terms of dynamic performance [7, 27].
- Synchronized space vector, pulse width modulation (PWM) techniques have been instrumental in achieving better DC bus voltage utilization and improvements to the output frequency spectrum of three-phase converters [9].
- Development of *Direct Torque control* algorithms for AC and Switched reluctance machines. Direct torque control for AC machines simplifies the overall drive technology given that the controller is directly interface with the drive circuitry of the switches, i.e., the modulator can be omitted. Direct torque control for switched reluctance drives (which do not utilize a modulator) empowers these highly non linear machines with servo drive performance capabilities [18].
- Development of control algorithms which make position and speed sensors superfluous [30]. In addition, control techniques have also been used to minimize the number of electrical (voltage/current) sensors needed. Furthermore, power devices are now available with integrated current sensors which enhances overall cost effectiveness.
- The availability of high performance (fast) fixed point as well as floating point digital signal processors (DSP) and micro-controllers ( $\mu$ C) have simplified the implementation of real time complex control algorithms as mentioned above.
- Availability of a range of programming tools for these DSP and  $\mu$ C units, which utilize high-level programming languages, such as C++, and graphical programming tools, such as MATLAB/SIMULINK or CASPOC, serve to shorten overall drive development times and enhance drive application flexibility.

These innovations related to embedded control have had a profound influence on drive development. Notably, the distinction between low and high perfor-



(a) DSP architecture



(b) DSP board

**Fig. 1.8** Example of DSP architecture, which demonstrate the flexibility available in terms of interfacing to other peripherals [1]

mance drives has become less pronounced because the same control platform can be used. Changes between the two is a matter of introducing different control algorithms and introducing or omitting electrical and/or position sensors. This implies that drives can be readily adapted to accommodate different industrial processes. Furthermore, changes to the power level of a drive can be carried through by using different converter packages. The net result

is that plug-and play concepts are increasingly used by drive manufacturers where the various components shown in Fig. 1.1 can be integrated and interchanged to suit a diverse range of drive applications. In all cases diverse standardized communication links are available to the user so that drives can be readily integrated in larger automated systems.

### 1.3 Drive Design Methodology

In this section, attention is given to drive design methodology, i.e., the processes used to develop and evaluate electrical drives. A thorough appreciation of these processes is important as they demonstrate the need for specialized software tools and above all a clear understanding of all the key drive components as well as the nature of the industrial process to be controlled.

Typically, a closed loop iterative design process is used which encompasses the complete drive as may be observed from the example given in Fig. 1.9. The example shown in Fig. 1.9 considers the design optimization process of a switched reluctance drive, but the approach is equally valid for other drives.

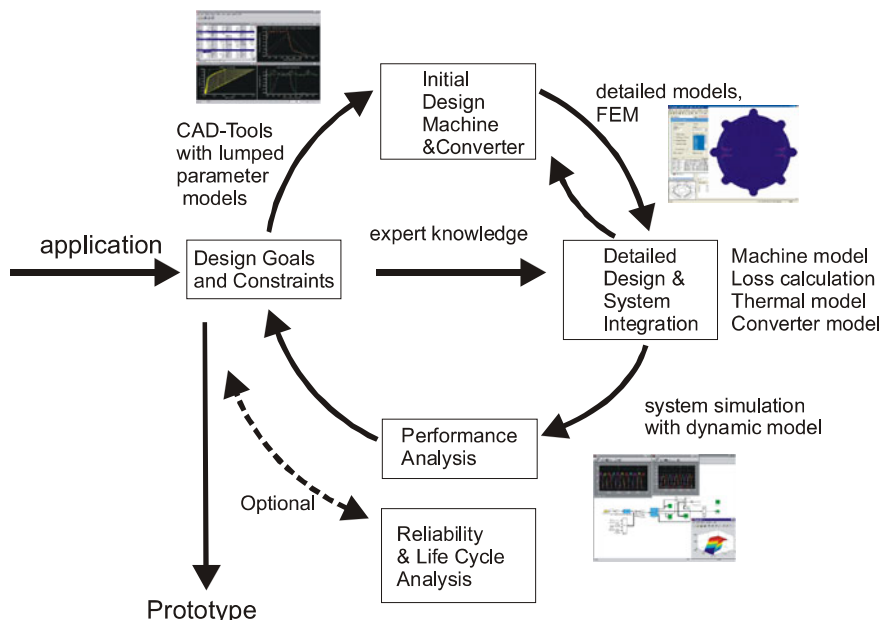


**Fig. 1.9** Typical design methodology used for electrical drives [61, 11, 65]

A brief discussion of the process shown in Fig. 1.9 may be initiated by considering the type of *application* for which the drive is intended. In this

context, knowledge of the industrial process to be controlled is essential. For example, drive development for an industrial process in the form of a compressor or fan is far less demanding than an off-shore drilling rig where dynamic load fluctuations must be controlled. Once the application is well defined, *design goals and constraints* can be established which form the basis for the *initial design of the machine and converter*. At this stage the type of machine and drive control algorithm to be used are also formulated, which may have a large impact on the time needed to complete the design process. For example, switched reluctance machines are highly non-linear by nature and the design of the machine is tied to the converter and envisaged control techniques. Use of ‘off-the-shelf’ rotating field AC machines, on the other hand, simplifies the design process as may be expected. In the latter case, which is typical for AC machines, manufacturer data is usually available and can be used to generate a well-defined set of parameters. For switched reluctance machines, a more extensive set of characteristics must be defined using computer aided design (*CAD-Tools*). Once the *initial design machine & converter* (see Fig. 1.9) has been established, the *detailed design and system integration* phase can be entered. This may be done in several layers. The first is to develop a global simulation model of the drive using ideal components. Software tools such as, for example, MATLAB/SIMULINK and CASPOC can be used to build dynamic simulation models of the complete drive. Such models utilize preplanned control algorithms which, for example, provide precise torque control. Usually additional control structures are added at this stage to empower the drive with the ability to control the intended industrial process. Subsequent *system simulation* of the model provides the transient and steady-state data needed to undertake a provisional *performance analysis*. On the basis of this information, further refinements to the model are undertaken which may involve the *initial design of the machine and converter* and *detailed design and system integration* elements shown in Fig. 1.9.

The level of design refinement is heavily dependent on the nature of the drive application. For example, applications involving aircraft and electric vehicles, need very high power-density levels, which can be achieved by undertaking more extensive computer modeling of the machine and converter. Such studies call for the use of sophisticated two- or three-dimensional *finite element* (FEM) simulation which can evaluate the magnetic behavior of the machine. In addition software tools exist to examine the thermal behavior of the machine and converter. Acoustical noise and vibration modes of the machine can also be considered well before the prototyping stage is reached.

A prime example of a drive, for which the design process described above has been applied is given in Fig. 1.10. The machine shown is a ninety-six phase spherical permanent magnet machine that is connected to a power converter. Each of the 96-phase converter modules was independently controlled by a dedicated control unit operating under field-oriented control. A global control algorithm was used to identify the appropriate phase currents to control the rotor with  $\mu\text{m}$  precision at high torque density level.

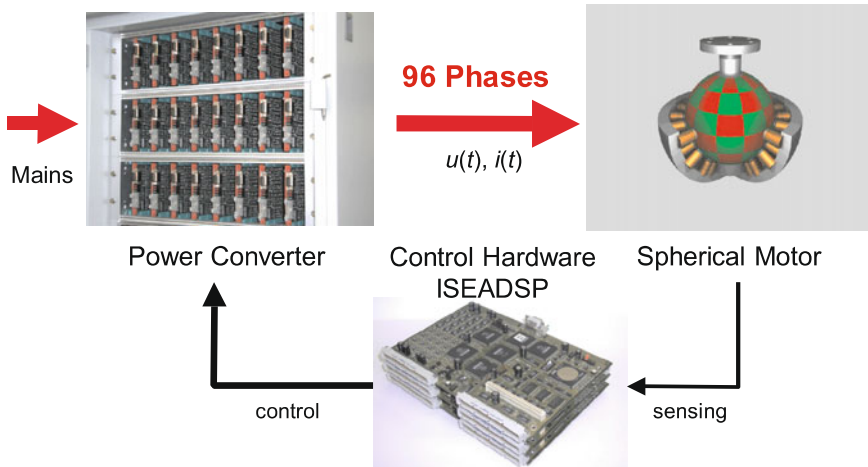


**Fig. 1.10** Ninety six phase spherical machine with corresponding converter and control platform with utilizes six DSP's [37]

After completion of the design stage, a drive prototype was built and evaluated. Overall experimental performance was generally consistent with the results obtained during the design phase. Projects of this kind demonstrate the need for drive engineers to have an in depth understanding of wide ranging technologies linked to electrical machines, mechanical industrial processes, power electronics, passive and active electronic circuitry, control hardware, software design tools, communication and control algorithms. Mastering and extending the boundaries of these technologies is a formidable challenge to the next generation of drive engineers.

## 1.4 Experimental Setup

In this book the developed control algorithms will be experimentally verified using a test-bench, that was developed for didactical work, as well as for research. The setup consists of four different machines, a DSP System and Power Rack, as shown in Fig. 1.11. The figure shows all used components, including the induction or asynchronous machine (ASM), the switched reluctance machine (SRM), the permanent magnet synchronous machine (PMSM) and the DC machine (DCM). Additionally, the figure shows a screen shot of the software AixScope, with which it is possible to on line read, write and display internal variables of the DSP.

To implement the control of each machine, a model of the control and the drive is first built in CASPOC (see Fig. 1.12). The models use the same basic blocks as the tutorials in each section. Using the C-code export function of

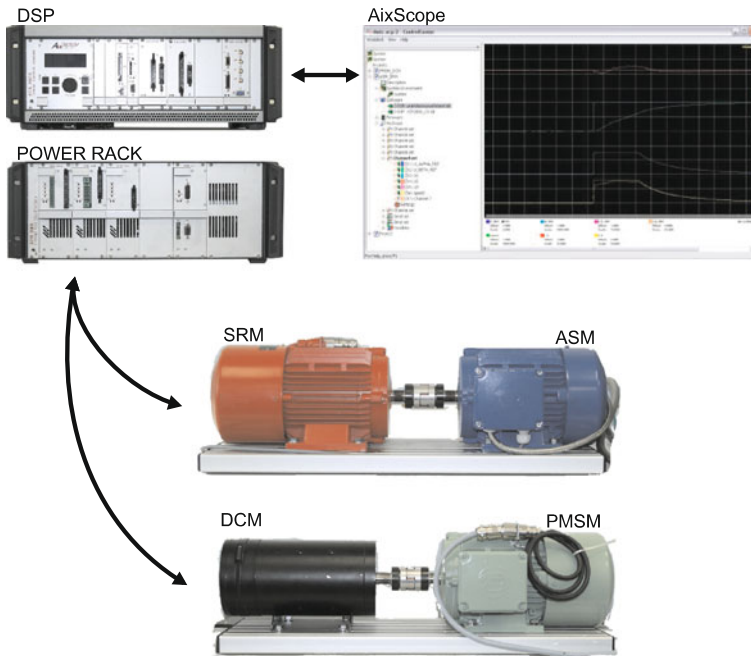


**Fig. 1.11** Setup of developed test-bench [1]

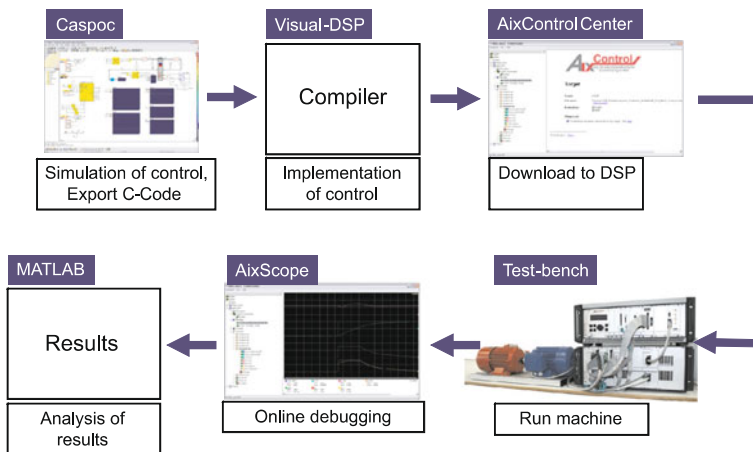


**Fig. 1.12** Process of control code development [60, 4, 1, 65]

CASPOC, the code of the control algorithm is transferred to Visual DSP, where it is embedded in the code of the test-bench. Using the software “Aixcontrol-Center”, the compiled code is subsequently uploaded to the test-bench and the machine can be tested. All experimental results in the following chapters are measured using the software AixScope. Figure 1.12 shows the developed process as used for all example machines.



# Chapter 2

## Modulation for Power Electronic Converters

### 2.1 Introduction

At present, voltage source converters are mostly used in electrical drives. These converters utilize capacitors in the DC-link to store temporarily electrical energy. Switching the power electronic devices allows the DC voltage to be modulated which can result in a variable voltage and frequency waveform. The purpose of the modulator is to generate the required switching signals for these switching devices on the basis of user defined inputs. For this purpose, the voltage-time integral was introduced [68], which in turn is tied to the average voltage per sample  $U(t_k)$  that may be written as

$$U(t_k) = \frac{1}{T_s} \int_{t_k}^{t_k + T_s} u(t) dt \quad (2.1)$$

where  $T_s$  is a given sample interval and  $u(t)$  represents the instantaneous voltage across a single-phase of a load. The introduction of the variable  $T_s$  assumes the use of a fixed sampling frequency which is normally judiciously chosen higher than the fundamental frequency range required to control electrical machines. The upper sampling frequency limit is constrained by the need to limit the switching losses of the converter semiconductor devices.

The ability to control the converter devices in such a manner that the load is provided with a user defined mean reference voltage per sample  $U^*(t_k)$  is instrumental to control current accurately. This statement can be made plausible by considering the incremental flux linkage for one sample interval of a load in the form of a coil with inductance  $L$  and resistance  $R$  which may be written as

$$\Delta\psi(t_k) = \int_{t_k}^{t_k + T_s} (u(t) - Ri(t)) dt \quad (2.2)$$

The corresponding incremental change of load current (over a sample interval  $T_s$ ) may be written as

$$\Delta i(t_k) = \frac{\Delta\psi(t_k)}{L} \quad (2.3)$$

in the event that magnetic saturation effects may be ignored. This expression can, with the aid of (2.2), be expressed as

$$\Delta i(t_k) = \frac{1}{L} \int_{t_k}^{t_k+T_s} u(t) dt - \frac{R}{L} \int_{t_k}^{t_k+T_s} i(t) dt \quad (2.4)$$

which may be reduced to

$$\Delta i(t_k) \cong \frac{U(t_k) T_s}{L} \quad (2.5)$$

when the time constant  $\tau = L/R$  of the load is deemed to be relatively large compared to  $T_s$ , as is normally the case for electrical machines. Central to the issue of controlling the incremental current is therefore, according to (2.5), the ability of the modulator to realize (within the constraint of this unit) the condition

$$U(t_k) = U^*(t_k) \quad (2.6)$$

for each sampling instance. Note that (2.6) simply states that the switching states of the converter must be controlled by the modulator to ensure that the average voltage (per sample) equals the user defined average reference value to ensure that the actual and reference incremental current change (per sample interval) are equal.

How this may be achieved will be outlined in subsequent sections for various converter topologies using an approach taken by Svensson [63]. In effect, this approach considers how the average voltage per sample  $U(t_k)$  varies as function of the converter switch on/off time within a sample interval. Once this relation is known for the converter under consideration, the function in question is compared with the user defined reference value to determine the converter switch state within each sample. Initially, a single-phase half-bridge converter, as discussed in [68], will be considered followed by an analysis of a single-phase full-bridge converter and three-phase converter. In the context of modulation for three-phase converters, the so-called *space vector modulation* [9] will also be considered, together with the need to impose a modulator strategy that can handle the finite switch on/off times of practical converter switches. In this chapter, a set of *build and play* tutorials are outlined, which will allow the reader to become better acquainted with the subject matter presented in this chapter.

## 2.2 Single-Phase Half-Bridge Converter

The so-called *half-bridge* converter configuration as shown in Fig. 2.1 consists of two switches which must be controlled by the modulator. The converter in question is connected to a single-phase symbolic load element  $Z$  (see Fig. 2.1).

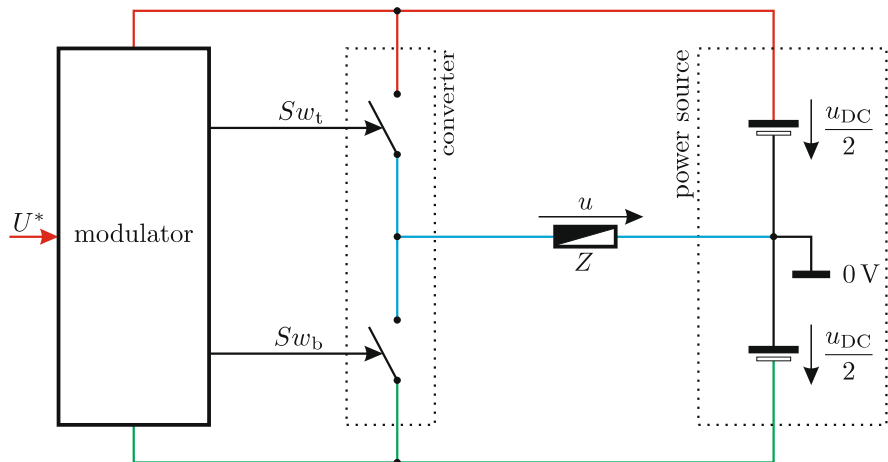


**Fig. 2.1** Two switch *half-bridge* converter with power source and modulator

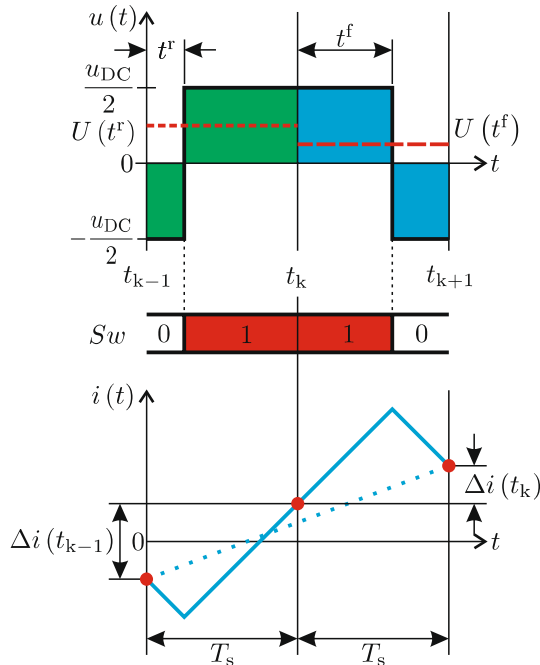
For drive applications, as considered in this book, the load element is typically a phase of an electrical machine which may be represented by a load impedance in the form of an inductance  $L$  and resistance  $R$  circuit connected in series, together with a voltage source  $e$ . The two *ideal* switches are controlled by two logic signals  $Sw_t$ ,  $Sw_b$ . Logic 1 corresponds to a *closed*, i.e., “on”, switch state and logic 0 to an *open* switch state. There are therefore four possible switch combinations possible as may be observed from Table 2.1. Of the four states shown in Table 2.1, the *shoot-through mode* must be avoided in voltage source converters, to prevent short-circuiting of the supply. The *idle* mode is normally used to disable the converter. Observation of Table 2.1 demonstrates that the two active switching states are complementary and can therefore be represented by a single logic switching state  $Sw$  with  $Sw_t = Sw$  and  $Sw_b = \overline{Sw}$ .

An example of a typical output voltage waveform, which appears in a half-bridge converter, is given in Fig. 2.2 for the sampling interval  $t_{k-1} \dots t_{k+1}$ , where the switching function  $Sw$  is assumed to be zero at  $t = t_{k-1}$  and changed to its logic state 1 at  $t = t_{k-1} + t^r$ . Subsequently,  $Sw$  is set to zero during the next sample interval at  $t = t_k + t^f$ , with  $t^r$  the instance at which  $Sw$  rises and  $t^f$  the instance at which  $Sw$  falls. This switching sequence is repeated every two samples where  $t^r$  and  $t^f$  may be varied within the limits of the interval  $t_{k-1} \dots t_k$  and  $t_k \dots t_{k+1}$  respectively. This modulation strategy

**Table 2.1** Half-bridge switching states

$Sw_t$	$Sw_b$	Voltage $u$	Comment
0	0	—	Idle mode
0	1	$-\frac{u_{DC}}{2}$	Active mode
1	0	$\frac{u_{DC}}{2}$	Active mode
1	1	—	Shoot-through mode

is known as *double edged* PWM, because the rising and falling edge of the load voltage waveform are varied as function of  $t^r$  and  $t^f$ . The latter waveform is also shown in Fig. 2.2 for two samples of operation. They constitute one period  $T_{PWM} = 2T_s = 1/f_{PWM}$  of modulator operation.

**Fig. 2.2** Variation of the average voltage per sample, with half-bridge converter

The corresponding average voltage functions  $U(t^r)$  and  $U(t^f)$  can be found by making use of (2.1), which leads to equation set (2.7)

$$U(t^r) = \frac{u_{DC}}{2} \left( 1 - \frac{2t^r}{T_s} \right); \quad 0 \leq t^r \leq T_s \quad (2.7a)$$

$$U(t^f) = \frac{u_{DC}}{2} \left( \frac{2t^f}{T_s} - 1 \right); \quad 0 \leq t^f \leq T_s \quad (2.7b)$$

where  $u_{DC}$  represents the DC bus voltage of the converter as shown in Fig. 2.1. Also shown in Fig. 2.2 is a typical load current trajectory in the event that the element  $Z$  is represented by an ideal (zero resistance) coil. The gradient of the current waveform is in this case dictated by the ratio  $u(t)/L$  while the incremental current change per sample  $\Delta i(t_k)$  (which is also shown in Fig. 2.2 for both sample intervals) is determined by the product  $UT_s$  (see expression (2.5)).

The average voltage functions according to equation set (2.7) are shown in Fig. 2.3 together with the user defined reference values for both sample intervals. The required switch state  $S_w$  may be found by comparing the defined reference average voltage values  $U^*(t_{k-1})$ ,  $U^*(t_k)$  (see Fig. 2.3) with the average voltage functions, as defined by equation set (2.7), which leads to the values  $t^r$  and  $t^f$  needed to meet the condition specified by (2.6). The latter may also be confirmed by observing the *green* and *blue* areas shown in the load voltage  $u(t)$  waveform which represent the actual voltage-time products  $U(t_{k-1}) T_s$  and  $U(t_k) T_s$  respectively as generated by the converter. Clearly identifiable in Fig. 2.3 are the switch  $S_w$  states over one period of modulator operation, where the *red* colored interval corresponds to logic level 1.

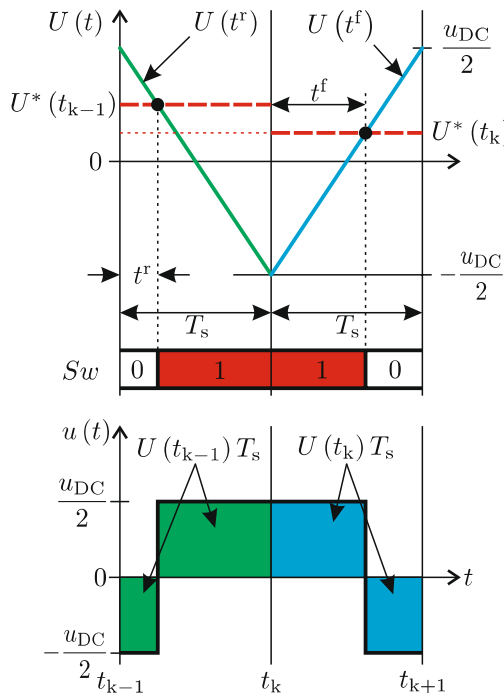


**Fig. 2.3** Double edged PWM strategy, with half-bridge converter

A generic implementation of a *double edged* PWM strategy, as given in Fig. 2.4, shows two A/D modules which are tied to the reference average voltage value (from the controller) and the measured DC bus voltage  $u_{DC}$  value (from the converter module). The sampled DC voltage is multiplied by a gain 1/2 to provide the maximum sampled average voltage value  $u_{DC}/2$ . This value is multiplied by a *triangular* function which results in the function  $U(t)$  defined by expression equation set (2.7). A summation module compares the two average voltage values  $U$  and  $U^*$ . Its output  $\varepsilon$  is used by a so-called comparator module with a transfer function of the form given by equation set (2.8).

$$\text{if } \varepsilon > 0 \quad \text{comparator output} = 1 \quad (2.8a)$$

$$\text{if } \varepsilon \leq 0 \quad \text{comparator output} = 0 \quad (2.8b)$$

The output of the comparator, known as switching function  $S_w$ , drives the two converter switches as discussed previously. Note that use of the measured DC bus voltage in the generic structure is beneficial because this provides the modulator with the capability to maintain the average voltage reference value, even when bus voltage variations occur.

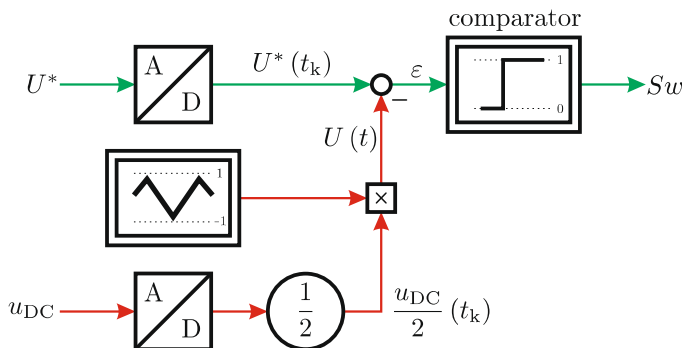


**Fig. 2.4** Generic model of double edged PWM based half-bridge modulator

Prior to introducing the full-bridge converter, it is helpful to introduce two modulation parameters which are applicable to sinusoidally varying average voltage reference signals that are commonly used in drive application. The first, known as the *amplitude modulation ratio*  $m_A$ , is defined as

$$m_A = \frac{\hat{U}^*}{u_{DC}/2} \quad (2.9)$$

where  $\hat{U}^*$  represents the peak value of the reference average phase voltage. The second modulation parameter in use is the *frequency modulation ratio*  $m_f$  which is defined as

$$m_f = \frac{f_{\text{PWM}}}{f^*} \quad (2.10)$$

where  $f_{\text{PWM}}$  represents the frequency of the triangular waveform shown in Fig. 2.3, which is half the sample frequency  $f_s = 1/T_s$ . The frequency of a sinusoidally varying average voltage reference signal is defined as  $f^*$ . In Tutorial 2.6.1, located at the end of this chapter, a simulation example is presented to underline the concepts presented in this section.

## 2.3 Single-Phase Full-Bridge Converter

The full-bridge, otherwise known as H-bridge converter, can be constructed by two half-bridge converters as shown in Fig. 2.3. A single-phase load impedance  $Z$  (as defined in the previous section) is again assumed, which in this case is represented by a virtual two-phase equivalent load, with a per phase impedance of  $Z/2$  and phase currents  $i_1 = i$ ,  $i_2 = -i$ . Use of a virtual two-phase load is particularly instructive for the development of a modulator structure given that this approach can be readily extended to three-phase systems. The virtual two-phase center point voltage with respect to the zero volt node is defined as  $u_0$ .

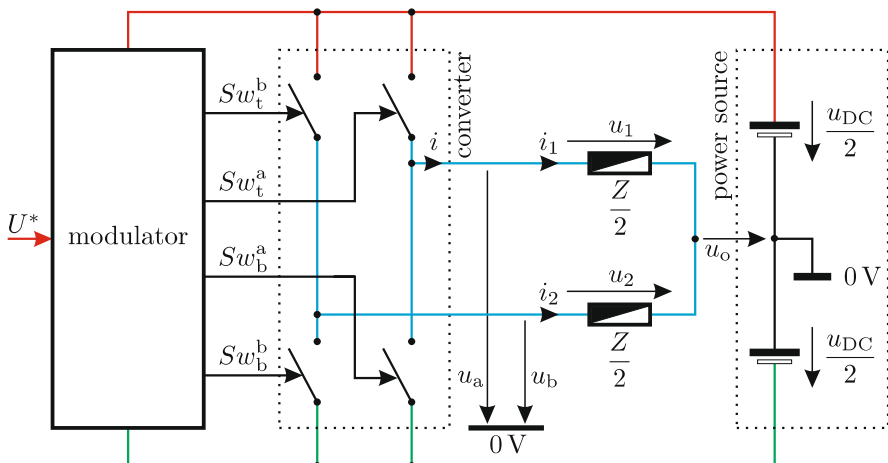


**Fig. 2.5** H-bridge converter

The key to determining the modulator strategy for this converter centers on the use of (2.1) which, with the aid of Fig. 2.5, may be written as

$$U(t_k) = \underbrace{\frac{1}{T_s} \int_{t_k}^{t_k+T_s} u_1(t) dt}_{U_1(t_k)} - \underbrace{\frac{1}{T_s} \int_{t_k}^{t_k+T_s} u_2(t) dt}_{U_2(t_k)}. \quad (2.11)$$

In expression (2.11), the terms  $U_1(t_k)$  and  $U_2(t_k)$  are introduced which represent the average (per sample) voltages for both virtual phases. These may in turn be written as

$$U_1(t_k) = \underbrace{\frac{1}{T_s} \int_{t_k}^{t_k+T_s} u_a(t) dt}_{U_a(t_k)} - \underbrace{\frac{1}{T_s} \int_{t_k}^{t_k+T_s} u_0(t) dt}_{U_0(t_k)} \quad (2.12a)$$

$$U_2(t_k) = \underbrace{\frac{1}{T_s} \int_{t_k}^{t_k+T_s} u_b(t) dt}_{U_b(t_k)} - \underbrace{\frac{1}{T_s} \int_{t_k}^{t_k+T_s} u_0(t) dt}_{U_0(t_k)} \quad (2.12b)$$

where  $U_a(t_k)$  and  $U_b(t_k)$  represent the half-bridge average voltage values. The required half-bridge average voltage references  $U_a^*(t_k)$ ,  $U_b^*(t_k)$  can with the aid of equation set (2.12), be written in terms of the user defined average voltage references  $U_1^*(t_k)$ ,  $U_2^*(t_k)$  as

$$U_a^*(t_k) = U_1^*(t_k) + U_0^*(t_k) \quad (2.13a)$$

$$U_b^*(t_k) = U_2^*(t_k) + U_0^*(t_k). \quad (2.13b)$$

In reality, a single-phase load exists, as mentioned above, to which a specified average voltage (per sample) value must be applied and this value is, according to (2.11), given by

$$U^*(t_k) = U_1^*(t_k) - U_2^*(t_k) \quad (2.14)$$

which, with the aid of equation set (2.13), may also be written as

$$U^*(t_k) = U_a^*(t_k) - U_b^*(t_k). \quad (2.15)$$

Equation (2.15) shows that the virtual average voltage value  $U_0^*(t_k)$  may be chosen freely (given that it is not present in this equation). This can also be observed from Fig. 2.6(a) where within two consecutive sample intervals the virtual average voltage value  $U_0^*(t_k)$  is arbitrarily selected at values greater and less than zero respectively, for the same average voltage reference value, i.e.,  $U^*(t_{k-1}) = U^*(t_k)$ . An observation of Fig. 2.6(a) shows that the output pulses correspond to the required average voltage-time reference values  $U^*(t_{k-1}) T_s$  and  $U(t_k) T_s$ , which in this example were chosen equal. The relative position of the output pulses within the sampling interval is defined by the virtual average voltage values  $U_0^*(t_{k-1})$  and  $U_0^*(t_k)$ . In this example, the values are arbitrarily chosen to be positive and negative respectively. Also

shown in Fig. 2.6 are the half-bridge voltages  $u_a$  and  $u_b$  which toggle between  $\pm u_{DC}/2$ .

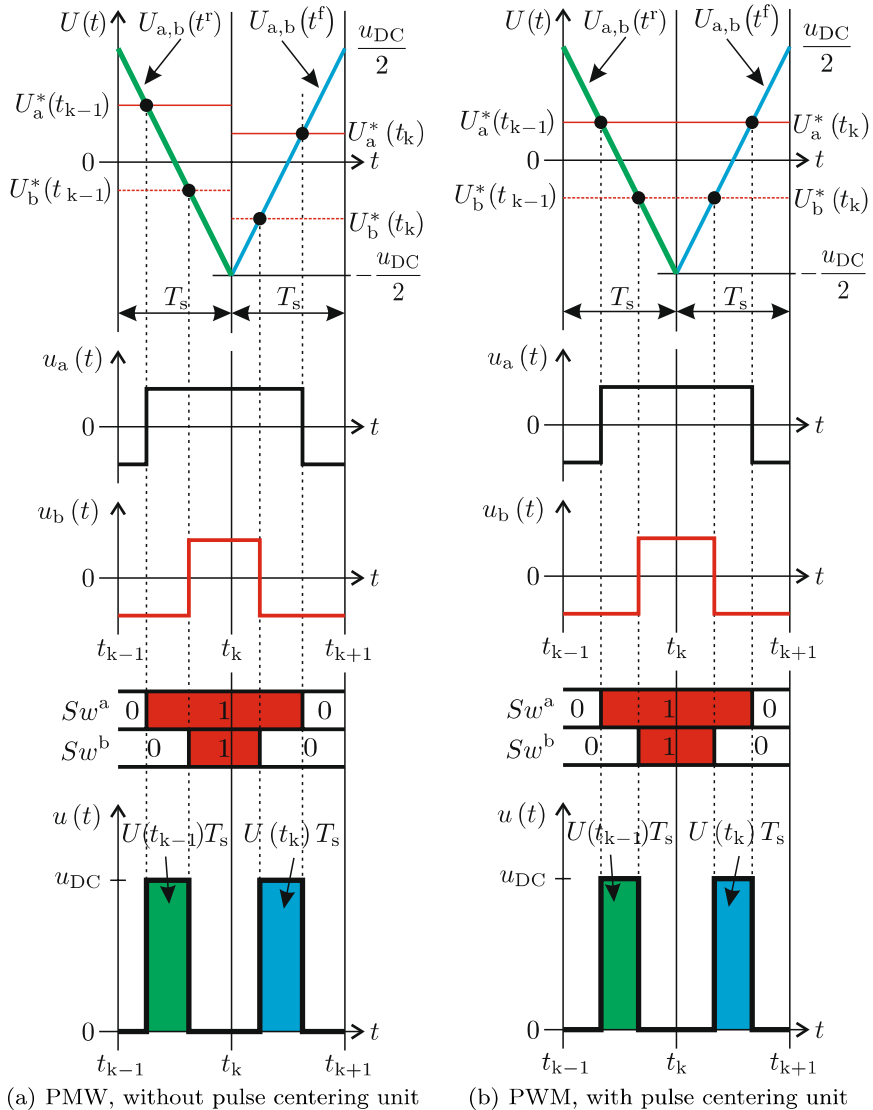


Fig. 2.6 Full-bridge converter with asymmetrically sampled PWM

From a practical perspective, it is prudent to choose the average voltage converter references  $U_a^*(t_k)$  and  $U_b^*(t_k)$ , during each sample interval in such a manner that they are symmetrically oriented with respect to the horizontal time axis. If this condition is maintained, the largest possible value of

$U^* = u_{DC}$  may be realized by the modulator/converter. Symmetrical orientation of the references  $U_a^*(t_k)$  and  $U_b^*(t_k)$  can be achieved by imposing the condition

$$\max\{U_a^*(t_k), U_b^*(t_k)\} + \min\{U_a^*(t_k), U_b^*(t_k)\} = 0. \quad (2.16)$$

With the aid of (2.13), this expression may also be written as

$$\max\{U_1^*(t_k), U_2^*(t_k)\} + \min\{U_1^*(t_k), U_2^*(t_k)\} + 2U_0^*(t_k) = 0 \quad (2.17)$$

which fully defines the required virtual average voltage reference level  $U_0^*(t_k)$  needed to satisfy (2.16). The control structure, which is referred to as a *pulse centering unit* and corresponds to (2.13) and (2.17), is given in Fig. 2.7.

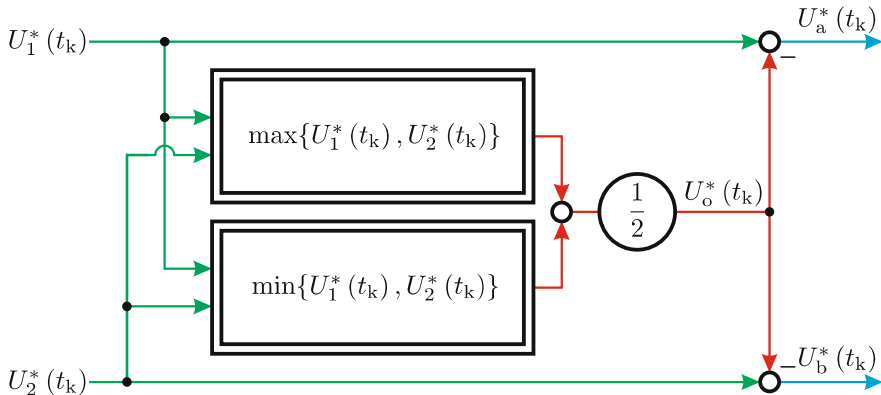


Fig. 2.7 Pulse centering module

Note that for the full-bridge modulator considered here, expression (2.16) may be written as

$$U_a^*(t_k) + U_b^*(t_k) = 0 \quad (2.18)$$

which symmetrizes the references with respect to the time axis. Input to the pulse centering reference value are the variables  $U_1^*$  and  $U_2^*$  while the input to the modulator is equal to  $U^*$  which, according to (2.14), is equal to the difference of said variables. Correspondingly, one of the two reference values can be chosen arbitrarily and a convenient choice is as follows

$$U_1^*(t_k) = U^*(t_k) \quad (2.19a)$$

$$U_2^*(t_k) = 0. \quad (2.19b)$$

The outputs from the pulse centering module are therefore of the form

$$U_a^*(t_k) = \frac{1}{2} U^*(t_k) \quad (2.20a)$$

$$U_b^*(t_k) = -\frac{1}{2} U^*(t_k). \quad (2.20b)$$

Figure 2.6(b) shows the impact of choosing the average voltage value  $U_0$  according to (2.17). Observation of the load voltage waveform demonstrates that it has now been centered with respect to the middle of the sample interval. Consequently, increasing the value of the reference average voltage value  $U^*$  will increase the area underneath the voltage pulse, but its position relative to the sampling interval remains unchanged. Without the use of this pulse centering unit an increase in the reference  $U^*$  will lead to a situation where one of the half-bridge references will exceed the maximum value. For example, reference  $U_a^*$  in Fig. 2.6(a) will exceed the absolute maximum value before reference  $U_b^*$ . With pulse centering, both half-bridge average voltage reference values will remain centered. Hence, they will reach their maximum value simultaneously.

A generic representation of the modulator for the H-bridge converter topology, is given in Fig. 2.8 and contains two comparators which provide the logic signals  $Sw^a$  and  $Sw^b$  that are in turn used to control the switches as discussed in the previous section. The tutorial given in Sect. 2.6.3 shows the use of the generic H-bridge modulator with a full-bridge converter connected to an inductive load.

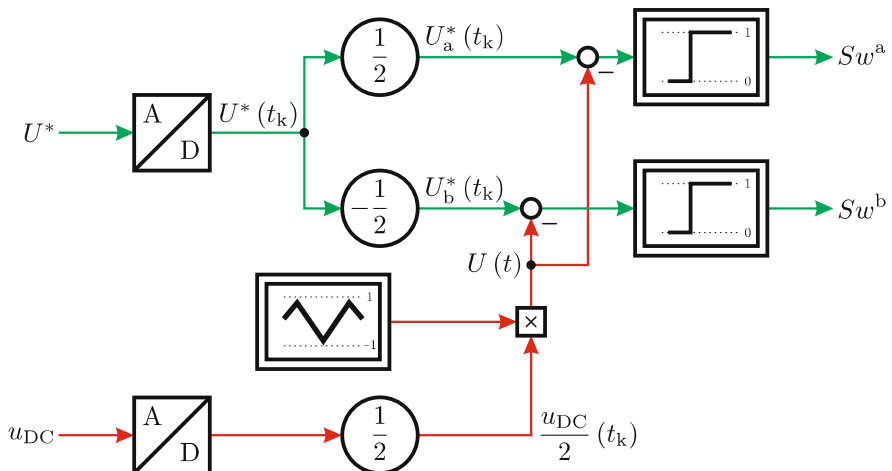


**Fig. 2.8** Generic model of double edged PWM based modulator for full-bridge converter

## 2.4 Three-Phase Converter

The three-phase converter topology, as shown in Fig. 2.9, consists of a symmetric balanced star connected load which is connected to three half-bridge converters as discussed in Sect. 2.2. The converter structure is similar to the virtual two-phase structure introduced in the previous section. Accordingly, the mathematical handling required to obtain the average voltage references for the three half-bridges is very similar as will become apparent shortly. The aim is to determine (for a given sampling interval) a switching strategy for the six switches of the converter, which ensures that the average load phase voltage values  $U_1(t_k)$ ,  $U_2(t_k)$ ,  $U_3(t_k)$  correspond with the three reference values  $U_1^*(t_k)$ ,  $U_2^*(t_k)$  and  $U_3^*(t_k)$ . The latter are in turn linked to the (power invariant) space vector average voltage reference value  $\vec{U}^*$  as given in (2.21), in its sampled form

$$\vec{U}^*(t_k) = \sqrt{\frac{2}{3}} (U_1^*(t_k) + U_2^*(t_k) e^{j\gamma} + U_3^*(t_k) e^{2j\gamma}) \quad (2.21)$$

where  $\gamma = 2\pi/3$ . Furthermore, a modulator generic structure is to be developed to produce the required switching signals for the converter on the basis of the user defined average voltage reference vector  $\vec{U}^*$ .

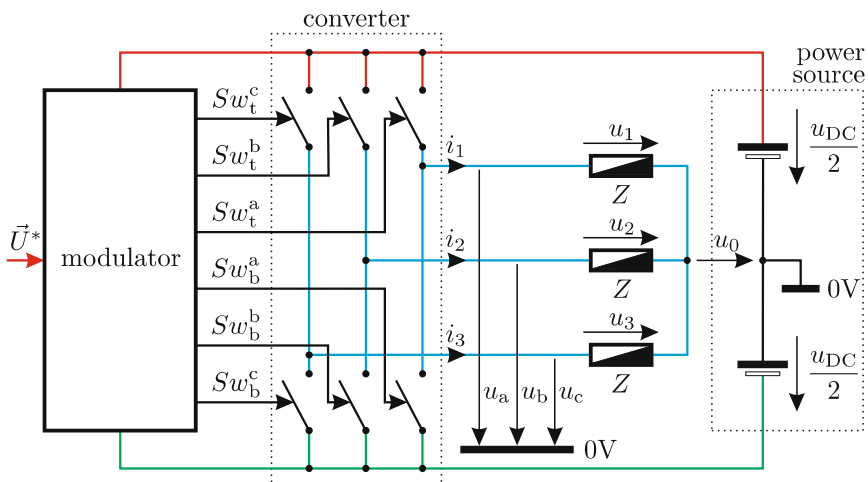


**Fig. 2.9** Three phase converter

The average voltage (per sample) values for the three-phase load can, with the aid of (2.1) and Fig. 2.9, be written as

$$U_1^*(t_k) = \underbrace{\frac{1}{T_s} \int_{t_k}^{t_k+T_s} u_a(t) dt}_{U_a(t_k)} - \underbrace{\frac{1}{T_s} \int_{t_k}^{t_k+T_s} u_o(t) dt}_{U_o(t_k)} \quad (2.22a)$$

$$U_2^*(t_k) = \underbrace{\frac{1}{T_s} \int_{t_k}^{t_k+T_s} u_b(t) dt}_{U_b(t_k)} - \underbrace{\frac{1}{T_s} \int_{t_k}^{t_k+T_s} u_o(t) dt}_{U_o(t_k)} \quad (2.22b)$$

$$U_3^*(t_k) = \underbrace{\frac{1}{T_s} \int_{t_k}^{t_k+T_s} u_c(t) dt}_{U_c(t_k)} - \underbrace{\frac{1}{T_s} \int_{t_k}^{t_k+T_s} u_o(t) dt}_{U_o(t_k)} \quad (2.22c)$$

where  $U_a(t_k)$ ,  $U_b(t_k)$  and  $U_c(t_k)$  represent the three half-bridge average voltages values. The required half-bridge average voltage references  $U_a^*(t_k)$ ,  $U_b^*(t_k)$  and  $U_c^*(t_k)$  can, with the aid of equation set (2.22), be written in terms of the user defined average voltage references  $U_1^*(t_k)$ ,  $U_2^*(t_k)$  and  $U_3^*(t_k)$  as

$$U_a^*(t_k) = U_1^*(t_k) + U_o^*(t_k) \quad (2.23a)$$

$$U_b^*(t_k) = U_2^*(t_k) + U_o^*(t_k) \quad (2.23b)$$

$$U_c^*(t_k) = U_3^*(t_k) + U_o^*(t_k) \quad (2.23c)$$

which contains a zero sequence average voltage (per sample) value  $U_o^*(t_k)$  that can be defined in terms of the user defined average voltage values according to the approach set out in the previous section. In practice, it is helpful to rewrite equation set (2.23) in a space vector format. Using equation set (2.23) and (2.21) gives

$$\begin{aligned} \vec{U}^*(t_k) &= \sqrt{\frac{2}{3}} (U_a^*(t_k) + U_b^*(t_k) e^{j\gamma} + U_c^*(t_k) e^{2j\gamma}) \\ &\quad - \sqrt{\frac{2}{3}} U_o^*(t_k) \underbrace{(1 + e^{j\gamma} + e^{2j\gamma})}_0. \end{aligned} \quad (2.24)$$

The second term of expression (2.24) contains a vector sum of value zero, together with the zero sequence average voltage value  $U_o^*(t_k)$ , which implies that the latter can be chosen freely. It is noted that the approach discussed here is almost identical to that used in the previous section. The choice of the *zero sequence average voltage* value is therefore of no concern with respect to the choice of the average voltage half-bridge references. However, it is prudent to choose the value of  $U_o^*(t_k)$  in such a manner that the maximum and minimum value of the half-bridge reference values are symmetrical with respect to the time axis. The reader is reminded of the fact that this same approach was purposefully introduced for the full-bridge modulator, which led to condition 2.16. This condition can simply be adapted to accommodate three instead of two variables allowing this expression to be written as

$$\begin{aligned} & \max\{U_a^*(t_k), U_b^*(t_k), U_c^*(t_k)\} \\ & + \min\{U_a^*(t_k), U_b^*(t_k), U_c^*(t_k)\} = 0. \end{aligned} \quad (2.25)$$

With the aid of equation set (2.23), this expression may also be written as

$$\begin{aligned} & \max\{U_1^*(t_k), U_2^*(t_k), U_3^*(t_k)\} \\ & + \min\{U_1^*(t_k), U_2^*(t_k), U_3^*(t_k)\} + 2U_o^*(t_k) = 0. \end{aligned} \quad (2.26)$$

Further development of (2.26) gives

$$\begin{aligned} U_o^*(t_k) = & -\frac{1}{2}[\max\{U_1^*(t_k), U_2^*(t_k), U_3^*(t_k)\} \\ & + \min\{U_1^*(t_k), U_2^*(t_k), U_3^*(t_k)\}] \end{aligned} \quad (2.27)$$

which fully defines the zero sequence average voltage value  $U_o^*(t_k)$  for each sampling interval. The pulse centering unit according to Fig. 2.7 is readily modified to a three output/three input structure, as given in Fig. 2.10 that complies with (2.27).

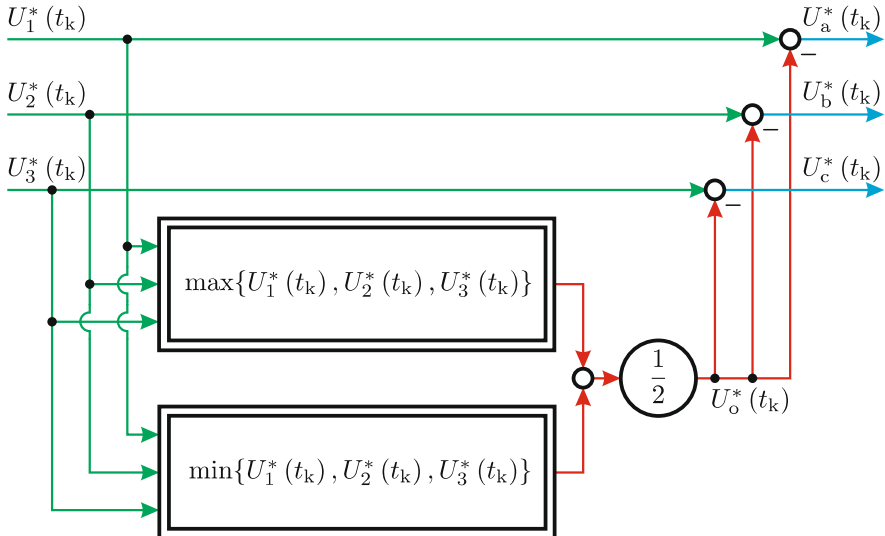


**Fig. 2.10** Three-phase pulse centering module

An example which demonstrates the omission and use of the pulse centering unit is given in Fig. 2.11 for the case where a reference vector  $\vec{U}^*(t_i)$  of constant amplitude  $\sqrt{3}/8 u_{DC}$  is rotated by  $\pi/6$  rad during a time interval  $T_s$ . The angle  $\rho^*(t_i)$  between the reference vector and the real axis of a stationary complex plane is chosen to be zero at time  $t_{k-1}$ , i.e.,  $\rho^*(t_{k-1}) = 0$ . The corresponding average load voltage reference values  $U_{1,2,3}^*$  for each sampling

interval may be found via a standard power invariant vector to three-phase conversion, which gives

$$U_1^*(t_i) = \sqrt{\frac{2}{3}} \Re \left\{ \vec{U}^*(t_i) \right\} \quad (2.28a)$$

$$U_2^*(t_i) = \sqrt{\frac{2}{3}} \Re \left\{ \vec{U}^*(t_i) e^{-j\gamma} \right\} \quad (2.28b)$$

$$U_3^*(t_i) = \sqrt{\frac{2}{3}} \Re \left\{ \vec{U}^*(t_i) e^{-j2\gamma} \right\}. \quad (2.28c)$$

Application of equation set (2.28) to the chosen reference vector for the two samples leads to the reference phase values given in Table 2.2, which also gives the value of  $U_o^*$  as calculated using (2.27). Note from Table 2.2 that the choice of reference space vector amplitude  $|\vec{U}^*| = \sqrt{3/8} u_{DC}$  is such that the phase variable  $U_1^*(t_k)$  is at the highest possible value of  $1/2 u_{DC}$ . This implies that the largest orbit of the reference vector that can occur *without* pulse centering may be represented by a circle with radius  $\sqrt{3/8} u_{DC}$ . The required half-bridge average voltage values  $U_{a,b,c}^*$  may be found with the aid of the pulse centering module given in Fig. 2.10 in which case the zero sequence average voltage reference value  $U_o^*$  is calculated using (2.27).

**Table 2.2** Reference vector:  $\vec{U}^*(t_{k-1}) = \sqrt{3/8} u_{DC}$ ,  $\vec{U}^*(t_k) = \sqrt{3/8} u_{DC} e^{j\pi/6}$

Phase reference	Time $t_{k-1}$	Time $t_{k1}$
$U_1^*$	$1/2 u_{DC}$	$\sqrt{3}/2 u_{DC}$
$U_2^*$	$-1/4 u_{DC}$	0
$U_3^*$	$-1/4 u_{DC}$	$-\sqrt{3}/2 u_{DC}$
$U_o^*$	$-1/8 u_{DC}$	0

In the first diagram, Fig. 2.11(a), no pulse centering is used, i.e.,  $U_o^*$  has been set to zero. An observation of the example given in Fig. 2.11(b) shows that the pulse centering unit symmetrizes the maximum and minimum average voltage references  $U_{a,b,c}^*$  with respect to the time axis. The use of the pulse centering unit has, as may be observed from Fig. 2.11(b), lowered the  $U_1^*(t_k)$  value to  $3/8 u_{DC}$  which implies that the average voltage reference vector amplitude may be further increased before reaching the supply voltage limits  $\pm u_{DC}/2$  of the converter. It will be shown in the next subsection that the introduction of pulse centering allows the user to increase the reference space vector amplitude from  $|\vec{U}^*| = \sqrt{3/8} u_{DC}$  to  $|\vec{U}^*| = \sqrt{1/2} u_{DC}$ , which is an increase of approximately 15%. For the second sample  $t_k \dots t_{k+1}$ , the half-bridge average voltage reference values were already balanced with respect to the time axis, which implies that the waveforms for this sample are identical to those shown in Fig. 2.11(a) for interval  $t_k \dots t_{k+1}$ . Also shown in Fig. 2.11 are the half-bridge voltages  $u_a, u_b, u_c$  which toggle between  $\pm u_{DC}/2$ ,

with respect to the zero bus voltage node. In addition, the three comparator output switch states  $Sw^a$ ,  $Sw^b$ ,  $Sw^c$  are shown in Fig. 2.11.

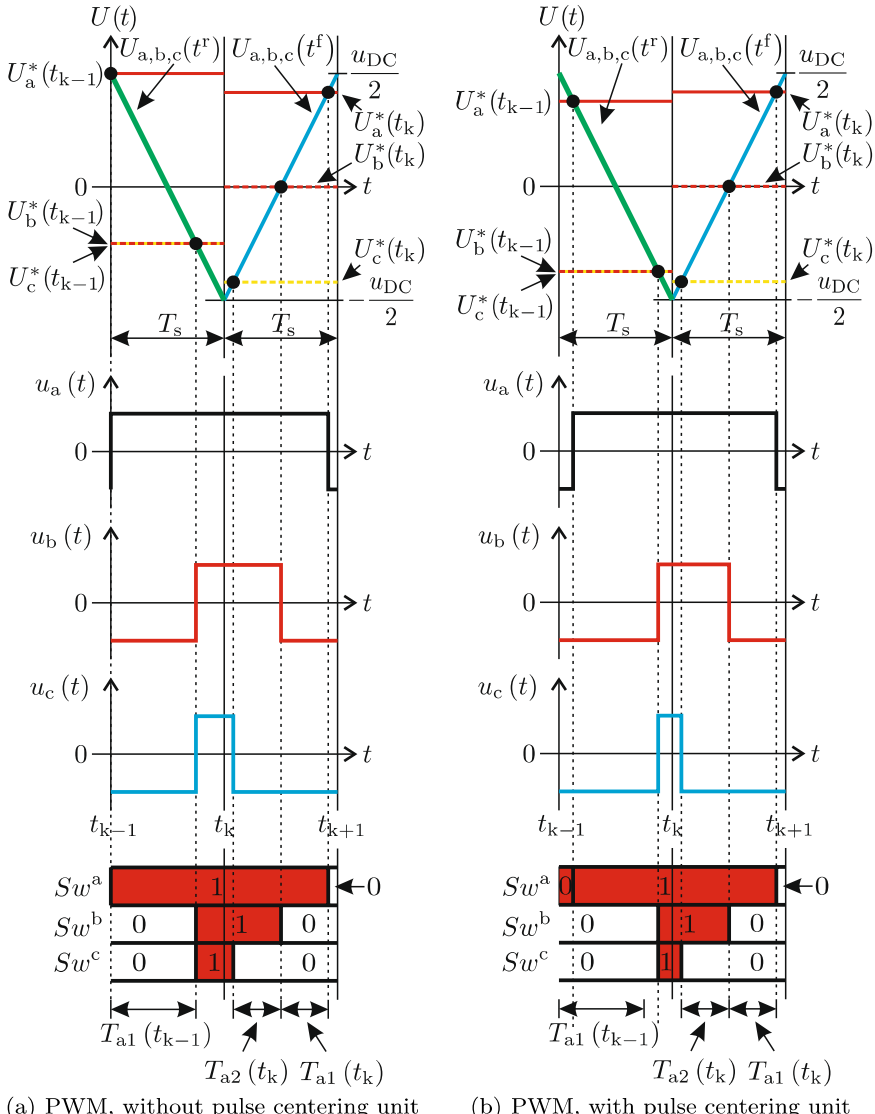


**Fig. 2.11** Asymmetrically sampled PWM, three-phase converter, use of pulse centering unit

The generic diagram for the three-phase converter as given in Fig. 2.12 is similar to the modulator concept described for the single-phase full-bridge converter. However, in this case the pulse centering module is used to generate

the average voltage reference value for the three half-bridges on the basis of the user defined space vector average voltage reference.

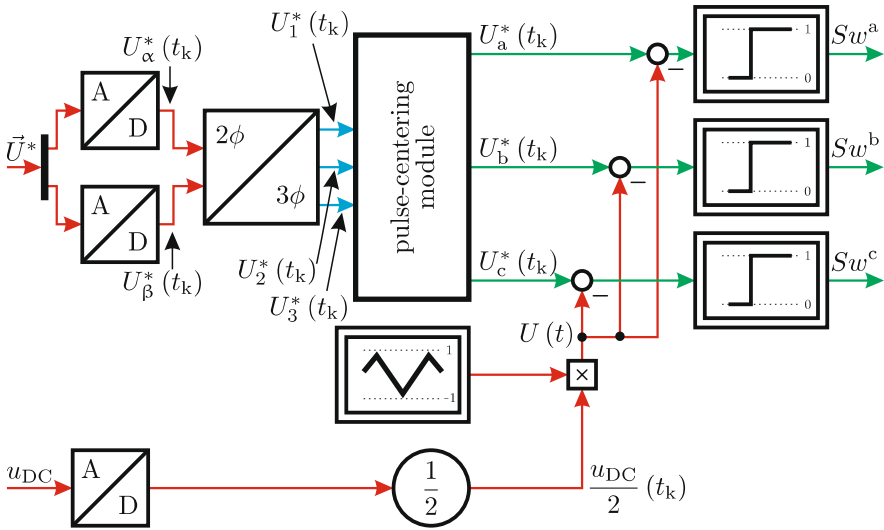


**Fig. 2.12** Generic model of double edged PWM based modulator for three-phase converter

### 2.4.1 Space Vector Modulation

It is also helpful to consider the above modulator scheme from a space vector perspective. The so-called *space vector modulation*, introduced by van der Broeck et al. [9], is directly based on the use of (2.21). Using a pulse centering unit is important to maximize the linear operating region of the converter. Hence, further discussion will focus on Fig. 2.11, which also shows the switch states that correspond with this example. These switch states and corresponding half-bridge converter outputs can, with the aid of (2.21), be interpreted as a set of voltage space vectors. The switch states shown in Fig. 2.11 represent a subset of the eight possible converter switching combinations  $\{Sw^a, Sw^b, Sw^c\}$  which gives

$$\vec{u}_{\{Sw^a, Sw^b, Sw^c\}} = \sqrt{\frac{2}{3}} u_{DC} \left\{ Sw^a + Sw^b e^{j\gamma} + Sw^c e^{j2\gamma} \right\}. \quad (2.29)$$

Evaluation of (2.29) shows that there are six active voltage vectors of magnitude  $\sqrt{2/3} u_{DC}$  that are displaced by  $\pi/3$  rad as indicated in Fig. 2.13. In addition, two zero vectors are present in this figure corresponding to converter

switch combinations  $\{000\}$  and  $\{111\}$ . The process by which the converter meets the condition specified by (2.30) may therefore be interpreted in terms of determining the two active voltage vectors adjacent to the reference average voltage vector  $\vec{U}^*$  and determining the time interval for which they must be active during the sampling time  $T_s$ . In addition, the duration of the zero vectors must be determined for each sampling interval.

$$\vec{U}(t_i) = \vec{U}^*(t_i) \quad (2.30)$$

A mathematical formulation of this strategy is of the form

$$\vec{U}^*(t_i) = \left( \frac{T_{a1}(t_i)}{T_s} \right) \vec{u}_{\bar{s}} + \left( \frac{T_{a2}(t_i)}{T_s} \right) \vec{u}_{\bar{s}} e^{j\frac{\pi}{3}} \quad (2.31)$$

where  $\vec{u}_{\bar{s}}$  is, according to (2.29), the active voltage vector which falls within the angle interval  $\rho^*(t_i)$ . In addition, the total duration of the time during which the active vectors can be deployed must satisfy the condition given in (2.32).

$$\frac{T_{a1}(t_i)}{T_s} + \frac{T_{a2}(t_i)}{T_s} \leq 1 \quad (2.32)$$

The equivalent space vector representation for the example discussed in the previous section with the aid of Fig. 2.11 is shown in Fig. 2.13. Included in both sub-figures are the eight possible converter voltage space vectors, together with the average voltage reference vectors for both samples  $t_{k-1}$  and  $t_k$ . The active voltage converter vector  $\vec{u}_{\bar{s}}$ , which must be used with (2.31), is in this case  $\vec{u}_{\{100\}}$ . Figure 2.13 shows that the PWM approach outlined earlier in this section determines the appropriate duration times for the active vectors as to satisfy equation set (2.31) and (2.32). Furthermore, the presence of the pulse centering unit ensures that the combined time interval in which active vectors are used is centered with respect to the *center* of the sampling interval. For the first sample  $t_{k-1} \dots t_k$ , the average voltage reference vector coincides with the active average voltage converter vector  $\vec{U}_{\{100\}}$ . In this case, the modulation strategy determines the required time needed to activate said vector during the sample interval. For the second sample interval, two active vectors adjacent to the average voltage reference vector are activated for a time interval sufficient to ensure that the condition given by (2.30) is met.

It is emphasized that the modulation technique discussed above determines, on the basis of the reference voltage, the duration of the active vectors used within each sample. Furthermore, the pulse centering unit is responsible for centering the combined active vector time interval within the sample. An often quoted alternative to the strategy discussed above, is the so-called *space vector modulation* [9] which is particularly suited to digital implementation as this approach calculates directly for a given sample interval ( $t_i$ ) the duration of the active vectors adjacent to the specified average voltage reference vector  $\vec{U}^*(t_i)$  with the aid of equation set (2.33), namely

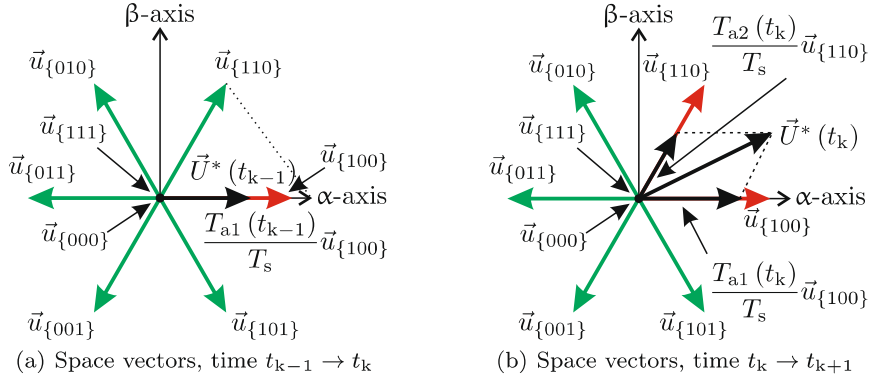


**Fig. 2.13** Space vector representation of Fig. 2.11

$$\frac{T_{a2}(t_i)}{T_s} = \frac{2}{\sqrt{3}} \Im \left\{ \frac{\vec{U}^*(t_i)}{\vec{u}_{\bar{s}}} \right\} \quad (2.33a)$$

$$\frac{T_{a1}(t_i)}{T_s} = \Re \left\{ \frac{\vec{U}^*(t_i)}{\vec{u}_{\bar{s}}} \right\} - \frac{1}{2} \frac{T_{a2}(t_i)}{T_s}. \quad (2.33b)$$

These expressions can be found using (2.31) and (2.32) and gives the user access to the required duration time of the active vectors, without having to implement a generic modular structure as given by, for example, Fig. 2.12.

The centering of the combined active time interval must however be carried out ensuring that a zero vector (if needed) is activated for the same time interval at the beginning and end of each sample interval. The choice of zero vectors used at any particular instance is decided on the basis of a minimum number of switch actions needed to reach the nearest zero vector from the last active vector in use. In terms of modulation, the overall result achieved with space vector modulation is identical in its execution to the pulse width modulation strategy as undertaken with the aid of the generic modulator structure given by Fig. 2.12.

Finally, it is considered important to determine the maximum reference average voltage amplitude  $\{U^*(t_i)\}^{\max}$  which may be used without imposing any constraints on the corresponding phase angle  $\rho^*(t_i)$ . Substitution of the active vector  $\vec{u}_{\bar{s}}$  (see (2.29)) into equation set (2.33) leads, after some mathematical manipulation, to

$$\left( \frac{T_{a1}(t_i)}{T_s} \right)^2 + \frac{T_{a1}(t_i) T_{a2}(t_i)}{T_s^2} + \left( \frac{T_{a2}(t_i)}{T_s} \right)^2 = \left( \frac{U^*(t_i)}{\sqrt{\frac{2}{3}} u_{DC}} \right)^2 \quad (2.34)$$

in which the active vector  $\vec{u}_s$  is arbitrarily chosen as  $\vec{U}_{\{100\}}$ . Equation (2.34) represents an ellipse in the  $T_{a1}/T_s, T_{a2}/T_s$  plane and its size is determined by the variable  $\nu = U^*(t_i)/\sqrt{2/3}u_{DC}$  as may be observed from Fig. 2.14.

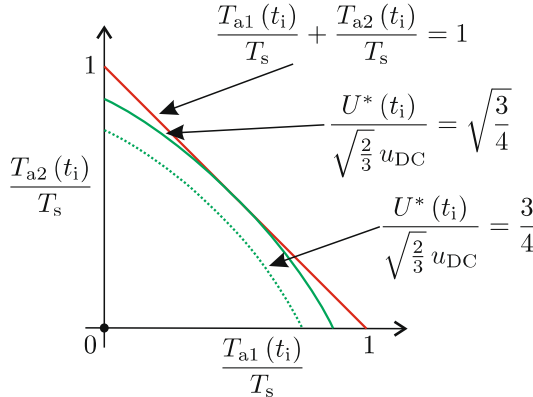


**Fig. 2.14** Active vector duty cycles for  $\nu = \frac{3}{4}$  and  $\nu = \sqrt{\frac{3}{4}}$

Figure 2.14 shows how the duty cycle of two adjacent active vectors can be selected to achieve a given voltage reference value  $U^*$  (amplitude only) as expressed by the variable  $\nu$ . Also shown in this diagram is a straight line which represents the sum of the two duty cycles which must be equal to one. Indeed, the time over which both vectors are activated cannot exceed the sample interval  $T_s$ . Observation of Fig. 2.14 shows two curves with values of  $\nu = 3/4$  and  $\nu = \sqrt{3/4}$  corresponding to a voltage reference amplitude of  $U^* = \sqrt{3/8} u_{DC}$  and  $U^* = \sqrt{1/2} u_{DC}$  respectively. The latter value is the largest reference value which can be produced given that it corresponds with the largest ellipse (shown partly in the first quadrant) that can be used, given the constraints imposed by the linear function and two axes shown in Fig. 2.14. For comparison purposes part of a second ellipse (dotted curve) has also been drawn in Fig. 2.14. This ellipse corresponds to the largest ellipse with reference voltage  $\sqrt{3/8} u_{DC}$  that can be used without the presence of a pulse centering module whilst maintaining the phase references within the supply limits  $\pm u_{DC}/2$ . This leads to an important observation, namely that centering the active vectors within a sample either by use of a pulse centering PWM unit or by calculation using the space vector modulation approach allows the user to extend the linear operating range by a factor of  $2/\sqrt{3} \approx 15\%$ , without encountering the supply level limits of the converter. Note that the ability to extend the linear operation of the modulator/converter by approximately 15% is particularly advantageous as it allows the converter to be operated with higher voltages and consequently lower currents. The latter implies that the kVA-rating of the converter can be increased by approximately 15% as a result of using pulse centering.

It is instructive to consider the circuit orbit which coincides with the highest allowable reference value, as discussed above, in a diagram together with the converter active and zero vectors. Such a diagram is given in Fig. 2.15 and shows that the circular orbit is the largest which can be located within a hexagon that is constructed from the six active vectors with length  $\sqrt{2/3} u_{DC}$ . Observation of Fig. 2.15 shows the presence of a right-angled triangle of which the hypotenuse is represented by the active vector  $\vec{u}_{\{100\}}$  and one of the legs which represents the radius  $u_{DC}/\sqrt{2}$  of the circle. The triangle in question is a  $30^\circ-60^\circ-90^\circ$  acute triangle, of which the sides are in the ratio  $1 : \sqrt{3} : 2$ . This also shows that the largest circle which can be placed inside the hexagon must have a radius that is  $\sqrt{3}/2$  smaller than the active vector amplitude.

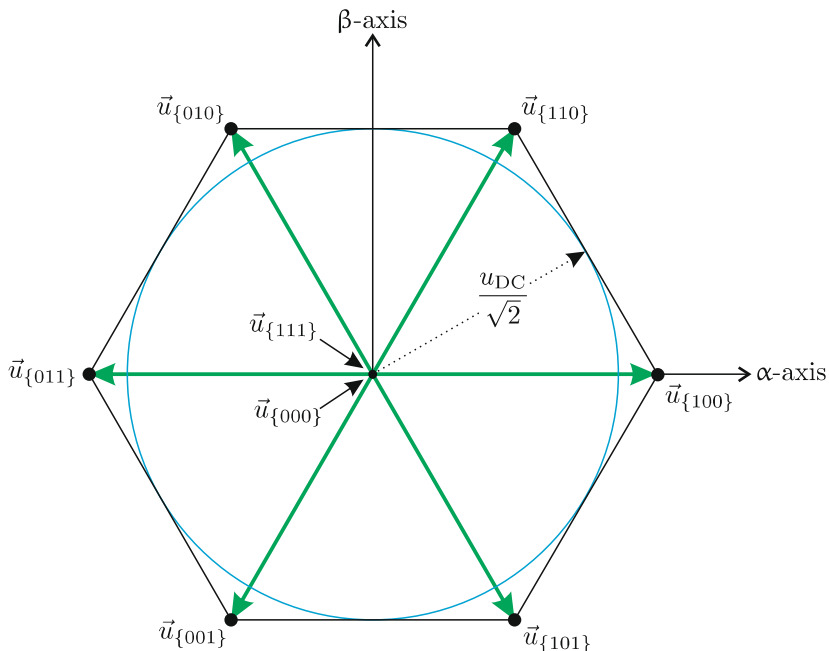


**Fig. 2.15** Maximum average voltage vector orbit and available converter vectors

Prior to considering the effect of dead time on the converter, it is instructive to examine a scenario where the reference voltage vector amplitude is increased beyond the maximum value of  $u_{DC}/\sqrt{2}$ . Under such conditions, the half-bridge reference values will exceed the DC supply limits during part of the circular orbit undertaken by the reference vector. This implies that the converter output voltage(s) may be held to the supply value for a period of time which is in excess of the sampling time. Consequently, the converter switching frequency will no longer be equal to half the sampling frequency. This mode of operation is referred to as *over-modulation* and will ultimately

lead (with increasing  $U^*$ ) to a situation where the converter waveforms are rectangular. In vector terms, this operation is characterized by switching from one active vector to the next, i.e., along the hexagon boundary shown in Fig. 2.15. This mode of operation is known as *six-step* operation and can be readily observed by increasing the reference voltage amplitude beyond the value  $u_{DC}/\sqrt{2}$  in the tutorial given in Sect. 2.6.5.

## 2.5 Dead-Time Effects

In the converter configuration shown in this chapter ideal switches were used, which implies that they may be turned on or off instantaneously. Consequently, the on and off switch signals were chosen complimentary (one signal set to logical 1, the other to logical 0), as shown in Fig. 2.3. In reality, semiconductor based switches and diodes are used which require a finite turn-on and turn-off time. This implies that a so-called *dead time*  $\Delta t_D$  must be imposed, which is the time when both switch signals are set to zero, to allow the switch turn-on/-off process to be completed. Failure to adhere to this policy can invoke the *shoot-through* mode as identified in Table 2.1 with usually disastrous consequences for the devices in question. The half-bridge configuration shown in Fig. 2.16 is representative of the converter topologies discussed in this section. Shown in Fig. 2.16 are two IGBT switches with corresponding diodes which are taken to be non-ideal, i.e., these require a finite turn-on/off time taken to be equal to  $\Delta t_D$ .

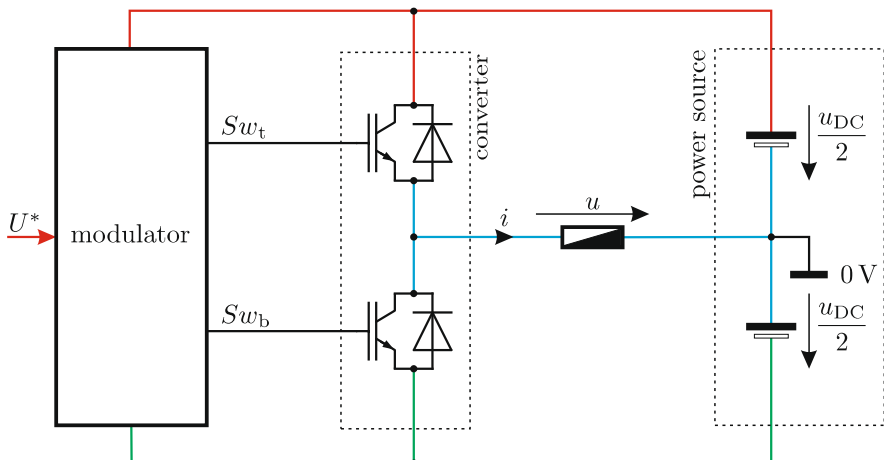


**Fig. 2.16** IGBT based *half-bridge* converter with power source and modulator

Consequently, the question arises how for example the generic modulator structure according the Fig. 2.4 may be modified to accommodate a *dead time* equal to at least  $\Delta t_D$ . This technique can subsequently be equally applied to the full-bridge and three-phase converter. The envisaged approach is to introduce two comparators (to control the switches individually) and adding an average voltage offset  $\pm U_D/2$  to the reference voltage value  $U^*$  as shown in Fig. 2.17. The value of  $U_D$  is defined as

$$U_D = u_{DC} \frac{\Delta t_D}{T_s} \quad (2.35)$$

which may be found by considering the absolute gradient of the function  $U(t)$  which is equal to  $u_{DC}/T_s$ . The value of  $\pm U_D/2$  and corresponding dead-time value shown in Fig. 2.17 is purposely chosen large, in comparison to the sample time  $T_s$  for didactic reasons.

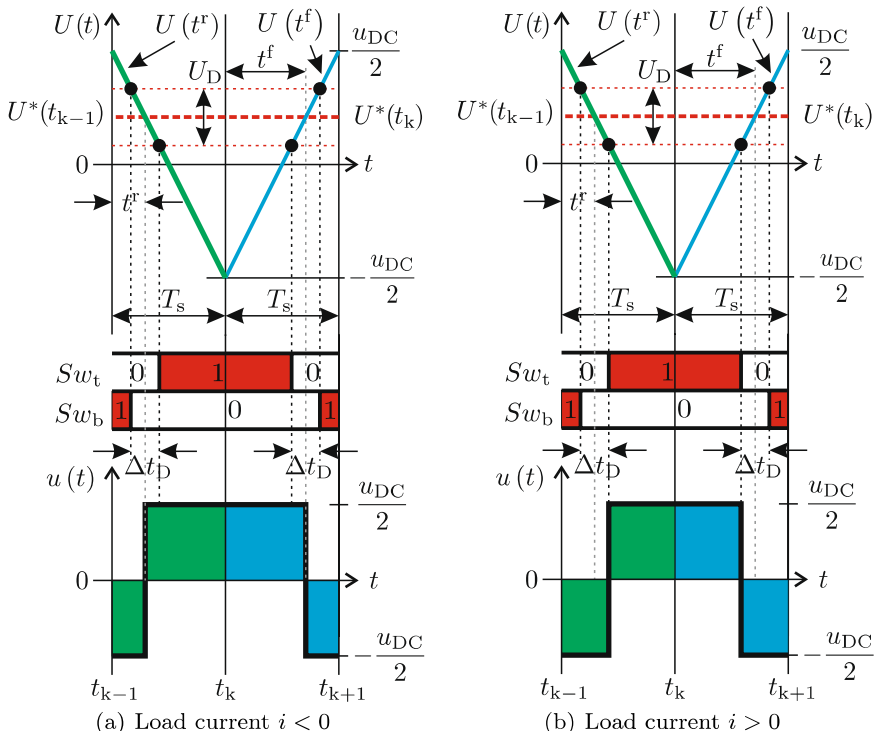


**Fig. 2.17** Double edged PWM strategy, with half-bridge converter and dead-time effects

The consequence of introducing converter dead time is that the modulator will not be able to set the control signals in such a manner that the delivered

average voltage–time area to the load (per sample interval) is exactly equal to the reference average voltage–time area (see (2.6)). The reason for this effect may be illustrated with the aid of Fig. 2.17, which shows two examples where the reference average voltage level is purposely kept constant. In the first example given in Fig. 2.17(a), the load current is assumed to be negative and the load will be connected to the negative DC rail voltage as long as the bottom switch is closed. However, when the switch signal for this device is set to zero the turn-off process will start and the current will be commutated immediately to the top diode. This implies that the load is connected to the top supply rail during the dead-time period. After this dead-time interval the top switch is activated which means that the load remains connected to the top rail either by virtue of negative current through the top diode or positive current through the (conducting) top switch. In this case, the average voltage (per sample) across the load is larger than the required reference average voltage level as shown by (2.36a). In the second example, shown in Fig. 2.17(b), a positive load current is assumed and events as described for the previous interval also occur with the difference that the bottom diode will remain conducting during the dead-time interval when the bottom switch turns off. Likewise, the bottom diode will also conduct during the dead-time interval as soon as the top switch turns off. Figure 2.17(b) demonstrates that the average voltage across the load will be less than the required reference average voltage value. The impact of the dead-time effect on the average load voltage may be observed with the aid of (2.36).

$$U = U^* + \frac{U_D}{2} \quad (i < 0) \quad (2.36a)$$

$$U = U^* - \frac{U_D}{2} \quad (i > 0) \quad (2.36b)$$

Observation of equation set (2.36) and (2.35) shows that the error in the average load voltage with respect to the reference average load voltage depends on the polarity of the load current as well as the ratio between dead time and sample time. The dead time is a semiconductor device dependent variable (typically set to a constant, safe value), whereas the sample time may be chosen by the user. If the sample frequency  $f_s = 1/T_s$  is increased, the ratio  $\Delta t_D/T_s$  increases and consequently a larger average voltage error  $U_D/2$  is introduced. In the tutorial section at the end of this chapter a simulation is shown (see Sect. 2.6.2) which demonstrates the issues set out in this subsection. Dead-time effects are not, for didactic reasons, included in the modulation strategies to be discussed in the remaining part of this book. However, dead-time effects must be accommodated in a practical power electronic converter using, for example, the techniques outlined in this section.

## 2.6 Tutorials

### 2.6.1 Tutorial 1: Half-Bridge Converter with Pulse Width Modulation

This tutorial is concerned with the implementation of a half-bridge converter structure as given in Fig. 2.1. The ideal switches are to be replaced by a combination of ideal semiconductors and diodes as shown in Fig. 2.16. A supply voltage  $u_{DC} = 300\text{ V}$  is assumed together with an impedance  $Z$  which in this case is reduced to an ideal inductance of  $100\text{ mH}$ . A modulator structure as shown in Fig. 2.4 is to be implemented with a sample interval setting of  $T_s = 1\text{ ms}$ . Furthermore, a sinusoidal  $50\text{ Hz}$  reference average voltage waveform  $U^*$  with an amplitude of  $100\text{ V}$  is to be used. The aim is to implement a simulation model and examine the sampled reference average voltage, voltage/current waveforms linked to the load, as well as the logic switch signals for this model. A  $20\text{ ms}$  simulation time interval is to be used.

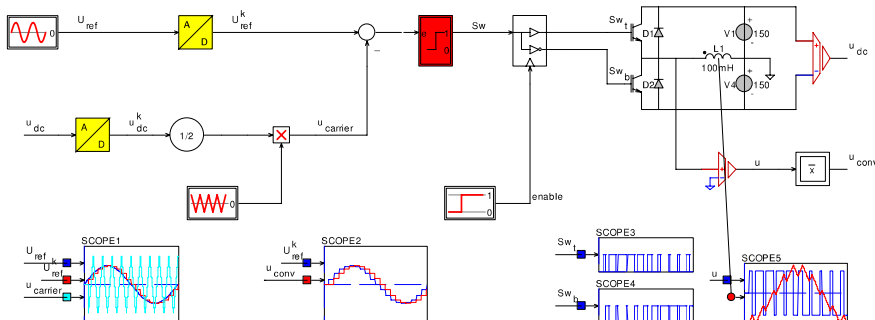


**Fig. 2.18** Simulation of half-bridge converter with PWM

An example of a simulation model which satisfies the needs for this tutorial is given in Fig. 2.18. Readily identifiable in this figure is the converter topology which consists of two ideal IGBT's and ideal diodes. The modulator structure is consistent with the generic structure shown in Fig. 2.4. An *enable* module is used together with a logic interface unit to activate the converter from time mark  $t = 1\text{ ms}$  onwards. Such a logic interface is usually implemented to ensure that the modulator circuit is enabled prior to the converter, to reduce the risk of accidental activation of both switches simultaneously during the power-up phase of operation.

The scope 5 waveforms in Fig. 2.19 represent the voltage across the load inductance and corresponding load current (depicted with a different amplitude scale). Observation of the load current waveform shows the presence of a series of incremental current steps. Two incremental current steps are made during each sample interval. The algebraic sum of each two steps is

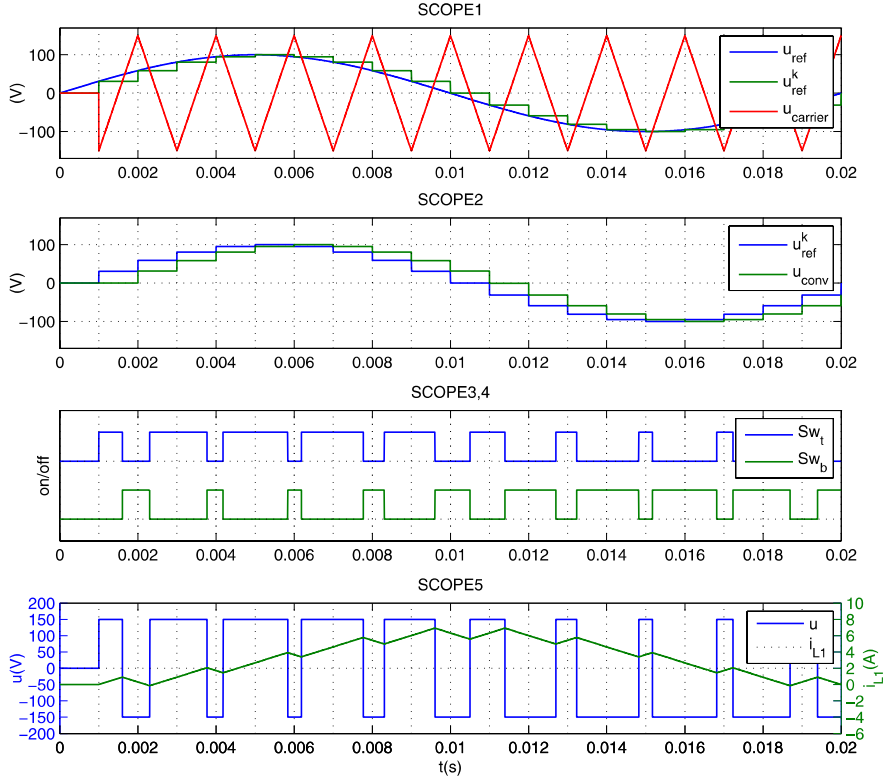
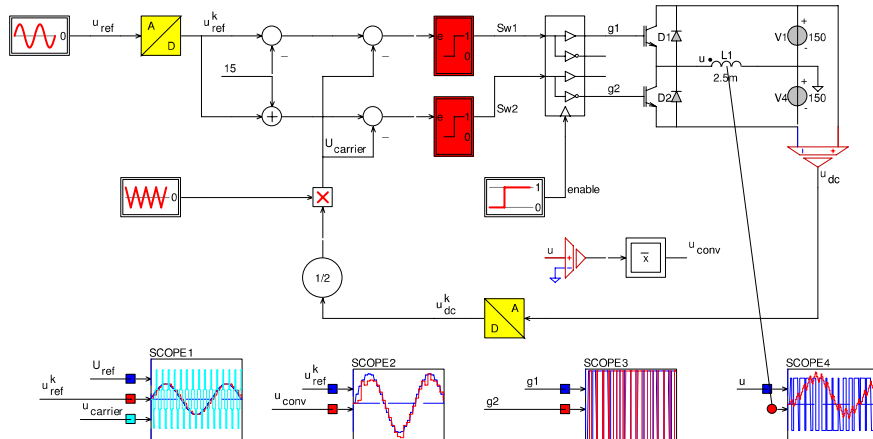


Fig. 2.19 Simulation results for half-bridge converter with PWM

defined by the load average voltage–time product  $U(t_k) T_s$  (for a given load inductance value  $L$ ) as shown earlier in Fig. 2.2. If the modulator operates correctly, the load average voltage  $U_{\text{conv}}(t_k)$  must be equal to the sampled reference average voltage  $U^*(t_k)$ . Both signals are shown in scope module 2. For this purpose, a module  $\bar{x}$  is introduced in the simulation which calculates the average voltage per sample time on the basis of the instantaneous input value, which is in this case the voltage across the load. Note that the output voltage of the  $\bar{x}$  module corresponds to the calculated average voltage value of the previous sample. The two complimentary switch signals given in scope modules 3 and 4 are directly tied to the comparator signal  $Sw$ . The ideal switches which are controlled by the signals  $Sw_t$ ,  $Sw_b$  (logic one corresponds to a switch on-state) connect the converter center node to the appropriate supply rail as shown in scope 5. The modular switch signal  $Sw$  is in turn determined by the average voltage function  $U(t)$  and the sampled reference average voltage  $U^*(t_k)$  shown in scope module 1.

### 2.6.2 Tutorial 2: Half-Bridge Converter with PWM and Dead-Time Effects

This tutorial considers the effects of dead time as discussed in Sect. 2.5. For this purpose the tutorial exercise as discussed above should be modified to accommodate an unrealistically high dead time of  $\Delta t_D = 100 \mu\text{s}$ , which, according to (2.35), corresponds to a band value  $U_D$  of 30 V, given the supply voltage and sample time value introduced in the previous section. Note that the dead-time value has been purposely chosen high to better illustrate the effect of including this phenomenon in the simulation. A CASPOC based implementation example which satisfies this tutorial is given in Fig. 2.20 and is unchanged with respect to the previous tutorial in terms of average voltage reference, assumed load and DC supply value. A full-bridge *logic interface module* is used to provide the appropriate switching signals for the two switches. The error input to two comparators is an error signal which is formed by the PWM signal  $U(t)$  and the sampled average voltage reference value. The latter is offset by a value of  $\pm 15 \text{ V}$  in order to realize the required dead-time average voltage band value of  $U_D = 30 \text{ V}$ . Again, a  $\bar{x}$  module has been added to this simulation which calculates the actual converter average voltage per sample value.



**Fig. 2.20** Simulation of half-bridge converter with PWM and dead-time effects

The waveforms generated by the simulation are again shown in Fig. 2.21. The waveforms given in scope 3 show that the switching signals for the converter are no longer complimentary. Instead a dead-time interval  $\Delta t_D = 100 \mu\text{s}$  is present between the two signals in question in order to facilitate the turn-on and turn-off sequence of the devices. The effects of including this dead time on, for example, the load voltage while changing polarity of the

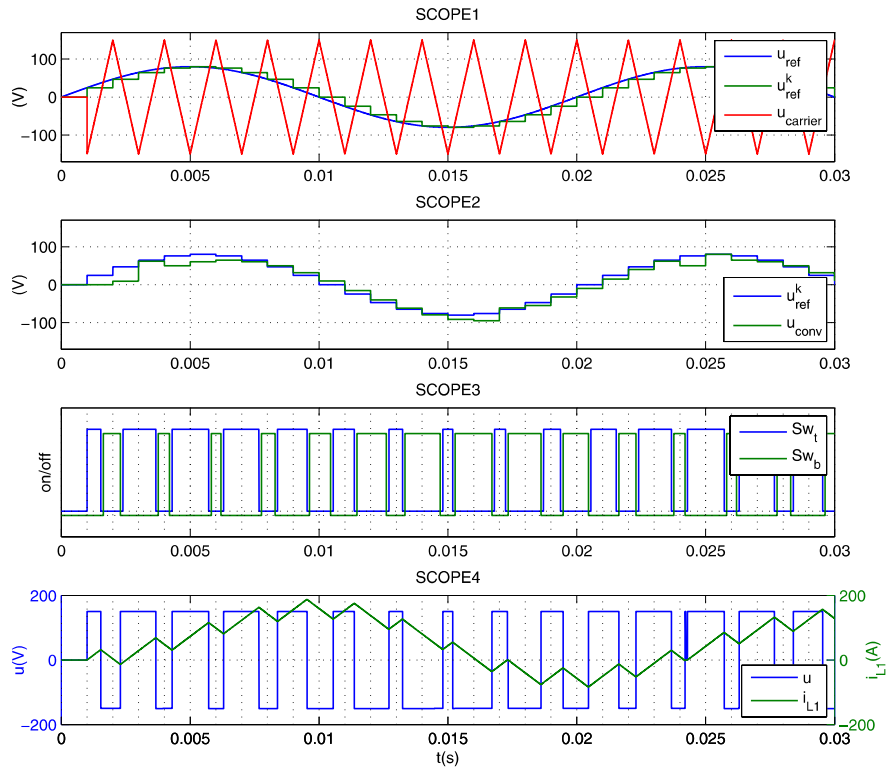


**Fig. 2.21** Simulation results for half-bridge converter with PWM

load current may be observed in scope 2, by comparing the average voltage value (calculated by the  $\bar{x}$  module) with the sampled reference voltage value.

### 2.6.3 Tutorial 3: Full-Bridge Converter with Pulse Width Modulation

This tutorial is concerned with a full-bridge converter concept as discussed in Sect. 2.3. For this purpose, the half-bridge based tutorial as discussed in Sect. 2.6.1 is to be modified to accommodate the new converter topology and the generic modulator structure shown in Fig. 2.8. The average voltage reference, load and supply variables remain unchanged with respect to those discussed in tutorial 1. However, to better understand the role of pulse centering, the voltage references  $U_a^*$ ,  $U_b^*$ , shown in Fig. 2.8, are to be provided by a two-phase pulse centering module as shown in Fig. 2.7. Inputs to this module are the voltage references  $U_1^*$ ,  $U_2^*$ . The voltage reference  $U_2^*$  is arbitrarily set to zero. Furthermore, a sinusoidal, 50 Hz reference average voltage waveform  $U^*$  with an amplitude of 100 V is to be used as introduced in tutorial 1, which will be used to represent  $U_1^*$ . An on/off switch is introduced to enable or disable the pulse centering unit. Disabling said unit will set the reference voltage  $u_o^*$  to zero, otherwise this value is calculated using expression (2.17). The introduction of the switch will enable the user to examine the role of the pulse centering, which is the main goal of this tutorial. The CASPOC based simulation model is given in Fig. 2.22 and clearly shows the use of two half-bridges with the ideal IGBT semiconductors and ideal diodes. A differential voltage probe measures the voltage across the inductive load. Furthermore, an average voltage module is used to calculate the actual average voltage per sample  $U_{\text{conv}}$  generated by the converter, so that this value can be compared with the required value during each sample of the simulation. A full-bridge *logic interface* module has been introduced which houses the logic components as required to generate the semiconductor gate signals from the comparator modules and step module which generates the drive *enable* signal, as discussed in Tutorial 2.6.2 for a single half-bridge. The pulse centering module used in this simulation model represents the generic structure according to Fig. 2.7, with the minor change that an analog switch has been introduced in the corresponding simulation module to set the output  $U_o^*$  to zero when the control input is set to logical zero by way of the on/off toggle switch. Outputs of the pulse centering unit are the two half-bridge reference variables and the variable  $U_o^*$ , which is particularly instructive, as they show the user how the pulse centering unit calculates this value based on the two reference input values. The remaining part of the modulator circuit is in accordance with the modulator generic diagram given in Fig. 2.8. As with the previous tutorials, a sampling time of  $T_s = 1 \text{ ms}$  is assumed.

The waveforms generated by the simulation are shown Fig. 2.23. The load voltage in scope 5 toggles between  $\pm 300 \text{ V}$ , which is double the value that is achievable with the half-bridge converter. This also means that the maximum average voltage level  $U_{\text{max}}$  is doubled when compared to the half-bridge converter topology. Furthermore, it is of interest to run the simulation with and

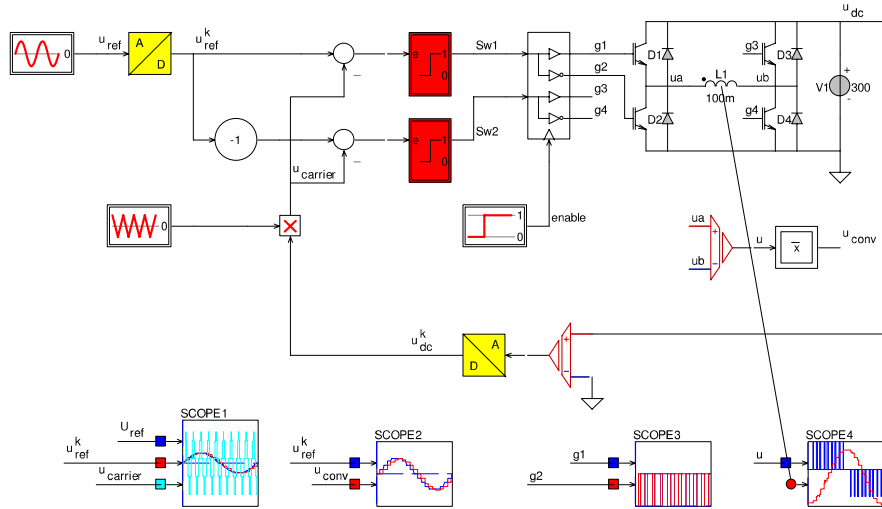


Fig. 2.22 Simulation of full-bridge converter with PWM

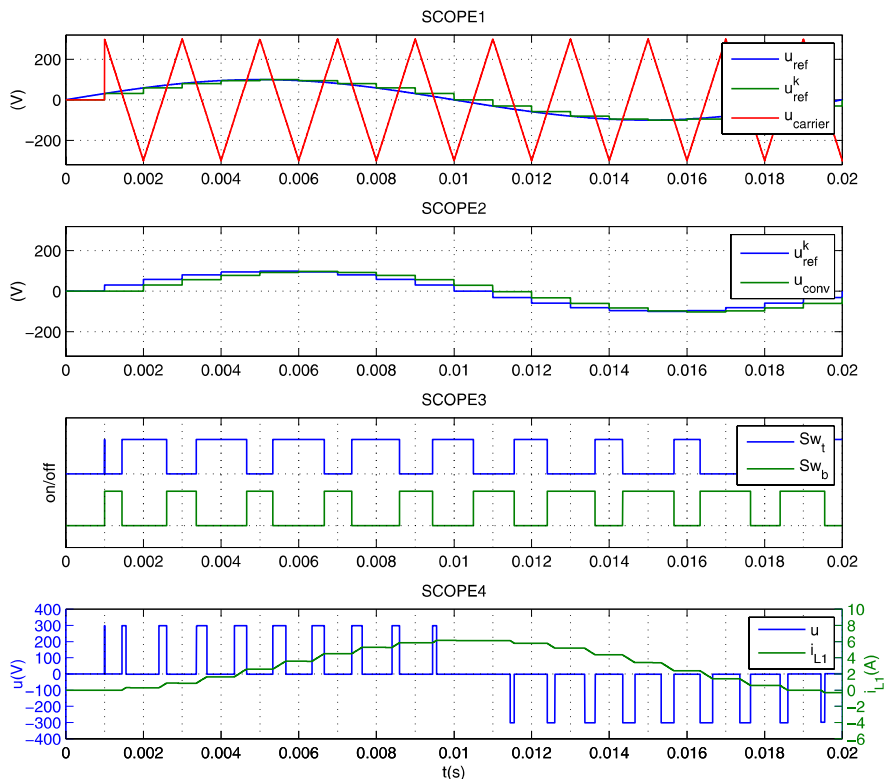


Fig. 2.23 Simulation results for full-bridge converter with PWM

without activation of the pulse centering unit to examine the orientation of the load voltage pulses (see scope 1 voltage waveform) relative to the center of each sampling interval. Observation of the results with the pulse centering unit active shows that the load voltage pulses are indeed centered with respect to the middle of the sample interval, in accordance with the waveforms given in Fig. 2.6(b). Furthermore, it may be verified that the largest reference voltage that can be used in this tutorial (without  $U_a^*$ ,  $U_b^*$  exceeding the supply voltage limits of the converter) with and without pulse centering is equal to 150 V and 300 V respectively.

#### ***2.6.4 Tutorial 4: Three-Phase Pulse Width Modulator with Pulse Centering***

The operation of the pulse centering technique for three-phase pulse width modulators, as discussed in Sect. 2.4 is to be considered in this tutorial. Of interest is to develop a simulation model of the generic structure shown in Fig. 2.12 that is able to generate the switching signals  $Sw^a$ ,  $Sw^b$ ,  $Sw^c$  on the basis of a rotating average voltage reference vector  $\vec{U}^*(t)$ . Furthermore, the required simulation should be able to display the converter voltage space vectors (as given in Fig. 2.15), which are used during each sample time step  $T_s$  for the duration of the chosen simulation time, which spans four periods. For this example, the average voltage reference vector at the start of the simulation is set to  $\vec{U}^*(t = 0) = \sqrt{3/8} u_{DC}$ , with  $u_{DC} = 300$  V, corresponding to the values chosen for the example given in Fig. 2.11 and Fig. 2.13(a). A sample time of  $T_s = 1$  ms is assumed together with a fixed amplitude rotating (average) voltage reference vector, with an angular frequency of  $\pi/6T_s$  rad/s. The latter has been purposely chosen to realize a 30° rotation of the vector over each sample interval, which is precisely in accordance with the example used to generate Fig. 2.11 and Fig. 2.13(b). This implies that the tutorial provides an opportunity for the reader to quantitatively verify the example discussed in Sect. 2.4, with and without the use of the pulse centering technique. Note that the selected angular frequency is relatively high in comparison with those used in drive applications. The reason for this is that this tutorial is aimed at showing the user how the converter vectors are generated to deliver the required average voltage vector during each sample interval, with and without the use of pulse centering, as was mentioned above.

The CASPOC based simulation model as given in Fig. 2.24 shows the three-phase modulator with an input in the form of a rotating average voltage vector. The latter is sampled and used with a two- to three-phase (power invariant) conversion module to obtain the three-phase load average voltage reference values  $U_1^*$ ,  $U_2^*$ ,  $U_3^*$ . The converter reference average voltage variables  $U_a^*$ ,  $U_b^*$ ,  $U_c^*$  used during each interval are generated with the submodule *Pulse Center Module*, the combination of which satisfies equation set (2.23).

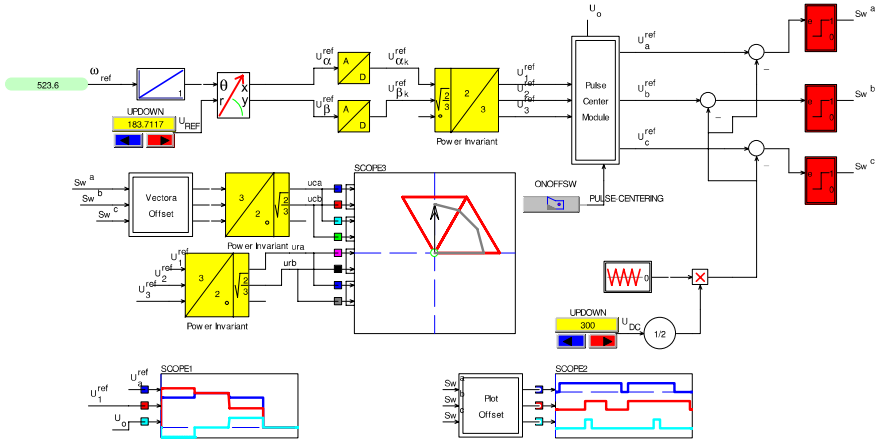


**Fig. 2.24** Simulation of three-phase modulator with pulse centering

The *Pulse Center Module*, as given in Fig. 2.12 calculates the required zero-sequence reference average voltage value  $U_o^*$  which is output variable of this module. A *toggle switch* is also shown in Fig. 2.24 which allows the user to enable/disable the pulse centering function. Setting the output value of the toggle switch to logic one enables the pulse centering module. With the value set to zero, the pulse centering module sets the zero-sequence reference average voltage to zero, in which case the output are equal to the input variables of the module.

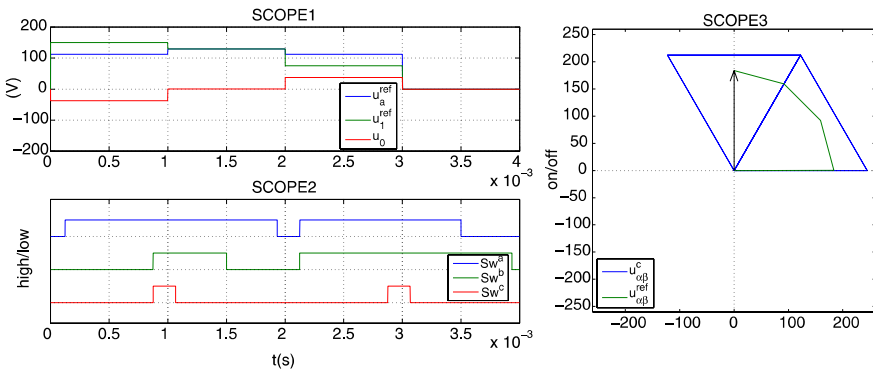


**Fig. 2.25** Simulation results of three-phase modulator with pulse centering

The waveforms generated by the simulation are shown in Fig. 2.25. Observation of the scope 3 vector diagram confirms that the sampled average voltage reference vector rotates from zero to  $30^\circ$  during the first two sample intervals  $0 \rightarrow 2T_s$  of the simulation. Also shown in this vector diagram

are the converter space vectors used to generate the required average voltage reference vector. In this context, note that converter *zero* vectors are shown as small circles at the origin. These change to arrow points when a converter active vector is selected during the simulation.

The corresponding switch states  $Sw^a$ ,  $Sw^b$ ,  $Sw^c$ , shown by scope module 2, are in accordance with those shown in Fig. 2.11(a) in case pulse-centering is not active. Note that a *plot offset* module is used in conjunction with this scope module for the purpose of showing all three switching waveforms in one diagram. The latter is achieved by introducing a vertical offset in the waveforms. It is instructive for the reader to repeat the simulation with active pulse centering, in which case the switch states for the first two samples of the simulation will correspond with those shown in Fig. 2.11(b). The *UP-DOWN* module, used in Fig. 2.24 to control the amplitude of the reference average voltage vector, may be increased from  $\sqrt{3}/8 u_{DC} \rightarrow u_{DC}/\sqrt{2}$ . With this setting, the modulator operates with the largest (without deforming the output waveform) possible reference incremental flux linkage amplitude, with pulse centering as was discussed in Sect. 2.4, i.e., the half-bridge reference value will remain within the supply limits  $\pm u_{DC}/2$  as may be observed from this exercise.

### 2.6.5 Tutorial 5: Three-Phase Converter with Pulse Width Modulator

This tutorial is concerned with the implementation of a three-phase converter and modulator structure as shown in Fig. 2.9 and Fig. 2.12 respectively. The generic load  $Z$  is assumed to be a 100 mH ideal inductance. The aim of this tutorial is to extend the previous tutorial activity by including a three-phase topology and modulator structure, together with a user defined average voltage reference vector. This should allow the user to examine the half-bridge voltage, load voltage, zero-sequence voltage and load current waveforms. In this example, the frequency of the rotating reference average voltage vector is (arbitrarily) set to 10 Hz, with a simulation time of 100 ms to allow visualization of one period of operation.

A simulation model of this tutorial, as given in Fig. 2.26, makes use of ideal IGBT's and diodes, in line with the approach set out in the previous tutorials. A *three-phase logic interface* modules has been introduced which hold the logic modules for the half-bridge converter stages as discussed earlier for the half and full-bridge interface modules. The interface module is connected to an *enable* module which is used within the simulation to enable the converter at  $t = 1$  ms. In the example given, the amplitude of the average voltage reference vector is determined by the product  $k_U$  and  $u_{DC}$ , which in this case are initially chosen to be equal to  $\sqrt{3}/8$  and 300 V respectively. A toggle switch is again introduced to allow the reader to enable/disable pulse centering.

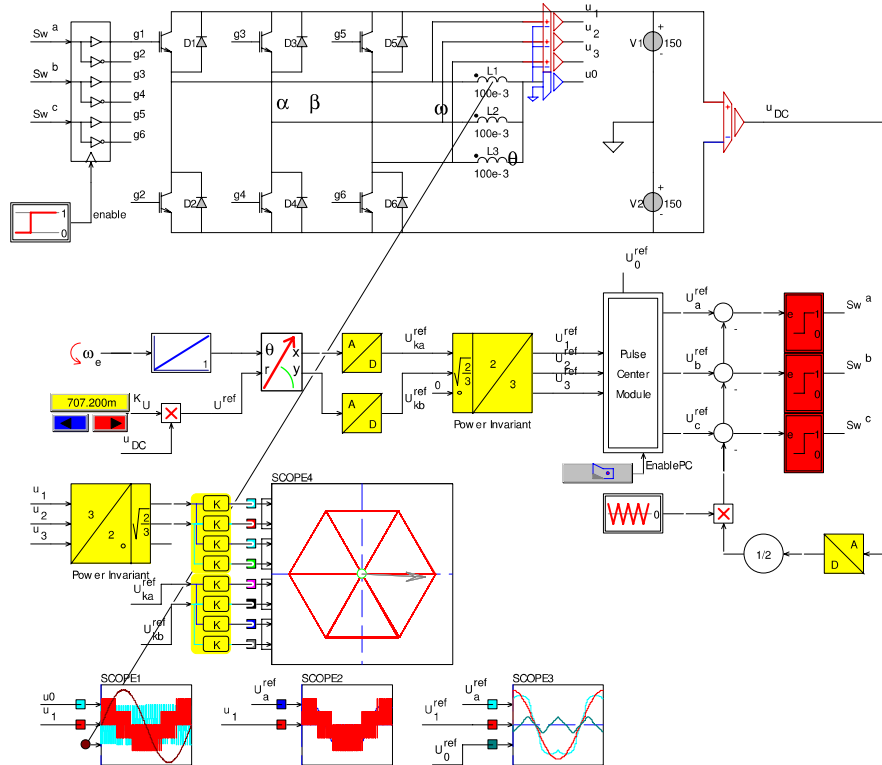


**Fig. 2.26** Simulation of three-phase converter with modulator

Setting the output of the toggle switch to zero disables pulse centering. Be sure to plot each time-step to observe all details.

The waveforms generated by the simulation are shown in Fig. 2.27. It is left as an exercise for the reader to reconsider the results from the simulation in the event that the factor  $k_U$  is increased to  $1/\sqrt{2}$  which represents the largest value that may be used, i.e., which will ensure that the absolute average voltage half-bridge reference values are less than or equal to  $u_{DC}/2$  when pulse centering is active. Disabling pulse centering with this value for  $k_U$  will lead to half-bridge average voltage reference values that exceed the supply window  $\pm u_{DC}/2$  and cannot therefore be implemented by the converter, as may be observed from this tutorial. It is particularly instructive to examine closely scope 4 during the course of the simulation because this module shows the reference vector together with the selected converter vectors used during each sample.

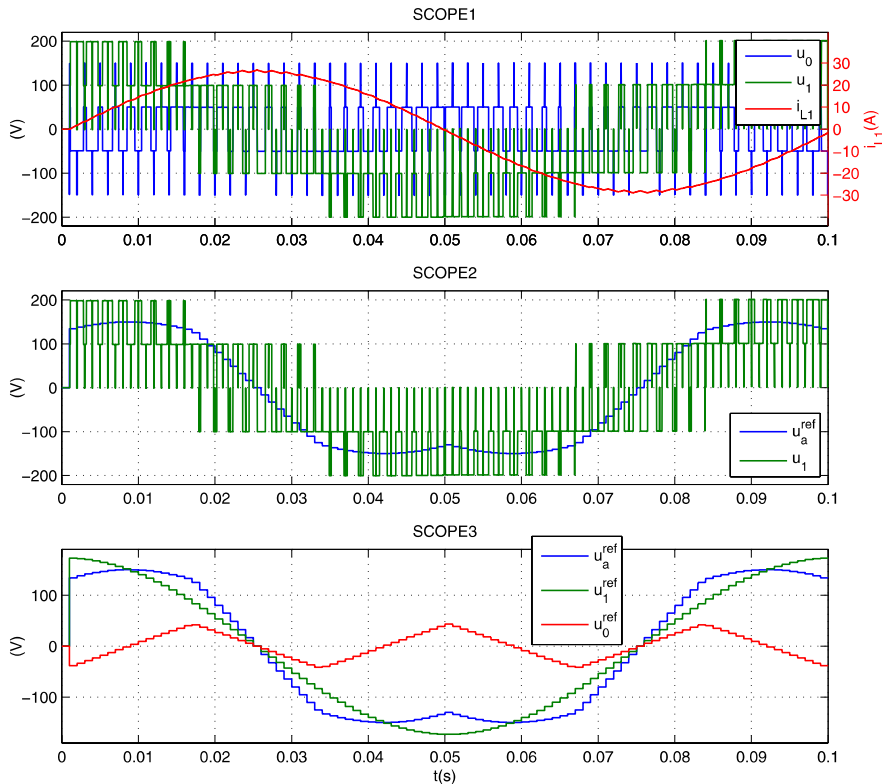


**Fig. 2.27** Simulation results of three-phase converter with modulator

### 2.6.6 Tutorial 6: Three-Phase Simplified Converter without PWM

In practice, the simulation of comprehensive models as discussed in the previous tutorials is inhibited by the need for a relatively small computation step time. In the example above, the computation step time was set to  $1\mu\text{s}$ . Consequently, such simulations are usually slow in terms of simulation run time. An often used approach, which speeds up the simulation, is to replace the converter with three supply limited  $\pm u_{\text{DC}}/2$  voltage sources, of which the input is derived from the half-bridge average reference generated by the pulse centering unit. The underlining concept of this approach is that the load is provided with a set of supply limited voltages which are in effect the mean (per sample) voltage generated by the modulator/converter as discussed in the previous tutorial. This tutorial aims to demonstrate this approach by removing the modulator/converter that was used in the previous tutorial and replacing the latter with a set of *supply limit* modules which ensures that the output is maintained within the supply voltage window  $\pm u_{\text{DC}}/2$ .

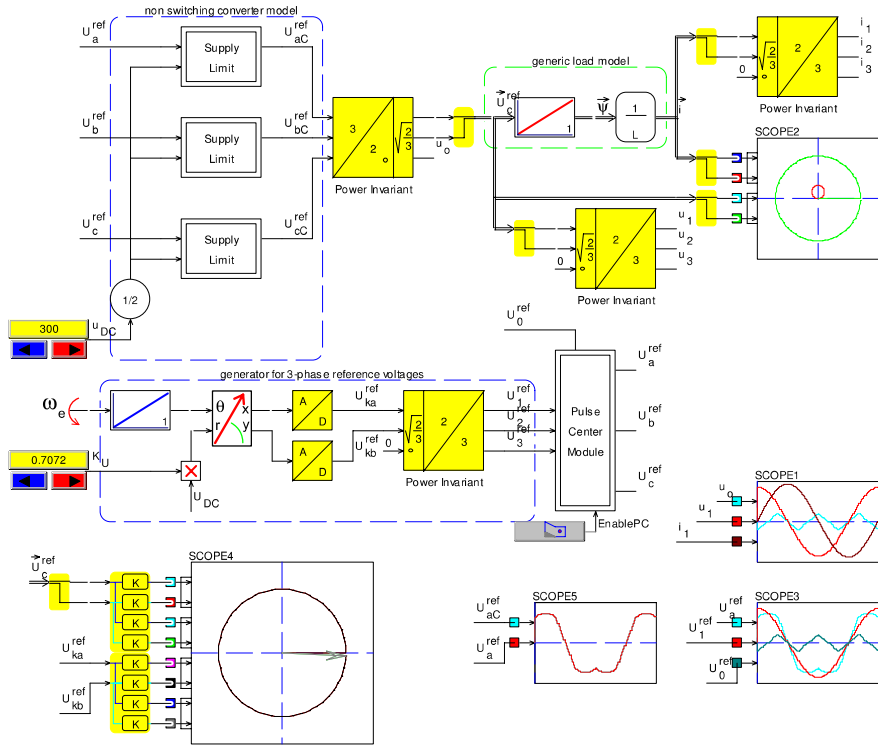


**Fig. 2.28** Simulation of three-phase converter with pulse centering, simplified model

The simulation model, given in Fig. 2.28, shows how the example discussed in the previous tutorial may be adapted to this new approach. Readily identifiable in this figure are the three *supply limit* modules which maintain the average voltage reference values from the pulse centering module within the range  $\pm u_{DC}/2$ . The outputs of these modules can also be conveniently used to accommodate dead time effects. For this purpose, the sign of the load current must be used together with an addition gain and summation module to generate a current polarity dependent average voltage offset for each phase according to equation set (2.36). In this example, the mean half-bridge voltages are used in conjunction with a three- to two-phase (power invariant) conversion as an input to the generic model of the load. The latter is in this case an ideal inductance, which is represented by an integrator and gain  $1/L$  module, the output of which represent the load current vector  $\vec{i}$ . Note also that the control of the current in the load is usually the aim of the simulation, as will become apparent in the next chapter. This implies that the need for a precise representation of the load voltage(s), other than their mean, may in most cases be avoided without comprising the purpose of the simulation.

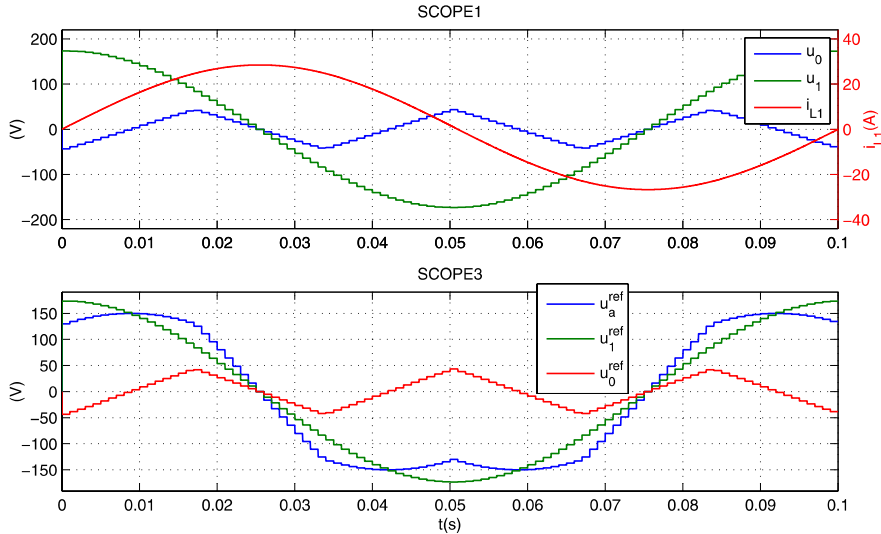


**Fig. 2.29** Simulation results of three-phase converter with pulse centering, simplified model

Some of the waveforms generated by the simulation, are shown in Fig. 2.29. A comparison of the load current waveform obtained with this and the previous tutorial shows that these are almost identical. The differences between the two are attributed to the PWM switching process which is no longer present in this simulation model. The operating conditions are otherwise identical as may be observed by comparing the average voltage reference waveforms of both simulations. The actual voltage waveforms are as expected vastly different, the average voltage per time sample  $T_s$  is however identical for both tutorials. With the present choice of average voltage reference amplitude  $u_{\text{DC}}/\sqrt{2}$ , a circular orbit of the load vector is still possible, provided pulse centering is active. However, this choice of reference voltage amplitude is at the limit of the linear operation, which may be verified by repeating the simulation with a disabled pulse centering unit (output of toggle-switch to zero). Under these conditions, the orbit of the load voltage vector is no longer a circle, which implies that the phase waveforms are no longer sinusoidal. Note that increasing the amplitude of the reference vector beyond  $u_{\text{DC}}/\sqrt{2}$  will lead to the six-step mode of operation as described towards the end of Sect. 2.4.1.



# Chapter 3

## Current Control of Generalized Load

The ability to control the currents in an electrical machine is essential for manipulating its mechanical torque and magnetic flux, as will become apparent in Chap. 4. This chapter considers current control techniques for single- and three-phase voltage-source converters which are connected to a *generalized load* as introduced in the previous chapter. The use of this type of load is instructive given that it reflects the electrical behavior of most electrical machines which are in use today. Consequently, the current control techniques discussed in this chapter may be applied for electrical machines discussed in this book. Attention has been given to the use of voltage-source converters because these are widely used in low- and medium-power drive applications. However, for high-power applications, current-source converters are often deployed which are considered outside the scope of this book. A bewildering variety of current control concepts have been developed. In this chapter two representative techniques for single- and three-phase converters will be considered. The two techniques in question are referred to as *hysteresis* and *model based* current control. Within these categories, different implementation techniques are possible. Two practical control techniques are introduced which have been used by the authors in electrical drive applications. The tutorial section at the end of this chapter deals with a range of simulation models which provide the reader with the ability to examine the control concepts explained in this chapter.

### 3.1 Current Control of Single-Phase Load

#### 3.1.1 *Hysteresis Current Control*

Prior to discussing this type of control it is helpful to define the so-called hysteresis concept with the aid of Fig. 3.1. Shown in this figure is a generic

module with input  $x$  and output  $y$ . The output has two states, which in this example are taken to be  $-1$  and  $1$  respectively, as is apparent from the transfer function shown in Fig. 3.1. The term hysteresis is used to describe a non-singular transitional process. If, for example, the output state  $y = -1$ , then the output will change to  $y = 1$  when the condition  $x \geq \varepsilon/2$  occurs. Vice-versa, when the output is  $y = 1$ , a change to  $y = -1$  will take place as soon as the condition  $x \leq -\varepsilon/2$  occurs. The transitions exhibit a degree of ‘hysteresis’ defined by the variable  $\varepsilon$  as shown in Fig. 3.1.

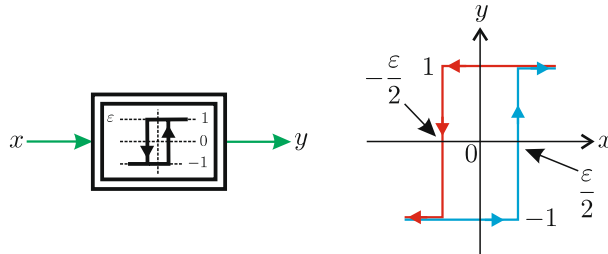


**Fig. 3.1** Generic hysteresis module and transfer function

In this section, a hysteresis based current control will be discussed with the aid of the half-bridge converter topology presented in Sect. 2.2. This topology is readily adapted to hysteresis type current control by adding a current controller module and a current sensor, as indicated in Fig. 3.2. The current controller module must provide the switching signals for the converter on the basis of the instantaneous measured load current and user defined reference current.

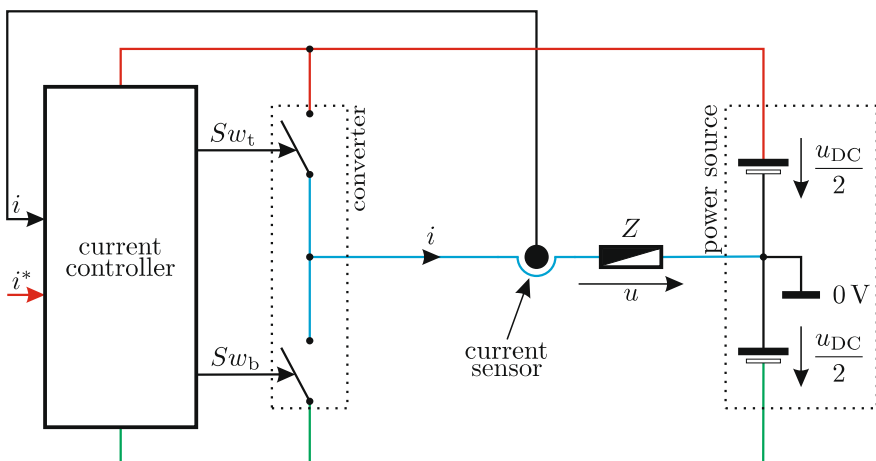


**Fig. 3.2** Single-phase converter with hysteresis current controller

An implementation example of such a module, in terms of its generic representation, is shown in Fig. 3.3. Figure 3.3 shows that this module contains two comparators of which the first (Comparator A) is a normal *hysteresis* type comparator with a bipolar output  $\pm 1$ . The output of the comparator is fed back to the input via a gain module with gain  $\Delta i/2$ . Consequently, the output state is determined by  $\varepsilon = i^* - i \pm \Delta i/2$ . Comparator B generates a logic signal  $Sw$  used by the two switches, where  $Sw = 1$  corresponds to a closed top switch  $S_{wt}$  and open bottom switch  $S_{wb}$ . Vice versa, a state  $Sw = 0$  corresponds to a closed bottom switch and open top switch. The basic action of the controller is to maintain the load current within the limits  $i^* \pm \Delta i/2$  where  $\Delta i$  and  $i^*$  are user defined parameters.

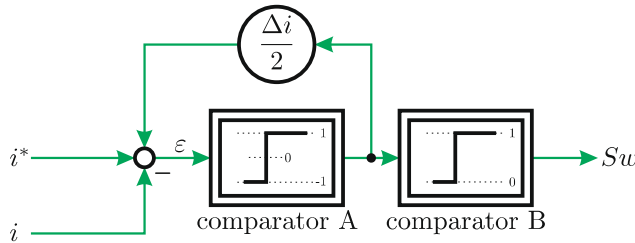


**Fig. 3.3** Generic structure of hysteresis current controller

Exemplary waveforms produced by this current controller are shown in Fig. 3.4. The waveforms shown are obtained with the aid of a simulation model, presented in Sect. 3.3.1. Clearly identifiable in subplot (a) are the load current (color blue) and the reference current (color red) waveforms, which confirm the ability of the controller to maintain the current within a specified hysteresis band. Also shown in subplot (b) of Fig. 3.4 are the load voltage (color red) and the assumed induced voltage  $u_e$ . More detailed views of these two subplots are shown in subplot (c) and subplot (d). In subplot (c) the selected current band  $\Delta i = 0.4$  A used for this simulation is visible, which confirms the ability of the controller to keep the current within the set limits. Observation of the converter voltage in particular shows that the switching frequency is not constant, which is particularly uninviting in case the load is in the form of an electrical machine, given the acoustic noise signature that may appear with this type of control strategy. The frequency spectrum of the converter voltage underlines this statement. The spectrum in question is discussed (for three-phase hysteresis control) in Sect. 3.2.4 where it is compared to the spectrum generated by three-phase model based current control.

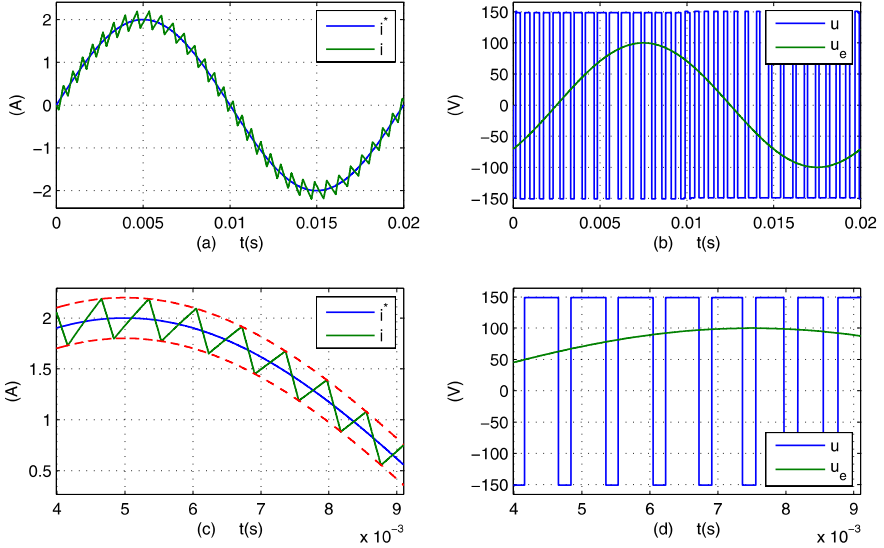


**Fig. 3.4** Single-phase hysteresis control example

### 3.1.2 Model Based Current Control

The term *model based control* refers to a control method which assumes that the nature of the load (electrical machine in our case) is known. Consequently, a controller may be designed which, on the basis of a known current error, calculates for each sampling interval the required voltage  $U_k^*$  (as defined by (2.6)) needed to drive said error to zero. The basic control structure as outlined in *Fundamentals of Electrical Drives* [68] is extended here to accommodate a full-bridge converter topology as discussed in Sect. 2.3. The converter shown in Fig. 3.5 is connected to a single-phase load  $Z$  as introduced in the previous chapter.

The modulator controls the converter switches in such a manner that the converter generates (during a given sampling interval  $T_s$ ) an average voltage quantity  $U(t_k)$  which corresponds to the reference average voltage value  $U^*(t_k)$  that is provided by the controller module. The basic task of the controller, shown in Fig. 3.5, is therefore to calculate the required average voltage per sample at the beginning of a sampling interval  $t_k$  that is required to drive the current error to zero at the end of said interval.

The nature of this control philosophy is shown with the aid of Fig. 3.6. Shown in this figure are the non-sampled reference current  $i^*(t)$  and typical (for PWM based control) converter current  $i(t)$ . These currents are sampled by the controller at time marks  $0, t_1, t_2, \dots$  etc. At time  $t = t_1$ , a current error between the sampled reference and sampled converter current  $i^*(t_1) - i(t_1)$  exists. The objective of the control approach is to determine the required

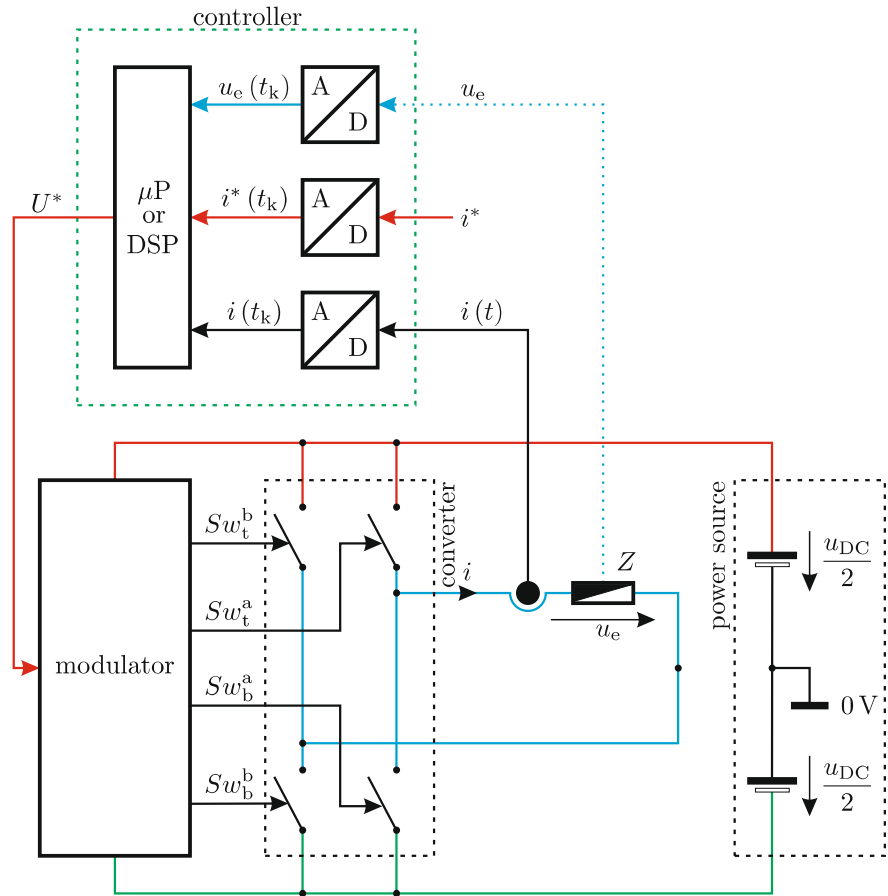


**Fig. 3.5** Single-phase model based current control

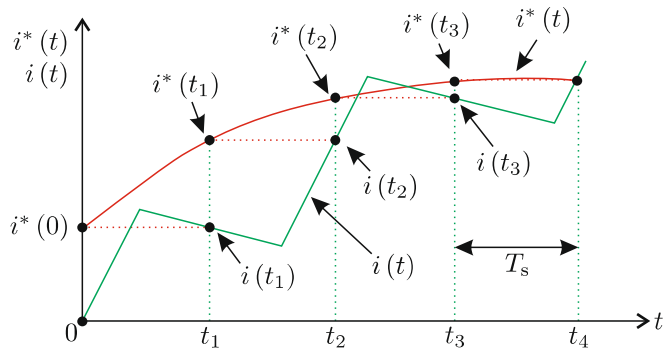


**Fig. 3.6** Model based current control

average voltage reference value needed to quickly zero this error. This leads to the condition  $i^*(t_1) = i(t_2)$ . The control objective aimed at driving the current error to zero during each sample interval may be written as

$$i(t_k + T_s) = i^*(t_k) \quad (3.1)$$

for a regularly sampled system with sampling time  $T_s$ . The modulator will control the converter switches in a manner needed to ensure that the condition as represented by (3.2) is satisfied, as was outlined in the previous chapter (see (2.6)).

$$U^*(t_k) = \frac{1}{T_s} \int_{t_k}^{t_{k+1}} u(\tau) d\tau \quad (3.2)$$

The variable  $u$ , shown in (3.2) represents the voltage across load  $Z$ , which may also be written as

$$u = Ri + L \frac{di}{dt} + u_e \quad (3.3)$$

given that the load is formed by a series network which consists of a resistance  $R$ , inductance  $L$  and voltage source  $u_e$ . The latter is usually referred to in machines as the back or counter EMF and represents a load dependent *disturbance*. In this analysis, access, by means of sensors, is assumed to the voltage  $u_e$  and load current  $i$ , where the latter represents the control variable. When the load is in the form of an electrical machine, an estimator/observer is normally used to compute the back EMF  $u_e$ , given that the latter cannot be measured directly. Use of (3.3) with (3.2) allows the latter to be written as

$$U^*(t_k) = \frac{R}{T_s} \int_{t_k}^{t_{k+1}} i(\tau) d\tau + \frac{L}{T_s} \int_{i(t_k)}^{i(t_{k+1})} di + \frac{1}{T_s} \int_{t_k}^{t_{k+1}} u_e(\tau) d\tau. \quad (3.4)$$

Equation (3.4) forms the basis for determining a generic control structure that is able to calculate the required average voltage capable of satisfying condition 3.1. It is noted that this value can only be determined on the basis of a detailed knowledge of the load  $Z$  with parameters  $R$  and  $L$  and back-EMF voltage  $u_e$ .

In practice, for a digital implementation, discretization of (3.4) is required. A first order approximation technique may be used, provided the sampling time is sufficiently small, which leads to

$$U^*(t_k) \cong Ri(t_k) + \left( \frac{L}{T_s} + \frac{R}{2} \right) (i^*(t_k) - i(t_k)) + u_e(t_k) \quad (3.5)$$

where use is made of expression (3.1). Furthermore, it is assumed that the sampling rate is sufficiently high to assure that the back EMF can be assumed constant over the duration  $T_s$ , in which case the average voltage  $U_e(t_k)$  is equal to  $u_e(t_k)$  as shown in (3.5). A control structure based

on (3.5) is basically a proportional type controller with a term  $u_e$ , otherwise referred to as a disturbance decoupling term. In practice, a proportional integrator type structure is preferable, because the process of zeroing the current error each interval is in practice not achievable due to parameter discrepancies between controller and load. Furthermore, the required average voltage cannot always be met, i.e., when the converter is used outside the linear voltage operating region, as discussed in the previous chapter. The replacement of the variable  $i(t_k)$  by a discrete integration term which utilizes the current error can be made plausible by considering Fig. 3.6. Observation of sampled reference and measured currents and  $i(t_3)$  in particular, shows that in the ideal case, i.e., when zeroing of the current error occurs each sample, the current  $i(t_3)$  may be represented as  $i(t_3) = (i^*(t_2) - i(t_2)) + (i^*(t_1) - i(t_1)) + i^*(0)$ . In general mathematical terms this error summation may be written as

$$i(t_k) \cong \sum_{ij=0}^{ij=k-1} (i^*(t_{ij}) - i(t_{ij})) \quad (3.6)$$

with  $t_0 = 0$  and  $i(0) = 0$ . Use of (3.6) with (3.5) leads to

$$\begin{aligned} U^*(t_k) &\cong R \sum_{ij=0}^{ij=k-1} (i^*(t_{ij}) - i(t_{ij})) \\ &+ \left( \frac{L}{T_s} + \frac{R}{2} \right) (i^*(t_k) - i(t_k)) + u_e(t_k). \end{aligned} \quad (3.7)$$

The generic structure which corresponds to (3.7), as shown in Fig. 3.7, contains a PI controller and disturbance decoupling term  $u_e(t_k)$ . The proportional  $K_p$  and integral  $K_i$  gain settings for the discrete controller are in this case defined as

$$K_p = \frac{L}{T_s} + \frac{R}{2} \quad (3.8a)$$

$$K_i = \frac{R}{T_s} \quad (3.8b)$$

In practice, the condition  $L/T_s > R/2$  is satisfied, which means that the proportional gain is reduced to  $L/T_s$ . As can be seen from (3.7), the multiplication factor in the discrete integrator equals  $R$ , the integral gain  $K_i$  corresponds to (3.8) and the controller's time constant  $K_p/K_i$  equals the time constant of the  $R-L$  circuit  $L/R$ . Note that model based current control utilizes a constant sampling and carrier frequency, which is decidedly advantageous when compared to hysteresis type control. The reason for this is that the frequency spectrum of the converter voltage is well defined (as shown in Sect. 3.2.4). Choosing the carrier frequency provides the ability to influence the acousti-

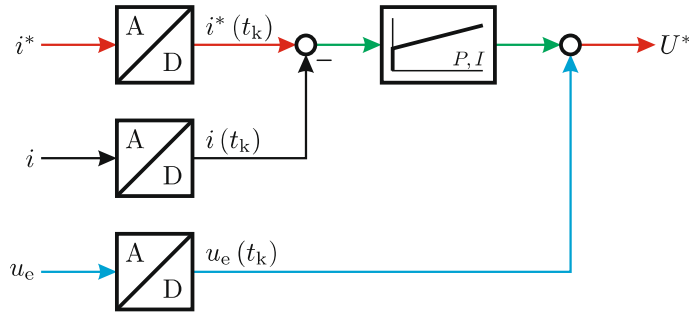


**Fig. 3.7** Model based current controller structure

cal spectrum, the switching losses and provides the ability to tailor design line-side grid filters. Furthermore, the control algorithm can easily be implemented in digital controllers.

In practical implementations, the PI controller is prone to *windup*, which occurs when the limits of the system are reached. Windup can occur in this case when the reference average voltage value generated by the PI controller exceeds the maximum value which can be delivered by the converter. Under such circumstances a current error occurs at the input of the controller, which will cause the integrator output to further ramp up or down. Practical controllers as those considered in the tutorials have an *anti-windup* feature which limits integrator action when the user defined limits are reached. For the controller in question, the limit values should be set to the  $\pm$  maximum average voltage per sample.

A disadvantage of model based control is that a priori knowledge of the load is required, which is not the case for hysteresis type current control. However, in practice, the advantage of not requiring access to the machine parameters does not outweigh the acoustical noise signature that comes with the use of a variable switching frequency hysteresis current controller.

An example of model based current control is given in Fig. 3.8, which is taken from the Tutorial 3.3.2 at the end of this chapter. The current reference and the load are identical to that used for the hysteresis control example, shown in Fig. 3.4.

For more details, the reader is referred to the tutorial given in Sect. 3.3.2. Also shown in Fig. 3.8 is the converter voltage  $u$  and voltage  $u_e$ . The averaged (per sample interval) load voltage waveform resembles the load voltage waveform  $u_e$ , which is to be expected because the load is predominantly inductive. Indeed, the mean voltage across an inductance must be zero, a statement also referred to as *voltage-second balancing*. The same set of waveforms were also given for the hysteresis controller, shown in Fig. 3.4. These show a similar behavior, given that the same load model is used in both examples. Subplots (c) and (d) in Fig. 3.8 show a zoomed section of the upper two subplots,

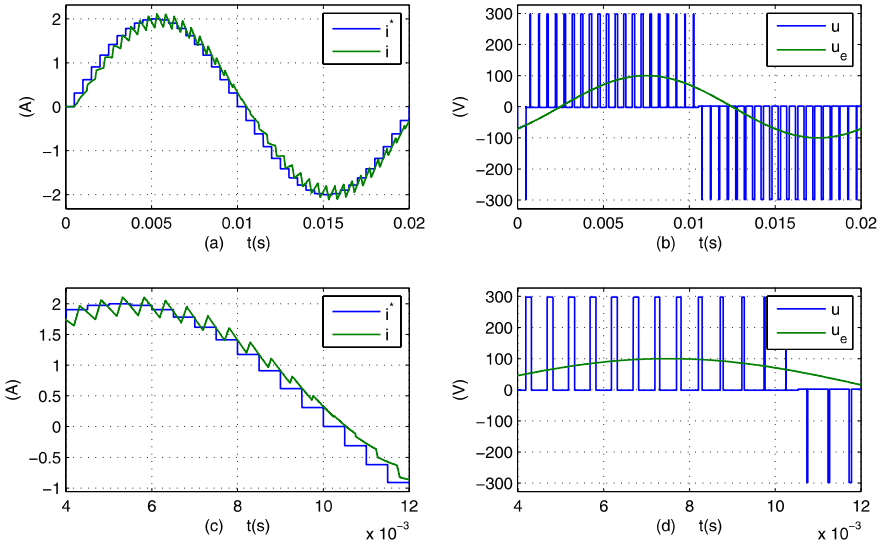


**Fig. 3.8** Single-phase model based current control example

which demonstrates the ability of the controller to zero the error between sampled converter and sampled reference current at the end of each sample.

### 3.1.3 Augmented Model Based Current Control

In the previous section, a disturbance decoupling terms  $u_e$  was added to the PI controller, of which the gains were derived using a model based control approach. A modified approach, referred to as *augmented model based control*, is based on the use of a discretized model of the load as indicated in Fig. 3.9. Input to this model are the (sampled) reference current  $i^*$  and load voltage  $u_e$ , while the output is in the form of the average voltage reference  $U_M^*(t_k)$ .

The contents of the discrete model is directly based on load (3.4), in which the measured current is replaced by the reference value. Furthermore, the integral boundaries are taken from  $t_{k-1} \rightarrow t_k$ , given the need to obtain an expression in terms of the variables  $i^*(t_k)$  and  $i^*(t_{k-1})$ . A process known as *backward time discretization*, which leads to

$$U_M^*(t_k) \cong R i^*(t_k) + \left( \frac{L}{T_s} - \frac{R}{2} \right) (i^*(t_k) - i^*(t_{k-1})) + u_e(t_k). \quad (3.9)$$

Typically, the parameters  $R$  and  $L$  and variable  $u_e$  are estimates of the actual load connected to the converter. Theoretically, this type of controller does not require access to the measured current, i.e., operates in an open loop

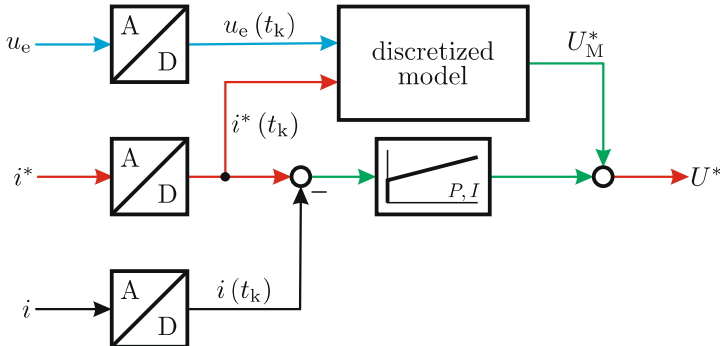


**Fig. 3.9** Augmented model based controller structure

control mode, assuming that there is no mismatch between the parameters used in the load and controller. In reality such errors exist in which case a PI controller with reduced gain (when compared to the previous case), as shown in Fig. 3.9, can be used to compensate for said errors. The gains  $K_p$  and  $K_i$  as calculated using equation set (3.8) represent a suitable upper limit for the PI controller shown in Fig. 3.9. However, in practice lower gains can be used because time constants associated with parameter changes are low. The use of an augmented model based current control approach must be considered with caution as the model may contain differential terms, which can be prone to noise. In the model shown here, the differential of the reference current is required, according to (3.9). Moreover, in this case, reference current signal is not a measured quantity and should not exhibit high noise levels.

### 3.2 Current Control of a Three-Phase Load

The extension to three-phase current control laws for voltage source converters is usually undertaken with the aid of space vectors. Such an approach is prudent on the grounds that the sum of the three-phase currents is zero, in which case the number of degrees of freedom to control current reduces to two. A space vector representation of the variables takes this into account and is therefore convenient. A further step in this process is to consider the control process in a synchronized reference frame linked to a suitable load vector as indicated in Fig. 3.10.

Shown in Fig. 3.10 is the load voltage vector  $\vec{u}_e$ , which in turn can be linked to a flux vector  $\vec{\psi}_e$ . If the load is in the form of an electrical machine, this vector may for example represent the rotor flux vector. At constant rotational speed  $\omega_e$ , the amplitude of the flux vector  $\vec{\psi}_e$  is equal to  $\hat{u}_e/\omega_e$ , where  $\omega_e$  represents the rotational speed of the vector. The *direct* d-axis of the dq coordinate system is tied to the flux vector, which is displaced by

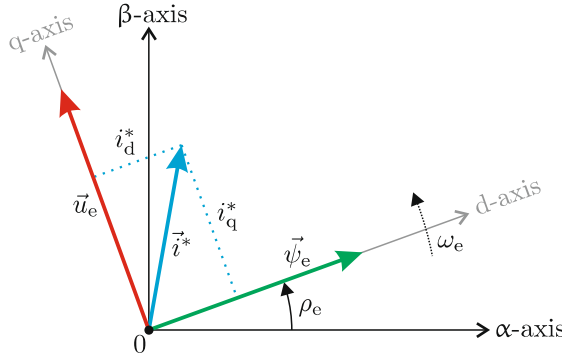


**Fig. 3.10** Synchronous reference frame for three-phase current control

an angle  $\rho_e$  with respect to the stationary reference frame. The *quadrature* q-axis is tied to the load vector  $\vec{u}_e$ . A user defined current reference vector  $\vec{i}^*$  is also shown in Fig. 3.10, which can be expressed in terms of the direct and quadrature reference current components  $i_d^*$  and  $i_q^*$ , respectively.

Prior to discussing two commonly used current control strategies, it is instructive to consider the basic principles which govern the current control process. A suitable starting point for this analysis is to consider Fig. 2.15 which shows the eight possible converter voltage vectors  $\vec{u}_{\{Sw^a, Sw^b, Sw^c\}}$  that can be realized with a three-phase voltage source converter. The converter in question is connected to a three-phase generalized load, as shown in Fig. 2.9. Each load phase consists of an inductance  $L$ , resistance  $R$  and phase load voltage  $u_e^i$ , with  $i = 1, 2, 3$ . The three load phases are represented in space vector format, for example by the vector  $\vec{u}_e = \hat{u}_e e^{j\omega_e t}$ . The corresponding load currents may be found by considering the terminal equation, in space vector format, namely

$$\vec{u}_{\{Sw^a, Sw^b, Sw^c\}} = L \frac{d\vec{i}}{dt} + R \vec{i} + \vec{u}_e. \quad (3.10)$$

For the loads considered in this book, the term  $R \vec{i}$  is small in comparison to the term  $L \frac{d\vec{i}}{dt}$  and is neglected in this analysis. A first order approximation of (3.10) gives

$$\Delta \vec{i}_{\{Sw^a, Sw^b, Sw^c\}} \simeq \frac{\Delta T}{L} (\vec{u}_{\{Sw^a, Sw^b, Sw^c\}} - \vec{u}_e) \quad (3.11)$$

where  $\Delta T$  represent the time interval in which the voltage vector  $\vec{u}_{\{Sw^a, Sw^b, Sw^c\}}$  is active. Equation (3.11) is significant as it shows that there are only a discrete set of possibilities for changing the instantaneous current vector from  $\vec{i} \rightarrow \vec{i} + \Delta \vec{i}$  over a time interval  $\Delta T$  in terms of the direction and amplitude. This may be observed from the example given in Fig. 3.11. This figure

shows a rotating voltage vector  $\vec{u}_e$  at a given point in time, which is arbitrarily positioned between two (adjacent) active converter vectors  $\vec{u}_{\{001\}}$  and  $\vec{u}_{\{110\}}$  (shown in red). Under these conditions, there are four converter vectors (which includes two zero vectors) that can be utilized by the current controller to change the direction of the instantaneous current. Note that the variable  $\Delta T$  determines the actual magnitude of current change in a particular direction as may be observed from (3.11) and Fig. 3.11.

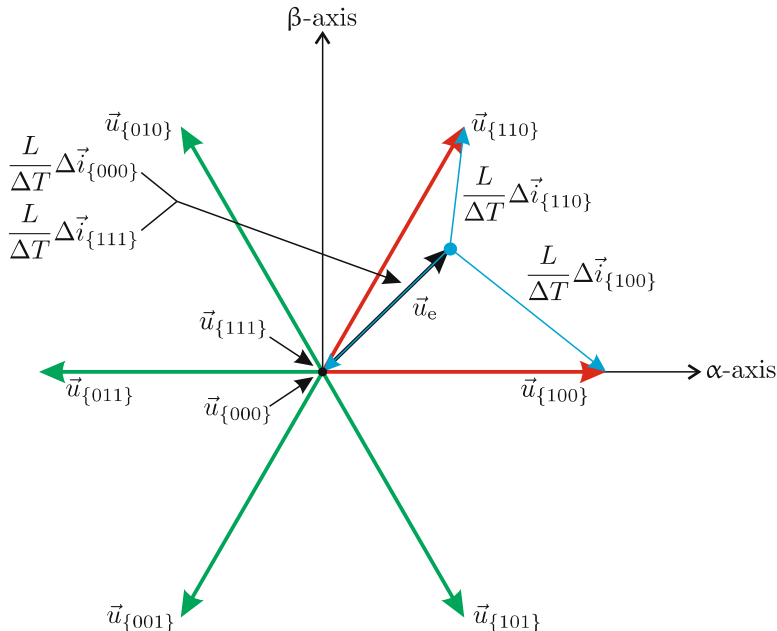


**Fig. 3.11** Choice of incremental current  $\Delta \vec{i}$  vectors

In terms of achieving three-phase current control, two specific techniques are possible. The first, as used for hysteresis type control, is to track the locus of the measured current and compare its trajectory relative to the reference current vector trajectory. The error current vector ( $\vec{i}^* - \vec{i}$ ) may be used in conjunction with a user defined boundary box to select the appropriate active or zero voltage vector needed to hold to the absolute current error within user defined limits. An alternative approach for regularly sampled systems, i.e., those which utilize a fixed sampling time  $T_s$ , is to identify the vector current error at the start of the interval and calculate the required average voltage reference vector  $\vec{U}^*(t_k)$  needed to drive this error to zero at the end of said interval. This model based current control type of approach, as applied to a single-phase system in the previous section, can be readily extended to three-phase systems. The three-phase PWM modulator as discussed in the previous chapter identifies the required active and zero vectors as well as the

duration for which these should be active during a sampling interval  $T_s$ , as will become apparent in Sect. 3.2.2.

### 3.2.1 Three-Phase Hysteresis Current Control

For this type of control, a current control module is required as given in Fig. 3.12, which has as inputs the measured current vector  $\vec{i}$ , reference current vector  $\vec{i}^*$  and load voltage vector  $\vec{u}_e$ . The *load* module consists of three star connected load phases. Each phase is represented by a resistive/inductance network and load voltage  $u_e$ , as discussed in the previous chapter. In this case, the load voltage vector  $\vec{u}_e$ , which represents the three-phase shifted load phase voltages is used as a reference for the synchronous current controller (see Fig. 3.10). However, in drive applications an estimated flux vector is commonly used for this purpose, as will become apparent at a later stage. The controller outputs are the three converter switch signals  $Sw^a$ ,  $Sw^b$ ,  $Sw^c$ .

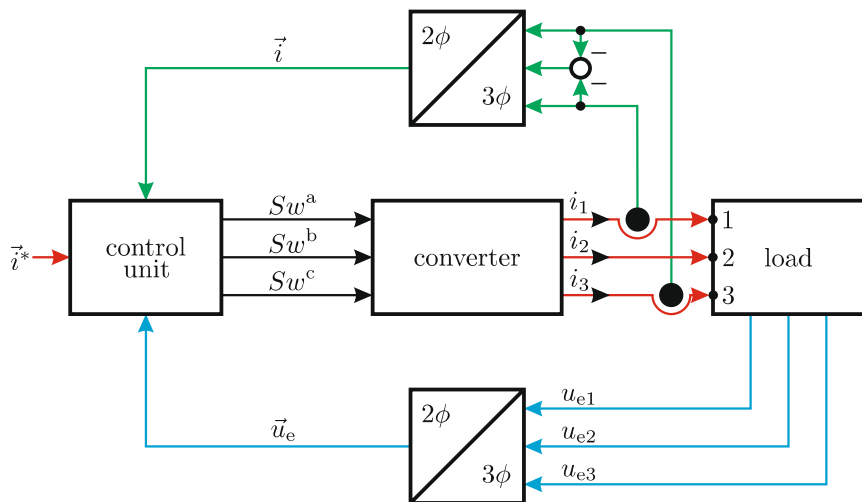


**Fig. 3.12** Three-phase hysteresis current control

(as defined in the previous chapter), which in effect identify the voltage vector  $\vec{u}_{\{Sw^a, Sw^b, Sw^c\}}$  and its required duration  $\Delta T$  to minimize the error between measured and reference current vectors.

The subject of hysteresis type current control for three-phase voltage source converters has received considerable attention in literature [8, 25, 43]. Consequently, there are a variety of algorithms which are able to perform hysteresis type current control. In this book, a hysteresis control approach is considered which is referred to as the *box* method [67]. This method utilizes

the current error  $\vec{i}_\delta$  in a synchronous reference frame that is tied to the orthogonal vectors  $\vec{u}_e$ ,  $\vec{\psi}_e$ , as shown in Fig. 3.10. The generic representation of this control concept, as given in Fig. 3.13, shows the coordinate conversion of the measured current vector to a synchronous reference frame. The orientation of this reference frame is realized with the aid of the voltage vector  $\vec{u}_e$  and a Cartesian to polar conversion module which identifies the instantaneous angle of vector  $\vec{u}_e$  with respect to a stationary reference frame. The imaginary axis of the synchronous frame controller is to be aligned with the voltage vector  $\vec{u}_e$ . Consequently, a phase angle shift of  $-\pi/2$  rad is introduced in the generic module to arrive at the required reference angle  $\rho_e$  for the direct axis of the synchronous reference frame. Also shown in Fig. 3.13 is a *box*

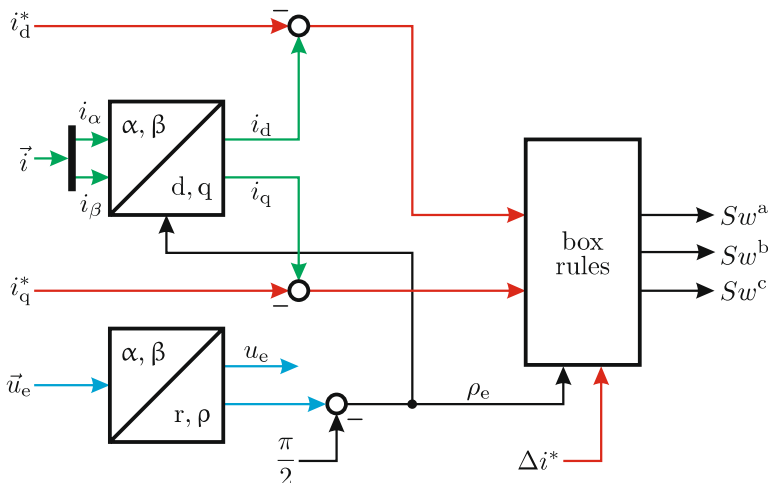


**Fig. 3.13** Generic diagram of the hysteresis, *box method* type controller

*rules* module which generates the required converter vector  $\vec{u}_{\{Sw^a, Sw^b, Sw^c\}}$  (in terms of the required converter switch states  $Sw^a, Sw^b, Sw^c$ ) on the basis of a direct and quadrature current error, defined as  $(i_d - i_d^*)$  and  $(i_q - i_q^*)$  respectively.

The process of selecting the appropriate voltage vector  $\vec{u}_{\{Sw^a, Sw^b, Sw^c\}}$  may be explained with the aid of Fig. 3.14. Shown in Fig. 3.14 are the eight converter voltage vectors, together with an arbitrarily chosen voltage vector  $\vec{u}_e$ , which in turn is linked to the flux vector  $\vec{\psi}_e$ . Tied to the current reference vector is a *box* shaped contour with sides numbered 1 to 4. These sides represent the boundary within which the instantaneous measured current vector  $\vec{i}$  should be held by the controller.

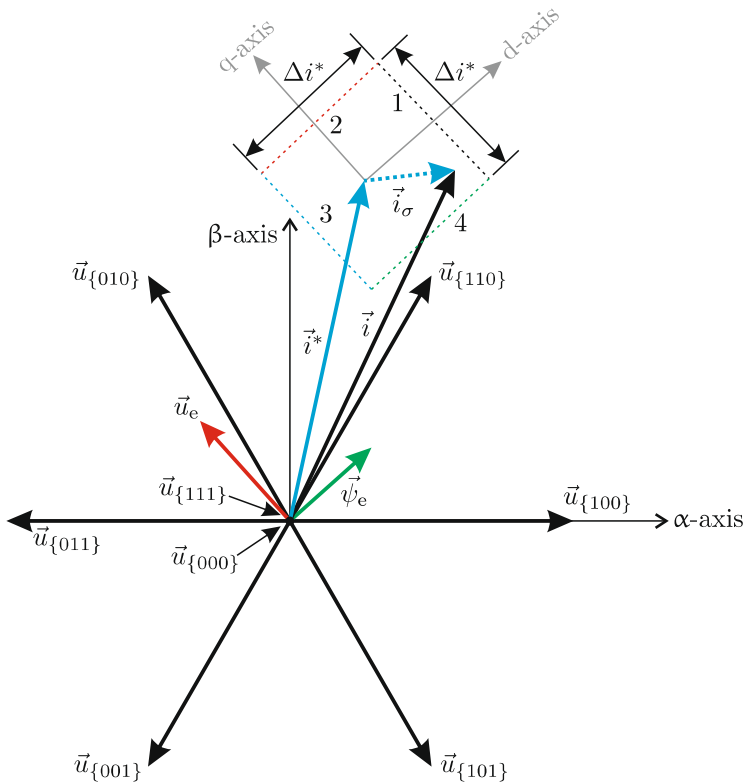


**Fig. 3.14** Switching algorithm for a hysteresis, *box method* type controller

The *box* is oriented with respect to the synchronous reference frame, as may be seen by the presence of the direct and quadrature axes shown in the box. These dq-axes match the orientation of the vectors  $\vec{u}_e$  and  $\vec{\psi}_e$  as may be observed from Fig. 3.14. Of key importance for the box method is to consider the vector endpoint of the error vector  $\vec{i}_\delta$  with respect to its location within the box, the size of which is determined by the variable  $\Delta i^*$ . If the error vector endpoint is located within the box, no action of the controller is taken. However, if the error vector endpoint meets or exceeds one of the four numbered boundaries of the box, specific action is undertaken namely at:

- Boundary 1: Check if the active vector  $\vec{u}_{\{Sw^a, Sw^b, Sw^c\}}$  currently in use *lags* the vector  $u_e$ . If this is the case, select the next *counter clockwise* active vector. If for example vector  $\vec{u}_{\{010\}}$  is the active vector in use, the controller would switch to vector  $\vec{u}_{\{011\}}$  when boundary 1 was encountered by the error vector endpoint.

- Boundary 2: Check which active vector  $\vec{u}_{\{Sw^a, Sw^b, Sw^c\}}$  is in use and switch to the nearest (with the minimum number of switching actions) zero vector. If for example vector  $\vec{u}_{\{010\}}$  is the active vector, then the controller would switch to zero vector  $\vec{u}_{\{000\}}$ , when boundary 2 was encountered by the error vector endpoint.
- Boundary 3: Check if the active vector  $\vec{u}_{\{Sw^a, Sw^b, Sw^c\}}$  currently in use leads the vector  $u_e$ . If this is the case, select the next clockwise active vector. If for example vector  $\vec{u}_{\{011\}}$  is the active vector in use, the controller would switch to vector  $\vec{u}_{\{010\}}$ , when boundary 3 was encountered by the error vector endpoint.
- Boundary 4: Check which active vector  $\vec{u}_{\{Sw^a, Sw^b, Sw^c\}}$  was used last and reactivate this vector. For example, if vector  $\vec{u}_{\{010\}}$  was active prior to encountering the zero vector  $\vec{u}_{\{000\}}$ , then the controller would switch to vector  $\vec{u}_{\{010\}}$ , when boundary 4 was encountered by the error vector endpoint.

The motivation behind the *box rules* can be understood by considering the current trajectory that will occur when for example an active or zero converter vector  $\vec{u}_{\{Sw^a, Sw^b, Sw^c\}}$  is selected. From Fig. 3.11 it may be observed that the incremental current vector  $\Delta \vec{i}$  is proportional to the vector  $(\vec{u}_{\{Sw^a, Sw^b, Sw^c\}} - \vec{u}_e)$ . This implies that the use of the active vector  $\vec{u}_{\{010\}}$  (see Fig. 3.14) would cause the current vector  $\vec{i}$  to move towards boundary 1. When boundary 1 is reached, the current direction must be changed, which for  $\omega_e > 0$  means activating converter vector  $\vec{u}_{\{011\}}$ . This is precisely the action taken by box boundary rule 1. Note that, for this rule, action is only undertaken provided that the currently active converter vector is lagging. The reason for this rule is that lagging vectors are capable of yielding an incremental current vector direction which will head towards the general direction of boundary 1. The reasoning outlined above can be similarly applied to understand the motivation for the remaining box rules.

The tutorial in Sect. 3.3.3 demonstrates this type of current control. The reader is urged to examine this tutorial and in particular view the reference current vector locus and actual current vector locus which appears during the course of this simulation. An example of the results achieved with this simulation are shown in Fig. 3.15. In this example, the direct axis and quadrature reference current were set to  $i_d^* = 0$  A and  $i_q^* = 15$  A respectively, while the error reference value  $\Delta i^*$  was taken to be 4.4 A. Hence, in this example, the reference current vector  $\vec{i}^*$  is aligned with the vector  $\vec{u}_e$ . Furthermore, a constant amplitude voltage vector  $\vec{u}_e$  is assumed which rotates at a speed of 3000 rpm. Shown in Fig. 3.15 are the current locus  $\vec{i}(t)$  and reference current locus  $\vec{i}^*(t)$  (red trace) for one 20 ms cycle of operation. An observation of Fig. 3.15 shows that the current controller is able to maintain the current within the limits of the box.

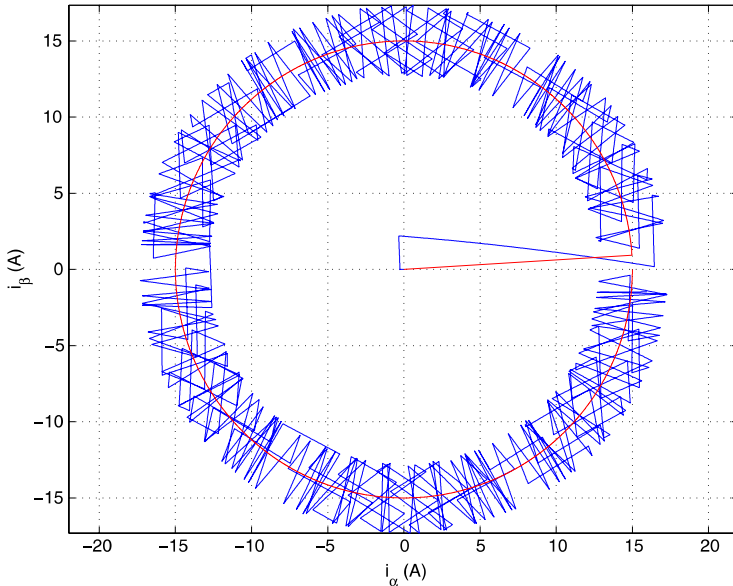


**Fig. 3.15** Current locus of the hysteresis *box method* example

The example discussed here assumes an analog control structure, but a digital implementation is equally feasible. With a digital implementation, the error vector can exceed the limits of the box, because changes to the trajectory will take place once during each sample. Furthermore, the measured current locus is built from a set of sub-trajectories which have a specified direction, as discussed earlier (see Fig. 3.11). It is instructive to consider the current error vector  $\vec{i}_\delta$ , for this example in a synchronous reference frame, i.e., with respect to the box shown in Fig. 3.14.

Figure 3.16 shows part of the 20 ms current error vector trace (green trace). Also shown in this figure is part of this trace (red trace), which is numbered to explain the sequence of actions undertaken by the controller. It is helpful in this context to note again that the error reference value  $\Delta i^*$  was taken to be 4.4 A and this determines the size of the box. Clearly observable from Fig. 3.16 is the fact that the measured current trace is kept within the box. The actions of the controller are in accordance with the *box rules* given earlier. Nonetheless it is instructive to examine the numbered trajectory in some detail. During current locus leg 1, an active vector has been selected which drives the error vector  $\vec{i}_\delta$  to the *top* limit (boundary 2 in Fig. 3.14) of the box. When this boundary is reached, a zero vector is activated, which results in current locus leg 2. When the *bottom* limit (boundary 4 in Fig. 3.14) of the box is reached, the controller switches back to the last active vector, i.e., the vector which was active for locus leg 1. Locus leg 3 is now active and the sequence of events described above repeats. This implies that during locus

leg 4 a zero vector is active and the last active vector is selected during leg locus 5. This locus leg meets the *left* box limit (boundary 3 in Fig. 3.14) where the active voltage vector is switched anti-clockwise by  $\pi/3$  rad, which results in locus leg 6. This locus leg meets the *right* box limit (boundary 4 in Fig. 3.14) in which case the active vector is switched clockwise by  $\pi/3$  rad leading to locus leg 7.

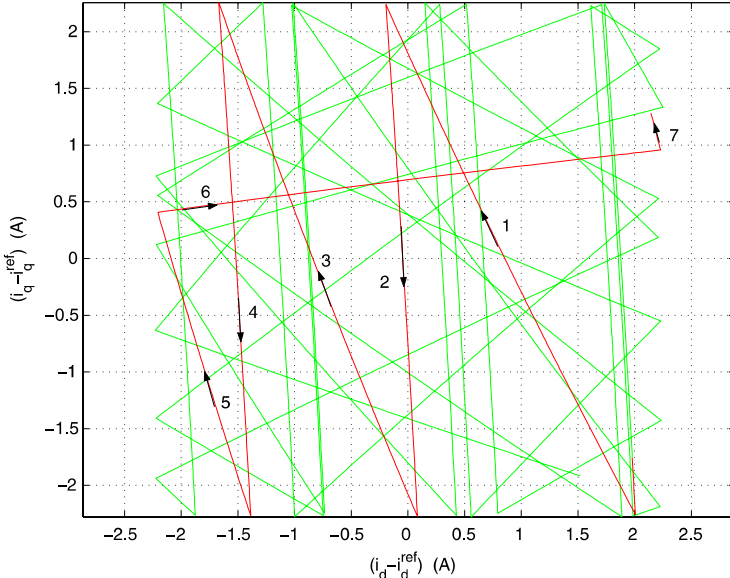


**Fig. 3.16** Current locus, hysteresis, *box method* example, current error

In the following, attention is given to the fact that trajectories with an active zero vector are slanted relative to the vertical axis of the plot shown in Fig. 3.16. A detailed explanation of the phenomenon is given below for those readers which have a desire or need to comprehend this issue. Note, however, that this effect does not affect the hysteresis control concept in a significant way. There may be an expectation that the trajectories in question should coincide with the *vertical* (*q*-axis) of the plot because the use of a zero vector leads to an error current trajectory which is in the direction of  $-\vec{u}_e$ , as indicated in Fig. 3.11. From a stationary reference frame perspective this is indeed the case. However, in a synchronous reference frame, the trajectory differs as may be explained with the aid of (3.10). This expression may also be written in terms of a synchronous reference frame namely

$$\bar{u}_{\{Sw^a, Sw^b, Sw^c\}}^{dq} = L \frac{d\vec{i}^{dq}}{dt} + j\omega_e L (\vec{i}^*)^{dq} + R (\vec{i}^*)^{dq} + \bar{u}_e^{dq} \quad (3.12)$$

where  $\vec{u}_e^{dq}$  is equal to  $ju_e$  and  $\omega_e$  represents the rotational frequency of the synchronous reference frame as mentioned earlier. To examine the direction of the incremental current for the case when the zero vector is active, it is helpful to rewrite  $(\vec{i}^*)^{dq}$  in the form of its direct and quadrature components  $i_d^*$  and  $i_q^*$  and ignore the resistive component (as undertaken with (3.10)), which after some manipulation gives

$$\Delta \vec{i}_0^{dq} \simeq \frac{\Delta T}{L} [\omega_e L i_q^* - j(\omega_e L i_d^* + u_e)] \quad (3.13)$$

In (3.13),  $\Delta \vec{i}_0^{dq}$  represents the current trajectory (in dq coordinates) which will occur when a zero vector is selected. Equation (3.13) shows that this current trajectory will be in the direction of the negative quadrature axis when  $i_q^* = 0$ . However, in the general case, the trajectory will be rotated, counter clockwise with respect to the *negative* quadrature axis by an angle  $\rho_0$  which, according to (3.13), equals

$$\rho_0 \simeq \arctan \left( \frac{L i_q^*}{L i_d^* + \psi_e} \right) \quad (3.14)$$

where  $\psi_e = u_e/\omega_e$  represents the amplitude of the flux vector  $\vec{\psi}_e$  (see Fig. 3.14). In the example shown in Fig. 3.16, the direct current reference value was set to zero  $i_d^* = 0$  and  $L i_q^*$  was chosen small in comparison to  $\psi_e$ . Consequently, the locus rotation as defined by (3.14) is relatively small. However, in some applications this rotation  $\rho_0$  of the current trajectory may become large. In this case, additional measures (which are outside the scope of this book) need to be taken in terms of the orientation of the box (see Fig. 3.14) in order for the *box method*, described in this section, to work satisfactorily.

### 3.2.2 Model Based Three-Phase Current Control

The approach used to obtain the generic controller structure for a three-phase load is very similar to the method described in Sect. 3.1.2, which was concerned with single-phase loads. The drive structure, given in Fig. 3.17 shows a three-phase load, modulator/converter and control module. The first two modules have been discussed. It is noted that a three-phase star connected load is assumed because this provides direct access to the load currents, which can be measured with only two current transducers (a third unit is not needed given that the sum of the currents must be zero for an unconnected star point). The three induced voltages  $u_{e1}$ ,  $u_{e2}$ ,  $u_{e3}$  are also measured as their inputs are required for the controller module. Two *three-phase to two-phase* converter modules are used to transform the measured variables to space vector form.

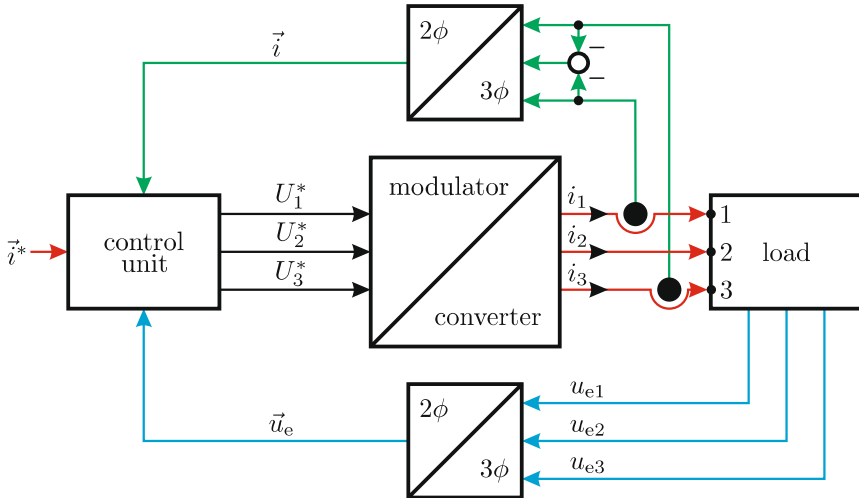


**Fig. 3.17** Model based three-phase current control

A discrete controller is assumed which should drive the error  $|\vec{i}(t_k + T_s) - \vec{i}^*(t_k)|$  to zero over a sample interval  $T_s$ . The design follows the single-phase approach where condition 3.1 was introduced, which may be rewritten in space vector form as

$$\vec{i}(t_k + T_s) = \vec{i}^*(t_k). \quad (3.15)$$

The task of the controller module is to determine the average voltage reference space vector  $\vec{U}^*(t_k)$  that is needed to satisfy condition 3.15. In Sect. 2.4, attention was given to the modulator/converter module with respect to determining the switching algorithm needed to satisfy the following condition

$$\vec{U}^*(t_k) = \frac{1}{T_s} \int_{t_k}^{t_k + T_s} \vec{u}(\tau) d\tau \quad (3.16)$$

where  $\vec{u}(t)$  represents the load voltage space vector of a star connected load. Each load phase is represented by a generic impedance  $Z$ , which represents a symmetric  $R, L, u_e$  circuit, similar as was discussed in the previous chapter. This implies that the load space vector may be expressed as

$$\vec{u} = R \vec{i} + L \frac{d\vec{i}}{dt} + \vec{u}_e. \quad (3.17)$$

The introduction of a synchronous reference frame, as shown in Fig. 3.10, is helpful from a control perspective, as was mentioned at the beginning of this chapter. Transformation of the vectors  $\vec{u}, \vec{i}, \vec{u}_e$  to this complex plane requires use of the general vector transformation  $\vec{x}^{dq} = \vec{x} e^{-j\rho_e}$ , in which case (3.16) can be rewritten as

$$(\vec{U}^{\text{dq}})^*(t_k) \frac{1}{1 - j\omega_e T_s} = \frac{1}{T_s} \int_{t_k}^{t_k + T_s} \vec{u}_s^{\text{dq}}(\tau) d\tau. \quad (3.18)$$

The sampling frequency  $1/T_s$  is normally much higher than the vector rotation speed  $\omega_e$  in which case the term  $1/(1 - j\omega_e T_s)$  can be taken at unity value. Transformation of the load (3.17) to a synchronous reference frame leads to

$$\vec{u}^{\text{dq}}(t) = R \vec{i}^{\text{dq}} + L \frac{d\vec{i}^{\text{dq}}}{dt} + \vec{u}_e^{\text{dq}} + j\omega_e L \vec{i}^{\text{dq}} \quad (3.19)$$

Substituting (3.19) into (3.18) and combining the real and imaginary terms of the latter yields

$$\begin{aligned} U_d^*(t_k) &= \frac{R}{T_s} \int_{t_k}^{t_k + T_s} i_d(\tau) d\tau + \frac{L}{T_s} \int_{i_d(t_k)}^{i_d(t_k + T_s)} di_d \\ &\quad - \frac{1}{T_s} \int_{t_k}^{t_k + T_s} \omega_e L i_q(\tau) d\tau, \end{aligned} \quad (3.20a)$$

$$\begin{aligned} U_q^*(t_k) &= \frac{R}{T_s} \int_{t_k}^{t_k + T_s} i_q(\tau) d\tau + \frac{L}{T_s} \int_{i_q(t_k)}^{i_q(t_k + T_s)} di_q \\ &\quad + \frac{1}{T_s} \int_{t_k}^{t_k + T_s} (\omega_e L i_d(\tau) + u_e(\tau)) d\tau. \end{aligned} \quad (3.20b)$$

A comparison of (3.4) and (3.20) shows that the three-phase control problem has been reduced to two single-phase control problems. This means that the discretization technique developed in Sect. 3.1.2 for the single-phase case may be directly applied to (3.20), which gives

$$\begin{aligned} U_d^*(t_k) &\cong R \sum_{ij=0}^{ij=k-1} (i_d^*(t_{ij}) - i_d(t_{ij})) \\ &\quad + \left( \frac{L}{T_s} + \frac{R}{2} \right) (i_d^*(t_k) - i_d(t_k)) \\ &\quad - \omega_e L i_q(t_k), \end{aligned} \quad (3.21a)$$

$$\begin{aligned} U_q^*(t_k) &\cong R \sum_{ij=0}^{ij=k-1} (i_q^*(t_{ij}) - i_q(t_{ij})) \\ &\quad + \left( \frac{L}{T_s} + \frac{R}{2} \right) (i_q^*(t_k) - i_q(t_k)) \\ &\quad + \omega_e L i_d(t_k) + u_e(t_k). \end{aligned} \quad (3.21b)$$

The generic diagram which corresponds to the control equation set (3.21a) and (3.21b) is given in Fig. 3.18. The diagram in question represents an embodiment of the control unit shown in Fig. 3.17.

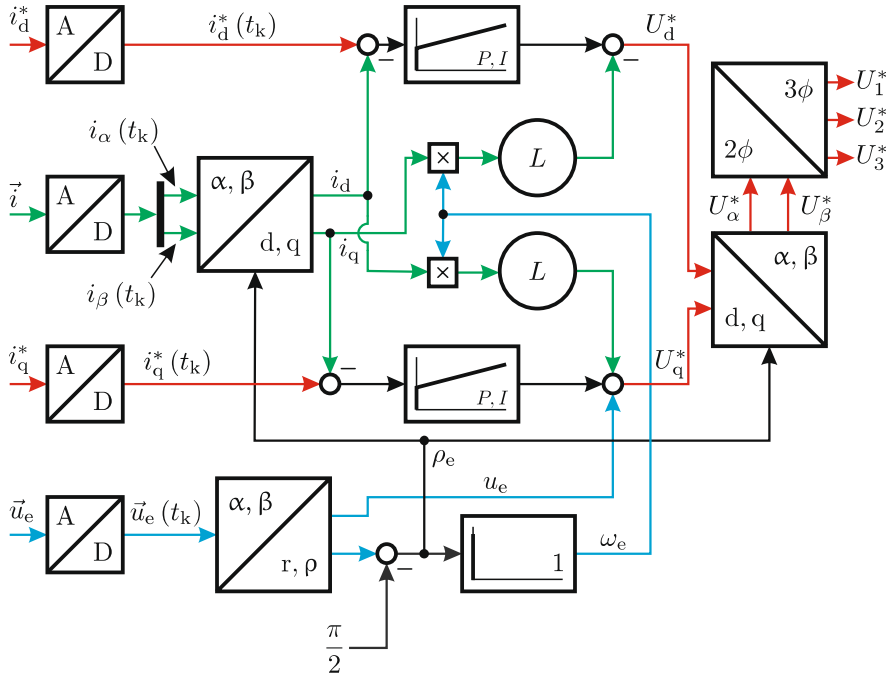


**Fig. 3.18** Model based three-phase controller structure

The PI gain settings  $K_p$  and  $K_i$  for the two current controllers are, as may be observed from (3.21a) and (3.21b), identical to those found for the single-phase case (see (3.9)). However, the  $dq$  disturbance decoupling terms are different, as may be observed from Fig. 3.18. Clearly identifiable are the terms with gain  $L$  which serve to decouple the direct axis (active) and quadrature axis (reactive) current components. Also present is the back-EMF voltage term  $u_e$  which appears in the quadrature axis. Furthermore, a differentiator module is used to determine the frequency  $\omega_e$  of the load vector  $\vec{u}_e$  or flux vector  $\vec{\psi}_e$ . In a mains connected load configuration, the frequency  $\omega_e$  is known and the controller structure can be simplified by omitting of the discrete differentiator module. Also shown in Fig. 3.18 are the two conversion modules used to generate the three average voltage phase references, which form the inputs to the modulator module.

It is noted that the current reference  $\vec{i}^*$  shown in Fig. 3.17 is formed by the direct and quadrature reference components  $i_d^*$  and  $i_q^*$  as shown in Fig. 3.10. Access to the direct and quadrature reference values  $(i_d^*, i_q^*)$  provides the user with the ability to control the position of the reference current vector (and thereby the actual current given condition 3.15) with respect to the flux vector  $\vec{\psi}_e$ . From a power definition perspective, control of the variables  $(i_d^*, i_q^*)$  gives the ability of controlling the real and reactive power components with respect

to the voltage vector  $\vec{u}_e$ . For most controller structures to be considered for electrical machines, the use of a flux vector will be of paramount importance, as will become apparent in this book. Given its perceived importance, the generic structure of the flux oriented model based current controller is shown in Fig. 3.19. A comparison between the voltage and flux oriented control structures shows that in the latter case the back-EMF voltage term  $u_e$  (see (3.21b)) is computed using  $u_e = \psi_e \omega_e$ .

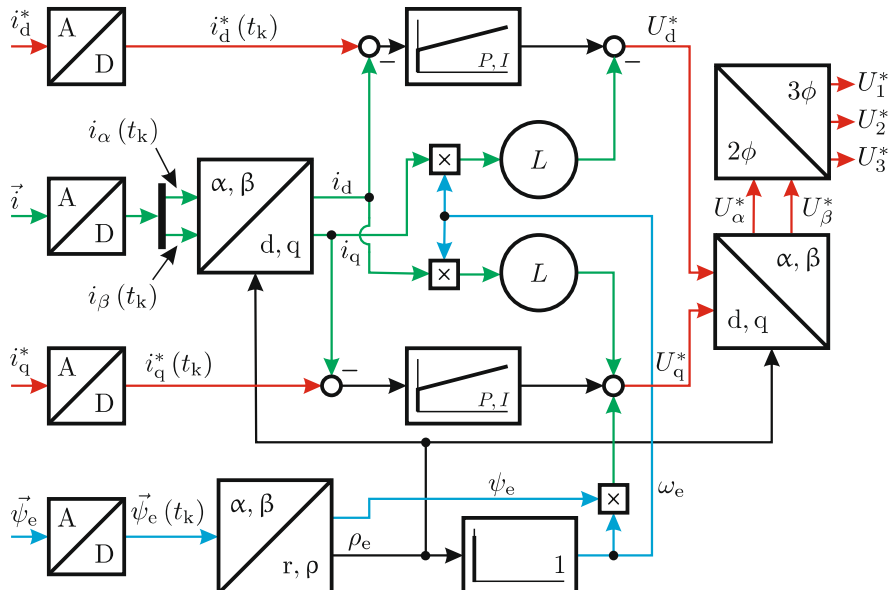


**Fig. 3.19** Model based three-phase, flux oriented controller structure

A detailed tutorial of the concepts outlined in this section is given in Sect. 3.3.4. This example, which is based on the model according to Fig. 3.18, is identical to that discussed for the three-phase hysteresis case, in terms of the load and direct/quadrature reference current setting, namely  $i_d^* = 0\text{ A}$ ,  $i_q^* = 15\text{ A}$  (reference vector  $\vec{i}^*$  aligned with the vector  $\vec{u}_e$ , which rotates at 3000 rpm). However, in this case, a modulator and controller structure were added as represented by Fig. 2.12 and Fig. 3.18 respectively. The sample and PWM carrier frequencies were set to 5 kHz and 2.5 kHz respectively. The values chosen are lower than normally used in practice, to clearly visualize the current endpoint trajectories. An example of the reference and actual current vector endpoint trajectories are given in Fig. 3.20 for one period of the fundamental component (one 20 ms rotation of the voltage vector  $\vec{u}_e$ ).

It is instructive to compare the results achieved with this type of control, as indicated by Fig. 3.20, with those obtained with the three-phase hysteresis type controller (see Fig. 3.15). With the model based controller, the current

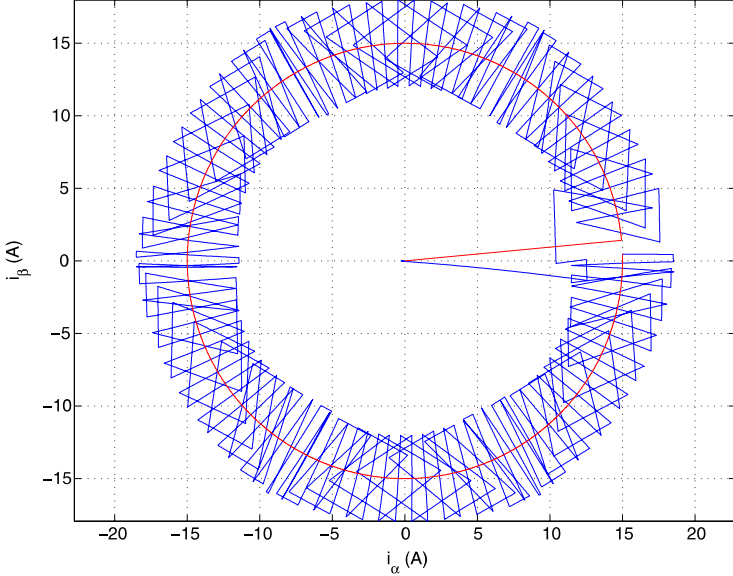


**Fig. 3.20** Current locus, model based control example

error is not specifically defined, but instead is governed by the load parameters and choice of sample and carrier frequencies. The present combination of these variables is such that an absolute current error is apparent in Fig. 3.20 that is larger than the one that was seen in Fig. 3.15. The other noticeable difference between the two current  $\vec{i}$  endpoint trajectories lies with the sequence and duration of active and zero voltage vectors for both methods. This may be demonstrated by considering the current error vector  $\vec{i}_\delta = \vec{i} - \vec{i}^*$  in a synchronous reference frame, as undertaken for the hysteresis type control approach. The endpoint locus for the current error  $\vec{i}_\delta$ , as shown in Fig. 3.21, is decidedly different in comparison with the hysteresis type result given in Fig. 3.16.

Figure 3.21 shows the first part of the 20 ms current error vector trace (green trace). Also shown in this figure are the trajectories over a time interval equal to  $2T_s$  of this simulation (red trace). The trajectories are numbered to explain the sequence of actions undertaken by the controller. The subinterval shown in red has been judiciously chosen in such a manner that it approximately coincides with the location of the load vector as shown in Fig. 3.11. The reader is reminded that the q-axis of the synchronous reference is aligned with the vector  $\vec{u}_e$ . Furthermore, in this particular example, the current reference vector  $\vec{i}^*$  is also aligned with this vector. The direction in which the error current endpoint will travel is dictated by the relative position of the load vector  $\vec{u}_e$  with respect to the two active vectors in use. During locus leg 1, the voltage vector  $\vec{u}_{\{110\}}$  is active for a given time interval after which vector

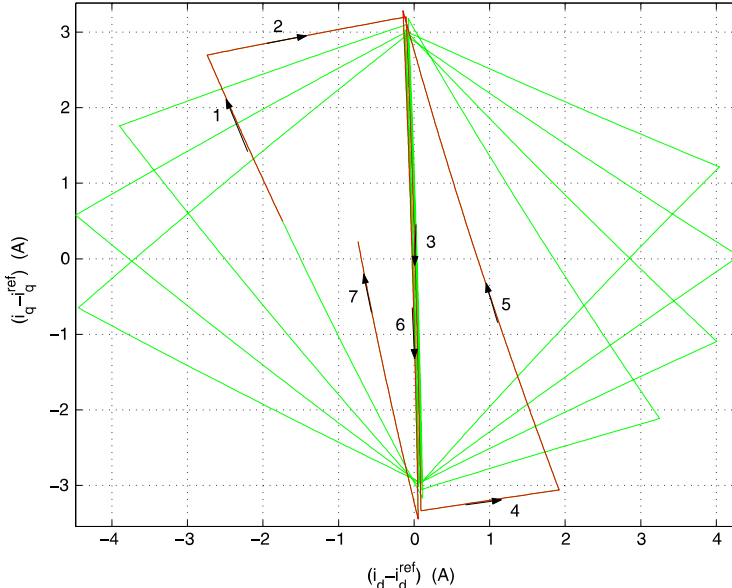


**Fig. 3.21** Current locus, model based control example: current error

$\vec{u}_{\{100\}}$  is activated which leads to the trajectory that corresponds to locus leg 2. With this type of control, typically two active vectors are sequentially activated after which a zero vector time interval occurs (as may be observed in Fig. 2.11(b) during a sample time interval  $t_k \rightarrow t_{k+1}$ ). This sequence of events is also identifiable in Fig. 3.21 in terms of the trajectory identified as locus leg 3. During this leg a zero vector is active, which in turn is followed by the reactivation of the last active vector  $\vec{u}_{\{100\}}$  during locus leg 4. The second active vector  $\vec{u}_{\{110\}}$  is then activated, which gives the trajectory path for locus leg 5. A zero vector is again initiated after every one or two active vectors which results in locus leg 6, which must coincide with leg three, given that the q-axis of the synchronous frame is tied to the voltage vector  $\vec{u}_e$ . After this zero vector has been applied, the active vector  $\vec{u}_{\{110\}}$  is selected, which leads to the trajectory locus leg 7. Note that the current error trajectories of, for example, locus legs 1 and 7 are not identical, despite the fact that they both utilize the same active vector. The reason is that during the course of this time interval the load vector  $\vec{u}_e$  has rotated clockwise with respect to the two active vectors shown in Fig. 3.11. Consequently, the error current direction must change as may be observed from Fig. 3.11. A final observation with respect to Fig. 3.21 is concerned with the trajectory undertaken when a zero vector is activated, i.e., locus legs 3 and 6. A detailed observation of Fig. 3.21 reveals that the trajectory is slanted relative to the vertical axis of the plot by an angle  $\rho_0$ . A similar observation was also made for the hystere-

sis controller and an explanation of this phenomenon was discussed with the aid of (3.14).

### 3.2.3 Augmented Three-Phase Model Based Current Control

The single-phase augmented model based control concept as discussed in Sect. 3.1.3 is extended to the three-phase case in this section. Accordingly, the approach taken to find a discrete representation of the model is similar. In this case, it is advantageous to make use of the synchronous model equation set (3.20). Backward discretization of equation set (3.20) along the lines undertaken for the single-phase case leads to

$$U_{\text{Md}}^*(t_k) \cong R i_d^*(t_k) + \left( \frac{L}{T_s} - \frac{R}{2} \right) (i_d^*(t_k) - i_d^*(t_{k-1})) - \omega_e L i_q^*(t_k), \quad (3.22a)$$

$$U_{\text{Mq}}^*(t_k) \cong R i_q^*(t_k) + \left( \frac{L}{T_s} - \frac{R}{2} \right) (i_q^*(t_k) - i_q^*(t_{k-1})) + \omega_e L i_d^*(t_k) + u_e(t_k). \quad (3.22b)$$

Equation set (3.22) form the basic algorithm which is located in the discretized model shown in Fig. 3.22. Output of this module are the direct and quadrature average voltage references  $U_{\text{Md}}^*(t_k)$  and  $U_{\text{Mq}}^*(t_k)$  which are used, together with the two PI controllers, to calculate the average voltage references  $U_d^*(t_k)$  and  $U_q^*(t_k)$ .

Deviations between the load parameters used in the controller and those actually present are compensated by the two PI controllers. The dynamics which need to be handled by these PI controllers are rather limited because they relate to parameter changes due to, for example, temperature. Hence, the gains can be chosen relatively low. An upper limit for these gains settings are given in equation set (3.21) respectively. A comparison between equation sets (3.22) and (3.21) shows that the discrete model given in Fig. 3.22 contains a number of elements which were also used in the controller shown in Fig. 3.18. However, the discrete model uses four additional terms  $R i_d^*(t_k)$ ,  $R i_q^*(t_k)$  and  $(L/T_s - R/2)(i_d^*(t_k) - i_d^*(t_{k-1}))$ ,  $(L/T_s - R/2)(i_q^*(t_k) - i_q^*(t_{k-1}))$  of which the latter two are current difference type equations which may be susceptible to noise. Consequently, bandwidth restrictions on the direct and quadrature reference current values should be imposed to avoid unwarranted excursions in the variables  $U_{\text{Md}}^*(t_k)$ ,  $U_{\text{Mq}}^*(t_k)$  due to the use of the differential terms present in equation set (3.22). Similarly, the process of generating the estimated rotational speed  $\omega_e$  from the rotor angle  $\rho_e$  by way of a differentiator module (see Fig. 3.22) may also cause unwarranted noise related disturbances in the out-

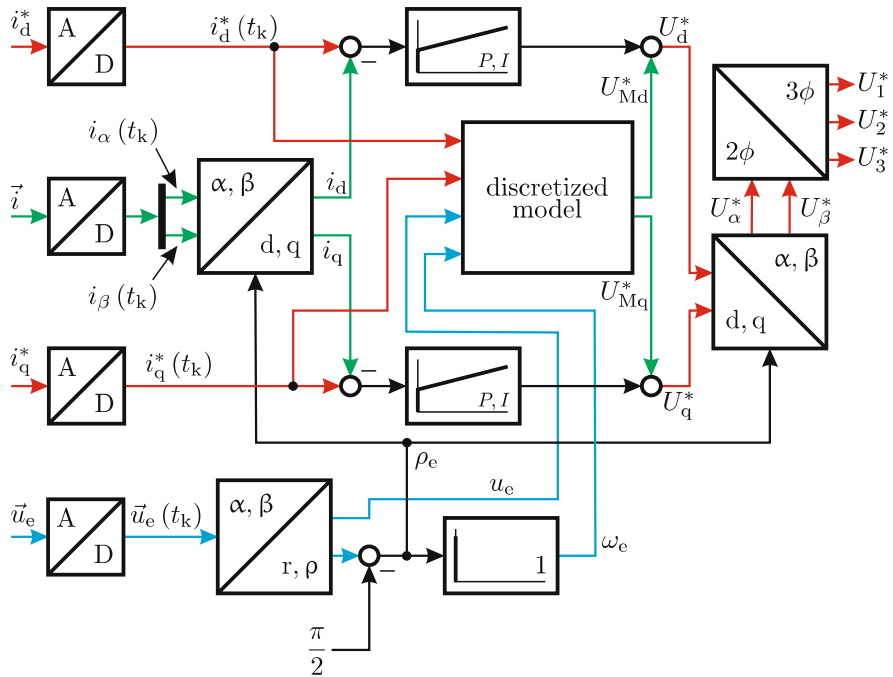


**Fig. 3.22** Augmented model based three-phase controller structure

puts of the discrete model. Note that in three-phase model based control the distinction between an augmented and non-augmented approach is not significant as both implement key decoupling elements of the same discrete model.

### 3.2.4 Frequency Spectrum of Hysteresis and Model Based Current Controllers

Both hysteresis and model based current control techniques are used widely in industry. It is deemed to be helpful for the reader to gain an appreciation of a typical frequency spectrum of the converter phase voltage for both current control methods.

For this purpose, the three-phase hysteresis and model based tutorials, discussed in Sect. 3.3.3 and Sect. 3.3.4 respectively, are analyzed. The load, supply and direct/quadrature reference current conditions for both examples have been chosen identical to compare the frequency spectra of the voltage across one phase of the load. Figure 3.23 shows the spectrum for both control techniques of the phase voltage with respect to the amplitude of the fundamental component over a frequency range  $0 \rightarrow 10\text{kHz}$ .

A general observation of Fig. 3.23 shows that the spectrum, in addition to the 50 Hz fundamental component, of the hysteresis controller approach

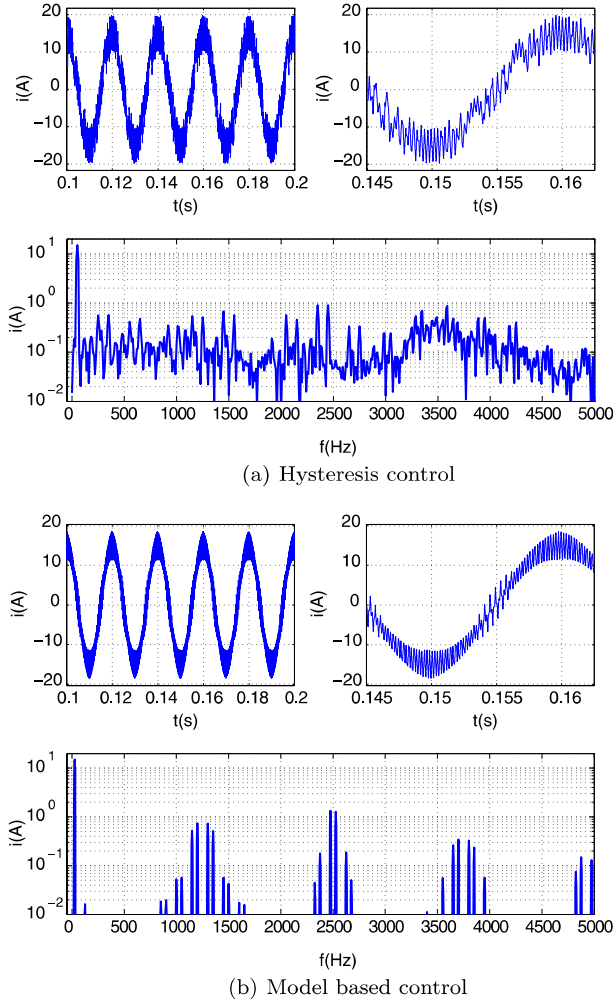


**Fig. 3.23** Frequency spectrum of the converter phase voltage for a three-phase drive operating under hysteresis and model based control

is wide spread in terms of the frequency components. The spectrum which will appear is dependent on the size of the box and the amplitude of the voltage vector  $\vec{u}_e$ . The spectrum of the fixed frequency model based control approach is more discrete in nature. In practice, this is reflected by an acoustical noise signature that is more predictable and can therefore be tuned to the application, for example machine-load combinations, as to avoid specific resonance frequencies [25, 45]. In the example given in Fig. 3.23 the PWM carrier and sample frequency were set to 2.5 kHz and 5.0 kHz respectively, which is reflected in the frequency spectrum shown in Fig. 3.23(b).

### 3.3 Tutorials

#### 3.3.1 Tutorial 1: Single-Phase Hysteresis Current Control

This tutorial is concerned with the implementation of a single-phase half-bridge converter connected to a load. The load is formed by a series connected resistance  $R = 20 \text{ m}\Omega$ , inductance  $L = 100 \text{ mH}$  and a sinusoidal voltage source  $u_e = \hat{u}_e \sin(\omega_e t + \xi_e)$ , with  $\hat{u}_e = 100 \text{ V}$ ,  $\xi_e = -\pi/4 \text{ rad}$  and  $\omega_e = 100\pi \text{ rad/s}$ . The half-bridge converter bus voltage  $u_{DC}$  is set to 300 V. The aim is to build a hysteresis type current controller with a hysteresis setting of  $\Delta i = 0.4 \text{ A}$  in accordance with the generic model shown in Fig. 3.3 so that the user can examine the various waveforms and switching activities as discussed in Sect. 3.1.1. The input current reference for this simulation is taken to be of the form  $i^* = \hat{i} \sin \omega_e t$ , with  $\hat{i} = 2 \text{ A}$ . A simulation model example for this tutorial, as given in Fig. 3.24, shows the half-bridge converter, load and current control structure. In this example, ideal IGBT type semi conductor switches are used. A *current probe* is used to measure the current for the current controller.

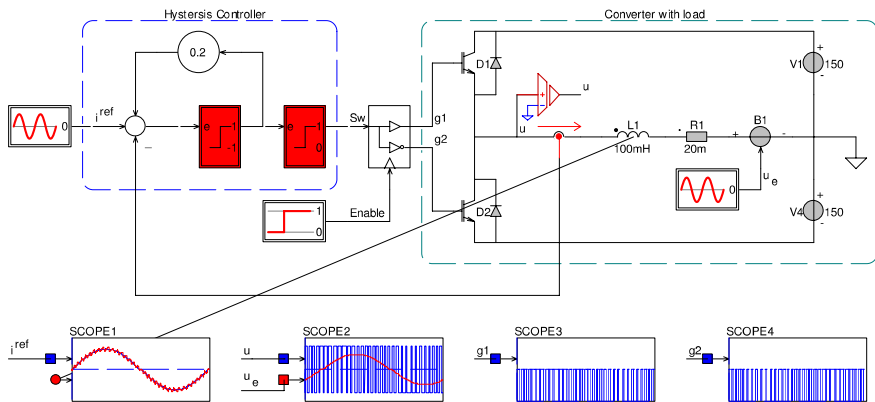


**Fig. 3.24** Simulation of single-phase hysteresis current control

The simulation results of the scope modules is given in Fig. 3.25. As with previous tutorials, a converter enable circuit is put in place to enable the converter switches from a specified time instance. In this example, the converter is enabled at  $t = 0 \text{ ms}$ , while the simulation run time is set to 20 ms. The reader is encouraged to examine closely the signals which appear within this simulation at various nodes to obtain a clear understanding of the operating principles.

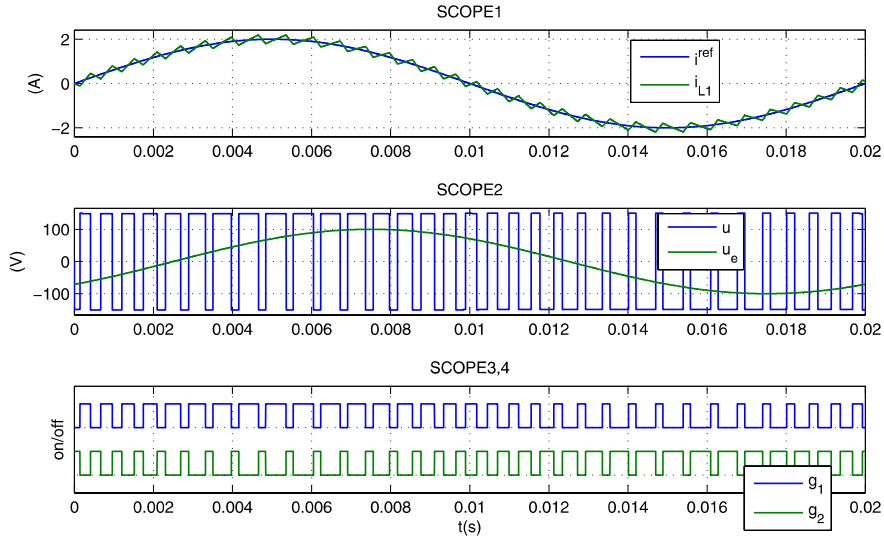


**Fig. 3.25** Simulation result of single-phase hysteresis current control

### 3.3.2 Tutorial 2: Single-Phase Model Based Current Control

A single-phase model based type controller is to be considered with a full-bridge converter/modulator topology that was discussed in Tutorial 2.6.3. The load parameters and current reference setting, as discussed in the previous tutorial, are also to be used for this example. A DC supply voltage  $u_{\text{DC}}$  of 300 V is used. Furthermore, a sampling time of  $T_s = 0.5 \text{ ms}$  is selected, which corresponds with a PWM carrier frequency of 1 kHz. The reader is encouraged to develop a current controller in accordance with the generic model given in Fig. 3.7 and plot the same variables by way of *scope* modules as introduced in the previous tutorial.

An example of a simulation model, as given in Fig. 3.26 shows the required controller structure with the PI controller and the  $u_e$  disturbance term. In the example given, an anti-windup PI controller *PIZ* is introduced of which the output limits are set to  $\pm 300 \text{ V}$ , which is the largest average voltage per sample that can be realized with this converter/supply combination. Inputs to the anti-windup PI controller are the current error and the disturbance decoupling signals. Note that in this example the proportional gain ( $L/T_s + R/2$ ) of the controller is dominated by the inductance term given that  $L/R \gg T_s/2$ , i.e., the time constant  $L/R$  is normally considerably higher than the sampling time.

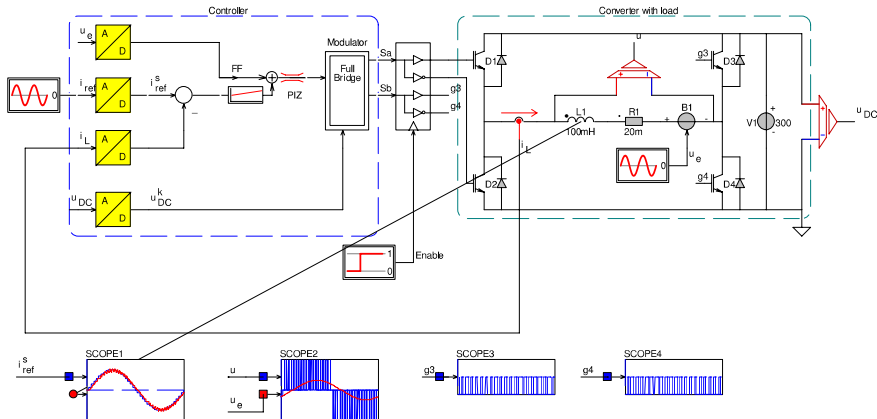


**Fig. 3.26** Simulation of single-phase model based current control

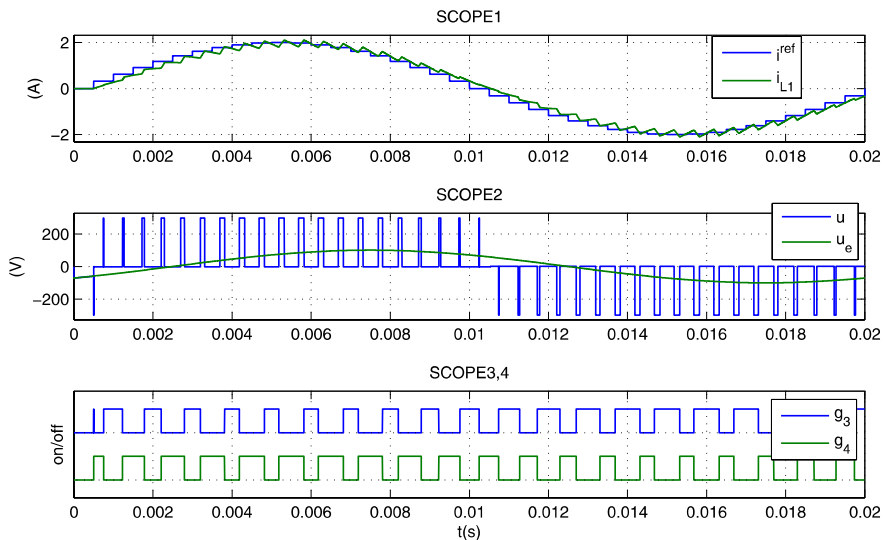


**Fig. 3.27** Simulation results of single-phase model based current control

The results as shown by scope modules in Fig. 3.27 are not significantly different than those obtained with the previous simulation (see Sect. 3.3.1). The control techniques used on the other hand are markedly different.

### 3.3.3 Tutorial 3: Three-Phase Box Method Type Hysteresis Current Control

This tutorial is concerned with the development of a three-phase converter with a *box-method* hysteresis type current control, that is connected to a symmetrical star connected load. Each load phase is formed by a series network formed by a resistance  $R = 20\text{ m}\Omega$ , inductance  $L = 3.4\text{ mH}$  and sinusoidal voltage source with a peak value of  $\sqrt{2} \cdot 150\text{ V}$  and frequency  $\omega_e = 100\pi\text{ rad}$ . In this example, an analog hysteresis *box method* type current controller is to be implemented according to method described in Sect. 3.2.1. Output of this controller should be a set signals:  $Sw^a$ ,  $Sw^b$ ,  $Sw^c$ , which can be used to control the converter switches. The load is to be represented in terms of a space vector based generic model, which must be interfaced to the converter circuit as used in the tutorial outlined in Sect. 2.6.5. A DC bus voltage of  $u_{DC} = 600\text{ V}$  is to be used with the converter. The direct and quadrature current reference values are taken to be  $i_d^* = 0\text{ A}$  and  $i_q^* = 15\text{ A}$  respectively. Furthermore, the box size is to be set to  $\Delta i^* = 4.4\text{ A}$ .

A possible CASPOC based implementation of the this tutorial, as shown in Fig. 3.28, contains the basic IGBT based converter structure which is linked to the space vector based representation of the three-phase load by way of a set of CASPOC based circuit/block conversion modules.

The voltage vector is of the form  $\vec{u}_e = \hat{u}_e e^{j\omega_e t}$ , with  $\hat{u}_e = \sqrt{3} \cdot 150\text{ V}$ . A vector to polar conversion module is used to derive the instantaneous argument of the vector  $\vec{u}_e$ , from which an angle  $\pi/2$  is subtracted to arrive at the reference angle  $\rho_e$  used for the synchronous reference conversion process. The generic load structure generates the *measured* load current vector  $\vec{i}$ , which is converted to a synchronous reference frame with variables  $i_d$  and  $i_q$ . These values are used in conjunction with the synchronous frame based reference currents to arrive at a current vector  $\vec{i}_\delta$ , which is used by the *Box Rules* module as indicated in the generic diagram linked to this control approach (see Fig. 3.13). In this tutorial, this module is represented by the sub-module *Box Rules* which has three outputs that represent the switching signals  $Sw^a$ ,  $Sw^b$ ,  $Sw^c$  for the converter. Note that this module has two additional inputs which are linked to the required box size and the angle  $\rho_e$ . The latter is used for the voltage vector rotation algorithm as discussed in Sect. 3.2.1. The simulation was used to generate the space vector currents  $\vec{i}$ ,  $\vec{i}^*$  and error current vector plot according to Fig. 3.15 and Fig. 3.16 respectively.

The simulation time for this tutorial was set to 20 ms which corresponds to one rotation of the (stationary coordinate oriented) reference current vector  $\vec{i}^*$ . A computation step time of 500 ns is used which has been purposely kept low, given that an analog control approach is in use, i.e., no sample and hold modules are present. The reader is urged to scrutinize the simulation as it unfolds, in particular with respect to the results shown on scopes 6 and 4.

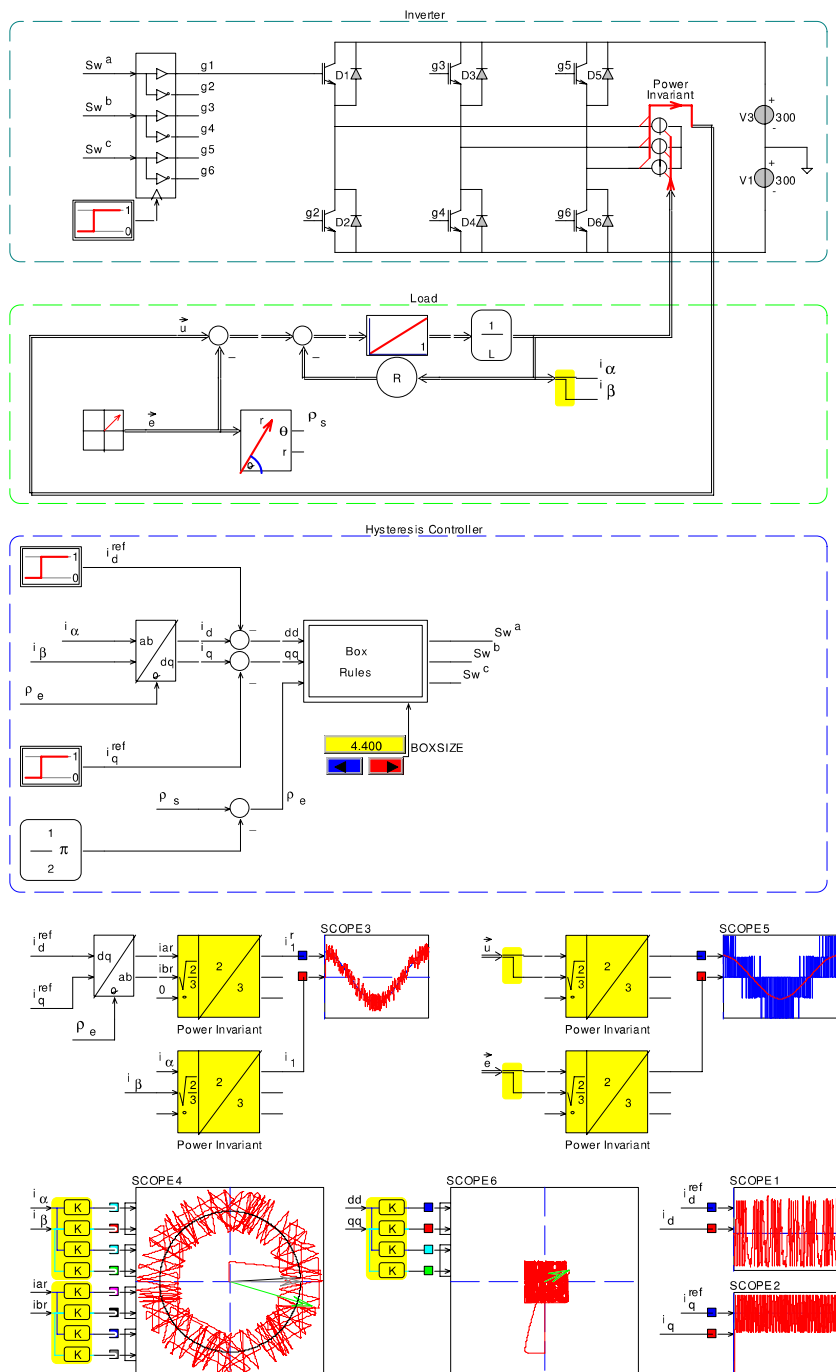
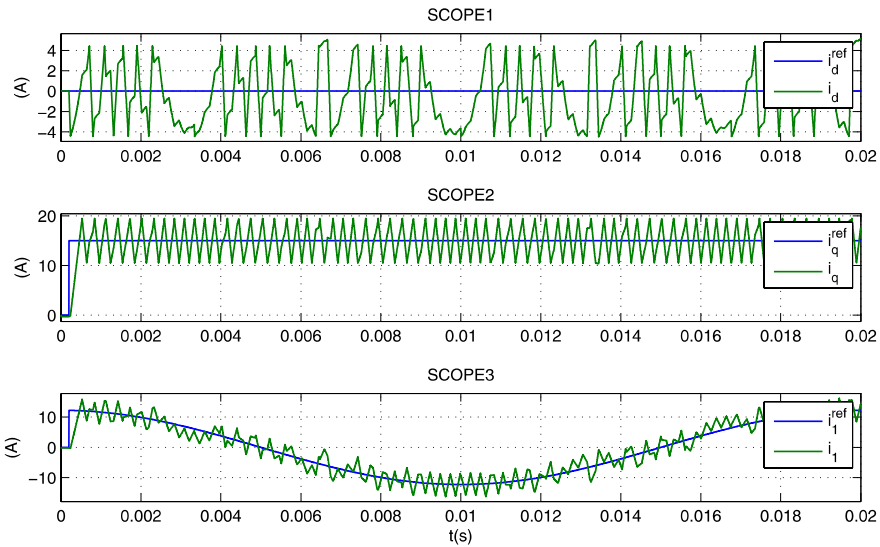
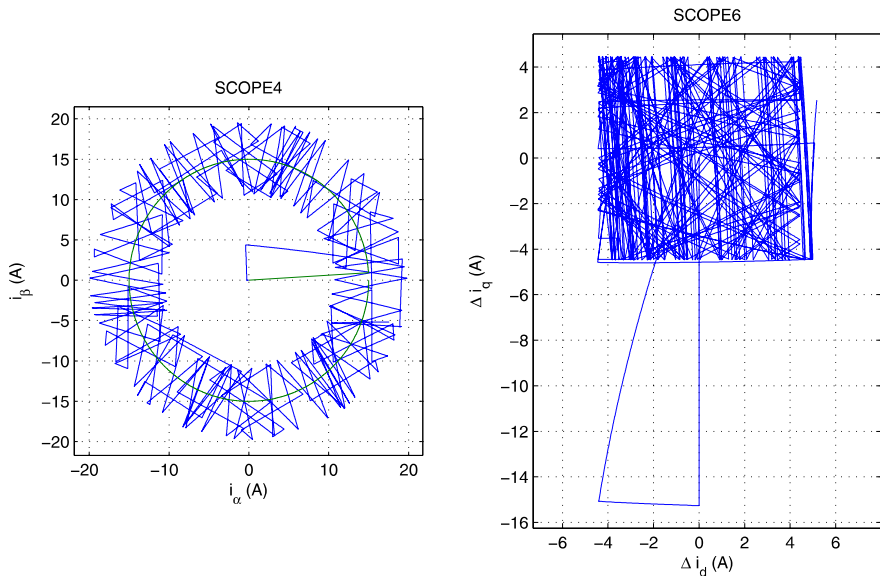


Fig. 3.28 Simulation of three-phase box method type hysteresis current control



**Fig. 3.29** Simulation results of three-phase *box method* type hysteresis current control



**Fig. 3.30** Simulation results of three-phase *box method* type hysteresis current control

### 3.3.4 Tutorial 4: Three-Phase Model Based Current Control

The aim of this tutorial is to replace the hysteresis based current controller as discussed in the previous subsection with a model based type controller as outlined in Sect. 3.2.2. For this purpose the CASPOC based simulation model outlined in tutorial 6, Sect. 2.6.6 is to be modified to accommodate the controller structure as shown in Fig. 3.18. The space vector based load structure that was used in the previous tutorial should also be incorporated in this simulation model. Furthermore, the load parameters, voltage vector  $\vec{u}_e$ , reference current settings and DC converter supply level are to remain unchanged when compared to the previous tutorial. A sample frequency  $1/T_s$  of 5 kHz is to be used, which corresponds to a PWM carrier frequency of 2.5 kHz.

The CASPOC based tutorial, as given in Fig. 3.31, shows the converter and space vector based load components as described in the previous tutorial. Also included in this figure is the three-phase modulator structure that was outlined in Sect. 2.6.6. Most importantly, an embodiment of a model based current controller is shown, which conforms with the generic structure shown in Fig. 3.18. The two PI controllers shown are anti-windup type controllers, as discussed in Sect. 3.3.2, which implies that the output limits must be specified. A convenient choice is to set the value to the length of the active converter vector, namely  $\pm\sqrt{2/3} u_{DC}$ , on the grounds that the output exceed the limits of the hexagon formed by the active converter vectors. The generation of the reference angle  $\rho_e$  from the voltage vector  $\vec{u}_e$  is according to the approach outlined in the previous section. However, in this tutorial a set of sample-and-hold elements are introduced, which implies that the controller utilizes the sampled reference angle  $\rho_e(t_k)$ . A direct consequence of this approach is the fact that the controller based synchronous reference frame lags on average, with respect to the actual reference frame, by an angle  $\omega_e T_s / 2$  rad. This must be compensated in the controller by introducing a phase angle shift of the same value, derived from different signals as shown in Fig. 3.33 yielding  $\rho_{ec}$ . For this simulation, the rotational frequency  $\omega_e$  is assumed to be constant and available for control purposes. The simulation model as described in this section was used to generate current locus plots and current error plots as shown in Fig. 3.20 and Fig. 3.21 respectively.

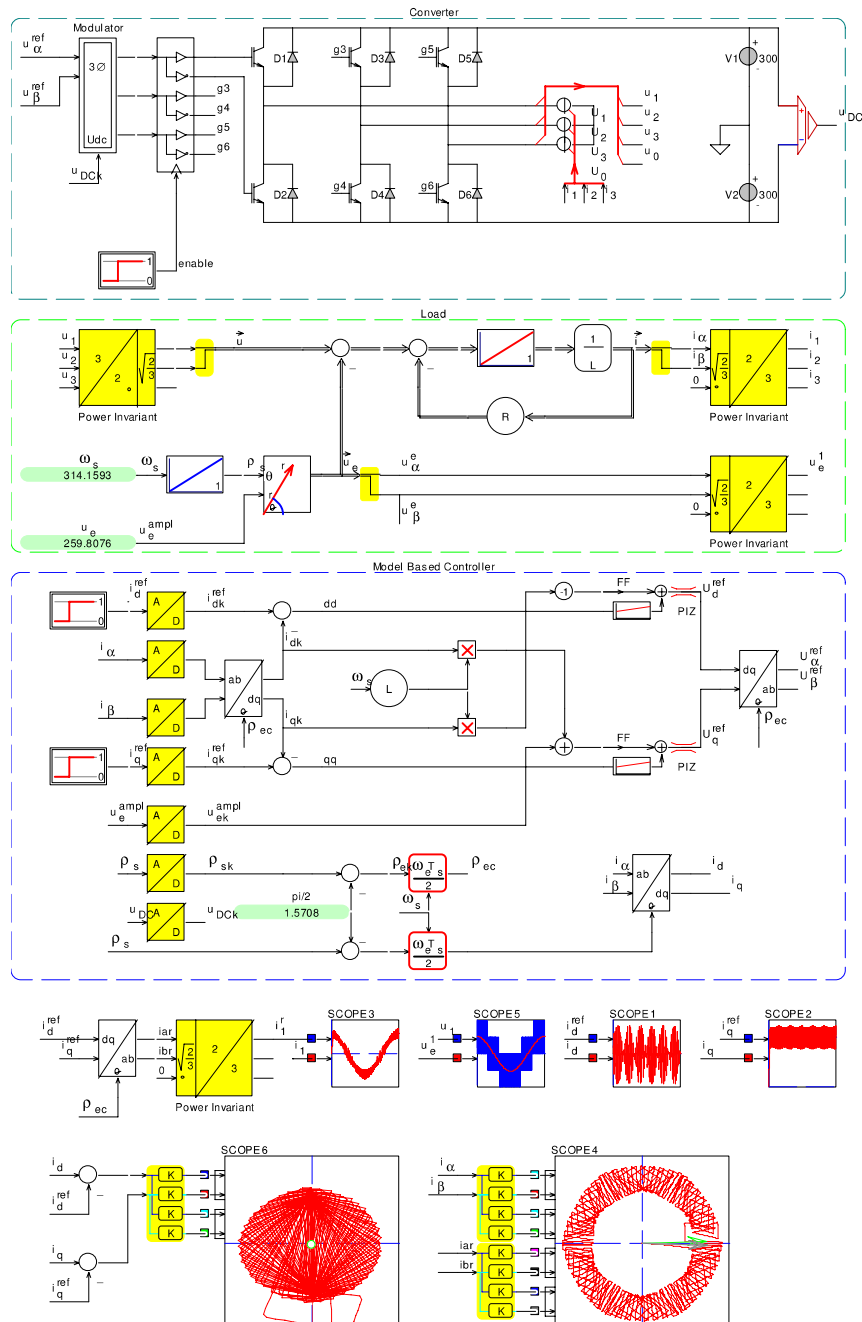
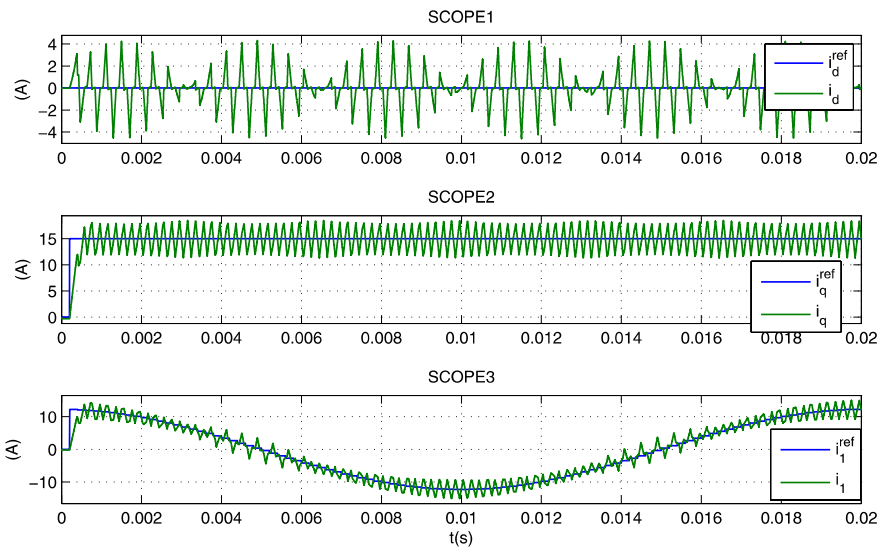
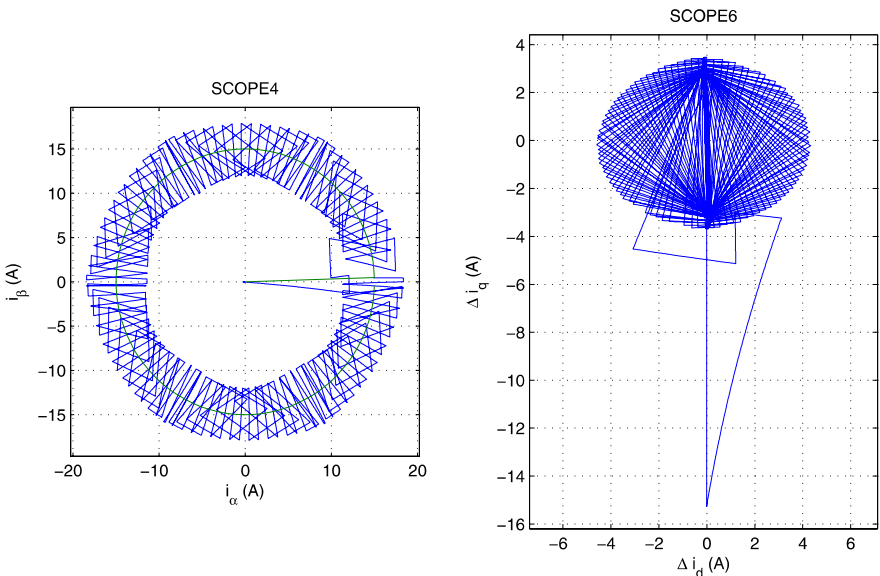


Fig. 3.31 Simulation of synchronous current controller



**Fig. 3.32** Simulation results of synchronous current controller



**Fig. 3.33** Simulation results of synchronous current controller

### 3.3.5 Tutorial 5: Three-Phase Model Based Current Control without PWM, Using Simplified Approach

In the previous tutorial the model based control concept was shown with the aid of a three-phase converter model with ideal semiconductor devices. This simulation approach may be simplified by omitting the modulator/converter structure, using the approach outlined in the tutorial given in Sect. 2.6.6. The aim of this tutorial is to modify the previous tutorial by making use of a set of ‘supply limit’ modules, as discussed in Sect. 2.6.6. In effect, this assumes that the average voltage load vector  $\vec{U}^*(t_k)$ , generated by current controller, corresponds to the load vector generated by the modulator/converter or linear amplifier. The latter will be the case provided that the average voltage half-bridge reference values are maintained within the supply window of the drive. The sampling time and reference current waveforms remain unchanged in comparison with the previous tutorial.

The CASPOC based model shown in Fig. 3.34 meets the requirements of this tutorial. Shown in this figure is an *Modulator* module which contains the pulse centering module and a supply limit. The latter generate the half-bridge voltage reference values, which are now assumed to be equal to those generated by the converter. Consequently, a three-to-two phase conversion module is used to generate the load voltage vector  $\vec{u}$  for the generic space vector based model of the load, as introduced in the previous tutorial. The load resistance and inductance values for the symmetrical load together with the sampling time  $T_s$  and DC bus voltage remain unchanged, in comparison to the previous example. The use of a fixed frequency voltage source allows the feed-forward gains to be simplified to fixed gain units (gain  $\omega_e L$ ). The simulation time remains unchanged and the results obtained with this model as shown in Fig. 3.35, are comparable to those given in Fig. 3.31. However, the converter switching action is not shown due to the use of the three *supply limit* modules. This implies that the role of the controller may be seen more easily, i.e., not masked by the switching actions of the converter. Figure 3.35 (scope 3) shows the reference phase current  $i_1^*$  (blue trace), together with the actual phase current  $i_1$ . The direct and quadrature current reference waveforms are given in Fig. 3.35 (scope 1 and 2 respectively, blue traces), together with the actual currents  $i_d$  and  $i_q$ . Also shown in Fig. 3.35 are the load voltage  $u_1$  (blue trace) and voltage  $u_e^1$  (green).

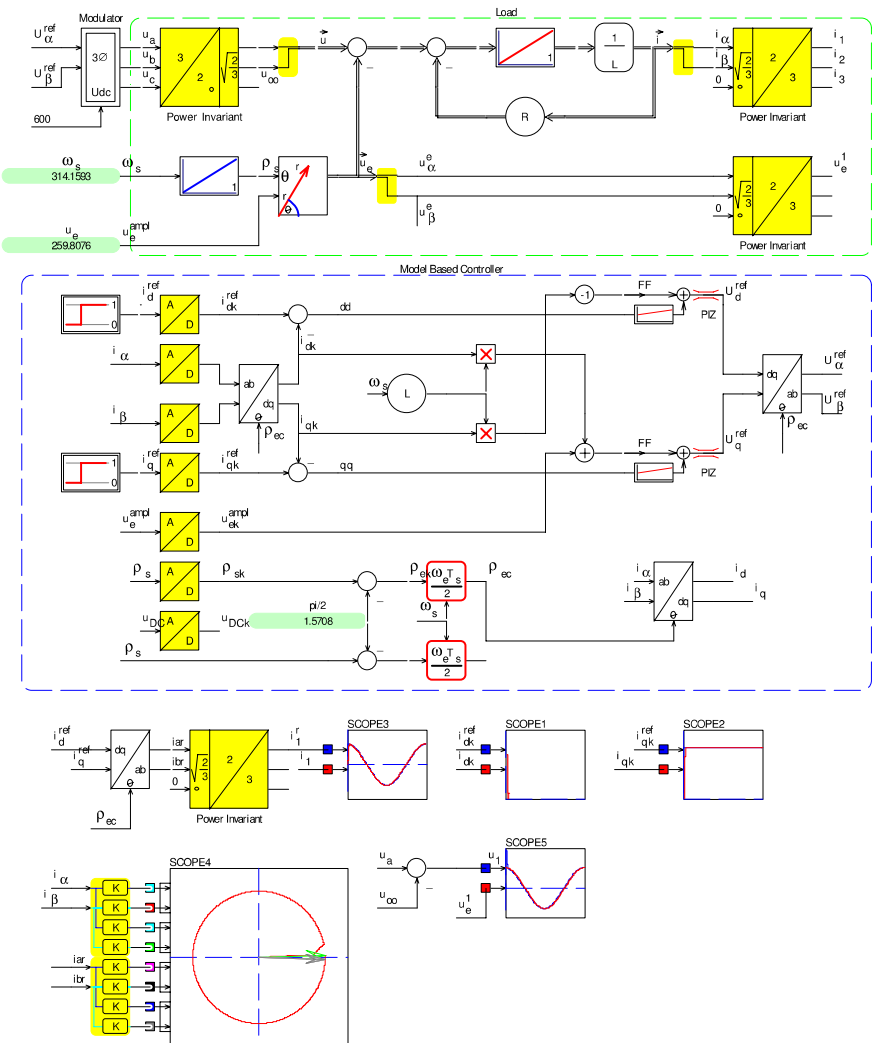
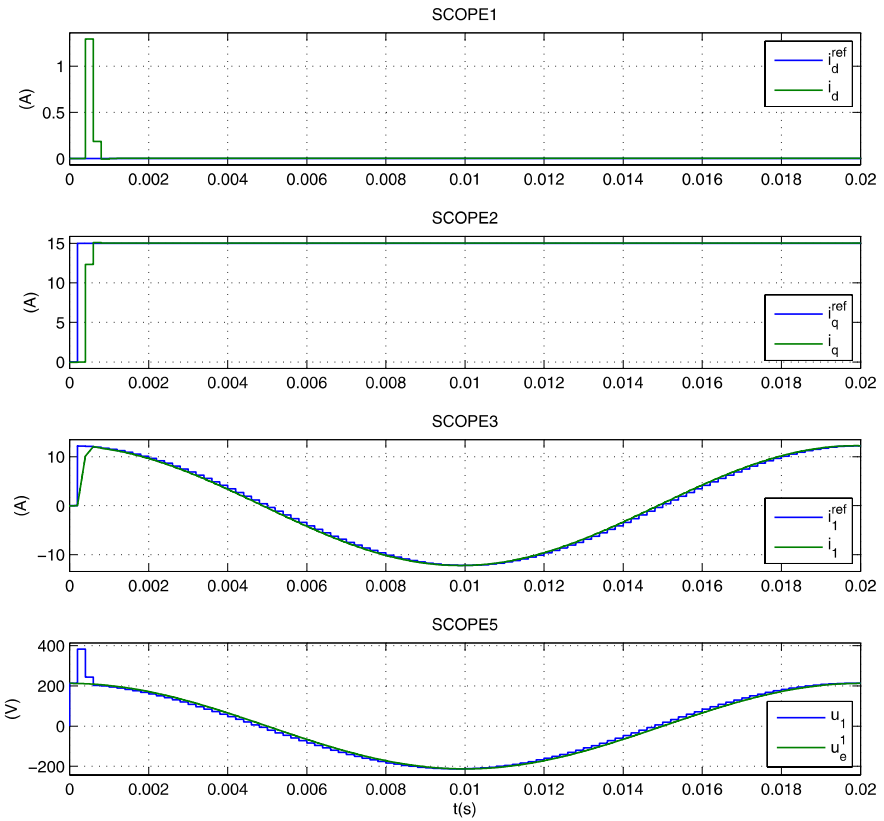


Fig. 3.34 Simulation of model based current control example, simplified approach



**Fig. 3.35** Simulation results of model based current control example, simplified approach

# Chapter 4

## Drive Principles

In successive chapters extensive attention will be given to the modeling and control of rotating field machines. Rotating field machines can be conveniently modeled with the aid of a so-called ideal rotating transformer (IRTF). The initial part of this chapter explores the IRTF concept. It will be shown that torque production may be described mathematically by the cross product of a flux and current space vector. In the previous chapter, three-phase current control was introduced with the precise aim of being able to manipulate the current space vector. The reason for this approach is to develop a set of fundamental drive concepts which aim to, at an elementary level, control torque in drive systems based on either a synchronous, asynchronous or brushed DC machine. Note that switched reluctance machines do not embrace the Lorentz force based concept, which implies that they are treated separately in this book at a later stage.

### 4.1 ITF and IRTF Concepts

The *ideal transformer* (ITF) and *ideal rotating transformer* (IRTF) concepts have been discussed extensively in the book *Fundamentals of Electrical drives* [68]. The IRTF was first used in [67]. The introduction of these concepts has proven to be effective for electrical machine modeling purposes. In this book, the ITF/IRTF concepts will be extended further. Hence, it is in the interest of readability to provide a brief review of these concepts prior to considering the machine models in this and following chapters.

#### Symbolic ITF Model

The symbolic ITF concept as shown in Fig. 4.1(a) represents a magnetically and electrically ideal transformer, i.e., without leakage inductances, copper or core losses and with a primary (subscript 1) to secondary winding ratio of

$n_1 : n_2$ . The ideal transformer requires no magnetizing current and can thus be regarded to have an infinite magnetizing inductance.

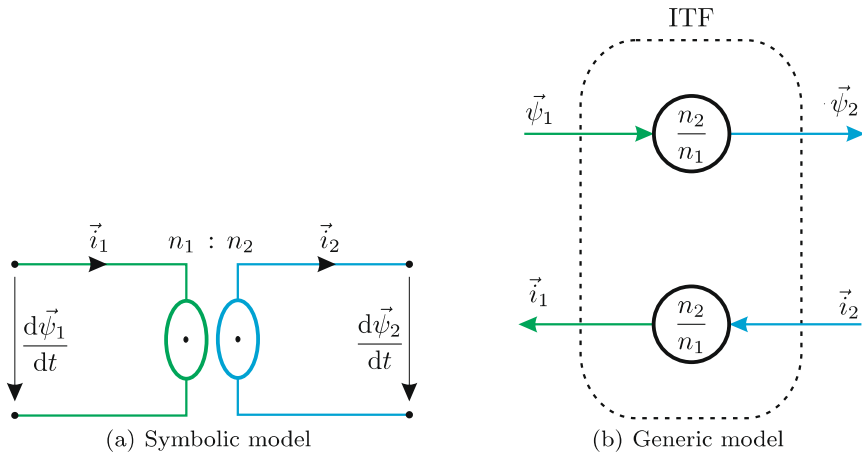


**Fig. 4.1** Symbolic and generic space vector based ITF models

The space vector equation set which corresponds with this model is of the form

$$\vec{\psi}_2 = \left( \frac{n_2}{n_1} \right) \vec{\psi}_1 \quad (4.1a)$$

$$\vec{i}_1 = \left( \frac{n_2}{n_1} \right) \vec{i}_2. \quad (4.1b)$$

### Flux- and Current-Based ITF Representation

The flux/current equation set (4.1) forms the basis for the generic model given in Fig. 4.1(b). Note that the generic model shown in Fig. 4.1(b) represents the so-called *ITF-flux* version, because the primary flux vector  $\vec{\psi}_1$  is designated as an input. The alternative so-called *ITF-current* version utilizes the primary current vector  $\vec{i}_1$  as an input. The version depends on the nature of the machine model in which it is applied. It is emphasized that the ITF model is based on the use of flux linkages and currents instead of voltages and currents.

### Symbolic IRTF Module

The *ideal rotating transformer* (IRTF) module, as given in Fig. 4.2, is a three-port transducer that describes the interactions between electrical quantities in stator and rotor (flux and current) and the mechanical quantities (torque and speed) on the shaft. The IRTF contains no means to store any energy, because there is neither mechanical inertia nor inductance. The IRTF describes how torque results from current and flux and how the moving shaft influences the relation between rotor and stator quantities. The IRTF can be

regarded as a model for the air-gap in rotating machines. A realistic dynamic machine model, valid for all electrical waveforms and speed transients, can be constructed by adding elements such as mechanical inertia, main inductance, leakage inductance, stator and rotor resistance to an IRTF.

In Fig. 4.2 a symbolic shaft (shown in red) enables the coupling to the mechanical world. The rotor port (shown in blue) allows electrical rotor components such as resistance to be added. The stator port (shown in green) provides the interface to connect stator related components.

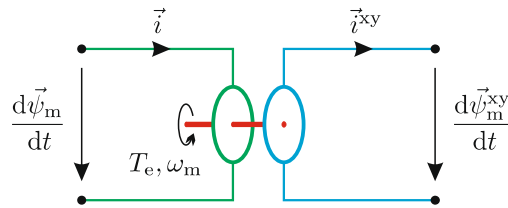


**Fig. 4.2** Symbolic IRTF representation

The magnetic flux linked with the stator and rotor is equal to  $\vec{\psi}_m$  and can be expressed in terms of the components, i.e., coordinates, seen by each winding, namely

$$\vec{\psi}_m = \psi_{m\alpha} + j \psi_{m\beta} \quad (4.2a)$$

$$\vec{\psi}_m^{xy} = \psi_{mx} + j \psi_{my}. \quad (4.2b)$$

### Space Vectors in the IRTF

An illustration of the flux linkage seen by the rotor and stator winding is given in Fig. 4.3(a).

The relationship between the stator and rotor oriented flux linkage and corresponding current space vectors, as shown in Fig. 4.3, may be written as

$$\vec{\psi}_m^{xy} = \vec{\psi}_m e^{-j\theta} \quad (4.3a)$$

$$\vec{i} = \vec{i}^{xy} e^{j\theta}. \quad (4.3b)$$

### Flux Linkage and Current Distribution in AC Machine

Figure 4.3 emphasizes the fact that there is only one flux linkage and one current space vector present in the IRTF. This fact is underlined by Fig. 4.4 which shows the cross-section of a typical AC machine with a three-phase sinusoidally distributed winding on the rotor and stator.

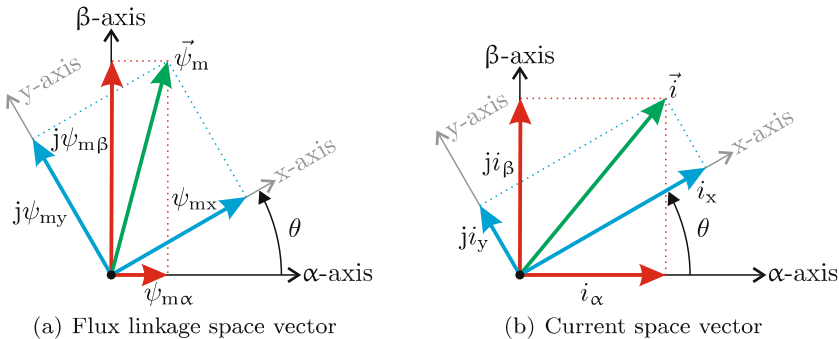


**Fig. 4.3** Flux linkage and current space vector diagrams

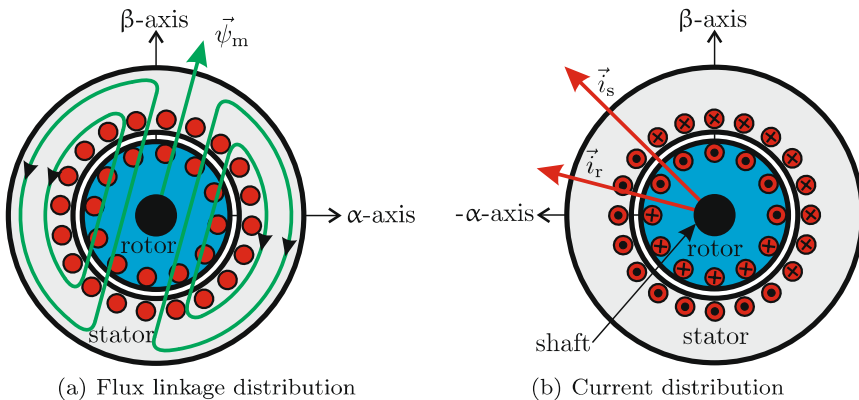


**Fig. 4.4** Flux linkage and current distribution in a typical induction machine

During operation the three-phase flux linkage and current contributions in a typical induction machine can be represented by a single flux linkage and two current distributions as shown in Fig. 4.4. These may in turn be represented by a space vector which for the flux is aligned with the resultant two-pole magnetic flux axis. The space vector  $\vec{i}_s$  is aligned with the current distribution of the stator, while the space vector  $\vec{i}_r$  is aligned with the current distribution in the rotor bars. When considering the current vector seen by the rotor, the IRTF module uses by convention the shown vector, whilst in reality the current distribution in the rotor is reversed in polarity. The reason for this is that the sum of stator and rotor magneto-motive forces (MMF) approaches zero when the permeability of the magnetic material of the IRTF model is taken towards infinity and the airgap is taken to be very small.

### Torque Production in the IRTF

The components of the space vectors shown in Fig. 4.3 can be projected onto a rotating orthogonal frame ( $\Re^{xy}, \Im^{xy}$ ) or stationary orthogonal reference frame ( $\Re, \Im$ ). If the angle  $\theta$  is set to zero, the IRTF model mirrors the ITF module with the exception that the IRTF has a unity winding ratio. According to the torque principles explained in the next section, the electrodynamic torque  $T_e$  produced by the two-pole IRTF module is of the form

$$T_e = \Im \left\{ \left( \vec{\psi}_m \right)^* \vec{i} \right\} \quad (4.4)$$

if the space vectors  $\vec{\psi}_m$  and  $\vec{i}$  are interpreted as complex numbers or

$$\vec{T}_e = \vec{\psi}_m \times \vec{i} \quad (4.5)$$

in vector form. Hence, the torque acting on the rotor is at its maximum value when the two vectors  $\vec{\psi}_m$  and  $\vec{i}$ , shown in Fig. 4.3, are perpendicular with respect to each other. The generic diagram of the IRTF module that corresponds to the symbolic representation shown in Fig. 4.2 is based on the use of (4.3a), (4.3b) and (4.5).

### Generic IRTF Module

The generic IRTF module as given in Fig. 4.5(a) is shown with a stator-to-rotor coordinate flux conversion module and rotor-to-stator current conversion module which complies with (4.3). The two coordinate conversion modules can also be reversed as shown in Fig. 4.5(b). The IRTF version used is application dependent as will become apparent in subsequent sections. The torque computation is not affected by the choice of coordinate system because both vectors use the factor  $e^{j\theta}$  and its conjugate  $e^{-j\theta}$ . Hence, these coordinate transformation in the form of vector rotation cancel out in expression (4.5).

The rotor angle  $\theta$  required for the IRTF module can be derived from the mechanical equation set of the (two-pole) machine, which is of the form

$$T_e - T_l = J \frac{d\omega_m}{dt} \quad (4.6a)$$

$$\omega_m = \frac{d\theta}{dt} \quad (4.6b)$$

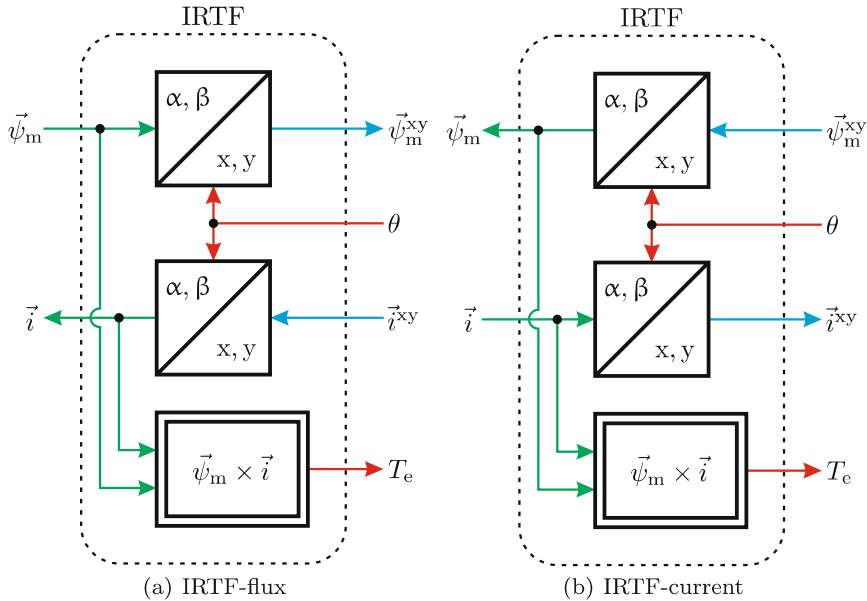


**Fig. 4.5** Generic representations of IRTF modules

with  $T_1$  and  $J$  representing the load torque and inertia of the rotor/load combination respectively.

## 4.2 Electromagnetic Torque Control Principles

In the previous chapter considerable attention was given to three-phase current control and the ability to generate a user defined current vector. In this section, it will be shown how such a current vector can be used for electromagnetic torque control in simplified AC and DC machines. The aim of this approach is to allow the reader to become more familiar with the use of the IRTF module for machine modeling and control design prior to undertaking more detailed studies in subsequent chapters. Furthermore, the introduction of simplified models will serve to emphasize the analogy that exists between the DC, synchronous and induction machine concepts.

Central to electromagnetic torque production is the interaction between the magnetic flux and the current sheet in the machine according to (4.5). The torque magnitude can be computed by the cross product of the IRTF vectors  $\vec{\psi}_m$  and  $\vec{i}$  as shown in Fig. 4.6.

This figure shows that torque control in an electrical machine may be realized by manipulating the current vector relative to the flux vector. The grey shaded area in Fig. 4.6 represents the torque magnitude. It may be readily

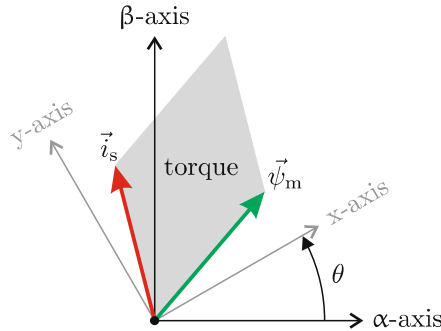


**Fig. 4.6** Relationship between IRTF current/flux linkage space vectors and torque

deduced that maximum torque (largest *grey area*) will be realized when the two vectors are orthogonal. For steady-state operation (constant torque), the two vectors must remain stationary with respect to each other. Changes in torque are usually instigated by changes of either the magnitude or the orientation of the current vector relative to the flux vector. The reason for this is that the dynamics linked to the flux vector are usually lower compared to the current vector. This explains why current control techniques, as discussed in the previous chapter, play a key role in electrical drives. Note that orientation of both vectors relative to the xy rotor reference frame (also shown in Fig. 4.6) is machine dependent, as will become apparent shortly.

In subsequent subsections, a simplified IRTF based synchronous, asynchronous and DC machine model will be introduced to which a space vector current source is connected. In practice, the latter is provided by the converter as discussed in the previous chapter. For each specific machine model additional components need to be introduced. In all cases, a magnetizing inductance  $L_m$  is required because machines are not magnetically ideal. For example, a finite air-gap between rotor and stator can be represented by a reluctance which is inversely proportional to the magnetizing inductance.

#### 4.2.1 DC Machine

In the context of explaining the basic torque control mechanism of a DC drive it is instructive to consider a DC machine which utilizes two orthogonal windings on the rotor as well as the stator. The converter of the drive generates a current vector  $\vec{i}_a$  which is supplied to the rotor windings via a set of slip-rings. As with the two previous cases, the question arises how torque control can be realized in such a drive concept. It will be shown in the next chapter that the DC drive shown here in fact characterizes the behavior of

the brush/commutator assembly of a DC machine. A symbolic representation of the DC drive, given in Fig. 4.7, shows a *salient* magnetizing inductance, which implies that the inductances as seen from either axis of the stationary reference frame are not equal.

In this case, the stator winding which is aligned with the real axis of the stationary reference frame is assumed to be the *field winding* that is connected to a current source  $i_f$ . The stator winding which is orthogonal to the field winding is known as the *compensating winding* and carries the armature (rotor) current  $i_{a\beta}$ . In space vector terms, the two currents in the field and compensation winding can be expressed as  $\vec{i} = i_f + j i_{a\beta}$  as shown in Fig. 4.7. The inductance of the field and compensating winding are named  $L_{m\alpha}$  and  $L_{m\beta}$  respectively. For DC machines that utilize a compensating winding the inductance as seen along the  $\beta$  axis is effectively zero, i.e.,  $L_{m\beta} = 0$ . The reason being that the MMF due to the armature (rotor) winding is effectively canceled by the MMF generated by the compensation winding.

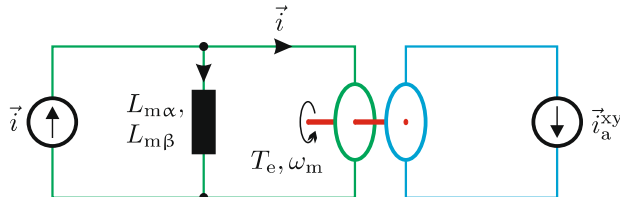


**Fig. 4.7** IRTF based DC drive model

The equation set, which corresponds to the symbolic model, is as follows

$$\vec{\psi}_m = L_{m\alpha} (i_f - i_{a\alpha}) \quad (4.7a)$$

$$\vec{i}_a = \vec{i}_{a\alpha} e^{j\theta} \quad (4.7b)$$

$$\vec{T}_e = \vec{\psi}_m \times \vec{i}_a. \quad (4.7c)$$

Shown in this expression is the current vector  $\vec{i}_a = i_{a\alpha} + j i_{a\beta}$ , which represents the current  $\vec{i}_{a\alpha}$  provided by the converter, but transformed to stationary coordinates. The field winding only carries the current  $i_f$  which implies that the component  $i_{a\alpha}$  must be zero. This in turn implies that the current vector  $\vec{i}_a$  can be defined as  $\vec{i}_a = jI$ , where  $I$  represents the reference current. A term  $L_{m\alpha} i_f$  is present in (4.7a), which corresponds to the flux linkage  $\psi_f$  due to either a field winding or permanent magnet. The introduction of a compensating winding which carries a current  $I$  (that is equal but opposite to that found in the armature), in effect insures that the flux vector  $\vec{\psi}_m$  remains aligned with the real axis of the stationary reference frame as shown in Fig. 4.8. The revised equation set which applies to this drive is therefore reduced to

$$\vec{\psi}_m = \psi_f \quad (4.8a)$$

$$\vec{i}_a^{xy} = jI e^{-j\theta} \quad (4.8b)$$

$$T_e = \psi_f I. \quad (4.8c)$$

Consideration of expression (4.8b) shows that in a positive (anti-clockwise) rotating motor, a backward (clockwise) rotating current vector (with the same rotational speed) is generated (see Fig. 4.8) on the rotor side of the IRTF. From a stationary reference perspective, the current vector will therefore remain stationary which is precisely the activity that is undertaken by the brush/commutator assembly in a brushed DC machine.

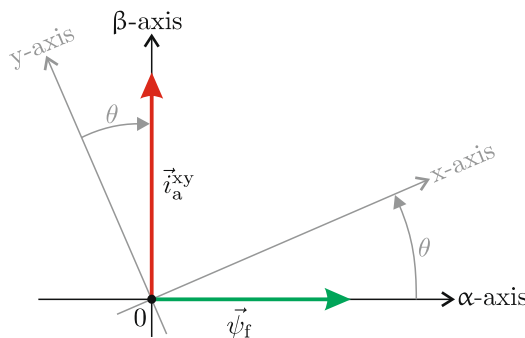


**Fig. 4.8** Current and flux linkage space vectors: DC drive

The generic model of the DC drive shown in Fig. 4.9 shows the IRTF module that is connected to a flux source on the stator side. On the rotor side a coordinate conversion module ( $\alpha, \beta \rightarrow x, y$ ) is used to generate the current vector  $\vec{i}_a^{xy}$ . In a DC machine, this conversion is effectively undertaken by the brush/commutator assembly. This will become apparent in Chap. 5, which deals with an extended model of the DC machine and design of a torque controller.

In Sect. 4.5.3, a tutorial is introduced which is directly based on the generic model given in Fig. 4.9.

#### 4.2.2 Synchronous Machine

Synchronous machines which utilize a field winding are often connected to an excitation source via a set of slip rings. In the IRTF based symbolic model given in Fig. 4.10, this excitation process is represented by the DC current source  $i_f$ . A magnetizing inductance  $L_m$  is also shown which has been arbitrarily positioned on the rotor side (this is allowed as the transformation ratio of the IRTF equals unity). The *converter* is represented by the current

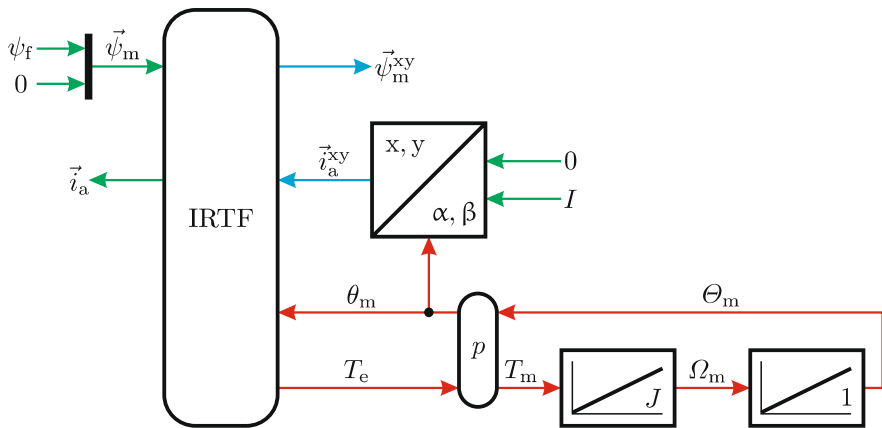


**Fig. 4.9** Generic IRTF model of a DC drive at no-load, with pole pair number  $p = 1$

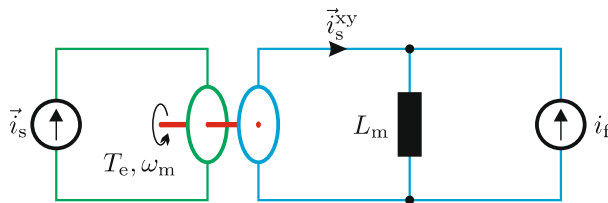


**Fig. 4.10** IRTF based synchronous drive

source  $\vec{i}_s$  and the question arises how this vector can be chosen to achieve torque control of the drive.

Observation of Fig. 4.10 and use of the IRTF equation set, as given in the previous section, shows that the following set of equations apply, namely

$$\vec{\psi}_m^{xy} = L_m \vec{i}_s^{xy} + L_m i_f \quad (4.9a)$$

$$\vec{T}_e = \vec{\psi}_m^{xy} \times \vec{i}_s^{xy}. \quad (4.9b)$$

The term  $L_m i_f$  represents the flux linkage  $\psi_f$  due to the excitation of either a field winding or permanent magnet. This variable is linked to a space vector  $\vec{\psi}_f^{xy} = \psi_f$ , which is tied to the real axis of the rotor coordinate system, as shown in Fig. 4.11. Use of the flux variables  $\vec{\psi}_f^{xy} = \psi_f$  with (4.9) leads to

$$\vec{\psi}_m^{xy} = L_m \vec{i}_s^{xy} + \vec{\psi}_f^{xy} \quad (4.10a)$$

$$T_e = \psi_f \Im \left\{ \vec{i}_s^{xy} \right\}. \quad (4.10b)$$

From (4.10b), optimum torque control (highest torque for the lowest current) is achieved by choosing the current vector  $\vec{i}_s^{xy} = jI$ , as shown in Fig. 4.11, where  $I$  represents the current magnitude of said vector. The corresponding

electromagnetic torque and current vector to be generated by the converter can be written as

$$T_e = \psi_f I \quad (4.11a)$$

$$\vec{i}_s = j I e^{j\theta}. \quad (4.11b)$$

An IRTF based generic model of the proposed synchronous drive structure given in Fig. 4.11 shows the IRTF module and a coordinate conversion module ( $x, y \rightarrow \alpha, \beta$ ) which implements expression (4.11b). Input to this module is the rotor shaft angle  $\theta$  which is derived from the torque using equation set (4.6) with  $T_l = 0$ , which implies that the machine is not connected to a load.

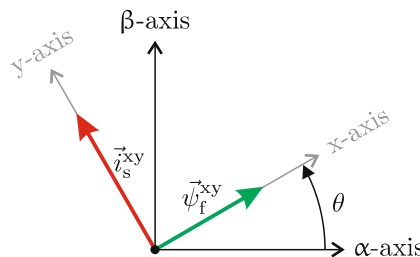


**Fig. 4.11** Current and flux linkage space vectors: synchronous drive

For the computation of the torque, the IRTF makes use of the vectors  $\vec{i}_s$  and  $\vec{\psi}_m$ , where the latter is found using (4.10a). Note that with the present choice of the current vector (orthogonal to the flux vector), the flux contribution  $L_m \vec{i}_s^{xy}$  will not affect the torque given that it is in phase with the current. Furthermore, it is emphasized that this type of drive requires access to the measured or estimated (by using electrical sensors and knowledge of the model) shaft angle  $\Theta_m$ .

Note that the torque production process, as discussed in this subsection, is remarkably similar to that shown for the simplified DC machine drive. The key difference is that the rotor and stator functions in the machine module have been exchanged. In the DC machine the excitation is provided by the stator, whilst in the synchronous machine it is the rotor which handles this task.

A tutorial based on Fig. 4.12 is given in Sect. 4.5.1 which underlines the concepts discussed in this subsection. The reader is reminded of the fact that the synchronous drive concept presented here is designed to provide a basic insight only. In reality, the machine design is more complex and, correspondingly, the control techniques to be deployed must be more extensive as will be shown in Chap. 6 and Chap. 7 respectively.

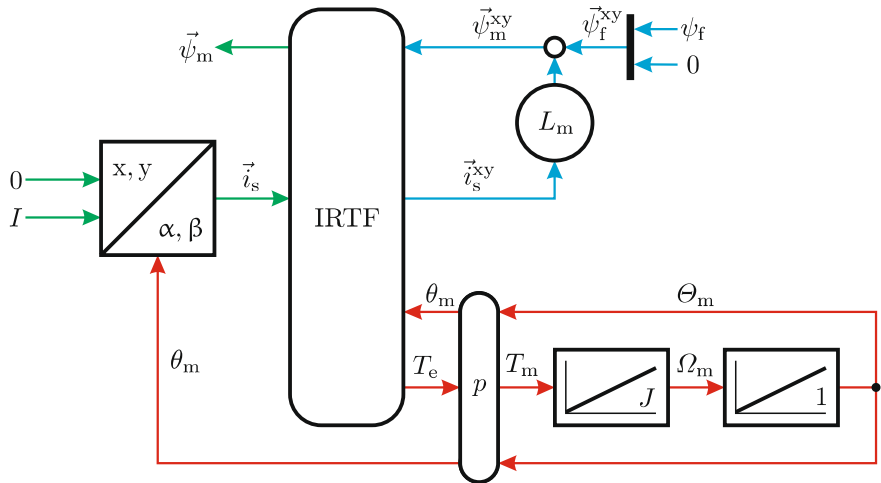


Fig. 4.12 Generic IRTF model of a synchronous drive at no-load

#### 4.2.3 Induction Machine

An induction machine which utilizes a squirrel-cage rotor [68] can in elementary form be represented with an IRTF based symbolic model as shown in Fig. 4.13. Readily apparent are the rotor resistance  $R_r$  of the squirrel cage and the magnetizing inductance  $L_m$ . The *converter* of the drive is represented by the current source  $\vec{i}_s$  which must be manipulated to achieve torque control. Unlike the synchronous drive discussed in the previous subsection, the flux  $\psi_m$  must be provided by the converter.

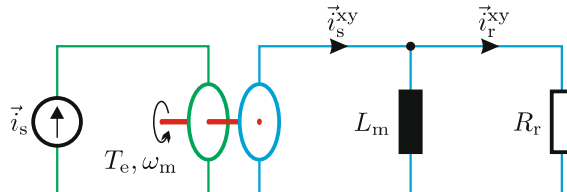


Fig. 4.13 IRTF based induction machine model

The equation set related to the flux and current can, with the aid of Fig. 4.13, be expressed as

$$\frac{d\vec{\psi}_m^{xy}}{dt} = R_r \vec{i}_r^{xy} \quad (4.12a)$$

$$\vec{\psi}_m^{xy} = L_m (\vec{i}_s^{xy} - \vec{i}_r^{xy}) \quad (4.12b)$$

$$\vec{T}_e = \vec{\psi}_m \times \vec{i}_s \quad (4.12c)$$

Also shown in equation set (4.12) is the torque expression which makes use of the flux space vector  $\vec{\psi}_m = \psi_m e^{j\theta_\psi}$ , where  $\theta_\psi$  represents the instantaneous angle between said vector and real axis of the stationary reference frame. This vector is shown in Fig. 4.14 together with a new orthogonal so-called *synchronous* coordinate system. The real axis  $\Re^{dq}$  of said coordinate system is tied to the flux vector in which case the latter can be expressed as  $\vec{\psi}_m^{dq} = \psi_m$ . The superscript dq identifies the reference frame in use. Also

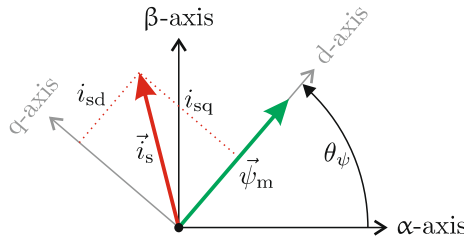


**Fig. 4.14** Current and flux linkage space vectors: induction machine drive

shown in Fig. 4.14 is the stator current vector  $\vec{i}_s$ , which can also be expressed in the synchronous reference coordinate frame as  $\vec{i}_s^{dq} = i_d + j i_q$ , where  $i_d$  and  $i_q$  are known as the direct axis and quadrature axis current components respectively. Subsequent transformation of equation set (4.12) to synchronous coordinates allows the flux and torque equations to be written as

$$\left( \frac{L_m}{R_r} \right) \frac{d\psi_m}{dt} + \psi_m = L_m i_d \quad (4.13a)$$

$$T_e = \psi_m i_q \quad (4.13b)$$

Equation set (4.13) is significant for this type of drive given that it shows that the direct axis component defines the flux level in the machine. Furthermore, changes to the current  $i_d$  will not lead to an instant change of the flux level, given that this is governed by the time constant  $L_m/R_r$ . Under quasi-steady state conditions, the flux level will be equal to  $\psi_m \cong L_m i_d$ . On the other hand, torque control can be virtually instantaneous (subject to the dynamics of the current controller), because it can be achieved by varying the value of the quadrature current  $i_q$  of the current source, which is set to the reference value  $I$  in this example. The corresponding electromagnetic torque and current vector to be generated by the converter for the induction machine drive can be written as

$$T_e = \psi_m I \quad (4.14a)$$

$$\vec{i}_s \simeq \left( \frac{\psi_m}{L_m} + j I \right) e^{j\theta_\psi} \quad (4.14b)$$

where  $\psi_m^*$  represents the reference flux value. A generic representation of the drive structure is illustrated in Fig. 4.15, showing the IRTF module at the center of the induction machine model. A Cartesian to polar conversion module is used to determine the required flux angle  $\theta_\psi$  that is required for the coordinate conversion module ( $d, q \rightarrow \alpha, \beta$ ), which generates the current vector  $\vec{i}_s$ .

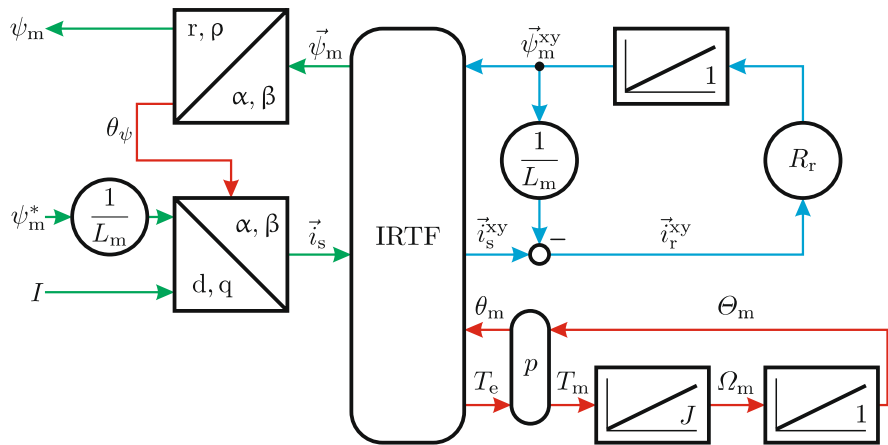


**Fig. 4.15** Generic model IRTF based induction machine drive

The tutorial given in Sect. 4.5.2 proves the opportunity to explore the drive concept as discussed in this subsection. It should come as no surprise that, in practice, induction machine models are more complex than shown here. This implies that more extensive control techniques are needed to achieve torque and flux control. Chapters 8 and 9 cover the advanced modeling and control aspects respectively.

### 4.3 Drive Dynamics

This section examines the mechanical interaction between the electrical machine and load. More specifically, Newton's laws of motion are introduced for linear and rotational based drive systems [35]. In addition, attention is given when an electrical machine is connected to a rotating and translatory load. Furthermore, the mechanical dynamics of a machine connected to a load are examined with the aid of a tutorial example outlined in Sect. 4.5.4.

### 4.3.1 Linear and Rotational Motion

#### Linear Motion

Prior to discussing rotational motion it is helpful to consider the linear or translatory motion of a point mass with the aid of Fig. 4.16. In this example, a point mass has been purposely chosen, so that the size of the body can be ignored for the ensuing analysis. Furthermore, the point mass is shown in a two-dimensional complex plane given that the rotational analysis will also be undertaken in such a reference frame. The reason for this is that rotating machines utilize rotors which exhibit a radial and axial symmetry, which justifies the use of a two-dimensional analysis.

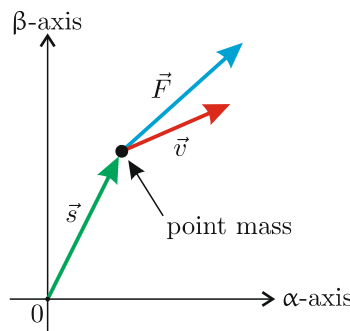


**Fig. 4.16** Linear motion of a point mass

The displacement vector  $\vec{s} = s_\alpha + j s_\beta$  defines the orientation of the point mass relative to the complex plane. The instantaneous velocity  $\vec{v} = v_\alpha + j v_\beta$  is defined according to

$$\vec{v} = \frac{d\vec{s}}{dt} \quad (4.15)$$

Newton's first law, known as the *law of inertia* states that a body (the point mass in this case) will be either at rest ( $\vec{v} = 0$ ) or moving at a constant velocity, when no net external forces are applied. If an external net force  $\vec{F}$  (as shown in Fig. 4.16) is applied to the point mass, an acceleration  $\vec{a}$  will occur according to

$$\vec{F} = m\vec{a} \quad (4.16a)$$

$$\vec{a} = \frac{d\vec{v}}{dt} \quad (4.16b)$$

where  $m$  represents the mass of the body, shown in Fig. 4.16. Expression (4.16a) is known as *Newton's second law*. Note that the force  $\vec{F}$  represents the vector sum of all applied forces. Consequently, a zero net force

yields zero acceleration, hence  $d\vec{v}/dt = 0$ , which implies motion at either constant velocity or rest (Newton's first law).

### Rotational Motion

The analysis given above can be readily extended to a rotating body such as the rotor of an electrical machine. Figure 4.17 shows a particle  $dm$  that is part of a rotating body (typically radially symmetric) which rotates around a fixed axis that is orthogonal to the origin 0 of the non-rotating complex plane.

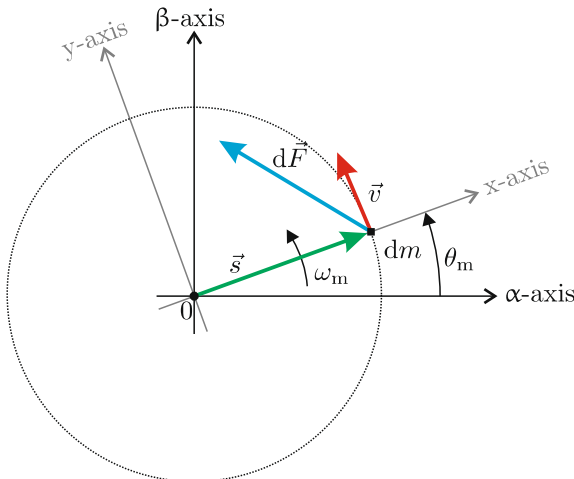


**Fig. 4.17** Non-uniform circular motion of a mass particle

The orientation of the mass particle is defined by the displacement vector  $\vec{s}$ , which can be expressed in its polar form as

$$\vec{s} = r e^{j\theta_m} \quad (4.17a)$$

$$\omega_m = \frac{d\theta_m}{dt} \quad (4.17b)$$

where  $|\vec{s}| = r$  represents the distance of the mass particle relative to the point of rotation, which is constant in this case, because it is part of a larger (solid) rotating body. Also shown in (4.17) is the angular frequency  $\omega_m$  of the mass particle which can, with the aid of (4.15) and (4.17a), be expressed as  $\vec{v} = j\vec{s}\omega_m$ . Note that the velocity is tangential to the circular orbit of the mass particle. It is also helpful to consider the speed in terms of an xy reference plane tied to the vector  $\vec{s}$  by making use of the conversion  $v^{xy} = \vec{v} e^{-j\theta_m}$ . Subsequent analysis shows that the rotating body referred velocity vector  $v^{xy}$  is equal to  $v^{xy} = \omega_m r$ , which is aligned with the  $\Im^{xy}$  axis of the rotating coordinate frame.

The incremental force  $d\vec{F}$  may be found with the aid of (4.16) (where  $m$  must be replaced by  $dm$ ) and (4.17), which gives

$$d\vec{F} = -\vec{s}\omega_m^2 dm + j\vec{s}dm \frac{d\omega_m}{dt}. \quad (4.18)$$

Equation (4.18) demonstrates that the incremental force consists of a so-called centripetal component which is oriented towards the point of rotation. Furthermore, a tangential force component exists, when non-uniform rotation  $d\omega_m/dt \neq 0$  occurs. The force equation can also be written in a rotor reference frame format as

$$d\vec{F}^{xy} = \underbrace{-r\omega_m^2 dm}_{dF_c} + \underbrace{j r dm \frac{d\omega_m}{dt}}_{dF_t} \quad (4.19)$$

where  $dF_c$  and  $dF_t$  represent the incremental centripetal and tangential force components respectively.

The incremental torque  $dT$  can be found using  $dT = r dF_t$ , which, with the aid of (4.19), may be written as  $dT = r^2 dm d\omega_m/dt$ . Computation of the torque associated with the entire rotating body volume  $V$  requires three-dimensional integration of the incremental torque expression, namely

$$T = \underbrace{\iiint_V r^2 dm}_{J} \frac{d\omega_m}{dt} \quad (4.20)$$

where  $J$  is referred to as the *moment of inertia*. This allows expression (4.20) to be written as

$$T = J \frac{d\omega_m}{dt} \quad (4.21)$$

which is the rotational equivalent of the linear expression  $\vec{F} = m d\vec{v}/dt$ . The torque  $T$  represents the net torque. In an electrical drive it is formed by the difference of the electromagnetic torque  $T_e$  produced by the electrical machine and the load torque  $T_l$ . The latter may be due to friction and/or mechanical loads, attached to the electrical machine. Expression (4.20) can be used to calculate the moment of inertia of rotating bodies. For example, the inertia of a solid disk with radius  $R$  and mass  $M$  is found to be equal to  $J = 1/2 M R^2$ . Following this section, a number of transmission examples will be discussed which makes use of the theory presented in this subsection.

### 4.3.2 Rotational to Translational Transmission

For applications which require linear motion, often a *rack and pinion* set of gears, as shown in Fig. 4.18, is used. The pinion, with radius  $r$ , is connected

to the shaft of the rotating electrical machine which generates a torque  $T_e$  with shaft speed  $\omega_m$ . The combined inertia of the electrical machine rotating parts connected to the shaft and pinion is defined as  $J$ . The rack is connected to the translatory load, which is represented in Fig. 4.18 by a force  $F_l$ . The total mass of rack and load is defined as  $m$ .

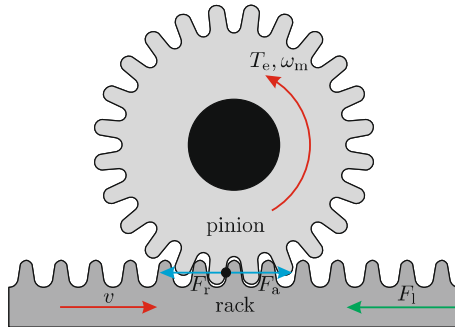


**Fig. 4.18** Rotational to translational transmission example: rack and pinion

The force exerted by the pinion gear on the rack is defined as  $F_a$ . Vice versa, the rack exerts an equal but opposite force  $F_r$  on the teeth of the pinion which gives

$$F_a = F_r. \quad (4.22)$$

Relationship (4.22) is known as Newton's third law which states that *to every action there is an equal but opposite reaction*. Application of Newton's second law to the set of gears shown in Fig. 4.18 leads to

$$T_e - rF_r = J \frac{d\omega_m}{dt} \quad (4.23a)$$

$$F_a - F_l = m \frac{dv}{dt}. \quad (4.23b)$$

Subsequent use of (4.22) with (4.23) and taking into account that the speed of the rack can be written as  $\vec{v} = \omega_m r$  gives

$$T_e - rF_l = \left( \underbrace{mr^2}_{J_e} + J \right) \frac{d\omega_m}{dt}. \quad (4.24)$$

Expression (4.24) shows that the introduction of a translatory load leads to an increase of the inertia seen by the rotating machine. The additional inertia  $J_e$  is defined as

$$J_e = mr^2 = m \left( \frac{v}{\omega_m} \right)^2. \quad (4.25)$$

This implies that a translational load which requires a large linear velocity  $v$  will lead to a substantial increase in the inertia experienced by the rotating machine/pinion combination.

### 4.3.3 Gear Transmission

A wide range of industrial rotational applications use a transmission device between load and electrical machine. Reasons for this may be due to physical load enclosure constraints, i.e., where the machine cannot be directly attached. In other instances, the mismatch between optimum load and machine speeds must be resolved by making use of a rotational to rotational transmission device. For this purpose gears or pulley's are used. Gears are wheels with teeth which mesh with each other, as shown in the example given in Fig. 4.19. The use of gears allows the transfer of forces without slippage, which is in contrast with pulley/belt systems, where this phenomenon can occur.

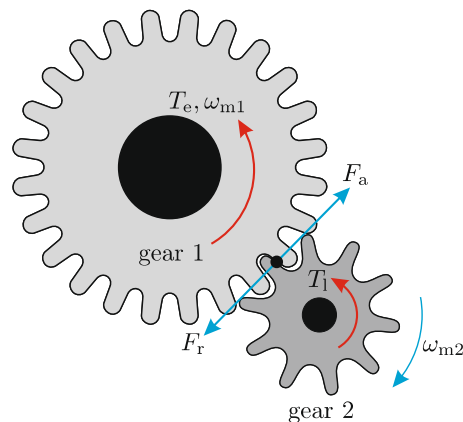


**Fig. 4.19** Gear transmission example: spur gearing

The relationship that exists between the torque and force of the two gears shown in Fig. 4.19 may be considered by application of Newton's second and third laws. In this example, the electrical machine is arbitrarily connected to gear 1 with radius  $r_1$  and provides a shaft torque  $T_e$  with rotational speed  $\omega_{m1}$ . The load is connected to gear 2 with radius  $r_2$  to which the load torque  $T_l$  is applied.

The relationship between the rotational speeds  $\omega_{m1}$  and  $\omega_{m2}$  follows from the observation that the tangential speed of both gears must be equal (no slippage), which gives

$$\omega_{m1}r_1 = \omega_{m2}r_2. \quad (4.26)$$

The relationship between machine driving torque and load torque may be found by taking into account that the driving gear (gear 1 in this example) exerts a force  $F_a$  (as shown in Fig. 4.19) on the teeth of gear 2. According to Newton's third law an equal but opposite force  $F_r$  will be exerted on gear 1. If the gears are replaced by a set of pulleys this force will be transferred via the belt. Observation of Fig. 4.19 and application of Newton's second law gives

$$T_e - r_1 F_r = J_1 \frac{d\omega_{m1}}{dt} \quad (4.27a)$$

$$r_2 F_a - T_l = J_2 \frac{d\omega_{m2}}{dt} \quad (4.27b)$$

where  $J_1$  and  $J_2$  represent the inertia of the electrical machine (with gear 1) and load (with gear 2) respectively. Subsequent elimination of the force variables  $F_a$  and  $F_r$  from (4.27) and using  $F_a = F_r$  (Newton's third law), as well as (4.26) gives

$$T_e - \left( \frac{r_1}{r_2} \right) T_l = \left( J_1 + \underbrace{\left( \frac{r_1}{r_2} \right)^2 J_2}_{J_{eq}} \right) \frac{d\omega_{m1}}{dt}. \quad (4.28)$$

Expression (4.28) represents Newton's second law expressed in terms of the machine variables  $T_e$ ,  $\omega_{m1}$ . The result shows that the load inertia  $J_2$  appears as an equivalent inertia  $J_e$  on the drive side of the transmission, which is computed according to

$$J_{\text{eq}} = \left( \frac{r_1}{r_2} \right)^2 J_2. \quad (4.29)$$

Hence, the inertia  $J_{\text{eq}}$  seen at the machine side of the transmission will be greater than the actual load inertia  $J_2$  in case  $r_1 > r_2$ , which is the case shown in Fig. 4.19.

#### 4.3.4 Dynamic Model of a Drive Train

The process of transmitting power from the electrical machine to the load is considered in this subsection with the aid of Fig. 4.20. Shown in Fig. 4.20 are two rotating masses with inertia  $J_1$  and  $J_2$ , which are assigned to the rotor of the electrical machine and load respectively. A coupling of some type, which may simply be a shaft, is used to link the two masses. If the coupling is sufficiently stiff, the two inertias may be simply represented by the sum of the two inertias  $J_{\text{total}}$ . In this case, Newton's second law for the drive train is given as

$$T_e - T_1 = J_{\text{total}} \frac{d\omega_m}{dt} \quad (4.30)$$

with  $J_{\text{total}} = J_1 + J_2$  and  $\omega_m = \omega_{m1} = \omega_{m2}$ . Furthermore, the relationship between angular frequency and shaft angle is reduced to  $\omega_m = d\theta/dt$ , with  $\theta_{m1} = \theta_m = \theta_{m2}$ . The power  $p_e$  delivered by the machine and the power supplied to the load  $p_l$  are given as  $p_e = T_e \omega_{m1}$  and  $p_l = T_1 \omega_{m2}$  respectively.

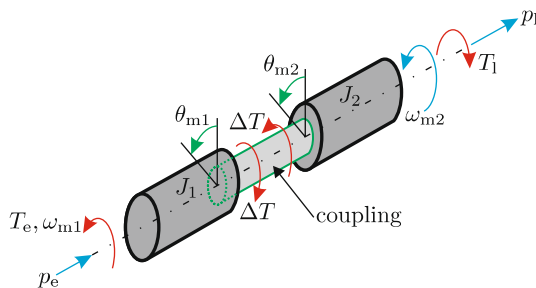


**Fig. 4.20** Dynamic model of a two-mass drive train

If the coupling between load and machine cannot be considered as stiff, a certain amount of twisting (torsion) of said coupling about its axis can occur, which depends on the torque  $\Delta T$  applied and the properties of the coupling.

The coupling properties typically are the torsion coefficient  $\kappa$ , also known as the *spring constant*, and damping coefficient  $c$ . Both coefficients are related to the applied torsional torque  $\Delta T$ , the instantaneous frequencies and rotor angles of the drive train according to (4.31).

$$\Delta T = \kappa (\theta_{m1} - \theta_{m2}) + c(\omega_{m1} - \omega_{m2}) \quad (4.31)$$

The formulation of Newton's second law for the drive train in question must take into account the twisting torque of the coupling, which leads to

$$T_e - \Delta T = J_1 \frac{d\omega_{m1}}{dt} \quad (4.32a)$$

$$\Delta T - T_l = J_2 \frac{d\omega_{m2}}{dt}. \quad (4.32b)$$

To study the interaction between load and machine under dynamic conditions it is helpful to develop a generic model of this system with the aid of (4.32) and (4.31) and the following expressions

$$\omega_{m1} = \frac{d\theta_{m1}}{dt} \quad (4.33a)$$

$$\omega_{m2} = \frac{d\theta_{m2}}{dt}. \quad (4.33b)$$

The latter defines the relationship between instantaneous shaft frequencies and shaft angles of the drive train under consideration. A generic diagram which satisfies the equation set given above is shown in Fig. 4.21.

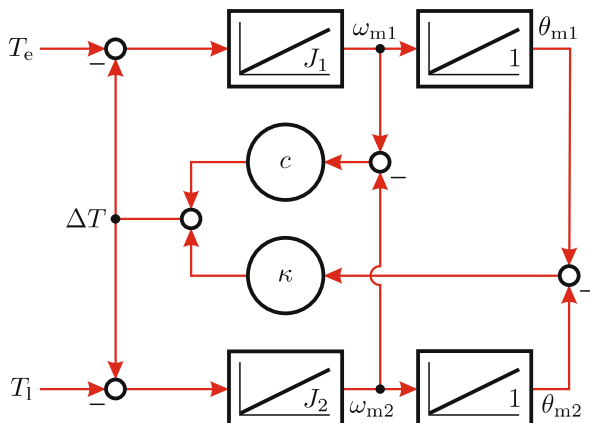


**Fig. 4.21** Generic model of a two-mass drive train

The tutorial given in Sect. 4.5.4 provides a numerical example which is directly based on the generic model given in Fig. 4.21. An example of the results obtained with this simulation model are given in Fig. 4.22.

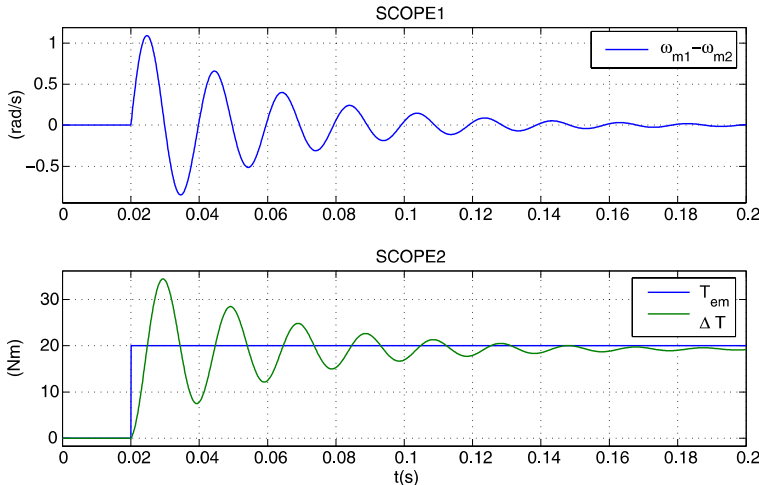


**Fig. 4.22** Dynamic response of a two-mass drive system with  $\kappa = 5000 \text{ Nm/rad}$ ,  $c = 2.5 \text{ Nms/rad}$ ,  $J_1 = 0.051 \text{ kg m}^2$  and  $J_2 = 1.35 \text{ kg m}^2$

Shown in Fig. 4.21 are the torque variable  $T_e$ ,  $\Delta T$  as function of time in the event that a shaft torque step of  $T_e = 20 \text{ Nm}$  is applied at  $t = 0 \text{ s}$ . Also shown in Fig. 4.21 is the angular frequency difference  $(\omega_{m1} - \omega_{m2})$  versus time, which must inevitably yield a zero steady state error given that both rotating masses ultimately accelerate at the same speed. The load torque in this example has been purposely set to zero. Note that the approach discussed in this section can be readily extended to more complex drive train structures. Note that in the tutorial the difference angle  $(\theta_{m1} - \theta_{m2})$  is calculated directly by integration of the speed difference. In this way, no special measures need to be taken to prevent increased rounding errors by subtracting two angles that would never stop growing.

## 4.4 Shaft Speed Control Loop Design Principles

In previous sections it was shown that torque control can be achieved by manipulating a current variable  $I$  which can be determined from the required reference torque  $T_e^*$  using

$$I = \frac{T_e^*}{\psi_m} \quad (4.34)$$

where  $\psi_m$  represents the magnetizing flux in the machine. However, in many applications control of the shaft speed is required which means that an additional outer control loop must be deployed. This so-called ‘cascaded control’ approach [20, 19] is typified by an *inner* current control loop and *outer* speed control loop. The time constant associated with the inner loop are usually small in comparison with the outer loop, which is dictated by mechanical time constants, as was mentioned earlier. Consequently, for the purpose of dimensioning the speed controller an ideal current controller may be assumed, which implies that the reference torque will be equal to the output torque of the drive. Under these conditions the drive is reduced to the generic model given in Fig. 4.23.

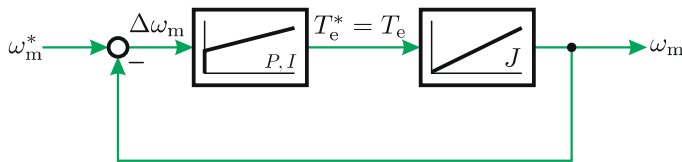


**Fig. 4.23** Continuous time domain block diagram of speed controller with simplified generic drive model

The drive, shown in none-discrete form, consists of a proportional-integral speed controller, of which the Laplace transform may be written as

$$\frac{T_e^*}{\Delta\omega_m} = K_p \left( 1 + \frac{1}{\tau_i s} \right) \quad (4.35)$$

where  $s$  is the Laplace operator. In steady state sinusoidal analysis,  $s$  can be considered as a complex variable, i.e., the *complex frequency*  $s = j\omega$ . Furthermore,  $\Delta\omega_m$  is defined as  $\Delta\omega_m = \omega_m^* - \omega_m$ . In this case, the controller is represented in terms of a proportional gain  $K_p$  and integral time constant  $\tau_i$  instead of an integral gain  $K_i = K_p/\tau_i$ , as used for the current controller. From a control perspective the use of variables  $K_p, \tau_i$  as opposed to  $K_p, K_i$  is often preferable, because they can be chosen independently.

The process of determining the controller parameters, may be undertaken by considering the Laplace transform of the drive representation according to Fig. 4.23 which is of the form

$$\frac{\omega_m}{\omega_m^*} = \frac{K_p (\tau_i s + 1)}{J \tau_i s^2 + K_p \tau_i s + K_p}. \quad (4.36)$$

A Bode amplitude plot of expression (4.36) is given in Fig. 4.24, where use is made of straight line asymptotic approximations. In the example shown the poles and zeros are assumed to be real, while the gradient of the linear functions is equal to 20 dB/decade.

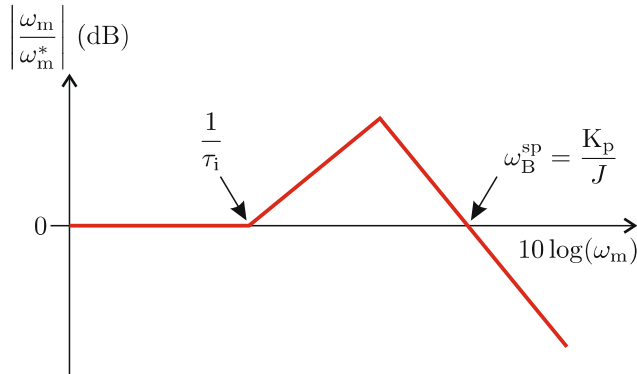


**Fig. 4.24** Bode amplitude plot example, with real poles and zeros

Observation of (4.36) and Fig. 4.24 demonstrates that for high frequencies the transfer function (in terms of its amplitude) may be written as

$$\left| \frac{\omega_m}{\omega_m^*} \right| \simeq \frac{K_p}{J\omega}. \quad (4.37)$$

The frequency  $\omega = \omega_B^{sp}$  (as shown in Fig. 4.24) at which the transfer function according to (4.37) reaches unity gain, effectively defines the bandwidth of the speed control loop. Accordingly, the proportional gain of the speed controller is given as

$$K_p = \omega_B^{sp} J \quad (4.38)$$

where  $J$  represents the total inertia of the drive. Consequently, it is necessary to have knowledge of the mechanical load that is attached to the machine, given the need to estimate the combined inertia  $J$ . Furthermore, a value for the effective bandwidth of the speed controller must be provided by the user. For typical high-performance drives the effective speed control bandwidth  $\omega_B^{sp}$  is in the order of  $\omega_B^{sp} = 100 \text{ rad/s}$ , which, together with the inertia  $J$ , fully defines the proportional gain of the controller.

Computation of the integrator time constant  $\tau_i$  may be undertaken by reconsidering (4.36), which upon substitution of (4.38) may be rewritten as

$$\frac{\omega_m}{\omega_m^*} = (\omega_B^{sp}) \frac{s + \frac{1}{\tau_i}}{s^2 + \omega_B^{sp}s + \omega_B^{sp}/\tau_i}. \quad (4.39)$$

The denominator of (4.39) can also be written as  $s^2 + 2\zeta\omega_o + \omega_o^2$ , where  $\zeta, \omega_o$  represent the damping and natural frequency respectively and which may be expressed as

$$\zeta = \frac{1}{2} \sqrt{\omega_B^{sp} \tau_i} \quad (4.40a)$$

$$\omega_o = \sqrt{\frac{\omega_B^{sp}}{\tau_i}}. \quad (4.40b)$$

The poles of the transfer function as defined by expression (4.39) determine the behavior of the model and in this context a value for the damping factor needs to be selected. According to general linear control theory principles [20, 19], two options are normally entertained namely:

- $\zeta = 1$ , which according to (4.40) corresponds to  $\tau_i = 4/\omega_B^{sp}$ ,  $\omega_o = \omega_B^{sp}/2$ . This option gives two poles  $s_1, s_s$  located in the complex  $s$  plane at  $s_{1,2} = -\omega_B^{sp}/2$ .
- $\zeta = 1/\sqrt{2}$ , which according to (4.40) corresponds to  $\tau_i = 2/\omega_B^{sp}$ ,  $\omega_o = \omega_B^{sp}/\sqrt{2}$ . This option yields two complex conjugate poles located in the complex plane at  $s_{1,2} = -\omega_B^{sp}/2 \pm j\omega_B^{sp}/2$ .

The choice of damping value must be considered in conjunction with the drive configuration in use and the nature of the transient response which will appear. For example, the step response of (4.39) for the two values of  $\zeta$  considered above are shown in Fig. 4.25 for the speed bandwidth frequency of  $\omega_B^{sp} = 100 \text{ rad/s}$ .

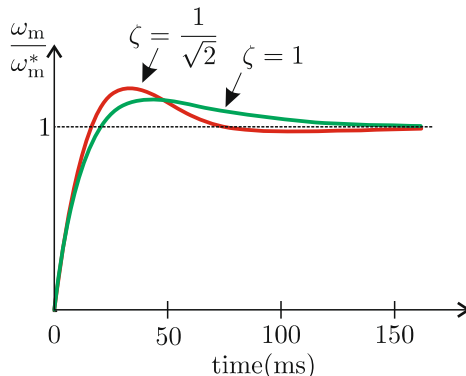


**Fig. 4.25** Step response ( $\omega_m/\omega_m^*$ ), with  $\omega_B^{sp} = 100 \text{ rad/s}$

A relatively high damping factor of  $\zeta = 1$  is particularly important for drives which are not capable of accepting energy from the mechanical side. Given that such drives must rely on the mechanical time constant of the motor/load to recover from a overspeed (speed in excess of the reference value) condition. For four quadrant drives a critical  $\zeta = 1/\sqrt{2}$  or under-damped  $\zeta < 1/\sqrt{2}$  response is warranted, particularly when short settling times are required, for example in servo applications. Given these considerations, a damping factor  $\zeta = 1$  is a prudent choice, in which case the resulting

set of controller parameters may be written as

$$K_p = \omega_B^{sp} J, \quad (4.41a)$$

$$\tau_i = \frac{4}{\omega_B^{sp}}. \quad (4.41b)$$

In a practical drive environment, as discussed in the accompanying tutorial (see Sect. 4.5.5), a discrete PI controller with *anti-windup* is required. This so-called *windup* effect occurs in all control systems which utilize an integrator to nullify steady state errors. An explanation of this phenomenon may be undertaken with the aid of Fig. 4.23 and imposing a practical constraint  $\pm T_e^{\max}$  on the torque level that can be delivered by the drive. If the torque level of the drive reaches the drive limit value, a situation can arise where a speed error occurs which causes the controller output to increase beyond the limit values  $\pm T_e^{\max}$  of the drive. An anti-windup controller has the capability to counteract the integrator action of the controller when the drive reaches a torque boundary.

A tutorial is given in Sect. 4.5.5 which outlines the concepts shown in this subsection. Notably this tutorial also demonstrates integrator windup effect and examines how this phenomenon can be countered.

## 4.5 Tutorials

### 4.5.1 Tutorial 1: Elementary Synchronous Drive

The purpose of this tutorial is to build a simulation model of the basic synchronous drive based on the generic model shown in Fig. 4.12. A simplified current source, IRTF based two pole machine model is to be developed with a set of parameters as given in Table 4.1.

**Table 4.1** Synchronous machine parameters

Parameters		Value	
Field flux	$\psi_f$	1.0	Wb
Magnetizing inductance	$L_m$	100	mH
Inertia	$J$	10 m	$\text{kg m}^2$

In this example, a machine without an external load is envisaged. Furthermore, a control input  $I$  for the drive, known as the *quadrature current*, is to be provided using an *UPDOWN* module with a range of  $\pm 10\text{ A}$ . Add a scope module to display the space vectors  $\vec{\psi}_f^{xy}$  and the scaled (by a factor 0.1) current vector  $\vec{i}_s^{xy}$  in a single diagram. In addition, provide a diagram which shows the torque  $T_e$  for the duration of the simulation, which must be set to  $T = 100\text{ ms}$ .

The simulation model as given in Fig. 4.26 satisfies the tutorial requirements outlined above. A simplified controller structure is shown which makes use of the *measured* shaft angle  $\theta$  and the reference current  $I$  to generate the reference current  $\vec{i}_s$ . Two scope modules are also shown which are tied to the variables given in Table 4.2. In the example given the control current is varied during the simulation and this affects the torque and current amplitude of the vector  $\vec{i}_s^{xy}$  as discussed in Sect. 4.2.2.

**Table 4.2** Scope variables

Scope number	Variables
Scope 1	$\vec{i}_s^{xy}$ ( <i>black</i> ), $\vec{\psi}_f^{xy}$ ( <i>green</i> )
Scope 2	$T_e$ ( <i>blue</i> )

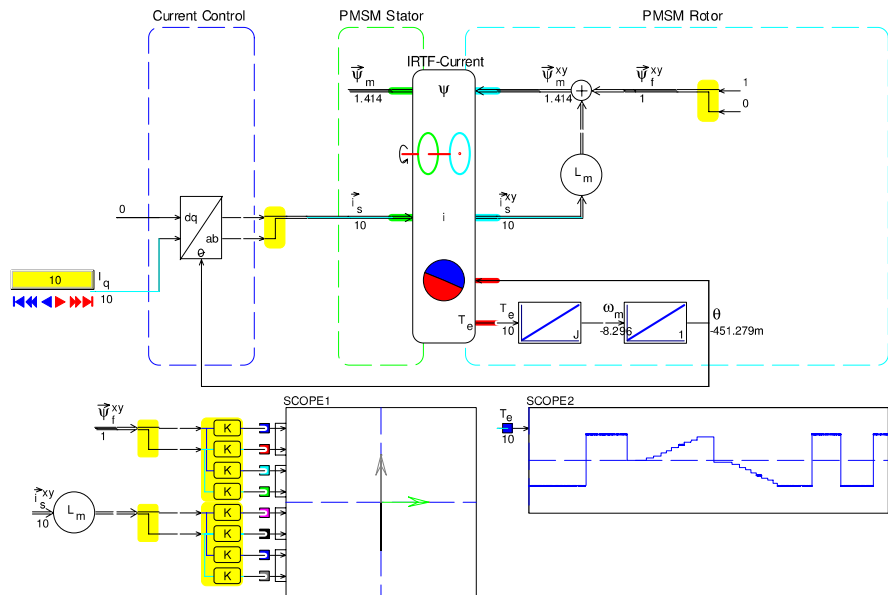


Fig. 4.26 Simplified synchronous drive simulation model

#### 4.5.2 Tutorial 2: Elementary Asynchronous (Induction) Drive

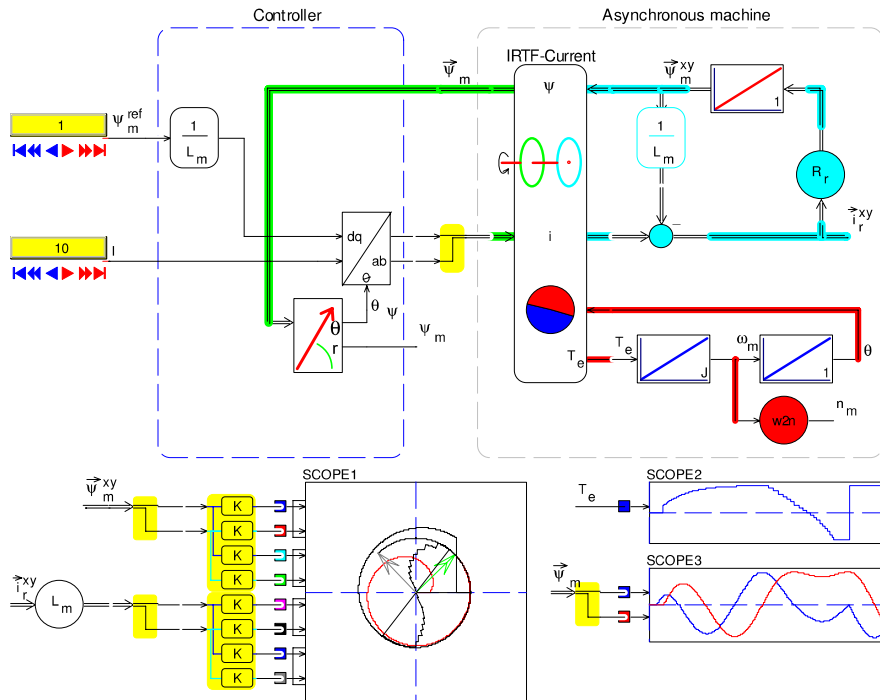
A simplified induction machine drive model is to be developed. The drive uses a current source connected to a two-pole induction machine with parameters as given in Table 4.3. No external mechanical load is required for this tutorial. Provide an IRTF based machine model and controller which corresponds to the generic model given in Fig. 4.15.

Table 4.3 Induction machine parameters

Parameters		Value	
Rotor resistance	$R_r$	10.0	$\Omega$
Magnetizing inductance	$L_m$	100	mH
Inertia	$J$	10 m	$\text{kg m}^2$

A set of *UPDOWN* modules is to be introduced to control the reference flux  $\psi_m^*$  and quadrature reference current  $I$  in the range of  $\psi_m^* = 0 \rightarrow 2 \text{ Wb}$  and  $I = -10 \text{ A} \rightarrow 10 \text{ A}$  respectively. Add a scope module to display the space vectors  $\vec{\psi}_{xy}^*$  and scaled (by a factor 0.1) current vector  $\vec{i}_{xy}$  in a single diagram. In addition, provide a diagram which shows the torque  $T_e$  for the duration of the simulation, which must be set to  $T = 100 \text{ ms}$ .

An implementation example of the posed problem as given in Fig. 4.27 shows the IRTF based induction machine model and controller. The latter makes use of the flux vector  $\vec{\psi}_m$ , of which the instantaneous angle  $\theta_\psi$  is used by the coordinate conversion module to generate the current  $\vec{i}_s$ . Shown in Fig. 4.27 are the two scope modules which in turn are linked to the variables given in Table 4.4.



**Fig. 4.27** Simulation of simplified induction machine drive model

**Table 4.4** Scope variables

Scope number	Variables
Scope 1	$\vec{i}_r^{xy}$ (black), $\vec{\psi}_m^{xy}$ (green)
Scope 2	$T_e$ (blue)

It is instructive to execute this tutorial in two phases. Firstly, use  $I = 0$  and a given  $\psi_m^*$  value. Under such circumstances the stator current  $\vec{i}_s$  will be aligned with the flux vector  $\vec{\psi}_m$ . This implies that the torque will be zero and the steady state flux will be equal to  $\psi_m = L_m i_d$  as may be confirmed with this exercise. Furthermore, it may be observed that step changes in  $\psi_m^*$

elicit a first order response in the machine flux  $\psi_m$  which is governed by the time constant  $L_m/R_r$ . In a second successive phase of this tutorial, operation under constant flux may be explored by maintaining  $\psi_m^*$  constant and varying the current  $I$ . Observation of the scope results shows that step changes in  $I$  are directly reflected in the torque. Note also that the spatial relationship between the flux and current is maintained with changes to the quadrature current which is consistent with the theory presented in Sect. 4.2.3.

### 4.5.3 Tutorial 3: Elementary DC Drive

This tutorial aims to demonstrate how torque production in a machine may be realized when the stator is provided with a fixed (with respect to a stationary reference frame) excitation flux  $\vec{\psi}_f = \psi_f$ . The approach to be taken follows the reasoning outlined in Sect. 4.2.1, where a compensation winding was introduced to offset the armature reaction of the machine. This implies that the magnetizing inductance  $L_{m\beta}$  is not required for this simulation exercise. Similarly, the magnetizing inductance  $L_{m\alpha}$  is not directly required because an excitation flux value  $\psi_f = L_{m\alpha}i_f$  is introduced. Consequently, the parameters for this machine may be reduced to those given in Table 4.5.

**Table 4.5** DC machine parameters

Parameters	Value		
Field flux	$\psi_f$	1.0	Wb
Inertia	$J$	10 m	$\text{kg m}^2$

The tutorial given in Fig. 4.28 shows a *machine module* which consists of an IRTF module with a set of integrators which represent the mechanical dynamics of the system. An excitation flux vector  $\vec{\psi}_f$  is provided to the stator side of the IRTF module as required. A counter-rotating current vector  $\vec{i}_{a\text{xy}}$  is generated by the controller and this is realized with the aid of an  $(\alpha, \beta \rightarrow d, q)$  coordinate conversion module. An *UPDOWN* module is used to provide the reference current for the controller module, which generates a stationary (with respect to the stationary reference frame) current vector  $\vec{i}_a$ . The latter is orthogonal to the excitation vector  $\vec{\psi}_f$  as may be observed from SCOPE2. Changes to the current reference directly affect the torque as can be deduced from the results shown on SCOPE1. The simulation model confirms that the controller acts as a brush/commutator assembly in a brushed DC machine. Hence, the combination of *machine* and *controller* module (shown in Fig. 4.28 as highlighted blocks) represent a simplified current source model of a brushed DC machine.

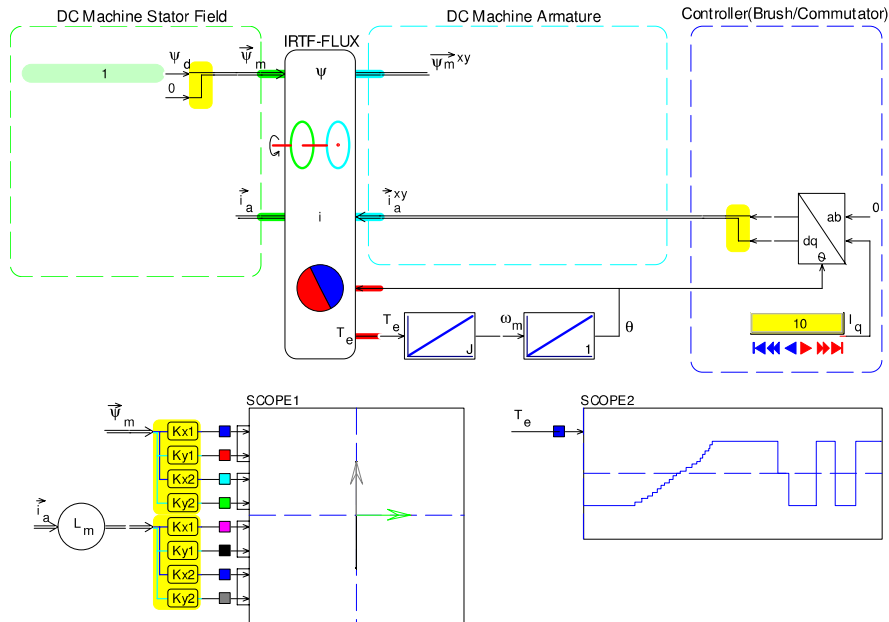


**Fig. 4.28** Simplified DC drive simulation model

#### 4.5.4 Tutorial 4: Drive Dynamics Example

In this tutorial, a dynamic model of a two-mass drive train is to be examined with the aid of a simulation model. The electrical machine and load inertia value are to be chosen to be  $J_1 = 0.051 \text{ kg m}^2$  and  $J_2 = 1.35 \text{ kg m}^2$  respectively. A coupling between the two inertias is to be used. The coupling has a torsion coefficient and damping coefficient of  $\kappa = 5000 \text{ Nm/rad}$  and  $c = 2.5 \text{ Nms/rad}$  respectively. A mechanical shaft torque step of  $T_e = 20 \text{ Nm}$  is to be applied at  $t = 0 \text{ s}$ . Furthermore, the drive is to be analyzed under no-load conditions.

A convenient approach to solving this problem is the use of the generic model discussed in Sect. 4.3.4, where the load torque  $T_l$  may be set to zero (no-load operation assumed). The simulation model as shown in Fig. 4.29 corresponds to the generic model given in Fig. 4.29, with the exception that only one angle integrator is used. Simulation results, based on the parameters and excitation conditions described above, are shown with the aid of the two SCOPES modules. The data from these two scopes have been introduced in Sect. 4.3.4 (see Fig. 4.22).

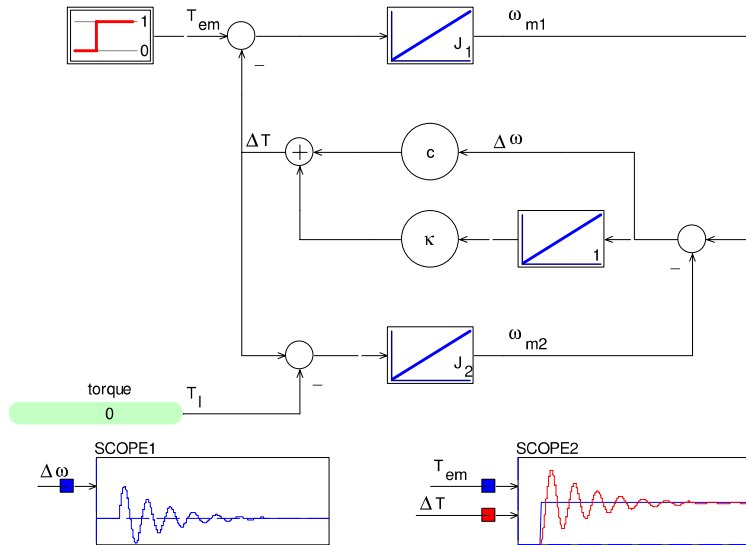


**Fig. 4.29** Dynamic model of two-mass drive train

#### 4.5.5 Tutorial 5: Speed Control Loop Design Example

This tutorial considers the design and implementation of a speed control loop according to the approach discussed in Sect. 4.4. A simulation model is to be developed which represents the drive model shown in Fig. 4.23. A discrete PI controller, as present in the CASPOC library, is to be used with a sampling frequency of  $f_s = 2$  kHz. In practical drives, machine and converter constraints limit the torque. This effect is to be modeled by introducing a limit module between the integrator and PI controller. The value of the limit controller is shown in Table 4.6. This table also shows the values to be used for the inertia and speed loop bandwidth.

**Table 4.6** Drive parameters

Parameters		Value	
Machine torque limits	$T_e^{\max}$	$\pm 8$	Nm
Inertia	$J$	0.005	$\text{kg m}^2$
Speed loop bandwidth	$\omega_B^{sp}$	100	rad/s

The issue of windup is also to be explored in this tutorial which uses a fixed 50% load torque. The shown anti-windup PI controller limits both the state of the internal integrator and the controller output to the chosen limits. When choosing controller limits that are beyond the drive limits (in this tutorial the controller limits are set to  $\pm 800$  Nm), windup of the speed con-

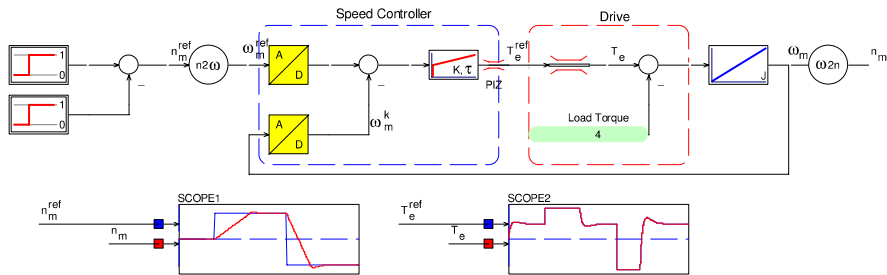


**Fig. 4.30** Simulation of speed control example

troller's integrator can occur. Note that during the ramp-up of the machine, a speed error causes the integrator output to increase even though the drive is already producing maximum torque. The bottom left graph in Fig. 4.31 shows that the controller is asking 200 Nm while the drive is only capable of producing a mere 8 Nm. It will require a significant negative speed error to work the integrator value back down. Figure 4.31 clearly shows that the speed overshoots its reference by a great amount. When proper controller limits are set, the integrator will stop to increase any further as soon as it reaches the set limit. The right two graphs in Fig. 4.31 show the simulation when the controller limits are set to  $\pm 8$  Nm, which results in a well behaved speed response that corresponds to the one shown in Fig. 4.25.

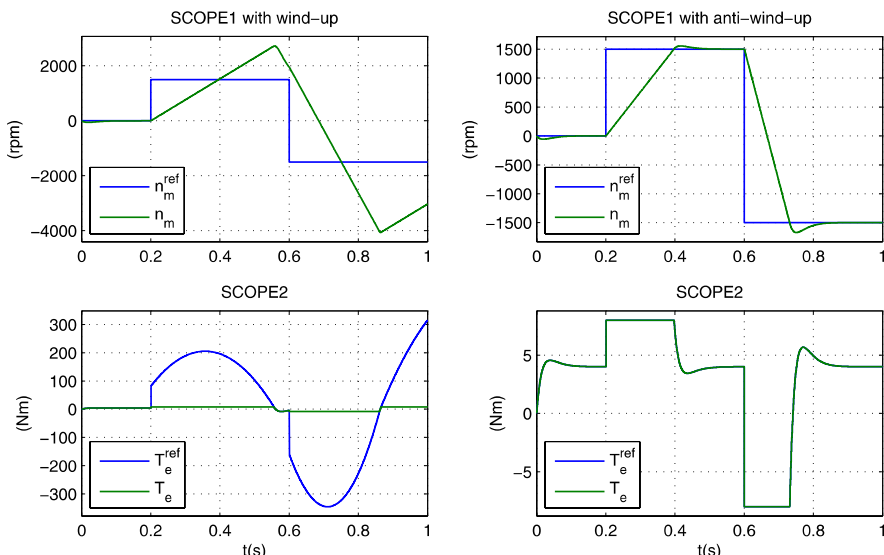


**Fig. 4.31** Simulation results for speed and reference torque versus time with and without anti-windup

A speed reference generator must be introduced which sets the speed to  $n_m^* = 1500 \text{ rpm}$  at  $t = 200 \text{ ms}$ , which is followed by a speed command  $n_m^*$  reversal from 1500 rpm to  $-1500 \text{ rpm}$  at  $t = 0.5 \text{ s}$ . Total simulation time  $T$  is assumed to be 1 s. Calculate the gain  $K_p$  and time constant  $\tau_i$  of the speed controller and undertake the simulation with PI controller torque limits that correspond to those of the machine. Examine in the first instance the shaft speed, machine torque  $T_e$  (torque after the limit module) and torque reference (output from the PI control module) for a controller without active anti-windup. Repeat the simulation for different limits of the PI controller and see how windup disappears as soon as the controller limits meet the drive limits. The gain  $K_p$  and time constant  $\tau_i$  of the speed controller are calculated using (4.41), with  $\omega_B^{\text{sp}} = 100 \text{ rad/s}$  (see Sect. 4.4), which gives  $K_p = 0.5 \text{ Nm}/(\text{rad/s})$  and  $\tau_i = 0.04 \text{ (Nm/rad)}$  respectively.

An implementation which complies with the requirements for this tutorial is given in Fig. 4.30. Readily apparent in this figure is the ‘drive’ which consists of an integrator with gain  $1/J$  and limit module. A discrete PI control module is also shown of which the limits were set to  $\pm 800 \text{ Nm}$  (left graphs) and  $\pm 8 \text{ Nm}$  (right graphs) in Fig. 4.31. The latter shows the preferred speed response with well-damped behavior and small overshoot.



# Chapter 5

## Modeling and Control of DC Machines

The brushed DC machine, which derives its excitation flux from a field winding or permanent magnets, remains commercially relevant in the field of drives. This despite the influx of brushless drive technologies which offer an inviting alternative to the use of a commutator/brush assembly, which is an inevitable component of the brushed DC machine. The use of well-established motor manufacturing techniques, together with low-complexity power electronic converters, has been instrumental in retaining its popularity in a diverse range of applications. For household goods and automotive products, the use of low cost, brushed permanent magnet motors remains virtually unchallenged. In particular, the brushed DC series machine known as the *universal machine* is widely deployed in domestic appliances. In the field of manufacturing automation, small high-dynamic brushed servo drives continue to play a critical role. Furthermore, the apparent simplicity of this technology (in comparison with *brushless* drive technologies) has ensured the survival of older larger drive concepts in applications where dynamic performance is considered not to be a key issue.

Given these considerations, it is prudent to consider the modeling and control of these machines in some detail. From a didactic perspective, there is decided merit in examining the brushed drive concept first. This approach provides the opportunity to introduce and demonstrate some basic modeling and control aspects, which are also highly relevant for AC drives that utilize rotating field machines. The introduction of an extended space vector based current source model of the machine, which builds on the simplified model given in the previous chapter, is both novel and helpful in the quest for building a *field-oriented* machine concept. The inversion of the current source field-oriented model, an approach which is one of the cornerstones of this book, is initially demonstrated for a brushed DC drive. In addition, attention will be given to the development of control strategies which ensure that drive operation is kept within the drive envelope dictated by voltage or current constraints. In this context, field weakening strategies for separately excited machines are introduced, together with a set of CASPOC based tutorials.

## 5.1 Separately Excited, Current-Controlled DC Machine

A brief review of this type machine concept is given in terms of a cross-sectional view, symbolic and generic models, together with relevant equations. A more extensive treatment is given in [68], which includes steady-state operation. A comprehensive treatment of basic machine concepts for the uninitiated reader is given, for example in [31] and [66].

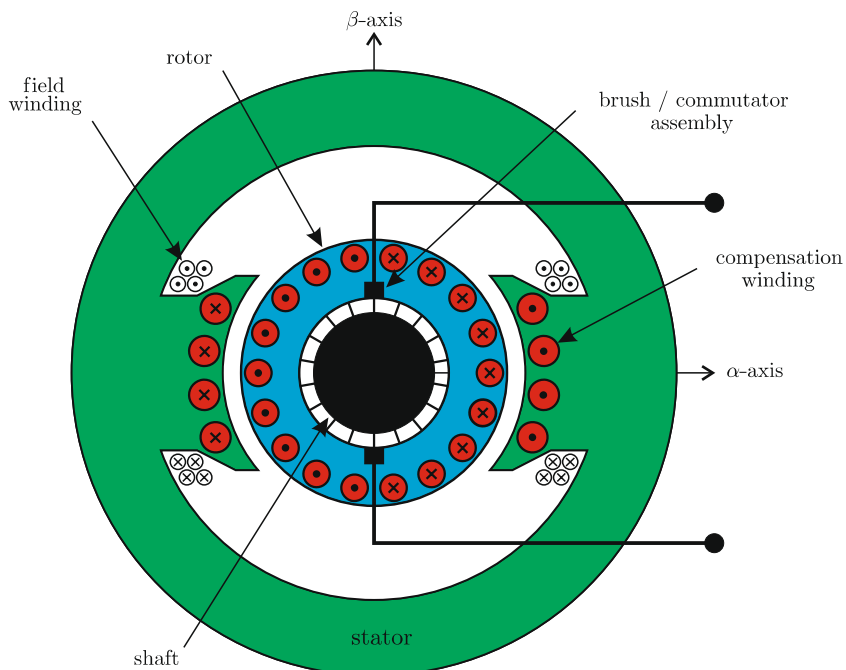


**Fig. 5.1** Cross-sectional view of a separately excited DC machine

A cross-sectional view of machine in question, as given in Fig. 5.1, is provided with a stator based excitation winding, referred to as the *field winding*, which carries a current  $i_f$ . The magnetizing inductances along both axes of the stationary  $\alpha$ ,  $\beta$  plane, also referred to as simply the real  $\alpha$ - and imaginary  $\beta$ -axis, are for this type of machine not necessarily equal, as may be observed from Fig. 5.1. For machines which carry a *compensation* winding (its principle is shown in Fig. 5.1), the magnetizing inductances along the two stationary axes are defined as  $L_{m\alpha}$  and  $L_{m\beta}$ . Also shown in Fig. 5.1 is the brush/commutator assembly used to realize a stationary (with respect to the stator) armature (rotor) current distribution. Both armature and compensating winding carry the same current (but in opposite direc-

tions, as shown in Fig. 5.1), which means that the magnetizing flux in the  $\beta$ -axis is effectively canceled. This implies that the magnetizing flux will remain oriented along the  $\alpha$ -axis and is equal to  $\vec{\psi}_m = \psi_f$ , with  $\psi_f = L_{m\alpha} i_f$  (no armature reaction). In addition to the magnetizing flux, a component perpendicular to the latter will appear due to the leakage inductance  $L_a$  of the armature winding. This flux component is not canceled by the use of a compensation winding. Note that in most field excited machines a non-linear relationship exists between the field flux and field current  $i_f$ . In permanently excited brushed DC machines the flux  $\psi_f$  is provided by a set of magnets. This reduces the overall diameter of the machine at the expense of losing one degree of freedom, namely the ability to alter the excitation flux level.

### 5.1.1 Symbolic Model of the DC Machine

The IRTF based model of this machine, as shown in Fig. 5.2, is based on the simplified model introduced in the previous chapter (see Sect. 4.2.1). The extensions introduced here are the armature inductance  $L_a$  (essentially the rotor and compensation winding leakage inductance) and armature resistance  $R_a$ . A commutator module as discussed in [68] is also shown in this figure. The commutator is taken to be ideal, i.e., an infinite set of commutator segments which in part ensures that the armature space vector current  $\vec{i}_a^{xy}$  remains stationary with respect to the stator, as discussed in Sect. 4.2.1. The relationship between the terminal DC current  $i_a$  and space vector armature current  $\vec{i}_a^{xy}$ , present on the rotor side of the IRTF, may be written as

$$\vec{i}_a^{xy} = j i_a e^{-j\theta}. \quad (5.1)$$

The corresponding voltage relationship between the rotating and stationary side of the commutator module may be found by making use of the power balance equation for said module namely

$$\underbrace{u_a i_a}_{p_a} + \underbrace{\Re \left\{ \vec{u}_a^{xy} \left( \vec{i}_a^{xy} \right)^* \right\}}_{p_a^{xy}} = 0. \quad (5.2)$$

Shown in expression (5.2) are the variables  $p_a^{xy}$  and  $p_a$  which represents the instantaneous power into the commutator from the rotor and stationary side respectively. For the IRTF module, positive electrical power on the stator and rotor side are defined to be towards and away of the module respectively [68]. For the DC machine, armature power is supplied to the stationary side when operating under motoring conditions, which implies that the power delivered by the current source  $i_a$  must be positive. Subsequent use of (5.1) with (5.2)

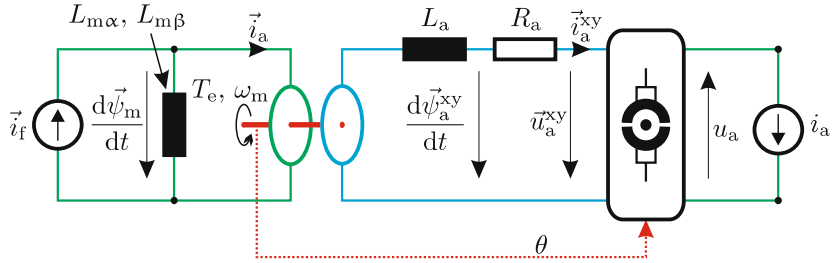


**Fig. 5.2** IRTF model of the separately excited DC machine, connected to a current source

leads to the required commutator voltage relationship

$$u_a = -\Re \{ \vec{u}_a^{xy} e^{j\theta} \}. \quad (5.3)$$

The equation set, which corresponds to this symbolic model of the machine, is given by equation set (5.4).

$$\vec{u}_a^{xy} = \frac{d\vec{\psi}_a^{xy}}{dt} - R_a \vec{i}_a^{xy} \quad (5.4a)$$

$$\vec{\psi}_a^{xy} = \vec{\psi}_m^{xy} - L_a \vec{i}_a^{xy} \quad (5.4b)$$

$$\psi_{m\alpha} = L_{m\alpha} (i_{f\alpha} - i_{a\alpha}) = L_{m\alpha} i_f = \psi_f \quad (5.4c)$$

$$\psi_{m\beta} = L_{m\beta} (i_{f\beta} - i_{a\beta}) = 0 \quad (5.4d)$$

Not shown in equation set (5.4) are the equations linked specifically to the IRTF module.

Some simplification of the symbolic model according to Fig. 5.2 may be achieved by introducing the field flux variable  $\psi_f = L_{m\alpha} i_f$ , which implicitly assumes a linear flux linkage/current relationship. Due to the presence of the compensation winding, the imaginary part of the magnetizing flux  $\psi_{m\beta}$  is compensated to zero. Additionally, the current component  $i_{a\alpha}$  is set to zero by defining the armature current according to (5.1), with  $\vec{i}_a = \vec{i}_a^{xy} e^{j\theta}$ . These two conditions lead to a magnetizing flux which equals the field flux ( $\vec{\psi}_m = \psi_f$ ). In the resultant equation set (5.5) a term  $\psi_f e^{-j\theta}$  appears, which is magnetizing flux seen in rotor coordinates, i.e.,  $\vec{\psi}_m^{xy} = \vec{\psi}_m e^{-j\theta}$ .

$$\vec{u}_a^{xy} = \frac{d\vec{\psi}_a^{xy}}{dt} - R_a \vec{i}_a^{xy} \quad (5.5a)$$

$$\vec{\psi}_a^{xy} = \psi_f e^{-j\theta} - L_a \vec{i}_a^{xy} \quad (5.5b)$$

Note, that in steady-state all variables as observed in rotational xy coordinates are sinusoidal.

### 5.1.2 Generic Model DC Machine

The generic model of the separately excited machine can be derived by using (5.5) and the corresponding IRTF equation set. An example of implementation is given in Fig. 5.3, which shows the *IRTF-current* based model. The flux  $\psi_f$  may be provided by either the field winding, which carries a current  $i_f$  or set of permanent magnets, as discussed previously.

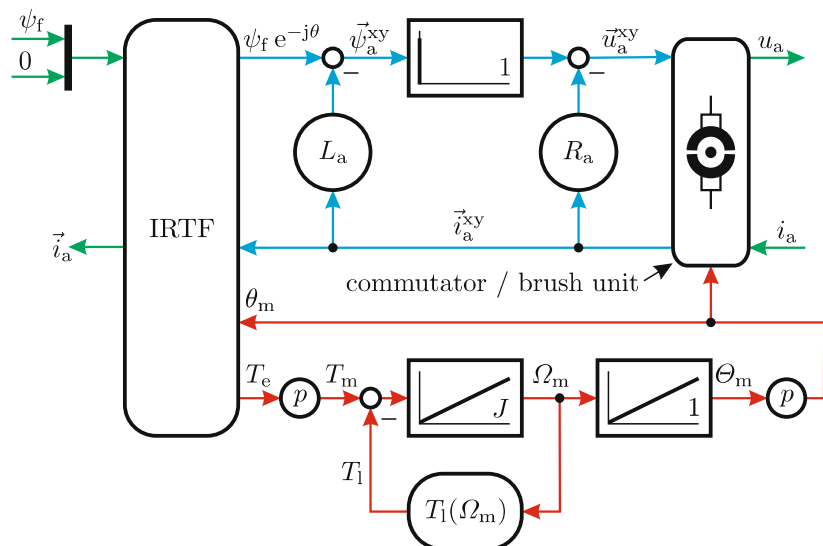


**Fig. 5.3** Generic model of a separately excited machine, connected to a current source

The tutorial given in Sect. 5.4.1 is concerned with a model of the machine, according to Fig. 5.3. This tutorial also shows the impact, of using a segmented brush/commutator assembly. Note that the ability to demonstrate the use of a non-ideal commutator is made possible by the use of an IRTF based modeling approach for this type of machine.

## 5.2 Field-Oriented Machine Model

In the machine models discussed previously, the current, voltage and flux linkage space vectors on the armature side of the machine were defined with respect to a shaft oriented reference frame. In this section, a *flux oriented* transformation is introduced which will prove to be of significance for three-phase AC drives. The introduction of this concept is deemed to be helpful for

the process of familiarizing the reader with the basic conversion principles. Central to the flux oriented coordinate transformation concept is the notion of aligning a complex plane consisting of a *direct*  $\Re^{dq}$  and *quadrature* axis  $\Im^{dq}$  with the flux vector  $\vec{\psi}_m^{xy}$ , as indicated in Fig. 5.4. Also shown in this diagram is the current vector  $\vec{i}_a^{dq}$  which is orthogonally oriented to the magnetizing vector when the brush assembly is positioned correctly. The corresponding transformation is (for the DC machine) of the form  $\vec{\psi}_m^{dq} = \vec{\psi}_m^{xy} e^{j\theta}$ , which in this case gives  $\vec{\psi}_m^{dq} = \vec{\psi}_f$ . A transformation along similar lines is also required for the armature flux and current vectors. The observant reader will note that the dq transformation is in this case a transformation to the stationary coordinate reference frame.

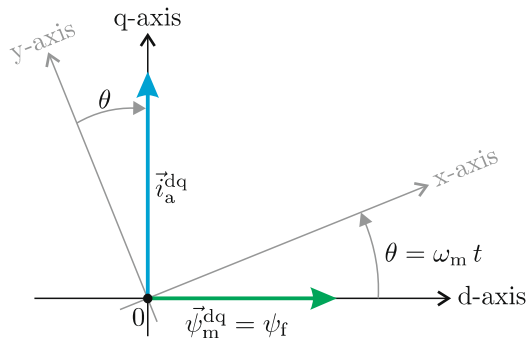


**Fig. 5.4** Vector diagram with direct and quadrature axis for separately excited DC machine

The coordinate transformation process which leads to a symbolic and generic representation of the field-oriented model of the DC machine may be undertaken with the aid of (5.5) and (5.1). The resultant equation set for the field-oriented model may be written as

$$\vec{u}_a^{dq} = \frac{d\vec{\psi}_a^{dq}}{dt} - R_a \vec{i}_a^{dq} - j \omega_m \vec{\psi}_a^{dq} \quad (5.6a)$$

$$\vec{\psi}_a^{dq} = \vec{\psi}_f - L_a \vec{i}_a^{dq} \quad (5.6b)$$

$$\vec{T}_e = \vec{\psi}_f \times \vec{i}_a^{dq}. \quad (5.6c)$$

Use of (5.6a) and (5.6b) with (5.3) and  $\vec{i}_a^{dq} = ji_a$  gives (after grouping the imaginary components) the following expression

$$u_a = R_a i_a + L_a \frac{di_a}{dt} + \omega_m \psi_f \quad (5.7a)$$

$$T_e = \psi_f i_a. \quad (5.7b)$$

Furthermore, equation set (5.7) also contains, for completeness, an expression for the torque. Observation of said expression shows that the complete generic

model of the current source connected DC machine (without the mechanical load equations) can be directly derived without the need for additional modules or use of an IRTF module. The underlying assumption is the presence of an ideal brush/commutator assembly. A symbolic representation of the quadrature axis based model, which corresponds with (5.7), is given in Fig. 5.5. In this case, the direct axis components of (5.6) are not relevant for the DC model because the direct axis current component is chosen to be equal to zero, as may be observed from Fig. 5.4.

The development of a current source based generic model, which corresponds to Fig. 5.5, may be undertaken with the aid of (5.7b), leading to the model shown in Fig. 5.6.

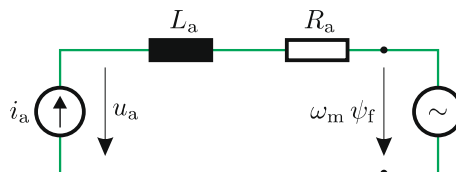


**Fig. 5.5** Symbolic field-oriented model: quadrature axis configuration

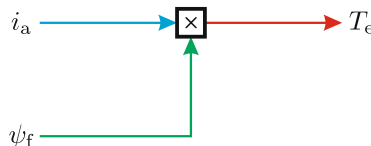


**Fig. 5.6** Generic model of current source connected separately excited DC machine

The importance of this simple model is not to be underestimated as it shows the importance of using current control with a DC machine. For example, the ability of the machine to respond quickly to a step change in the torque is dictated by the current controller in use. This will become apparent in the control section of this chapter. Furthermore, there is complete decoupling between the current and field flux variables. The latter can also be used to control the torque. However, the time constant associated with controlling this variable is significantly larger than those linked with the armature circuit (see Fig. 5.5). The reason for this is that the time constant linked to the field winding is defined as  $L_f/R_f$  with  $L_f = L_{m\alpha} + L_{\sigma f}$ . The variables  $L_{\sigma f}$  and  $R_f$  represent the field leakage inductance and field winding resistance respectively. Typically,  $L_f$  is much larger than  $L_a$ . Therefore, the armature time constant is considerably shorter than the time constant of the field winding. It is noted that current control leads to more efficient drive operation because the dissipative losses are reduced (when compared to a voltage-controlled machine), as may be deduced from the tutorial discussed in Sect. 5.4.2.

### 5.3 Control of Separately Excited DC Machines

The interpretation of the term *control* is primarily considered from the perspective of achieving a specified dynamic torque and excitation response. The basic approach envisaged is to *invert* the dynamic current source field-oriented model with the purpose of generating the required reference current(s) for a given user defined torque reference value. A second *control* objective is to integrate the control concept with a voltage source machine, using the current control and modulation strategies discussed in the previous two chapters. In addition to these two *control* objectives, there is a need to consider the optimum use of the drive within the constraints imposed by the maximum DC supply voltage source and maximum current of machine or power electronic devices. Henceforth, attention is given to the issue of establishing the optimum performance trajectories and control techniques which may be deployed.

#### 5.3.1 Controller Concept

The process of developing a DC drive controller may be initialized by making use of the generic model given in Fig. 5.6 and reconfiguring this topology with the torque as an input variable. Application of this *inversion* principle using the generic model, according to Fig. 5.6, shows that it may be reduced to the configuration given in Fig. 5.7.

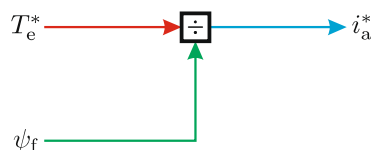


**Fig. 5.7** Inversion of DC machine current control structure

Input to this model is the required torque reference value  $T_e^*$  for the drive and the field flux value  $\psi_f^*$  of the DC machine in use. Output of the controller is the current reference value  $i_a^*$  which will act as an input for a single-phase current controller (as discussed in Sect. 3.1.1 and Sect. 3.1.2) to maintain the condition  $i_a = i_a^*$ . In permanent magnet DC machines, where the field excitation is provided by magnets, the flux  $\psi_f$  will be inevitable constant. In this case, the armature reference current is the only control variable available for controlling the torque. However, this value must be constrained to ensure that the maximum current limits of the machine or the converter are not exceeded. Consequently, it prudent to introduce a current control variable  $i_a^c$  which will be equal to  $i_a^*$ , provided the machine is operating within its

intended design envelope. When specific drive limits (maximum current or voltage limits of machine or converter) are reached, the controller should act to reduce the value of  $i_a^c$  in which case its value will not be equal to  $i_a^*$ .

In electrically excited DC machines, the variable  $\psi_f$  can be set by the controller. As such, an additional degree of control flexibility is provided, which will prove to be beneficial at high speed operation. When operating within the normal design envelope, the flux value will normally be set to its highest level, designated as  $\psi_f^{\max}$ , which will ensure that torque production is realized with the lowest armature current level. Such an approach will serve to minimize armature copper loss, which will in turn improve the efficiency of the machine. However, in some cases the controller may need to vary the value of the field by introducing a control variable  $\psi_f^c$ . The *extended DC control structure* as given in Fig. 5.8 contains an additional (compare to Fig. 5.7) control module which generates the required control variables  $i_a^c$  and  $\psi_f^c$ , which are to be used by the armature current controller and field excitation converter (if present) respectively.

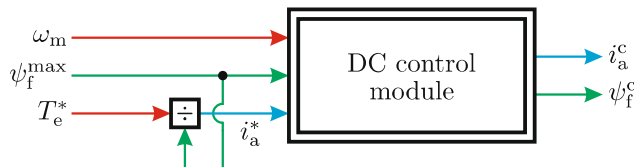


**Fig. 5.8** Extended DC machine control structure

The introduction of the DC control unit simply ensures that the machine can be optimally utilized within its steady-state operational limitations.

### 5.3.2 Operational Drive Boundaries

To visualize the control laws and operating limits imposed by the maximum voltage and current values, it is helpful to utilize the complex plane linked to the real (direct) d-axis which is tied to the positive axis of the flux vector  $\vec{\psi}_m^{dq}$  (see Fig. 5.4). In this diagram, henceforth referred to as the *current locus diagram* or *synchronous Blondel diagram*, the reference current vector  $\vec{i}_a^{dq}$  will be shown together with the operating limits of the drive. Note that for a DC drive, the orientation of the current vector is determined solely by the brush/commutator assembly, as was discussed in Sect. 4.2.1.

For the purpose of identifying the limits of the drive it is helpful to reconsider (5.6c) and (5.7b), which show that lines of constant torque may be represented as  $\Im\{\vec{i}_a^{dq}\} = i_a = T_e/\psi_t$  in the current locus diagram. Furthermore, the current constraint  $|\vec{i}_a^{dq}| \leq i_a^{\max}$  may be interpreted as the operating

region within a (red) maximum ampere (MA) circle with radius  $i_a^{\max}$ , as shown in the current locus diagram given in Fig. 5.9.

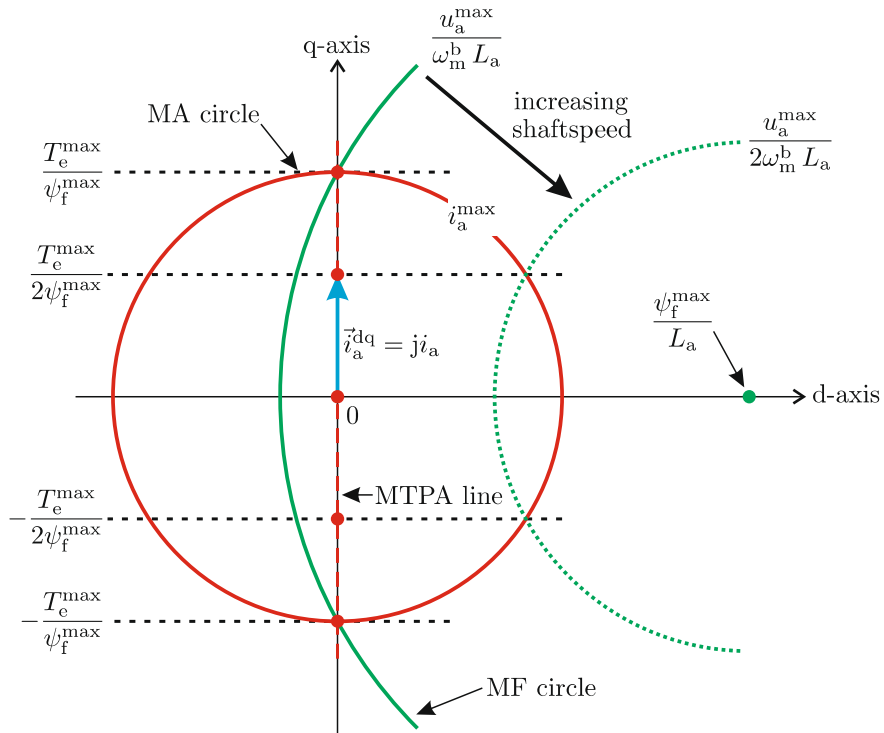


**Fig. 5.9** Operational drive limits: DC drive

This diagram also shows the lines of constant torque as discussed above. In this context, the lines  $\Im\{\vec{i}_a^{\text{dq}}\} = \pm i_a^{\max}, \pm 1/2 i_a^{\max}$  are shown in terms of the maximum torque value which is defined as  $T_e^{\max} = i_a^{\max} \psi_f$ , with  $\psi_f = \psi_f^{\max}$ .

Also shown in this diagram is a set of so-called *maximum flux* MF circles (shown partly to limit the figure size) which are tied to the maximum voltage constraint  $u_a^{\max}$ . The introduction of these circles is based on the use of (5.6a) and the underlying assumption of quasi-steady state operation, i.e., differential terms may be ignored. This implies that the dominant term in this expression is formed by the induced voltage term  $\omega_m |\vec{\psi}_a^{\text{dq}}|$ , i.e., the resistive term is ignored in this analysis. With this assumption in mind, the stator flux variable  $\psi_a^\omega$  is introduced, which represents the magnitude of the vector  $\vec{\psi}_a^{\text{dq}}$ . This variable can, according to (5.6a), with  $|\vec{v}_a^{\text{dq}}| = u_a^{\max}$  and  $\vec{v}_a^{\text{dq}} \cong j\omega_m \vec{\psi}_a^{\text{dq}}$ , be written as

$$\psi_a^\omega \cong \frac{u_a^{\max}}{\omega_m}. \quad (5.8)$$

From an operational perspective, the variable  $\psi_a^\omega$  represents the maximum armature flux value which may be realized by the converter for a given speed  $\omega_m$  and voltage  $u_s^{\max}$ . Use of  $|\vec{\psi}_a^{dq}| = \psi_a^\omega$  with (5.6b) and equating the real and imaginary components of  $\vec{i}_a^{dq}$  gives

$$\left( i_{ad} - \frac{\psi_f}{L_a} \right)^2 + i_{aq}^2 = \left( \frac{\psi_a^\omega}{L_a} \right)^2. \quad (5.9)$$

Observation of (5.9) shows that this expression is indeed a circle with its origin at coordinates  $(\psi_f/L_a, 0)$  and radius  $(\psi_a^\omega/L_a = u_s^{\max}/\omega_m L_a)$ , as shown in the so-called synchronous Blondel diagram (Fig. 5.9). The circles of maximum available armature flux will increase in radius as the shaft speed is reduced. Consequently, an operating speed will occur where the MF circle (see Fig. 5.9) will completely encompass the MA circle. This implies that the direct axis current value  $i_{ad} = \Re\{\vec{i}_a^{dq}\}$  for the controller may hypothetically be chosen (within the area bound by the MA circle) with impunity for a given quadrature current value  $i_{aq}$  in the range  $\pm i_a^{\max}$ . In practice, this is not realizable given the need to rotate the brush/commutator assembly to achieve the rotation of the vector  $\vec{i}_a^{dq}$ . Alternatively, the compensation winding could be fed by a separate current source ( $i_{cw} \neq i_a$ ), which is prohibitive from a cost viewpoint. However, from a didactic perspective, it is instructive to entertain this concept. Given a choice of current orientation in the  $dq$  plane it is prudent to set the direct axis current to zero, which implies an operating trajectory along the imaginary axis of the Blondel diagram. This so-called *maximum torque per ampere MTPA* operating line as shown in Fig. 5.9 represents the control law according to

$$i_{ad} = 0 \quad (5.10a)$$

$$i_{aq} = 0 \rightarrow \pm i_a^{\max}. \quad (5.10b)$$

This signifies an operating trajectory where the highest torque is obtained with the lowest armature current value, which is precisely how the brush/commutator assembly orientation is determined for a DC machine (see (5.1) and Sect. 4.2.1). As the shaft speed increases, the maximum flux circle reduces in radius until a speed referred to as the *base operating speed*  $\omega_m^b$  is reached where the MF circle intersects the MTPA line at coordinates  $0, \pm i_a^{\max}$ . This speed corresponds to an operating point often referred to as the *saturation point* or *corner point* of the drive. It represents the highest operating speed where the control law according to (5.10) can be used without any constraints imposed by the maximum armature flux value  $\psi_a^\omega$ . Subsequent mathematical evaluation of (5.9) and (5.10) shows that the base speed may be written as

$$\omega_m^b = \left( \frac{u_s^{\max}}{\psi_f^{\max}} \right) \frac{1}{\sqrt{1 + \frac{1}{\kappa_{DC}^2}}} \quad (5.11)$$

with

$$\kappa_{DC} = \frac{\psi_f^{max}}{L_a i_a^{max}}. \quad (5.12)$$

For DC machines, the coefficient  $\kappa_{DC}$  represents the ratio between the excitation flux and leakage flux defined by the term  $L_a i_a^{max}$ . To ensure seamless commutation, i.e., with minimum sparking under the brushes, the condition  $\kappa_{DC} \gg 1$  is enforced in DC machines. The reason for this is that the brush/commutator assembly is oriented in such a manner that the armature winding section being commutated has the lowest possible induced voltage. This will be the case when the winding section being commutated is orthogonal to the excitation flux direction. With increasing armature current, the excitation flux direction will be rotated by an orthogonal leakage flux component. This leads to a higher induced voltage in the winding being commutated, which in turn can cause current discontinuities (referred to as *under commutation*) during the commutation process. This phenomenon is associated with sparking in the brush/commutator assembly. It is therefore important to ensure that the resultant flux direction seen by the armature winding does not significantly deviate from the field or PM excitation flux, otherwise the brush/commutator assembly would need to be either rotated. The latter is in most cases not practical. So-called *interpoles*, in effect similar to compensation windings, may be introduced to improve the commutation process.

Further observation of Fig. 5.9 shows that for machines with a fixed  $\psi_f^{max}$  value, e.g. permanent magnet based machines, a maximum shaft speed  $\omega_m^{max}$  exists where the MF flux circle no longer intersects the MTPA line. The shaft speed at which this occurs may be found by inspection of Fig. 5.9 which leads to

$$\omega_m^{max} = \frac{u_s^{max}}{\psi_f^{max}}. \quad (5.13)$$

For most machines, the maximum shaft speed is also approximately equal to the base speed, given that the condition  $\kappa_{DC} \gg 1$  holds, in which case (5.11) reduces to (5.13), hence  $\omega_m^b \simeq \omega_m^{max}$ .

For machines with a field winding, the prospect of varying the field flux by changing the field current is viable. Consider for example a machine operating with  $i_a = i_a^{max}$  and speed  $\omega_m = \omega_m^b$  (intersection of the MTPA line with the MA circle, see Fig. 5.9) at the saturation point of the drive. Operation at the saturation point of the drive may be maintained beyond the base operating speed provided that the field flux is adjusted to ensure that the MF circle is kept on the drive saturation point as exemplified by Fig. 5.10.

In this figure, the coefficient  $\kappa_{DC}$  has been purposely set to an unrealistically low value, as would be the case when no armature current flows in the compensation windings, to demonstrate the field weakening concept in a single diagram. It is emphasized that in practical machines the coefficient  $\kappa_{DC}$  will be significantly greater than the value used in Fig. 5.10, as was mentioned earlier. Subsequent mathematical analysis based on the use

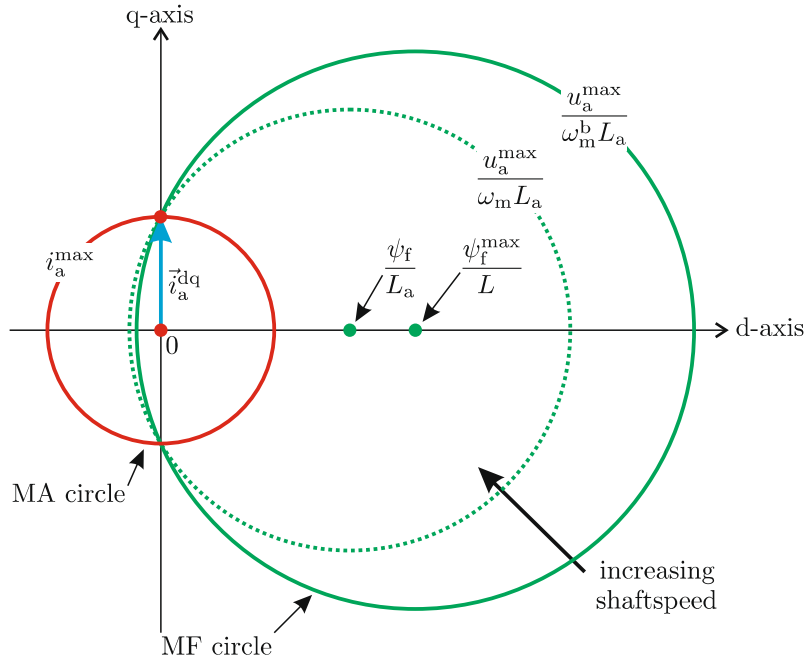


**Fig. 5.10** Field weakening  $\psi_f < \psi_f^{\max}$ : Operation for  $\omega_m > \omega_m^b$

of Fig. 5.10 shows that the relationship between flux and speed as given by (5.14) must be maintained to keep the operating point of the drive on the *saturation point* of the drive.

$$\psi_f = \sqrt{\left(\frac{u_a^{\max}}{\omega_m^b}\right)^2 \left(\left(\frac{\omega_m^b}{\omega_m}\right)^2 - 1\right) + (\psi_f^{\max})^2} \quad (5.14)$$

Substitution of (5.11) with  $\kappa_{DC} \gg 1$  into expression (5.14) leads to

$$\psi_f \simeq \psi_f^{\max} \left( \frac{\omega_m^b}{\omega_m} \right) \quad (5.15)$$

which is valid for  $\omega_m \geq \omega_m^b$ . Note that the above example was undertaken with  $i_a = i_a^{\max}$ . In theory, operation along the MTPA line can be extended in the range  $\omega_m^b < \omega_m < \omega_m^{\max}$  for armature currents somewhat less than  $\pm i_a^{\max}$ . However, for DC machines this is not practical given the typical large value of  $\kappa_{DC}$ , which leads to the previously stated condition  $\omega_m^b \simeq \omega_m^{\max}$ . Hence, the flux weakening control law according to (5.15) is assumed for operation above the base speed for all currents in the range  $0 \rightarrow \pm i_a^{\max}$ . In the so-called *field weakening mode* of operation, the ratio between leakage flux  $L_a i_a$  and field flux  $\psi_f$  will increase as the shaft speed becomes larger.

A limit is imposed on said ratio to ensure that the commutation process is not significantly affected by under-commutation) at high speeds. Hence, a user set shaft speed  $\omega_m^k$  is defined which corresponds to the largest acceptable ratio  $i_a^{\max}/\psi_f$ . For operation beyond this speed the flux will be kept constant, in which case the current  $i_a$  needs to be reduced to maintain the armature voltage at the value  $u_a^{\max}$ . It is emphasized that this mode of operation also acts as a protection against *over-speeding* and is put in place as a safety precaution. The maximum speed obtainable under minimum flux conditions is found using (5.13), where  $\psi_f^{\max}$  must be replaced with the value of  $\psi_f$  as calculated with the aid of expression (5.15) and  $\omega_m = \omega_m^k$ . This leads to

$$\omega_m^{F,\max} = \omega_m^{\max} \left( \frac{\omega_m^k}{\omega_m^b} \right). \quad (5.16)$$

The current during the interval  $\omega_m^k < \omega_m < \omega_m^{F,\max}$  is given as

$$i_a^F = i_a \left( \frac{\omega_m - \omega_m^{F,\max}}{\omega_m^k - \omega_m^{F,\max}} \right). \quad (5.17)$$

In the following subsection, the control laws which need to be implemented in the DC control module, shown in Fig. 5.8, are developed. The operational sequence that is used in the simulation will also be used for the synchronous and induction machine drives. Initially, the machine is assumed to be at standstill, at which point in time a torque step equal to half maximum torque is applied. The behavior of the drive under quasi-steady state conditions is examined for operation over a given speed range to understand speed and current limits of the drive. Application of the above mentioned operation sequence for the DC drive causes the controller to change the armature current and flux values as function of speed, as may be observed from Fig. 5.11.

Observation of Fig. 5.11 shows that the flux (*red* trace) and current variables are normalized with respect to  $\psi_f^{\max}$  and  $i_a^{\max}$  respectively. Furthermore, the horizontal speed axis has also been normalized with respect to the base speed  $\omega_m^b$  of the drive. Also shown in Fig. 5.11 is the corresponding normalized (with respect to the maximum output power level) output power versus normalized shaft speed characteristic of the drive for the chosen operating sequence.

Shown in Fig. 5.11 are three regions identified as A, B and C respectively, which are linked to the following operating limits namely:

- Base speed area (region A): operating speed range  $0 \rightarrow \omega_m^b$ , in normalized form from  $0 \rightarrow 1$ . Flux  $\psi_f$  is set to its maximum value  $\psi_f^{\max}$ . Operation from zero to rated current  $i_a^{\max}$  provides torque output from zero to maximum (rated) torque  $T_e^{\max}$ . The output torque can be maintained at constant level in this region.

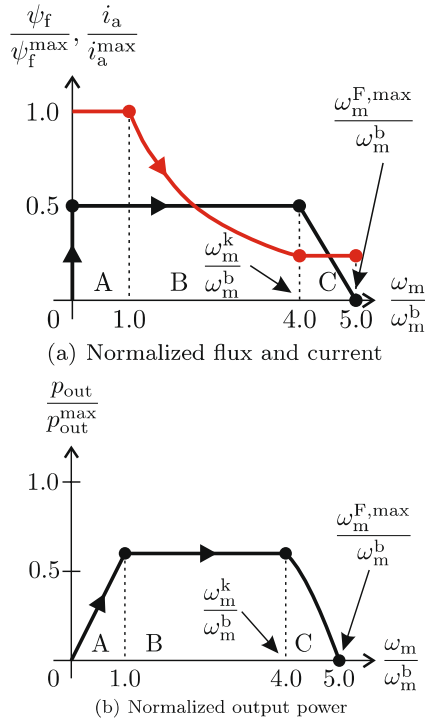


**Fig. 5.11** Operational drive trajectory of a separately excited DC machine under quasi-steady state conditions with armature current set to 50% of  $i_a^{\max}$

- Field weakening area (region B): operating speed range  $\omega_m^b \rightarrow \omega_m^k$ , in normalized form from 0 → 4, where in the numerical example given  $\omega_m^k$  is arbitrarily set to  $4\omega_m^b$ . Flux becomes inversely proportional to the shaft speed (5.15). Operation from zero to rated current  $i_a^{\max}$  provides output power from zero to maximum (rated) output power  $p_{out}^{\max}$ . The output power can be maintained at a constant level (whilst keeping the current constant), which is why this region is also referred to as the *constant power region*.
- Overspeed region (region C): operating speed range  $\omega_m^k \rightarrow \omega_m^{F,\max}$ , in normalized form from 4 → 5, where in the numerical example given  $\omega_m^{F,\max}$  is arbitrarily set to  $5\omega_m^b$ . Flux level set to the minimum recommended level set by the machine manufacturer to avoid excessive arcing in the brush/commutator assembly. Armature current reduced to zero according to (5.17).

For the selected operational sequence used to derive Fig. 5.11, a current step to  $1/2i_a^{\max}$  was initiated at zero shaft speed. In addition, the controller flux was set to its highest value, namely  $\psi_f^{\max}$ . The operating point for

operation below the base speed, is represented in Fig. 5.9 by the vector  $\vec{i}_a^{dq}$  which is positioned on the MTPA line of the drive. When the drive reaches the base speed, the MF flux circle will intersect with the vertical axis of the synchronous Blondel diagram at the saturation point(s) of the drive. For operation beyond the base speed, the controller keeps the MF flux circle on the saturation point of the drive by changing the flux level in accordance with (5.16). As speed increases in the field weakening region of the drive, the ratio  $L_a i_a^{\max} / \psi_f$  increases. This is why an upper limit  $\omega_m^k$  to the field weakening mode is usually enforced, as may be observed from Fig. 5.11.

### 5.3.3 Use of Current Source IRTF Based Model

The process of integrating the control concepts with the electrical drive may be initially undertaken with the aid of a current source model of the DC machine. This approach, which is also used for synchronous and induction machine drives, is effective given that the dynamics of the current controller are removed from the drive. Ignoring (initially) the dynamics and implementation details of the current controller is warranted because the electrical time constant associated with current control is usually much shorter than those linked with the mechanical side of the drive (at least for machines which utilize a compensation winding). A generic representation of the IRTF based current-controlled DC machine (see Fig. 5.3), with a control structure as given by Fig. 5.8, is shown in Fig. 5.12. This controller has torque  $T_e^*$  as input control variable. Outputs of the DC control module are the current reference  $i_a^c$  and field flux reference value  $\psi_f^c$ . For the current based approach considered in this section, the current reference value  $i_a^c$  will be equal to the current in the machine. Likewise, the field flux  $\psi_f$  is deemed to be equal to the flux reference  $\psi_f^c$ .

In this drive controller example, the shaft speed is assumed to be measurable, i.e., a speed/or position encoder is attached to the shaft, as shown in Fig. 5.12. This approach may not be viable in some applications, either because only one shaft end is available (for the load), or robustness and reliability considerations may preclude the use of a shaft sensor, in which case sensorless techniques must be used. In the accompanying tutorial given in Sect. 5.4.3, a drive model according to Fig. 5.3 is discussed which exemplifies the controller concepts outlined in this and the previous section.

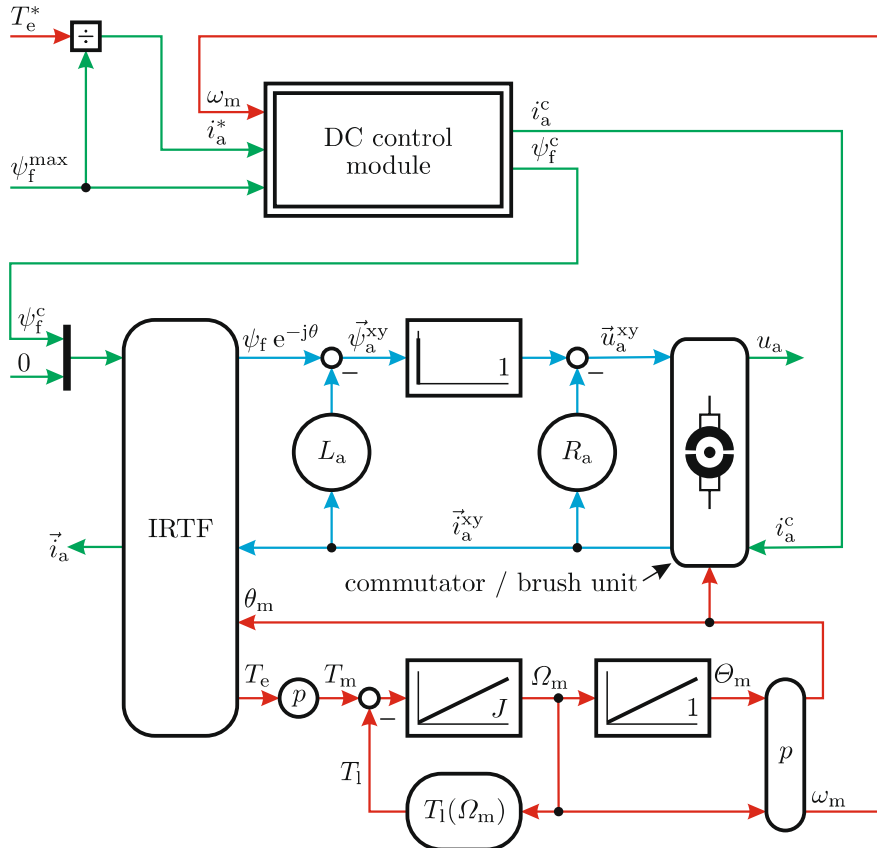


**Fig. 5.12** DC drive with current source IRTF based machine model

### 5.3.4 Use of a Voltage Source with a Model Based Current Control

In modern drives voltage source power converters are used as discussed in Sect. 2.3. In terms of current control, a hysteresis type controller as discussed in Sect. 3.1.1, or a model based controller approach (see Sect. 3.1.2) may be used. Regularly sampled controllers are most commonly used, which is why the model based control technique discussed in the previous chapter is used in this section. A voltage source connected model is required and for this purpose the field-oriented model which is based on equation set (5.7). The complete electrical drive, with the DC controller as introduced in the previous section, is shown in Fig. 5.13. It brings together a range of concepts introduced in this and the previous two chapters.

The required proportional and integral gain values are calculated using (3.8), where the variables  $L$  and  $R$  represent the armature inductance and

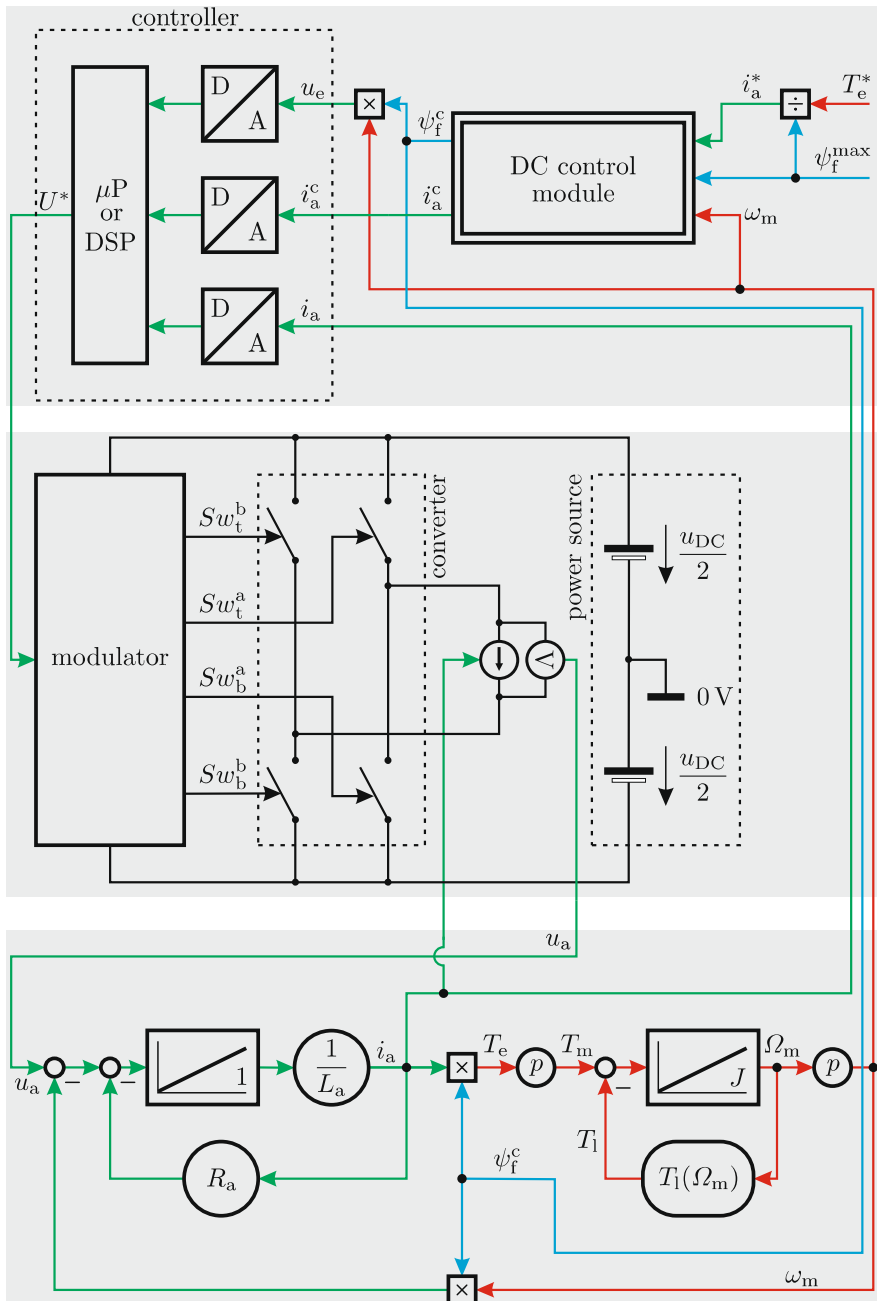


**Fig. 5.13** DC drive with model based current control and voltage source based machine model

armature resistance respectively. In addition to the above, it is favorable to generate the term  $u_e = \psi_f^c \omega_m$ , i.e., the induced voltage or back EMF of the machine, for the current controller (see (3.7)). This is realized by making use of the DC controller field flux value  $\psi_f^c$  and measured shaft speed  $\omega_m$ . In most cases the controller flux reference  $\psi_f^c$  is used and converted to a field current reference value  $i_f^c$  which requires knowledge of the inverse magnetization characteristic  $i_f^c(\psi_f^c)$ . A second current controller is then used to control the field current in the machine. A tutorial is given in Sect. 5.4.4 which gives the reader the opportunity of examining in detail the waveforms and variables introduced in the drive model discussed in this section. Note that the effects of converter *dead time* are not included in these models, as was mentioned in Sect. 2.5.

## 5.4 Tutorials

### 5.4.1 Tutorial 1: Current Source Model of a Brushed DC Machine with Segmented Commutation Module

The aim of this tutorial is to build a dynamic, current controlled DC machine model with parameter values as specified in Table 5.1. The model in question is to be built according to the generic diagram for this machine, as given in Fig. 5.3. An example of the proposed simulation model is given in Fig. 5.14.

**Table 5.1** DC machine parameters

Parameters	Value		
Armature inductance	$L_a$	0.05	H
Armature resistance	$R_a$	10	$\Omega$
Field flux	$\psi_f$	1.0	Wb
Inertia	$J$	0.005	$\text{kg m}^2$
Initial rotor speed	$\omega_m^o$	0	rad/s

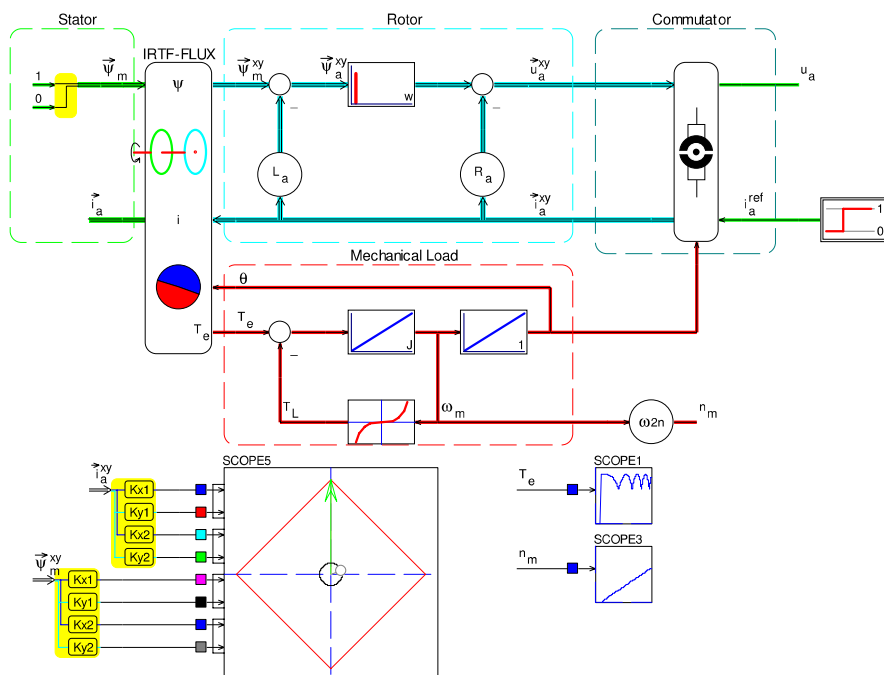


**Fig. 5.14** Simulation of current controlled brushed DC motor with  $N_{\text{seg}} = 4$

The commutator segmentation unit, which is the module that provides the angle input for the commutator module shown in this figure, requires the user to specify the number of segments  $N_{\text{seg}}$  of the machine. Set the value initially to  $N_{\text{seg}} = 40$ , which is sufficiently high to represent the *ideal* (infinite segment) model. The segmentation module may of course be removed, in the event that segmentation effects are not required to be modeled. In this tutorial, the segmentation module has been included to illustrate the effects of segmentation, given the uniqueness of being able to demonstrate this phenomenon using an IRTF based model.

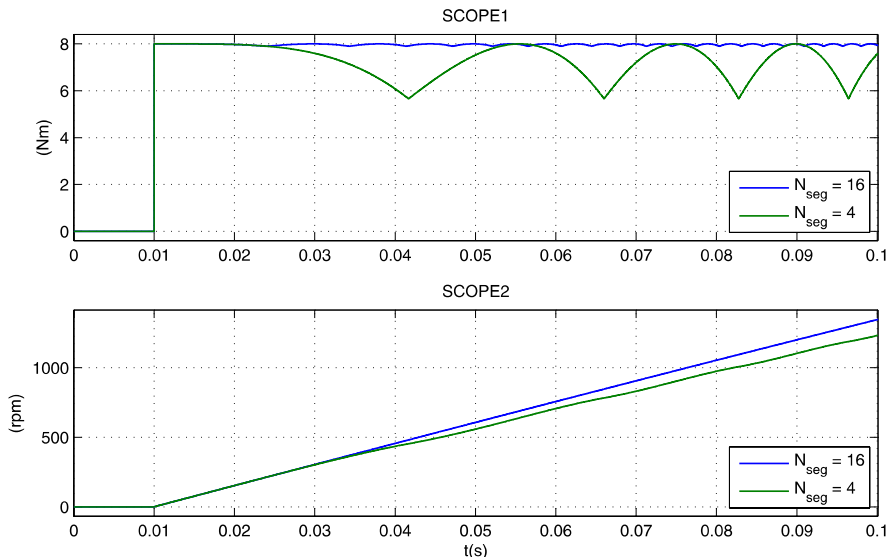


**Fig. 5.15** Simulation results for a current controlled DC machine, using a current source and  $N_{\text{seg}} = 16$  and  $N_{\text{seg}} = 4$

The machine is to be studied by considering a start-up sequence from zero shaft speed with a mechanical load connected. The load torque/speed curve is assumed to be a quadratic function. The load module settings are selected to produce a load torque of 2 Nm at 3000 rpm. Electrically, a current step of  $i_a = 8$  A is to be applied to the machine at  $t = 10$  ms. Add a set of display modules as indicated in Fig. 5.14, to visualize the shaft speed (in rpm) and shaft torque during the simulation process. Under the *simulation/simulation parameters* dialog window, select a step size of 10  $\mu$ s and run the simulation for a time interval of 0.1 s. An example of the results which should appear with the chosen armature current, field flux and load module settings is given in Fig. 5.15 for both  $N_{\text{seg}} = 16$  and  $N_{\text{seg}} = 4$ . In addition, an xy plot (*scope 3* in Fig. 5.14) has been included to allow the user to examine the vectors  $\bar{i}_a^{\text{xy}}$  and  $\bar{\psi}_{\text{in}}^{\text{xy}}$  which will rotate in a clock-wise direction in this case, given that

a counter clock-wise, positive shaft speed will appear in this simulation. Of particular interest is the change in the current vector which will take place when the segmentation variable  $N_{\text{seg}}$  is set to a low value. The reader is advised to observe the motion of the flux and current space vectors during the simulation sequence, as they provide fundamental insights to the operating principles of the DC machine.

### 5.4.2 Tutorial 2: Modeling of a Current and Voltage Source Connected Brushed DC Motor

This tutorial is concerned with comparing a voltage controlled and identical current controlled brushed DC machine, with a view to determine which is preferable in terms of operating efficiency. For this purpose, a machine with parameters according to Table 5.1 is to be deployed. It is to be used under no-load conditions, i.e., no external mechanical load connected.

A voltage step of  $u_a^* = 80 \text{ V}$  is to be applied at  $t = 10 \text{ ms}$  to the voltage source connected machine which is assumed to be initially at standstill. The no-load shaft speed  $\omega_m^v$  is to be obtained at  $t = 200 \text{ ms}$ , which represents the time mark where steady-state operation is achieved for the machine in question. The no-load machine shaft speed  $\omega_m^v$  of the voltage source connected machine is to be used to calculate the required armature current  $i_a^*$  which must be applied at  $t = 10 \text{ ms}$  to the current source connected machine to achieve the same shaft speed as the voltage source connected machine at  $t = 200 \text{ ms}$ . Determine for both machines the dissipated energy over the designated run period and on the basis of these results, identify which mode of operation is preferred in terms of operating efficiency. To obtain an answer to the posed question, a voltage source based symbolic model according to Fig. 5.5 may be used which must be transformed to its generic representation as shown in the simulation given in Fig. 5.16.

In terms of the current controlled model topology, we could also have used Fig. 5.6, together with the appropriate mechanical modules needed to obtain the shaft speed  $\omega_m$ . Alternatively, the IRTF based model, as discussed in the previous tutorial, may be deployed. This is the approach taken in this tutorial as may be observed from Fig. 5.16. Computation of the required current  $i_a^*$  needed for the current source connected machine to reach the shaft speed  $\omega_m^v$  may be undertaken with the aid of equation set (4.6), with  $T_l = 0$  and (5.7b), which gives

$$i_a^* = \frac{J \omega_m^v}{\psi_f \Delta T} \quad (5.18)$$

where  $\Delta T$  represents the run-time of machine, which in this case, equals  $\Delta T = 190 \text{ ms}$ . The energy dissipation during the run-up interval may be found by evaluation of the integral  $E_d = \int R_a i_a^2 dt$ . This task is carried out in the simulation via the two sub-modules named *Energy module*.

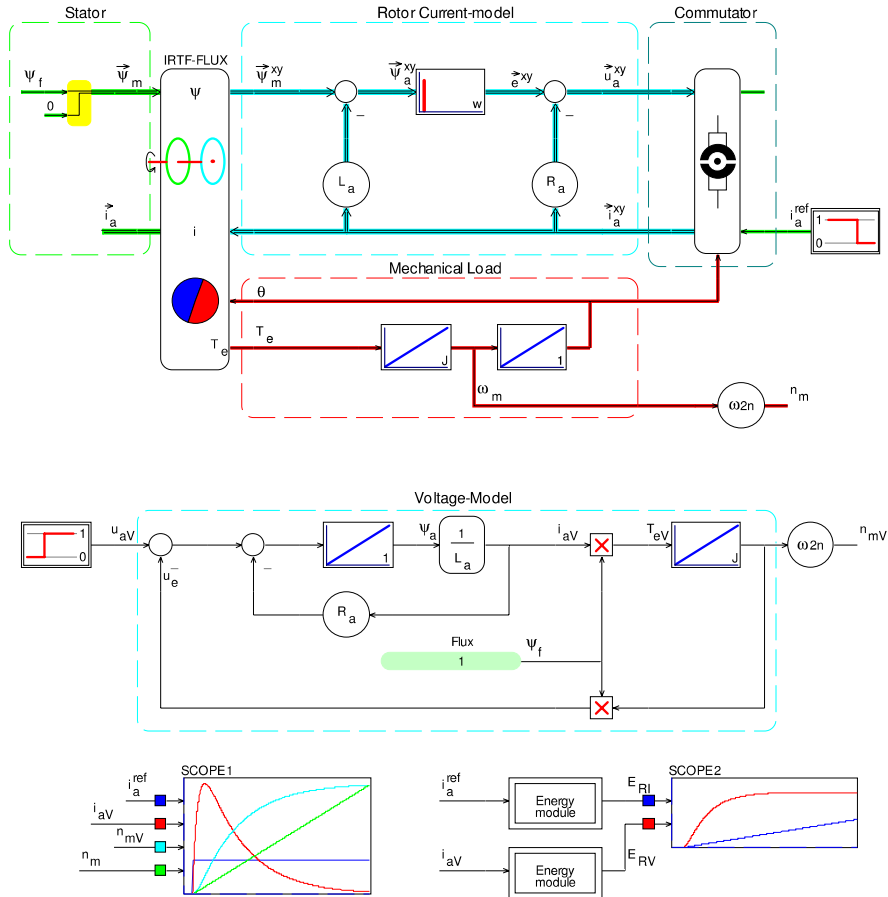


**Fig. 5.16** Simulation of current and voltage source connected brushed DC motor

The results obtained with the aid of the simulation, as given in Fig. 5.16, show the shaft speed, current and energy dissipated for both machines (green curves represent the voltage source connected machine). Observation of Fig. 5.16 shows that both machines reach the same shaft speed of  $\omega_m^v = 751$  rpm, which is approximately equal to the theoretical no-load speed of  $\omega_m^o = u_a^*/\psi_f$  namely  $\omega_m^o = 763$  rpm. A comparison between the dissipated energy levels of the two machines at the end of the operating sequence demonstrates that the current-source connected machine is able to reach the required operating speed with a reduction in dissipated energy of 46% relative to using a constant voltage-source connected machine. Apart from improved dynamic performance, this is another important reason, why current controlled machines are preferable in drive applications.

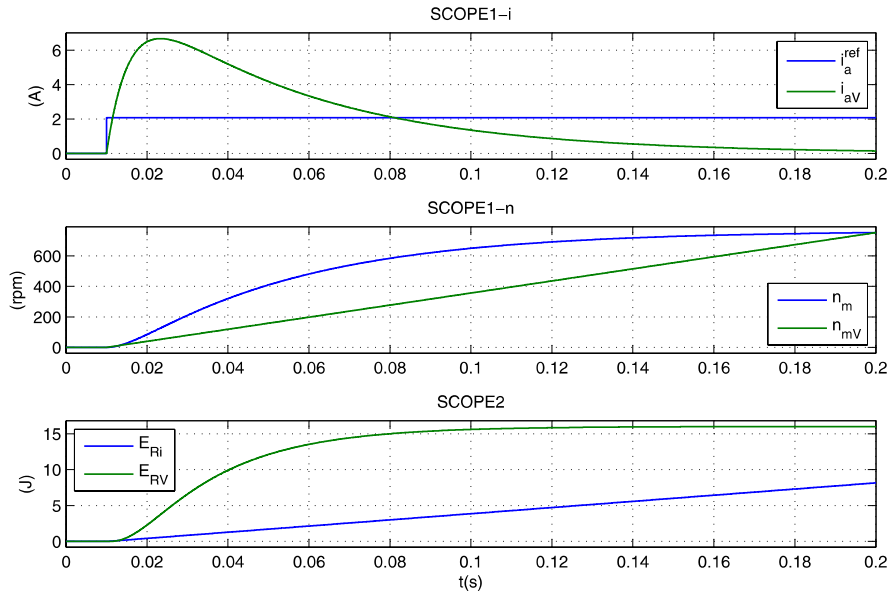


**Fig. 5.17** Voltage (green) and current (blue) controlled DC machines: armature current  $i_a$ , mechanical speed  $\omega_m$ , and dissipated energy  $E_d$  during run-up from standstill

#### 5.4.3 Tutorial 3: Current Source Connected Brushed DC Motor with Field Weakening Controller

This tutorial aims to examine the functioning of a current controller which operates in accordance with the control laws discussed in Sect. 5.3.2. For this purpose the IRTF based brushed DC machine, as introduced in Sect. 5.4.1, is to be connected to a DC current controller module which requires as inputs the reference armature current  $i_a^*$  and shaft speed  $\omega_m$ . Control input for the drive should be a torque reference value which should be adjustable between the limits  $\pm T_e^{\max}$ . The operating drive parameters for the drive are given in Table 5.2.

**Table 5.2** DC Drive parameters

Parameters	Value	
Maximum armature current	$i_a^{\max}$	8.0 A
Maximum supply voltage	$u_a^{\max}$	200.0 V
Maximum field flux	$\psi_f^{\max}$	1.0 Wb

Calculate the base speed  $\omega_m^b$  of the drive, using the data provided in Table 5.1 and Table 5.2. Observe quasi-steady state drive operation with the aid of a synchronous Blondel diagram. The diagram in question should show

the maximum flux circle, maximum current circle and current vector  $\vec{i}_a^{xy}$  (as given in Fig. 5.3), which is to be represented in a synchronous dq reference frame. A quadratic load torque versus speed characteristic is assumed. This load produces a torque of 30 Nm at 3000 rpm.

Calculation of the base speed may be undertaken with the aid of (5.11), which shows that its value is equal to  $n_m^b = 1733$  rpm. The simulation model as given in Fig. 5.18, shows the IRTF based current model together with the current controller. A torque reference input module is provided in the form of an *updown* module which is set to operate within the range  $\pm 8$  Nm. These are the torque limits of this drive. The DC drive module main outputs are the field flux  $\psi_f^c$  and armature current  $i_a^c$ , which in this example serve as inputs to the current based model (ideal current control is assumed). The controller module controls the flux in accordance with the control law defined by (5.14). Note that the *over-speed* mode of operation is not implemented in the DC controller module used in this tutorial. A number of additional outputs are provided by the DC control module to visualize the synchronous Blondel diagram (see Fig. 5.10). These are the variables  $i_s^c = \psi_f^c / L_a$  (which defines the circle of the maximum flux curve),  $i_a^{\max}$  (defines the maximum current circle) and  $i_{av} = u_a^{\max} / (\omega_m L_a)$ , which is the radius of the maximum flux circle. Its value is constrained to the value  $(i_s^c + i_a^{\max})$  to limit the circle size at low speeds. The current vector  $\vec{i}_a^{xy}$  is connected to a coordinate conversion module with input  $\theta$  which produces the vector  $\vec{i}_a^{dq}$ .

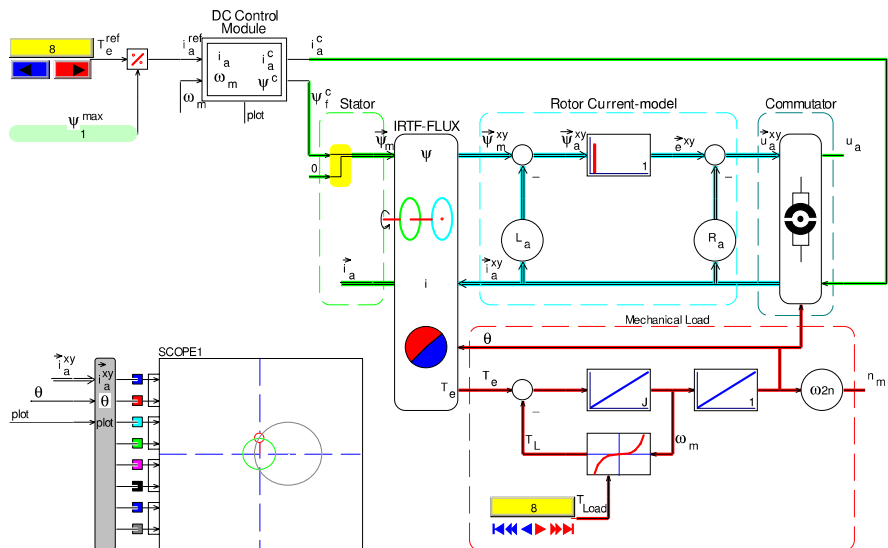


**Fig. 5.18** Current source connected brushed DC motor with field weakening controller

Observation of drive operation should confirm that the amplitude of the vector  $\bar{e}_a^{xy}$  will indeed be limited to the maximum voltage value of 200 V, when the armature current is set to its maximum value and the drive speed is increased beyond the base speed. Note, however, that the armature voltage  $u_a$  will be greater than this value as the control approach does not take into account the voltage drop across the armature resistance. In this model the armature resistance is relatively large. In practice, the value of the resistive voltage drop is small in comparison to the back-EMF component, but its contribution should nevertheless be taken into account.

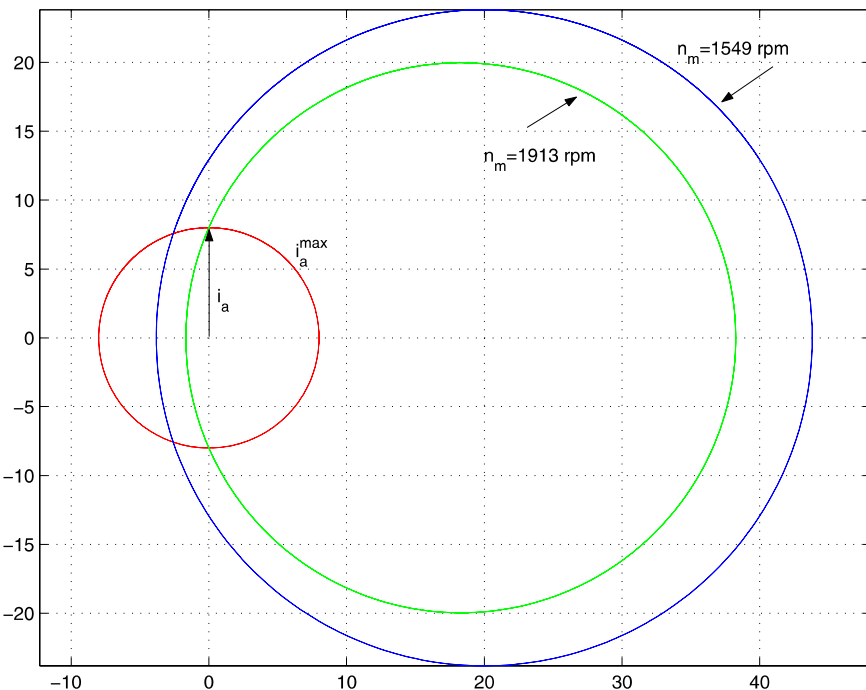


**Fig. 5.19** Simulation results for synchronous Blondel diagram, current controlled DC machine, with field weakening

The results given in Fig. 5.19 show the synchronous Blondel diagram of the drive for an operating speed above and below the base speed of  $n_m^b = 1733 \text{ rpm}$ . In addition, the maximum current vector  $\bar{i}_a^{dq}$  is shown. As mentioned earlier, the ratio between field flux and armature reaction flux was purposely chosen to be relatively high, to show a the maximum flux circle and maximum current circle in a single diagram for didactic purposes.

#### 5.4.4 Tutorial 4: DC Drive Operating under Model Based Current Control and a Field Weakening Controller

A single-phase model based current controller is to be considered with a full-bridge converter/modulator topology as discussed in Tutorial 3.3.2. The controller is connected to a brushed DC machine. The machine parameters and operating drive voltage/current limits to be used are in accordance with those discussed in the previous tutorials. Asymmetric pulse width modulation, with a sampling time of  $T_s = 0.5$  ms is to be used, which corresponds with a PWM carrier frequency of 1 kHz. Modify the model given in Tutorial 3.3.2 in accordance with the DC drive concept presented in Sect. 5.3.4. In the context of this exercise, determine the new gains settings for the current controller and plot the reference torque and machine torque in a single diagram as well as the shaft speed over the simulation period to be specified. An anti-windup PI controller is to be used, for which the output limit values must be found. The machine is deemed to operate without any external mechanical load. A torque reference step of  $T_e^* = 4$  Nm (50% rated torque) is applied at  $t = 10$  ms and the control value is reversed at  $t = 100$  ms. Examine the behavior of the drive over a simulation period of  $T = 200$  ms and use a computational step size of 5  $\mu$ s. Explain why such a relatively small computation step size is required.

An example of a simulation model, as given in Fig. 5.20, shows the required controller structure with the PI controller and back-EMF term  $u_e$  as calculated using the measured shaft speed and DC controller field flux value  $\psi_f^c$ . Note, that in this example, the proportional gain  $L/T_s + R/2$  of the controller is dominated by the inductance term given that  $L/R > T_s/2$ . Hence, its value is equal to  $K_p = 105.0$ , while the integral gain value was found to be  $K_i = 10$ . A discrete anti-windup PI controller is introduced which has as input the disturbance-decoupling signal (top input) and the current error signal. The output voltage limits for this controller should be set to the maximum average voltage per sample values that may be realized. In this case the limits should be set to  $\pm 200$  V given that the supply voltage is set to 200 V.

The IGBT based H-bridge shows a circuit-generic model interface unit that provides the voltage input to the generic model of the separately excited brushed (with ideal commutator) DC machine. Output of the model is the armature current  $i_a$ , that is fed back to the circuit model and the current controller, as may be observed from Fig. 5.20. Note that the use of a modulator/circuit model has a significant impact on the computation time, given the need to accommodate a representative number of simulation time steps within the chosen sampling time. For this reason, simulations that support control design are often undertaken with the average voltage  $U^*$  output of the PI controller(s), as discussed in Sect. 3.3.5.

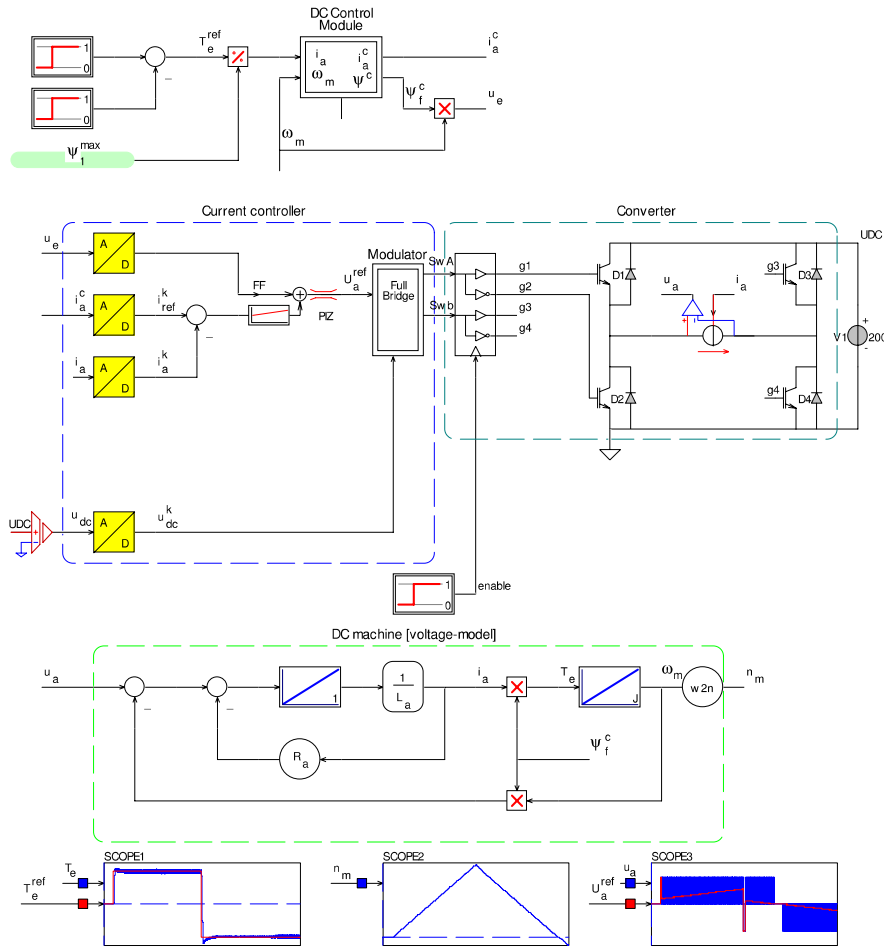


**Fig. 5.20** Simulation of current source connected brushed DC motor with field weakening controller

The results obtained from the simulation are collected with the aid of scope modules as shown in Fig. 5.21. Observation of Fig. 5.21 shows that the drive is able to deliver the required torque response. A torque ripple component due to the use of a regularly sampled switched converter can be observed. The maximum operating shaft speed, shown in Fig. 5.21, is in this example below the base speed. This implies that the DC controller maintains the field flux  $\psi_f^c$  at its maximum value of 1 Wb for the entire simulation. The reader is encouraged to reconsider this tutorial with a hysteresis type current controller, as discussed in Sect. 3.3.1.

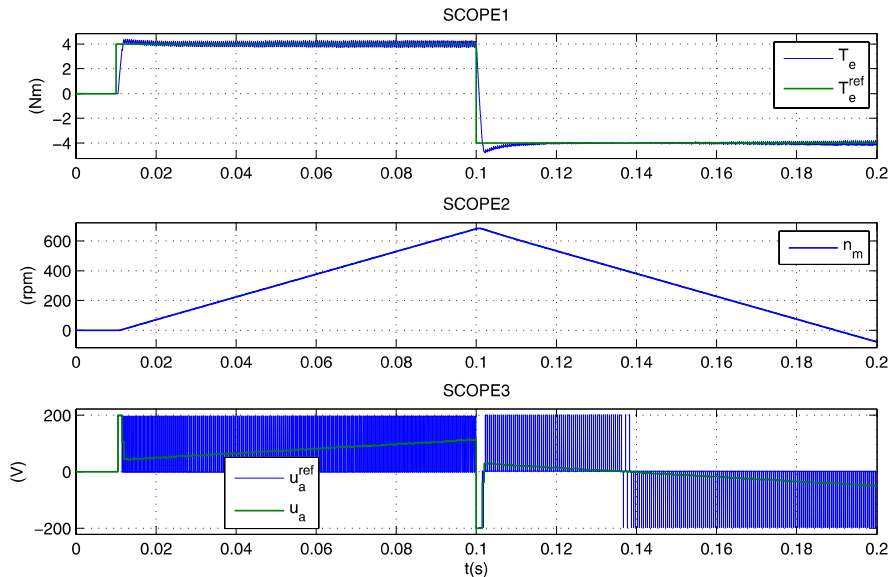
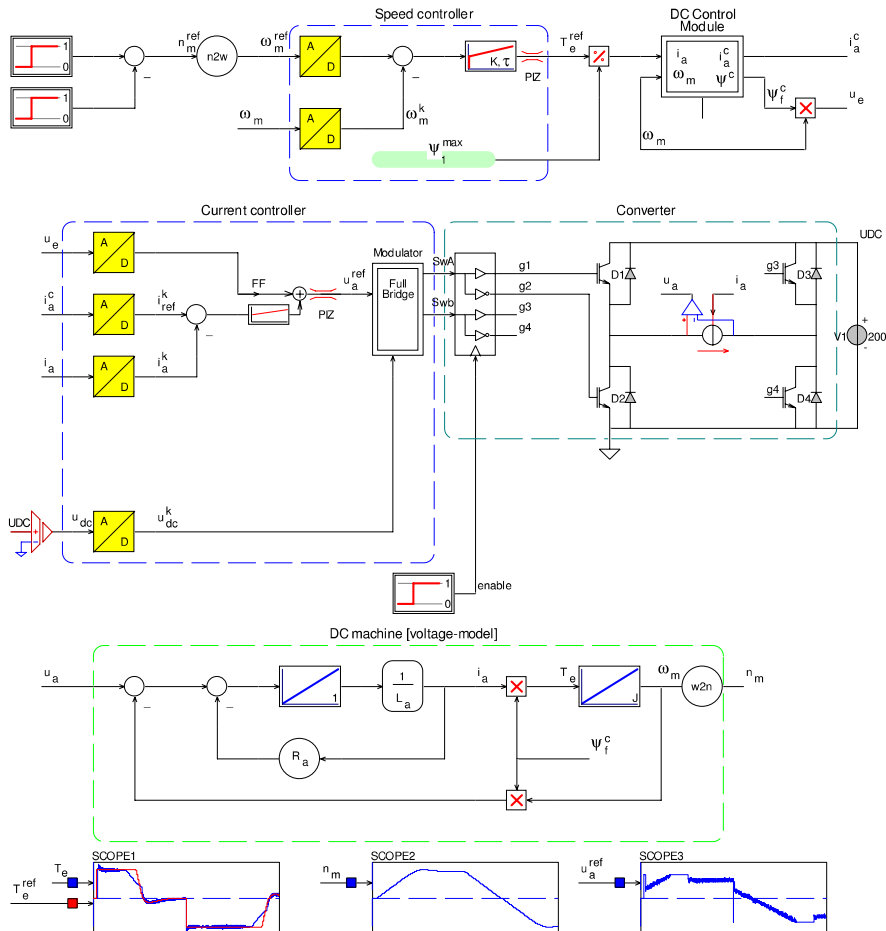


Fig. 5.21 Simulation results for DC drive with model based current control

#### 5.4.5 Tutorial 5: DC Drive with Model Based Current Control and Shaft Speed Control Loop

This tutorial aims to extend the previous model by introducing an outer shaft speed control loop as discussed in Sect. 4.4. For this purpose, add a discrete *anti-windup* PI speed controller to the drive and calculate the required proportional gain and time constant values. Set the output limits of the speed controller to  $\pm T_e^{\max}$  and determine a value for the anti-windup factor  $k_w$ . Choose a simulation run time of 0.5 s and apply a step  $n_m^{\text{ref}} = 0 \rightarrow 1500$  rpm at  $t = 10$  ms. Reverse the speed reference at  $t = 0.25$  s and plot the measured and reference shaft speed over the specified time interval. Likewise, plot the measured and reference torque versus time waveforms. The remaining parameters and simulation setting remain unchanged.

The simulation model, shown in Fig. 5.22, contains a speed control loop that features a discrete anti-windup PI control module, which has as inputs the sampled reference speed  $\omega_m^*$  and sampled measured shaft speed  $\omega_m$ . The gain  $K_p$  and time constant  $\tau_i$  of the speed controller are calculated using (4.41), with  $\omega_B^{\text{sp}} = 100 \text{ rad/s}$ , as mentioned in Sect. 4.4. The resulting speed gain and time constant values, for the given drive parameters  $J$  and  $T_s$ , are  $K_p = 0.5 \text{ Nms/rad}$  and  $\tau_i = 0.04 \text{ Nm/rad}$  respectively. The values found are identical to those found in the tutorial shown in Sect. 4.5.5, which implies that the same anti-winding factor  $k_w = 16m$  can be used.



**Fig. 5.22** Simulation of DC drive with model based current control and shaft speed control loop

The results from the simulation, as given in Fig. 5.23, show two plots that represent the shaft speed and torque curves obtained after running the simulation. The results, shown in Fig. 5.23, demonstrate that points A and B mark the start of a time interval in which the reference and actual torque are not equal. Basically two effects may cause this. The first is that field weakening could become active. However, this is not the case here as the controller base speed corresponds to  $n_m^b = 1733$  rpm (same controller as discussed in Sect. 5.4.3). In this case, the torque reduction is caused by the current controller because it fails to track the reference current as the required supply voltage to maintain a reference current of 8 A is outside the supply limit of 200 V. In a practical drive, the voltage limit in the field controller should be set lower because the armature resistive voltage potential  $R_a i_a$  must be

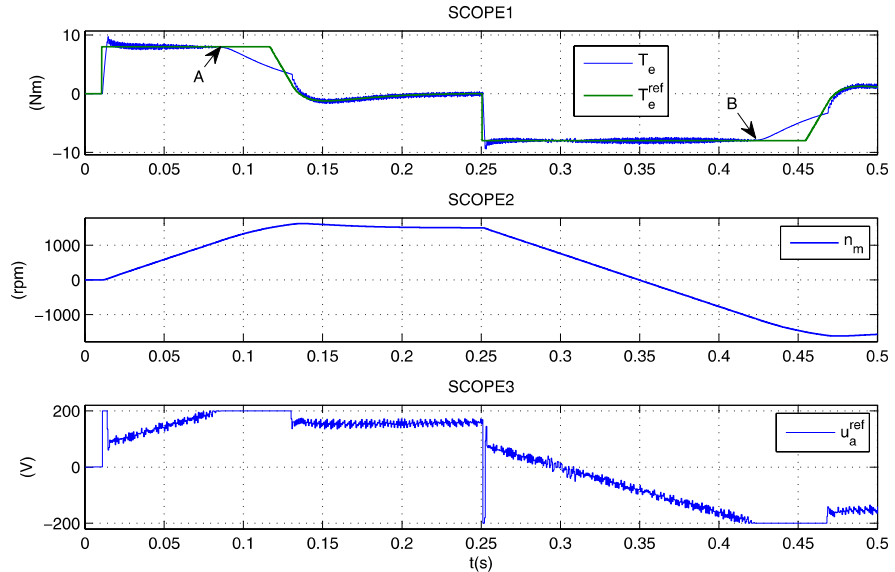


**Fig. 5.23** Simulation results for DC drive with model based current control and shaft speed control loop

taken into account. Hence, in this example it would be prudent to reduce the maximum supply voltage (to achieve a base speed of approximately 1100 rpm in this example) of the field controller to ensure that current control is maintained over the entire speed range. This implies that field weakening should start at points A and B. This reasoning illustrates the need for comprehensive modeling so that a good understanding of drive operation is achieved prior to experimental implementation.

#### 5.4.6 Tutorial 6: Experimental Results of DC Machine

The test bench described in Sect. 1.4 is used as an example to show the functionality of the previous described control algorithms. The control of the DC machine was implemented and tested using a simulation model of the drive, as shown in Fig. 5.24. The figure shows three main blocks, consisting of the controller, the converter and the model of the DC machine. The control block (called TEST\_BENCH\_DC) consists of a speed and torque controller, chosen by the variable DCM\_T\_OR\_S. In addition, the control algorithm needs, the reference speed (DCM\_N\_REF), the reference torque (DCM\_T\_REF), the maximum field flux (DCM\_PSI\_F\_MAX), the measured armature current (DCM\_I\_A\_MEASURED) and speed (DCM\_OMEGA\_M). As output, the controller calculates the reference armature voltage(DCM\_U\_A\_REF) and

the reference field flux (DCM\_PSL\_REF). The armature voltage is then applied to a full bridge modulator to calculate the switching signals for the converter. The resulting voltage  $u_a$  is applied to a voltage model of the DC machine to calculate the current and the torque of the machine. The two scopes at the end of Fig. 5.24 show the results of a simulated speed reversal.

The TEST\_BENCH\_DC block was generated using the C-code export function of CASPOC C-code of and embedded in the test-bench code. The specifications of the DC machine are given in Table 5.3.

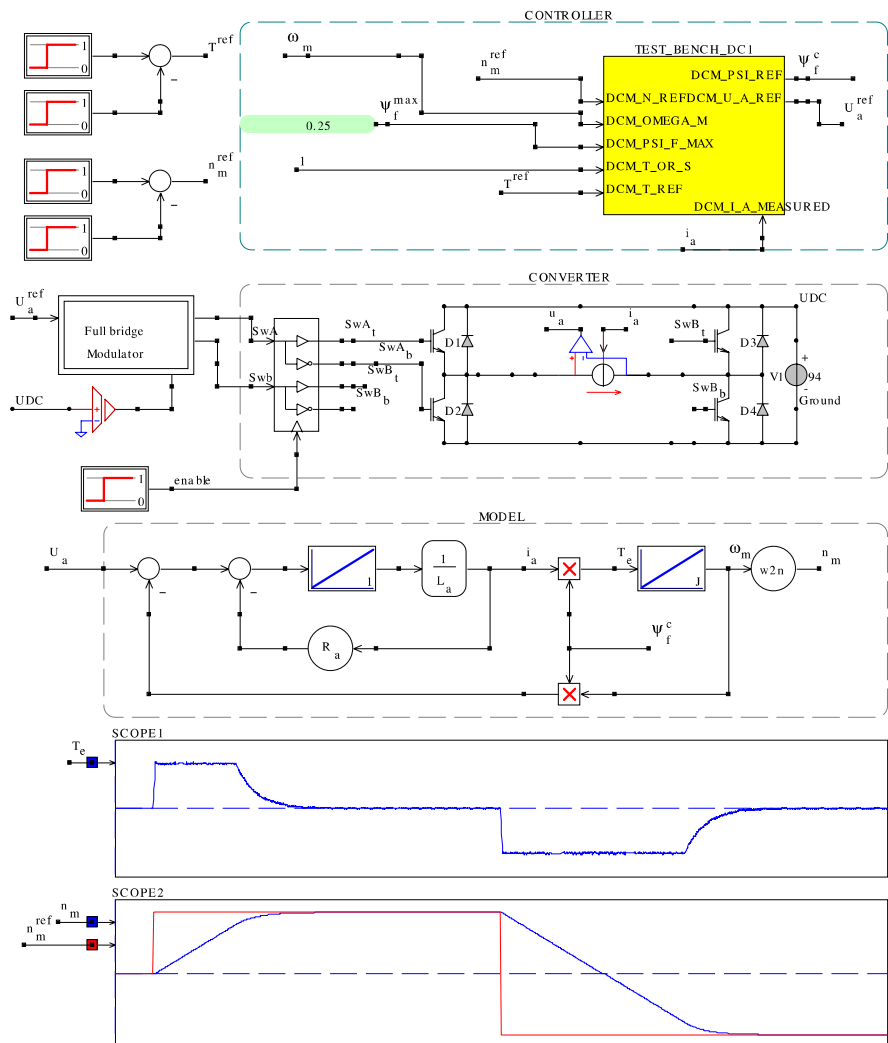
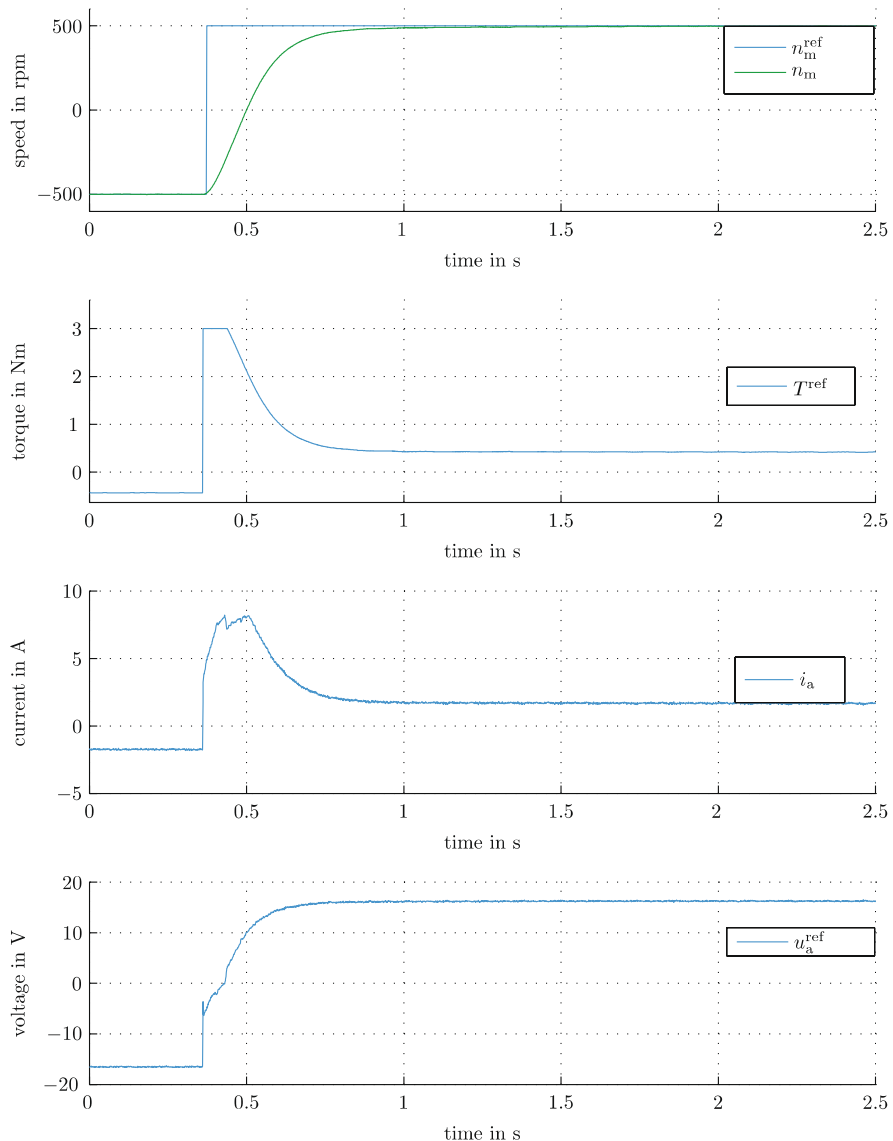


Fig. 5.24 Simulation of DC drive

**Table 5.3** Specifications of example DC machine

Parameters		Value
Nominal power	$P$	0.75 kW
Maximum armature voltage	$u_a^{\max}$	25 V
Maximum armature current	$i_a^{\max}$	8 A
Armature inductance	$L_a$	2.5 mH
Maximum field flux	$\psi_f$	0.25 Wb

**Fig. 5.25** Experimental results for speed reversal with DC machine

To show the function of the developed control, a speed reversal from  $-500\text{ rpm}$  to  $500\text{ rpm}$  at no-load was performed. Figure 5.25 shows the reference speed  $n_m^{\text{ref}}$ , the measured speed  $n_m$ , the reference torque  $T^{\text{ref}}$ , the armature current  $i_a$  and the armature voltage  $u_a^{\text{ref}}$ . At approximately  $0.4\text{ s}$ , a speed step is applied. The controller immediately commands the maximum allowed torque of  $3\text{ Nm}$ . The voltage  $u_a^{\text{ref}}$  is determined using an anti-windup PI current controller.

# Chapter 6

## Synchronous Machine Modeling Concepts

In this chapter, attention is given to modeling three-phase AC synchronous machines with quasi-sinusoidally distributed stator windings. The excitation may be provided by a rotor winding which is connected via a brush/slipping set to an electrical excitation source [40, 31, 66]. Alternatively, use can be made of permanent magnets which produce a quasi-sinusoidal magnetic flux density distribution in the air-gap. Both non-salient and salient IRTF based machine models are considered in this chapter from a dynamic and quasi-steady-state perspective.

The field-oriented modeling approach, briefly introduced in Chap. 4, is extended to encompass a rotor flux oriented model of the non-salient and salient machine. Such an approach is deemed to be important in the context of the *model inversion* control principle embraced in this book. In contrast to the previous chapter, the modeling and control sections have been separated to facilitate readability. Subsequent to this chapter, a comprehensive set of tutorials is introduced to provide the reader with the opportunity to interactively examine the key concepts discussed in this chapter.

### 6.1 Non-salient Machine

In this section, a brief review of the symbolic and generic models and the relevant equations of a *non-salient* synchronous machine is given. Furthermore, attention is given to the steady-state characteristics of a voltage source connected machine. For a detailed discussion the reader may refer to our previous book [68].

In a synchronous machine, the excitation may be provided by permanent magnets or by a rotor based excitation winding which carries a field current  $i_f$ . In both cases, the flux density distribution due to the excitation is assumed to be sinusoidal. Furthermore, it is assumed that the magnetizing inductance is equal along both axes of the xy plane. A cross-sectional view of a four-pole

PM non-salient machine is given in Fig. 6.1. It shows the stator and the rotor with a set of surface mount magnets. Note the presence of a dual set of xy axes, because a four-pole machine is shown in Fig. 6.1. The machine does not

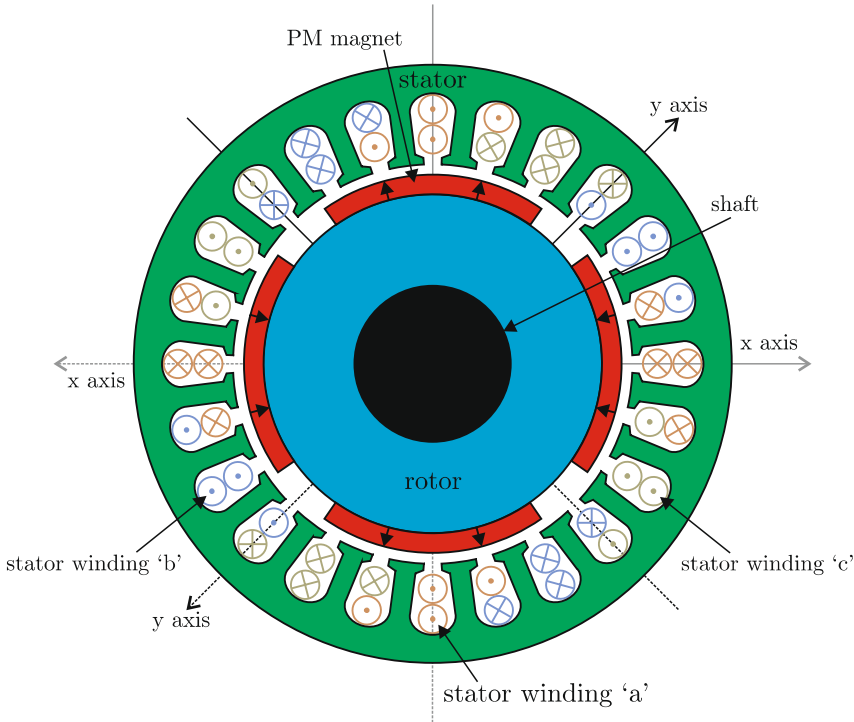


**Fig. 6.1** Non-salient PM synchronous machine

carry any damper windings given that (to avoid losses) these are normally not found in servo-drive applications which are predominantly considered in this book.

### 6.1.1 Symbolic Model of a Non-salient Machine

The machine can be described by an IRTF based model as shown in Fig. 6.2. The model was derived from the elementary model introduced in Sect. 4.2.2 by accommodating the stator resistance  $R_s$  and the stator leakage inductance  $L_{\sigma s}$ . The magnetizing inductance  $L_m$  is shown on the rotor side of the machine. In general, inductances of non-salient machines may be placed on either side of the IRTF module. For salient machines the magnetizing inductance depends on the orientation relative to the rotor and thus it is prudent

to place it on the rotor side. For this reason, it is beneficial to also locate the magnetizing inductance of the non-salient machine on the rotor side.

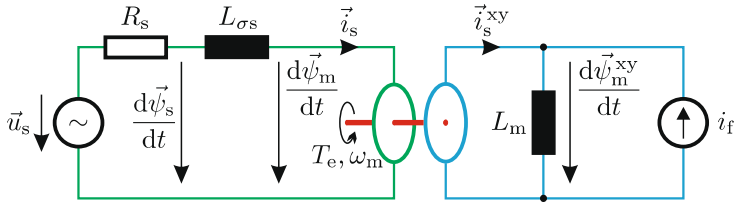


**Fig. 6.2** Non-salient synchronous machine

The equation set which corresponds to this machine is given by

$$\vec{u}_s = R_s \vec{i}_s + \frac{d\vec{\psi}_s}{dt} \quad (6.1a)$$

$$\vec{\psi}_s = L_{\sigma s} \vec{i}_s + \vec{\psi}_m \quad (6.1b)$$

$$\vec{\psi}_m^{xy} = L_m (\vec{i}_s^{xy} + i_f) \quad (6.1c)$$

In the symbolic model in Fig. 6.2, a linear relationship  $\psi_f = L_m i_f$  between the field flux linkage  $\psi_f$  and excitation current  $i_f$  is assumed, as was done earlier in Sect. 4.2.2. In case of saturation,  $\psi_f$  is a non-linear function of current.

Using the transformation  $\vec{A} = \vec{A}^{xy} e^{j\theta}$ , (6.1b) can be written in rotor coordinates  $\vec{\psi}_s^{xy} = L_{\sigma s} \vec{i}_s^{xy} + \vec{\psi}_m^{xy}$ . Combining this equation with (6.1c), grouping the two inductances  $L_{\sigma s}$  and  $L_m$  and replacing  $L_m i_f$  by  $\psi_f$ , the stator flux linkage can be written as

$$\vec{\psi}_s^{xy} = \underbrace{(L_{\sigma s} + L_m)}_{L_s} \vec{i}_s^{xy} + \psi_f. \quad (6.2)$$

The sum of the two inductances in (6.2) is the stator inductance  $L_s$ . Equation (6.2) is the general flux linkage relationship including the field current  $i_f$ . In case of permanent magnet excitation, the flux linkage  $\psi_f$  is converted to an equivalent current  $i_f = \psi_f / L_m$ , because a flux linkage source cannot be modeled in the symbolic model directly. This equation will be used in the development of the generic model in the next section.

### 6.1.2 Generic Model

A generic model of the non-salient synchronous machine can be built by either using a current-based or a flux-based IRTF model. In this section, a flux-based

IRTF model is used. The generic machine model is directly found by using (6.1a) at the stator side and (6.2) at the rotor side of the IRTF. The resulting model is shown in Fig. 6.3.

At the stator side, an integrator is used to calculate the stator flux linkage  $\vec{\psi}_s$ . This integrator must be provided with an initial value  $\vec{\psi}_s(t=0) = \psi_f e^{j\theta}$  in the (normal) event that excitation of the machine is provided at the start of machine operation.

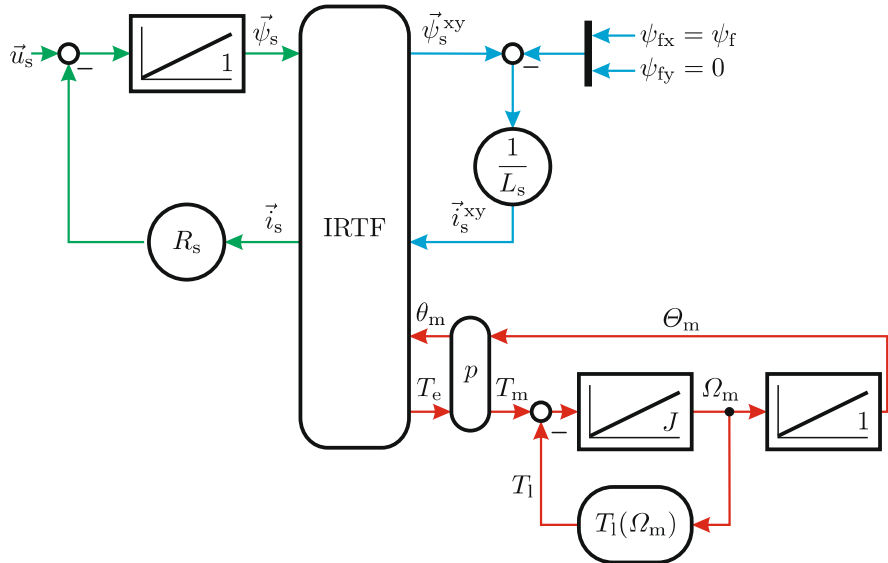


**Fig. 6.3** Generic model of a synchronous machine which corresponds with equation set (6.1) and (6.2)

The machine torque can be derived from IRTF (4.5), using the stator flux linkage  $\vec{\psi}_s$  and the stator current  $\vec{i}_s$  resulting in  $\vec{T}_e = \vec{\psi}_s \times \vec{i}_s$ . The use of (6.1b) with said torque equation gives

$$\vec{T}_e = \vec{\psi}_m \times \vec{i}_s + L_{\sigma s} \underbrace{\vec{i}_s \times \vec{i}_s}_{=0} \quad (6.3)$$

of which the second term equals zero. This implies that the torque is not affected by the leakage inductance  $L_{\sigma s}$ . Hence, either the stator flux linkage vector  $\vec{\psi}_s$  or the magnetizing flux linkage vector  $\vec{\psi}_m$  can be used for torque calculation. Also shown in Fig. 6.3 is a mechanical load module which represents the relationship between load torque and shaft speed. A tutorial based on the generic model shown in Fig. 6.3 is discussed in Sect. 6.3.1.

### 6.1.3 Rotor-Oriented Model: Non-salient Synchronous Machine

In the machine models discussed previously, the current, voltage and flux linkage space vectors were defined with respect to a stationary or a shaft oriented reference frame. In this section, a so-called *rotor-oriented* transformation is introduced where the stator and rotor based space equations are tied to the flux linkage vector  $\vec{\psi}_f^{dq} = \psi_f$ , as shown earlier in Sect. 4.2.2. The development of a rotor-oriented model is important for creating a field-oriented control for the non-salient synchronous machine as will be done in the next chapter. The equation set for the non-salient rotor flux based model may be written as

$$\vec{u}_s^{dq} = R_s \vec{i}_s^{dq} + \frac{d\vec{\psi}_s^{dq}}{dt} + j\omega_s \vec{\psi}_s^{dq} \quad (6.4a)$$

$$\vec{\psi}_s^{dq} = L_s \vec{i}_s^{dq} + \psi_f \quad (6.4b)$$

$$T_e = \psi_f i_{sq}. \quad (6.4c)$$

The coordinate transformation which leads to a symbolic and generic representation of the rotor-oriented model is initiated by transforming (6.1a) in a rotor-oriented dq-reference frame using  $\vec{A} = \vec{A}^{dq} e^{j\theta}$ . Due to the coordinate transformation, a term  $j\omega_s \vec{\psi}_s^{dq}$  appears in the voltage (6.4a) as a result of using the product rule on  $d(\vec{\psi}_s e^{j\theta})/dt$ , with  $d\theta/dt = \omega_s$ . The flux linkage expression (6.4b) is unchanged from (6.2), apart from replacing the superscript, given that the xy and dq coordinate reference frames are fully aligned in this case, as may be observed from Fig. 6.4. The general torque expression  $\vec{T}_e = \vec{\psi} \times \vec{i}$  along with  $\vec{\psi} = \vec{\psi}_s^{dq}$  and  $\vec{i} = \vec{i}_s^{dq}$  leads directly to (6.4c).

Figure 6.4 graphically depicts the process of constructing the stator flux linkage vector based on a given stator current  $\vec{i}_s^{dq}$ , as described by (6.4b). In case of permanent magnet machines, the stator current vector  $\vec{i}_s^{dq}$  normally has a negative direct current component for reasons that will become apparent in the next chapter.

The process of finding a symbolic rotor flux model representation may be further pursued by combining the voltage and flux linkage expressions shown in equation set (6.4). Separating the real and imaginary components leads to

$$u_{sd} = R_s i_{sd} - \omega_s L_s i_{sq} + L_s \frac{di_{sd}}{dt} \quad (6.5a)$$

$$u_{sq} = R_s i_{sq} + \omega_s L_s i_{sd} + L_s \frac{di_{sq}}{dt} + \omega_s \psi_f. \quad (6.5b)$$

Equation set (6.5) shows the existence of cross-coupling between the phases. For example, the q-axis current  $i_{sq}$  causes a d-axis voltage compo-

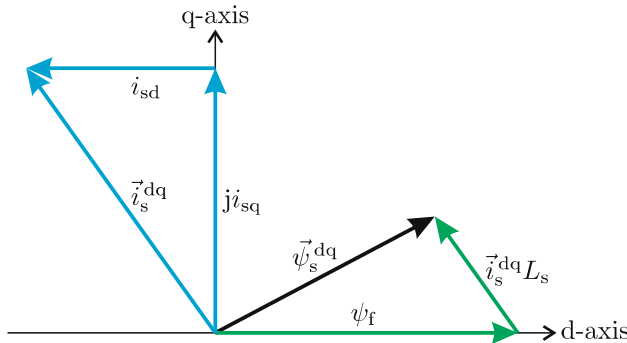


**Fig. 6.4** Vector diagram with direct and quadrature axis for non-salient machine

nent  $u_{sd}$ . One important feature of a machine control is to compensate or to decouple the cross-coupling, as will be described in the next chapter. From equation set (6.5), a symbolic representation for the rotor flux based model can be derived, as shown in Fig. 6.5.

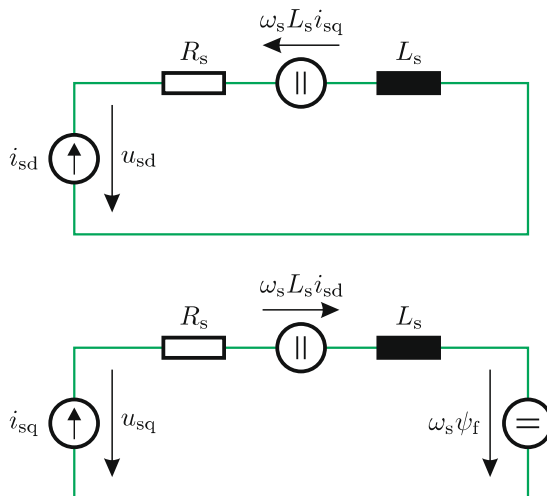


**Fig. 6.5** Symbolic rotor-oriented model of a non-salient machine

A current based generic model for a rotor flux based machine, which corresponds to Fig. 6.5, is given in Fig. 6.6 and directly derived from the torque (6.4c). From (6.4c), it can be seen that in a flux based reference system, torque is produced by the  $i_{sq}$  component of the current, allowing a simple torque control similar to the DC-machine. The symbolic model shown in Fig. 6.5 is discussed in Tutorial 6.3.3.

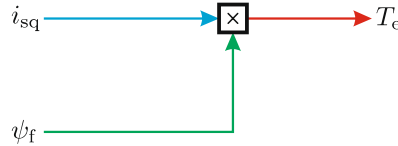


**Fig. 6.6** Generic current based rotor-oriented non-salient synchronous machine model

### 6.1.4 Steady-State Analysis

A brief overview of the steady-state operation of non-salient machines is presented here. The reader is referred to [68] for a more extensive analysis. The aim of this section is to derive an operational diagram referred to as *Blondel diagram* which can be used to show the impact of changing the mechanical load on the current phasor locus  $\underline{i}_s$ . Operational diagrams of this type utilize a complex plane of which the real axis is aligned with the terminal voltage phasor  $\underline{u}_s$ .

The behavior of the machine in steady-state operation can be derived from equation set (6.4) taking into account that time-dependent derivatives are zero in steady-state.

$$\vec{u}_s^{\text{dq}} = R_s \vec{i}_s^{\text{dq}} + j\omega_s \vec{\psi}_s^{\text{dq}} \quad (6.6a)$$

$$\vec{\psi}_s^{\text{dq}} = L_s \vec{i}_s^{\text{dq}} + \underline{\psi}_f \quad (6.6b)$$

In the following, it is assumed that the machine is connected to a (three-phase) voltage source with constant amplitude  $\hat{u}_s$  and adjustable angular frequency  $\omega_s$ . In space vector terms that voltage source may be represented by  $\vec{u}_s = \underline{u}_s e^{j\omega_s t} = \hat{u}_s e^{j\omega_s t}$ . In steady-state all space vectors in equation set (6.6) are rotating at the same speed, which is zero in dq coordinates and equals  $\omega_s$  in stator coordinates. Therefore, the system is fully described by the relative position of the space vectors to each other and phasors (here using peak values) can be used to describe the machine variables, resulting in the following equation set

$$\underline{u}_s = R_s \underline{i}_s + j\omega_s \underline{\psi}_s \quad (6.7a)$$

$$\underline{\psi}_s = L_s \underline{i}_s + \underline{\psi}_f. \quad (6.7b)$$

The stator voltage phasor is aligned with the real axis and therefore  $\underline{u}_s = \hat{u}$ . The phasor relations are shown in Fig. 6.7. Shown in this diagram are the voltage  $\underline{u}_s$ , the flux linkage  $\underline{\psi}_f$ , and the current  $\underline{i}_s$  which are linked by equation set (6.7). The complex phasor coordinate plane is shown in gray. The real axis is tied to the voltage phasor  $\underline{u}_s$ . The load angle  $\rho_m$  is defined as the angle between the voltage phasor  $\underline{u}_s$  and the back-EMF phasor  $j\omega_s \underline{\psi}_f$ . Subsequent observation of Fig. 6.7 shows that the field flux linkage phasor  $\underline{\psi}_f$  can be

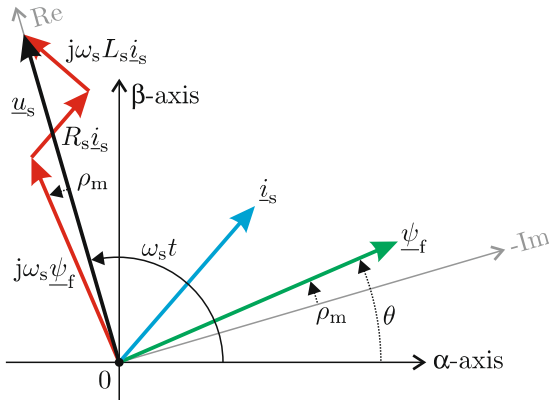


**Fig. 6.7** Load angle definition ( $\rho_m$ ) in phasor diagram

written as  $-j\psi_f e^{j\rho_m}$  resulting in the equations

$$\underline{u}_s = R_s \underline{i}_s + j\omega_s \underline{\psi}_s \quad (6.8a)$$

$$\underline{\psi}_s = L_s \underline{i}_s - j\psi_f e^{j\rho_m}. \quad (6.8b)$$

An expression for the current phasor  $\underline{i}_s$  can now be found by eliminating the flux linkage phasor  $\underline{\psi}_s$

$$\underline{i}_s = \frac{\hat{u}_s - \omega_s \psi_f e^{j\rho_m}}{R_s + j\omega_s L_s} \quad (6.9)$$

Expression (6.9) may also be presented by an equivalent circuit as given in Fig. 6.8. It includes two voltage sources, the supply voltage  $\underline{u}_s = \hat{u}_s$  and the back EMF  $\omega_s \underline{\psi}_f$ . Observation of the complex network shows that the current  $\underline{i}_s$  can also be found by superposition of the current components for each voltage source separately, leading to

$$\underline{i}_s = \underbrace{\frac{\hat{u}_s}{R_s + j\omega_s L_s}}_{i_{s1}} + \underbrace{\frac{-\omega_s \psi_f e^{j\rho_m}}{R_s + j\omega_s L_s}}_{i_{s2}}. \quad (6.10)$$

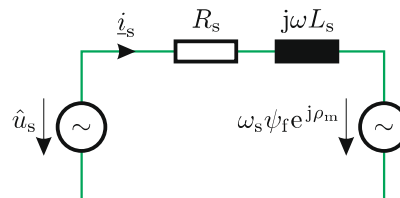


**Fig. 6.8** Non-salient synchronous, phasor based, machine model

A graphical representation of (6.10) is given in Fig. 6.9. If the equation is factorized it can be written as

$$\underline{i}_s = \frac{\hat{u}_s}{R_s} \left( \frac{1}{1 + j \frac{\omega_s L_s}{R_s}} + \frac{-\frac{\omega_s \psi_f}{\hat{u}_s} e^{j \rho_m}}{1 + j \frac{\omega_s L_s}{R_s}} \right). \quad (6.11)$$

In Fig. 6.9,  $\omega_s \psi_f / \hat{u}_s$  was set at 0.7 and  $\omega_s L_s / R_s$  was set at 1.96. The figure shows the two current components  $\underline{i}_{s1}$  and  $\underline{i}_{s2}$ , together with circles of constant output power  $p_{out}$ . Note that in practical machines the stator current  $\underline{i}_s$  is limited. This limit can be represented by a circle around the origin of the Blondel plot as will be explained in detail in the next chapter. This constraint is not taken yet into consideration for the analysis presented here. The lines of constant output power  $p_{out}$  can be derived by using the energy balance equation and assuming that the machines produce only ohmic losses.

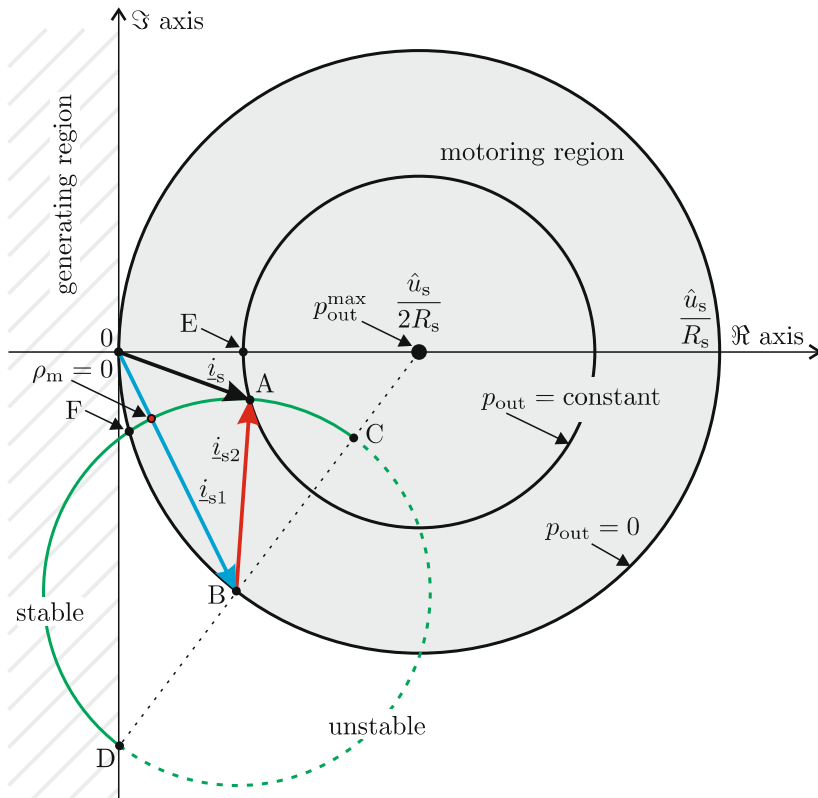


**Fig. 6.9** Blondel diagram of synchronous machine

$$\underbrace{\Re \{ \underline{u}_s \underline{i}_s^* \}}_{\text{electrical power}} - \underbrace{R_s \Re \{ \underline{i}_s \underline{i}_s^* \}}_{(\text{ohmic}) \text{ losses}} = \underbrace{p_{\text{out}}}_{\text{mechanical output power}} = \text{const.} \quad (6.12)$$

After some mathematical handling, (6.12) gives

$$\left( \Re \{ \underline{i}_s \} - \frac{\hat{u}_s}{2R_s} \right)^2 + \Im \{ \underline{i}_s \}^2 = \left( \left( \frac{\hat{u}_s}{2R_s} \right)^2 - \frac{p_{\text{out}}}{R_s} \right). \quad (6.13)$$

Equation (6.13) states that the lines of constant power are circles in the complex plane with their centers on the real axis at  $(\hat{u}_s/2R_s, 0)$  and with radii equal to  $\sqrt{(\hat{u}_s/2R_s)^2 - p_{\text{out}}/R_s}$ . The circles of constant power are also shown in Fig. 6.9. The zero output power circle has a radius of  $\hat{u}_s/2R_s$ . Furthermore, the theoretical maximum output power of the machine can be found by matching the source, i.e., the electrical machine, and the load impedances resulting in  $p_{\text{out}}^{\max} = \hat{u}_s^2/4R_s$ . The maximum output power is shown in Fig. 6.9 at coordinates  $(\hat{u}_s/2R_s, 0)$ . It is noted that for a given shaft speed the output power is proportional to the output torque. The Blondel diagram has a number of characteristic operating points which are discussed below:

- If the field flux linkage  $\psi_f$  is zero, the stator current component  $\underline{i}_{s2}$  is zero and thus the stator current  $\underline{i}_s$  will be positioned on the zero output power circle  $p_{\text{out}} = 0$ , e.g. at point B.
- During motor operation the stator current is inside and during generator operation outside the zero power circle  $p_{\text{out}} = 0$ .
- For a given field flux linkage ( $\omega_s \psi_f / \hat{u}_s = \text{const.}$ ) and a variable load angle  $\rho_m$ , the stator current lies on the green circle. The radius of this circle is proportional to the field flux linkage  $\psi_f$ . If no torque is produced, the operating point is located at point F with  $\rho_m = 0$ . As load torque is increased ( $\rho_m < 0$ ), the motoring region is entered and the output power increases. The distance from the operating point to the maximum output power point  $p_{\text{out}}^{\max}$  determines the output power. The shorter this distance, the higher the output power. This means that operation with a current phasor at point C gives the highest output power achievable for a given field flux linkage. This operating point also represents the limit for stable (steady-state) operation.
- For a given output power at, for example, point A, it is possible to minimize the stator current by changing the excitation flux linkage. Minimum stator current is achieved at point E, which corresponds to unity power factor.
- The Blondel diagram according to Fig. 6.9 is shown with a ratio  $\omega_s \psi_f / \hat{u}_s = 0.7$  and  $\omega_s L_s / R_s = 1.96$ . The current endpoint trajectory can be made to intersect with the maximum power point in case the ratio  $\omega_s \psi_f / \hat{u}_s$  is increased to a value of 1.1.

The output power as a function of the load angle can be found using (6.7b) and (6.9) in conjunction with the torque expression  $\vec{T}_e = \underline{\psi}_s \times \underline{i}_s$ . Alternatively, the power balance equation can be used, as defined by expression (6.12). The resulting expression is normalized using  $p_{out}^n = p_{out}/p_{out}^{\max}$ . A graphical representation of the normalized output power as a function of the load angle is shown in Fig. 6.10, with  $\omega_s \psi_f / \hat{u}_s = 0.7$  and  $\omega_s L_s / R_s = 1.96$ . The parameters deployed here are identical to those used for Fig. 6.9. Also,

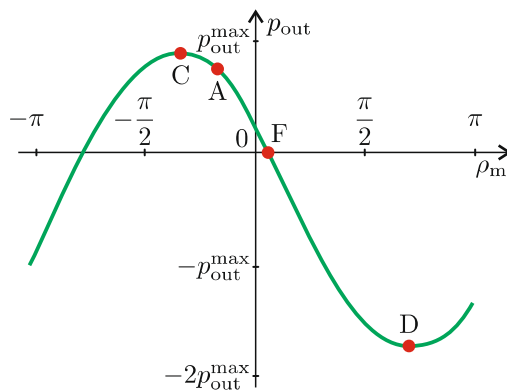


**Fig. 6.10** Output power versus load angle curve

the same operating points are shown in Fig. 6.10 for comparative purposes. A tutorial example which demonstrates the use of the Blondel diagram is given in Sect. 6.3.2.

## 6.2 Salient Synchronous Machine

Salient synchronous machines have a reluctance that is rotor position dependent. A common type of salient synchronous machines is the *interior permanent magnet machine* which carries magnets within the rotor lamination. A cross section of an interior magnet machine with four poles is shown in Fig. 6.11. In the direction of the x-axis, the magnets are in the flux path, increasing the effective air-gap due to their low permeability. In the direction of the y-axis, the magnets have no effect and thus the effective air-gap is unchanged [66]. Consequently, the magnetizing inductances  $L_{mx}$  and  $L_{my}$  related to the x- and y-axes are different. In the example given,  $L_{my}$  is larger than  $L_{mx}$ . This is typical for interior magnet machines and contrary to *salient pole machines* where  $L_{my}$  is usually smaller than  $L_{mx}$ . The IRTF based model of a salient machine is given in Fig. 6.12, showing the magnetizing inductance on the rotor side. The inductance is composed of the two

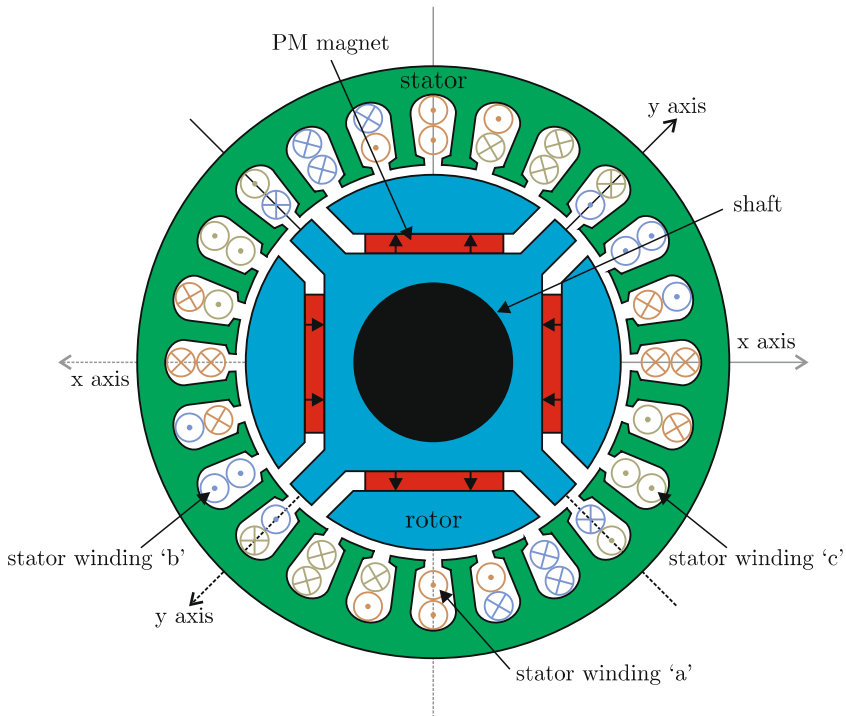


**Fig. 6.11** PM synchronous machine, with saliency

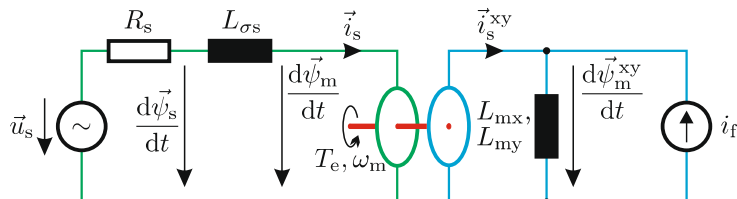


**Fig. 6.12** Synchronous machine, with a salient rotor

components  $L_{mx}$  and  $L_{my}$  which act on the real and imaginary part of the current. It is emphasized that the freedom of locating these inductances to the stator side of the IRTF is lost due to the rotor saliency. Transferring the inductance to the stator side would result in an angle dependent inductance, which is rotating with the rotor, making the model unnecessarily complex. No other changes compared to the non-salient IRTF model, shown in Fig. 6.2, are needed and the stator resistance  $R_s$  and stator leakage inductance  $L_{\sigma s}$  remain in place.

The equations which correspond to this machine are given by equation set (6.14). Equation (6.14b) was derived from (6.1b) by transforming it to rotor coordinates using  $\vec{A} = \vec{A}^{xy} e^{j\theta}$  for any vector  $\vec{A}$ .

$$\vec{u}_s = R_s \vec{i}_s + \frac{d\vec{\psi}_s}{dt} \quad (6.14a)$$

$$\vec{\psi}_s^{xy} = L_{\sigma s} \vec{i}_s^{xy} + \vec{\psi}_m^{xy} \quad (6.14b)$$

$$\psi_{mx} = L_{mx} (i_{sx} + i_f) \quad (6.14c)$$

$$\psi_{my} = L_{my} i_{sy} \quad (6.14d)$$

As with the non-salient case, some simplification of the symbolic model according to Fig. 6.12 may be achieved by rearranging the inductances  $L_{\sigma s}$ ,  $L_{mx}$  and  $L_{my}$  and by introducing the variable  $\psi_f = L_{mx} i_f$ , which allow (6.14c), (6.14d) and (6.14b) to be written as

$$\psi_{sx} = \underbrace{(L_{mx} + L_{\sigma s})}_{L_{sd}} i_{sx} + \psi_f \quad (6.15a)$$

$$\psi_{sy} = \underbrace{(L_{my} + L_{\sigma s})}_{L_{sq}} i_{sy}. \quad (6.15b)$$

The two parameters  $L_{sd}$  and  $L_{sq}$  represent the direct and quadrature synchronous inductances respectively. Note that the *direct* and *quadrature* axis terminology is normally used to represent a complex plane which is oriented with respect to a designated flux linkage vector. For synchronous machines, the designated flux linkage vector is normally chosen to be the field flux linkage vector  $\vec{\psi}_f^{xy} = \vec{\psi}_f^{dq} = \psi_f$ , which is aligned with the x axis. Hence, for the synchronous machine, the complex plane formed by the direct and quadrature axes is aligned with the rotor based xy complex plane.

### 6.2.1 Generic Model

The generic model of the salient synchronous machine follows directly from the non-salient model, according to Fig. 6.3. For the salient model, the gain module  $1/L_s$  shown in Fig. 6.3 must be replaced by a gain  $1/L_{sd}, 1/L_{sq}$  as illustrated in Fig. 6.13. The input and output vectors for this gain module are unchanged, while the gain variables are defined by equation set (6.15). As with the non-salient case, the field flux linkage  $\psi_f$  may be supplied by an excitation winding which carries a current  $i_f$  or by permanent magnets, as shown in Fig. 6.11.

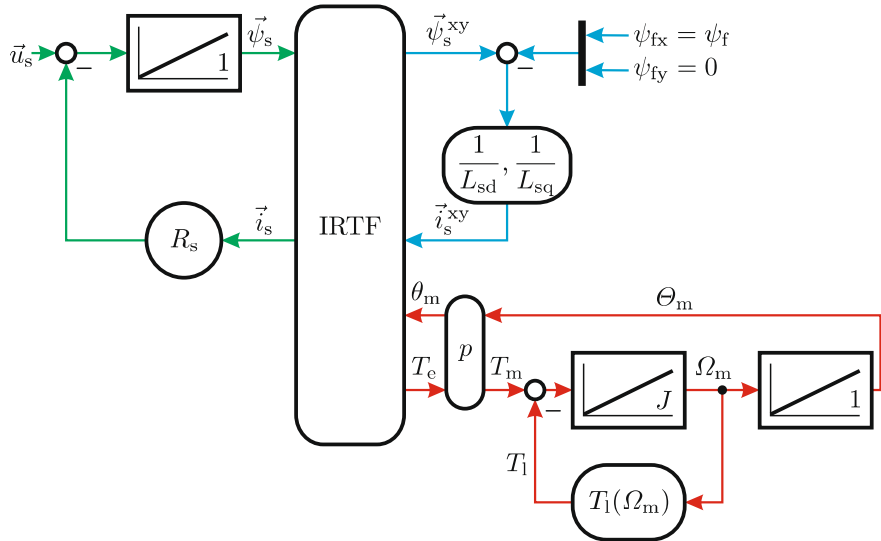


**Fig. 6.13** Generic synchronous machine model, with a salient rotor

### 6.2.2 Rotor-Oriented Model of the Salient Synchronous Machine

The coordinate transformation process for deriving a symbolic and generic representation of the rotor-oriented model of the salient machine, is similar to that undertaken for the non-salient case in Sect. 6.1.3. The process is initiated with the aid of (6.14a) and (6.15). For a rotor flux based model the synchronous reference frame with the direct and quadrature axis is linked to the field flux linkage vector  $\psi_f$ , as shown in Fig. 6.14.

The equation set for the salient rotor flux based model may be written as

$$\vec{u}_s^{\text{dq}} = R_s \vec{i}_s^{\text{dq}} + \frac{d\vec{\psi}_s^{\text{dq}}}{dt} + j\omega_s \vec{\psi}_s^{\text{dq}} \quad (6.16a)$$

$$\vec{\psi}_s^{\text{dq}} = L_{sd} i_{sd} + jL_{sq} i_{sq} + \psi_f \quad (6.16b)$$

$$T_e = \underbrace{\psi_f i_{sq}}_{\text{electromagnetic torque}} + \underbrace{(L_{sd} - L_{sq}) i_{sd} i_{sq}}_{\text{reluctance torque}}. \quad (6.16c)$$

The stator voltage (6.16a) for the salient rotor flux based model in synchronous coordinates is identical to that found for the non-salient case (see (6.4a)). The flux linkage relationship given by (6.16b) differs from equation set (6.15) by the coordinate reference frame used. However, the xy reference frame is fully aligned with the dq reference frame. Equation (6.16c) is derived using the general torque equation  $\vec{T}_e = \vec{\psi} \times \vec{i}$ . Expression (6.16b) can be rewritten as

$$\vec{\psi}_s^{dq} = L_{sd}\vec{i}_s^{dq} + j(L_{sq} - L_{sd})i_{sq} + \psi_f \quad (6.17)$$

and is used to graphically depict the process of constructing the stator flux linkage vector based on a given stator current  $\vec{i}_s^{dq}$ . Figure 6.14 shows a flux linkage and current vector diagram for the salient synchronous machine.

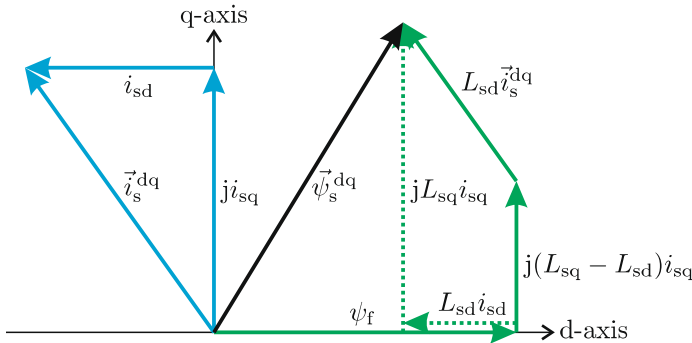


**Fig. 6.14** Vector diagram with direct and quadrature axis for salient machine

The torque equation (6.16c) shows that the introduction of a salient rotor leads to an additional torque component  $(L_{sd} - L_{sq})i_{sd}i_{sq}$ . Recalling that torque in a machine is formed by the cross-product of flux linkage and current, Fig. 6.14 shows that there are two torque producing components, namely one *electromagnetic component* due to the interaction of  $\psi_f$  and  $i_{sq}$  (shown as providing a positive torque) and a *reluctance component* due to the interaction of  $(L_{sq} - L_{sd})i_{sq}$  and  $i_{sd}$  (also shown as providing a positive torque). The flux linkage component  $L_{sd}\vec{i}_s^{dq}$  is parallel with  $\vec{i}_s^{dq}$  and therefore does not produce torque. Note that  $L_{sq} < L_{sd}$  would lead to a negative reluctance torque contribution (as long as  $i_{sd}$  stays negative).

By using (6.16a) and (6.16b), as well as by grouping the real and imaginary components, the following d- and q-axis voltage expressions can be derived:

$$u_{sd} = R_s i_{sd} - \omega_s L_{sq} i_{sq} + L_{sd} \frac{di_{sd}}{dt} \quad (6.18a)$$

$$u_{sq} = R_s i_{sq} + \omega_s L_{sd} i_{sd} + L_{sq} \frac{di_{sq}}{dt} + \omega_s \psi_f. \quad (6.18b)$$

A symbolic representation of the rotor-oriented model which corresponds with equation set (6.18) is given in Fig. 6.15. Note that the model for the salient machine reduces to the model of the non-salient machine shown in Fig. 6.5, with  $L_{sd} = L_{sq} = L_s$ . The corresponding generic model is given in Fig. 6.16.

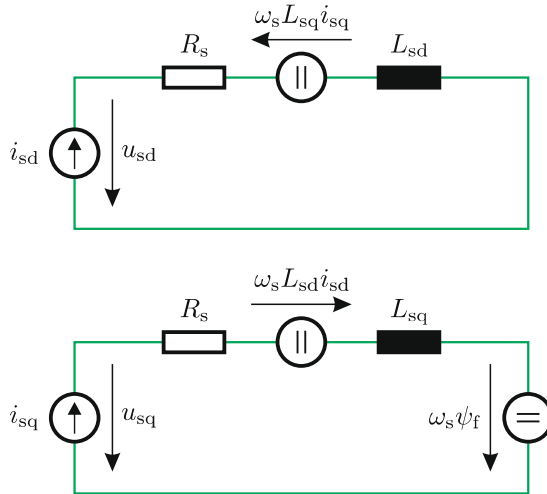


**Fig. 6.15** Symbolic rotor-oriented model: salient machine

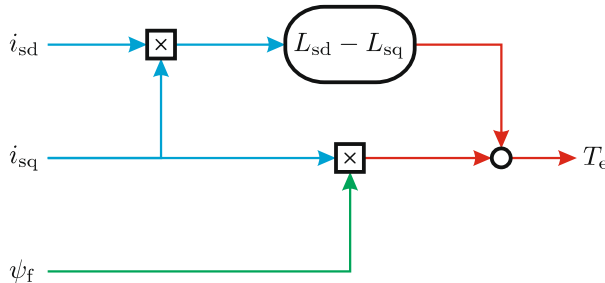


**Fig. 6.16** Generic current based rotor-oriented salient synchronous machine model

### 6.2.3 Steady-State Analysis

Similar to the non-salient machine the steady-state behavior of the salient machine is analyzed in this chapter. Consequently, only a broad outline of the steps needed is shown. It is helpful to define the saliency factor  $\chi$  as

$$\chi = \frac{L_{sq} - L_{sd}}{2L_{sd}}. \quad (6.19)$$

Use of (6.19) with expression (6.17) allows the stator flux linkage vector  $\vec{\psi}_s^{dq}$  to be written as

$$\vec{\psi}_s^{dq} = L_{sd} \vec{i}_s^{dq} + j2\chi L_{sd} i_{sq} + \psi_f. \quad (6.20)$$

This expression reduces to the non-salient case as in (6.2), with  $L_{sd} = L_{sq} = L_s$ , i.e., the saliency factor  $\chi$  equals zero. The torque expression can likewise be rewritten as

$$T_e = \psi_f i_{sq} - 2\chi L_{sd} i_{sd} i_{sq}. \quad (6.21)$$

If  $\chi > 0$ , then a field weakening current component ( $i_{sd} < 0$ ) leads to an additional reluctance torque component as in interior magnet machines. In salient pole machines with field excitation the saliency factor  $\chi$  is negative. The current components in (6.20) can be replaced by  $\vec{i}_s^{dq}$  and its complex conjugate  $(\vec{i}_s^{dq})^*$  which leads to

$$\vec{\psi}_s^{dq} = (1 + \chi) L_{sd} \vec{i}_s^{dq} - \chi L_{sd} (\vec{i}_s^{dq})^* + \psi_f. \quad (6.22)$$

The Blondel diagram for the salient machine is found by making use of the voltage (6.16a) and the flux linkage expression (6.22). As for the non-salient machine both expressions are converted to their phasor form, based on the general transformation from stator to rotor coordinates  $\vec{A}^{dq} = \vec{A} e^{-j\theta}$  and from phasor to space vector quantities  $\vec{A} = \underline{A} e^{j\omega_s t}$ . Note that the phasors are representing sinusoidal functions in time, using peak values. Using the relationship  $\theta - \omega_s t = \rho_m - \pi/2$  (cp. Fig. 6.7), this leads to the expression  $\vec{A}^{dq} = \underline{A} e^{-j(\rho_m - \frac{\pi}{2})}$ . Inserting this in (6.16a) and (6.22), we obtain the expression

$$\underline{u}_s = R_s \underline{i}_s + j\omega_s \underline{\psi}_s \quad (6.23a)$$

$$\underline{\psi}_s = (1 + \chi) L_{sd} \underline{i}_s + \chi L_{sd} \underline{i}_s^* e^{j2\rho_m} - j\psi_f e^{j\rho_m}. \quad (6.23b)$$

Elimination of the flux linkage phasor  $\underline{\psi}_s$  from equation set (6.23), leads to the following current phasor expression.

$$\underline{i}_s + \underbrace{\left[ \frac{j\omega_s L_{sd} \chi e^{j2\rho_m}}{R_s + j\omega_s (1 + \chi) L_{sd}} \right]}_{\underline{K}} \underline{i}_s^* = \underbrace{\frac{\hat{u}_s - \omega_s \psi_f e^{j\rho_m}}{R_s + j\omega_s (1 + \chi) L_{sd}}}_{\underline{i}_s^\circ} \quad (6.24)$$

For the non-salient case with  $\chi = 0$ , (6.24) reduces to expression (6.9). It is helpful to introduce the phasors  $\underline{K}$  and  $\underline{i}_s^\circ$  as defined in (6.24). This allows the former expression to be written as

$$\underline{i}_s + \underline{K} \underline{i}_s^* = \underline{i}_s^\circ. \quad (6.25)$$

The current phasor  $\underline{i}_s$  can be expressed as a function of the load angle  $\rho_m$  by rewriting the complex coefficient  $\underline{K}$  as  $\underline{K} = K_x + jK_y$  and the phasor  $\underline{i}_s^\circ$  as  $\underline{i}_s^\circ = i_{sx}^A + j i_{sy}^A$ . Subsequent use of the aforementioned approach with (6.25) gives

$$\Re \{i_s\} = \frac{(1 - K_x) i_{sx}^A - K_y i_{sy}^A}{1 - K_x^2 - K_y^2} \quad (6.26a)$$

$$\Im \{i_s\} = \frac{(1 + K_x) i_{sy}^A - K_y i_{sx}^A}{1 - K_x^2 - K_y^2}. \quad (6.26b)$$

A graphical representation of equation set (6.26) as given in Fig. 6.17, shows the Blondel diagram of the machine with (green line) and without saliency (red line). For the salient example, the value of  $\chi$  was arbitrarily chosen as 0.75, corresponding to a ratio  $L_{sq}/L_{sd} = 2.5$ . The parameters  $\omega_s \psi_f / \hat{u}_s = 0.7$  and  $\omega_s L_{sd} / R_s = 1.96$  are identical to those used for the non-salient machine to demonstrate the impact of saliency in the Blondel diagram. As with the non-salient Blondel diagram the current locus is shown for a given shaft speed while the load angle  $\rho_m$  varies from  $-\pi$  to  $\pi$ .

Figure 6.17 also shows the vectors  $i_s^\circ$  and  $K i_s^*$  as defined by (6.25). The endpoint trajectory of the phasor  $i_s^\circ$  is circular for the non-salient case when

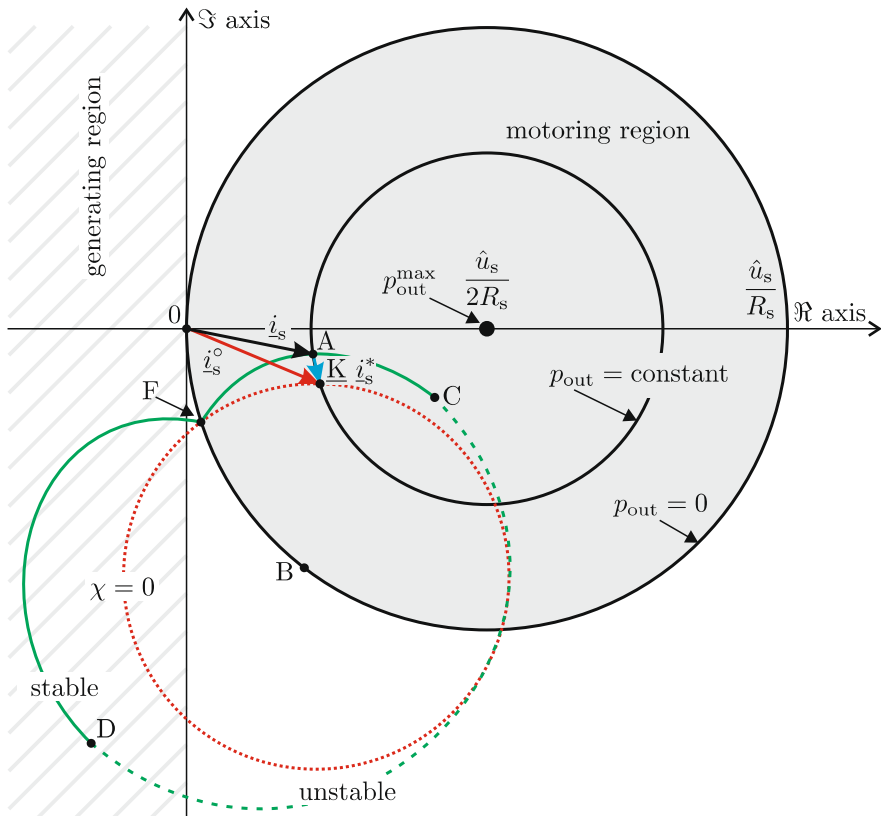


**Fig. 6.17** Blondel diagram of synchronous machine with  $\omega_s \psi_f / \hat{u}_s = 0.7$ ,  $\omega_s L_{sd} / R_s = 1.96$  and  $\chi = 0.75$

the load angle is varied from  $-\pi$  to  $\pi$ . For the salient case the radius of the circle will be slightly larger as may be deduced from (6.24). Also, for the salient case the current  $i_s$  is additionally determined by the phasor  $\underline{K}i_s^*$ . Given that its rotation is governed by the term  $2\rho_m$ , a deviation from the circle occurs resulting in a *cardioidal* shape, which is a special case of the *Limaçon of Pascal*. A negative saliency factor results in a stator current phasor with a differently shaped endpoint trajectory, also a member of the Limaçon class. Additionally, if stator frequency, stator voltage and machine speed are constant, the introduction of saliency increases the maximum available output power of the machine, because the current locus is closer to the theoretical power limit at  $p_{out}^{\max}$ .

The output power versus load angle diagram may be found by making use of the power equation  $p_{out} = \omega_s \Im\{\underline{\psi}_s^* \underline{i}_s\} = \Re\{\underline{u}_s \underline{i}_s^*\} - R_s \underline{i}_s \underline{i}_s^*$ , together with equation set (6.26) and the stator voltage phasor  $\underline{u}_s = \hat{u}_s$ . As with the non-salient case a normalization with  $p_{out}^n = p_{out}/p_{out}^{\max}$  is introduced leading to Fig. 6.18. For comparison, this figure also shows the non-salient case according to Fig. 6.10 with  $\omega_s \psi_f / \hat{u}_s = 0.7$  and  $\omega_s L_s / R_s = 1.96$ . Note that the theoretical maximum output power  $p_{out}^{\max}$  is not affected by the introduction of rotor saliency, given that the voltage supply amplitude  $\hat{u}_s$  and stator resistance  $R_s$  remain the same. As can be observed from Fig. 6.18, the slope of the output power is less steep in the stable (motoring) area. This effect results in a reduced stiffness of the salient machine with  $\chi > 0$  compared to the non-salient machine. To increase the stiffness of grid connected, electrically excited machines, the machines are typically designed with a negative saliency factor. In drive applications with a power electronic converter, usually a positive saliency factor is preferable, as will become apparent in the next chapter. The effect of the saliency factor on the stiffness is discussed in more detail in a tutorial given in Sect. 6.3.5.

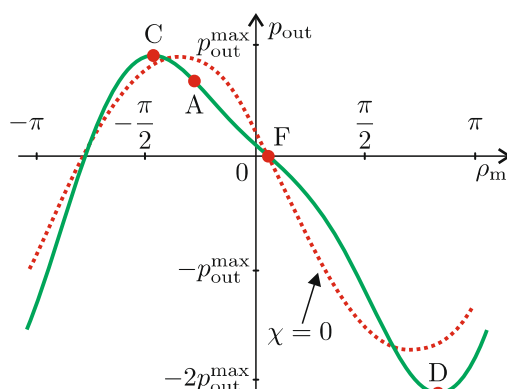
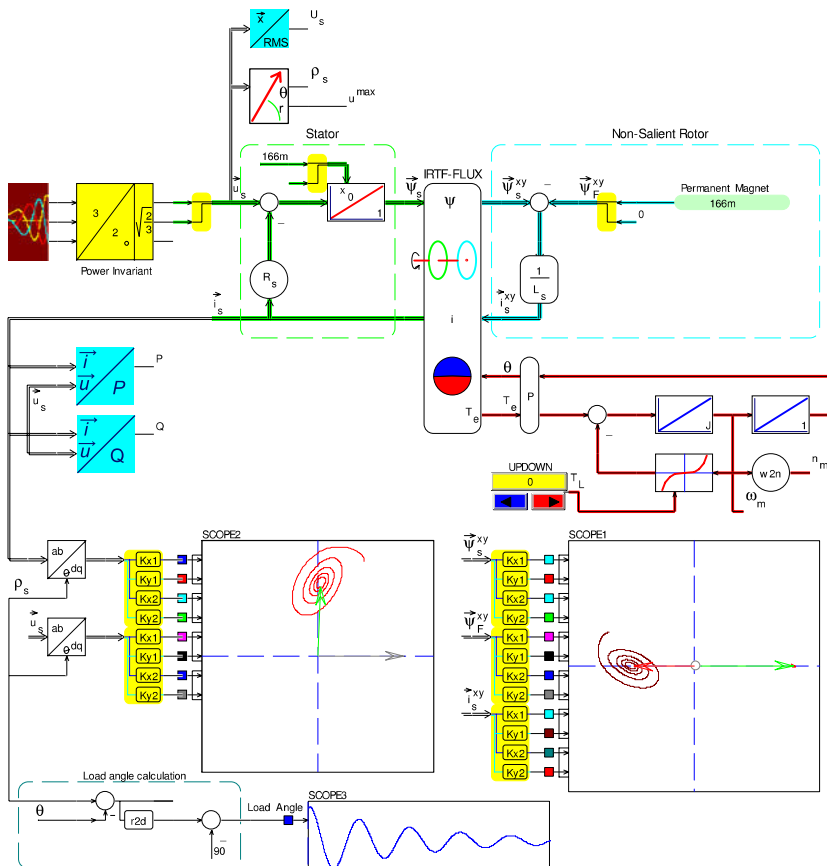


**Fig. 6.18** Normalized output power versus load angle curves of salient and non-salient machine, with  $\omega_s \psi_f / \hat{u}_s = 0.7$ ,  $\omega_s L_s / R_s = 1.96$  and  $\chi = 0.75$

## 6.3 Tutorials

### 6.3.1 Tutorial 1: Dynamic Model of a Non-salient Synchronous Machine

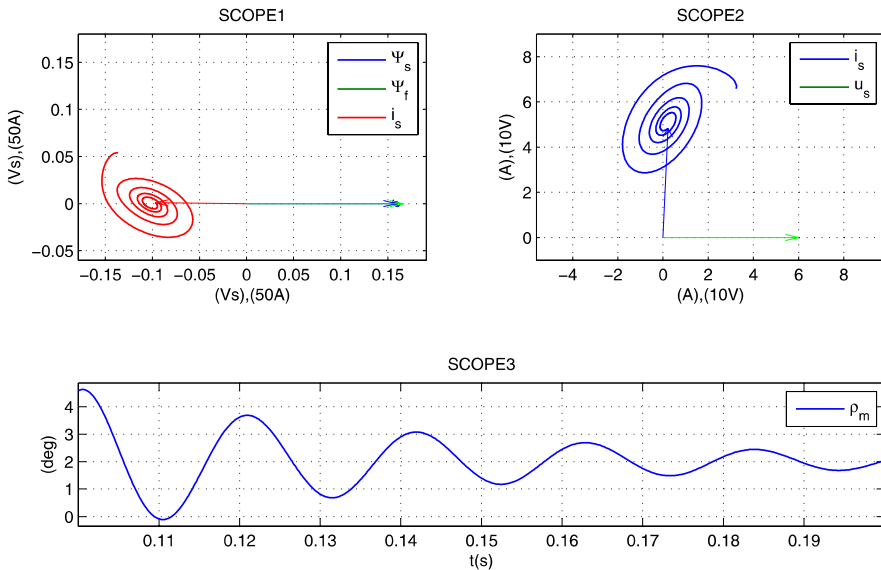
This tutorial considers a dynamic model of a four pole PM synchronous machine, as introduced in [68]. The set of parameters used is defined in Table 6.1. A three-phase variable frequency voltage source with  $\vec{u}_s = \hat{u}_s e^{j2\pi f_s t}$  is connected to the machine model. At the start of the simulation the frequency  $f_s = 0 \rightarrow 60$  Hz and the amplitude  $\hat{u}_s = 7 \rightarrow 60$  V are ramped up over a period of  $t = 0.1$  s. A quadratic load-speed characteristic is assumed, providing a load torque  $T_L = 20$  Nm at synchronous shaft speed  $n_m = 1800$  rpm.



**Fig. 6.19** Simulation of the synchronous machine, non-salient model

**Table 6.1** Parameters for PM synchronous machine

Parameters	Value
Stator inductance $L_s$	1.365 mH
Stator resistance $R_s$	0.416 Ω
PM flux linkage amplitude $\psi_f$	0.166 Wb
Inertia $J$	$3.4 \cdot 10^{-4}$ kg m <sup>2</sup>
Pole pairs $p$	2
Initial rotor speed $\omega_m^A$	0 rad/s

**Fig. 6.20** Simulation results of the synchronous machine, non-salient model

The simulation model according to Fig. 6.19 shows the dynamic model of the machine together with a  $V/f$  module which generates the required excitation vector  $\vec{u}_s$ . A vector to polar conversion module determines the instantaneous angle  $\rho^s$  of the voltage vector  $\vec{u}_s$ . This reference angle is used for the transformation of the current vector  $\vec{i}_s$  and voltage vector  $\vec{u}_s$  to the synchronous reference frame. Furthermore, the load angle (in degrees) is calculated by introducing a vector  $\vec{u}_{s/j\omega_s}$ , which is used as an input vector to the *load angle* module together with the electrical shaft angle  $\theta$ . Results obtained with this simulation are shown in Fig. 6.20 with the aid of three scope modules. Also shown in the simulation model are the real and reactive power levels which show that the reactive power is capacitive with the present choice of excitation, as may also be observed from scope 2 (current vector leading the voltage vector).

### 6.3.2 Tutorial 2: Steady-State Analysis of a Non-salient Synchronous Machine

A steady-state analysis of the model given in Fig. 6.19 is to be carried using the approach outlined in Sect. 6.2.3. The aim is to plot the Blondel diagram for the machine defined in the previous tutorial when operating under steady conditions with a phasor voltage of  $|u_s| = \hat{u}_s = 60\text{ V}$  and frequency  $f_s = 60\text{ Hz}$ , which are the end values used in the ramped space vector generator (see Fig. 6.19). The plot in question should show the zero output power circle, maximum power point (with the corresponding power value) and phasors  $\underline{i}_{s1}, -\underline{i}_{s2}$  as shown in Fig. 6.9, as well as the stator current phasor locus for operation of the machine for a load angle of  $\rho_m = 0 \rightarrow -\pi/2\text{ rad}$ . The locus is to be calculated using the model given in Fig. 6.8. In addition, show in the Blondel diagram the output power circle which corresponds with the maximum achievable power level  $p_{a,out}$  of the machine for the given excitation flux linkage value  $\psi_f$ . Finally, add to your plot the steady-state current vector  $\vec{i}_s e^{-j\rho_m}$  endpoint coordinates, with the model shown in Fig. 6.19 for a set of load torque values (with an incremental step of  $1\text{ Nm}$ ) in the range  $0 \rightarrow 10\text{ Nm}$ .

A solution to this problem may be initialized by firstly considering the zero power circle which, according to Sect. 6.2.3, is a circle with its origin at  $\hat{u}_s/2R_s, 0$  and radius  $\hat{u}_s/2R_s$ , as shown in Fig. 6.21. The maximum power  $p_{out}^{\max}$  point of the machine, which is located on the origin of the output power circles, is found using (6.13) and (with the given parameters and excitation) is equal to  $p_{out}^{\max} = 2.16\text{ kW}$ . A synchronous shaft speed of  $n_s = 1800\text{ rpm}$  is present, which means that the maximum achievable shaft torque that can be delivered by this machine equals  $11.48\text{ Nm}$ . Note that these values are theoretical limit values which are normally not realizable given the thermal constraints, which limit the current to an (assumed) maximum value  $i_s^{\max} = 20\text{ A}$ . The current phasors  $\underline{i}_{s1}, -\underline{i}_{s2}$  and current phasor  $\underline{i}_s$  may be found using (6.10). Changing the load angle  $\rho_m$  over the required angle range gives the current phasor locus illustrated in Fig. 6.21.

Careful observation of Fig. 6.21 shows that the current phasor endpoint for  $\rho_m = 0$  is outside the zero output power circle, hence this point is not feasible for motoring operation. When a load torque is applied, the current phasor will move to a point of the locus which corresponds to the required output level. However, observation of Fig. 6.21 demonstrates that an output power level  $p_{a,out}$  exists, which corresponds to a power circle that coincides with the locus at one single operating point. This limit also defines the stability range of the machine, because a load angle setting less than the value  $\rho_m = -\arctan(\omega_s L_s/R_s)$  will result in a power level that is less than  $p_{a,out}$ . The relationship between the radius  $r_p$  of power circle and output power is of the form  $p_{out} = p_{out}^{\max} - R_s r_p^2$ , with  $r_p = [0 \dots \hat{u}/2R_s]$ . At the maximum achievable power level, the power radius

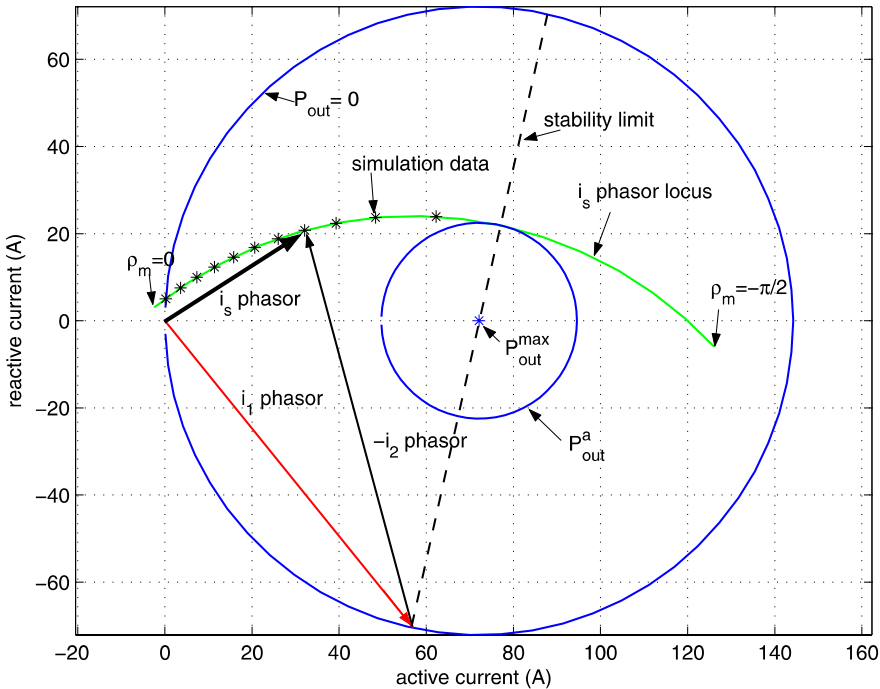


**Fig. 6.21** Blondel diagram, non-salient voltage source connected machine

$r_p = |\omega_s \psi_f / \sqrt{R_s^2 + (\omega_s L_s)^2} - \hat{u}/2 R_s|$ , which corresponds to  $p_{a,out} = 1.95 \text{ kW}$  and a corresponding shaft torque level of  $10.3 \text{ Nm}$ . The simulation model given in the previous tutorial was used to obtain the steady-state current vector  $\vec{i}_s e^{-j\rho_m}$  for the predetermined range of load torque settings. As expected, the resultant set of current endpoints (identified by an ‘asterisk’ in Fig. 6.21), are located on the current locus calculated using the steady-state phasor model.

### 6.3.3 Tutorial 3: Stator Flux Linkage Excited Dynamic Model of a Synchronous Machine to Demonstrate the Rotor Flux Oriented Concept

The purpose of this tutorial is to introduce the reader to the concepts which are linked to the rotor flux oriented model approach as outlined in Sect. 6.1.3. The machine model, described in the previous two tutorials, is again used with the important difference that a stator flux linkage space vector, defined

as  $\vec{\psi}_s = \hat{\psi}_s e^{j\omega_s t}$ , is to be used as an input to the IRTF based model shown in Fig. 6.3. For this example, the stator flux linkage amplitude  $\hat{\psi}_s$  and excitation frequency  $f_s$  are set to 0.166 Wb and 200 Hz (which is the rated value) respectively. Make use of a quadratic load torque module as discussed previously and set its internal speed reference to the synchronous speed of the machine. Assume a load torque range of  $0 \rightarrow 5$  Nm as input to this module. The current vector  $\vec{i}_s$  from the IRTF based model is in turn to be used as an input for a rotor flux oriented model as shown in Fig. 6.5. For this purpose, the IRTF current output vector is to be converted to a synchronous reference frame that is tied to the rotor angle  $\theta$ , leading to the vector  $\vec{i}_s^{dq}$ . Build a rotor flux oriented model of the machine using circuit elements which have as outputs the torque  $T_e$  (which requires use of (6.4c)) and the voltage vector  $\vec{u}_s^{dq}$ . To compare operation of the two machine models, add a scope module which should display the vector  $\vec{u}_s^{dq}$  as obtained from the rotor flux oriented model. In addition, show in the same scope the voltage vector  $\vec{u}_s$ , which is to be derived for the IRTF based model. Make use of a coordinate conversion module to realize the transformation  $\vec{u}_s e^{-j\theta}$  and add this vector to the scope module.

The module as given in Fig. 6.22 satisfies the criteria for this tutorial. Shown in this figure is a ‘scope module’ set in xy mode which has as input the vectors  $\vec{u}_s^{dq}$ ,  $\vec{u}_s e^{-j\theta}$ . The vector  $\vec{u}_s$  is calculated using (6.1a) in which the differentiator function is undertaken with the aid of an ‘alternative differentiator’ module. A set of circuit modules and controllable voltage/current sources has been introduced to generate the circuit current and voltage source modules for the rotor flux model.

A set of voltage amplifiers (with unity gain) is introduced to find the variables  $u_{sd}, u_{sq}$ , which are shown in the scope. An ( $\alpha\beta \rightarrow dq$ ) coordinate conversion unit is used to achieve the conversion  $\vec{u}_s e^{-j\theta}$ , where  $\vec{u}_s$  represent the voltage vector generated by the IRTF based machine module. Set the initial load torque value to  $T_l = 2$  Nm and observe the locus of the two vectors and note that these are in fact identical. Likewise, the torque generated by the IRTF and rotor flux based models must be the same. Note also that changes of the load parameters reflect in damped oscillatory movements of the two vectors. As the load is reduced, the damping reduces, given that in this model there is no electrical damping (due to the stator resistance) present, i.e., the damping is only provided by the mechanical load.

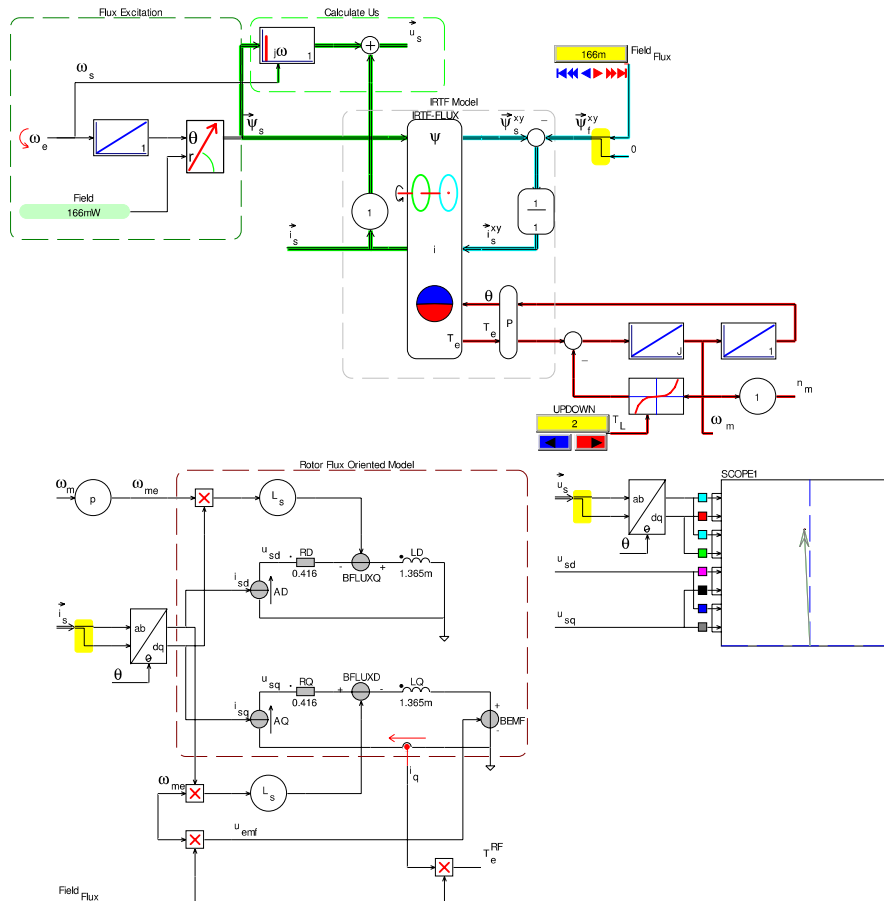


**Fig. 6.22** Simulation of non-salient synchronous machine, with stator flux linkage space vector as input variable

### 6.3.4 Tutorial 4: Dynamic Model of a Synchronous Machine with Adjustable Saliency

In this section the non-salient model discussed in tutorial 1 is to be extended to accommodate rotor saliency. On the basis of the generic model shown in Fig. 6.13, modify the non-salient model (see Fig. 6.19) by introducing a saliency module  $1/L_{dq}$  which realizes the gains  $1/L_{sd}$ ,  $1/(2\chi+1)L_{sd}$  in the real and imaginary axis respectively. The factor  $\chi$  is known as the saliency factor and is to be connected to an UPDOWN module which must be varied over the range  $-0.4 \rightarrow 0.75$ . The excitation and parameters as introduced in tutorial 1 remain unchanged, whereby it is noted that the inductance  $L_{sd}$  is set to  $L_s$  as defined in Table 6.1. The purpose of the exercise is to familiarize the

reader with rotor saliency and to demonstrate how the voltage/current and flux linkage space vectors introduced in this tutorial will change when the load torque is adjusted. The simulation model given in Fig. 6.23 shows the changes needed to arrive at a generalized model, where the user can choose the saliency factor of the machine.

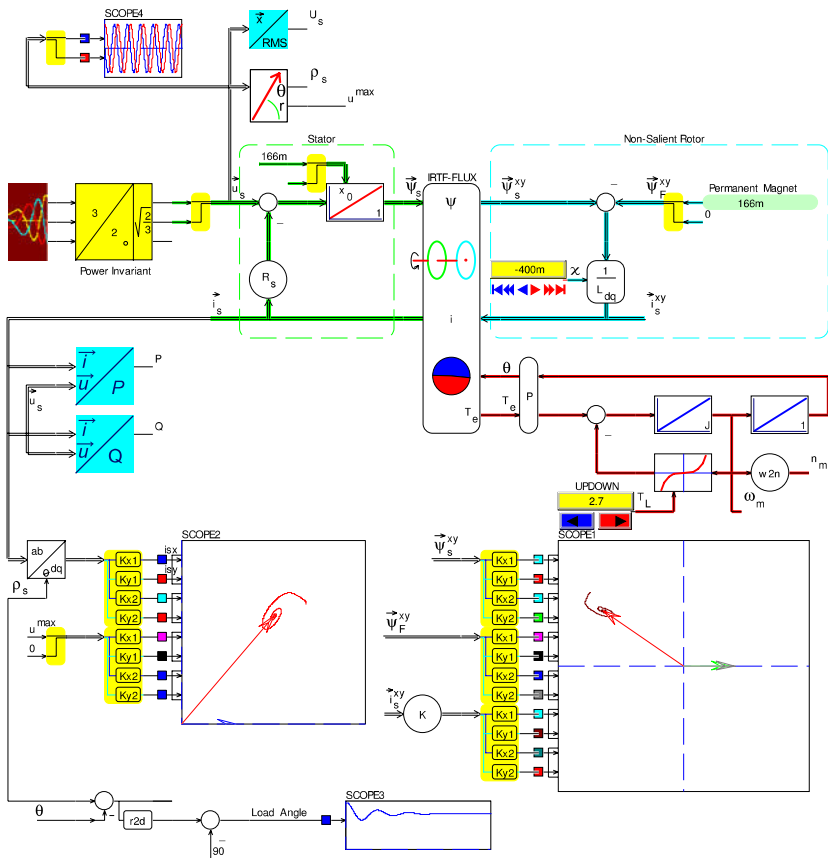


**Fig. 6.23** Simulation of synchronous machine, full model with adjustable saliency factor

### 6.3.5 Tutorial 5: Steady-State Analysis of a Salient Synchronous Machine

The final tutorial in this section examines the steady-state behavior of the machine that was introduced in the previous tutorial. A similar approach was taken in tutorial 2 for the non-salient machine, where the stator current phasor trajectory was calculated and compared with the simulation model operating under quasi-steady-state conditions. In this tutorial the steady-state output power versus load angle characteristic of the machine is to be calculated using the theory outlined in Sect. 6.2.3. For the purpose of this exercise restrain the load angle  $\rho_m$  range to  $-\pi/2 \rightarrow 0$  rad and undertake this task for saliency factors of  $\chi = -0.4, 0$  and  $\chi = 0.75$  respectively. The parameters and excitation are those given in tutorials 1 and 4. In addition to the above, use the model given in Fig. 6.23 and vary the load torque in the range of  $0 \rightarrow 10$  Nm in increments of 1 Nm. At each step, allow the model to settle to its steady-state and then record the load angle. Add the results obtained to the calculated torque versus load angle characteristics for the three saliency factors considered.

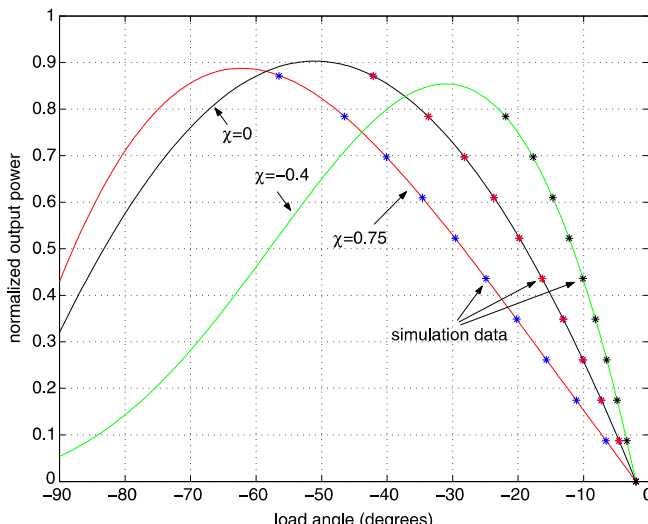


**Fig. 6.24** Normalized output power versus load angle of a voltage source connected machine, with saliency factors of  $\chi = -0.4, 0$  and  $\chi = 0.75$  respectively

The results shown in Fig. 6.24 confirm an earlier observation that the stiffness of the machine, i.e., its sensitivity to load angle variations when the load torque changes, is reduced when the saliency factor increases. Also shown in Fig. 6.24 are the simulation results (asterisks) as obtained with the dynamic model operating under quasi-steady-state conditions.



# Chapter 7

## Control of Synchronous Machine Drives

This chapter deals with field-oriented control of synchronous machines. Field-oriented control has become common choice for many servo-drive applications due to the availability of affordable digital signal processors (DSPs). This chapter builds on the machine models introduced in the previous chapter and extends the electromagnetic torque control principle introduced in Sect. 4.2.2. Controls are derived for both non-salient and salient synchronous machines. The operation in field weakening with constant stator flux linkage and with unity power factor is analyzed. At the end of the chapter, the controls are interfaced with a current-controlled and a voltage-controlled converter. A set of tutorials is provided to interactively illustrate the concepts and the proposed control strategies.

### 7.1 Controller Principles

The drive structure of a synchronous machine under field-oriented control is shown in Fig. 7.1. It consists of a field-oriented control module, a converter with a current control unit, and a synchronous machine which is connected to a mechanical load [40]. In case the machine is not permanently excited, an additional single-phase converter is connected to the excitation winding of the machine. For current control, any of the methods outlined in Chap. 3 can be used. Input to the field-oriented control module is the reference torque  $T_e^*$  which is either set by the user or by a superimposed control (e.g. speed control). From the reference torque  $T_e^*$  and the mechanical rotor angle  $\Theta_m$ , the field-oriented control module generates the command currents  $i_{sd}^c$ ,  $i_{sq}^c$ , and  $i_f^c$  and calculates the control angle  $\theta^c$ . The rotor or shaft angle  $\Theta_m$  is provided by a shaft encoder which is attached to the machine shaft. In an ideal case the control angle matches the shaft angle  $\theta^c = \theta_m = p\Theta_m$ .

The field-oriented control module uses an orthogonal control grid formed by the direct axis d and the quadrature axis q, as shown in Fig. 7.2. The

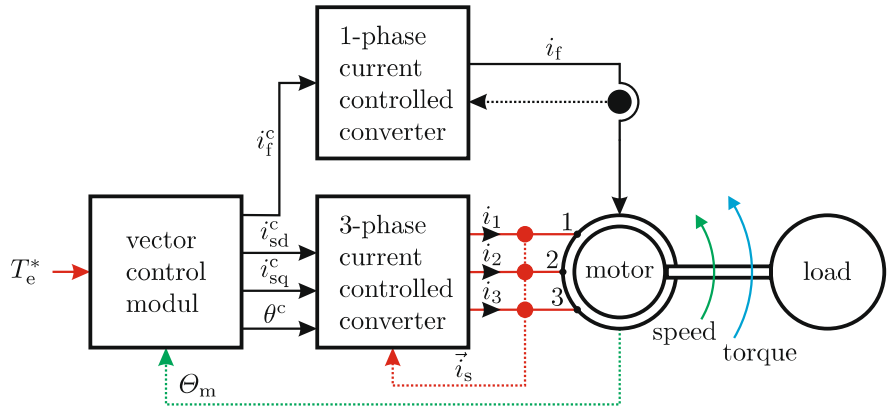


Fig. 7.1 Drive structure of a field-oriented controlled synchronous machine

d-axis is aligned with the flux linkage vector  $\vec{\psi}_f$ , giving the field-oriented control its name. In a synchronous machine, the flux linkage vector  $\vec{\psi}_f$  has a fixed orientation relative to the rotor, such that the rotor reference system (xy) matches the rotor-oriented reference system (dq). This is why this type of control is also referred to as rotor flux or rotor-oriented control. Rotor-oriented control is most suited for synchronous drives because it has the benefit of easily decoupling the direct and quadrature currents in non-salient machines as discussed in Sect. 6.1.3. Given the above, rotor-oriented control is exclusively considered in this chapter.

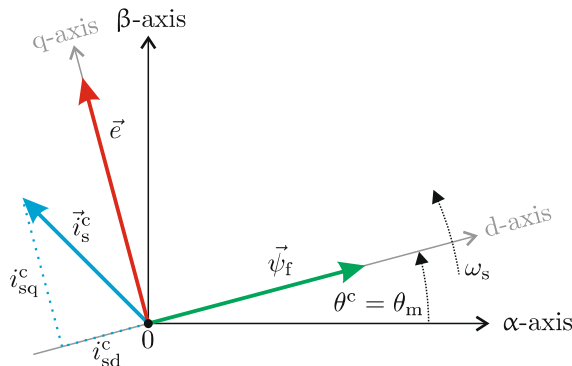


Fig. 7.2 Space vector diagram for rotor-oriented control

Careful attention must be given to ensure that the control angle  $\theta^c$  matches the rotor position  $\theta_m$ . Two methods exist to achieve this, namely:

- Indirect field-oriented control (IFO), which makes use of a mechanically connected sensor to measure the shaft angle  $\Theta_m$ .

- Direct field-oriented control (DFO), which estimates the angle  $\theta^c$  by making use of the flux linkage vector  $\psi_f$  or the back-EMF vector  $\vec{e}$ . The latter can be achieved by making use of sensors in the machine or an observer which uses measured electrical quantities.

In this chapter attention is given exclusively to IFO, because of its widespread use in industry.

The basic question to be addressed in the ensuing sections is how the d-axis and q-axis components  $i_{sd}^c$  and  $i_{sq}^c$  of the reference current should be chosen. In case a machine with electrical excitation is used, this question further includes the reference excitation current  $i_f^c$ . Besides the desired torque, also issues like field weakening at high speed or operation with constant stator flux linkage or unity power factor (for machines with electrical excitation) determine the variables  $i_{sd}^c$ ,  $i_{sq}^c$  and  $i_f^c$ .

## 7.2 Control of Non-salient Synchronous Machines

In this section, the control of permanently and electrically excited non-salient synchronous machines is considered. More specifically, the generic implementation of the field-oriented control module as given in Fig. 7.1 is discussed.

Following the key concept of this book, the control for the non-salient synchronous machine can be derived by model inversion. Starting from the current source connected machine model shown in Fig. 6.6 and (6.4c), the rotor-oriented control model can easily be derived, giving

$$i_{sq}^* = \frac{T_e^*}{\psi_f^*}. \quad (7.1)$$

The resulting control structure is shown in Fig. 7.3. The control is identical to that found for the DC machine (compare Fig. 5.8). Its simplicity stresses the advantage of rotor flux orientation. The output of this model is the quadrature reference current  $i_{sq}^*$ . It is used as an input to the non-salient control module which generates the command current values  $i_{sd}^c$  and  $i_{sq}^c$  for the current controller of the converter.

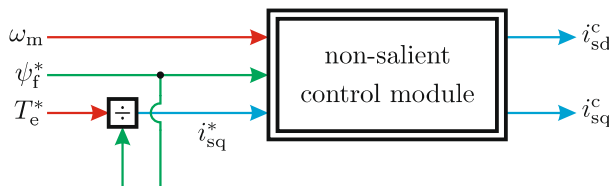


**Fig. 7.3** Structure of the field-oriented control module for a non-salient machine

The purpose of the non-salient control module is to moderate the reference current values  $i_d^c$  and  $i_q^c$ . The control laws used within the control module are dependent on the type of control used and will be discussed in the next subsections. In this context, operation in field weakening, under constant stator flux linkage, and with unity power factor (for electrically excited machines) will be examined.

### 7.2.1 Operation under Drive Limitations

The control has to ensure that the reference values for the controller currents are chosen in such a manner that maximum stator current  $i_s^{\max}$  and maximum stator voltage  $u_s^{\max}$  are not exceeded. At the same time, the reference values should be chosen to deliver the required torque with highest efficiency. In line with the approach taken for the DC drive, use is made of the current locus diagram in which the reference current vector  $\vec{i}_s^{dq}$  is shown together with the operating limits of the drive (see Fig. 7.4).

#### Lines of Constant Torque

Equation (7.1) shows that the torque is independent of the d-axis current  $i_{sd}$  and therefore the choice of the current vector  $\vec{i}_s^{dq}$  is not unique for one reference torque value.

$$i_{sq} = \frac{T_e}{\psi_f} \quad (7.2)$$

In the current locus diagram, the lines of constant torque are horizontal lines. Four lines of constant torque are shown in Fig. 7.4 at  $i_{sq} = \pm i_s^{\max}$  and  $i_{sq} = \pm 1/2 i_s^{\max}$  (black dotted lines) as a function of the maximum torque  $T_e^{\max} = i_s^{\max} \psi_f$ . By choosing the operating point dependent currents, the controller has obey the following limits:

#### Current Limit (Maximum Ampere, MA)

A first limit is given by the maximum current of the drive. It limits the operating region to

$$|\vec{i}_s^{dq}| \leq i_s^{\max} \quad (7.3)$$

as shown in the current locus diagram by the maximum ampere (MA) circle (red).

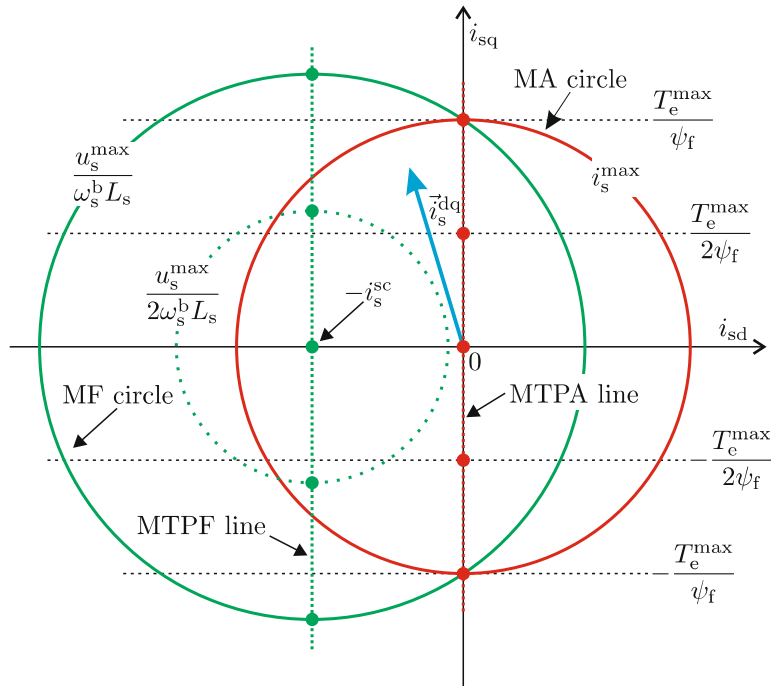


**Fig. 7.4** Operational drive limits for non-salient synchronous drives

### Voltage Limit (Maximum Flux Linkage, MF)

A second limit is the maximum available stator flux linkage which arises from the voltage constraint  $u_s^{\max}$ . For quasi-steady-state conditions, i.e., neglecting time derivatives, equation set (6.4) may be rewritten as

$$\vec{u}_s^{dq} \simeq \vec{i}_s^{dq} R_s + j\omega_s \vec{\psi}_s^{dq} \quad (7.4a)$$

$$\vec{\psi}_s^{dq} = \psi_f + L_s \vec{i}_s^{dq}. \quad (7.4b)$$

Assuming that the dominant term in (7.4a) is formed by the induced voltage, the resistive component is ignored. Thus,

$$\vec{u}_s^{dq} \cong j\omega_s \vec{\psi}_s^{dq}. \quad (7.5)$$

With  $|\vec{u}_s^{dq}| = u_s^{\max}$ , the maximum stator flux linkage can be written as

$$\psi_s^{\max} \cong \frac{u_s^{\max}}{\omega_s}. \quad (7.6)$$

The variable  $\psi_s^{\max}$  represents the maximum stator flux linkage which can be realized by the converter for a given speed  $\omega_s$  and a given maximum voltage  $u_s^{\max}$ . Voltage  $u_s^{\max}$  is typically limited by the converter's DC bus voltage. By

using  $|\vec{\psi}_s^{dq}| = \psi_s^{\max}$ , (7.4b) and (7.6), and by equating the real and imaginary components of  $\vec{i}_s^{dq}$  the following expression is derived:

$$(i_{sd} + i_s^{sc})^2 + i_{sq}^2 = \left( \frac{\psi_s^{\max}}{L_s} \right)^2 \quad (7.7)$$

where  $i_s^{sc} = \psi_f/L_s$  represents the short circuit current of the machine (if  $R_s$  is neglected). Equation (7.7) describes the stator current limit due to the maximum flux linkage. It can be represented by a circle with its origin at coordinates  $(-i_s^{sc}, 0)$  and a radius  $(\psi_s^{\max}/L_s = u_s^{\max}/\omega_s L_s)$  as shown in Fig. 7.4 (green).

The circles of maximum (available) stator flux linkage will increase in radius when the shaft speed is reduced. Consequently, an operating speed will occur where the MF circle (see Fig. 7.4) will completely encompass the MA circle. This implies that the direct axis current value for the controller may be chosen freely within the area bound by the  $i_s^{\max}$  circle.

To simplify the equations in the following, it is helpful to introduce the ratio between the short circuit current  $i_s^{sc}$  and maximum current  $i_s^{\max}$ , as well as the normalized stator current components  $i_{sd}^n$  and  $i_{sq}^n$

$$\kappa = \frac{i_s^{sc}}{i_s^{\max}} \quad (7.8a)$$

$$i_{sd}^n = \frac{i_{sd}}{i_s^{\max}} \quad (7.8b)$$

$$i_{sq}^n = \frac{i_{sq}}{i_s^{\max}}. \quad (7.8c)$$

The value of  $\kappa$  is determined by the current ratings of machine and converter. While the short circuit current  $i_s^{sc}$  is a machine parameter, usually the inverter limits the maximum current  $i_s^{\max}$ . A value of  $\kappa < 1$  signifies that short circuit operation occurs within machine and converter limits. In the example shown, a value of  $\kappa = 0.66$  was assumed. Normalizing (7.7) with the maximum stator current  $i_s^{\max}$ , the following equation is derived:

$$(i_{sd}^n + \kappa)^2 + (i_{sq}^n)^2 = \left( \frac{\psi_s^{\max}}{L_s i_s^{\max}} \right)^2. \quad (7.9)$$

Equation (7.1) showed that for the non-salient synchronous machine, the control rule for maximum torque per ampere is remarkably simple: always choose the highest available q-axis current. Taking into account the current and voltage limit derived above, the following operation point dependent trajectories are derived:

### Maximum Torque per Ampere (MTPA) Line

Operation with lowest ohmic losses in the machine is achieved by choosing an operating condition where the required torque is delivered with the lowest amplitude of the current vector  $\vec{i}_s^{dq}$ . For a non-salient machine, this may be achieved by choosing an operating trajectory along the imaginary axis of the current locus diagram, known as the maximum torque per ampere (MTPA) operating line shown in Fig. 7.4. Operation along this line corresponds to the following control law:

$$i_{sd}^n = 0 \quad (7.10a)$$

$$-1 < i_{sq}^n < 1. \quad (7.10b)$$

The maximum speed at which nominal torque can be produced, i.e., before the voltage limit is reached, is called *base speed*. It is derived from (7.9) and (7.10a)

$$\omega_s^b = \frac{u_s^{\max}}{L_s \sqrt{\kappa^2 + 1}}. \quad (7.11)$$

### Maximum Torque per Flux Linkage (MTPF) Line

Above base speed, the maximum torque at first occurs where the MA and the MF circles intersect. For machines-converter combinations with  $\kappa < 1$ , maximum torque is eventually only limited by the maximum stator flux linkage when speed is increased further. Consequently, the operating points are found on the MF circle with radius  $u_s^{\max}/2\omega_s L_s$ . They form the maximum torque per flux linkage (MTPF) line (cp. Fig. 7.4). The operating points on this line are those with the largest possible quadrature current value and the following control law applies

$$i_{sd} = -i_s^{sc} \quad (7.12a)$$

$$i_{sq} = \frac{u_s^{\max}}{\omega_s L_s}. \quad (7.12b)$$

Operation along the MTPF line signifies drive operation far above the base speed with the highest possible torque level. Operation on the MTPF line is restricted by the maximum current constraint. This implies that operation along the MTPF line is possible for that part of the trajectory which is within the MA circle. Obviously, for drives where the short circuit current exceeds the maximum current value ( $\kappa > 1$ ) no operation on the MTPF line is feasible. This is generally the case when the converter is not excessively overrated.

In the next three subsections, specific operating strategies are discussed that are commonly used for PM or electrically excited machines. To develop control strategies a drive sequence is used where the torque command is ramped up to  $0.5 T_e^{\max}$  while accelerating from standstill to one half rated speed. Then, the torque command stays constant and the speed is increased further well beyond base speed. Quasi-steady operation of the drive is considered.

### 7.2.2 Field Weakening Operation for PM Non-salient Drives

For electrically excited machines, field weakening is readily achieved by reducing the field current as discussed for the DC machine. Permanent magnet machines are able to achieve field weakening by using the direct axis current to produce a flux linkage component that opposes the magnet flux linkage and thus reduces the back EMF. The current locus and the corresponding direct and quadrature current versus speed characteristics will be examined. Two cases, namely  $\kappa < 1$  and  $\kappa > 1$  are considered, corresponding to machines with a short circuit current less and greater than the maximum stator current value  $i_s^{\max}$ .

#### Machines with $\kappa < 1$ ( $i_s^{\text{sc}} < i_s^{\max}$ )

The current space vector locus, which corresponds to the case  $\kappa < 1$ , is given in Fig. 7.5. It shows three specific operating trajectories.

##### First Trajectory, $0 \rightarrow A$ , MTPA

The first trajectory, from  $0 \rightarrow A$  corresponds to the 50% maximum torque ramp applied while the machine accelerates from standstill to one half rated speed. This operation trajectory is on the MTPA line. As speed increases, the maximum flux linkage circle radius decreases. Operation at point A is possible until speed  $\omega_s^A$  is reached, where the MF circle intersects with said operating point. The normalized speed  $\omega_s^A$  can be expressed with the aid of (7.6), (7.7), (7.10a) and (7.11):

$$\frac{\omega_s^A}{\omega_s^b} = \sqrt{\frac{\kappa^2 + 1}{\kappa^2 + (i_{sq}^n)^2}}. \quad (7.13)$$

##### Second Trajectory, $A \rightarrow B$ , Basic Field Weakening

For shaft speeds greater than  $\omega_s^A$ , field weakening must take place given the need to ensure that the current space vector remains on or within the MF circle. Note that the shaft speed at which field weakening must start

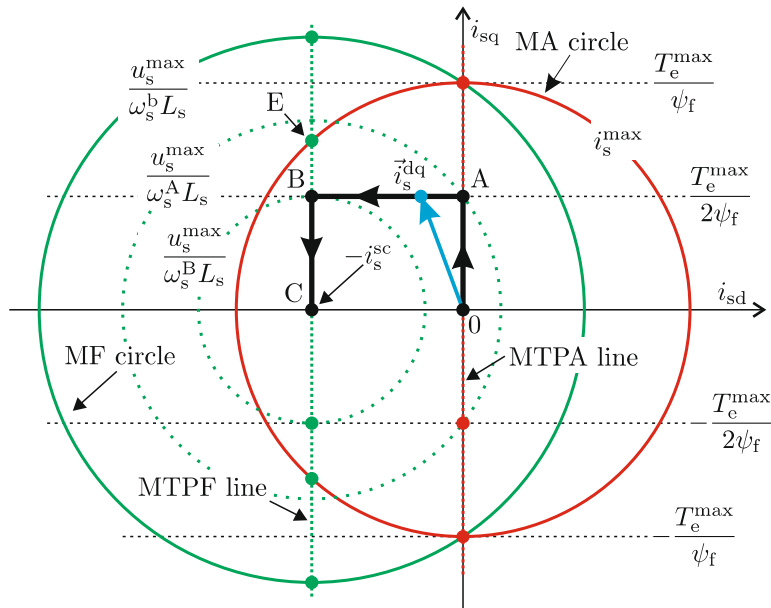


**Fig. 7.5** Current locus diagram: operational drive trajectory  $0 \rightarrow \omega_s^C$  for non-salient synchronous drives with  $i_s^{sc} < i_s^{\max}$

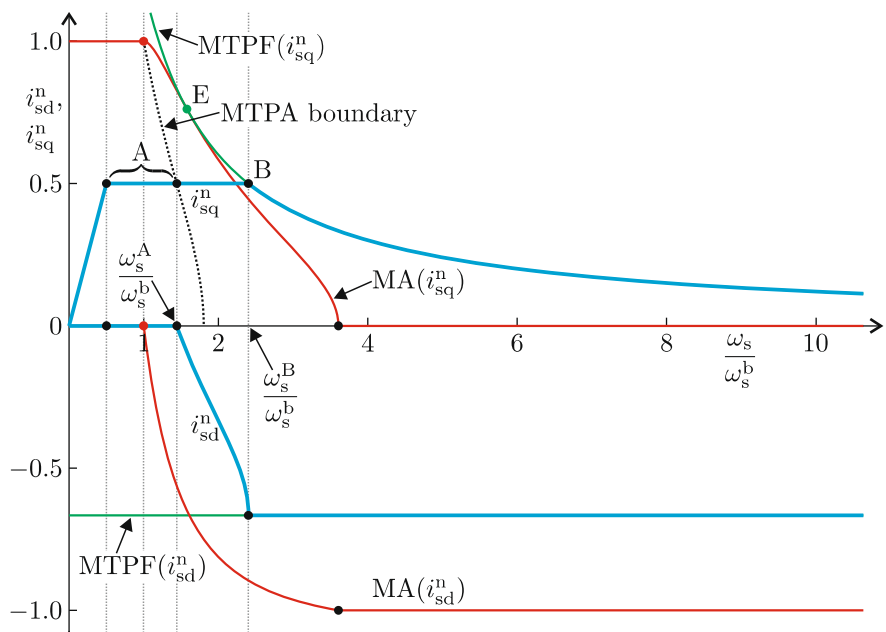


**Fig. 7.6** Current-speed diagram: operational drive trajectory  $0 \rightarrow \omega_s^C$  for non-salient synchronous drives with  $i_s^{sc} < i_s^{\max}$

is dependent on  $i_{sq}^n$  which may vary over the range  $-1 \rightarrow 1$ . During the operating trajectory A → B, the current space vector is kept on the maximum flux linkage circle and at the same time on the q-reference current value  $i_{sq}^n = 0.5$  (for the chosen example scenario). Subsequent application of goniometric laws linked to the MF flux linkage circle and constant torque line shows that the trajectory can be expressed as

$$i_{sd}^n = -\kappa + \sqrt{\kappa^2 \left(\frac{\omega_s^A}{\omega_s}\right)^2 + \left[\left(\frac{\omega_s^A}{\omega_s}\right)^2 - 1\right] (i_{sq}^n)^2} \quad (7.14a)$$

$$i_{sq}^n = \text{const.} \quad (7.14b)$$

### Third Trajectory, B → C, MTPF

The final trajectory B → C occurs when shaft speed  $\omega_s^B$  is reached. Operation on the basic field weakening trajectory cannot be continued. For operation beyond shaft speed  $\omega_s^B$ , the operating point is on the MTPF line. In this operating mode, the currents are given by

$$i_{sd}^n = -\kappa \quad (7.15a)$$

$$i_{sq}^n = \frac{\omega_s^B}{\omega_s} \sqrt{\kappa^2 + 1}. \quad (7.15b)$$

Recalling that the torque is directly proportional to the q-axis current, it is obvious that the maximum available torque drops below the set value  $0.5 T_e^{\max}$ . The torque is readily calculated by substituting (7.15b) in the torque (7.1). Theoretically, the speed can be increased infinitely while the torque decreases  $\propto 1/\omega_s$ , assuming  $R_s = 0$ . The output power remains constant. Note that operation under field weakening conditions allows the drive to operate far beyond the base speed within the voltage limit. This is achieved by the use a substantial direct axis current in the machine. If for some reason, i.e., malfunction of the drive this current is removed, an over voltage occurs that has the potential to damage substantially the converter.

### Current-Speed Diagram

An alternative approach to the use of the current locus diagram for representing the current locus is to consider the normalized direct and quadrature current components as function of the normalized (with respect to the base speed) shaft speed. The so-called *current-speed diagram* is given in Fig. 7.6. In this diagram, the green and red curves correspond to the maximum direct and quadrature axis currents at the given speed. In the current locus diagram, they encompass the MTPA line (motoring only) up to the maximum torque point and then along the MA circle. The red dotted curve represents the base speed (7.13). The intersection of this line with the selected quadrature current value  $i_{sq}^n$  occurs at speed  $\omega_s^A$  above which field

weakening must be used. The green dashed curve represents the quadrature component of the MTPF line. The blue colored lines show the normalized direct current  $i_{sd}^n$  and the normalized quadrature current  $i_{sq}^n$  for currents that correspond to operation with half maximum torque. In the current locus diagram these lines corresponds to the trajectory  $0 \rightarrow A \rightarrow B$  and part of the trajectory  $B \rightarrow C$  ( $C$  is reached when  $\omega_s \rightarrow \infty$ ). Included in Fig. 7.6 is operating point E which identifies the speed from where operation along the MTPF trajectory is feasible. The diagram shows that the d-axis current is equal to the short circuit current for  $\omega_s \geq \omega_s^B$ . It further shows that the quadrature current curve  $i_{sq}^n$ , coincides with the q-component of the MTPF trajectory as defined in current locus diagram for  $\omega_s \geq \omega_s^B$ .

### Short Circuit Operation

In the final part of this section attention is given to operation under short circuit conditions when the operating point is point C. This happens not only at very high speeds under field weakening, but also in case the supply voltage becomes zero, given that the radius of the maximum flux linkage circle is determined by the ratio  $u_s^{\max}/\omega_s$ . Observation of the current locus diagram shows that the machine would then operate under zero torque conditions. In practice, this is not the case because the winding resistance is not-zero. As a consequence, a relatively low, but non-zero, torque will be present in the machine at high speeds. A brief analysis of the quasi-steady-state operation under short-circuited condition may be undertaken with the aid of the synchronous, phasor-based machine model from Fig. 6.8 by setting  $|\underline{u}_s| = 0$ . If the rotor flux linkage is represented by the phasor  $\psi_f = \psi_f$ , the current amplitude  $|i_s|$  and the machine torque  $T_e$  may be rewritten.

$$|i_s| = \frac{\omega_s \frac{\psi_f}{R_s}}{\sqrt{1 + \left(\omega_s \frac{L_s}{R_s}\right)^2}} \quad (7.16a)$$

$$T_e = -\frac{\omega_s \frac{\psi_f^2}{R_s}}{1 + \left(\omega_s \frac{L_s}{R_s}\right)^2} \quad (7.16b)$$

An illustrative example based on the use of equation set (7.16) is shown in Fig. 7.7. Observation of this figure and the above equation shows that the torque versus speed characteristic is very similar to that of an induction machine operating under DC injection braking conditions (compare (9.4)). The speed which corresponds to the maximum absolute torque level  $\psi_f^2/2L_s$  is defined by the ratio  $R_s/L_s$  as may be observed from Fig. 7.7. Braking energy is in this case fully dissipated in the machine. The example also shows that the short circuit current is equal to  $i_s^{sc}$  as anticipated.

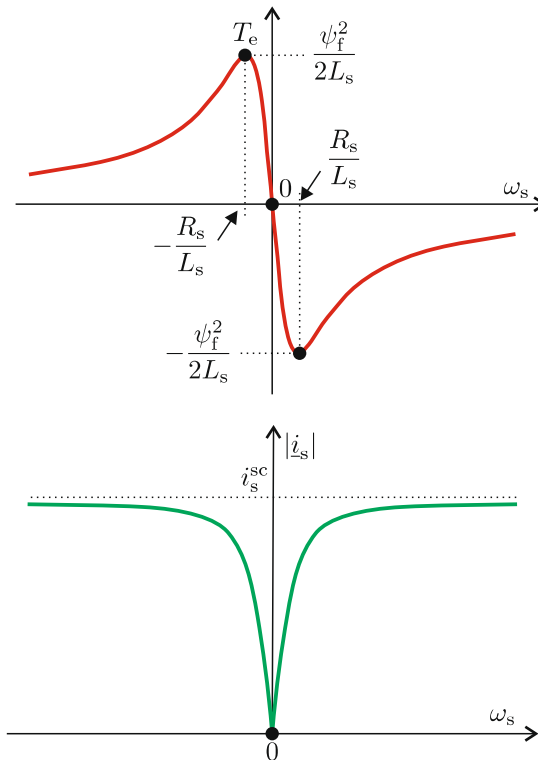


**Fig. 7.7** Short circuit operation of non-salient synchronous machines

### Machines with $\kappa > 1$ ( $i_s^{sc} > i_s^{\max}$ )

The second case to be discussed in this section is a machine converter configuration with  $\kappa > 1$ . This is the case, when the short circuit current of the machine is larger than the maximum current rating of the converter. Shown in the diagram is the current locus for the chosen control sequence 0 → A → B → C.

#### First and Second Trajectory, 0 → A → B

The first and second trajectory are identical to the case with  $\kappa < 1$ .

#### Third Trajectory, B → C, Maximum Current (MA)

The final trajectory B → C occurs when shaft speed  $\omega_s^B$  is reached. In this case the operation is limited to a locus that is part of the maximum current circle. An operation along the MTPF line is not possible, given that this trajectory is outside the maximum current circle, i.e.,  $\kappa > 1$ . The trajectory is defined by the expressions

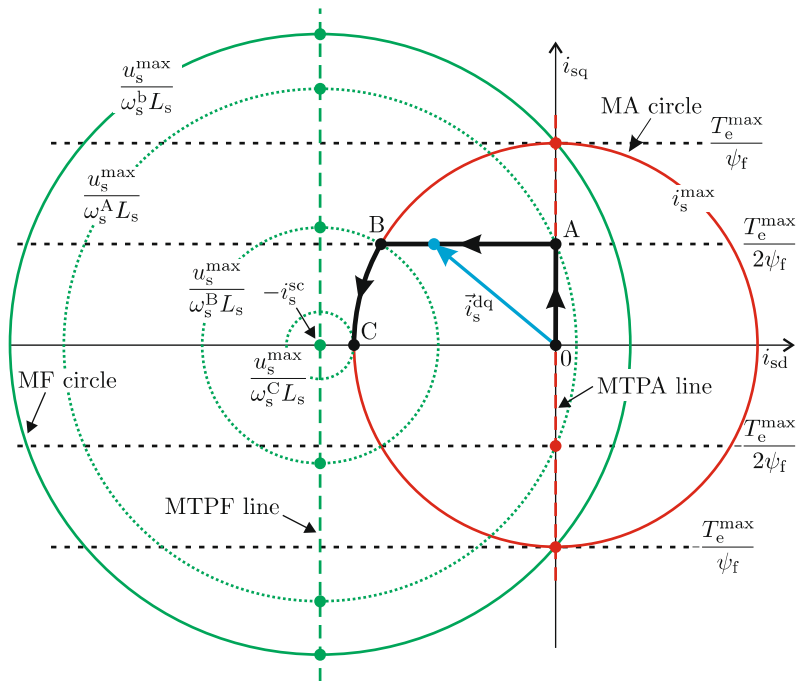


Fig. 7.8 Current locus diagram: operational drive trajectory  $0 \rightarrow \omega_s^C$  for non-salient synchronous drives with  $i_s^{sc} > i_s^{\max}$

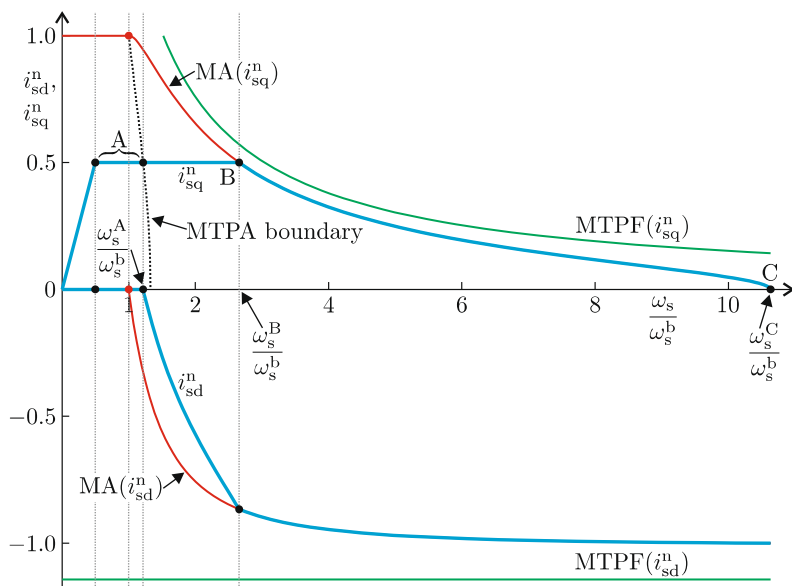


Fig. 7.9 Current-speed diagram: operational drive trajectory  $0 \rightarrow \omega_s^C$  for non-salient synchronous drives with  $i_s^{sc} > i_s^{\max}$

$$i_{\text{sd}}^{\text{n}} = \frac{\kappa^2 + 1}{2\kappa} \left[ \left( \frac{\omega_s^{\text{b}}}{\omega_s} \right)^2 - 1 \right] \quad (7.17\text{a})$$

$$i_{\text{sq}}^{\text{n}} = \sqrt{1 - (i_{\text{sd}}^{\text{n}})^2}. \quad (7.17\text{b})$$

The highest drive operating speed  $\omega_s^{\text{C}}$  is reached when the maximum flux linkage circle and maximum current circle coincide at a single operating point C, as may be observed from Fig. 7.8. Note that in this case torque production continues only up to the maximum speed  $\omega_s^{\text{C}}$ , which is markedly different when compared to the case  $\kappa < 1$ .

### Current-Speed Diagram

The corresponding current-speed diagram is given in Fig. 7.9. The colors used are identical to those in the previous case. It can be seen that operation occurs along the MA circle for  $\omega_s \geq \omega_s^{\text{B}}$  once point B is reached. Operation along the MTPF line (green dashed curve) is not possible because it lies outside the maximum current circle. Eventually, the maximum speed  $\omega_s^{\text{C}}$  is reached.

A simulation based tutorial is given in Sect. 7.6.1 in which the reader can examine the operation of the drive for both cases discussed above.

### 7.2.3 Field Weakening for PM Non-salient Drives, with Constant Stator Flux Linkage Control

When operating under MTPA conditions, as discussed in the previous section, the stator flux linkage will increase as the torque reference value is increased. For some machines this may lead to saturation of the stator yoke, which is not desirable. To avoid this problem, a control strategy is discussed in this section which maintains the stator flux linkage constant and equal to the field flux linkage  $\psi_f$ . An illustration of the proposed control strategy is given in Fig. 7.10. The direct axis current  $i_{\text{sd}}^c$  is manipulated to maintain the stator flux linkage amplitude constant for a given value of quadrature axis current  $i_{\text{sq}}^c$ . Figure 7.10 shows that the relationship between stator flux linkage, field flux linkage, and stator current components  $i_{\text{sd}}^c$  and  $i_{\text{sq}}^c$  can be written as

$$\psi_s = \sqrt{(\psi_f + L_s i_{\text{sd}}^c)^2 + (L_s i_{\text{sq}}^c)^2}. \quad (7.18)$$

The stator flux linkage magnitude is set to  $\vec{\psi}_s = \psi_f$ , which is the value that must be accommodated in case  $i_{\text{sd}} = 0$  and  $i_{\text{sq}} = 0$ . Equation (7.18) can then be expressed in normalized form as

$$i_{\text{sd}}^n = -\kappa \pm \sqrt{\kappa^2 - (i_{\text{sq}}^n)^2} \quad (7.19)$$

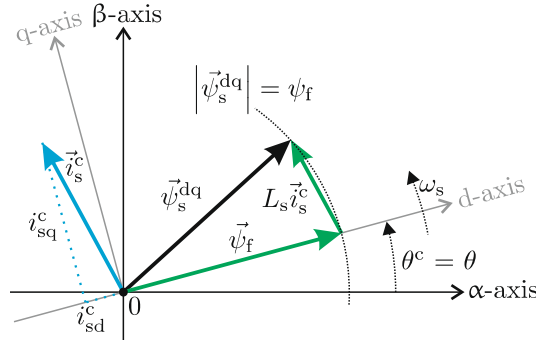


**Fig. 7.10** Rotor-oriented control with constant stator flux linkage

with  $\kappa = i_s^{sc}/i_s^{\max}$  and  $i_s^c = \psi_f/L_s$ . The current locus diagram given in Fig. 7.11 shows the operating locus of the current space vector. It has three specific trajectories. The first trajectory,  $0 \rightarrow A$ , represents operation as defined by the control law according to equation set (7.19). The quadrature current  $i_{sq}^n$  is increased from 0 to 0.5 and then remains constant.

Figure 7.11 shows that for shaft speeds below the speed  $\omega_s^{bS}$ , constant stator flux linkage is realizable for a quadrature current range which is limited to point D. The corresponding (normalized) currents are given by equation set (7.20). They confirm that the maximum torque capability of the drive has been reduced as a result of constant stator flux linkage control strategy. The extend of this limitation is dependent on the value of  $\kappa$ , as may be deduced from (7.20b) (under the assumption that  $\kappa > 0.5$ ).

$$i_{sd}^n = -\frac{1}{2\kappa} \quad (7.20a)$$

$$i_{sq}^n = \sqrt{1 - \frac{1}{4\kappa^2}} \quad (7.20b)$$

Operation under constant stator flux linkage conditions can be maintained, provided that the maximum flux linkage circle is outside the circle which coincides with trajectory  $0 \rightarrow A$ . As speed increases, the maximum flux linkage circle radius reduces until the speed  $\omega_s^{bS}$  is reached.

$$\frac{\omega_s^{bS}}{\omega_s^b} = \sqrt{\frac{\kappa^2 + 1}{\kappa^2}} \quad (7.21)$$

Note that the speed  $\omega_s^{bS}$  exceeds the base speed  $\omega_s^b$ , which is to be expected, given that operation is not along the MTPA line. For speeds greater than  $\omega_s^{bS}$ , field weakening operation occurs for the trajectory  $A \rightarrow B \rightarrow C$  as discussed in the previous section.

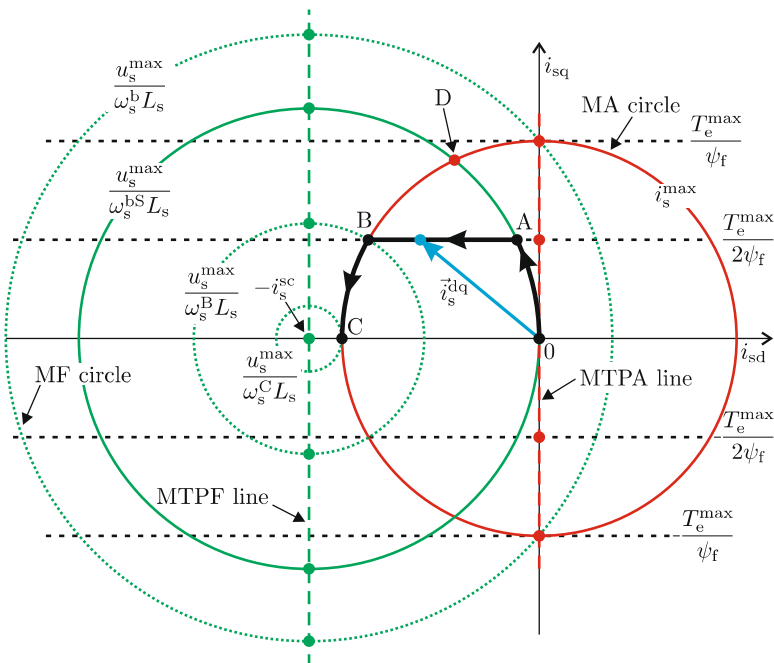


**Fig. 7.11** Current locus diagram: operational drive trajectory  $0 \rightarrow \omega_s^C$  for non-salient synchronous drives with  $i_s^{sc} > i_s^{\max}$  and constant stator flux linkage control

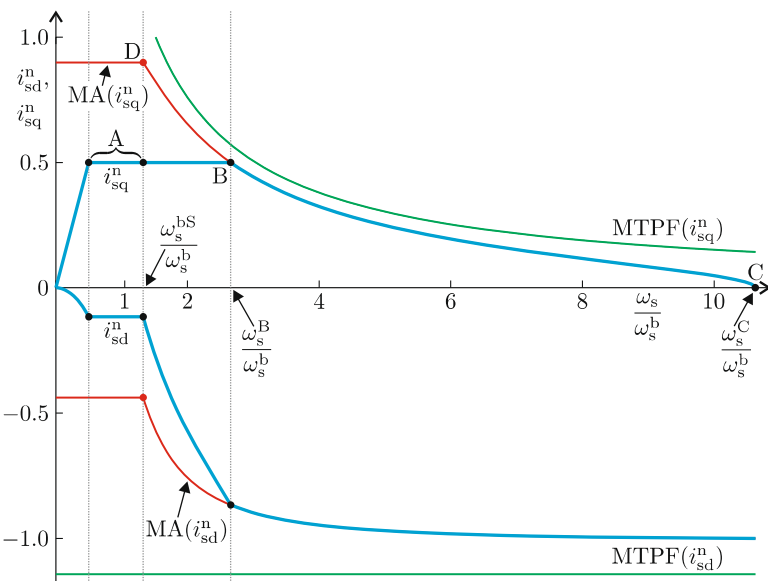


**Fig. 7.12** Current-speed diagram: operational drive trajectory  $0 \rightarrow \omega_s^C$  for non-salient synchronous drives with  $i_s^{sc} > i_s^{\max}$  and constant stator flux linkage control

The current-speed diagram given in Fig. 7.12 shows that field weakening operation is required for  $\omega_s > \omega_s^{bS}$ . Also clearly noticeable from this figure is the torque limitation caused by the need to couple the direct and quadrature currents in order to maintain constant stator flux linkage in the speed range  $\omega_s \leq \omega_s^{bS}$ . The tutorial given in Sect. 7.6.2 shows a simulation of a drive which utilizes the constant stator flux linkage control strategy.

#### 7.2.4 Field Weakening for Electrically Excited Non-salient Drive, with Constant Stator Flux and Unity Power Factor Control

Machines which utilize a field winding have an additional degree of freedom which may be utilized to achieve unity power factor operation. As a consequence, the converter is not required to provide any reactive power. In addition, constant stator flux linkage operation  $\psi_s = \psi_f$  is achieved as discussed in the previous section. The basic control strategy may be deduced by realizing that the voltage  $\vec{u}_s^{dq}$  can be approximated as  $\vec{u}_s^{dq} \simeq j\omega_s \vec{\psi}_s^{dq}$  given that the voltage drop across the stator resistance is assumed to be low. Consequently, unity power factor is achieved by ensuring that the voltage vector  $\vec{u}_s^{dq}$  and current vector  $\vec{i}_s^{dq}$  are kept in phase. This condition implies that the current vector should remain orthogonal to the stator flux linkage vector  $\vec{\psi}_s^{dq}$  as shown in Fig. 7.13. This again implies that the field flux linkage amplitude  $\psi_f$  must be varied for a given user defined value of the quadrature current  $i_{sq}$ .

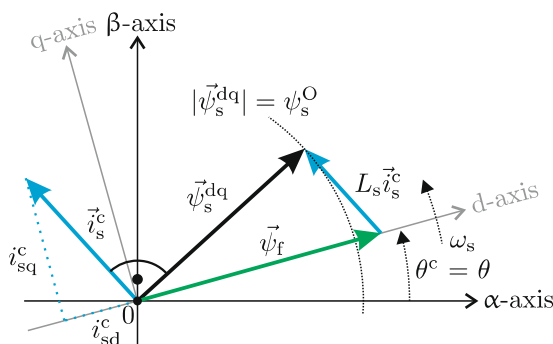


**Fig. 7.13** Rotor-oriented control with constant stator flux linkage and unity power factor

The concept of manipulating the field flux linkage  $\psi_f$  and therefore the short circuit current  $i_s^{sc}$  below the speed  $\omega_s^{bS}$  of the drive implies that

the variable  $\kappa = i_s^{sc}/i_s^{\max}$  is no longer constant. For the sake of comparison with the previous case, the normalized short circuit current variable  $\kappa^O$  is introduced which is equal to the constant value of the rated short circuit current ratio used above. The flux linkage level  $\psi_s^O$  as shown in Fig. 7.13 is chosen to be the same value as assumed in the previous section. Consequently, the defined base speed  $\omega_s^{bs}$  of the drive remains unchanged.

The process of determining how the field flux linkage  $\psi_f$  and the corresponding short circuit current  $i_s^{sc}$  must be chosen to maintain unity power factor operation is undertaken with the aid of the current locus diagram given in Fig. 7.14. Shown in Fig. 7.14 is the trajectory  $0 \rightarrow A$  which corresponds to operation below the base speed. This trajectory coincides partly with the dashed locus  $0 \rightarrow A \rightarrow D$  which is no longer circular as was the case previously (see Fig. 7.11). The reason for this is that the field flux linkage level must be adjusted as a function of the user defined torque reference value to maintain the stator flux linkage vector  $\vec{\psi}_s^{dq}$  orthogonal to the current reference vector  $\vec{i}_s^{dq}$  as discussed above.

Note that this objective is reached at the cost of a reduced operating quadrature current range as may be observed by the location of operating point D on the maximum current curve relative to the previous case (see Fig. 7.11). After some goniometric manipulations it may be shown that this point is linked to the normalized current values

$$i_{sd}^{n,D} = -\frac{1}{\sqrt{(\kappa^O)^2 + 1}} \quad (7.22a)$$

$$i_{sq}^{n,D} = \frac{\kappa^O}{\sqrt{(\kappa^O)^2 + 1}} \quad (7.22b)$$

$$i_s^{sc,n,\max} = i_s^{sc,n,D} = \kappa^D = \sqrt{(\kappa^O)^2 + 1}. \quad (7.22c)$$

The measure of quadrature current reduction may be quantified by comparing the  $i_{sq}^n$  values according to (7.20) and (7.22) where the latter corresponds to stator flux linkage control without power factor control. A careful analysis of Fig. 7.14 gives that the dashed locus  $0 \rightarrow A \rightarrow D$  may be expressed as

$$i_{sd}^n = -\frac{(i_{sq}^n)^2}{\sqrt{(\kappa^O)^2 - (i_{sq}^n)^2}} \quad (7.23a)$$

$$i_{sq}^n \propto T^* \quad (7.23b)$$

$$i_s^{sc,n} = \kappa = \frac{(\kappa^O)^2}{\sqrt{(\kappa^O)^2 - (i_{sq}^n)^2}}. \quad (7.23c)$$

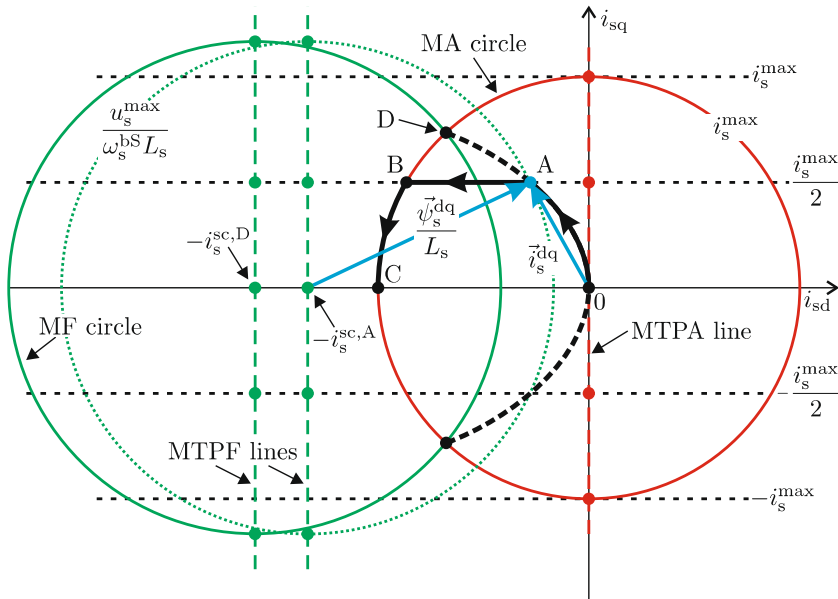


**Fig. 7.14** Operational drive trajectory  $0 \rightarrow \omega_s^C$  for non-salient synchronous drives with constant stator flux linkage and unity power factor control

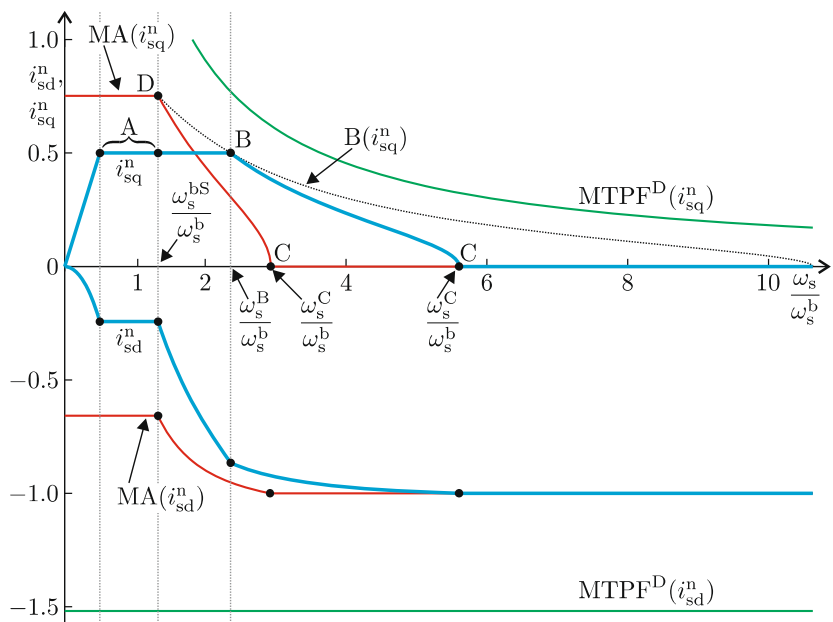


**Fig. 7.15** Current-speed diagram for non-salient synchronous drives with constant stator flux-linkage and unity power factor control

where  $i_{\text{sq}}^{\text{n}}$  corresponds to the user defined normalized current reference. The variable  $i_s^{\text{sc},n}$  represents the normalized short circuit flux linkage (in PM applications referred to as  $\kappa$ ) and its value must be increased as the quadrature current reference is increased. The changing short circuit current value is noticeable in Fig. 7.14 by the displacement of the constant stator flux linkage circles which is required to maintain the combination of constant stator flux linkage and unity power factor below the base speed. For operation above the base speed, which is the remaining part of the chosen excitation trajectory A → B → C, field weakening is activated. Due to the changing normalized short circuit current, the relationship for A → B trajectory slightly deviates from equation set (7.14) and may be expressed as

$$i_{\text{sd}}^{\text{n}} = -\kappa + \sqrt{\left(\frac{\omega_s^{\text{b}}}{\omega_s}\right)^2 \left(1 + (\kappa^{\text{o}})^2\right) - (i_{\text{sq}}^{\text{n}})^2} \quad (7.24\text{a})$$

$$i_{\text{sq}}^{\text{n}} = \text{const.} \quad (7.24\text{b})$$

For the same reason, trajectory B → C in this case is based on relationship

$$i_{\text{sd}}^{\text{n}} = \frac{1}{2\kappa} \left[ \left(\frac{\omega_s^{\text{b}}}{\omega_s}\right)^2 \left(1 + (\kappa^{\text{o}})^2\right) - (1 + \kappa^2) \right] \quad (7.25\text{a})$$

$$i_{\text{sq}}^{\text{n}} = \sqrt{1 - (i_{\text{sd}}^{\text{n}})^2} \quad (7.25\text{b})$$

and also differs from equation set (7.17). As may be seen in Fig. 7.15 and equation set (7.25), the maximum normalized speed of the drive operating under constant stator flux linkage and unity power factor control varies depending on the actual value of normalized short circuit current  $\kappa$

$$\frac{\omega_s^{\text{C}}}{\omega_s^{\text{b}}} = \sqrt{\frac{1 + (\kappa^{\text{o}})^2}{(1 - \kappa)^2}}. \quad (7.26)$$

Note that the linear relationship between torque and quadrature current is no longer maintained with this control strategy given that the field flux linkage  $\psi_f$  is a function of the quadrature current. In the approach taken here, the initial field flux linkage  $\psi_f$  (for  $i_{\text{sq}} = 0$ ) was chosen equal to the value used in the previous section. Consequently, the field flux linkage level  $\psi_f$  increases as the quadrature current is increased. Normally, the field flux linkage  $\psi_f$  must not exceed its rated value which implies that the rated field flux linkage is realized when the machine is operating under maximum torque conditions, i.e., point D in Fig. 7.14. A consequence of this control approach is that the initial field flux linkage level  $\psi_f$  must be chosen lower than the rated value. This will become apparent from the tutorial given in Sect. 7.6.3.

## 7.3 Control of Salient Synchronous Machines

The operating principles discussed previously for the non-salient machine were primarily aimed at determining an optimum trajectory for the controller current vector  $\vec{i}_s^{dq}$  for drive operation over a given shaft speed range. For this purpose, specific operating trajectories such as MTPA and MTPF were introduced, together with transition regions between these two. For the salient machine, similar control strategies can be defined, despite the fact that the torque is determined by the direct and quadrature current as was discussed in Sect. 6.2. Consequently, the process of determining the required current references  $i_d^c$  and  $i_q^c$  for a rotor-oriented current control algorithm is more sophisticated.

### Lines of Constant Torque

A convenient starting point for this analysis is the salient field-oriented model discussed in Sect. 6.2.2. The torque equation (6.21) can be rewritten in a normalized form using the saliency factor  $\chi$  from (6.19):

$$T_e^n = \frac{T_e}{\psi_f i_s^{\max}} = i_{sq}^n \left( 1 - \frac{2\chi}{\kappa} i_{sd}^n \right). \quad (7.27)$$

Note that the normalization is undertaken with respect to the maximum torque level of a non-salient machine. The variable  $\chi$  is less than zero for  $L_{sd} < L_{sq}$ . Furthermore, the normalized short circuit current  $\kappa$  is assumed to be constant (i.e., excitation is provided by permanent magnets). Equation (7.27) confirms an earlier observation that torque is a function of both currents. Consequently, the lines of constant torque in the salient synchronous current locus diagram of Fig. 7.4 are no longer horizontal lines. The constant torque contours (black dashed lines) shown in the salient synchronous current locus diagram are defined by (7.27). The analysis in this section concentrates on motor operation in the second quadrant of the current locus diagram for  $\chi > 0$ . The trajectories for the third quadrant can be found by mirroring the shown trajectories along the d-axis.

### Current Limit (Maximum Ampere, MA)

As for the non-salient machine, the MA circle is shown in Fig. 7.16.

### Maximum Torque per Ampere (MTPA) Line

Maximum torque  $T_e^{\max}$  is given where the MA circle touches the lines of constant torque in one point. This operating point produces the largest torque which can be realized with the chosen value of  $i_s^{\max}$ . It is referred to as the *maximum torque point*, which is part of the MTPA trajectory of the salient machine. The entire MTPA trajectory is found by introducing a set of concentric circles centered on the origin with radius  $0 \rightarrow i_s^{\max}$ . For a given  $i_s$  value the MTPA point is the point in which the circle touches a line of constant torque in one point:

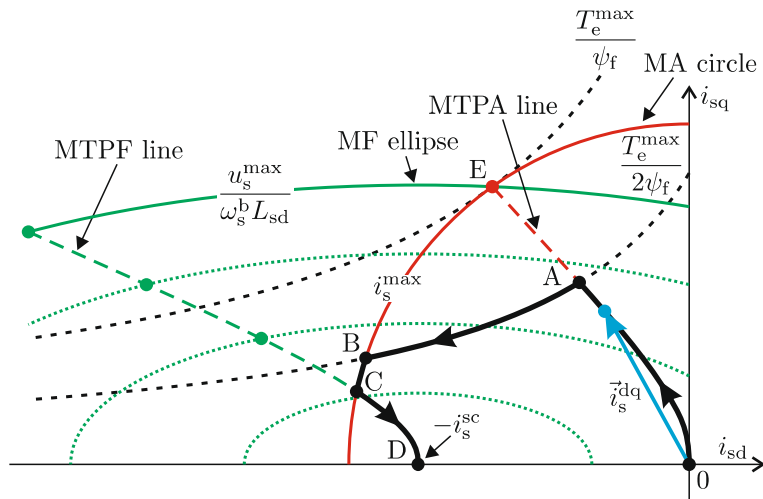


**Fig. 7.16** Current locus diagram: Operational drive trajectory  $0 \rightarrow \omega_s^C$  for salient synchronous drives with  $i_s^{sc} < i_s^{\max}$

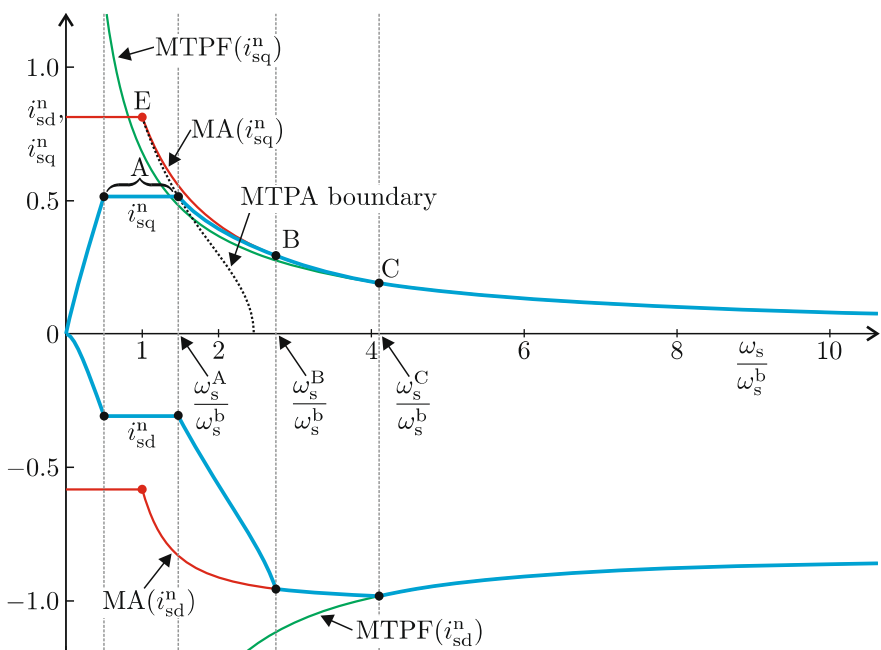


**Fig. 7.17** Current-speed diagram: Operational drive trajectory normalized current versus speed plane for salient synchronous drives with  $i_s^{sc} < i_s^{\max}$

$$(i_{sd}^n)^2 + (i_{sq}^n)^2 = (i_s^n)^2 \quad (7.28)$$

with  $i_s^n = i_s / i_s^{\max}$ . Subsequent use of (7.28) with (7.27) leads to an expression for the torque as function of the normalized direct axis current  $i_{sd}^n$ . Differentiation gives the MTPA value of  $i_{sd}^n$  as function of  $i_s^n$ , which can in turn be used to find the corresponding  $i_{sq}^n$  value. The resulting set of coordinates which define the MTPA trajectory are given in the following equation set:

$$i_{sd}^n = \frac{\kappa}{8\chi} - \sqrt{\frac{(i_s^n)^2}{2} + \left(\frac{\kappa}{8\chi}\right)^2} \quad (7.29a)$$

$$i_{sq}^n = \sqrt{(i_s^n)^2 - (i_{sd}^n)^2} \quad (7.29b)$$

From a control objective it is helpful to re-map the variable  $i_s^n$  as function of the torque  $T_e^n = T_e / T_e^{\max}$ , using (7.29) and (7.27), where  $T_e^{\max}$  is the torque in the maximum torque point. The resulting direct and quadrature reference values are shown in Fig. 7.18 for operation below the base speed. These values can be used as input to the current controller for MTPA.

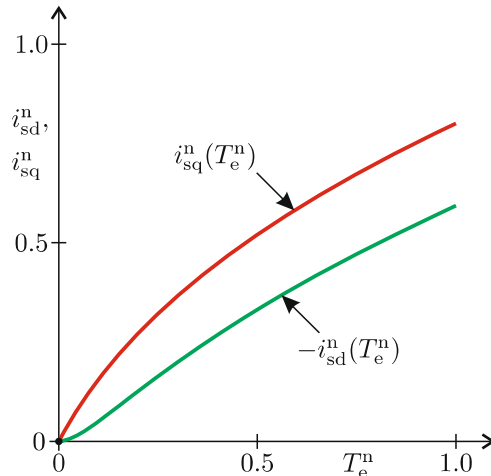


**Fig. 7.18** Direct and quadrature current as a function of torque in MTPA mode below base speed for a salient synchronous drive

### Voltage Limit (Maximum Flux Linkage, MF)

The maximum flux linkage (MF) lines can be found in a similar way as done for the non-salient case starting from (6.16):

$$(i_{sd}^n + \kappa)^2 + (i_{sq}^n)^2 (2\chi + 1)^2 = i_O^2 \quad (7.30)$$

The variable  $i_O = \psi_s^{\max}/L_{sd} i_s^{\max}$  is directly linked to the maximum flux linkage  $\psi_s^{\max} = u_s^{\max}/\omega_s$ . In case of zero saliency ( $\chi = 0$ ) expression (7.30) reduces to (7.9), assuming  $L_{sd} = L_s$ . For a salient machine the MF lines are elliptical as may be deduced from expression (7.30). The major axis coincides with the d-axis, while the minor axis is parallel with the q-axis. The intersection of both axes is at the short circuit current point D as is shown in Fig. 7.16. As the shaft speed increases, the maximum flux linkage ellipse reduces in size given that the variable  $i_O$  is inversely proportional to the speed  $\omega_s$ . This implies that the available operating region of the drive is constrained by the area within the ellipse as speed increases. This behavior is the same to the one of non-salient machines. A saliency factor  $\chi < 0$  would force operation below the base speed to the first quadrant of the current locus diagram. In this case, operation at high speed is severely compromised, given that the maximum flux linkage circles would need to extend to the first quadrant.

The *base speed* corresponds to the MF ellipse which coincides with the maximum torque point. Operation along the MTPA contour remains viable for shaft speeds up to the base speed. Computation of the base speed may be undertaken by making use of (7.29), with  $i_s^n = 1$  which provides the (normalized) drive saturation coordinates of the current vector  $\bar{i}_s^{dq}$ . Use of these coordinates with (7.30) leads to the base speed  $\omega_s^b$ .

### Maximum Torque per Flux Linkage (MTPF) Line

For deriving a field weakening strategy, the MTPF trajectory is used. The MTPF trajectory is given by the operating points in which the MF ellipses and the constant torque curves touch in one point. Expressed differently, they are the points on the MF ellipses which represent maximum torque. A mathematical representation can be found by using (7.30) with (7.27) and by differentiation, resulting in an expression for  $i_{sd}^n$  as function of  $i_O$ . This can in turn be used to find the corresponding  $i_{sq}^n$  value. The resulting set of equations which defines the MTPF trajectory is given as follows

$$i_{sd}^n = -\kappa + (1 + 2\chi) \frac{\kappa}{8\chi} - \sqrt{\frac{i_O^2}{2} + \left( (1 + 2\chi) \frac{\kappa}{8\chi} \right)^2} \quad (7.31a)$$

$$i_{sq}^n = \frac{1}{2\chi + 1} \sqrt{i_O^2 - (\kappa + i_{sd}^n)^2} \quad (7.31b)$$

The MTPF trajectory is shown in Fig. 7.16 for  $\kappa = 0.6$  and  $\chi = 0.75$ . It is partly within the MA circle, because in this example the short circuit is less than  $i_s^{\max}$ .

### Operating Sequence

In the final part of this section, the control strategy under field weakening condition will be discussed using the excitation scenario introduced for previous examples. The torque is increased from 0 to  $0.5 T_e^{\max}$  while the machine accelerates from standstill. This corresponds to the trajectory  $0 \rightarrow A$  in the

current locus diagram. Operation under MTPA conditions will remain until a shaft speed  $\omega_s^A$  is reached when the MF contour coincides with point A. Above  $\omega_s^A$ , constant torque operation is possible by maintaining the current vector  $\vec{i}_s^{dq}$  on the maximum flux MF linkage ellipse and on the chosen torque curve A → B. This control strategy can be used as long as the currents are within the MA circle and on the right of the MTPF line. This is possible up to speed  $\omega_s^B$ , when the MA circle is reached. Above  $\omega_s^B$ , operation proceeds along the MA circle until the MTPF line is reached at point C. For even higher speeds, operation proceeds along the MTPF trajectory C → D.

The operating sequence described above can also be shown with the aid of a current-speed diagram as given in Fig. 7.17, where the *blue* curves represent the currents  $i_{sq}^n$  and  $i_{sd}^n$ . In this figure, the *green* and *red* curves represent the direct and quadrature current curves for operation along the MA contour and the MTPA trajectory. For operation below the base speed, the current references are defined by Fig. 7.18 for the chosen torque reference value. Above the speed  $\omega_s^A$ , the normalized currents must be found using (7.27) and (7.30) until speed  $\omega_s^B$  is reached. For speeds in excess of  $\omega_s^B$ , the currents are defined by (7.28), with  $i_s^n = 1$  and (7.30) until the MTPF line is reached, in which case equation set (7.31) must be used. For an implementation of the control strategies lookup tables are used, which give the required reference current values based on the reference torque and maximum stator flux linkage  $\psi_s^c$ . The reason for this is that saturation affects the values of  $L_{sd}$  and  $L_{sq}$  making it difficult to find analytical expressions. In this case, the look-up tables are usually derived from measurements or from finite-element analysis. Nevertheless, the introduction of the equations is useful to give the reader an appreciation of the relationship between variables that control the current reference values.

A tutorial is given in Sect. 7.6.4, which exemplifies and visualizes the control strategies discussed in this section. For this purpose, a current source salient machine model is introduced and used in conjunction with a controller that delivers the appropriate current reference values as a function of shaft speed and a user defined torque reference value.

## 7.4 Interfacing the Field-Oriented Control Module with a Current-Controlled Synchronous Machine

The process of integrating the controller with the machine is discussed in this section. Use is made of a current source based model of the machine because by using the current source based model concepts can be readily examined without having to consider the dynamics of the current controller. In practice, this approach is realistic given that the time constants linked to the current controllers are small in comparison to those of the machine. Figure 7.19 shows a salient machine model although the approach discussed

here is equally applicable to non-salient machines by setting  $L_{sd} = L_{sq} = L_s$ . The field flux linkage  $\psi_f$  may be provided by permanent magnets or a field winding. In the latter case, the synchronous machine control module may be used to regulate the field flux linkage in order to control the power factor as was explained in Sect. 7.2.4.

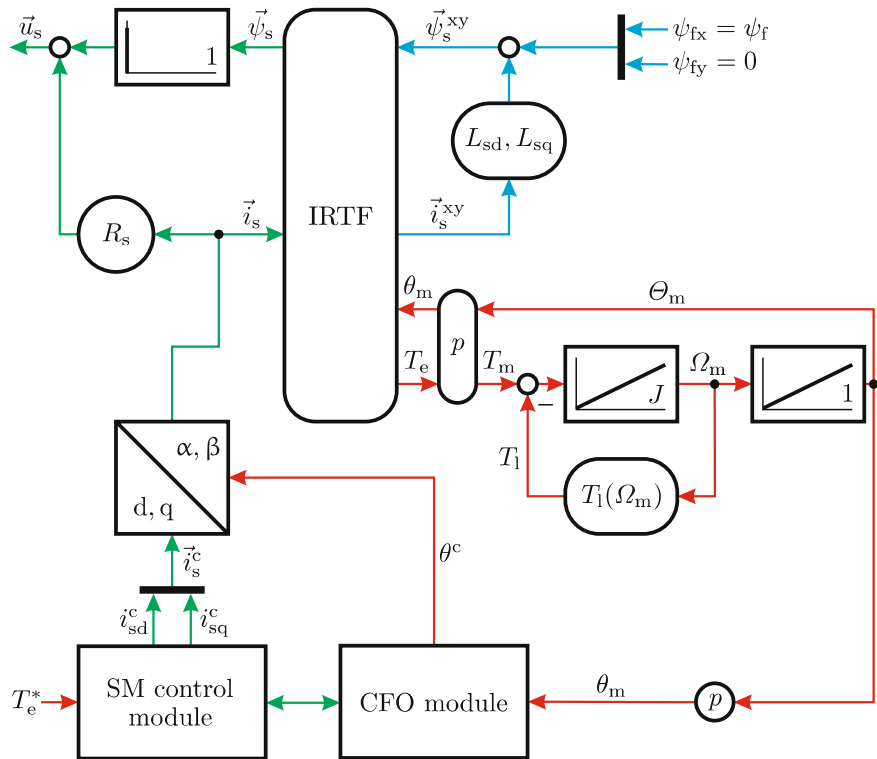


**Fig. 7.19** Field-oriented control with current source synchronous machine model

The main purpose of the SM control module is to generate the required synchronous coordinate reference currents  $i_{sd}^c$  and  $i_{sq}^c$  based on the user defined torque reference value. A number of field weakening control strategies has been introduced in the previous sections for both salient and non-salient machines which ensure that the machine can operate within the design envelope. Also shown in Fig. 7.19 is a CFO (coordinate calculator for field orientation) module which provides the reference rotor angle  $\theta^c$  for the synchronous controller and the  $dq \rightarrow \alpha\beta$  conversion module which yields the current vector  $\vec{i}_s$  used as an input to the machine (in this case) or current controller. For position sensorless applications, i.e., those which do not use a mechanical shaft sensor, use is made of the electrical variables, which then

serve as inputs to the CFO module. In most cases an encoder is used (as shown) which provides the shaft angle position for the controller.

Interfacing a non-salient machine with a controller is a relatively straightforward task provided that the machine parameters are known. For the salient synchronous machine this process is more laborious given the need to generate look-up tables which is an approach more akin with the switched reluctance drive that will be discussed in Chap. 10.

## 7.5 Interfacing the Field-Oriented Control Module with a Voltage-Source Connected Synchronous Machine

Practical implementation of the current-controlled machine discussed in the previous section calls for the use of a voltage-source converter. Consequently, a three-phase current-control approach as discussed in Sect. 3.2 must be integrated with the drive. In this section, a three-phase model based current controller is used because these are generally favored in practical drive applications. The generic representation of the current controller in question as shown in Fig. 3.19 is connected to a generalized load which defines the parameters for the discrete model based synchronous current controller which is tied to a flux vector  $\vec{\psi}$ .

For the synchronous drive, the latter vector must be replaced by the field flux linkage vector  $\vec{\psi}_f = \psi_f e^{j\theta}$ . Furthermore, the parameters used for the controller need to be redefined given that the load is in this case a synchronous machine. For the purpose of determining the parameters, it is helpful to consider the synchronous direct and quadrature axis salient symbolic models of the machine shown in Fig. 6.15. For the direct axis current controller, calculation of the sampled average voltage reference  $U_s^*(t_k)$  is carried out with the aid of (3.21a) in which the parameters  $R$  and  $L$  must be replaced by the variables  $R_s$  and  $L_{sd}$ . A similar approach must be used for the computation of quadrature axis controller sampled average voltage reference  $U_s^*(t_k)$  where use is made of (3.21b) in which case the parameters  $R$  and  $L$  must be replaced by the machine parameters  $R_s$  and  $L_{sq}$ . Furthermore, this expression shows the presence of a disturbance decoupling term  $u_e = \omega_e \psi_e$ , which corresponds to the term  $\omega_m \psi_f$  in a synchronous drive. Note that in the discussion given above, a salient synchronous model has been purposely entertained given that the non-salient machine model is readily accommodated by choosing the direct and quadrature axis inductances equal.

The resulting drive structure as shown in Fig. 7.20 brings together key concepts such as modulation and current control introduced in earlier chapters of this book. Readily apparent in Fig. 7.20 is the *predictive model based current controller* which uses the current reference values produced by the *SM control module* as discussed in the previous section. The observant reader will note

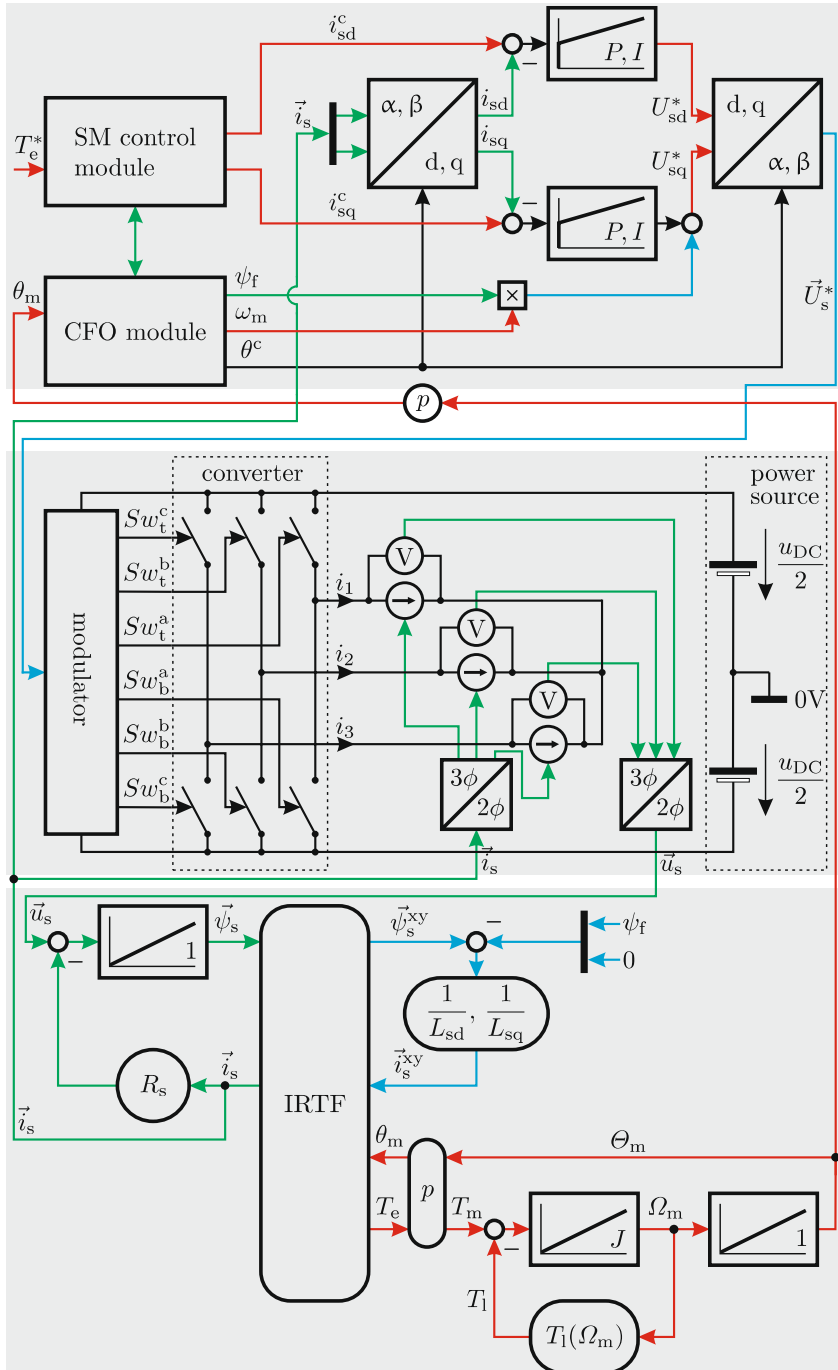


Fig. 7.20 Field-oriented control with voltage source synchronous machine model

that only the predominant disturbance decoupling terms  $\omega_m \psi_f$  is shown in the current controller module. The remaining terms  $\omega_m L_{sd}$  and  $-\omega_m L_{sq}$  are not shown for the sake of readability. However, these terms are included in the accompanying tutorial given in Sect. 7.6.5 which is concerned with a voltage source converter that is connected to a salient synchronous machine operating with a model based current controller. Also shown in Fig. 7.20 is the generic model of the IRTF based salient synchronous machine according to Fig. 6.13. From a simulation perspective, the voltage source converter/modulator structure is often replaced by an alternative module which calculates the required supply vector directly from the average voltage references generated by the current controller. This approach as outlined in Sect. 3.3.5 reduces the simulation run-time because a larger computational step size may be entertained. For the sake of clarity, it is emphasized the model shown is equally applicable to the non-salient machine provided the appropriate control algorithm is used within the *SM control* and *CFO* modules. Furthermore, the generic machine model according to Fig. 6.3 must be used instead of the salient model, which in effect calls for the introduction of a common stator inductance  $L_s$  as discussed previously.

## 7.6 Tutorials

### 7.6.1 Tutorial 1: Non-salient Synchronous Drive

This exercise is aimed at examining the drive concept presented in Fig. 7.19, whereby use is to be made of the non-salient machine as discussed in Sect. 6.3.1. For the purpose of visualizing the Blondel diagram the inductance value shown in Table 6.1 will be increased by a factor of four. The drive voltage and current limit values are set to  $u_s^{\max} = 60 \text{ V}$  and  $i_s^{\max} = 20 \text{ A}$  respectively. A simulation model is to be developed which satisfies the drive representation shown in Fig. 7.19. Furthermore, the control strategy for the SM controller module should satisfy the approach outlined in Sect. 7.2.1 and Sect. 7.2.2 respectively.

For the purpose of this simulation, the quadrature current to the controller and mechanical shaft speed are taken to be the user defined variables. The stator resistance  $R_s$  is set to zero, given that the voltage drop linked to this parameter is usually low in comparison with the back-EMF term. Moreover, from a didactical perspective it is helpful to observe the stator voltage amplitude without having to consider the contribution caused by the resistance. Calculate the base speed (in rpm) of the drive and determine the synchronous Blondel diagram of the drive which shows the maximum current circle and maximum flux circle at the base speed as indicated in Fig. 7.8. In addition, set the input quadrature current for the controller to  $i_{sq} = 10 \text{ A}$  and increase the shaft speed in ten incremental steps of 300 rpm starting from the base speed. Record the coordinates of the current vector produced by the controller in the Blondel diagram. Also record the shaft speed  $n_m^B$  where the requested output torque can no longer be maintained.

An implementation example which satisfies this tutorial, as given in Fig. 7.21, shows the IRTF based machine and *Control Module* which meets the desired control strategy requirements for the drive in question. Two UP-DOWN modules are shown in the simulation model which represent the desired quadrature current value and selected mechanical shaft speed (in rpm). An xy scope module shows the maximum flux circle for the selected speed as well as the maximum current circle. In addition, the machine current vector  $\vec{i}_s^{dq}$ , as generated by the controller, is also presented in this diagram. Note that the maximum flux circles are constrained once these fully encompass the maximum current circle. Computation of the base speed may be undertaken with the aid of (5.11) and the data given in this section which gives a mechanical shaft speed of  $n_m^b = 1442 \text{ rpm}$ . Observation of the simulation model in terms of the SM controller generated current vector over the designated speed range leads to a discrete current trajectory for the drive as shown in Fig. 7.22.

Also shown in Fig. 7.22 is the speed  $n_m^B = 3242 \text{ rpm}$  which corresponds to operating point  $P$  in (for example) the current-speed diagram (see Fig. 7.9)

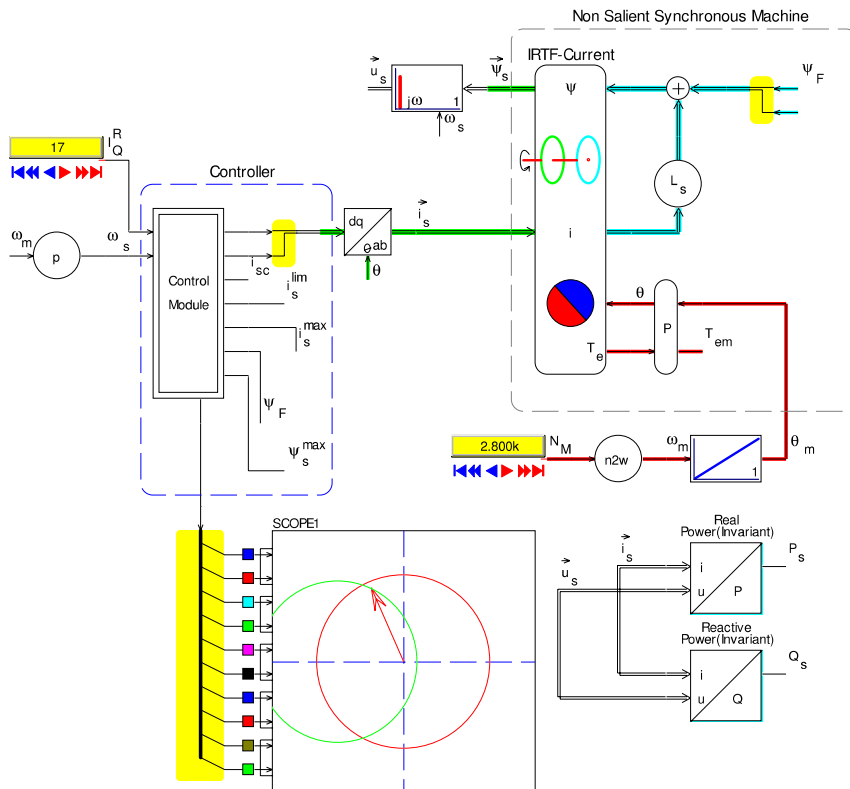


Fig. 7.21 Simulation of non-salient synchronous drive

where the required torque output can no longer be maintained. Note that the amplitude of the supply voltage is held to  $u_s^{\max} = 60$  V as field weakening is enforced when the speed is increased.

The reader is urged to reconsider the problem discussed in this section for the case where the excitation flux  $\psi_f$  is halved, which corresponds to the case where the short circuit current point lies within the maximum current circle (see Fig. 7.5). Included in the Blondel diagram are the short circuit current point and drive saturation points for the drive.

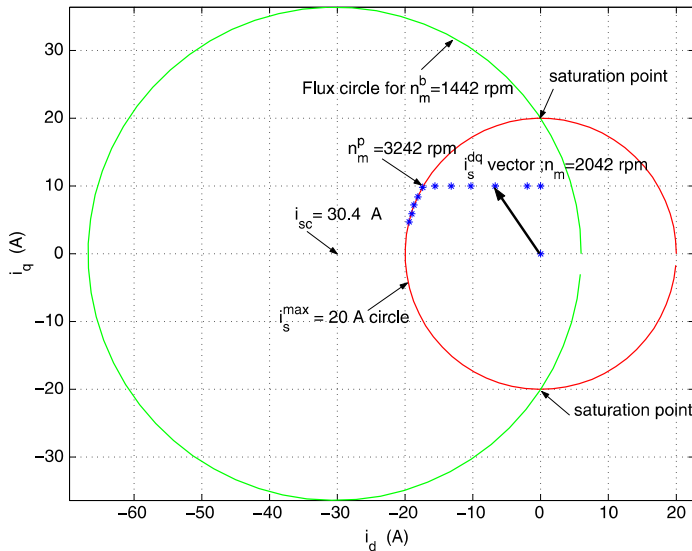
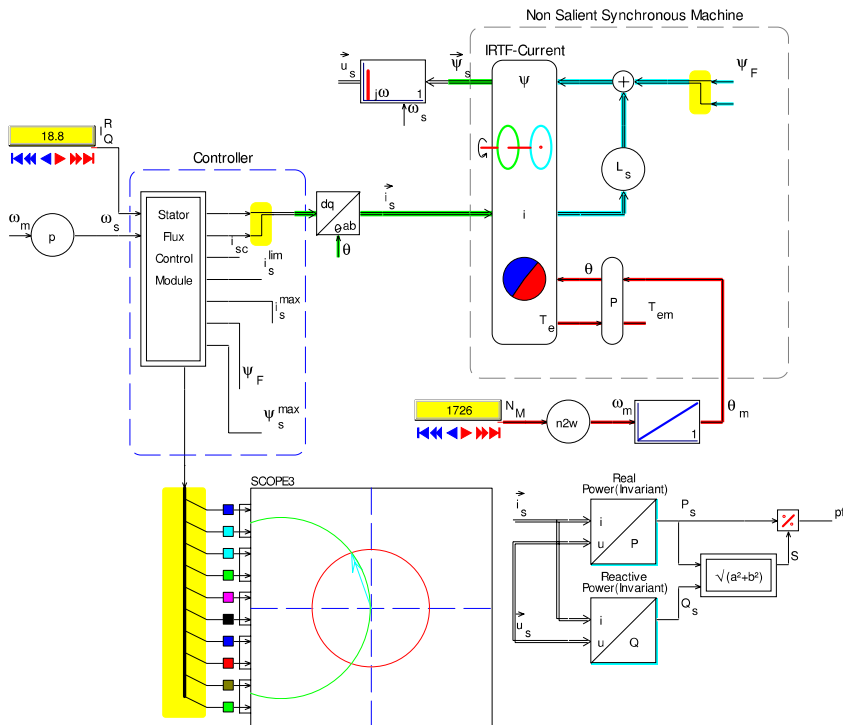


Fig. 7.22 Blondel diagram non-salient current source connected machine

### 7.6.2 Tutorial 2: Non-salient Synchronous Drive, Constant Stator Flux Operation

An extension to the previous tutorial is considered here, which is concerned with drive operation under constant stator flux, as discussed in Sect. 7.2.3. The drive concept and parameters are not changed, only a new controller is to be deployed which meets the requirements of maintaining the condition  $|\vec{\psi}_s| = \psi_f$  below the base speed  $\omega_m^{BS}$ . Calculate the mechanical shaft speed (in rpm) which corresponds to  $\omega_m^{BS}$  and determine the percentage reduction in torque capability, which must be tolerated for achieving constant flux operation. Furthermore, provide a Blondel diagram which shows the maximum flux circle at the new base speed as well as the maximum current circle. Set the simulation model shaft speed to  $\omega_m^{BS}$  and vary the quadrature input current (for the controller) in steps of 2 A to achieve a discrete current locus that traverses a trajectory from the 2<sup>nd</sup> quadrant saturation point to the 3<sup>rd</sup> quadrant saturation point.

Calculation of the revised base speed  $\omega_m^{BS}$  may be undertaken with the aid of (7.21). This gives the new value relative to the base speed found in the previous tutorial. Subsequent analysis using the parameters given shows that the new base speed is equal to  $n_m^{BS} = 1725$  rpm, which is the highest speed under which constant stator flux operation at the desired flux level can be realized for this drive. The maximum achievable torque for this drive may be found by determining the largest quadrature current as defined by (7.20) (shown in its normalized form). The



**Fig. 7.23** Simulation of non-salient synchronous drive, constant stator flux operation

field flux level remains unchanged. Hence, the torque reduction can be readily calculated using the parameters given. This leads to a maximum quadrature current of  $i_{sq}^* = 18.8 \text{ A}$ , with a corresponding reduction in torque capability of 5.5%. The simulation model shown in Fig. 7.23 utilizes an *stator flux control module* which has as inputs the shaft speed ( $n_m^{bs} = 1725 \text{ rpm}$ ) and input quadrature current variable set to operate in the range  $i_q^* = 18.8 \rightarrow -18.8 \text{ A}$ , as required for this simulation exercise.

The process of acquiring the required discrete current locus trajectory may be undertaken by varying the quadrature current reference and recording the current components. In the process ascertain that the stator flux amplitude is indeed held at a constant value of  $|\vec{\psi}_s| = 0.166 \text{ Wb}$  as required. The revised Blondel diagram given in Fig. 7.24 shows the maximum flux and maximum current circles, together with the discrete current locus trajectory for the chosen excitation scenario.

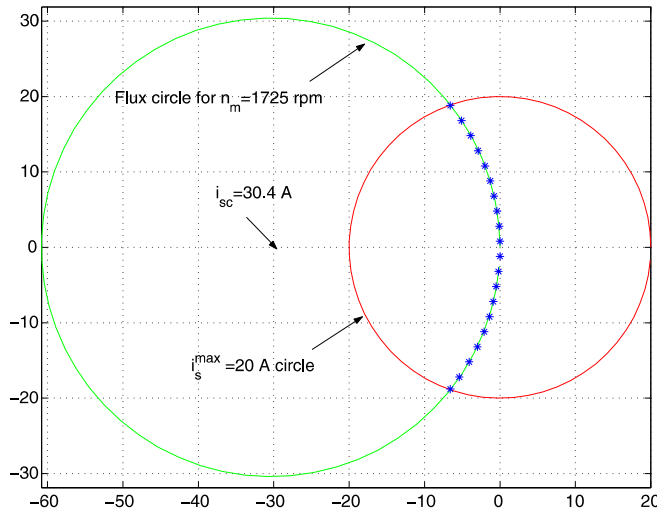


**Fig. 7.24** Blondel diagram non-salient current source connected machine, operation with constant stator flux and  $n_m^{bS} = 1725$  rpm

### 7.6.3 Tutorial 3: Non-salient Synchronous Drive, Unity Power Factor Operation

The drive concept discussed in the previous section is to be modified to accommodate unity power factor operation as discussed in Sect. 7.2.4. For this purpose the simulation model is to be provided with an alternative controller which meets the requirements for this exercise. The field flux is now deemed to be a variable and is chosen in such a manner that the rated flux value of  $\psi_f = 0.166$  Wb is realized with the largest allowable quadrature current  $i_{sq}^{max}$  (whilst maintaining unity power factor operation).

Calculate this current value and the stator flux level which should be used in the drive. In addition, calculate the corresponding base speed  $\omega_m^{bS}$  using the parameters given in Sect. 7.6.1 and determine the percentage reduction in maximum torque capability of the drive in comparison to operation along the MTPA curve (as discussed in Sect. 7.6.1). Furthermore, provide a Blondel diagram which shows the maximum flux circle at the new base speed as well as the maximum current circle. Set the simulation model shaft speed to  $\omega_m^{bS}$  and vary the quadrature input current (for the controller) in steps of 2 A in order to achieve a discrete current locus that traverses a trajectory from the 2<sup>nd</sup> quadrant saturation point to the 3<sup>rd</sup> quadrant saturation point.

Computation of the flux level  $\psi_{fA}$  (which is the required field flux level, for  $i_{sq} = 0$ ) to be used for the new controller requires access to the variable  $\kappa^A =$

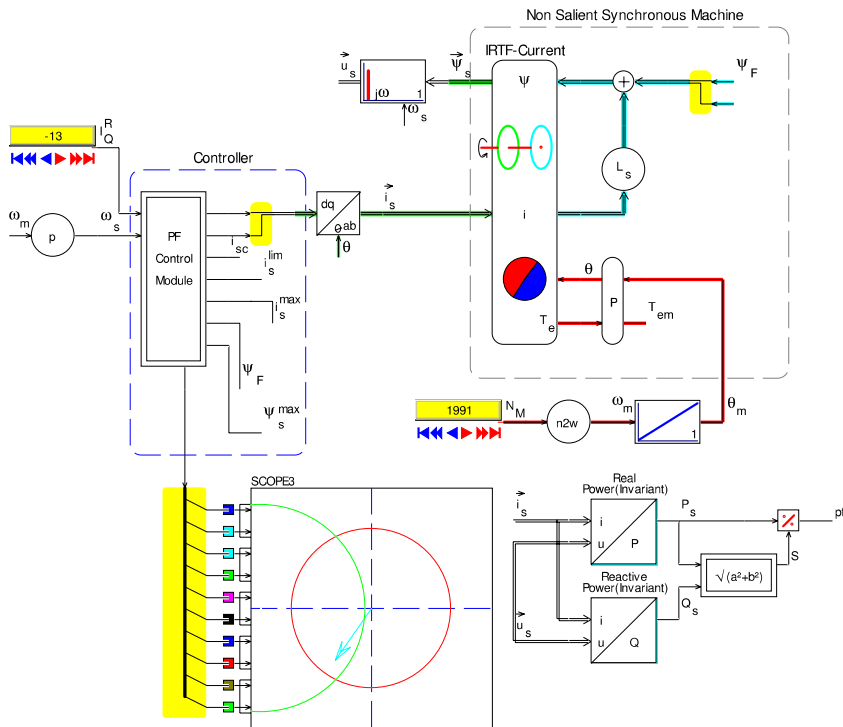


**Fig. 7.25** Simulation of nonsalient synchronous drive, unity power factor operation

$\psi_{fA}/L_s i_s^{max}$  and use of the variable  $i_s^{sc,max} = \psi_f/L_s i_s^{max}$ , with  $\psi_f = 0.166$  Wb. Subsequent use of (7.22c) demonstrates that the required flux value is equal to  $\psi_{fA} = 0.125$  Wb, which is also the required stator flux value, for reasons discussed in Sect. 7.2.3. The corresponding base speed may be found with the aid of (5.11) and (7.21) with  $\kappa = \kappa^A$ , which gives  $n_m^{BS} = 2291$  rpm. The maximum quadrature current may be calculated with the aid of (7.22b). It is equal to  $(i_{sq})^{max} = 15.0$  A. If this current is used, then the field flux will be at the rated value  $\psi_f = 0.166$  Wb as used for operation under MTPA conditions. Hence, the percentage maximum torque reduction is equal to 25%, which must be accepted for operating under zero reactive input power conditions.

The simulation model given in Fig. 7.25 utilizes a *power factor control module* which allows the drive to operate under unity power factor conditions. The power factor is calculated with the aid of a real and reactive power module and the reader may ascertain that its value remains at the required value (within an acceptable tolerance band) when the quadrature current reference is varied over the range  $i_q^* = 15.0 \rightarrow -15.0$  A, as required for this simulation exercise. The shaft speed for this simulation should be set to the base speed value of  $n_m^{BS} = 2291$  rpm.

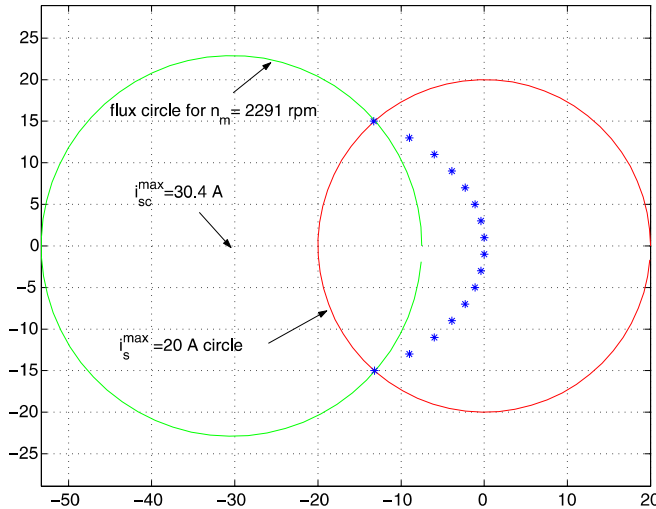


**Fig. 7.26** Blondel diagram non-salient current source connected machine, operation with constant stator flux/unity power factor and  $n_m^{bS} = 2291$  rpm

Computation of the discrete current trajectory is carried along the lines discussed in the previous tutorials and in this case variation of the quadrature current takes place with a stator flux level of  $\psi_s = 0.125$  Wb and unity power factor as may be observed. The Blondel diagram given in Fig. 7.26 shows the base speed flux circle and maximum current circle as well as the discrete current locus for this exercise.

#### 7.6.4 Tutorial 4: Salient Synchronous Drive

The non-salient drive concept discussed in the previous tutorials can be readily modified to accommodate saliency, as has already been shown in Sect. 6.3.4. For this exercise set the direct axis inductance to  $L_{sd} = 5.5$  mH (which is the value for  $L_s$  used in previous cases) and choose a saliency factor of  $\chi = 0.75$ . Furthermore, maintain the drive parameters  $u_s^{\max}$ ,  $i_s^{\max}$  as chosen above. Calculate the mechanical base speed (in rpm) of the drive and the corresponding maximum shaft torque. A simulation model is provided, as shown in Fig. 7.27, which utilizes a *salient control module*, which satisfies the control strategies outlined in Sect. 7.3. The model in question, which is based on the generic diagram given in Fig. 7.19 (with  $R_s = 0$ ), allows the user to set the mechanical shaft speed and reference shaft torque value for the controller module.

Set the initial shaft speed to the base speed of the drive and plot the current locus of the vector  $\vec{i}_s^{dq}$  endpoint under the following conditions:

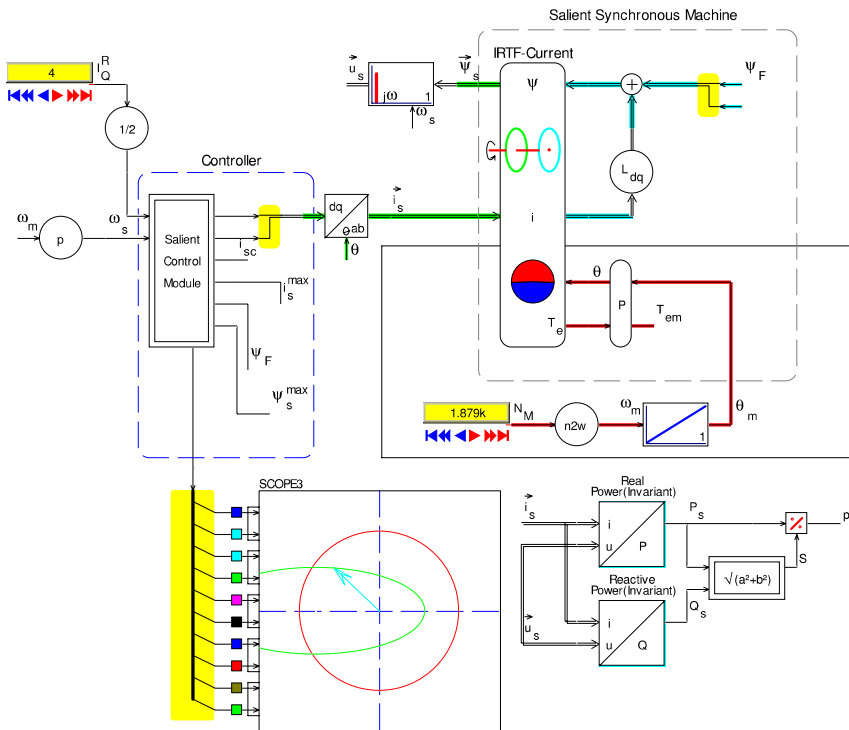


**Fig. 7.27** Simulation of salient synchronous drive

- MTPA operation: set the operating point on the drive saturation point in the third quadrant and vary the reference torque in incremental steps of 1 Nm until a torque of 4 Nm is reached. Maintain the base operating speed.
- Constant torque operation: Maintain the torque reference at 4 Nm and increase the shaft speed in incremental steps of 300 rpm until the current vector endpoint reaches the maximum current circle. Confirm that the controller maintains constant torque during operation in this region (as required).

Provide a Blondel diagram which shows the maximum flux circle at the base operating speed and the maximum current circle of the drive. Add to this diagram the discrete current locus as derived with the aid of your simulation model.

Computation of the vector  $\vec{i}_s^{dq}$  endpoint coordinates at the drive saturation point may be undertaken with the aid of (7.29), with  $i_s^n = 1$ . Subsequent use of these coordinates with torque expression (7.27) leads to the maximum shaft torque of the drive which was found to be  $T_{em}^{max} = 6.0 \text{ Nm}$ . The same set of coordinates may also be used with (7.30), which yields the variable  $i_A$

that is linked to the base speed  $\omega_m^b$  of the drive. Evaluation of said expression along the suggested lines shows that the base speed (expressed in terms of the mechanical shaft speed) is equal to  $n_m^b = 1279$  rpm. The Blondel diagram of the drive showing the maximum flux circle at the base speed together with the maximum current circle is given in Fig. 7.28.

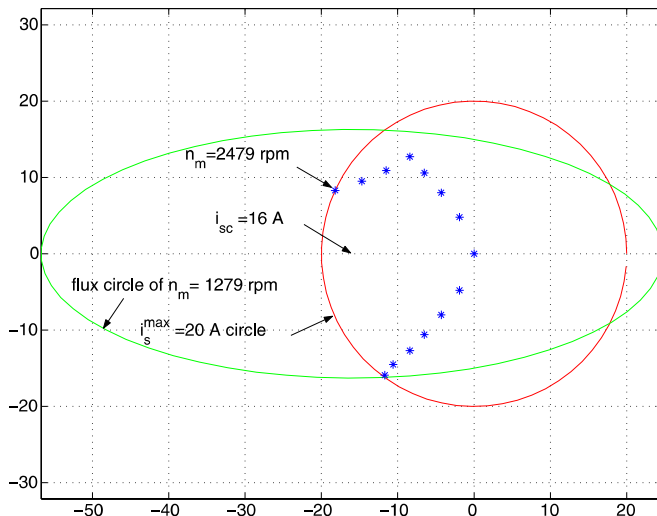


**Fig. 7.28** Blondel diagram salient current source connected synchronous machine

Also shown in Fig. 7.28 is the discrete current locus for operation under MTPA conditions for the reference torque range  $T_e^* = -6.0 \rightarrow 4$  Nm. The second part of the trajectory shown, corresponds to operation under constant torque conditions, i.e with  $T_e^* = 4.0$  Nm, and increasing speed which culminates at speed  $n_m = 2479$  rpm, which is where the maximum current circle is reached by the vector  $\vec{i}_s^{dq}$  endpoint.

### 7.6.5 Tutorial 5: PM Salient Synchronous Drive with Model Based Current Control

The final tutorial in this chapter examines the operation of a voltage-source connected machine operating with a model based current controller. The proposed concept as discussed in Sect. 7.5 utilizes a four pole salient machine as discussed in the previous example. In this exercise the current references produced by the (same) current controller are used as inputs  $i_d^c$ ,  $i_q^c$  for the current controller as may be observed from Fig. 7.20. The parameters of the machine are those presented in the previous section, with exception of the

inertia which has been arbitrarily set to  $J = 0.005 \text{ kg m}^2$ . A sampling rate of 10 kHz is assumed for the discrete current controllers. For this example the input reference torque is set to  $T_e^* = 6.0 \text{ Nm}$  at  $t = 10 \text{ ms}$  and this is to be followed by a torque reversal  $T_e^* = 6.0 \rightarrow -3.0 \text{ Nm}$  at  $t = 175 \text{ ms}$ . A first order filter with a time constant of  $\tau = 2 \text{ ms}$  is to be placed between torque reference and synchronous drive controller, to limit the torque variations to realistic values. Requesting an instantaneous change in torque is not realistic in any practical drive system, due to limitations imposed by the converter DC bus-voltage. Total simulation run time is to be set to 250 ms while the DC supply is equal to  $u_{\text{DC}} = 200 \text{ V}$ . Both shaft speed and shaft angle are assumed to be available for the controllers. In this simulation the modulator and converter are not to be implemented at circuit level, i.e., the switching effects should be excluded (as discussed Sect. 3.3.5) to better visualize the operation of the drive.

The first task to be undertaken is to calculate the gains for the two current controllers and in addition identify the disturbance decoupling terms which must be introduced. Secondly examine the simulation model of the drive as given in Fig. 7.29 and plot the following results:

- Sampled direct/quadrature reference  $i_{\text{sd}}^c, i_{\text{sq}}^c$  and *measured* currents  $i_{\text{sd}}, i_{\text{sq}}$ .
- Controller shaft input torque reference  $T_e^*$  and *actual* shaft torque  $T_{em}$ .
- Shaft speed  $n_m$  (in rpm and scaled by a factor 1/20) and stator voltage vector amplitude  $|\vec{u}_s|$ .

The computation of the current controller gains follows the approach taken for the tutorial shown in Fig. 3.31, where use was made of a resistive/inductive load. Furthermore, the converter/modulator modules were introduced, which are excluded in this tutorial. For the salient machine the direct and quadrature inductance calculated with equation set (3.21) differ. Hence, the direct and quadrature proportional gains will reflect the reluctance transformation in use. The integral terms will be equal for both controllers. Said equations also define the disturbance decoupling terms which must be used, keeping in mind the salient nature of the machine. A torque reference module is shown in Fig. 7.29, which also contains the first order filter used to moderate the torque reference signal supplied to the *salient control module*. This module is the same unit used in the previous example and makes use of the converter limits  $u_s^{\max} = 60 \text{ V}, i_s^{\max} = 20 \text{ A}$ . Note that the actual supply vector may become larger as the control strategy deployed does not take into account the voltage potential across the stator resistance.

Four scope modules are given in Fig. 3.31 which show the required variables for this tutorial. The results are reproduced in Fig. 7.30 by way of MATLAB subplots and show the operation of the drive in some detail. Subplot Fig. 7.30(a) shows the torque reference step at  $t = 10 \text{ ms}$  as provided to the salient control module, which in turn set the required reference direct and quadrature currents as may be observed from Fig. 7.30(c), (d). The

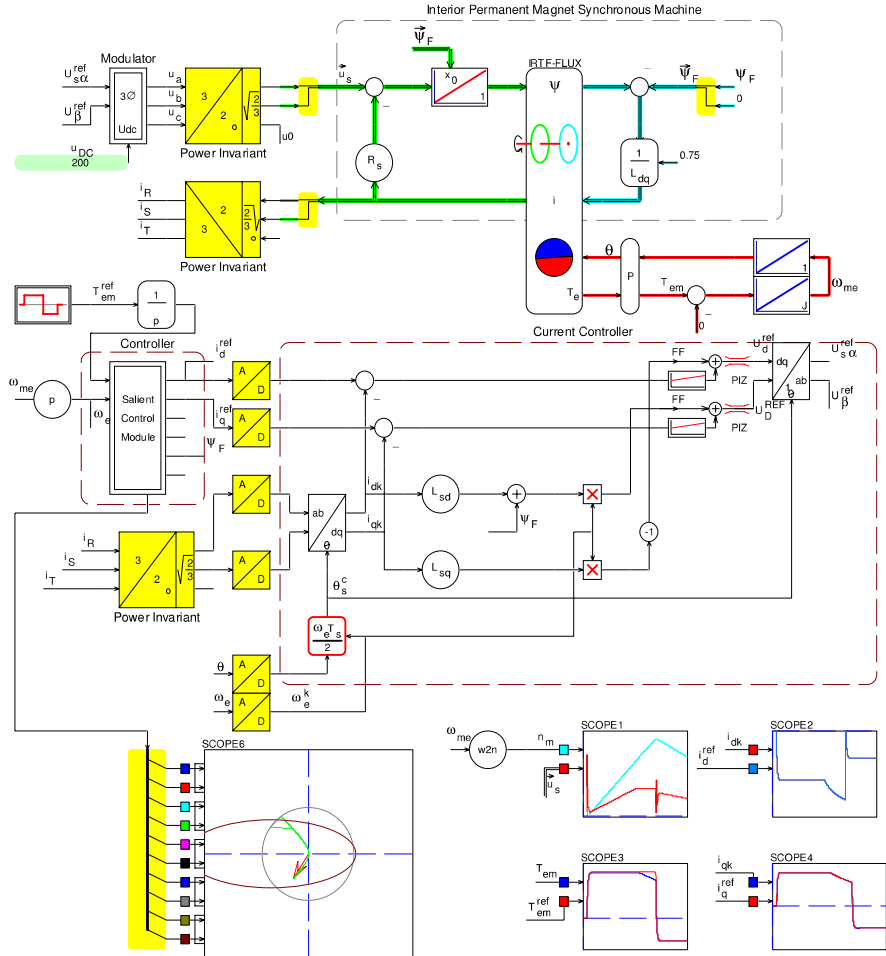
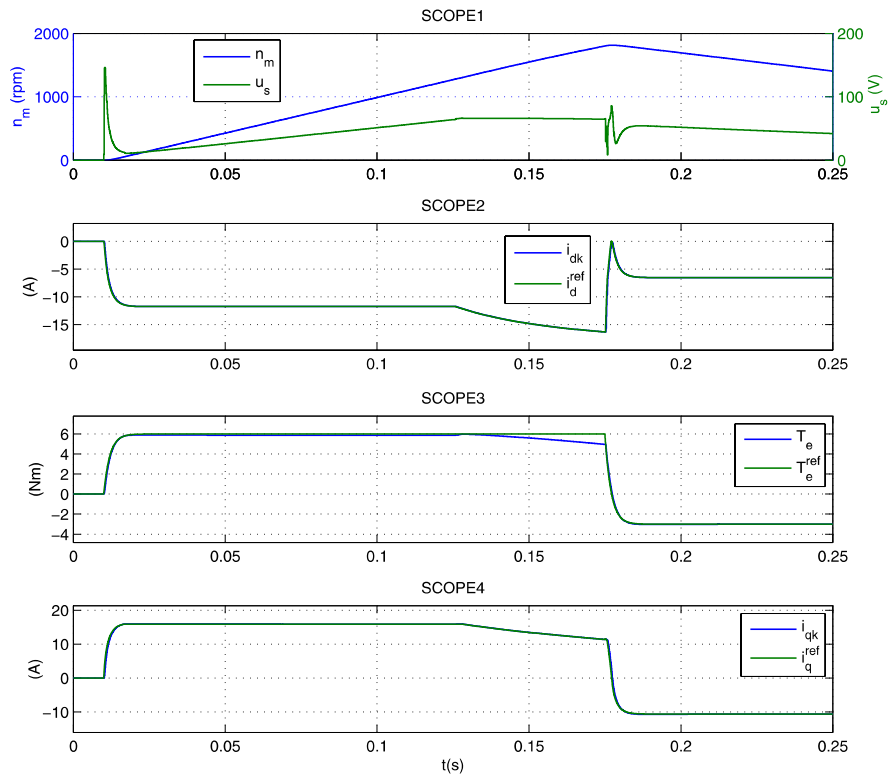


Fig. 7.29 Simulation of salient synchronous drive with voltage source converter

current controller average voltage per sample values are changed, as noticeable from the supply voltage transient (Fig. 7.30(b)) and change in measured direct and quadrature currents. These in turn serve to deliver the required shaft torque as shown in Fig. 7.30(a). Speed increases linearly as long as the shaft torque remains constant. At approximately  $t = 0.13$  s the current controller reference values (and therefore the currents in the machine) change because the drive reaches the *drive saturation point*, which occurs at shaft speed  $n_m^b = 1279$  rpm in this example. As speed increases beyond the base speed, field weakening is active as may be observed from Fig. 7.30. The supply voltage amplitude is somewhat higher than the required value of  $|\vec{u}_s| = 60$  V due to the presence of a finite stator resistance, as mentioned above. At  $t = 0.175$  s a reference torque reversal to half rated (negative) torque occurs



**Fig. 7.30** Simulation results for salient synchronous drive with voltage source converter

which is matched by an appropriate shaft torque change. The drive example shown was undertaken with a model based current controller. It is left as an exercise for the reader to reconsider this problem for the case where a hysteresis controller as shown in Fig. 3.13 is used with the drive in question.

### 7.6.6 Tutorial 6: Experimental Results of a PM Non-salient Synchronous Drive

The test-bench described in chapter Sect. 1.4 is used as an example to show the functionality of the previous described control algorithms. The control for a non-salient synchronous drive was implemented using a CASPOC simulation, similar to the control in tutorial 1. Figure 7.31 shows the built simulation model. The model has two basic blocks. The first block is the controller, which calculates the reference voltages  $U_1$ ,  $U_2$  and  $U_3$  depending on the reference torque  $T_e^{\text{ref}}$  or the reference speed  $n_m^{\text{ref}}$ . The type of control can be chosen by the variable T-OR-S, which stands for torque or speed control. Additionally, the model needs to know the actual rotor position  $\theta$  and the measured phase currents  $i_R$ ,  $i_S$  and  $i_T$ . The calculated reference phase voltages are then applied to the machine to calculate the currents and the torque of the machine. The scopes at the bottom of Fig. 7.31 show the results of a simulated speed reversal.

The developed control algorithm can be implemented on the DSP using the C-code export functionality of CASPOC as explained in Sect. 1.4. The exported code is embedded in the test-bench software. To measure the rotor position of the machine an incremental encoder with 720 pulses per revolution is used. The specifications of the used machine are given in Table 7.1.

**Table 7.1** Specifications of example PM synchronous machine

Parameters		Value
Nominal power	$P$	0.75 kW
Voltage	$U$	50 V
Stator inductance	$L_s$	3.5 mH
Stator resistance	$R_s$	0.11 Ω
Field flux	$\psi_f$	0.089 Wb
Number of polepairs	$p$	1

To demonstrate the control a speed reversal is performed. A speed reversal is useful to show the speed, torque and current control, for both motoring and generating operation. Figure 7.32 shows a measured speed reversal of the machine from  $-500$  rpm to  $500$  rpm with no load. Shown are the reference and measured speed,  $n_m^{\text{ref}}$  and  $n_m$ , the reference torque  $T^{\text{ref}}$ , the measured  $i_d$  and  $i_q$  currents and the phase voltages  $U_1$ ,  $U_2$  and  $U_3$ . It can be seen, that the  $i_q$  current is following the torque command. The  $i_d$  current is almost zero, as the machine is not in field weakening. Regarding the phase voltages, the functionality of the pulse centering technique, as explained in Fig. 2.10, can be seen.

With AixScope [1] it is possible to show variables which are in the  $\alpha, \beta$ -plane as rotating vectors. Figure 7.33 shows plots of the stator reference voltages  $u_{\alpha, \beta}$  and the currents  $i_{\alpha, \beta}$  in a polar plot, as well over time. Shown

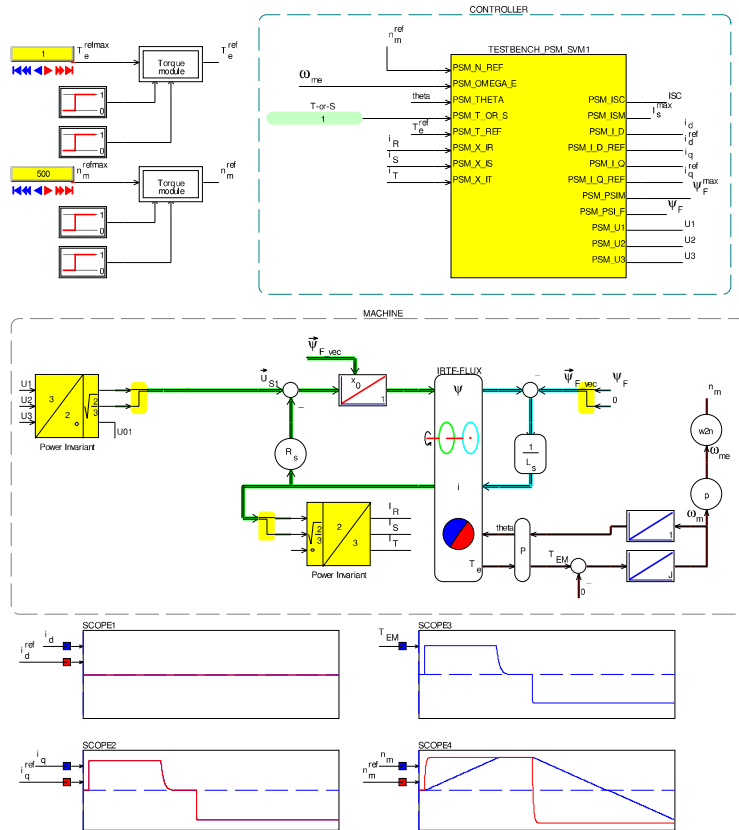
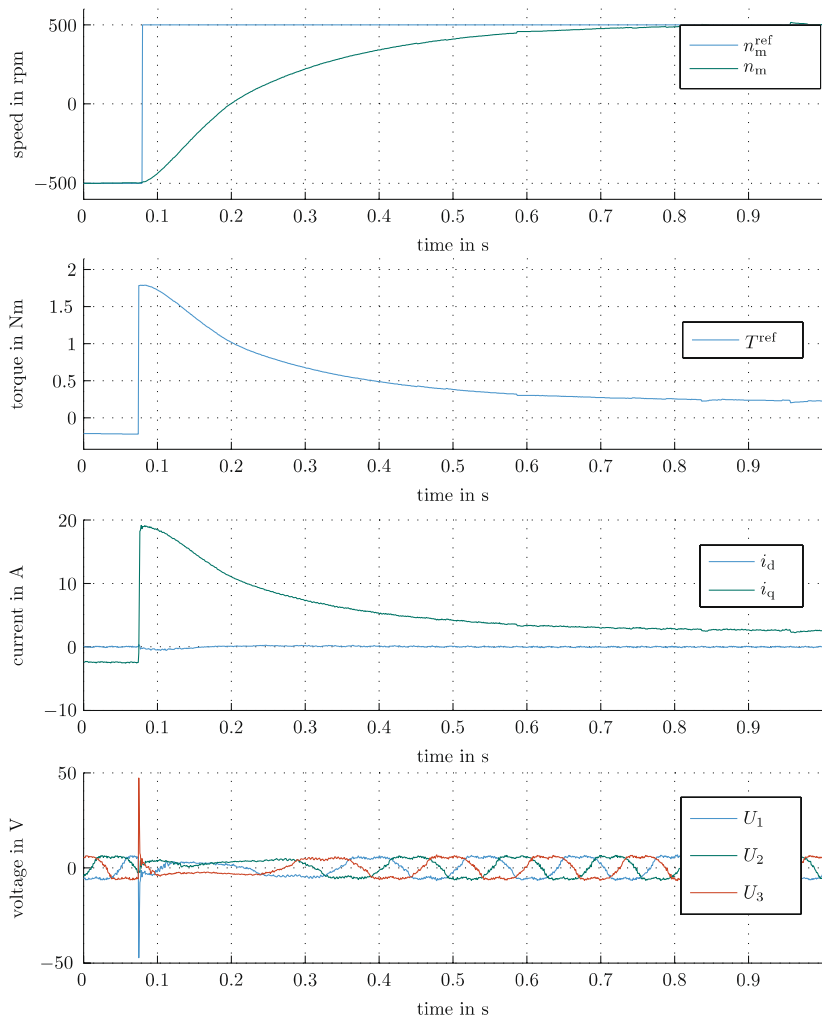
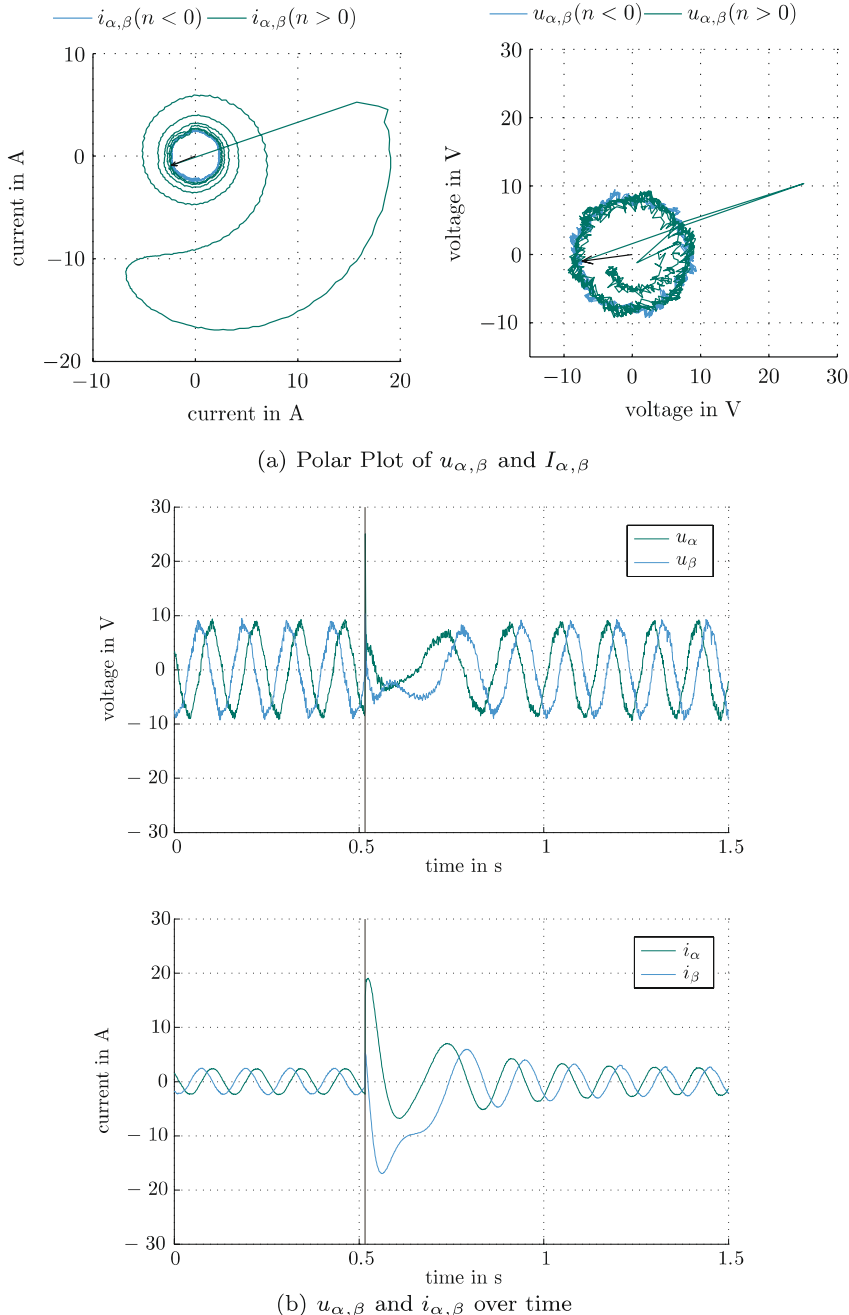


Fig. 7.31 Simulation of PM synchronous machine

is, as in the example before, a speed reversal from  $-500$  rpm to  $500$  rpm. The black arrow or the line in each figure marks the time, where the reference speed is changed. At the beginning voltage and currents rotate clockwise, corresponding to negative speed. In Fig. 9.43(a) the corresponding voltage and currents are colored blue. After the speed step, the rotation direction changes. The voltage and current curves in the polar plot for  $n > 0$  are colored green, for a better readability.



**Fig. 7.32** Experimental results for speed reversal with PM synchronous machine



**Fig. 7.33** Experimental result for voltage and currents in  $\alpha\beta$ -reference system at speed reversal



# Chapter 8

## Induction Machine Modeling Concepts

Electrical drives with induction machines remain the dominant market leader in the field. The combination of a robust low cost squirrel-cage machine, high power density converter, and versatile controller yields a highly adaptable drive for wide ranging rugged industrial applications.

In this chapter, induction machine models are developed which will be used in successive chapters of this book, e.g. with voltage source inverters and field-oriented controls. Initially, a brief review of the induction machine with squirrel-cage rotor is given in terms of a cross-sectional view and simplified symbolic and generic models. A detailed description of the fundamentals can be found in [31, 40, 48], and [68]. As a platform for introducing field-oriented models, first models without leakage inductances are derived showing the essence of torque production of the machine. Central to this chapter is the introduction of a *universal* flux linkage model which allows a three-to-two inductance transformation leading to a simplified IRTF machine model. This universal model is the stepping stone to the *universal field-oriented* (UFO) machine model which gives a basic understanding of the transient behavior of induction machines [19]. Furthermore, this model forms the cornerstone for the development of field-oriented control. At the end of this chapter, attention is given to single-phase induction machines. These machines are widely used in domestic appliances and as such it is important to have access to dynamic and steady-state models. A set of tutorials is provided which allows the user to interactively explore the concepts presented in this chapter.

### 8.1 Induction Machine with Squirrel-Cage Rotor

Figure 8.1 shows the cross-section of a induction machine with a so-called *squirrel-cage* rotor. The squirrel cage consists of a set of conductors (shown in red), which are short-circuited at both ends by a conductive ring. The cage is

embedded in the rotor lamination as may be observed from Fig. 8.1. A three-phase two-layer winding is housed in the stator of a four-pole machine.

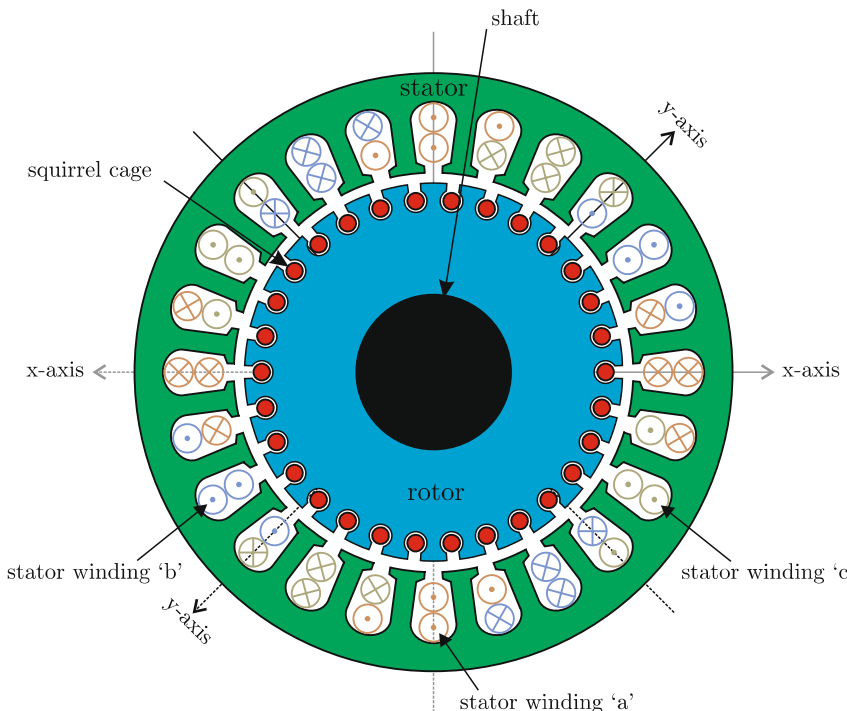


**Fig. 8.1** Induction machine with squirrel-cage rotor

A rotating field created by the stator winding is penetrating the rotor. If the rotor is rotating asynchronously to the stator field (which means it is rotating at a different speed), alternating currents are induced in the squirrel cage. These currents, together with the stator field, are responsible for the torque production of the machine. This is why asynchronous machines are also known as *induction machines*. If stator field and rotor were rotating synchronously, no currents would be induced and no torque could be produced. Note, that, regardless of the rotor speed, the rotor field and stator field are still rotating synchronously with a phase shift. The difference between the speed of the rotor and the fields is compensated by the frequency of the rotor currents, the so-called rotor slip frequency. The asynchronous nature of the machine is the reason why for the control of induction machines, only the position of stator field and rotor field are required and not the absolute rotor position.

Squirrel cage based induction machines are widely used in industry. However, other configurations include *single-phase machines* and *doubly-fed in-*

*duction machines.* Single-phase machines are discussed in Sect. 8.5. Modeling and control of doubly-fed induction machines can be found in literature [47]. These machines are found in wind turbines and large pump drives. These machines make use of a rotor that is provided with a set of three-phase windings which are connected to a stationary converter (or set of resistors) via a set of slip-rings.

## 8.2 Zero Leakage Inductance Models of Induction Machines

For the purpose of understanding the basic dynamic and steady-state behavior of the induction machine, it is helpful to initially ignore the presence of stator and rotor leakage inductances. Therefore, symbolic and generic models will be introduced first without leakage inductances showing the essence of torque production of the machine. Furthermore, the zero leakage approach serves as an effective platform for introducing field-oriented models.

### 8.2.1 IRTF Based Model of the Induction Machine

As a first step in the development of dynamic models for induction machines, it is instructive to consider a simplified IRTF based symbolic concept as given in Fig. 8.2. Using an IRTF means to deploy a dual coordinate reference frame which is linked to the stator and to the rotor of the machine.

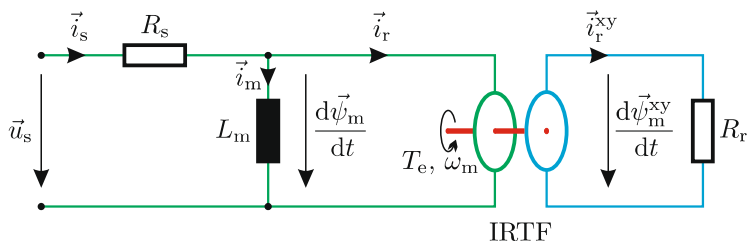


**Fig. 8.2** Zero leakage IRTF based induction machine model

The mathematical equation set that conforms to the model according to Fig. 8.2 is as follows:

$$\vec{u}_s = R_s \vec{i}_s + \frac{d\vec{\psi}_m}{dt} \quad (8.1a)$$

$$\vec{\psi}_m = L_m (\vec{i}_s - \vec{i}_r) \quad (8.1b)$$

$$0 = -R_r \vec{i}_r^{xy} + \frac{d\vec{\psi}_m^{xy}}{dt}. \quad (8.1c)$$

Note that the model presented here is very similar to that shown in Fig. 4.13. In the latter case, current excitation was assumed whereas here voltage excitation is imposed for connecting the machine to a voltage source converter. Furthermore, the magnetizing inductance is shown on the other side of the IRTF which can be done with impunity.

The development of a corresponding generic model representation of this simplified two-pole machine model is readily undertaken with the aid of (8.1) and the two IRTF related (4.5) for electromagnetic torque calculation and (4.6) as a load model. An implementation example is given in Fig. 8.3. It makes use of a differentiator module which is unavoidable in the case leakage inductance has been ignored. Note that, for reasons of numerical stability, the use of differentiators should be avoided in a simulation environment whenever possible. The tutorial in Sect. 8.6.1 is based on the generic model presented in this chapter.

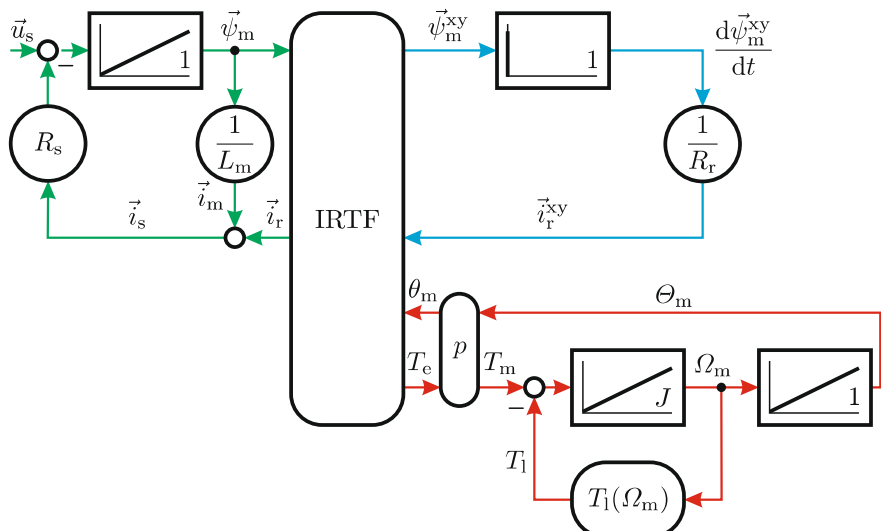


**Fig. 8.3** Generic model, zero leakage IRTF based induction motor model

### 8.2.2 Field-Oriented Model

A suitable starting point for the development of a field-oriented model is the IRTF based machine model shown in Fig. 8.2 and the vector diagram given in Fig. 8.4. The latter diagram shows the stator current and magnetizing flux linkage space vectors  $\vec{i}_s$  and  $\vec{\psi}_m$  respectively. The latter vector may be represented as  $\vec{\psi}_m = \psi_m e^{j\theta_\psi}$ , where  $\psi_m$  is the amplitude and  $\theta_\psi$  the angle between the flux linkage vector and real axis of the stationary reference plane.

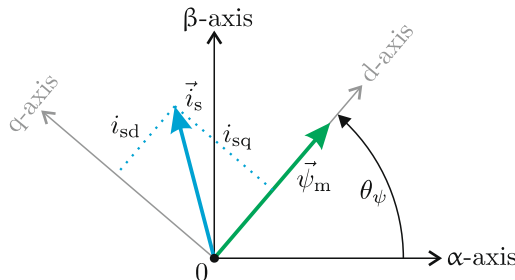


**Fig. 8.4** Vector diagram, zero leakage model

Stationary based equations are transformed to the dq plane using  $\vec{A} = \vec{A}^{dq} e^{j\theta}$  with  $\omega_s = d\theta/dt$ . The conversion process of rotor-oriented equations to a synchronous reference frame, linked to the flux linkage vector  $\vec{\psi}_m$ , is achieved by a two-step process. Firstly, the rotor based equations are transformed to a stationary reference frame after which the transformation to a synchronous reference frame can be implemented. Equation set (8.1) may be transformed to the dq plane with the aid of the approach outlined above which leads to

$$\vec{u}_s^{dq} = R_s \vec{i}_s^{dq} + \frac{d\vec{\psi}_m^{dq}}{dt} + j\omega_s \vec{\psi}_m^{dq} \quad (8.2a)$$

$$\frac{\vec{\psi}_m^{dq}}{L_m} = \vec{i}_s^{dq} - \vec{i}_r^{dq} \quad (8.2b)$$

$$\frac{d\vec{\psi}_m^{dq}}{dt} = R_r \vec{i}_r^{dq} - j(\omega_s - \omega_m) \vec{\psi}_m^{dq}. \quad (8.2c)$$

It is noted that in this case some further simplification is possible given that  $\vec{\psi}_m^{dq} = \psi_m$ , i.e., the vector is real because the direct axis is aligned with this vector. All the remaining vectors have both a real (direct) and a imaginary (quadrature) component, for example  $\vec{i}_s^{dq} = i_{sd} + j i_{sq}$ . Further development of equation set (8.2) in terms of grouping the real components leads to:

$$u_{sd} = R_s i_{sd} + \frac{d\psi_m}{dt} \quad (8.3a)$$

$$\frac{\psi_m}{L_m} = i_{sd} - i_{rd} \quad (8.3b)$$

$$\frac{d\psi_m}{dt} = R_r i_{rd}. \quad (8.3c)$$

Grouping the imaginary components of equation set (8.2) leads to:

$$u_{sq} = R_s i_{sq} + \omega_s \psi_m \quad (8.4a)$$

$$i_{rq} = i_{sq} \quad (8.4b)$$

$$\omega_s \psi_m = R_r i_{rq} + \omega_m \psi_m. \quad (8.4c)$$

The symbolic direct and quadrature model as given in Fig. 8.5 satisfies equation sets (8.3) and (8.4) respectively.

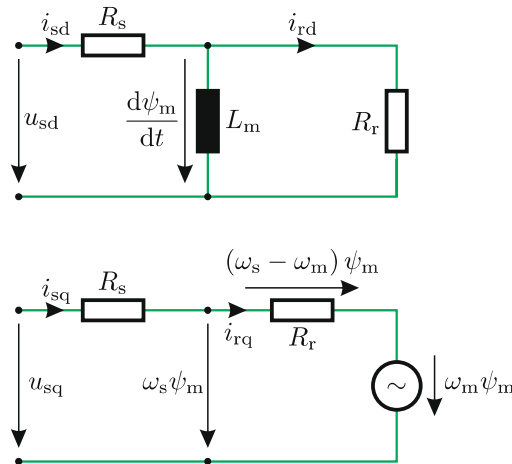


**Fig. 8.5** Direct and quadrature field-oriented symbolic model with zero leakage inductance

The corresponding generic current-fed induction machine model with currents  $i_{sd}$  and  $i_{sq}$  as input variables, which corresponds to the symbolic field-oriented model, is given in Fig. 8.6.

The model according to Fig. 8.5 and Fig. 8.6 provides some fundamental insights with respect to the operation of the machine. If for example, a current  $i_{sd}$  is applied to the machine at  $t = 0$ , the flux linkage  $\psi_m$  will assume a steady-state value  $\psi_m = L_m i_{sd}$  after a transitional period which is governed by the time constant  $L_m/R_r$ . Once the flux linkage reaches its steady-state value, the variables  $d\psi_m/dt$  and  $i_{rd}$  (see Fig. 8.5) will be equal to zero.

The torque  $T_e$  is determined by the product of  $\psi_m$  and  $i_{sq}$  and these components can be controlled independently as is the case for a DC machine

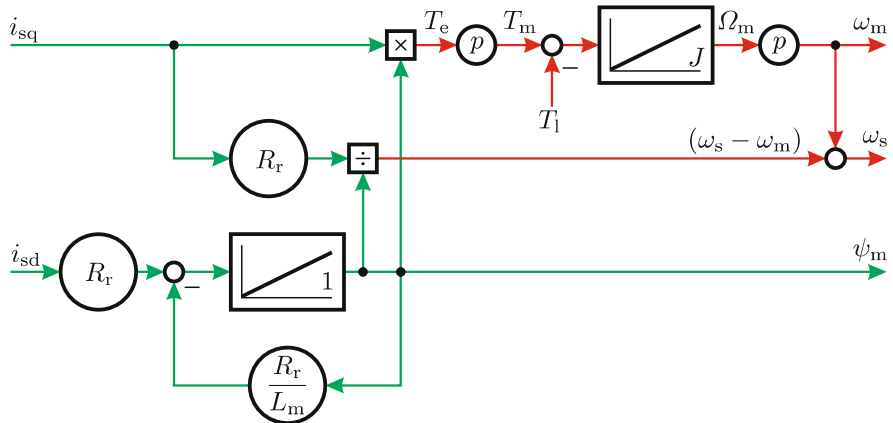


**Fig. 8.6** Generic representation of current source, field-oriented induction machine model, with zero leakage inductance

with a field winding. In the latter case, the variables  $\psi_m$  and  $i_{sq}$  are replaced by the field flux linkage  $\psi_f$  and armature current  $i_a$  respectively. A voltage variable  $\omega_s \psi_m$  as shown in Fig. 8.5, is defined by the sum of the voltages  $\omega_m \psi_m$  and  $R_r i_{sq}$  (cp. (8.4c)). The latter is equal to the product of the *slip frequency*  $\omega_{sl} = \omega_s - \omega_m$  and flux linkage  $\psi_m$ . If a step increase in the current  $i_{sq}$  is made, whilst maintaining a constant  $i_{sd}$  value, the torque and slip frequency must also increase stepwise.

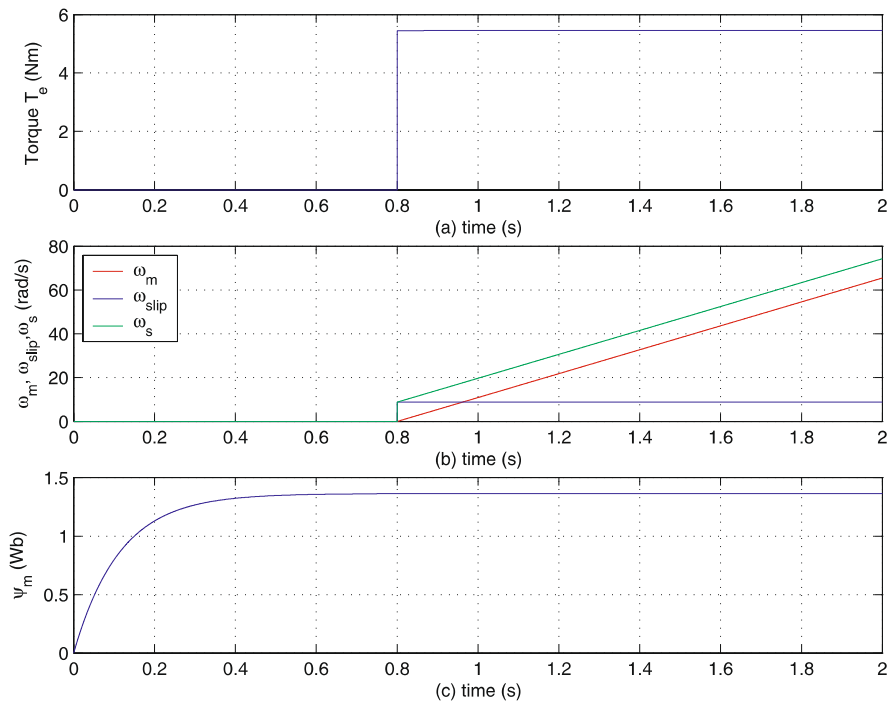
### Tutorial Results

Figure 8.7 shows a typical transient response for a machine in its current form, without a mechanical load, in terms of the torque  $T_e$ , shaft speed  $\omega_m$ , slip frequency  $\omega_{sl}$ , and electrical frequency  $\omega_s$ . In this example, a current  $i_{sd} = 4.0$  A is applied at  $t = 0$  and a quadrature stator current step  $i_{sq} = 0 \rightarrow 4.0$  A is made at  $t = 0.8$  s. The results shown are obtained with the model given in the tutorial (see Sect. 8.6.4). The reader is referred to Sect. 8.6.4 for further details of the simulation model.

### Flux/Current Diagram

Further insight with regard to this type of model can be obtained by considering the flux/current diagram of the machine taken at a particular instance in time. Figure 8.8 shows the flux lines  $\phi_d$  linked with the flux linkage  $\psi_m$ . A current distribution in the stator windings and squirrel-cage rotor is shown for both cases. The current and flux distributions tied to the dq plane rotate at speed  $\omega_s$ , while the rotor rotates with a shaft speed  $\omega_m$ .

The direct axis flux distribution (Fig. 8.8(a)) shows the d-axis which is aligned with the flux linkage vector  $\psi_m$ . The current  $i_{sd}$  is shown in distributed form on the stator side. Note that the rotor component shows no current, i.e.,  $i_{rd} = 0$ . The quadrature model, see Fig. 8.8(b), shows the flux



**Fig. 8.7** Transient response of field-oriented model with zero leakage inductance

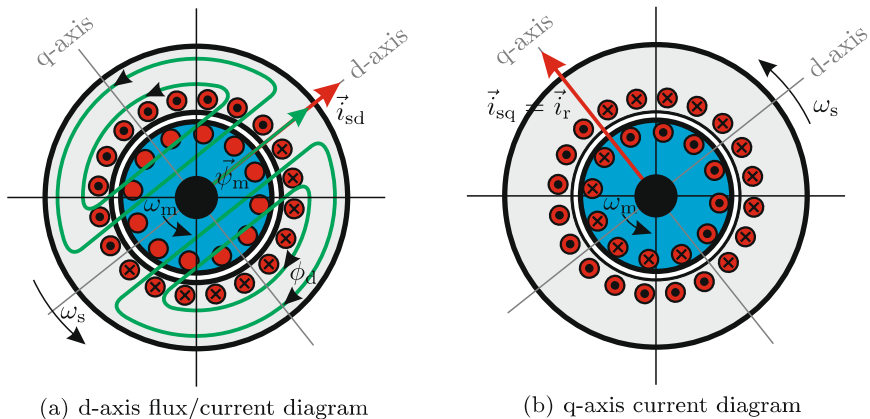


**Fig. 8.8** Direct and quadrature flux/current diagram in steady-state

distribution  $\phi_d$  and the stator and rotor current distributions which correspond to  $i_{sq}$  and  $i_{rq}$  respectively. It is noted that the two current distributions are in opposition in the actual machine given, whilst the model assumes the condition  $i_{sq} = i_{rq}$ . The reason for the supposed discrepancy is linked to the choice of input/output power conventions of the IRTF model. The resultant current distribution in the stator is formed by the two stator components shown in Fig. 8.8.

## 8.3 Machine Models with Leakage Inductances

In practical machines, not all the magnetic flux linkage is fully coupled between the stator windings and the rotor squirrel-cage. So-called leakage flux paths are present on the stator and rotor side of the machine, which in modeling terms are represented by leakage inductances  $L_{os}$  and  $L_{or}$  respectively. In this section, the IRTF and field-oriented modeling approach used in the previous section is extended to accommodate magnetic flux leakage of the machine. In this context, a *universal field-oriented* (UFO) approach will be introduced, which will prove to be instrumental for the development of a field-oriented controller in the next chapter [16].

### 8.3.1 Fundamental IRTF Based Model

The simplified model according to Fig. 8.2 is extended to include the rotor and stator based leakage inductances  $L_{or}$  and  $L_{os}$  respectively. The rotor leakage inductance has been conveniently relocated to the stator side of the IRTF module to form a three-element circuit network which consists of the two leakage inductances and the magnetizing inductance  $L_m$ . Note that the use of an IRTF module allows the positioning of an inductance to either side without having to change its value, and that relocating the leakage inductance does not affect the torque  $T_e$ , as seen in Sect. 4.1.

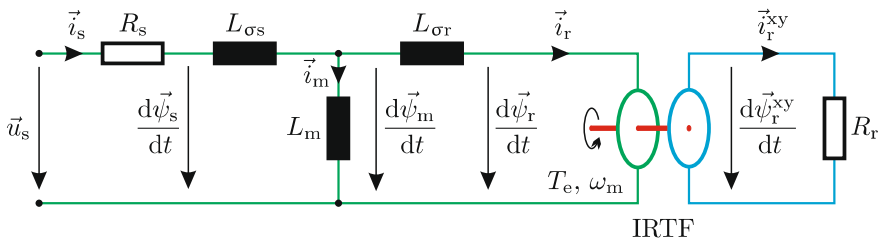


**Fig. 8.9** Three inductance, IRTF based induction machine model

The equation set which corresponds to Fig. 8.9 is as follows:

$$\vec{u}_s = R_s \vec{i}_s + \frac{d\vec{\psi}_s}{dt} \quad (8.5a)$$

$$\vec{\psi}_s = \vec{\psi}_m + L_{os} \vec{i}_s \quad (8.5b)$$

$$\vec{\psi}_r = \vec{\psi}_m - L_{or} \vec{i}_r \quad (8.5c)$$

$$\vec{\psi}_m = L_m (\vec{i}_s - \vec{i}_r) \quad (8.5d)$$

$$0 = -R_r \vec{i}_r^{xy} + \frac{d\vec{\psi}_r^{xy}}{dt}. \quad (8.5e)$$

On the basis of the symbolic model given in Fig. 8.9 and equation set (8.5), a generic IRTF based symbolic model can be developed. However, particular attention must be given in terms of its numerical implementation to avoid algebraic loops. The cause of this problem is the presence of two leakage inductance circuit elements which may be avoided as will become apparent in the following section. Furthermore, it is difficult to determine individual values for these two inductances in a squirrel-cage motor. The reason for this is that these values are usually determined by a *locked rotor* test [68] which yields an estimate for the combined leakage inductance  $L_{os} + L_{or}$ . The combined leakage inductance value is then (usually) arbitrarily divided by two in order to arrive at values for the individual elements. As a result, the rotor leakage inductance is measured at line frequency (50 Hz or 60 Hz). Due to rotor deep bar and saturation effects [13, 42], the rotor leakage inductance value can deviate strongly when operating under field-oriented control.

### 8.3.2 Universal IRTF Based Model

The IRTF model according to Fig. 8.9 can be transformed to a so-called *universal* three-inductance configuration which makes use of a transformation coefficient  $a$ . By changing the value of this parameter, the user is able to alter the model from, for example, a three- to two-inductance type model where the circuit element which represents the leakage inductance can be located on either side of the equivalent magnetizing inductance component. The term *universal* reflects the flexibility of this new model in terms of being able to change the inductance parameters simultaneously without affecting the no-load or short circuit impedance of the original inductance network. It will be shown in Sect. 8.3.4 that such a transformation capability is of importance for the development of a so-called *universal field-oriented* (UFO) machine model [16].

### Parameter Definition for the Universal Model

The aim of this section is therefore to define a set of inductance parameters  $L_M$ ,  $L_{\sigma S}$ , and  $L_{\sigma R}$  for a revised symbolic machine model as given in Fig. 8.10 which is able to replace the three-element inductance network of the original model (see Fig. 8.9). The impedance as viewed from either side of the revised inductance network must correspond to the values found in the original inductance network and should not be affected by changes in the transformation factor  $a$ . In order to achieve this aim, an ITF module with transformation ratio  $a : 1$  is introduced in the new model.

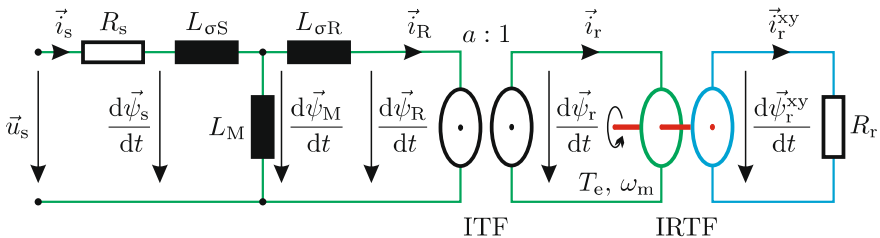


**Fig. 8.10** Universal, IRTF based induction machine model, with ITF module

The transformation process is initiated by considering equation set (8.5) which is linked to the model given in Fig. 8.9. In particular, it is helpful to consider (8.5b) and (8.5d) which may also be written as

$$\vec{\psi}_s = L_s \vec{i}_s - L_m \vec{i}_r - a L_m \vec{i}_s + a L_m \vec{i}_R \quad (8.6)$$

with  $L_s = L_m + L_{\sigma S}$ . This expression may then be written as

$$\vec{\psi}_s = \underbrace{(L_s - a L_m)}_{L_{\sigma S}} \vec{i}_s + \underbrace{a L_m}_{L_M} (\vec{i}_s - \vec{i}_R) \quad (8.7)$$

where the parameters  $L_{\sigma S}$  and  $L_M$  are introduced, representing a generalized leakage inductance and magnetizing inductance. Furthermore, a scaled rotor current vector  $\vec{i}_R$  is introduced in (8.7) which along with the scaled rotor flux linkage vector  $\vec{\psi}_R$  is defined as

$$\vec{i}_R = \frac{\vec{i}_r}{a} \quad (8.8a)$$

$$\vec{\psi}_R = a \vec{\psi}_r. \quad (8.8b)$$

The scaled rotor flux linkage vector  $\vec{\psi}_R$  represents the scaled (by the transformation factor  $a$ ) rotor flux linkage vector  $\vec{\psi}_r$ . The choice of scaling for  $\vec{i}_R$  and  $\vec{\psi}_R$  is such that the product of the current and flux linkage vectors as well as the impedance remain unaffected by the scaling. In the *universal* model

(see Fig. 8.10) (8.8) is represented by the ITF module with winding ratio  $a : 1$ . Equations (8.8b) and (8.8c) form the basis for the second part of the proposed model transformation. Use of these two equations to represent the scaled rotor flux linkage vector  $\vec{\psi}_R$  gives

$$\vec{\psi}_R = a L_m \vec{i}_s - a^2 L_r \vec{i}_R - a L_m \vec{i}_R + a L_m \vec{i}_R \quad (8.9)$$

with  $L_r = L_m + L_{\sigma R}$ . This expression may also be rewritten as

$$\vec{\psi}_R = \underbrace{a L_m (\vec{i}_s - \vec{i}_R)}_{L_M} - \underbrace{(a^2 L_r - a L_m)}_{L_{\sigma R}} \vec{i}_R \quad (8.10)$$

where a second leakage inductance parameter  $L_{\sigma R}$  is introduced. The resultant flux linkage vector based equation set as given by (8.7) and (8.10) may also be written as

$$\vec{\psi}_s = L_{\sigma S} \vec{i}_s + L_M \vec{i}_M \quad (8.11a)$$

$$\vec{\psi}_R = L_M \vec{i}_M - L_{\sigma R} \vec{i}_R \quad (8.11b)$$

where  $\vec{i}_M = \vec{i}_s - \vec{i}_R$  represents the scaled magnetizing current vector. The flux linkage equation set (8.11) contains a set of leakage inductances and magnetizing inductance which are a function of the transformation variable  $a$ . This new set on inductances is conveniently summarized in equation set (8.12):

$$L_{\sigma S} = L_m \left( \frac{L_s}{L_m} - a \right) \quad (8.12a)$$

$$L_{\sigma R} = a L_r \left( a - \frac{L_m}{L_r} \right) \quad (8.12b)$$

$$L_M = a L_m. \quad (8.12c)$$

Observation of equation set (8.12) shows that if the transformation variable  $a$  is bound by the condition

$$\frac{L_m}{L_r} \leq a \leq \frac{L_s}{L_m} \quad (8.13)$$

then the leakage inductances  $L_{\sigma S}$  and  $L_{\sigma R}$  remain greater than or equal to zero.

The variation of  $a$  as defined by (8.13) is relatively small, hence it is helpful to introduce a percentage transformation coefficient  $\Gamma_a$  which is defined over the range  $\pm 100\%$ , with  $\Gamma_a = 0\%$  set to correspond to a universal model with  $a = 1$ . The relationship between  $\Gamma_a$  and  $a$  may be written as

$$\text{if } \Gamma_a \geq 0 : \quad a = 1 + \frac{\Gamma_a}{100} \left( \frac{L_s}{L_m} - 1 \right) \quad (8.14\text{a})$$

$$\text{if } \Gamma_a < 0 : \quad a = 1 + \frac{\Gamma_a}{100} \left( 1 - \frac{L_m}{L_r} \right). \quad (8.14\text{b})$$

Hence, a value of  $\Gamma_a = 100\%$  corresponds to a universal model with  $a = L_s/L_m$  and  $L_{\sigma S} = 0$ , conversely setting  $\Gamma_a = -100\%$  gives  $a = L_m/L_r$  and  $L_{\sigma R} = 0$ .

### Vector Representation of the Universal Model

It is instructive to consider the model transformation from a graphical perspective. This may be achieved by considering the flux linkage/current vector (8.5b) and (8.5d) for the original model and representing these in a vector diagram for an arbitrarily chosen set of currents  $\vec{i}_s$  and  $\vec{i}_r$  and a set of inductances  $L_m$ ,  $L_{\sigma S}$ , and  $L_{\sigma R}$ .

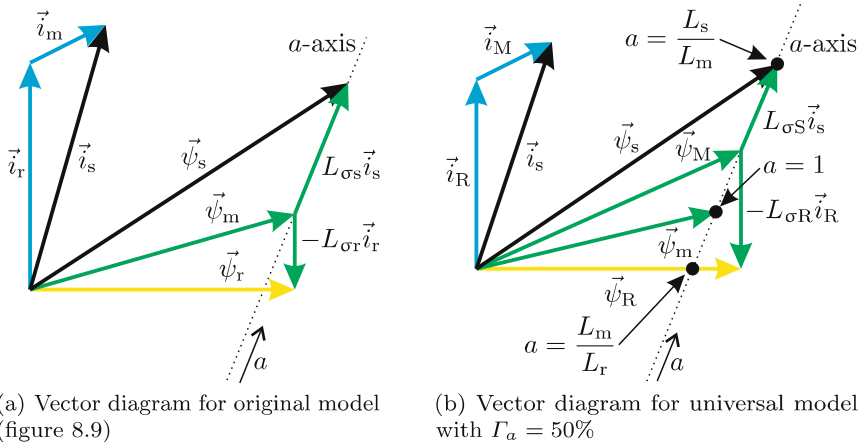


**Fig. 8.11** Comparison of vector diagrams for original and universal induction machine model

An example of such a vector plot is shown in Fig. 8.11(a). A similar exercise can also be undertaken for the universal model which requires access to the flux linkage/current (8.11a) and (8.11b). In this case, the transformation variable must be given a specific value in order to derive the vector plot which corresponds to the current vectors and inductances chosen for the original model. The universal model-based vector diagram as given in Fig. 8.11(b) is shown with a transformation variable of  $\Gamma_a = 50\%$ . Figure 8.11(a) and Fig. 8.11(b) show an  $a$ -axis which is a line defined by the endpoints of the vectors  $\vec{\psi}_s$  and  $\vec{\psi}_m$  respectively. This line is significant because it represents the locus of the vector  $\vec{\psi}_M$  endpoint as function of the transformation variable  $a$  [16]. For any user defined value of  $a$  the transformation defines the

location of the vector  $\vec{\psi}_M$  and corresponding vectors  $\vec{\psi}_R$  and  $\vec{i}_R$ , whereby the latter two vectors are only changed (with respect to the vectors  $\vec{\psi}_r$  and  $\vec{i}_r$ ) in terms of their magnitude (see (8.8)), as may also be observed from Fig. 8.11(b).

### Symbolic Representation of the Universal Model

The universal model in its present form makes use of an ITF module to transform the vectors  $\vec{\psi}_R$  and  $\vec{i}_R$  to their original values  $\vec{\psi}_r$  and  $\vec{i}_r$ . It is from a modeling perspective not strictly necessary to undertake such a transformation provided that the user takes into account the fact that a scaling of these rotor based variables takes place which is dependent on the choice of transformation factor  $a$ . The ITF module may be omitted by relocating the IRTF and rotor resistance  $R_r$  to the primary side of the ITF module. Relocating the IRTF module will not affect the torque but the referred rotor resistance  $R_R$  must be calculated using

$$R_R = a^2 R_r. \quad (8.15)$$

The resultant universal IRTF based symbolic machine model is shown in Fig. 8.12.

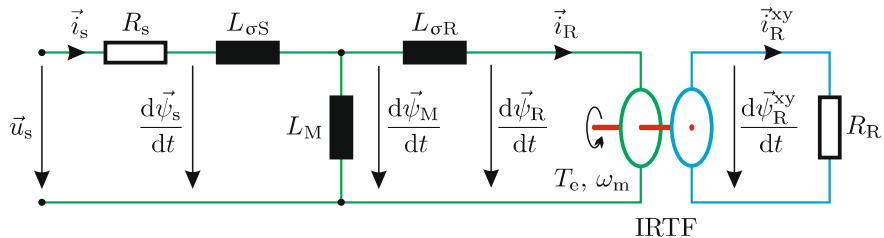


**Fig. 8.12** Universal, IRTF based induction machine model

The corresponding equation set for the universal IRTF based model is of the form:

$$\vec{u}_s = R_s \vec{i}_s + \frac{d\vec{\psi}_s}{dt} \quad (8.16a)$$

$$\vec{\psi}_s = \vec{\psi}_M + L_{\sigma S} \vec{i}_s \quad (8.16b)$$

$$\vec{\psi}_R = \vec{\psi}_M - L_{\sigma R} \vec{i}_R \quad (8.16c)$$

$$\frac{\vec{\psi}_M}{L_M} = \vec{i}_s - \vec{i}_R \quad (8.16d)$$

$$0 = -R_R \vec{i}_R^{xy} + \frac{d\vec{\psi}_R^{xy}}{dt}. \quad (8.16e)$$

The significance of the universal model transformation can be demonstrated by considering the following three values (of which two are chosen at opposite ends of the scale, see (8.13)) for the transformation variable  $a$ , namely:

- $a = \frac{L_m}{L_r}$  ( $\Gamma_a = -100\%$ ): Under these conditions, the model shown in Fig. 8.12 is reduced to two inductances  $L_{\sigma S}$  and  $L_M$ , i.e.,  $L_{\sigma R} = 0$ . Furthermore, the vector  $\vec{\psi}_M$  equals  $\vec{\psi}_R$  as may also be observed with the aid of Fig. 8.11(b). This model will be referred to the *rotor flux based IRTF model*.
- $a = 1$  ( $\Gamma_a = 0\%$ ) The universal model is reduced to the *original five-parameter model* as given in Fig. 8.9.
- $a = \frac{L_s}{L_m}$  ( $\Gamma_a = 100\%$ ) The universal model according to Fig. 8.12 is reduced to an *alternative two-inductance model* with  $L_{\sigma S} = 0$ . Furthermore, the vector  $\vec{\psi}_M$  is equal to  $\vec{\psi}_s$  under these circumstances as may also be observed with the aid of Fig. 8.11(b). This model will be referred to the *stator flux based IRTF model*.

### Generic Representation of the Universal Model

A generic representation of the symbolic model as given in Fig. 8.13 may be developed with the aid of the terminal (8.16a) and (8.16e).

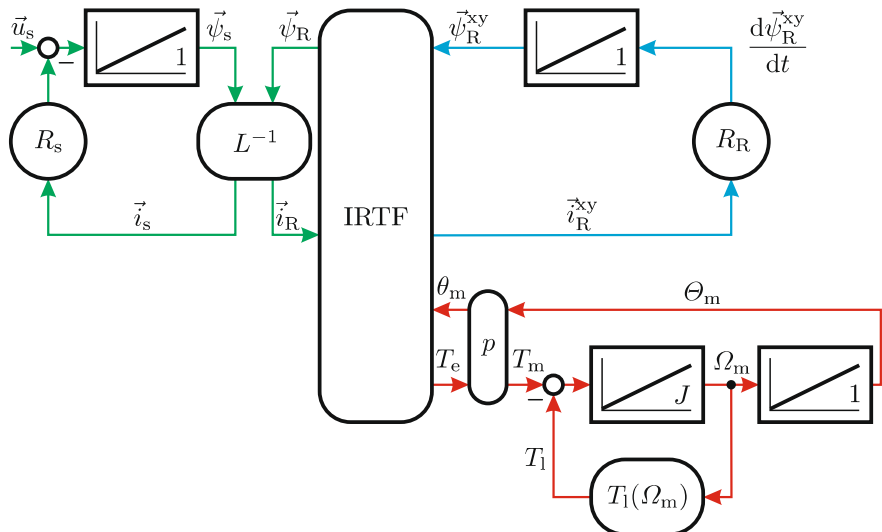


**Fig. 8.13** Generic model representation of a universal IRTF based induction machine

The model in question makes use of a generic module identified by the name  $L^{-1}$  which represents the matrix  $[L^{-1}]$  defined by (8.17).

$$\begin{bmatrix} \vec{i}_s \\ \vec{i}_R \end{bmatrix} = \underbrace{\frac{1}{L_s L_R - (L_M)^2}}_{[L^{-1}]} \begin{bmatrix} L_R & -L_M \\ L_M & -L_s \end{bmatrix} \begin{bmatrix} \vec{\psi}_s \\ \vec{\psi}_R \end{bmatrix} \quad (8.17)$$

with  $L_s = L_M + L_{\sigma S}$  and  $L_R = L_M + L_{\sigma R}$ , where  $L_M$ ,  $L_{\sigma S}$ , and  $L_{\sigma R}$  are defined by (8.12). Expression (8.17) is found with the aid of (8.11) in which the vector  $\vec{i}_M$  is redefined in terms of the current vectors  $\vec{i}_s$  and  $\vec{i}_R$ . The model according to Fig. 8.13 does not generate the vector  $\vec{\psi}_M$  explicitly, instead this variable can be calculated using (8.16c). It is emphasized that this generic model can be used for any transformation factor  $a$  within the range defined by (8.13) without encountering any algebraic loops in the simulation. The reader is reminded of the fact that changes in the transformation variable  $a$  affect the matrix  $L^{-1}$  terms as well as the variable  $R_R$ . In some cases, it is beneficial to represent (8.17) in terms of the variables  $L_m$ ,  $L_{\sigma s}$ , and  $L_{\sigma r}$ , which represent the inductances of the original model (see Fig. 8.9). Use of (8.12) with (8.17) leads to

$$\begin{bmatrix} \vec{i}_s \\ \vec{i}_R \end{bmatrix} = \underbrace{\frac{1}{\sigma_u L_s} \begin{bmatrix} 1 & -\frac{1}{a} \left( \frac{L_m}{L_r} \right) \\ \frac{1}{a} \left( \frac{L_m}{L_r} \right) & -\frac{1}{a^2} \left( \frac{L_s}{L_r} \right) \end{bmatrix}}_{[L^{-1}]} \begin{bmatrix} \vec{\psi}_s \\ \vec{\psi}_R \end{bmatrix} \quad (8.18)$$

where  $\sigma_u = 1 - L_m^2 / (L_s L_r)$  represents the leakage factor [16, 40, 48], which is a machine characteristic and not a function of the transformation variable  $a$ . The tutorial given in Sect. 8.6.2 is directly based on the generic model (see Fig. 8.13) and demonstrates the use of the *universal* transformation concept as discussed in this section.

### 8.3.2.1 Rotor Flux Based IRTF Model

Use of the transformation variable  $a = L_m / L_r$  ( $\Gamma_a = -100\%$ ) with the model according to Fig. 8.12 leads to the symbolic model shown in Fig. 8.14.

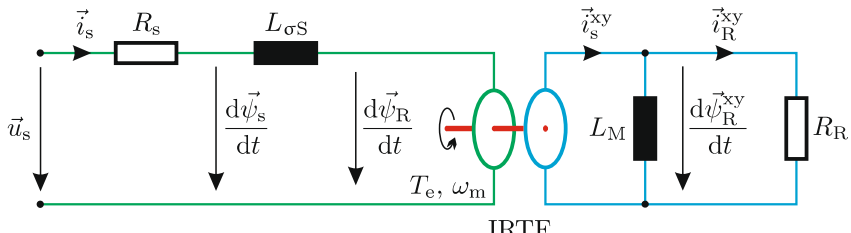


**Fig. 8.14** IRTF based induction machine model with  $a = L_m / L_r$

The corresponding equation set for the rotor flux based IRTF based model is of the form

$$\vec{u}_s = R_s \vec{i}_s + \frac{d\vec{\psi}_s}{dt} \quad (8.19a)$$

$$\vec{\psi}_s = \vec{\psi}_R + L_{\sigma S} \vec{i}_s \quad (8.19b)$$

$$\frac{\vec{\psi}_R^{xy}}{L_M} = \vec{i}_s^{xy} - \vec{i}_R^{xy} \quad (8.19c)$$

$$0 = -R_R \vec{i}_R^{xy} + \frac{d\vec{\psi}_R^{xy}}{dt}. \quad (8.19d)$$

The symbolic model according to Fig. 8.14 will be used for representing the *standard* induction machine. The generic dynamic model as given in Fig. 8.15 corresponds to this symbolic model and equation set (8.19). It is emphasized that the rotor flux based IRTF model is able to accommodate dynamic as well as steady-state operation. However, for the latter a phasor type analysis may be more convenient as will be shown in Sect. 8.3.6.

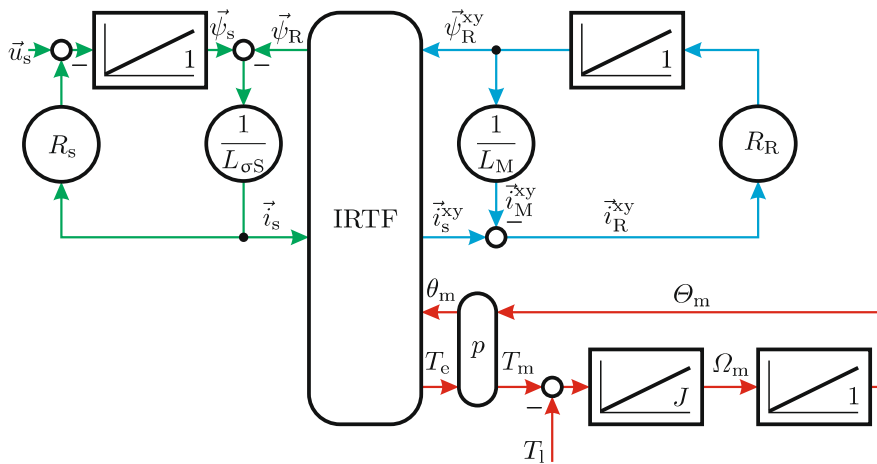


**Fig. 8.15** Four-parameter, IRTF based induction motor model

Note that the IRTF model can be readily extended to include (among others) homopolar effects, rotor skin effect, however such models are not included here as these are outside the scope of this book.

### Tutorial Results

In Sect. 8.6.7, a simulation example is given which is based on the model described above. In this tutorial, the model is used to examine the line start of a 22 kW four-pole delta-connected induction machine. An exam-

ple of the results obtained with this simulation model, as indicated in Fig. 8.16, shows the machine shaft torque, shaft speed, and line current over a 2 s start up sequence, where a load torque step is applied at  $t = 1$  s. The reader is referred to the tutorial given in Sect. 8.6.7 for further details and the opportunity to interactively examine this model concept.

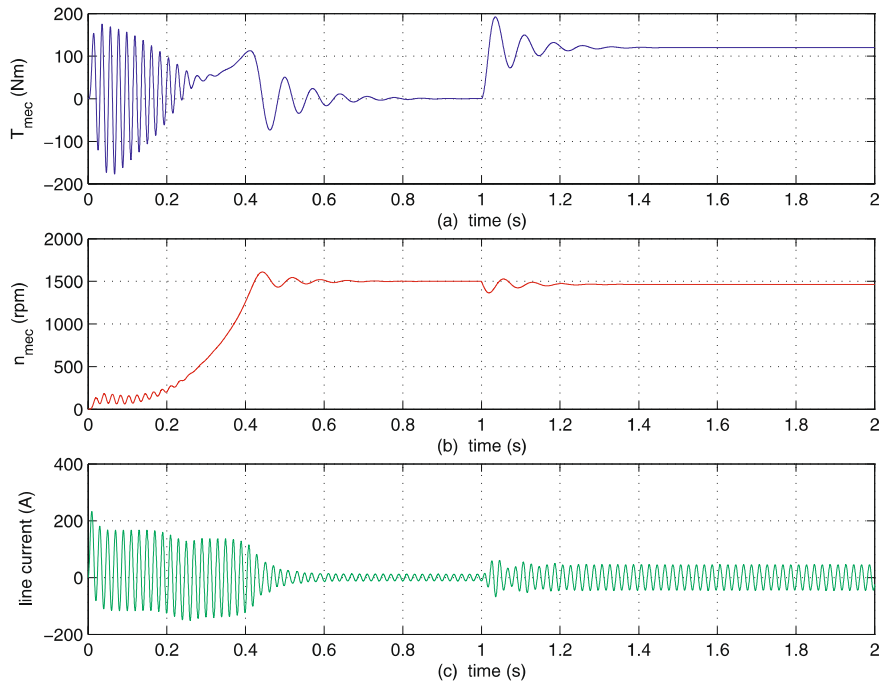


**Fig. 8.16** Line start simulation of a 22 kW delta connected machine, showing shaft torque, speed and line current

### 8.3.2.2 Stator Flux Based IRTF Model

Setting the transformation variable to  $a = L_m/L_r$  ( $\Gamma_a = 100\%$ ) reduces the symbolic model given in Fig. 8.12 to the form shown in Fig. 8.17 [71]. This model is instructive because it shows how the rotor current is affected by the series impedance formed by the leakage inductance  $L_{\sigma R}$  and rotor resistance  $R_R$ .

The corresponding equation set for the stator flux based IRTF model may be found by making use of equation set (8.16) with  $L_{\sigma S} = 0$ ,  $L_M = L_s$ , and  $\vec{\psi}_M = \vec{\psi}_s$ , which gives

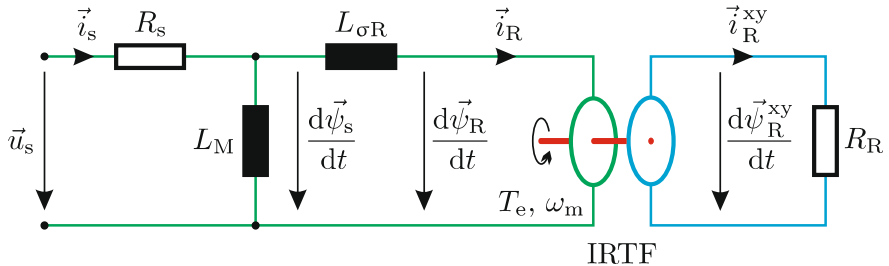


**Fig. 8.17** IRTF based induction machine model with  $a = L_s/L_m$

$$\vec{u}_s = R_s \vec{i}_s + \frac{d\vec{\psi}_s}{dt} \quad (8.20a)$$

$$\vec{\psi}_s = \vec{\psi}_R + L_{\sigma R} \vec{i}_s \quad (8.20b)$$

$$\frac{\vec{\psi}_s}{L_M} = \vec{i}_s - \vec{i}_R \quad (8.20c)$$

$$0 = -R_R \vec{i}_{Rxy} + \frac{d\vec{\psi}_{Rxy}}{dt}. \quad (8.20d)$$

### 8.3.3 Universal Stationary Frame Oriented Model

The IRTF based models introduced in Sect. 8.3.2 have components which are linked to vectors in a stationary as well as a shaft-oriented reference frame. To simplify analysis, a model is derived where all voltage, current, and flux linkage vectors are linked to a *common stationary reference frame*. To realize this aim, the rotor coordinate based (8.16e) must be converted to stationary coordinates. The general space vector conversion required for this task is of the form  $\vec{A} = \vec{A}^{xy} e^{j\theta}$  with  $\theta = \omega_m t$ . The revised rotor based equation in stationary coordinates is of the form

$$0 = -R_R \vec{i}_R + \frac{d\vec{\psi}_R}{dt} - j\omega_m \vec{\psi}_R. \quad (8.21)$$

Use of (8.21) and the stationary frame oriented elements of equation set (8.20) leads to the symbolic model given in Fig. 8.18 which appears in the drives literature with different values for the transformation variable  $a$ . Note that the conversion process used here is convenient when dealing with steady state sinusoidal supplies. In this case, the space vectors that can be readily transformed to stationary phasor diagrams.

The corresponding generic model representation as shown in Fig. 8.19 makes use of the generic module  $L^{-1}$  introduced in the Sect. 8.3.2. A tutorial which is based on the generic model given here is discussed in Sect. 8.6.3.

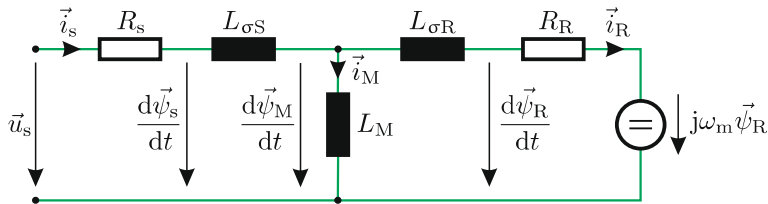


Fig. 8.18 Universal, stationary frame oriented symbolic machine model

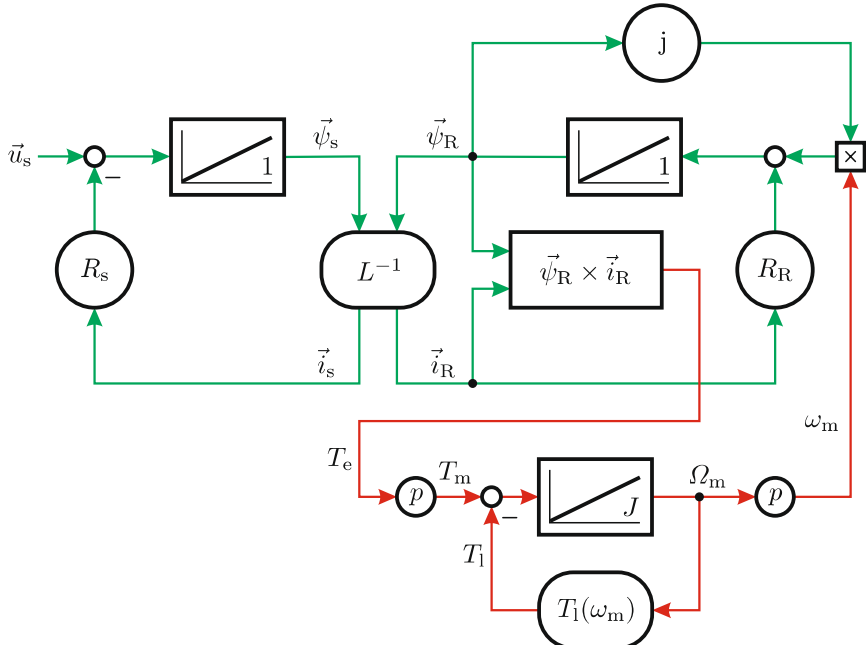


Fig. 8.19 Generic representation, stationary frame oriented model

### 8.3.4 Universal Field-Oriented (UFO) Model

In the machine models discussed previously, the current, voltage, and flux linkage space vectors were defined with respect to a stationary and/or shaft-oriented reference frame. In this section, a so-called *universal field-oriented* (UFO) transformation is introduced where the stator and rotor based space equations are tied to the flux linkage vector  $\vec{\psi}_M$ .

This approach combines the advantages of a universal inductance model, as discussed in Sect. 8.3.2, with a so-called field-oriented transformation that leads to synchronous model representation. The development of UFO based models in this section is particularly instructive for the development of field-oriented control concepts in Chap. 9. In this context, the models to be dis-

cussed are current-excited because vector-controlled drives often utilize some form of current control as discussed in Chap. 3.

### Development of a Symbolic UFO Model

The development of a UFO type model is based on the field-oriented (synchronous) reference frame with a so-called *direct* and *quadrature* axis, i.e.,  $\vec{x}^{\text{dq}} = x_d + jx_q$ . The direct axis is aligned with flux linkage vector  $\vec{\psi}_M$ , hence  $\psi_{Md} = \psi_M$  and  $\psi_{Mq} = 0$ , as can be observed in Fig. 8.20.

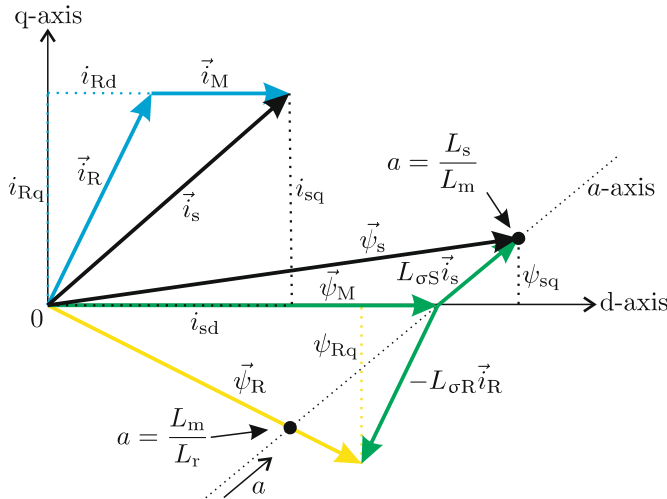


**Fig. 8.20** Vector diagram with direct and quadrature axis

The approach required to derive the symbolic and generic model of the UFO model with leakage inductances  $L_{\sigma S}$  and  $L_{\sigma R}$  (see Fig. 8.12) is similar to the method described for the zero leakage case. Consequently, the coordinate transformation process may be undertaken with the aid of (8.16) and (8.21). However, in this case the stator and rotor flux linkage space vectors  $\vec{\psi}_s$  and  $\vec{\psi}_R$  must in the course of this transformation be expressed in terms of the magnetizing vector  $\vec{\psi}_M$ , given that the d-axis of synchronous reference frame is aligned with this variable (as shown in Fig. 8.20). The equation set for the generalized UFO based model may be written as

$$\vec{u}_s^{\text{dq}} = R_s \vec{i}_s^{\text{dq}} + \frac{d\vec{\psi}_s^{\text{dq}}}{dt} + j\omega_s \vec{\psi}_s^{\text{dq}} \quad (8.22a)$$

$$\vec{\psi}_s^{\text{dq}} = \vec{\psi}_M + L_{\sigma S} \vec{i}_s^{\text{dq}} \quad (8.22b)$$

$$\vec{\psi}_R^{\text{dq}} = \vec{\psi}_M - L_{\sigma R} \vec{i}_R^{\text{dq}} \quad (8.22c)$$

$$\frac{\vec{\psi}_M}{L_M} = \vec{i}_s^{\text{dq}} - \vec{i}_R^{\text{dq}} \quad (8.22d)$$

$$\frac{d\vec{\psi}_R^{dq}}{dt} = R_R \vec{i}_R^{dq} - j(\omega_s - \omega_m) \vec{\psi}_R^{dq}. \quad (8.22e)$$

The symbolic direct and quadrature models, as shown in Fig. 8.21, are found by rearranging equation set (8.22) and by grouping the real and imaginary terms. The real terms for the direct axis model are:

$$u_{sd} = R_s i_{sd} - \omega_s L_{\sigma S} i_{sq} + L_{\sigma S} \frac{di_{sd}}{dt} + \frac{d\psi_M}{dt} \quad (8.23a)$$

$$\frac{\psi_M}{L_M} = i_{sd} - i_{Rd} \quad (8.23b)$$

$$\frac{d\psi_M}{dt} = L_{\sigma R} \frac{di_{Rd}}{dt} - (\omega_s - \omega_m) L_{\sigma R} i_{Rq} + R_R i_{Rd}. \quad (8.23c)$$

The imaginary terms for the quadrature axis model form the following equation set:

$$u_{sq} = R_s i_{sq} + L_{\sigma S} \frac{di_{sq}}{dt} + \omega_s L_{\sigma S} i_{sd} + e_q \quad (8.24a)$$

$$i_{sq} = i_{Rq} \quad (8.24b)$$

$$e_q = L_{\sigma R} \frac{di_{Rq}}{dt} + (\omega_s - \omega_m) L_{\sigma R} i_{Rd} + R_R i_{Rq} + \omega_m \psi_M. \quad (8.24c)$$

The impact of including the leakage inductance components of the machine in the symbolic direct and quadrature models is significant as may be observed by comparing Fig. 8.21 with the zero leakage model in Fig. 8.5. The model complexity increases as the rotor current vector  $\vec{i}_r^{dq}$  is no longer perpendicular to the main magnetizing flux vector  $\vec{\psi}_m$ .

### Development of a Generic UFO Model

The development of a generic stator current model which corresponds to Fig. 8.21 may be undertaken with the aid of (8.23c) and (8.24c), and replacing the variables  $i_{Rd}$  and  $i_{Rq}$  with the variables  $i_{sd}$ ,  $i_{sq}$ , and  $\psi_M$  as defined by (8.23b) and (8.24b). Subsequent mathematical manipulation gives

$$\frac{d}{dt} \left( \frac{L_R}{L_M} \psi_M \right) + \frac{R_R}{L_M} \psi_M = R_R i_{sd} + L_{\sigma R} \frac{di_{sd}}{dt} - \omega_{sl} L_{\sigma R} i_{sq} \quad (8.25a)$$

$$\omega_{sl} \left( \frac{L_R}{L_M} \psi_M - L_{\sigma R} i_{sd} \right) = L_{\sigma R} \frac{di_{sq}}{dt} + R_R i_{sq} \quad (8.25b)$$

with  $L_R = L_{\sigma R} + L_M$  and slip frequency  $\omega_{sl} = (\omega_s - \omega_m)$  as defined previously. Equation (8.25a) yields the basic set of generic modules which are needed to generate the flux linkage variable  $\psi_M$  with inputs  $i_{sd}$ ,  $i_{sq}$ , and  $\omega_{sl}$ . However, to complete this model the slip frequency must also be expressed in terms of the input variables  $i_{sd}$ ,  $i_{sq}$ , and  $\psi_M$ . The latter can readily be achieved by rewriting (8.25b) as follows:

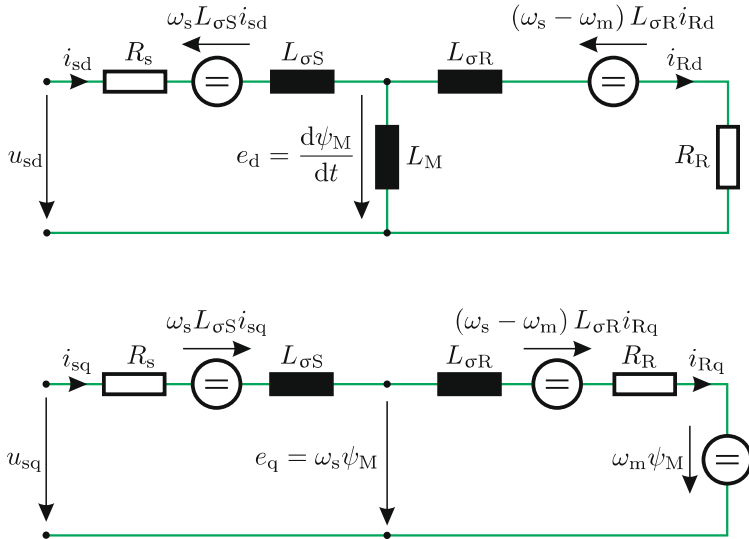


**Fig. 8.21** Symbolic UFO model: direct/quadrature axis configuration, with leakage inductance

$$\omega_{sl} = \frac{L_{\sigma R} \frac{di_{sq}}{dt} + R_R i_{sq}}{\frac{L_R}{L_M} \psi_M - L_{\sigma R} i_{sd}}. \quad (8.26)$$

Equations (8.25) and (8.26) together with the torque equation  $T_e = \psi_M i_{sq}$ , define the complete generic direct/quadrature model of the UFO machine concept shown in Fig. 8.22. Some indication with respect to its functioning is possible at this stage by considering this model without rotor leakage, in which case the parameter  $L_{\sigma R}$  should be set to zero. The model according to Fig. 8.22 is particularly useful for considering two special cases where the d-axis and corresponding  $\vec{\psi}_M$  is aligned with either the rotor flux linkage vector  $\vec{\psi}_R$  or stator flux linkage vector  $\vec{\psi}_s$ . Both cases will be discussed in the next two subsections.

### 8.3.4.1 Rotor Flux Oriented Model

If a transformation value of  $a = L_m/L_r$  is used in the generalized UFO model, a d-axis alignment with the rotor flux linkage vector  $\vec{\psi}_R$  takes place as may be observed from Fig. 8.23. This vector diagram shows the spatial orientation of the current/flux linkage vectors for rotor flux oriented models. As such, this figure is a specific case of the more generalized case shown in Fig. 8.20.

With the present choice of transformation value, the symbolic direct and quadrature models shown in Fig. 8.21 convert to the form indicated in

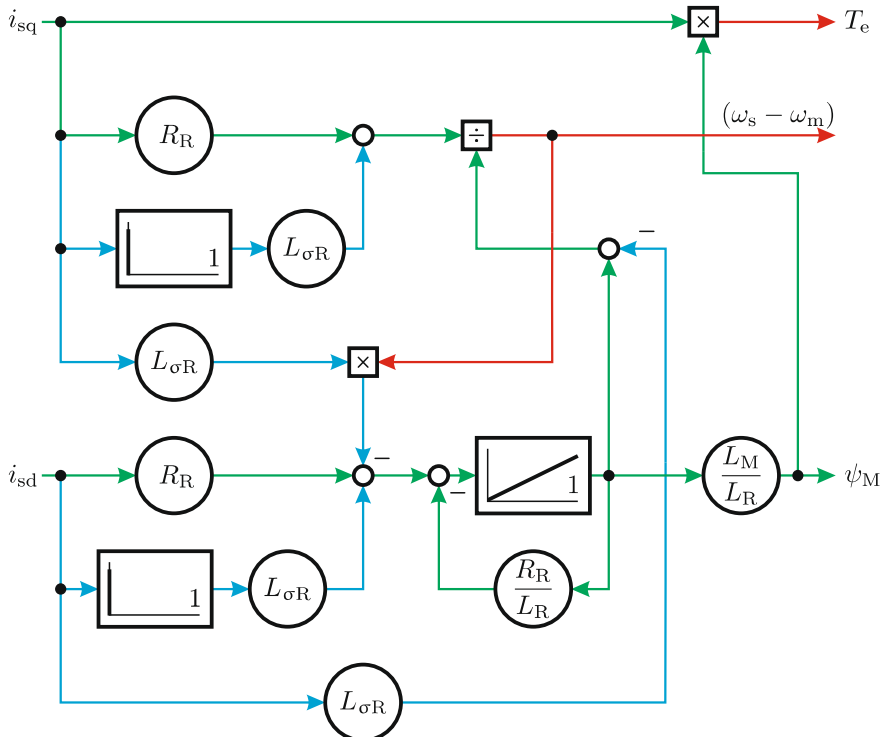


**Fig. 8.22** Generic direct and quadrature UFO based, stator current source induction machine model

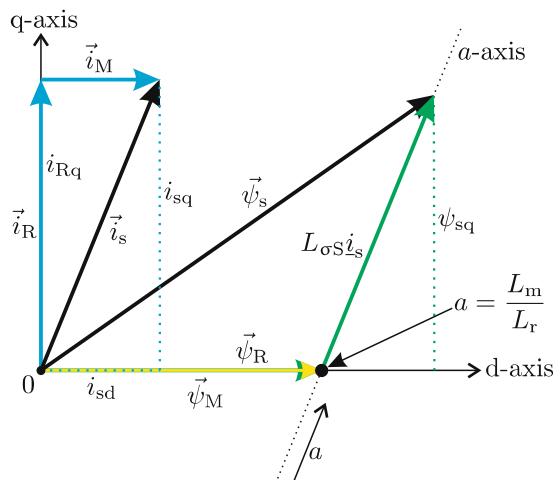


**Fig. 8.23** Rotor flux oriented vector diagram

Fig. 8.24. The reason for this is that the leakage inductance  $L_{\sigma R}$  will be zero for the selected  $a$  value (see (8.12b)).

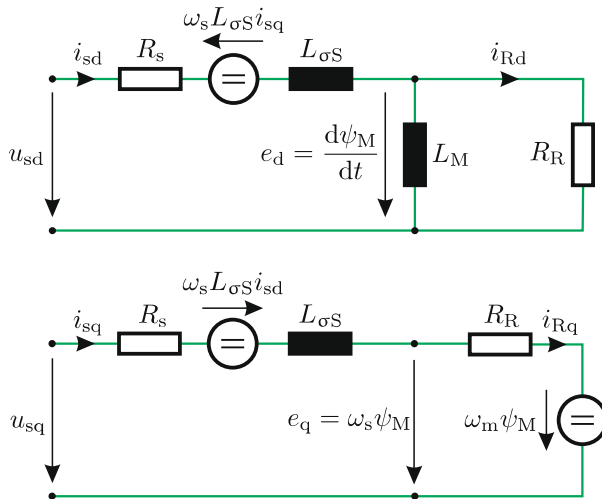
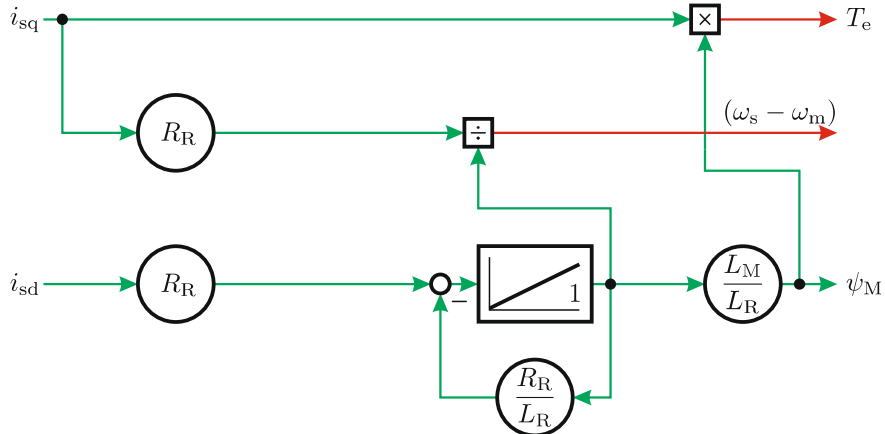


Fig. 8.24 Symbolic rotor flux oriented model: direct and quadrature axis topologies

The implications for the generic model which is linked with the choice of dq coordinates may be observed with the aid of Fig. 8.25. This figure is based on Fig. 8.22 where all  $L_{\sigma R}$  related terms are omitted as  $L_{\sigma R} = 0$  for rotor flux orientation ( $a = L_m/L_r$ ). Under these circumstances, the model reduces to the form given by Fig. 8.6 (where here, due to the choice of  $a$ ,  $R_R$  replaces  $R_r$  and  $L_R$  replaces  $L_m$ ), which represents the zero rotor leakage model. The latter is perhaps not surprising given that the model assumes current excitation, which implies, as may be observed from the symbolic model in Fig. 8.24, that only the voltages  $e_d$  and  $e_q$  are affected by the parameters and variables to the right of these diagrams. An important benefit of a rotor-oriented flux model is that there is a complete decoupling between the direct and quadrature currents. This implies that a change in torque may be undertaken by changing the quadrature current only as may be observed from Fig. 8.6. Likewise, a change in direct current will only affect the flux linkage magnitude  $\psi_M = \psi_r$ . Given the simplicity of these models, they were used first by the inventors of field-oriented control in a time when no digital implementation of the algorithm was possible [7, 27]. A model representation with a single leakage inductance  $L_{\sigma S}$  on the stator side of the magnetizing inductance  $L_M$  is often used.

### Tutorial Results

The tutorial given in Sect. 8.6.5 is based on the UFO generic model concept shown in Fig. 8.22. The current excitation and parameters  $R_r$  and  $L_m$  used



**Fig. 8.25** Block diagram for rotor flux based, current source induction machine model

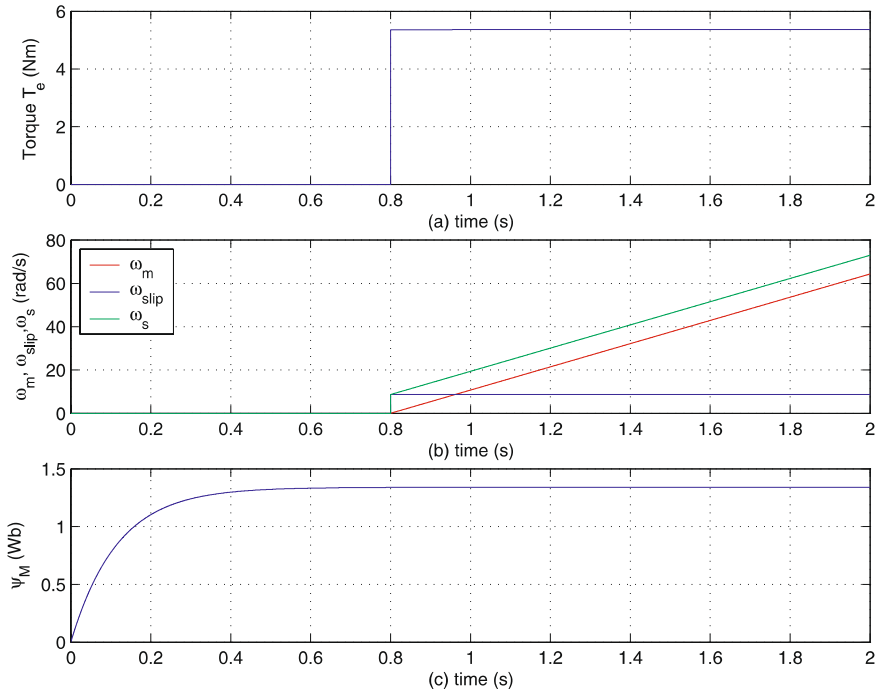
here, to derive the results shown in Fig. 8.26 are the same as those used to derive the zero leakage results given in Fig. 8.7. However, the model has been extended to accommodate the leakage inductance parameters  $L_{\sigma s}$  and  $L_{\sigma r}$  and the transformation variable  $a$  is introduced. Variable  $a$  may be varied to allow the model to be used in any UFO reference. Here, the model is set to a rotor flux oriented reference frame, and the transient results shown in Fig. 8.26 underline the fact that the direct and quadrature models are decoupled, given that a change in the torque does not affect the flux linkage  $\psi_M$ .

A qualitative comparison of the results shown in Fig. 8.7 and Fig. 8.26 demonstrates that the results are similar. This implies that the use of a rotor flux oriented model leads to a transient response which matches that of a machine without leakage inductance. It is precisely the combination of using direct/quadrature current excitation and setting the leakage inductance parameter  $L_{\sigma R}$  to zero which leads to a decoupled model that may be readily used for realizing field-oriented control in a rotor flux oriented reference frame.

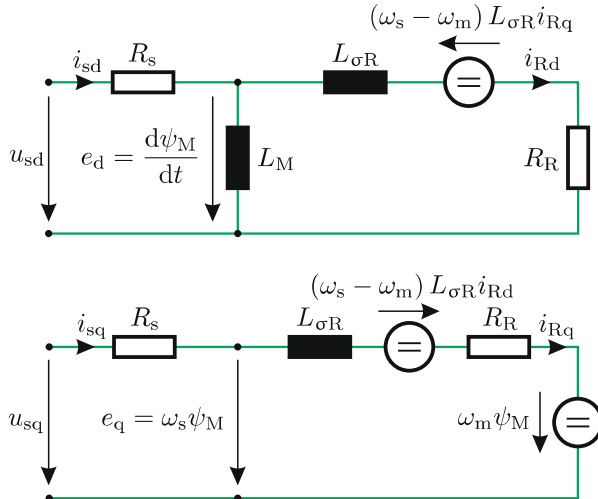
### 8.3.4.2 Stator Flux Oriented Model

If the transformation variable is set to  $a = L_s/L_m$ , the dq symbolic model is reduced from the configuration shown in Fig. 8.21 to that indicated in Fig. 8.27. The reason for this is that the leakage inductance  $L_{\sigma S}$  will be zero for this  $a$  value (see (8.12b)).

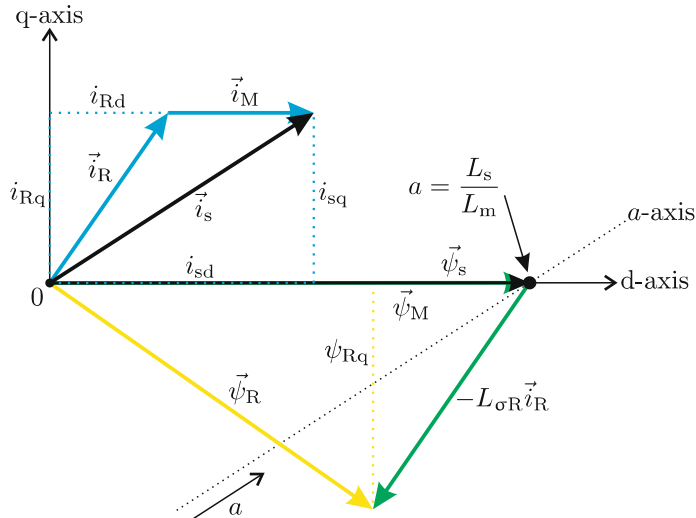
The corresponding vector diagram for this model representation as shown in Fig. 8.28 highlights the fact that the flux linkage vector  $\vec{\psi}_M$  (and therefore the d-axis) is now aligned with the vector  $\vec{\psi}_s$ . A further observation of



**Fig. 8.26** Transient response of rotor flux oriented UFO model



**Fig. 8.27** Symbolic stator flux oriented model: direct/quadrature axis configurations



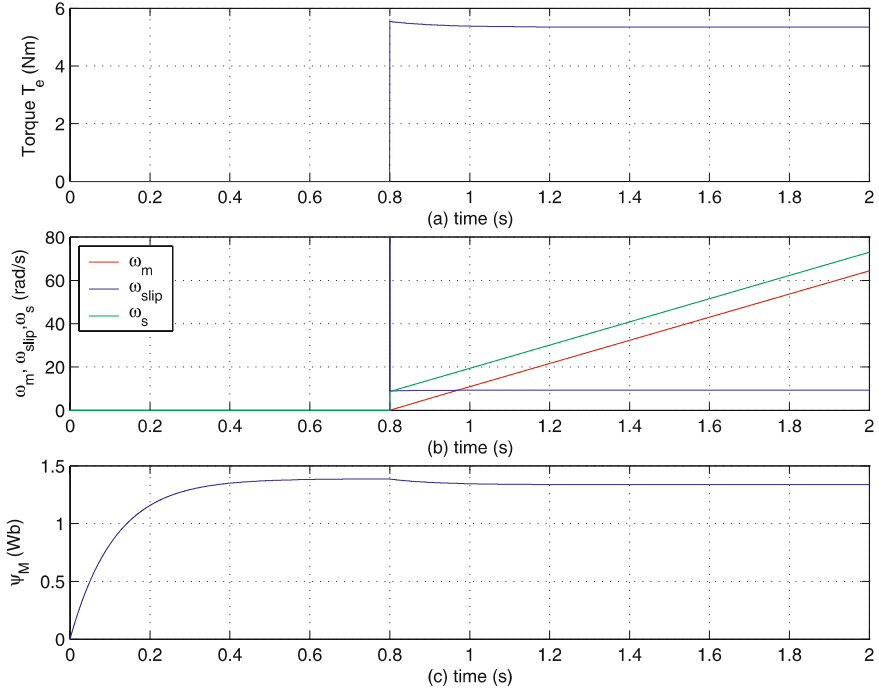
**Fig. 8.28** Stator flux oriented vector diagram

Fig. 8.28 shows that the magnitudes of the vectors  $\vec{\psi}_R$  and  $\vec{i}_R$  are changed. However, their spatial orientation with respect to the vectors  $\vec{\psi}_r$  and  $\vec{i}_r$  remains unaffected. In contrast to the rotor flux oriented symbolic models, the direct and quadrature models exhibit a degree of cross-coupling which is dictated by the leakage inductance  $L_{\sigma R}$ .

### Tutorial Results

The tutorial (see Sect. 8.6.5) used in the previous section for the presentation of machine transient results may be conveniently used in this section, provided that the transformation value is set to  $a = L_s/L_m$ . With this choice of transformation variable, the UFO based simulation model will operate with a stator flux oriented reference frame. The current excitation and machine parameters used to derive the results given in Fig. 8.26 are also applied to the numerical results given in Fig. 8.29.

A qualitative comparison between the results shown in Fig. 8.29 and Fig. 8.26 demonstrates that they are markedly different. For example, a Dirac type response occurs in the slip frequency  $\omega_{sl}$  which in turn appears in the electrical frequency  $\omega_s$ . The cause of this phenomenon is the step change in the quadrature current which leads to an instantaneous change of the flux linkage vector  $\vec{\psi}_s$  with respect the vector  $\vec{\psi}_R$ . In addition to this Dirac function, a step in the slip frequency occurs which leads to a change in the flux linkage  $\psi_M = \vec{\psi}_s$ . The results given in Fig. 8.29 confirm the presence of coupling between the direct and quadrature models and the impact of a torque step on the instantaneous slip frequency. Inverting the model in question for the purpose of developing stator flux oriented control is therefore a more demanding task as will become apparent in Chap. 9.



**Fig. 8.29** Transient response of stator flux oriented UFO model

### 8.3.5 Synchronous Frame Oriented Heyland diagram

As mentioned earlier, most drives assume some type of direct/quadrature axis current control, where the flux linkage  $\psi_M$  is maintained at a constant value. It is therefore of interest to consider the quasi-stationary stator current  $\vec{i}_s^{dq}$  locus under varying slip conditions and constant flux linkage  $\psi_M$ . This analysis may be undertaken by considering the *steady-state* form of (8.23c) and (8.24c) which upon elimination of  $\omega_{sl} = (\omega_s - \omega_m)$  and after some mathematical manipulation leads to:

$$\left( i_{sd} - \frac{\psi_M}{2} \left( \frac{1}{L_{\sigma R}} + \frac{1}{L_M} \right) \right)^2 + i_{sq}^2 = \frac{\psi_M^2}{4} \left( \frac{1}{L_{\sigma R}} - \frac{1}{L_M} \right)^2. \quad (8.27)$$

This expression represents a circle in the complex dq plane with its center at coordinates  $(\psi_M/2(1/L_{\sigma R} + 1/L_M), 0)$  and radius  $\psi_M/2(1/L_{\sigma R} - 1/L_M)$  as indicated in Fig. 8.30(a). This type of current locus diagram, known as a *Heyland diagram* [28, 29, 36] shows the interaction between the stator current vector  $\vec{i}_s$  (in this case represented in synchronous coordinates), the torque  $T_e$  and the slip frequency  $\omega_{sl}$ . The circle shows that a given  $\psi_M$  value corresponds to a maximum quadrature current and maximum torque  $T_e^{\max}$  value.

In practice, this maximum quadrature current value is normally outside the rated value, given that  $L_{\sigma R} \ll L_M$ . The influence of the transformation vari-

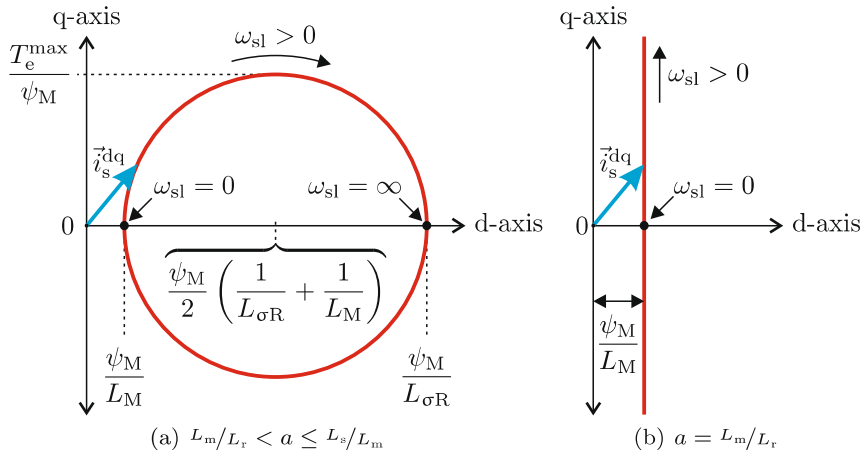


**Fig. 8.30** Current locus  $\vec{i}_s^{dq}$  for UFO model and two transformation values

able is clearly apparent in Fig. 8.30(b) given the dependency of the latter on the parameters  $L_{\sigma R}$  and  $L_M$  (see (8.12)). When this transformation ratio is changed from  $L_s/L_m \rightarrow L_m/L_r$  the radius increases to infinity, given the variation of the leakage inductance from  $L_{\sigma R} \rightarrow 0$ . This implies that the current locus at  $a = L_m/L_r$  is reduced to a straight line as shown in Fig. 8.30(a).

### 8.3.6 Steady-State Analysis of Voltage-Source-Connected Induction Machines

The steady-state characteristics of the induction machine are studied with the aid of Fig. 8.14, where it is assumed that the stator is connected to a three-phase sinusoidal supply which is represented by the space vector  $\vec{u}_s = \hat{u}_s e^{j\omega_s t}$ . The basic characteristics of the machine are deemed to be the Heyland diagram of the  $p$  pole pair machine and torque/speed curve. For the development of this type of model, it is helpful to redefine the relevant space vector equations in terms of phasors. The general relationship in steady-state between a space vector  $\vec{x}$  and phasor  $x$  is of the form  $\vec{x} = x e^{j\omega_s t}$  [68]. Given this relationship, the supply voltage phasor may be expressed as  $\underline{u}_s = \hat{u}_s$ . Furthermore, the phasor representation of the rotor flux linkage on the stator and rotor side of the IRTF may be written as

$$\vec{\psi}_R = \underline{\psi}_R e^{j\omega_s t} \quad (8.28a)$$

$$\vec{\psi}_R^{xy} = \underline{\psi}_R e^{j(\omega_s t - \theta)} \quad (8.28b)$$

where  $\theta$  is equal to  $\omega_m t$  (constant speed operation). Use of (8.19) and (8.28) leads to the following phasor based equation set for the machine

$$\underline{u}_s - \underline{e}_R = R_s \underline{i}_s + j\omega_s L_{\sigma S} \underline{i}_s \quad (8.29a)$$

$$\underline{e}_R = j\omega_s \underline{\psi}_R \quad (8.29b)$$

$$\underline{e}_R^{xy} = j(\omega_s - p\omega_m) \underline{\psi}_R \quad (8.29c)$$

$$\underline{i}_R^{xy} = \frac{\underline{e}_R^{xy}}{R_R} \quad (8.29d)$$

$$\underline{\psi}_R^{xy} = L_M (\underline{i}_s^{xy} - \underline{i}_R^{xy}). \quad (8.29e)$$

Elimination of the flux linkage phasor from (8.29b) and (8.29c) leads to an expression for the air-gap EMF on the stator and rotor side of the IRTF namely

$$\underline{e}_R^{xy} = \underline{e}_R s \quad (8.30)$$

where  $s$  is known as the slip of the machine and is given by

$$s = 1 - \frac{\omega_m}{\omega_s}. \quad (8.31)$$

The slip according to (8.31) is simply the ratio between the rotor rotational frequency  $\omega_{sl} = \omega_s - \omega_m$  (as apparent on the rotor side of the IRTF) and the stator rotational frequency  $\omega_s$ . The Heyland diagram for this model is found by making use of (8.29) which leads to the following expression for the phasor based stator current:

$$\underline{i}_s = \frac{\hat{u}_s \left( \frac{R_R}{s} + j\omega_s L_M \right)}{j\omega_s L_M \frac{R_R}{s} + (R_s + j\omega_s L_{\sigma S}) \left( \frac{R_R}{s} + j\omega_s L_M \right)}. \quad (8.32)$$

The equivalent circuit which corresponds with (8.32) is shown in Fig. 8.31.

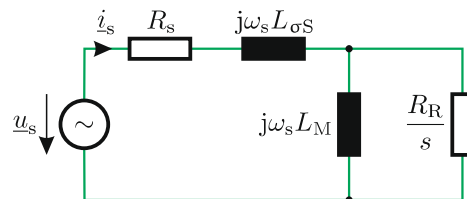


**Fig. 8.31** Equivalent circuit of an induction machine with  $L_{\sigma S}$ ,  $R_s$  and  $L_M$ , and voltage source (steady-state version of dynamic model in Fig. 8.14)

A normalization of expression (8.32) is convenient, which is of the form  $\underline{i}_s^n = \underline{i}_s / (\hat{u}_s / \omega_s L_{\sigma S})$ . An example of an Heyland diagram as calculated using (8.32) (in normalized form) is given in Fig. 8.32(a), for a slip range of  $-1 \leq s \leq 1$  using parameters of the 22 kW machine discussed in the tutorial linked to this part of the book (see Sect. 8.6.8).

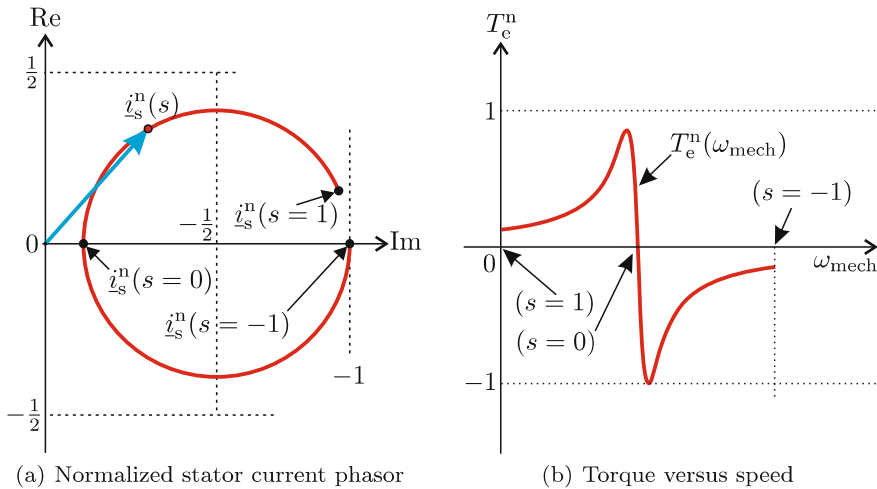


**Fig. 8.32** Steady-state characteristics of voltage source connected induction machine, complete model according to Fig. 8.31

The corresponding torque  $T_e$  of this machine may be calculated as

$$T_e = \frac{1}{\omega_s} \underbrace{(\Re \{\underline{u}_s \underline{i}_s^*\} - R_s \underline{i}_s \underline{i}_s^*)}_{p_{\text{air-gap}}} \quad (8.33)$$

Equation (8.33) underlines the fact that the torque can be calculated on the basis of the *air-gap power*  $p_{\text{air-gap}}$ , i.e., the power which crosses the air-gap to the rotor (see (8.36)). A normalization of (8.33) (as introduced in [68]) of the form  $T_e^n = T_e / \hat{T}_e$ , with  $\hat{T}_e = \hat{u}_s^2 / 2\omega_s^2 L_{\sigma S}$  leads, with the aid of (8.32), to the torque speed curve given in Fig. 8.32(b).

## 8.4 Parameter Identification and Estimates for Stator and Rotor Flux Linkage Magnitude

The direct and quadrature stator flux model as given by Fig. 8.27 is also useful in terms of obtaining estimates for the parameters  $L_s$ ,  $L_{\sigma R}$ , and  $R_R$  on the basis of the measured stator resistance  $R_s$ , measured no-load stator

current, and given nameplate data. Furthermore, the approach given here provides a guideline for the flux linkage magnitudes to be used for vector control. The first part of this section outlines the calculation steps which leads to these parameters. Under no-load steady-state conditions, the stator flux oriented model is greatly simplified given that  $i_{sq} = 0$  and  $\omega_m = \omega_s$ . This means that the d-axis and q-axis voltages are given by  $u_{sd} = R_s i_{sd}$  and  $u_{sq} = \omega_s \vec{\psi}_s$  respectively. The no-load stator current (vector amplitude)  $i_s^{noload} = i_{sd}$ . Consequently, the stator flux linkage can be calculated according to

$$\psi_s = \frac{1}{\omega_s} \sqrt{u_s^2 - (R_s i_s^{noload})^2} \quad (8.34)$$

where  $u_s$  represents the applied rated stator voltage (vector amplitude, power invariant). The self inductance  $L_s = L_M$  is, according to Fig. 8.27, of the form

$$L_s = \frac{\psi_s}{i_s^{noload}} \quad (8.35)$$

where  $\psi_s$  is calculated using (8.34). An estimate for the rotor resistance  $R_R$  is found by considering Fig. 8.27 under steady-state rated torque conditions. Hence, we assume the machine is operating at its nameplate rated speed value  $\omega_m^{nom}$  (electrical rated shaft speed in  $rad/s$ ). The rated electrical torque  $T_e^n$  is then estimated by calculating the so-called *air-gap power*  $T_e \omega_s$ , which is equal to the terminal input power minus the stator copper losses which gives

$$T_e^{nom} = \frac{1}{\omega_s} \left( \underbrace{u_s i_s^{nom} \cos(\rho_s)}_{p_{in}} - R_s (i_s^{nom})^2 \right) \quad (8.36)$$

where  $\omega_s$  represents the electrical stator frequency  $2\pi f$ , with frequency  $f$  in Hz. The variable  $i_s^{nom}$  represents the rated stator current vector amplitude, while  $\rho_s$  represents the angle between the stator voltage vector and stator current vector (this parameter comes directly from the nameplate data, i.e., power factor). On the basis of the rated torque we can calculate the rated quadrature current  $i_{sq}^{nom}$  using (8.34) and (8.36) as

$$i_{sq}^{nom} = \frac{T_e^n}{\psi_s}. \quad (8.37)$$

From the quadrature model, shown in Fig. 8.27, we can derive, under steady-state rated conditions, the voltage equation  $e_{sq} = (\omega_s - \omega_m)L_{\sigma R} i_{sd} + R_R i_{sq} + \omega_m \psi_s$ , which under the assumption of  $L_{\sigma R} i_{sd} \ll \psi_s$  reduces to

$$R_R \simeq \frac{(\omega_s - \omega_m^{nom}) \psi_s}{i_{sq}^{nom}} \quad (8.38)$$

The remaining parameter, being the leakage inductance  $L_{\sigma R}$ , comes from Fig. 8.30(a) (with  $a = L_s/L_m$ ). This figure shows that the direct axis current

value  $i_{sd}$  increases as the torque increases. The Heyland diagram circle is a direct function of the leakage. It may be shown that we can approximate the direct current  $i_{sd}$  versus  $i_{sq}$  function as

$$i_{sd} \simeq \underbrace{\frac{\psi_s}{L_s}}_{i_s^{noload}} + L_{\sigma R} \frac{i_{sq}^2}{\psi_s}. \quad (8.39)$$

Equation (8.39), when used under rated conditions, i.e.,  $i_{sd} = i_{sd}^{nom}$  and  $i_{sq} = i_{sq}^{nom}$ , gives us a direct estimate for the leakage inductance namely

$$L_{\sigma R} \simeq (i_{sd}^{nom} - i_s^{noload}) \frac{\psi_s}{(i_{sq}^{nom})^2} \quad (8.40)$$

where  $i_{sd}^{nom}$  is calculated using the stator current  $i_s^{nom}$  and (8.37) as

$$i_{sd}^{nom} = \sqrt{(i_s^{nom})^2 - (i_{sq}^{nom})^2}. \quad (8.41)$$

The conversion to a model with  $a = 1$  is based on the assumption of equal rotor and stator leakage inductances, i.e.,  $L_{\sigma s} = L_{\sigma r}$  and  $L_s = L_r$ . Use of (8.12b), with  $a = L_s/L_m$  gives

$$L_m = \sqrt{\frac{L_s^3}{L_{\sigma R} + L_s}} \quad (8.42a)$$

$$L_{\sigma s} = L_s - L_m \quad (8.42b)$$

$$R_r = \left(\frac{L_m}{L_s}\right)^2 R_r. \quad (8.42c)$$

The stator flux linkage magnitude  $\psi_s$  as given by (8.34) and rated currents  $i_{sd}^{nom}$  and  $i_{sq}^{nom}$  provides the basis for calculating a value for the flux linkage  $\psi_M$  and use of (8.16b), namely

$$\psi_{Md} = \psi_s - L_{\sigma S} i_{sd}^{nom} \quad (8.43a)$$

$$\psi_{Mq} = -L_{\sigma S} i_{sq}^{nom} \quad (8.43b)$$

which leads to the required flux linkage magnitude  $\psi_M$  for any given transformation value  $a$ .

$$\psi_M = \sqrt{\psi_{Md}^2 + \psi_{Mq}^2} \quad (8.44)$$

The tutorial at the end of this chapter gives an example of using this approach for calculating the rated flux linkage values and motor parameters for a given machine.

## 8.5 Single-Phase Induction Machines

In this section, we will consider the use of the IRTF based concept for representing single-phase, squirrel-cage based induction machines. The machine in question is provided with two orthogonal-oriented stator windings referred to as the *run winding* (main winding) and *auxiliary winding* respectively as indicated in Fig. 8.33. The number of winding turns per phase may in this case differ, hence the phase resistance of the run winding and auxiliary winding are defined as  $R_{\text{aux}}$  and  $R_{\text{run}}$  respectively. Furthermore, a factor  $k_{\text{aux}}$  is introduced which represents the auxiliary-to-run winding turns ratio. A single-phase sinusoidal supply is assumed which is directly connected to the run winding.

### Types of Single-Phase Induction Machines

There are various types of single-phase induction machines. For so-called *split-coil* machines, the auxiliary winding is also connected directly to the supply source. For *capacitor-start* type machines, a capacitor  $C$  is placed in series with the auxiliary winding and the supply (see Fig. 8.33) and a shaft speed operated switch (also shown in Fig. 8.33) disconnects the auxiliary winding when the speed reaches a predetermined operating speed. So-called *capacitor-run* machines, first proposed by Steinmetz, are provided with a fixed capacitor between supply and winding which removes the need for a switch. A combination of phase winding topologies described above are found in the industry, hence it is of interest to present a generalized modeling approach in this section which will allow the user to examine the dynamic and steady-state behavior of such machines.

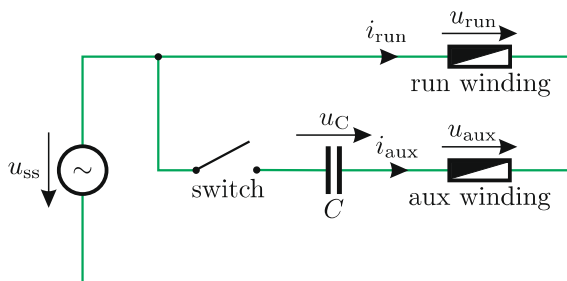


**Fig. 8.33** Generalized wiring diagram of single-phase motor

### Dynamic Model of Single-Phase Induction Machine

A convenient starting point for this modeling process is the rotor flux based machine model discussed in Sect. 8.3.2.1. The use of a space vector model is particularly helpful given that this is in fact a two-phase representation of the induction machine. On the stator side of the IRTF components and variables

linked to the  $\alpha$ -axis may, for example, be assigned to the auxiliary winding as is the case in this section. With this choice of axis assignment, the run winding parameters and variables are tied to the  $\beta$ -space vector axis hence the supply voltage and current space vectors  $\vec{u}_{ss}$  and  $\vec{i}_{ss}$  may be written as

$$\vec{u}_{ss} = u_{aux} + j u_{run} \quad (8.45a)$$

$$\vec{i}_{ss} = i_{aux} + j i_{run} \quad (8.45b)$$

where  $u_{aux}$ ,  $u_{run}$ ,  $i_{aux}$ , and  $i_{run}$  are given in Fig. 8.33. For the generalized model assumed here, a capacitor  $C$  is connected in series with the auxiliary winding in which case the winding voltage  $u_{aux}$  may be found using

$$u_{aux} = u_{ss} - \frac{1}{C} \int i_{aux} dt \quad (8.46)$$

where  $u_{ss}$  represents the supply voltage to the machine which is arbitrarily defined as

$$u_{ss} = \hat{u}_{ss} \cos \omega_s t. \quad (8.47)$$

The development of a symbolic model for single-phase induction machines is readily initiated by considering the rotor flux based IRTF model according to Fig. 8.14. The parameters  $L_{\sigma S}$ ,  $L_M$ , and  $R_R$  used to model standard three-phase machines as discussed in Sect. 8.3.2.1 are based on the stator referred parameters  $L_{\sigma S}$ ,  $L_{\sigma S}$ ,  $L_m$ , and  $R_r$ . Here, the number of turns on the run and auxiliary winding may differ and a choice needs to be made in terms of referring said parameters to a specific winding. The run winding is assigned as the reference winding and the machine parameters are referred to this winding. The resulting symbolic model for the single-phase machine as given in Fig. 8.34 has resemblance with the rotor flux based machine model for the three-phase machine from Fig. 8.14 which was the starting point of the modeling process.

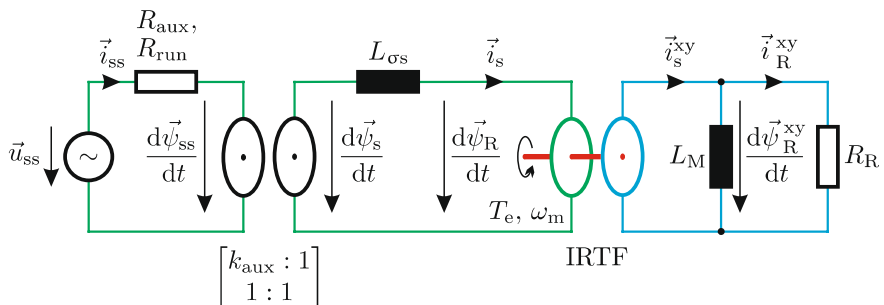


**Fig. 8.34** IRTF/ITF based symbolic model for single-phase induction machine

However, in this case an *asymmetric* ITF module is introduced in order to accommodate the difference in run/auxiliary winding turns. The latter is achieved by introducing an ITF module where the  $\alpha$ -axis (assigned to the auxiliary winding) winding ratio is set to  $k_{\text{aux}} : 1$ , while the  $\beta$ -axis winding ratio is set to unity. The ITF equation set is therefore of the form

$$i_{s\alpha} = k_{\text{aux}} i_{\text{aux}} \quad (8.48a)$$

$$i_{s\beta} = i_{\text{run}} \quad (8.48b)$$

while the corresponding ITF flux linkages may be defined as

$$\psi_{\text{aux}} = k_{\text{aux}} \psi_{s\alpha} \quad (8.49a)$$

$$\psi_{\text{run}} = \psi_{s\beta} \quad (8.49b)$$

where the variables  $\psi_{\text{aux}}$  and  $\psi_{\text{run}}$  are introduced which are linked with the space vector  $\vec{\psi}_{ss} = \psi_{\text{aux}} + j\psi_{\text{run}}$ . The equation set which corresponds to Fig. 8.34 is of the form

$$u_{\text{aux}} = R_{\text{aux}} i_{\text{aux}} + \frac{d\psi_{\text{aux}}}{dt} \quad (8.50a)$$

$$u_{\text{run}} = R_{\text{run}} i_{\text{run}} + \frac{d\psi_{\text{run}}}{dt} \quad (8.50b)$$

$$\vec{\psi}_s = \vec{\psi}_R + L_{\sigma s} \vec{i}_s \quad (8.50c)$$

$$\frac{\vec{\psi}_R^{xy}}{L_M} = \vec{i}_s^{xy} - \vec{i}_R^{xy} \quad (8.50d)$$

$$\vec{e}_R^{xy} = \frac{d\vec{\psi}_R^{xy}}{dt} \quad (8.50e)$$

$$\vec{e}_R^{xy} = R_R \vec{i}_R^{xy} \quad (8.50f)$$

where the parameters  $R_{\text{aux}}$  and  $R_{\text{run}}$  represent the resistance of the auxiliary and run winding respectively. Note that the single-phase symbolic model and corresponding equation set reduce to the rotor flux oriented model from Sect. 8.3.2.1 in case the auxiliary and run windings are identical in terms of the winding configuration. Under these circumstances, the phase resistances will be equal and the winding ratio  $k_{\text{aux}}$  will be equal to 1, in which case the ITF module can be omitted from the symbolic diagram.

The generic model as given by Fig. 8.35 which corresponds to the symbolic model shown in Fig. 8.34 and equation set (8.50) shows the introduction of scalar variables on the primary side of the (asymmetric) ITF module.

## Tutorial Results

In Sect. 8.6.9, a simulation example is given which is based on the model described above. In this tutorial, the model is used to examine the line start of a 150 W four-pole, capacitor-run type single-phase induction machine. For this purpose, the model voltage input  $u_{\text{run}}$  is connected to a 50 Hz sinusoidal

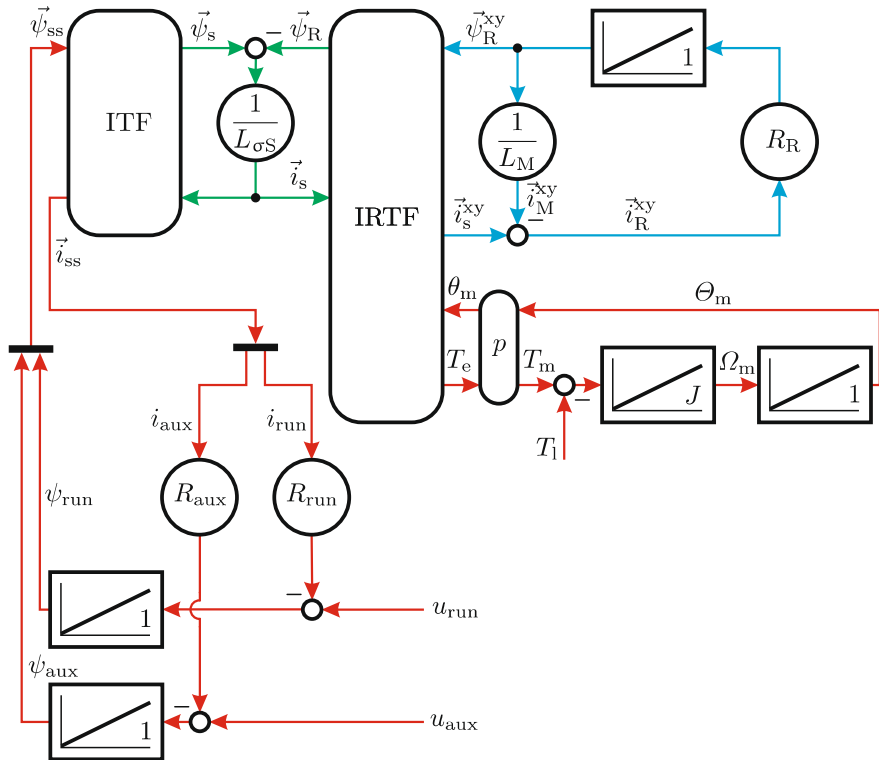
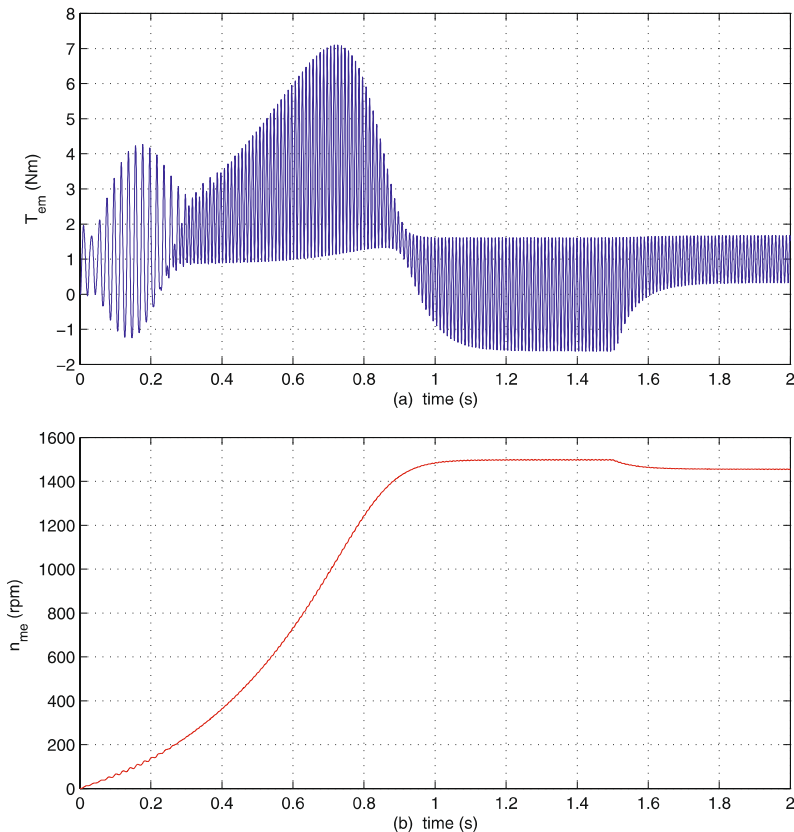


Fig. 8.35 Generic model for single-phase induction machines

voltage source as defined by (8.47). Furthermore, the model voltage  $u_{aux}$  is derived with the aid of (8.46) which may be implemented with the aid of an additional integrator module and gain module with gain  $1/C$ . An example of the results obtained with this simulation model, as indicated in Fig. 8.36, shows the machine shaft torque and shaft speed during a 2 s start-up sequence where a load torque step is applied at  $t = 1.5$  s. The reader is referred to the tutorial given in Sect. 8.6.9 for further details and the opportunity to interactively examine this model concept.

It is emphasized that the capacitor-run machine model can be readily adapted to different single-phase machine concepts. For the purpose of modeling a capacitor start machine, a speed dependent switch may be introduced which purposely sets the auxiliary winding resistance  $R_{aux}$  to a substantially larger (in comparison with the auxiliary winding resistance) value. For the purpose of modeling a split-phase induction machine, the capacitor gain module  $1/C$  may be simply set to zero in which case both voltage inputs of the model are connected to the same sinusoidal voltage source. Modeling of, for example, a TRIAC controlled single-phase machine can be undertaken by



**Fig. 8.36** Line start example of a capacitor-run single-phase induction machine

the introduction of circuit based CASPOC elements such as a TRIAC and a circuit/block conversion module (see Fig. 3.28).

### 8.5.1 Steady-State Analysis of Capacitor-Run Single-Phase Induction Machines

A phasor based analysis of the generalized single-phase model is considered here to determine the steady-state run and auxiliary peak (or RMS) currents, average torque, and torque ripple as function of the shaft speed for capacitor-run single-phase induction machines.

#### Capacitor as Integral Part of the Machine

For the purpose of this analysis, it is helpful to consider the capacitor in series with the auxiliary winding as an integral part of the machine, i.e., instead of

defining the stator voltage space vector  $\vec{u}_{ss}$  as

$$\vec{u}_{ss} = u_{aux} + j u_{run}$$

as in (8.45) we redefine it as

$$\vec{u}_{ss} = u_{ss\alpha} + j u_{ss\beta} \quad (8.51)$$

where  $u_{ss\alpha}$  is now the voltage drop over the capacitor in series with the auxiliary winding while  $u_{ss\beta}$  remains the resulting voltage drop over the run winding, compare Fig. 8.33. Due to the parallel connection to the single-phase supply voltage, both  $u_{ss\alpha}$  and  $u_{ss\beta}$  equal  $u_{ss}$  (with  $u_{ss}$  defined in (8.47)). The orientation of the space vector components with the auxiliary winding in the  $\alpha$ -direction and the run winding in the  $\beta$ -direction remains unchanged.

For  $u_{ss\alpha}$ , (8.50a) is substituted into (8.46) which leads to

$$\begin{aligned} u_{ss\alpha} &= u_{aux} + \frac{1}{C} \int i_{aux} dt \\ \Leftrightarrow u_{ss\alpha} &= R_{aux} i_{aux} + \frac{1}{C} \int i_{aux} dt + \frac{d\psi_{aux}}{dt} \end{aligned} \quad (8.52)$$

where  $u_{ss}$  is defined by (8.47). The run winding is directly connected to the supply source and hence  $u_{ss\beta}$  is formed by

$$\begin{aligned} u_{ss\beta} &= u_{run} \\ \Leftrightarrow u_{ss\beta} &= R_{run} i_{run} + \frac{d\psi_{run}}{dt}. \end{aligned} \quad (8.53)$$

### Phasor Notation of Voltage Equations

In steady-state, the auxiliary and run voltages  $u_{ss\alpha}$  and  $u_{ss\beta}$  are sinusoidal functions of time. A sinusoidal quantity is represented by the expression  $u = \hat{u} \cos(\omega_s t + \rho)$  and can be expressed as  $u = \Re\{\underline{u} e^{j\omega_s t}\}$  where the phasor  $\underline{u} = \hat{u} e^{j\rho}$  is introduced. In phasor notation and matrix format, (8.52) and (8.53) can therefore be rewritten as

$$\begin{bmatrix} \underline{u}_{ss\alpha} \\ \underline{u}_{ss\beta} \end{bmatrix} = \begin{bmatrix} \underline{Z}_{aux} & 0 \\ 0 & R_{run} \end{bmatrix} \begin{bmatrix} \underline{i}_{run} \\ \underline{i}_{aux} \end{bmatrix} + j\omega_s \begin{bmatrix} \underline{\psi}_{aux} \\ \underline{\psi}_{run} \end{bmatrix} \quad (8.54)$$

where the impedance  $\underline{Z}_{aux} = R_{aux} + 1/j\omega_s C$ .

Equation set (8.54) is now referred to the secondary side of the ITF module shown in Fig. 8.34. This is achieved by multiplying (8.54) by a factor  $1/k_{aux}$  which gives

$$\begin{bmatrix} \underline{u}_{s\alpha} \\ \underline{u}_{s\beta} \end{bmatrix} = \underbrace{\begin{bmatrix} \underline{Z}_{s\alpha} & 0 \\ 0 & R_{s\beta} \end{bmatrix}}_{\underline{Z}_{sp}} \begin{bmatrix} \underline{i}_{s\alpha} \\ \underline{i}_{s\beta} \end{bmatrix} + j\omega_s \begin{bmatrix} \underline{\psi}_{s\alpha} \\ \underline{\psi}_{s\beta} \end{bmatrix} \quad (8.55)$$

with

$$\begin{aligned}\underline{u}_{s\alpha} &= \frac{\underline{u}_s}{k_{aux}} \\ \underline{u}_{s\beta} &= \underline{u}_s \\ \underline{i}_{s\alpha} &= k_{aux} \underline{i}_{aux} \\ \underline{i}_{s\beta} &= \underline{i}_{run} \\ \underline{\psi}_{s\alpha} &= \frac{\underline{\psi}_{aux}}{k_{aux}} \\ \underline{\psi}_{s\beta} &= \underline{\psi}_{run}\end{aligned}$$

and

$$\begin{aligned}\underline{Z}_{s\alpha} &= \frac{\underline{Z}_{aux}}{k_{aux}^2} \\ R_{s\beta} &= R_{run}.\end{aligned}$$

### Positive and Negative Sequence Phasors

With the aid of Euler's formula, the time domain quantities  $u_{s\alpha}$  and  $u_{s\beta}$  can be expressed by their phasor from the above (8.55) as

$$u_{s\alpha} = \frac{1}{2} (\underline{u}_{s\alpha} e^{j\omega_s t} + \underline{u}_{s\alpha}^* e^{-j\omega_s t}) \quad (8.56a)$$

$$u_{s\beta} = \frac{1}{2} (\underline{u}_{s\beta} e^{j\omega_s t} + \underline{u}_{s\beta}^* e^{-j\omega_s t}). \quad (8.56b)$$

An observation of (8.56) shows that the two sinusoidal scalar quantities  $u_{s\alpha}$  and  $u_{s\beta}$  may be represented by two counter-rotating space vectors and two phasors  $\underline{u}_{s\alpha}$  and  $\underline{u}_{s\beta}$ .

The two time domain quantities  $u_{s\alpha}$  and  $u_{s\beta}$ , according to the symbolic and generic diagram of the machine, represent the space vector  $\vec{u}_s = u_{s\alpha} + j u_{s\beta}$ . Use of (8.56) with this expression and grouping the phasors linked to the terms  $e^{j\omega_s t}$  and  $e^{-j\omega_s t}$  gives

$$\vec{u}_s = \underbrace{\left( \frac{1}{2} \underline{u}_{s\alpha} + j \frac{1}{2} \underline{u}_{s\beta} \right)}_{\underline{u}_{s+}} e^{j\omega_s t} + \underbrace{\left( \frac{1}{2} \underline{u}_{s\alpha}^* + j \frac{1}{2} \underline{u}_{s\beta}^* \right)}_{\underline{u}_{s-}^*} e^{-j\omega_s t}. \quad (8.57)$$

The resultant equation as represented by expression (8.58) shows that the space vector  $\vec{u}_s$  may also be represented by two counter-rotating space vectors which in turn are linked to two phasors  $\underline{u}_{s+}$  and  $\underline{u}_{s-}$  that are tied to the rotation direction. The subscript notation  $+, -$  underlines the fact that these phasors are referred to as the so-called *positive* and *negative sequence phasors*,

$$\vec{u}_s = \underline{u}_{s+} e^{j\omega_s t} + \underline{u}_{s-}^* e^{-j\omega_s t}. \quad (8.58)$$

Observation of (8.57) shows that the relationship between the phasors  $\underline{u}_{s\alpha}$  and  $\underline{u}_{s\beta}$  and phasors  $\underline{u}_{s+}$  and  $\underline{u}_{s-}$  may be expressed in terms of a matrix based expression (8.59),

$$\begin{bmatrix} \underline{u}_{s+} \\ \underline{u}_{s-} \end{bmatrix} = \underbrace{\frac{1}{2} \begin{bmatrix} 1 & j \\ 1 & -j \end{bmatrix}}_A \begin{bmatrix} \underline{u}_{s\alpha} \\ \underline{u}_{s\beta} \end{bmatrix} \quad (8.59)$$

where  $A$  is referred to as the transformation matrix. For three-phase machines operating under symmetrical conditions, the two phasors  $\underline{u}_{s\alpha}$  and  $\underline{u}_{s\beta}$  will be orthogonal and symmetric. If, for example, the two phasors are set to  $\underline{u}_{s\alpha} = \hat{u}_s$  and  $\underline{u}_{s\beta} = -j\hat{u}_s$  respectively, (8.58) is reduced to  $\vec{u}_s = \hat{u}_s e^{j\omega_s t}$ , i.e., the negative sequence phasor  $\underline{u}_{s-}$  will then be zero.

The positive and negative phasor variables may be transformed to the  $\alpha$  and  $\beta$ -phasor as

$$\begin{bmatrix} \underline{u}_{s\alpha} \\ \underline{u}_{s\beta} \end{bmatrix} = \underbrace{\begin{bmatrix} 1 & 1 \\ -j & j \end{bmatrix}}_{A^{-1}} \begin{bmatrix} \underline{u}_{s+} \\ \underline{u}_{s-} \end{bmatrix}. \quad (8.60)$$

This transform is the inverse of (8.59). The matrix  $A^{-1}$  is the inverse matrix of the matrix  $A$ .

### Positive and Negative Sequence Model

The transformation process described above for the two scalar variables  $u_{s\alpha}$  and  $u_{s\beta}$  can be equally applied to other machine variables such as the flux linkage and current. Consequently, the conversion process in question may be used to develop a so-called positive and negative sequence phasor model of the machine, with inputs  $\underline{u}_{s+}$  and  $\underline{u}_{s-}$ .

The transformation to positive and negative sequence based phasors is achieved by multiplying both sides of (8.55) with the transformation matrix  $A$  as given in (8.59). The resulting equation is

$$\begin{bmatrix} \underline{u}_{s+} \\ \underline{u}_{s-} \end{bmatrix} = \underbrace{\frac{1}{2} \begin{bmatrix} Z_{s\alpha} + R_{s\beta} Z_{s\alpha} - R_{s\beta} \\ Z_{s\alpha} - R_{s\beta} Z_{s\alpha} + R_{s\beta} \end{bmatrix}}_{Z_{pn}=A Z_{sp} A^{-1}} \begin{bmatrix} \underline{i}_{s+} \\ \underline{i}_{s-} \end{bmatrix} + j\omega_s \begin{bmatrix} \underline{\psi}_{s+} \\ \underline{\psi}_{s-} \end{bmatrix}. \quad (8.61)$$

In this expression, the terms  $\underline{\psi}_{s+}$  and  $\underline{\psi}_{s-}$  need to be considered in detail. This is achieved by rewriting (8.50c) in terms of positive and negative sequence phasors. The resultant equation set, which has been multiplied by factor  $j\omega_s$  to simplify the ensuing analysis, becomes

$$j\omega_s \underline{\psi}_{s+} = j\omega_s L_{\sigma} i_{s+} + j\omega_s \underline{\psi}_{R+} \quad (8.62a)$$

$$j\omega_s \underline{\psi}_{s-} = j\omega_s L_{\sigma} i_{s-} + j\omega_s \underline{\psi}_{R-} \quad (8.62b)$$

where the phasors  $j\omega_s \underline{\psi}_{R+}$  and  $j\omega_s \underline{\psi}_{R-}$  appear. These may be further developed by making use of expression (8.50e) in which the space vectors are shown in rotating coordinates. For the conversion to positive and negative sequence phasors using the approach outlined above, it is helpful to reconsider the relationship between stationary and rotating space vectors, namely  $\tilde{A} = \tilde{A}^{xy} e^{j\theta}$  where  $\theta$  represents the shaft angle which may also be written as  $\theta = \omega_m t$ . The positive/negative phasors linked to expression (8.50e) may after some mathematical handling be written as

$$\underline{e}_{R+} = \left(1 - \frac{\omega_m}{\omega_s}\right) j\omega_s \underline{\psi}_{R+} \quad (8.63a)$$

$$\underline{e}_{R-} = \left(1 + \frac{\omega_m}{\omega_s}\right) j\omega_s \underline{\psi}_{R-}. \quad (8.63b)$$

Some simplification of equation set (8.63) may be realized by introducing the *slip*  $s$  as defined by expression (8.31). Note that the slip relationship was defined for a unidirectional set of space vectors. In the case here, two counter rotating space vectors are used, hence we will arbitrarily assume that the slip is determined with respect to the positive rotating vectors. The left-hand side of equation set (8.63) may also be developed further with the aid of (8.50c), (8.50d), and (8.50f) and converting the latter to positive/negative phasors. Subsequent manipulation of (8.63) using the approach outlined and substitution of the phasor based equation into (8.62) gives

$$j\omega_s \underline{\psi}_{s+} = \underbrace{i_{s+} \left( j\omega_s L_{\sigma S} + \frac{j\omega_s L_M \frac{R_R}{s}}{\frac{R_R}{s} + j\omega_s L_M} \right)}_{Z_{s+}} \quad (8.64a)$$

$$j\omega_s \underline{\psi}_{s-} = \underbrace{i_{s-} \left( j\omega_s L_{\sigma S} + \frac{j\omega_s L_M \frac{R_R}{2-s}}{\frac{R_R}{2-s} + j\omega_s L_M} \right)}_{Z_{s-}} \quad (8.64b)$$

where  $Z_{s+}$  and  $Z_{s-}$  represent a positive and negative sequence impedance network which consists of the leakage inductance in series with a parallel network formed by a slip-dependent rotor resistance and magnetizing inductance. Note that the positive sequence impedance  $Z_{s+}$  is in fact the network shown in Fig. 8.31 for the steady-state of the three-phase induction machine (without the resistance  $R_s$ ), while the negative sequence is similar but utilizes a different slip-dependant rotor resistance.

The positive and negative sequence currents are obtained by substituting the flux linkage expression (8.64) into the voltage (8.61),

$$\begin{bmatrix} \underline{u}_{s+} \\ \underline{u}_{s-} \end{bmatrix} = \frac{1}{2} \begin{bmatrix} Z_{s\alpha} + R_{s\beta} + 2Z_{s+} & Z_{s\alpha} - R_{s\beta} \\ Z_{s\alpha} - R_{s\beta} & Z_{s\alpha} + R_{s\beta} + 2Z_{s-} \end{bmatrix} \begin{bmatrix} \underline{i}_{s+} \\ \underline{i}_{s-} \end{bmatrix}. \quad (8.65)$$

Hence, on the basis of a given steady-state sinusoidal voltage excitation  $u_s$ , the voltage phasors  $\underline{u}_{s+}$  and  $\underline{u}_{s-}$  may be found using (8.57). In turn, these phasors are used as an input for expression (8.65) from which the currents  $\underline{i}_{s+}$  and  $\underline{i}_{s-}$  for a given shaft speed may be derived. These current phasors can with the aid of (8.60) (for currents instead of voltages) be used to obtain the run and auxiliary currents (in phasor form). For the purpose of developing a steady-state equivalent model it is helpful to rewrite (8.65) as

$$\begin{aligned} \underline{u}_{s+} &= (R_{\text{run}} + Z_{s+}) \underline{i}_{s+} \\ &\quad + \left\{ \frac{1}{2} \left( \frac{R_{\text{aux}}}{k_{\text{aux}}^2} - R_{\text{run}} \right) + \frac{1}{j2\omega_s C k_{\text{aux}}^2} \right\} (\underline{i}_{s+} + \underline{i}_{s-}) \end{aligned} \quad (8.66a)$$

$$\begin{aligned} \underline{u}_{s-} &= (R_{\text{run}} + Z_{s-}) \underline{i}_{s-} \\ &\quad + \left\{ \frac{1}{2} \left( \frac{R_{\text{aux}}}{k_{\text{aux}}^2} - R_{\text{run}} \right) + \frac{1}{j2\omega_s C k_{\text{aux}}^2} \right\} (\underline{i}_{s+} + \underline{i}_{s-}) \end{aligned} \quad (8.66b)$$

where the auxiliary and run winding variables are reintroduced as defined for the dynamic model in order to enhance the readability of the resultant expression. A model representation as introduced in Fig. 8.37 is consistent with mathematical expression (8.66). Readily apparent in this model are the two impedances  $Z_{s+}$  and  $Z_{s-}$  as defined in (8.64).

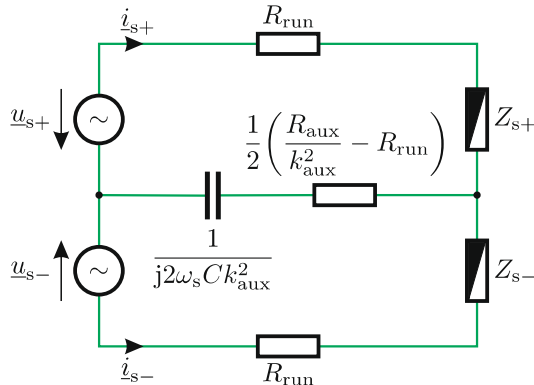


**Fig. 8.37** Equivalent steady-state circuit of a single-phase induction machine with auxiliary capacitor

### Torque Calculation in Steady-State

We will now consider the calculation of the average torque and peak amplitude of the pulsating torque under steady-state conditions using the model given in Fig. 8.37. A suitable starting point for this analysis is the general torque expression in phasor notation

$$T_e = \Im \left\{ \underline{\psi}_s^* \underline{i}_s \right\}. \quad (8.67)$$

This expression may be rewritten in terms of the positive and negative sequence flux linkage and current phasors  $\underline{\psi}_{s\pm}$  and  $\underline{i}_{s\pm}$  by making use of (8.58) in which the voltage variables must be replaced by the appropriate space vectors and phasors. Subsequent mathematical manipulation using this approach gives

$$\begin{aligned} T_e &= \underbrace{\Im \left\{ \underline{\psi}_{s+}^* \underline{i}_{s+} \right\} + \Im \left\{ \underline{\psi}_{s-} \underline{i}_{s-}^* \right\}}_{T_e^{\text{av}}} \\ &\quad + \underbrace{\Im \left\{ \underline{\psi}_{s-} \underline{i}_{s+} e^{j2\omega_s t} \right\} + \Im \left\{ \underline{\psi}_{s+}^* \underline{i}_{s-}^* e^{-j2\omega_s t} \right\}}_{T_e^{\text{ripple}}}. \end{aligned} \quad (8.68)$$

Observation of (8.68) shows that the torque expression has an average (non-time-dependent) component  $T_e^{\text{av}}$  that may be found with the aid of the positive and negative current phasors. Equation (8.68) also shows a sinusoidal torque ripple component  $T_e^{\text{ripple}}$  which has a frequency that is double the voltage supply excitation frequency  $\omega_s$ . The torque  $T_e$  can be rewritten as

$$T_e = T_e^{\text{av}} + T_e^R \sin(2\omega_s t) + T_e^X \cos(2\omega_s t). \quad (8.69)$$

with

$$\begin{aligned} T_e^R &= \Re \left\{ \underline{\psi}_{s-} \underline{i}_{s+} \right\} - \Re \left\{ \underline{\psi}_{s+}^* \underline{i}_{s-}^* \right\} \\ T_e^X &= \Im \left\{ \underline{\psi}_{s-} \underline{i}_{s+} \right\} + \Im \left\{ \underline{\psi}_{s+}^* \underline{i}_{s-}^* \right\}. \end{aligned}$$

The peak amplitude  $\hat{T}_e^{\text{ripple}}$  of this torque ripple component is

$$\hat{T}_e^{\text{ripple}} = \sqrt{(T_e^R)^2 + (T_e^X)^2}. \quad (8.70)$$

### Tutorial Results

A numerical example of a steady-state analysis for the single-phase capacitor run induction machine used for the dynamic model example is given in Fig. 8.38. The results represent the average torque, peak torque ripple, peak auxiliary, and peak run currents as function of the ratio between shaft speed and synchronous speed  $p\omega_s$  over a slip range from  $s = 0$  to  $s = 2$ .

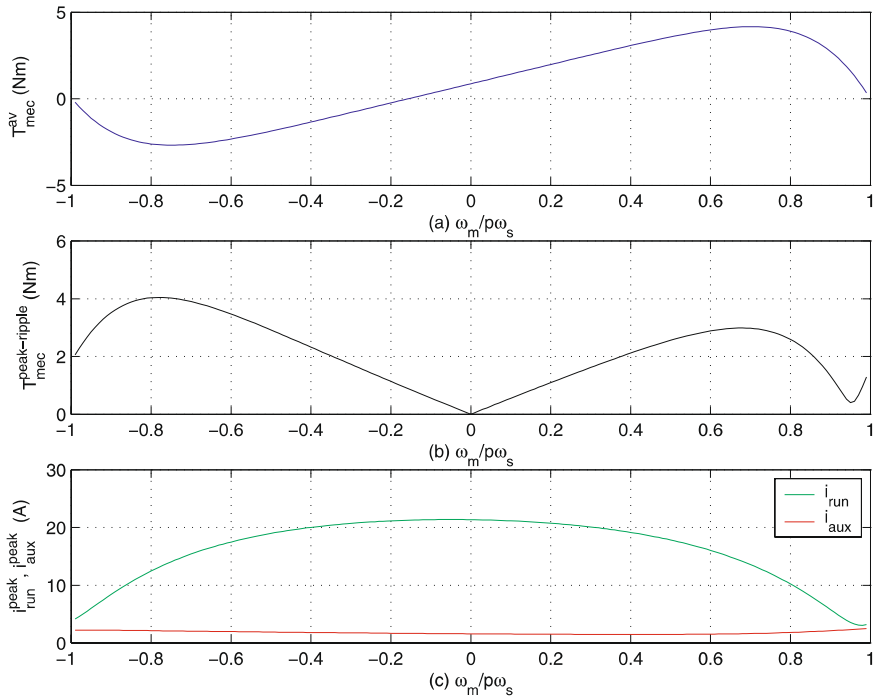


**Fig. 8.38** Steady-state analysis example of a capacitor-run single-phase induction machine

## 8.6 Tutorials

### 8.6.1 Tutorial 1: Simplified Induction Machine Model

In this tutorial, a simulation is considered which is based on the generic model as shown in Fig. 8.3. A rotating flux vector  $\vec{\psi}_m$  with angular frequency  $\omega_s = 100\pi \text{ rad/s}$  and amplitude  $\psi_m = 1.25 \text{ Wb}$  is assumed as an input to this model. This means that the integrator with output  $\vec{\psi}_m$  (see Fig. 8.3) can be omitted in this tutorial. Use of a flux vector as an input emphasizes the fact that it is flux which plays a key role with respect to the operation of the machine. Furthermore, the use of constant flux vector allows the introduction of an *alternative* differentiation module [68], which requires a constant amplitude input vector, on the rotor side of the IRTF module. This approach avoids the use of standard differentiator modules which may cause simulation problems. The generation of the vector  $\vec{\psi}_m$  is realized with the aid of a polar to Cartesian conversion module which has as input the required vector amplitude  $\psi_m$  and angle  $\omega_m t$ . The machine is connected to a mechanical load with a quadratic torque speed curve, where we are able to vary the load torque value (so we can achieve variable speed motor operation).

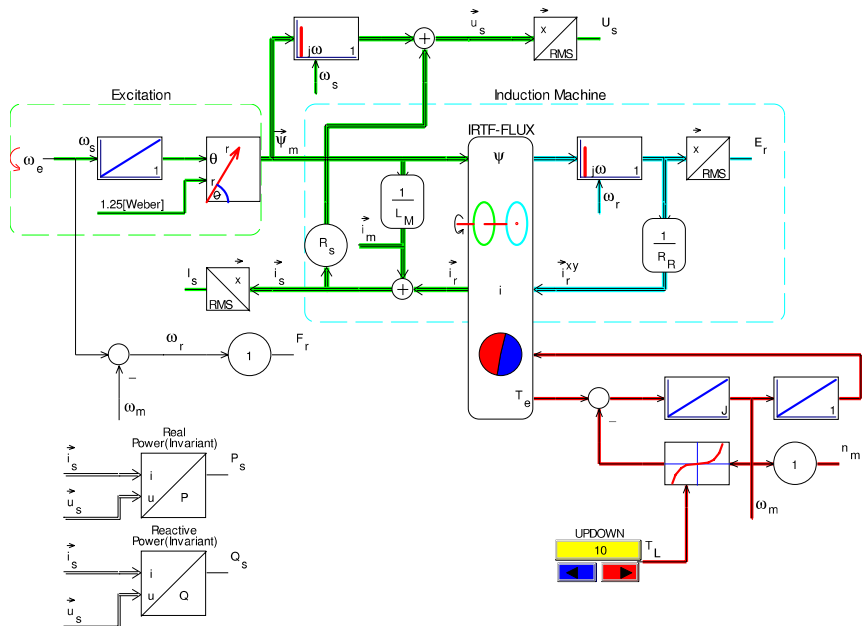


**Fig. 8.39** Simulation of induction machine using the simplified model

The aim of this example is to examine the steady-state operation, hence the use of modules which represent key RMS values and real/reactive power modules. The machine in question has the following parameters: inertia of  $J = 0.001 \text{ kg m}^2$ , stator resistance  $R_s = 6.9 \Omega$ , rotor resistance  $R_r = 3.0 \Omega$  and magnetizing inductance  $L_m = 340.9 \text{ mH}$ . The simulation model as given in Fig. 8.39 satisfies the requirements for this tutorial. It is instructive to activate the CASPOC feature *animate nodal voltages* prior to running the simulation, as this allows the user to visualize the numerical value at named nodes. Space vectors also show a value, namely the amplitude. Furthermore, the simulation should be set to run continuously, by way of the *hand* button on the CASPOC toolbar. In this simulation example the supply voltage is calculated using (8.1a).

### 8.6.2 Tutorial 2: Universal Induction Machine Model

This tutorial is concerned with the development of a simulation model that represents a universal IRTF based machine concept. The aim is to develop a model which reflects the generic model given in Fig. 8.13. Furthermore, the user should be able to vary the transformation variable  $a$  so that the impact of this transformation can be seen on a vector diagram of the type given in Fig. 8.11(b). To achieve this objective the flux vectors  $\vec{\psi}_s$ ,  $\vec{\psi}_M$  and  $\vec{\psi}_R$ , should be transformed to a coordinate reference frame that is tied to the flux vector  $\vec{\psi}_m$  (as given in Fig. 8.11(a)). For this tutorial, the model as developed in the previous section is to be extended with the following set of inductance parameters: stator inductance  $L_s = 346.9 \text{ mH}$  and rotor inductance  $L_r = 346.9 \text{ mH}$ . The remaining set of parameters are as given in the previous tutorial. With this choice of parameters the limits of the transformation variable  $a$  are (see (8.13)) as follows  $0.9827 \leq a \leq 1.0177$ .

An implementation example as given in Fig. 8.40 shows the presence of the inductance matrix  $L^{-1}$  together with an *UPDOWN* module which allows the user to vary the transformation variable  $a$ . As with the previous example, a rotating flux vector is assumed, which in this example represents the stator flux vector  $\vec{\psi}_s$ . Furthermore, the gain module  $R_R$  have been replaced by a new variable gain module which has a second input representing the transformation variable  $a$ . The gain for this new module is equal to  $R_R = a^2 R_r$  (see (8.15)).

A set of three coordinate transformation modules is introduced in Fig. 8.40 which transform the flux vectors  $\vec{\psi}_s$ ,  $\vec{\psi}_M$ ,  $\vec{\psi}_R$ , to a synchronous reference frame linked to the vector  $\vec{\psi}_m$ . This vector is calculated with the aid of (8.5b), with  $L_{os} = L_s - L_m$ . Furthermore, the instantaneous angle  $\rho_m$  of this vector, as found with the aid of a Cartesian to polar conversion unit, is connected to said coordinate conversion modules to realize the required representation of the flux vectors. When the simulation is active, the user

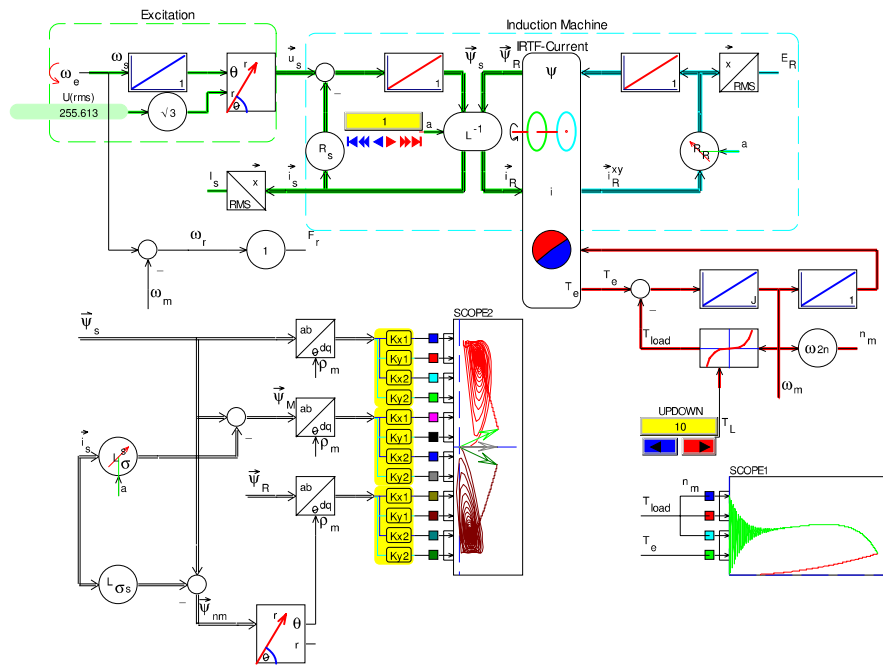


Fig. 8.40 Simulation of induction machine, universal model

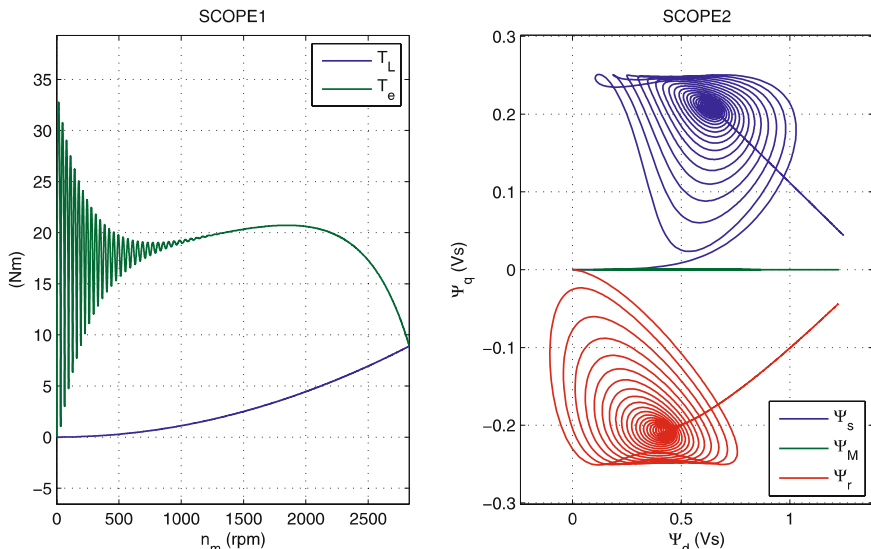
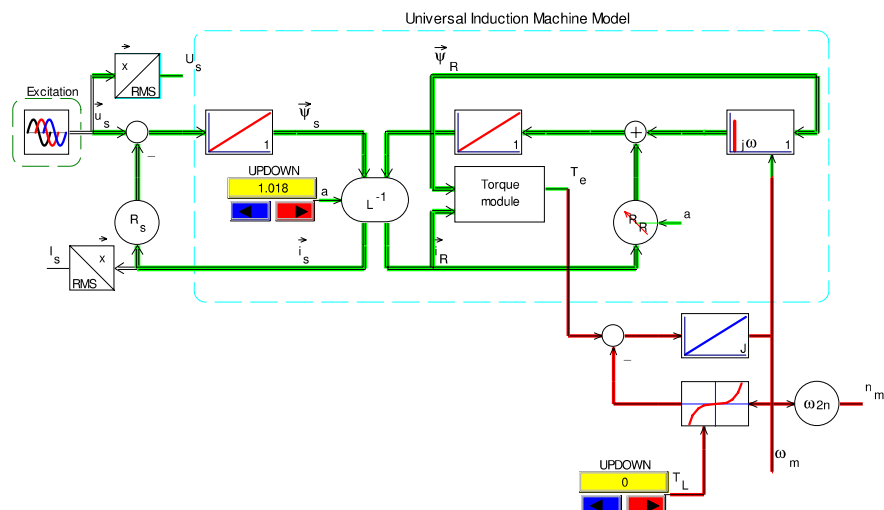


Fig. 8.41 Simulation results of induction machine, universal model

is able to change the transformation variable and observe the effects on the flux vectors and the remaining nodes of the simulation, as discussed in the previous tutorial. Note in particular that the values for the (steady state) output torque/shaft speed and RMS stator voltage/current are unaffected by the changes to the parameter  $a$ . Finally, it is instructive to vary the load torque setting and observe the changes to the flux vectors and node values of the simulation model.

### 8.6.3 Tutorial 3: Universal Stationary Oriented Induction Machine Model

This tutorial is concerned with the implementation of a stationary oriented model of the induction machine as discussed in Sect. 8.3.3. The aim is to develop a simulation model which is based on the generic structure given in Fig. 8.19. The machine is to be connected to a three-phase 220 V, 50 Hz sinusoidal source. The machine inductances and resistances are according to those specified in the previous two tutorials. A combined machine/load inertia of  $J = 0.01 \text{ kg m}^2$  will be used in this simulation. Furthermore, a quadratic load torque versus shaft speed characteristic is assumed. Of interest is to examine the model under steady state conditions by viewing the shaft torque and shaft speed for a given load torque value and to examine the effect on these variables by changing the transformation factor  $a$ .



**Fig. 8.42** Simulation of universal model with stationary oriented reference frame

The simulation model as given in Fig. 8.42 satisfies the requirements for this tutorial. Excitation for the model is provided by making use of a rotating voltage supply vector  $\vec{u}_s$ , the amplitude of which is set to  $U_s \sqrt{3}$ , where  $U_s = 220$  V represents the RMS phase voltage value. The inclusion of the factor  $\sqrt{3}$  follows from the fact that power invariant space vectors are used throughout this book. Also shown in this figure are the inverse matrix element  $L^{-1}$  and gain unit  $R_R$  both of which are affected by changes to the transformation variable  $a$ . If the simulation is executed for different transformation values  $a$ , in this case realized by using the UPDOWN *a value*, the user may ascertain that the torque and speed readings remain unaffected. Changes to the load torque setting, realized by way of the load module torque setting, give the user the ability to examine, for example, the steady state torque speed curve of this machine.

#### **8.6.4 Tutorial 4: Current Controlled Zero Leakage Flux Oriented Machine Model**

This tutorial is concerned with the development of a zero leakage, UFO based model as discussed in Sect. 8.2.2. A simulation model is envisaged, which complies with the generic structure shown in Fig. 8.6. The machine inductance and resistance parameters are according to those used in the previous tutorial. Furthermore, the machine, which has an inertia of  $J = 0.1 \text{ kg m}^2$ , is deemed to operate under no-load conditions. A direct and quadrature current are to be used as inputs, where the direct axis is to be set to  $i_d = 0 \text{ A}$  at the start of the simulation. A step in the quadrature current from  $0 \rightarrow 4 \text{ A}$  is required, at  $t = 0.8 \text{ s}$ . The aim is to build a model of the machine and examine the transient response in terms of the shaft torque  $T_e$ , flux linkage  $\psi_m$  and speed variables  $\omega_m$ ,  $\omega_{sl}$ ,  $\omega_s$ . An implementation example which satisfies the requirements for this tutorial, as shown in Fig. 8.43, was used to derive the result shown in Fig. 8.7. A simulation step time of  $100 \mu\text{s}$  and run time of  $2.0 \text{ s}$  has been assumed to give the reader a clear visualization of the machine torque, flux linkage and speed response over time. It is helpful to active the *cross hairs/red dot* button in the CASPOC tool bar, which activates the node animation feature of the program. This allows the reader access to the numerical values of labeled nodes during the simulation. This feature in combination with the *replay* feature (activated with the *red dot* button on the bottom tool bar) allows the user to examine the node variables at any instant of the simulation sequence. The scopes used to present the results are shown in Fig. 8.44.

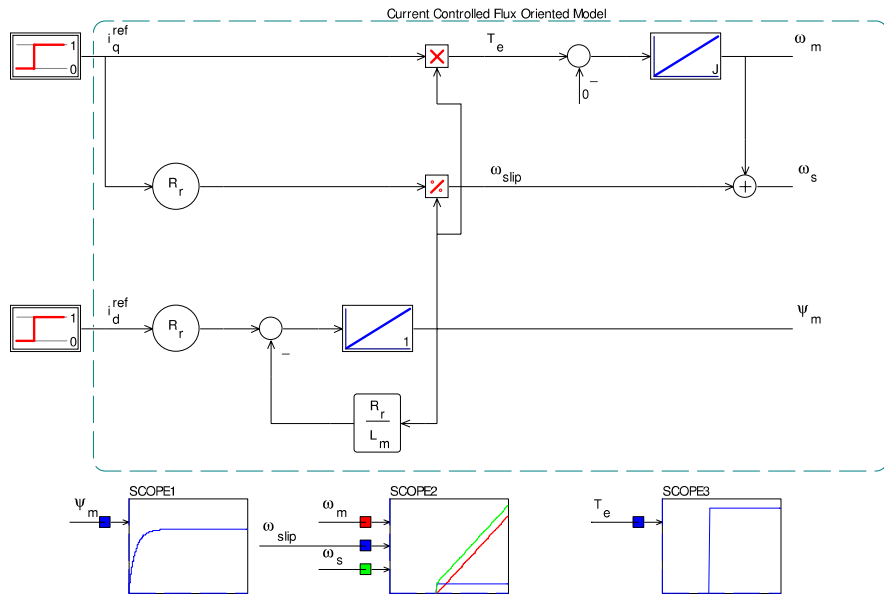


**Fig. 8.43** Simulation of current controlled, flux oriented model with zero leakage

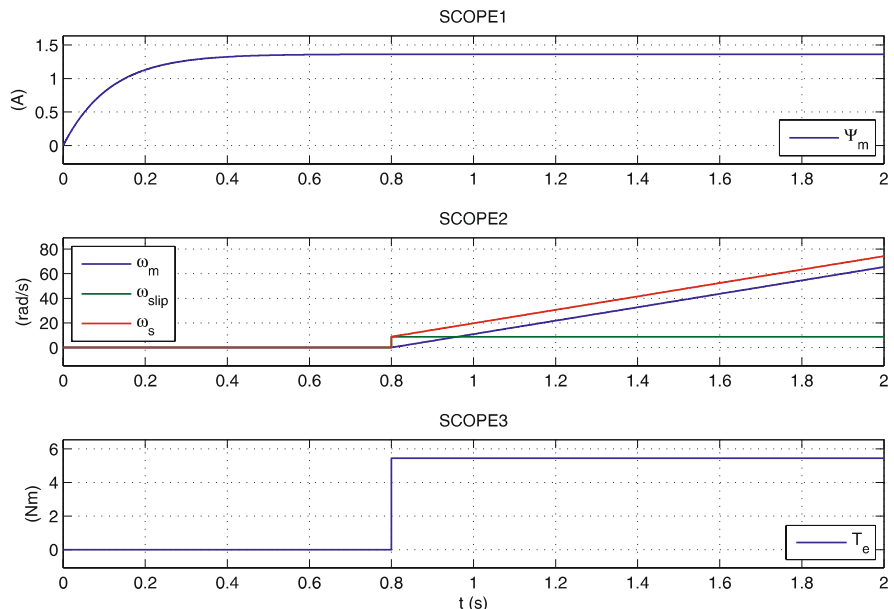


**Fig. 8.44** Simulation results of current controlled, flux oriented model with zero leakage

### 8.6.5 Tutorial 5: Current Controlled Universal Field Oriented (UFO) Model

In this tutorial a generalized UFO model, with leakage inductances, is to be developed which is based on the generic structure shown in Fig. 8.22. The aim is to consider the transient response of the model in question, whereby the user is able to alter the transformation ratio  $a$ . For this purpose the current excitation and machine inertia as given in the previous tutorial are again used in this example. Furthermore, the machine resistance and inductance parameters for this tutorial are given in Sect. 8.6.2. The simulation model, as shown in Fig. 8.45, complies with the generic model of the machine in its present form (see Fig. 8.22). Setting the transformation variable  $a$  to either side of its scale using the UPDOWN module leads to a rotor or stator flux oriented model, with corresponding transient results given by Fig. 8.26 and Fig. 8.29 respectively. The scopes used to present the results are similar to Fig. 8.44.

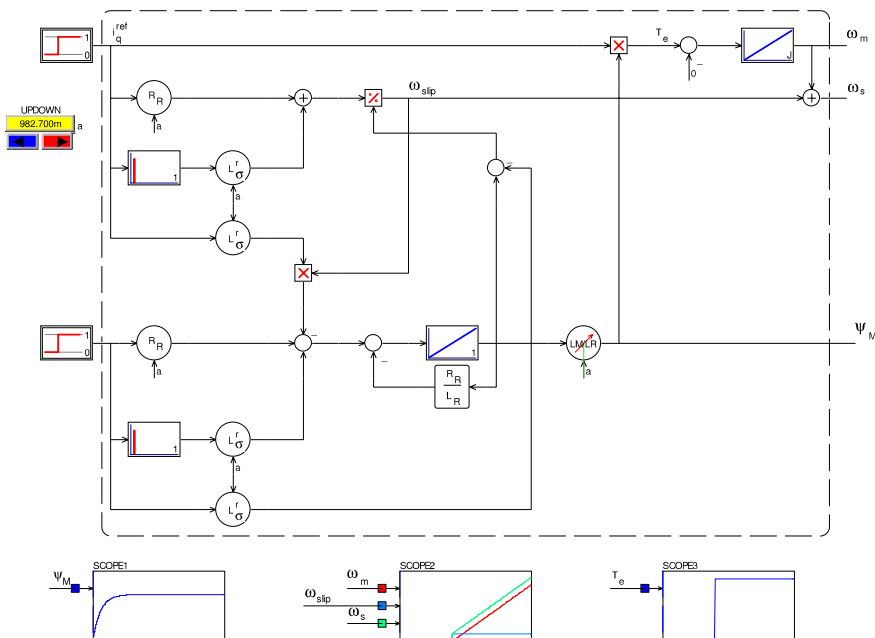


**Fig. 8.45** Simulation of current controlled, flux oriented model with leakage inductance

### 8.6.6 Tutorial 6: Parameter Estimation Using Name Plate Data and Known Stator Resistance

The name plate data given in Table 8.1 corresponds to a *delta* connected motor, of which the measured RMS no-load line current and resistance between two terminals (with the machine at standstill) were found to be equal to  $I_l^{\text{noload}} = 8.4 \text{ A}$  and  $R_l = 0.35 \Omega$  respectively. On the basis of the approach set out in Sect. 8.4 build a MATLAB m-file which calculates the parameters  $L_s$ ,  $L_{\sigma s}$ ,  $L_{\sigma r}$  and  $R_r$  whereby it may be assumed that the leakage inductances are equal. Furthermore, calculate the rated stator flux  $\vec{\psi}_s$ , magnetizing flux  $\psi_M$  and the parameters  $L_{\sigma S}$ ,  $L_M$ ,  $R_R$  for a rotor flux field oriented model.

**Table 8.1** Name plate data

Parameters	Value
Rated power	$P_{\text{out}}^{\text{nom}}$ 22 kW
Rated shaft speed	$n_m^{\text{nom}}$ 1465 rpm
Number of pole pairs	$p$ 2
Rated RMS line voltage	$U_l^{\text{nom}}$ 415 V
Rated RMS line current	$I_l^{\text{nom}}$ 33.4 A
Supply frequency	$f_s$ 50 Hz
Rated power factor	$\text{pf}^{\text{nom}}$ 0.88

A possible approach to this problem may be initiated by examining the measured resistance  $R_l$  between two terminals of the machine. For a delta connected machine, the equivalent resistance *seen* by two terminals is equal to resistance of one phase with the other two series connected phases in parallel. Hence, the stator resistance is equal to  $R_s = 3/2R_l$ . The RMS no-load phase current and RMS rated phase current are equal to  $i_D^{\text{noload}} = I_l^{\text{noload}}/\sqrt{3}$  and  $i_D^{\text{nom}} = I_l^{\text{nom}}/\sqrt{3}$  respectively, given the use of a delta connected machine. Furthermore, the conversion from RMS phase variables to power invariant space vector amplitude is realized by multiplying the former with a factor  $\sqrt{3}$  [68]. Hence, the magnitude of the current and voltage space vectors defined in (8.34) are equal to  $u_s = U_l^{\text{nom}} \sqrt{3}$ ,  $i_s^{\text{noload}} = I_l^{\text{noload}}$ , which allows the calculation of the stator flux linkage vector amplitude  $\vec{\psi}_s$  and inductance  $L_s$  given that  $\omega_s = 2\pi f_s$ . Calculation of the rated electromechanical torque proceeds with the aid of (8.36) which requires access to the rated (space vector) current amplitude  $i_s^{\text{nom}} = I_l^{\text{nom}}$  (note that the amplitude of a power invariant current space vector is equal to the RMS line current value, in case the machine is delta connected). The remaining variables required for this calculation are found with the aid of Table 8.1. Computation of the parameters  $L_s$ ,  $L_{\sigma s}$ ,  $L_{\sigma r}$ ,  $R_r$ , with the assumption of  $L_{\sigma s} = L_{\sigma r}$ , proceeds using the approach set out in Sect. 8.4 which leads to the data shown in Table 8.2. Also included (for completeness) in this table is the measured stator resistance and homopolar inductance  $L_{\text{hom}}$ .

**Table 8.2** Estimated machine parameters

Parameters		Value
Stator inductance	$L_s$	272.4 mH
Magnetizing inductance	$L_m$	260.7 mH
Leakage inductance	$L_{\sigma s}$	11.7 mH
Leakage inductance	$L_{\sigma r}$	11.7 mH
Rotor resistance	$R_r$	0.5377 $\Omega$
Stator resistance	$R_s$	0.5250 $\Omega$
Homopolar inductance	$L_{hom}$	6.0 mH

The second part of this tutorial requires the conversion of the parameters given in Table 8.2 to a revised set of universal model parameters as defined by (8.12) and (8.15) with  $a = L_m/L_r$ . The new set of parameters as given in Table 8.3 correspond to a rotor flux oriented UFO model which in turn are used in conjunction with (8.43) and (8.44) to calculate the required (rated) magnetizing flux amplitude  $\psi_M^{\text{nom}} = \psi_R^{\text{nom}}$ . This flux linkage value together with the earlier found stator flux linkage value and measured stator resistance are also shown in Table 8.3.

**Table 8.3** Estimated machine parameters and flux linkage values for a rotor flux oriented model

Parameters		Value
Magnetizing inductance	$L_M$	249.6 mH
Leakage inductance	$L_{\sigma s}$	22.8 mH
Leakage inductance	$L_{\sigma r}$	0 mH
Rotor resistance	$R_R$	0.4927 $\Omega$
Stator resistance	$R_s$	0.5250 $\Omega$
Rated stator flux linkage	$\psi_s^{\text{nom}}$	2.29 Wb
Rated rotor flux linkage	$\psi_R^{\text{nom}}$	2.00 Wb

### M-File Code:

```
% 22kW machine, delta connected
VsR = 415; % RMS line voltage in V
IsR = 33.4; % rated RMS line current in A
IsN = 8.4; % noload RMS line current in A
Rlin = 0.35; % measured line-to-line resistance in Ohms
%nameplate data
PoutR = 22000; % rated output power in W
pfR = 0.88; % rated power factor
p = 2; % fourpole machine
nR = 1465; % rated shaft speed in r/min
fs = 50; % supply frequency in Hz
%
ws = 2*pi*fs; % electrical freq in rad/sec
wm = p*2*pi*nR/60; % rated electrical shaft freq in rad/sec
Rs = 3/2*Rlin; % stator resistance in Ohms
isR = sqrt(3)*IsR/sqrt(3); % power invariant vector is value
```

```

isN = sqrt(3)*IsN/sqrt(3); % power invariant noload is value
usR = sqrt(3)*VsR; % power invariant supply voltage vector
Te = (usR*isR*pfR-isR^2*Rs)/ws; % rated electrical torque in Nm
% calculate remaining data
psi_s = 1/ws*sqrt(usR^2-isN^2*Rs); % stator flux amplitude in Vs
Ls = psi_s/isN; % self inductance stator in H
isqR = Te/psi_s; % rated isq value in A
isdR = sqrt(isR^2-isqR^2); % rated isd value in A
RR = (ws-wm)*psi_s/isqR; % rotor resistance with a=Ls/Lm
Lrsig = (isdR-isN)/(isqR^2/psi_s); % leakage inductance with a=Ls/Lm
% calculate parameters for a=1 assume Lsig=Lsigs
Lr = Ls; % rotor inductance equal to stator inductance
Lm = sqrt(Ls^3/(Lrsig+Ls)); % magnetizing inductance in H
Lsigs = Ls-Lm; % stator leakage inductance in H
Rr = (Lm/Ls)^2*RR; % rotor resistance in Ohms
% parameters and flux for any 'a': example rotor flux orientation
a = Lm/Lr;
Lssig = Lm*(Ls/Lm-a);
L_M = a*Lm;
R_R = a^2*Rr;
psiMd = psi_s-Lssig*isdR;
psiMq = -Lssig*isqR;
psi_M = sqrt(psiMd^2+psiMq^2); % rated magnetizing flux in Vs

```

### 8.6.7 Tutorial 7: Grid Connected Induction Machine

A dynamic model of a three-phase delta connected induction machine, with an inertia of  $J = 0.1 \text{ kg m}^2$  is to be considered which is to be connected to a 415 V (RMS line to line voltage) 50 Hz supply. A four parameter, two pole pair machine representation is envisaged, with a stator oriented leakage inductance and a set of parameters as given in Table 8.3. Provide a simulation model of this machine with the required supply source and plot the shaft torque  $T_e$ , line current  $i_1$ , stator flux amplitude  $|\vec{\psi}_s|$  and shaft speed  $\omega_m$  over a 2 s period. The machine is initially assumed to operate without a mechanical load. However, at time mark  $t = 1 \text{ s}$  a 120 Nm (rated) torque step is to be applied. Furthermore, add a set of modules to your simulation which provide a numerical indication of the input power, RMS line current  $I_1$  and RMS phase voltage  $U_D$ .

A possible implementation of this problem may be realized by making use of the generic machine model shown in Fig. 8.15, where the IRTF module needs to be extended by a pole pair module in [68]. The introduction of this pole pair module is readily apparent in the model for this tutorial shown in Fig. 8.46. Shown in this simulation model is a space vector generator which has as output a power invariant rotating (at a speed of 3000 rpm) space vector with an amplitude of 415 V. Note that for power invariant space vectors the amplitude is equal to the RMS value of the three individual phases times a factor  $\sqrt{3}$ . A set of conversion modules is introduced which realizes the

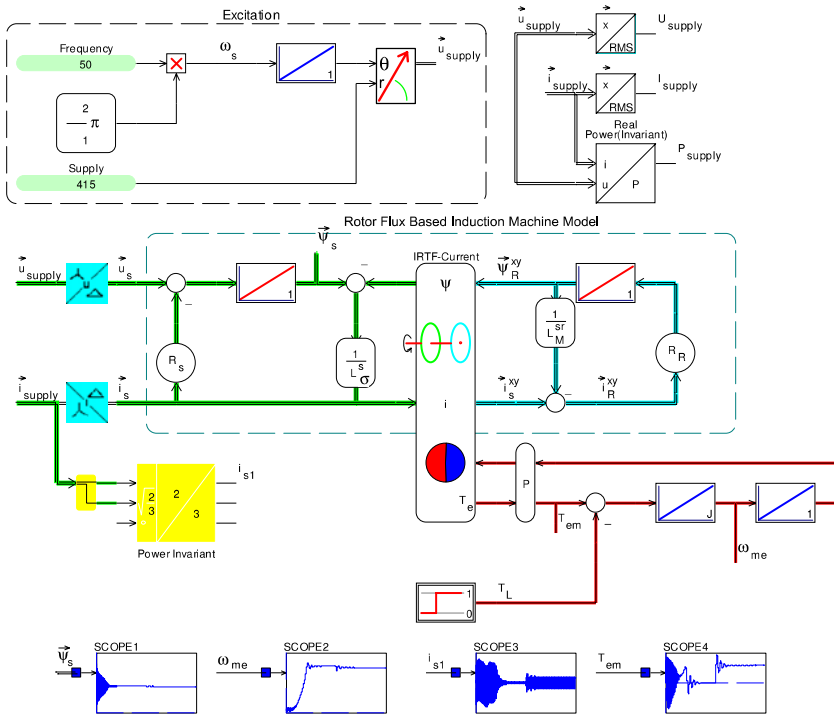


**Fig. 8.46** Simulation of grid connected induction machine

star-delta conversion  $\vec{u}_{\text{supply}} \rightarrow \vec{u}_s$ , where  $\vec{u}_s$  is the input voltage space vector for the machine model. Conversely, a similar set of modules is introduced in order to realize the delta-star conversion process for the stator current vector  $\vec{i}_s$ . Also shown in Fig. 8.46 are a set of modules which generate the RMS supply current  $I_l$ , RMS phase voltage  $U_D$  and input power  $p_{\text{in}}$ .

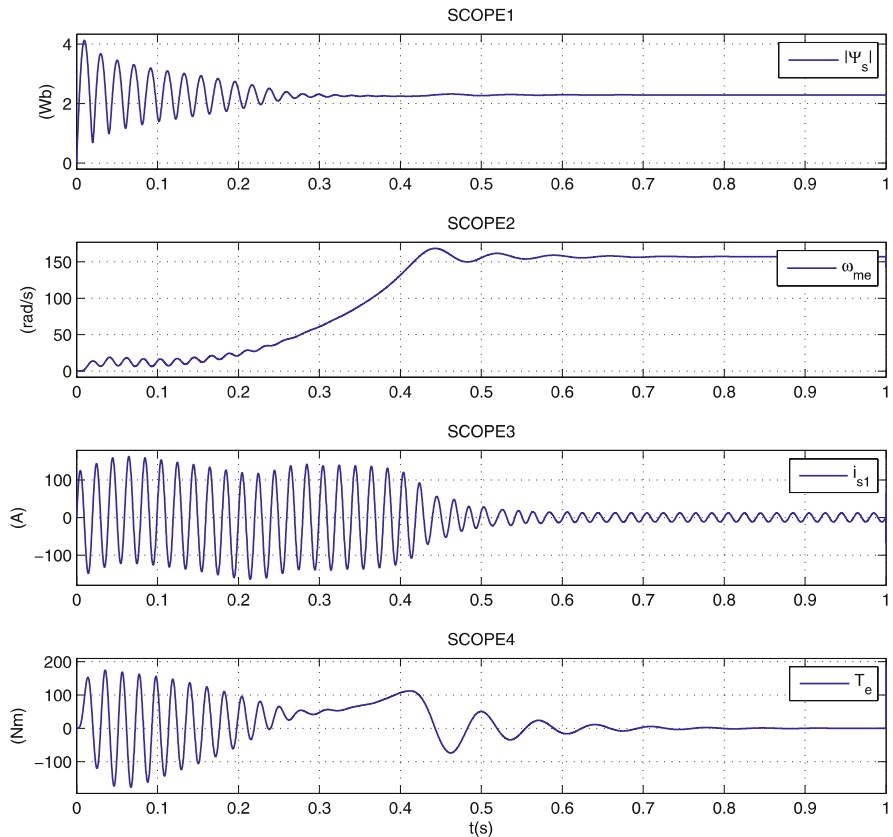
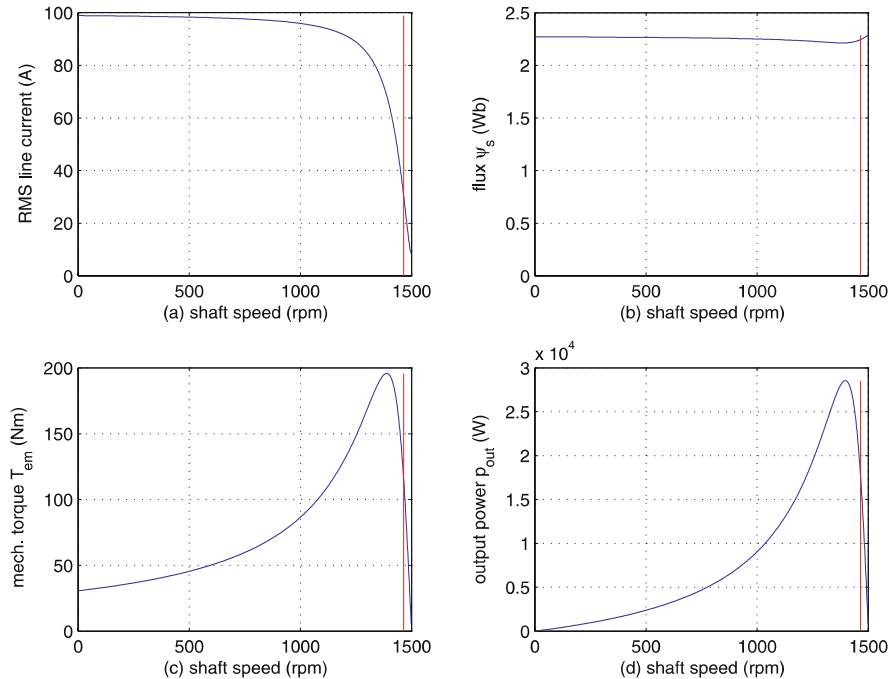


Fig. 8.47 Simulation results of grid connected induction machine

### 8.6.8 Tutorial 8: Steady State Characteristics, Grid Connected Induction Machine

This tutorial is concerned with the computation of the steady-state characteristics:  $T_e$ ,  $I_1$ ,  $\vec{\psi}_s$ ,  $P_{out}$  of the delta connected machine discussed in the previous subsection. Provide a MATLAB m-file which contains a phasor based analysis for the machine in question when connected to a three phase sinusoidal supply as used in the previous example. Assume the machine input voltage phasor  $\underline{u}_s$  as real and calculate the corresponding stator current phasor and torque of the machine using the approach set out in Sect. 8.3.6. Display your results by way of a set of subplots which represent (as function of the shaft speed) the mechanical torque  $T_e$ , RMS line current  $I_1$ , flux linkage  $|\psi_s|$  and output power  $P_{out}$ . Choose the shaft speed range for your plots so that they coincide with a slip variation of  $s : 1 \rightarrow 0$ .



**Fig. 8.48** Steady-state characteristics of 22 kW induction machine

A possible solution to this problem may be found by considering the equivalent circuit of the machine given in Fig. 8.31. The model in question utilizes a stator based leakage inductance, hence the machine parameters must be converted as discussed in the tutorial given in Sect. 8.6.6. The machine is delta connected, hence the input voltage phasor is of the form  $\underline{u}_s = 415\sqrt{3}$ , which in turn may be used in conjunction with (8.32) to find the stator current phasor  $\underline{i}_s$ . For a delta connected machine, the RMS line current magnitude is equal to  $i_s$ , as calculated above. Computation of the torque may be realized with the aid of for example (8.33) which must be converted to its phasor equivalent format. This expression requires access to the flux phasor  $\underline{\psi}_R$  which may be found with the aid of (8.29b).

### 8.6.9 Tutorial 9: Grid Connected Single-Phase Induction Machine

This tutorial is concerned with the implementation of a dynamic simulation model of a single-phase, capacitor run induction machine connected to a 110 V(RMS), 50 Hz supply. For this purpose a machine prototype with pa-

rameters as given in Table 8.4 will be considered in terms of its dynamic behavior when subjected to line-start conditions. Of interest is to examine the instantaneous torque, shaft speed and phase currents during the run up sequence of the motor. Central to the approach given here are the concepts discussed in Sect. 8.5 which, as may be observed, provides a more general approach to the topic of modeling single-phase machines. This tutorial is restricted to a capacitor run machine, but the model may be readily adapted to split-coil and capacitor start type machines. In the latter case, the auxiliary winding resistance must be controlled in a manner outlined in the previous tutorial.

**Table 8.4** Single-phase, capacitor run machine parameters

Parameters		Value
Leakage inductance	$(L_{\sigma s})$	12.8 mH
Stator resistance (run winding)	$(R_{\text{run}})$	2.02 $\Omega$
Stator resistance (aux winding)	$(R_{\text{aux}})$	7.14 $\Omega$
Rotor resistance	$(R_R)$	3.87 $\Omega$
Magnetizing inductance	$(L_M)$	171.8 mH
Asymmetric ITF winding ratio	$(k_{\text{aux}})$	1.18
Capacitor size	$(C)$	31.0 $\mu\text{F}$
Inertia	$(J)$	$1.46 \cdot 10^{-2} \text{ kg m}^2$
Pole pairs	$(p)$	2
Initial rotor speed	$(\omega_m^0)$	0 rad/sec

A suitable starting point for the proposed analysis is the generic model of the single-phase machine as shown in Fig. 8.35 in which the auxiliary winding must (in this case) be connected to the run winding via a capacitor  $C$ . Given this approach, an additional set of generic modules must be provided to implement (8.46). The model as given in Fig. 8.49 shows the ITF and IRTF modules as present in the generic model. In this case the IRTF module is extend with a additional gain module  $p$  given that a four pole machine is used for this tutorial. Also shown is a *source* module, which is used to apply a 1 Nm load torque step to the machine at  $t = 1.5$  s.

For the purpose of understanding the torque production mechanism of this machine, it is instructive to consider the locus of the space vectors  $\vec{i}_s^{xy}$ ,  $\vec{\psi}_R^{xy}$  during the simulation sequence. A set of scopes is used to generate the results and these are presented with the aid of MATLAB based subplots as shown in Fig. 8.50. These results clearly show that the presence of a large pulsating torque component, in addition to an average torque component, which (under steady-state conditions) corresponds to the (1.0 Nm) applied load torque value. It is also instructive to examine the interaction between the rotor flux  $\vec{\psi}_R^{xy}$  and stator current vector  $\vec{i}_s^{xy}$  (in rotor coordinates) of the machine, given that these define the instantaneous torque in the machine. The vector plot as given in Fig. 8.51 shows that the relationship between flux and current vectors is by no means constant over the course of the simulation.

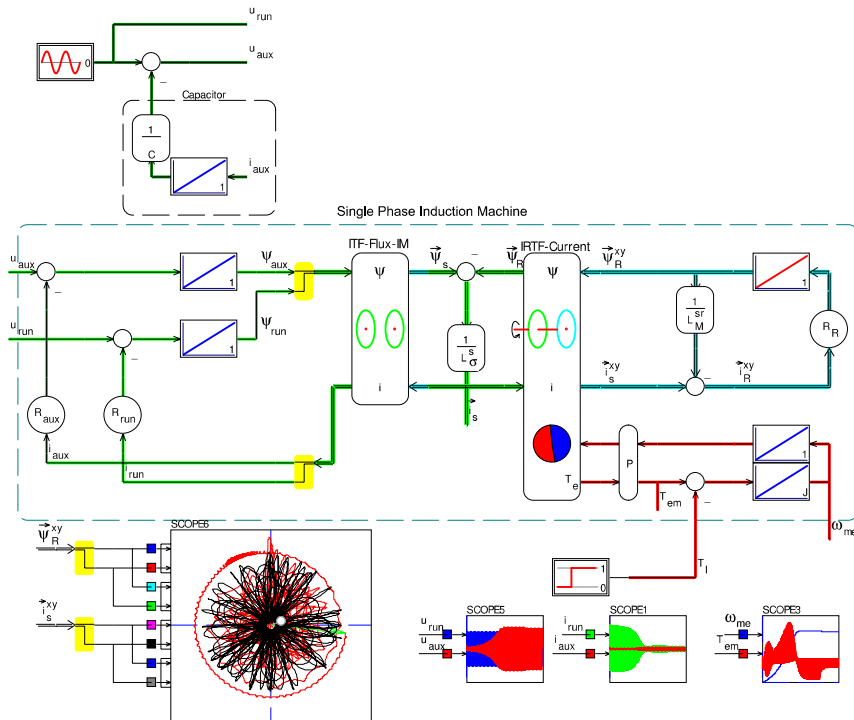
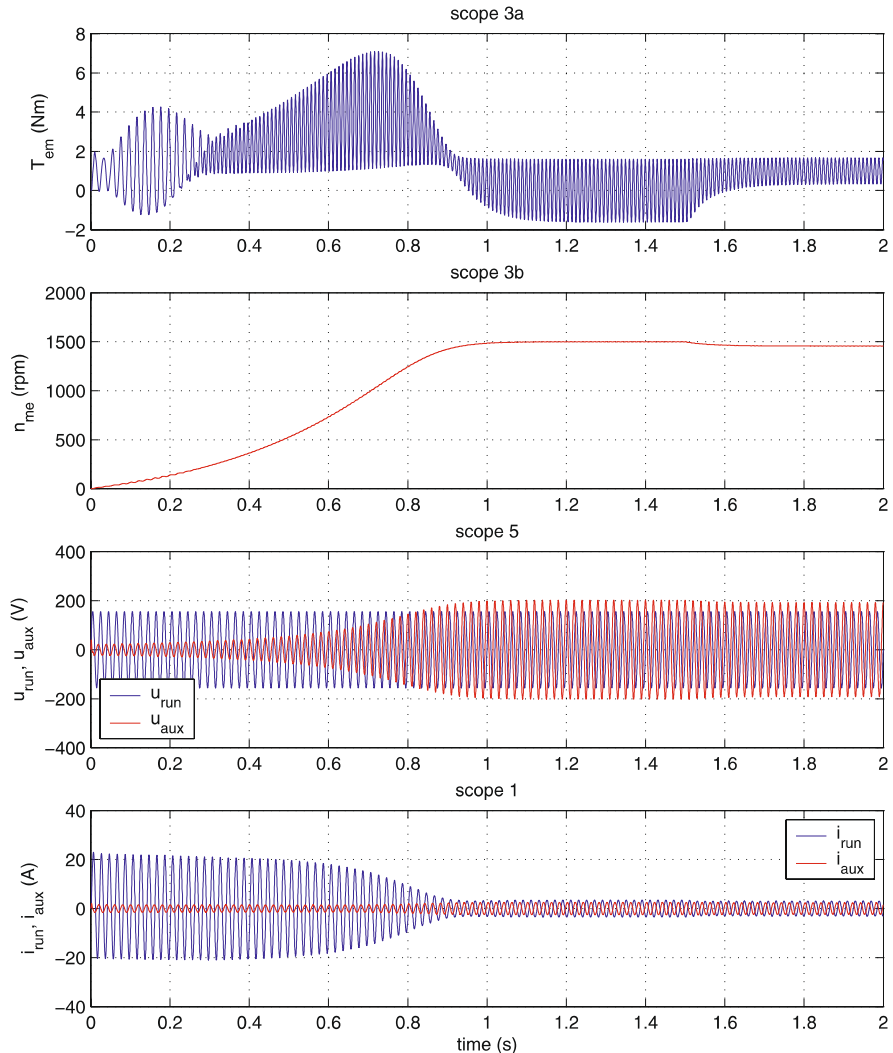
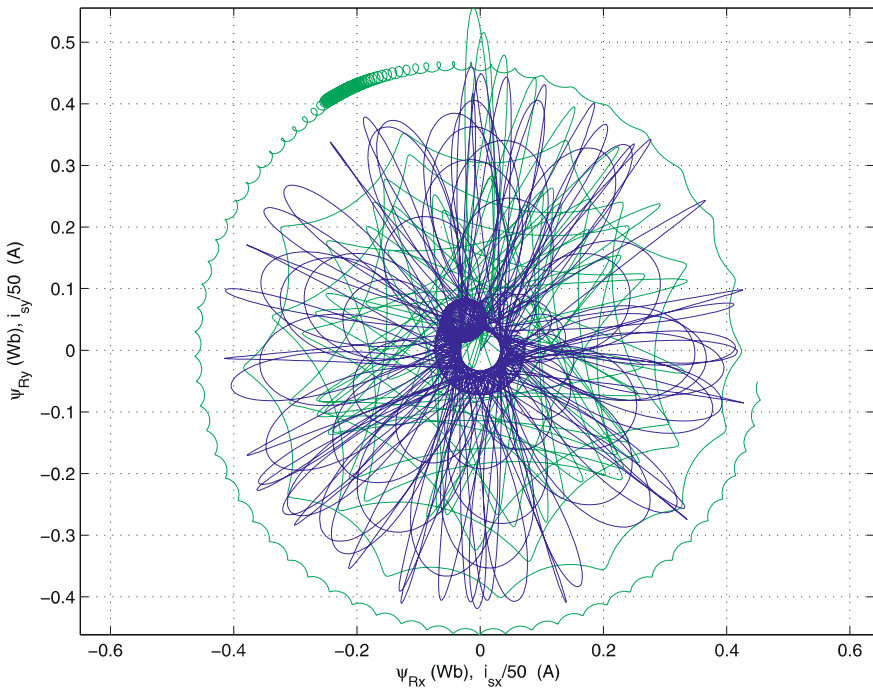


Fig. 8.49 Simulation of single-phase capacitor run motor

This points to the presence of a large torque ripple component as apparent in the result shown on SCOPE3a (see Fig. 8.50).



**Fig. 8.50** Simulation results of a line start of single-phase capacitor run induction machine



**Fig. 8.51** Line start of single-phase capacitor run induction machine, vector plot  $\vec{\psi}_R^{xy}$  (green trace) and  $\vec{i}_s^{xy}/50$  (blue trace)



# Chapter 9

## Control of Induction Machine Drives

In this chapter, attention is given to the control concepts that can be used to achieve independent torque and flux linkage control of induction machines over a wide speed range. Following the *machine model inversion principles*, the machine models introduced in the previous chapter will again be used for deriving suitable controller structures.

First, classical  $V/f$  control concepts with very limited dynamic performance capabilities will be discussed. Next, field-oriented control techniques will be discussed which build on the fundamental model given in Sect. 4.2.3. A key role is assigned to the presentation of a *universal field-oriented* (UFO) model which is used in conjunction with a current source induction machine model. At a later stage, this model is replaced with a voltage source induction model which is connected to a synchronous current-controlled converter. Finally, attention is given to the operational aspects of the drive which takes into account the maximum supply voltage and current constraints. In this context field weakening techniques are also discussed. A set of tutorials is again provided to further familiarize the reader with the concepts presented in this chapter.

### 9.1 Voltage-to-Frequency ( $V/f$ ) Control

In many applications the issue of controlling torque or speed of a mechanical load connected to an induction motor is not critical in terms of required dynamic performance. For these applications, the classical *voltage-to-frequency* ( $V/f$ ) control can be used resulting in a very simple drive control which can easily be implemented in analog hardware. It was therefore extensively used before digital hardware was available. The key concepts of the  $V/f$  control are presented in the following.

The drive structure in question does not utilize closed loop current control as discussed in Chap. 3. Instead, only the stator voltage  $\hat{u}_s$  and the stator

frequency  $\omega_s$  are controlled in a way that

$$\psi_s = \text{const.} \quad (9.1)$$

The lack of a current control in V/f control is a key issue which distinguishes this low-dynamic drive concept from, for example, the dynamic field-oriented control concepts to be discussed in the subsequent section of this chapter. Furthermore, it will be shown in this section that the omission of current control can in some applications lead to instability. The ensuing discussion is undertaken for a two-pole machine to facilitate the readability of the figures and equations.

### Steady-State Equations for V/f Control

Prior to examining the algorithms and generic models which may be invoked for this type of control it is helpful to consider the steady-state relationship which exists between the torque  $T_e$ , flux linkage  $\psi_s$ , and angular frequency  $\omega_s$ .

For this purpose, the stator flux oriented model, discussed in Sect. 8.3.4.2, is introduced because it is advantageous given the simplicity of the control algorithm that can be achieved. Under these conditions, the variables  $\psi_M$  and  $L_M$  shown in Fig. 8.27 may be written as  $\psi_s$  and  $L_s$  respectively. The equation set which corresponds to the stator flux model, viewed under steady-state conditions may be written as

$$u_{sd} = R_s i_{sd} \quad (9.2a)$$

$$u_{sq} = R_s i_{sq} + \omega_s \psi_s \quad (9.2b)$$

$$\omega_s \psi_s = \omega_{sl} L_{\sigma R} i_{Rd} + R_R i_{sq} + \omega_m \psi_s \quad (9.2c)$$

$$i_{sd} = \frac{\psi_s}{L_s} + \underbrace{\frac{\omega_{sl} L_{\sigma R} i_{sq}}{R_R}}_{i_{Rd}} \quad (9.2d)$$

$$i_{sq} = \frac{T_e}{\psi_s}. \quad (9.2e)$$

Elimination of the variable  $i_{Rd}$  from expression (9.2c), by making use of expression (9.2d), gives

$$L_{\sigma R} i_{sq} = \frac{\psi_s}{\frac{\hat{\omega}_{sl}}{\omega_{sl}} + \frac{\omega_{sl}}{\hat{\omega}_{sl}}} \quad (9.3)$$

with  $\hat{\omega}_{sl} = R_R/L_{\sigma R}$  and  $\omega_{sl} = \omega_s - \omega_m$ . Use of the latter equation with expression (9.2e) leads to the following torque equation known as *Kloss formula*:

$$T_e = \frac{2\hat{T}_e}{\frac{\hat{\omega}_{sl}}{\omega_{sl}} + \frac{\omega_{sl}}{\hat{\omega}_{sl}}} \quad (9.4)$$

with

$$\hat{T}_e = \frac{\psi_s^2}{2L_{\sigma R}} \quad (9.5)$$

represents the *pullout torque* and  $\hat{\omega}_{sl}$  the *slip frequency* at which the pullout torque occurs. Use of (9.4), with a given reference stator frequency  $\omega_s = \omega_{s1}^*$ , leads to the torque versus shaft speed curve shown as the blue curve in Fig. 9.1. When increasing the stator frequency at constant stator flux linkage  $\hat{\psi}_s$ , as given in (9.1), another curve shown in Fig. 9.1 arises for stator frequency reference values  $\omega_{s2}^*$  with  $\omega_{s1}^* < \omega_{s2}^*$ . Note, by maintaining constant flux linkage  $\psi_s$  the amplitude of the pullout torque  $\hat{T}_e$  is constant as can be seen from (9.5).

A typical load-torque/shaft-speed characteristic  $T_l(\omega_m)$  is also shown in Fig. 9.1 to show the *steady-state* operating point of the drive, which is found when the load torque is equal to the torque produced by the machine.

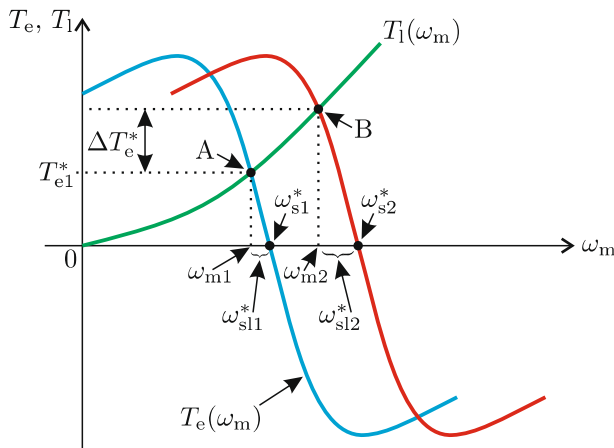


**Fig. 9.1** Classical voltage-to-frequency (V/f) drive concept

In the following two subsections V/f controllers for speed and torque control will be discussed.

### 9.1.1 Simple V/f Speed Controller

This control approach is based on the use of the reference  $\omega_s^*$  and strives to maintain, without consideration of the stator resistance, a constant stator

flux linkage value. The required supply voltage amplitude  $\hat{u}_s$  and phase angle  $\rho_s$  are determined with the aid of equation set (9.2). Input to the controller is the stator frequency  $\omega_s$  in which case the phase angle is given as  $\rho_s = \omega_s t$ . The required voltage amplitude may be written as  $\hat{u}_s = \sqrt{u_{sd}^2 + u_{sq}^2}$ . In most cases the leakage term in (9.2d) can be ignored and the voltage  $u_{sd}$  can be written as

$$u_{sd} \simeq \psi_s^* \frac{R_s}{L_s} \quad (9.6a)$$

$$u_{sq} \simeq \omega_s^* \psi_s^*. \quad (9.6b)$$

The quadrature voltage component  $u_{sq}$  shown in (9.6b) is derived from expression (9.2b) with the implicit assumption that the term  $\omega_s \psi_s$  is usually larger than the term  $R_s i_{sq}$ . Note that in most applications the reference stator flux linkage matches the nominal stator flux linkage to avoid saturation. By neglecting the stator resistance, the term  $\frac{u_{sq}}{\omega_s}$  is held constant, which is why this type of control is referred to as a V/f control. The generic representation of the simple V/f speed controller is given in Fig. 9.2.

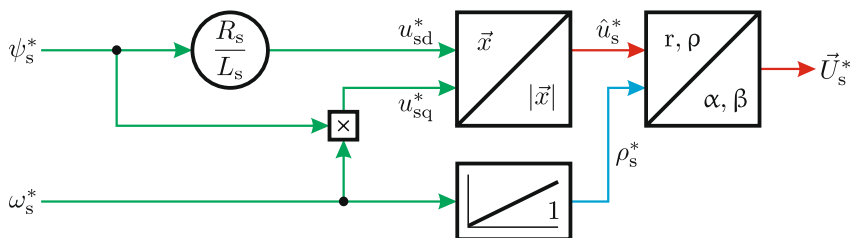


**Fig. 9.2** V/f control structure with stator frequency reference input

If for example the speed reference is set to  $\omega_{s1}^*$ , the steady-state shaft speed will settle to  $\omega_{m1}$  for the assumed load torque versus speed characteristic. A frequency shift from  $\omega_{s1} \rightarrow \omega_{s3}$  in effect translates the torque speed curves as may be observed from Fig. 9.1. Note that this type of controller does not require a shaft speed sensor, which is advantageous for applications where such a device is either unpractical (for robustness reasons) or not possible (in case the load machine combination excludes the possibility of fitting a sensor). The real machine speed differs from the reference speed by the slip frequency since the latter is not calculated by the controller.

### Tutorial Results

An example of a drive which utilizes the control concept shown in Fig. 9.2 is given in Tutorial 9.7.2. It uses the same delta connected 22 kW machine as in the previous chapter. An example of the results achieved with this simulation are given in Fig. 9.3, showing the stator flux linkage amplitude  $|\vec{\psi}_s|$ , shaft

speed and shaft torque as function of time. The flux linkage reference was set to  $\psi_s^* = 2.29 \text{ Wb}$  which is the rated stator flux linkage value for this machine. The reference stator frequency, represented in terms of a reference speed, was set to  $n_m^* = 1465 \text{ rpm}$ . A quadratic load torque versus shaft speed function is introduced which provides rated torque  $T_l^{\text{nom}} = 120 \text{ Nm}$  at rated speed  $n_m^{\text{nom}} = 1465 \text{ rpm}$ . An observation of the results given in Fig. 9.3 shows that the steady-state shaft speed and stator flux linkage amplitude are in reasonable agreement with the corresponding control input values. The steady-state shaft speed will be lower than the controller reference value given that the difference between the two speed settings is proportional to the (load dependent) slip frequency. Further details of the simulation are provided in Tutorial 9.7.1.

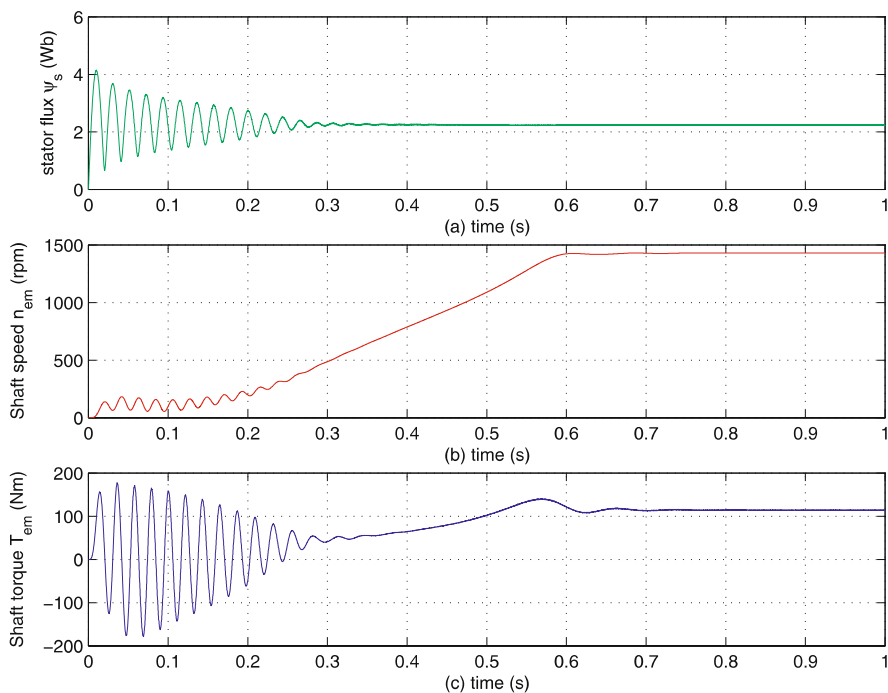


**Fig. 9.3** Delta connected 22 kW machine with simplified V/f based drive controller

Note that the controller in its present form has no provision for ensuring that the stator currents are kept within specified limits. In a practical drive this must be undertaken given that changes to the stator frequency reference can lead to large current perturbations. The nature of control can be compared to that of a voltage source connected DC machine. This can be shown using the model given in Fig. 5.5, where the current source is replaced with a voltage source, which is similar to the quadrature model of the stator flux

oriented machine (see Fig. 8.27). Observation of the quadrature model shows that a frequency  $\omega_s$  step change will lead to a step change in  $u_{sq}$ , which in turn causes a change in current  $i_{sq}$  that is dictated among others by machine operating conditions, i.e., the shaft speed in use. To avoid large current changes, it is therefore prudent to rate limit the stator frequency reference input to the controller.

In the second part of the tutorial given in Sect. 9.7.1 an operating example is discussed where the stator frequency is ramped up with a constant rate of  $\frac{d\omega_s^*}{dt} = 10 \text{ rad/s}^2$ . This case is of interest because drives based on the V/f controller concept discussed in this section may exhibit instability [2, 41, 69] under certain conditions. To ascertain this phenomenon, a bipolar rectangular shaped load torque of 0.2 Nm amplitude and frequency of 4 Hz is introduced in the tutorial given in Sect. 9.7.2. A numerical example showing the behavior of the drive during a 20 s ramp up interval, with the machine initially at standstill is given in Fig. 9.4. The result shown were undertaken with a rotor resistance which is 10% less than the nominal value calculated for this machine on the basis of name plate data (see Sect. 8.6.6), to better demonstrate this resonance phenomenon.

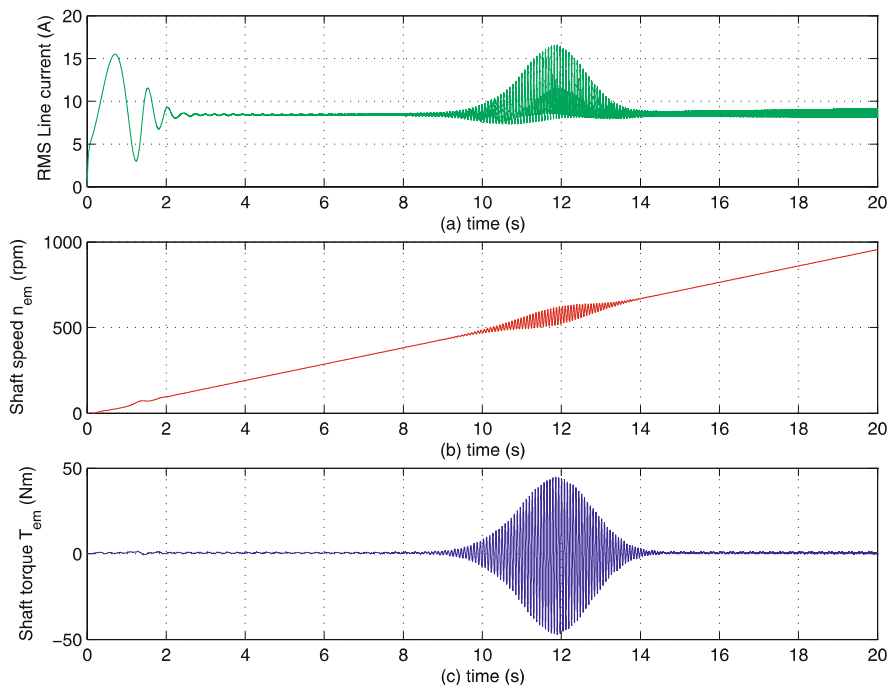


**Fig. 9.4** Delta connected 22 kW machine with simplified V/f based drive controller exhibiting instability

Observation of the results shows that drive instability occurs at shaft speed of approximately 580 rpm, which has severe effects on the stator currents and torque. Note that the instability is substantially reduced when the machine operates with the nominal rotor resistance. Nevertheless, the results demonstrate that induction machines operated (open loop) at low and medium frequencies may exhibit instability. Manufacturers of V/f type drives usually deploy counter measures to alleviate operating speeds where instability can occur. It is also emphasized that the instability depends on a particular combination of machine parameters and operating conditions as is apparent from the example given in Fig. 9.4. Note that running the simulation without the load disturbance torque leads to a result where the instability effect is not triggered.

### 9.1.2 V/f Torque Controller with Shaft Speed Sensor

For drives which have access to the estimated or measured shaft speed  $\omega_m$  a V/f torque control can be implemented. It uses a torque reference  $T_e^*$  and flux linkage reference  $\psi_s^*$  as inputs. The derivation of the generic model of the V/f torque controller is similar to that used in the previous subsection.

The required voltage amplitude  $\hat{u}_s = \sqrt{u_{sd}^2 + u_{sq}^2}$  is again derived using the stator flux oriented model discussed in Sect. 8.3.4.2. In this case, the stator frequency control input is replaced by the torque reference  $T_e^*$ . This implies that the stator frequency  $\omega_s^*$  must now be calculated with the aid of the estimated or measured shaft speed  $\omega_m$ . The stator flux  $\psi_s^*$  control input is unchanged and calculation of the direct axis voltage is undertaken with the aid of equation set (9.6). Computation of the stator frequency reference may be undertaken using  $\omega_s^* = \omega_{sl}^* + \omega_m$ , where the slip frequency variable  $\omega_{sl}^*$  is introduced. The latter may be found using (9.2c) in which the term containing the leakage inductance  $L_{sr}$  is assumed to be small in comparison to the other two terms. Under this condition the slip frequency may be expressed as

$$\omega_{sl}^* \simeq \frac{R_R i_{sq}^*}{\psi_s^*}. \quad (9.7)$$

The quadrature current  $i_{sq}$  variable which appears in expression (9.7) may be found using (9.2e) with  $\psi_s = \psi_s^*$  and  $T_e = T_e^*$ . Computation of the outstanding quadrature voltage variable  $u_{sq}$  is readily undertaken using (9.2b). The resulting generic model which complies with (9.2) and (9.7) under the conditions given above is shown in Fig. 9.5. It includes a module which determines the magnitude of the vector  $\tilde{u}_s^{dq}$  and a polar to Cartesian conversion module to calculate the reference stator voltage vector from the variable  $\hat{u}_s^*$  and  $\rho_s^*$ . The angle  $\rho_s^*$  is found through integration of the calculated stator frequency reference  $\omega_s^*$ .

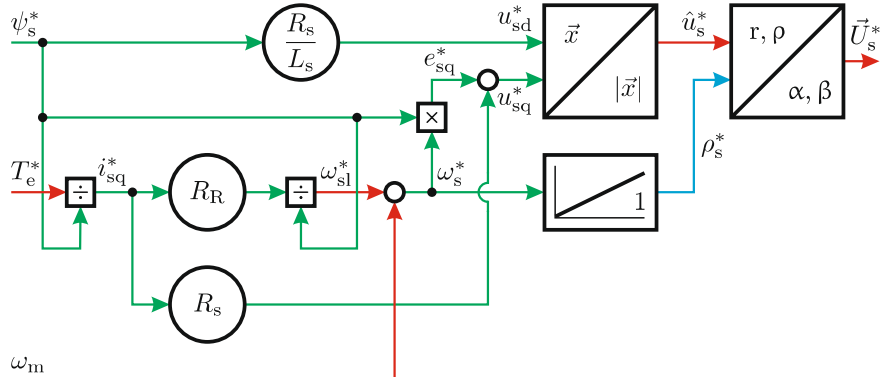


**Fig. 9.5** V/f control structure with shaft speed input

For shaft speeds  $\omega_m \gg \omega_{sl}^{nom}$ , where  $\omega_{sl}^{nom}$  represents the rated slip frequency, the voltage amplitude  $\hat{u}_s^*$  is largely determined by the back EMF  $e_s^* = \psi_s^* \omega_s^*$ . At low stator frequencies the controller terms  $u_{sd}^*$  and  $R_s i_{sq}^*$  become more prevalent in comparison to the term  $e_{sq}^*$  which causes the function  $\hat{u}_s^*(\omega_s^*)$  to deviate from the  $e_{sq}^*(\omega_s^*)$  characteristic in this operating region. The latter operating region is referred to as *low speed voltage boost* [31] and in effect compensates the voltage drop across the stator resistance.

In point A in Fig. 9.1, the machine operates with a shaft speed of  $\omega_{m1}$  whilst delivering a torque  $T_e = T_1$ , which in turn is assumed to be equal to the reference torque  $T_{e1}^*$  of the control unit. The task of the controller is in this case reduced to determining (for a given value of the flux linkage reference  $\psi_s^*$ ) the required slip frequency reference  $\omega_{sl1}^*$ , which together with the measured shaft speed produces the required stator flux linkage frequency  $\omega_s^*$ . If a reference torque step  $\Delta T_e^*$  is applied, the controller will determine the new reference slip frequency  $\omega_{sl2}^*$  which leads to the revised stator frequency  $\omega_{s2}^*$  as shown in Fig. 9.1. The increased machine (steady-state) shaft torque accelerates the machine until the new steady-state operating point B is reached. In this point the reference stator frequency is  $\omega_{s3}^*$ .

### Tutorial Results

In Tutorial 9.7.2 an example of this type of drive is given which makes use of the delta connected 22 kW machine used earlier. An example of the results achieved with this simulation are given in Fig. 9.6, which shows the stator flux linkage amplitude  $|\vec{\psi}_s|$ , shaft speed and shaft torque as function of time. The flux linkage reference was set to  $\psi_s^* = 2.29$  Wb, which is the rated stator flux linkage value for this machine. The reference shaft torque for the controller was set to  $T_e^* = 120$  Nm. An observation of the results given in Fig. 9.6 show that the steady-state shaft torque and stator flux linkage amplitude are in reasonable agreement with the above mentioned control input values.

Further details of the simulation are provided in Tutorial 9.7.2. Note that the V/f torque controller did not decouple torque and flux linkage under transient conditions. Oscillations occur as magnetic and mechanical energy are exchanged during transients.

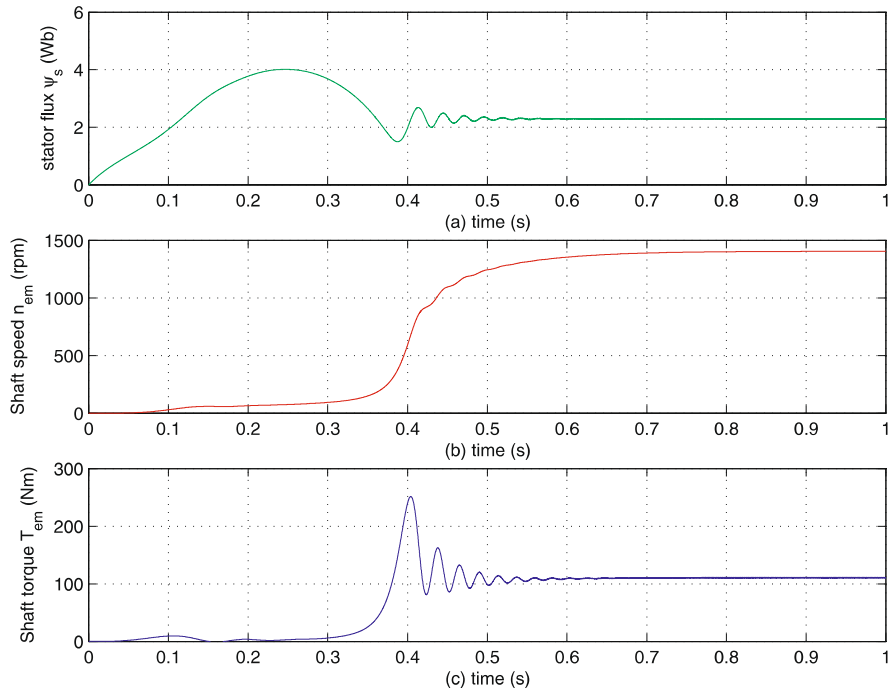


**Fig. 9.6** Delta connected 22 kW machine with V/f based drive controller and shaft speed sensor

## 9.2 Field-Oriented Control

The advent of affordable high-performance digital signal processors has enabled the introduction of field-oriented control for a plethora of applications involving the use induction machines.

Field-oriented control allows independent control of torque and flux linkage under transient conditions. To provide this decoupling, the design of the controller uses the model inversion approach introduced in the previous chapters for the DC and synchronous machine. The drive structure as given in Fig. 9.7 shows the presence of a vector control module which generates a set of reference signals for use with an induction machine operating under current control. The current control methods outlined in Chap. 3 are directly

transferable to the theory and application examples to be discussed in this section.

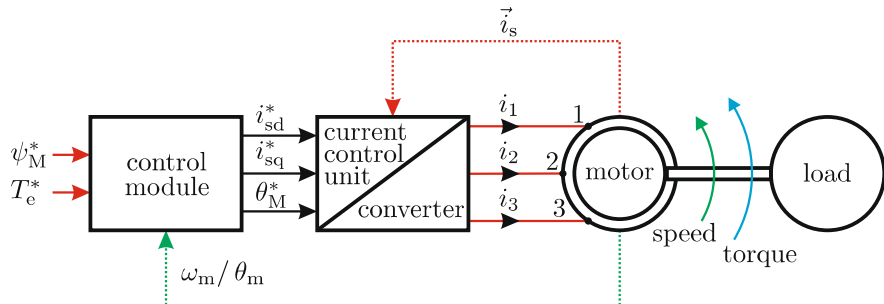


**Fig. 9.7** Field-oriented control drive structure

First, attention is given to the underlying control principles which in turn lead to an in depth treatment of various vector control module implementations which make use of the so-called *direct* or *indirect* field-oriented control of which the principles are developed by K. Hasse [27] and F. Blaschke [7]. In the sequel of this section the integration of the vector control module with the current-controlled induction machine is examined using the current control techniques hitherto presented in Chap. 3. Tutorial examples related to this subject matter are given at the end of this chapter.

### 9.2.1 Controller Principle

#### Torque Control

It is instructive to consider first the rotor flux oriented symbolic and generic model as given in Fig. 8.24. The direct and quadrature machine models play an important role in terms of understanding the basic principles by which to achieve decoupled magnetizing flux linkage and precise torque control. Observation of the direct axis model shows that control of the direct axis current  $i_{sd}$  provides direct control of the magnetizing flux linkage  $\psi_M$ . The time constant by which these flux linkage variations can occur is  $L_M/R_R$ . A constant  $i_{sd}$  value will therefore result in a constant rotor flux linkage magnitude and constant (zero)  $e_{sd}$  value. Torque control is governed by the quadrature stator current component  $i_{sq}$ , given that the latter can be varied without affecting the flux linkage  $\psi_M$ . For example, a torque step with constant magnetizing flux linkage  $\psi_M$  value is realized by changing the  $i_{sq}$  value in accordance with equation

$$i_{\text{sq}} = \frac{T_e}{\psi_M}. \quad (9.8)$$

Hence, the required  $i_{\text{sq}}$  value corresponds to a specified torque and flux linkage value.

Observation of the quadrature model shown in Fig. 8.24 shows that this current change corresponds to a voltage change across the rotor resistance  $R_R$ . This voltage change must be equal to the product of the slip frequency  $\omega_{\text{sl}} = \omega_s - \omega_m$  and magnetizing flux linkage  $\psi_M$ . Since flux linkage and shaft speed cannot change instantaneously, a step increase in the slip frequency is needed. The latter corresponds to an increase in the induced rotor voltage which in turn gives a larger rotor current  $i_{\text{rq}}$  equal to the new stator quadrature current. Hence, the only variable (besides  $i_{\text{sq}}$  and  $i_{\text{rq}}$ ) which can and must be changed instantaneously is the stator frequency  $\omega_s$ . Furthermore, the required stator frequency change must be precise as to ensure that the condition according to (9.9) is always satisfied.

$$(\omega_s - \omega_m) \psi_M = R_R i_{\text{sq}} \quad (9.9)$$

This expression follows directly upon application of Kirchhoff's Voltage Law to the quadrature model shown in Fig. 8.5.

From the previous section it is clear that a current controller is required which is able to deliver the required direct and quadrature currents to the machine. These may in turn be used as inputs to a three-phase current-controlled converter as discussed in Chap. 3.

### Calculation of Field Orientation (CFO)

As mentioned before, torque control can be achieved by controlling the direct and quadrature currents separately. It is obvious, that the controllers reference dq coordinate system must be aligned with the synchronous dq coordinate system formed by the vectors  $\vec{\psi}_M$  and  $\vec{e}_M = j\omega_s \vec{\psi}_M$ . Both systems are rotated by the angle  $\theta_M$  and  $\theta_M^c$  respectively. There are two methods how the controller can determine the angle  $\theta_M^c$  namely:

- *Direct field-oriented control (DFO)* which estimates the angle  $\theta_M^c$  by making use of the flux linkage vector  $\vec{\psi}_M$  or voltage vector  $\vec{e}_M$ . This may be achieved by making use of sensors in the machine or an observer which makes use of measured electrical quantities at the terminals of the machine. This so-called *sensorless* (better *encoderless*) control approach generally refers to operation without mechanical position sensors.
- *Indirect field-oriented control (IFO)* which makes use of mechanical sensors which measure the shaft angle  $\Theta_m$  (position encoder) or integrate the measured shaft speed  $\Omega_m$  (tachogenerator).

There may however be a misalignment between the controller reference and motor reference coordinate systems as indicated in Fig. 9.8. This misalignment causes an error  $\Delta\theta_M = \theta_M^c - \theta_M$  between the reference and actual current values which in turn will affect the torque and magnetizing flux linkage level of the machine. In the case shown, the machine will in steady-state produce a lower magnetizing flux linkage level namely  $\psi_M = L_M i_{sd}$  than the required value  $\psi_M^* = L_M i_{sd}^*$  given that  $i_{sd} < i_{sd}^*$ . In addition, the actual  $i_{sq}$  is slightly higher than the reference value, however, in this case, the torque of the machine will be lower than  $T_e^*$  given that the magnetization level of the machine is lower ( $T_e = i_{sq}\psi_M$ ). The coordinate system misalignment, or so-called de-tuning, should be reduced to a minimum.

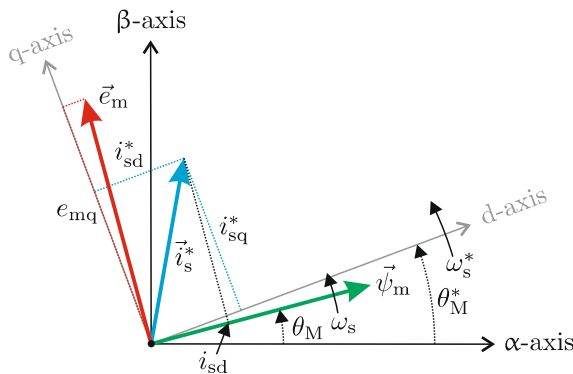


**Fig. 9.8** dq-space vector diagram for motor and controller under detuned conditions

### 9.2.2 Controller Structure

In the previous section the basic controller principles were presented based on a model without leakage inductances. In this section, the leakage inductances are included. The basic *universal field-oriented* UFO model as discussed in Sect. 8.3.4 is used for the development of a generalized controller concept.

The concept is shown Fig. 9.9. It consists of two basic modules, the *UFO control module*, which decouples torque and flux linkage, and the calculation of the flux orientation *CFO control module*.

The UFO module generates the required reference currents  $i_{sd}^*$  and  $i_{sq}^*$  which corresponds to the user defined torque reference  $T_e^*$  and flux linkage reference  $\psi_M^*$  inputs.

The CFO module calculates the d-axis grid reference angle  $\theta_M^c$  for aligning the field-oriented control coordinate system and (in some applications) estimates the flux linkage magnitude  $\psi_M$ . Inputs to the CFO module are, among

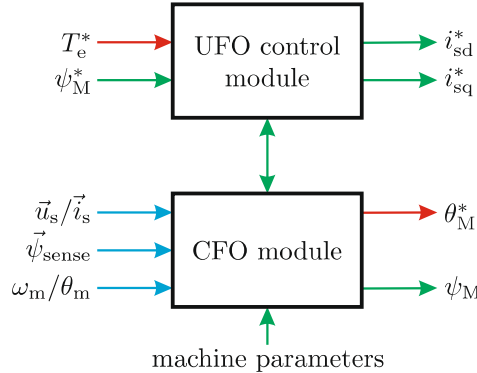


**Fig. 9.9** UFO controller structure

others, the measured stator voltages  $\vec{u}_s$  and stator currents  $\vec{i}_s$ . In addition, the input vector  $\vec{\psi}_{\text{sense}}$  is shown, which represents the flux linkage vector, which is measured with the aid of sensors located inside the machine. The remaining inputs  $\omega_m$  and  $\theta_m$  represent the measured angle or speed using position encoders or tachogenerators. The reader should be keenly aware of the fact that not all input variables of the CFO are required at any one time. The choice of inputs used depends on the control strategy envisaged for a particular drive implementation.

It is noted that invariably a number of estimated machine parameters are required for the controller. The number and choice of parameters is again strongly influenced by the choice of (direct and indirect) field orientation. Last but not least, the required drive performance and the sensitivity of the latter to de-tuning effects caused by parameter variations, as a result of temperature variations, magnetic saturation, or the like within the machine will strongly influence the type of controller to be implemented.

### 9.2.3 UFO Module Structure

A generic representation of the UFO module can be developed by inverting the UFO based dq module given in Fig. 8.22 [16, 50]. The inverse model can be obtained by making use of (8.25b) and (8.26), leading to the generic controller model given in Fig. 9.10.

A comparison between Fig. 9.10 and Fig. 8.22 shows the commonality between the two models. Also apparent from the controller generic diagram is the significance of the inductance parameter  $L_{\sigma R}$ . Setting this variable to zero, i.e., choosing rotor flux oriented control, will significantly reduce the overall controller complexity. This may be directly observed from Fig. 9.10, given that the blue signal paths will then become non-operative.

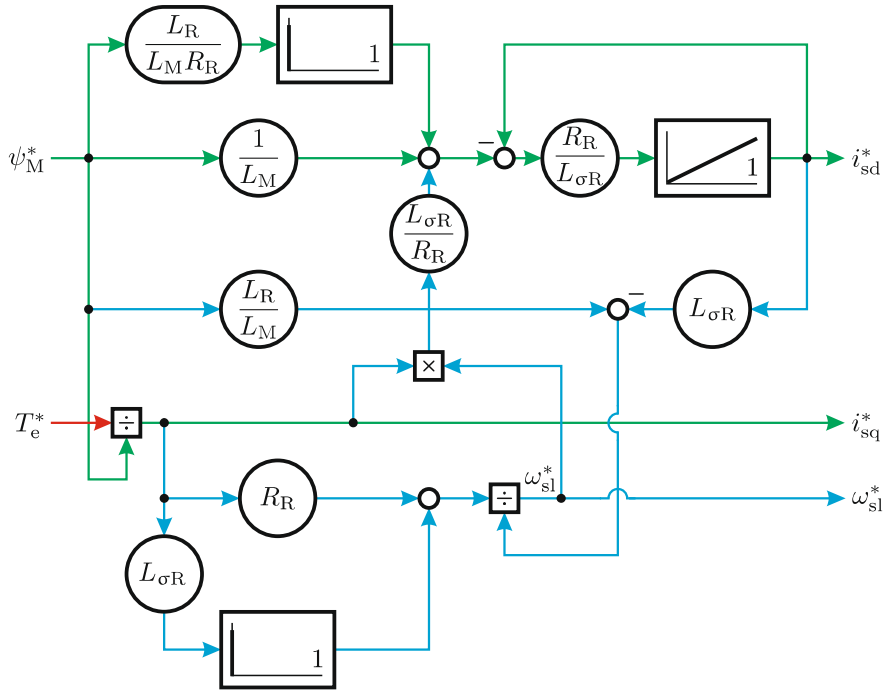


Fig. 9.10 UFO decoupling control structure

The diversity of overall controller implementations precludes the possibility of considering all feasible configurations of the modules shown in Fig. 9.9. Instead, a number of realistic controller configuration will be discussed in the following subsections, which includes both *direct* and *indirect* based field-oriented concepts. The merits of the various configurations, their performance, operating range and sensitivity to detuning will be presented. Tutorials at the end of this chapter will allow the reader to gain additional insight by way of simulations.

#### 9.2.4 IFO Using Measured Shaft Speed or Shaft Angle

In fact, the implementation of a CFO module with indirect field orientation (IFO) requires the relative shaft position as an input. If shaft speed is measured, the following equation can be used:

$$\theta_M^* = \int (\omega_{sl}^* + \omega_m) dt \quad (9.10)$$

where  $\omega_{sl}$  is the rotor slip frequency. This slip frequency can be approximated by the estimated value  $\omega_{sl}^*$ , given by (8.26), which is already computed in the UFO decoupler, shown in Fig. 9.10. The implementation of the CFO module with measured shaft speed is given in Fig. 9.11.

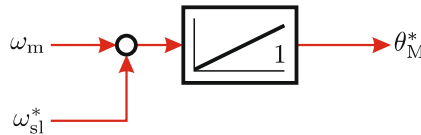


**Fig. 9.11** CFO module: IFO using measured shaft speed

Note that measurement and offset error in the shaft speed, in particular at low speeds, may significantly detune the controller, given the fact that typically  $\omega_{sl} \ll 1$ .

The IFO concept can be readily adapted to make use of an incremental shaft encoder instead of a shaft speed tachometer. Use of a digital encoder is not sensitive to offset errors and can be easily integrated in a digital controller. The CFO module for this approach makes use of the fact that the last term  $\int \omega_m dt$  represents the shaft angle  $\theta_m$ , which is in this case the input variable. The revised generic implementation of the CFO modules with measured shaft speed is shown in Fig. 9.12.

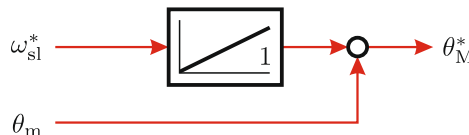


**Fig. 9.12** CFO module: IFO with measured shaft angle

For both implementations with measured shaft speed and shaft position, the transformation variable  $a$  may be set to any value within the range of  $L_m/L_r \leq a \leq L_s/L_m$ . As can be seen from Fig. 9.10, a step in the quadrature current, which corresponds to a step in torque, leads to a step on the inputs of the differentiator. This must be avoided by introducing a rate limiter for  $i_{sq}^*$ . Otherwise a Dirac impulse would lead a step in the slip frequency  $\omega_{sl}$ . In terms of parameters dependency, the method discussed, requires estimates for the parameters  $L_M$  and  $R_R$  as well as the leakage inductance  $L_{\sigma R}$ . The latter may change under varying load conditions, depending on the type of squirrel-cage rotor in use. Also, the rotor resistance is particularly sensitive to temperature variations.

One disadvantage of the approaches is the need to add a sensor to the shaft, which reduces the overall robustness of the drive, i.e., addition of a signal cable between motor and controller. Furthermore, most ‘off-the-shelf’

machines are provided with one drive shaft (used to connect the mechanical load), which further exacerbates the problem of fitting an encoder. On the other hand, the IFO controller with measured shaft angle can function properly at standstill (zero frequency) because no integrators are used to detect flux linkage position.

### 9.2.5 DFO with Air-Gap Flux Sensors

Direct field orientation (DFO) may be realized by measuring the flux density inside the air-gap by way of Hall effect sensors. Figure 9.13 shows the location of two sensors on the real and imaginary axis of a stator based complex plane [7].

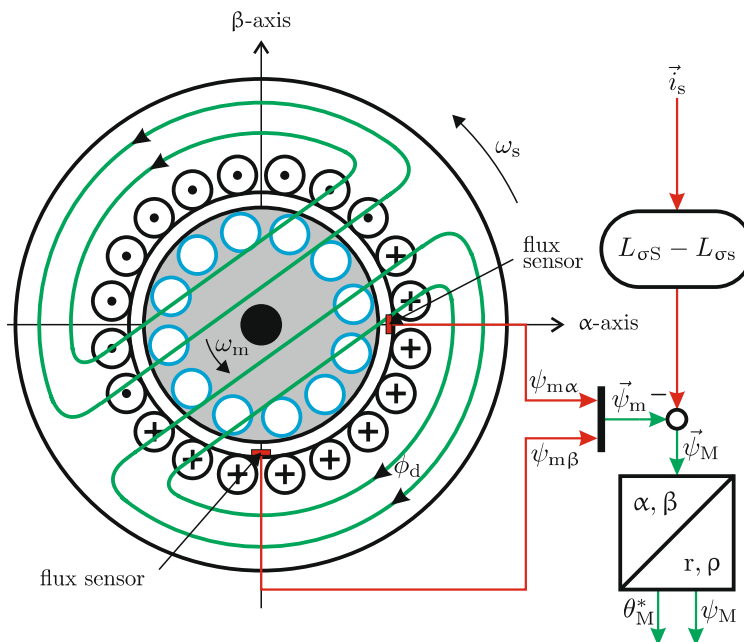


**Fig. 9.13** CFO module: DFO with air-gap flux sensors

A scalar-to-vector module is used to combine the two scalar flux linkage values  $\psi_{m\alpha}$  and  $\psi_{m\beta}$  into a single vector  $\vec{\psi}_m = \psi_{m\alpha} + j\psi_{m\beta}$ . The choice of reference frame for the field-oriented UFO controller is directly linked to the CFO module, which in this case must generate the required output vector  $\vec{\psi}_M$  on the basis of the measured vector  $\vec{\psi}_m$  and stator current vector  $\vec{i}_s$ . The relationship between these vectors may be found with the aid of (8.11), which leads to

$$\vec{\psi}_M = \vec{\psi}_m - (L_{\sigma S} - L_{\sigma s}) \vec{i}_s. \quad (9.11)$$

Also shown in Fig. 9.13 are the generic modules linked with this equation and the Cartesian to Polar conversion module which generates the reference angle  $\theta_M^*$ . It is instructive to consider the implications of choosing a specific transformation ratio. For example, use of a transformation value of  $a = 1$  in the CFO unit, gives an output vector  $\vec{\psi}_M = \vec{\psi}_m$  ( $L_{\sigma s} = L_{\sigma S}$  in (9.11)). This implies that the rotor leakage inductance  $L_{\sigma r}$ , or stator current vector  $\vec{i}_s$  is not required for this unit, under these circumstances. Hence, the reference angle calculation is devoid of parameter dependency. However, the UFO module, as shown in Fig. 9.10, does require the (non-zero) leakage inductance  $L_{\sigma r}$  in the controller as it uses the air-gap flux oriented controller ( $a = 1$ ). Hence, its complexity is increased when compared with a rotor flux oriented controller  $L_{\sigma r} = 0$ . Controlling the air-gap flux linkage is however an attractive option given that the machine design is usually based on a specific air-gap flux density value. Consequently, maintaining this level under varying load conditions makes optimum use of the machine.

A rotor flux oriented controller may also be used, in which case the CFO module (as defined by (9.11)) and UFO module must be used with a transformation variable of  $a = L_m/L_R$ . Note in this context that any arbitrarily chosen reference frame may be used provided that the transformation factor is varied within its range in both modules.

Hall effect sensors are often used in laboratories for the air-gap flux density measurement. However, use of air-gap sensors, confines the user to a none standard machine and severely limits the maximum temperature range of the drive (typically less than 120 °C). Hence, the issue of sensor reliability and drive robustness needs to be addressed when pursuing this control approach.

### 9.2.6 DFO with Sensor Coils

The use of a set of sensor coils located in the stator windings on the stationary real and imaginary axis, as shown in Fig. 9.14, provides the stator flux linkage by integration of the induced voltage. Alternatively, taps on stator windings can provide the same information [17, 49].

The induced sensor voltages  $e_{s\alpha}$  and  $e_{s\beta}$  must be integrated to obtain the estimated stator flux linkage vector  $\vec{\psi}_s$ . This task is performed in the CFO module which also generates a reference vector  $\vec{\psi}_M$  for the UFO controller and making use of (9.12).

$$\vec{\psi}_M = \vec{\psi}_s - L_{\sigma S} \vec{i}_s \quad (9.12)$$

where  $\vec{i}_s$  represents the measured current and  $L_{\sigma S}$  is the estimated leakage inductance as defined by (8.12a). The latter is a function of the transformation variable  $a$ , which must be given the same value for both UFO and CFO

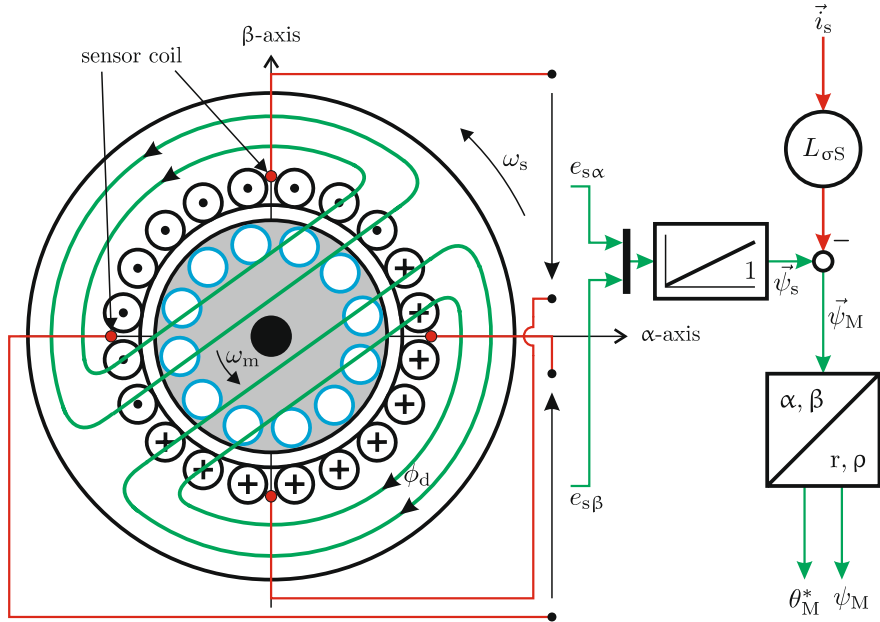


**Fig. 9.14** CFO module: DFO with sensor coils

modules. Setting this value to  $a = L_s/L_m$  corresponds to a value of  $L_{\sigma s} = 0$ , hence  $\vec{\psi}_M = \vec{\psi}_s$  (see (9.12)) which is beneficial in this case because it avoids the need to measure the stator currents. This type of approach requires the insertion of sensor coils in the machine, which precludes its use for standard ‘off-the-shelf’ machines. Furthermore, the need to integrate the sensor voltages, makes this method unsuitable for applications where the frequency of the rotating magnetic field becomes zero.

### 9.2.7 DFO with Voltage and Current Transducers

A alternative approach to deriving the required flux linkage vector  $\vec{\psi}_M$  is to consider the machine from the stator terminal side [26, 71, 70]. This approach makes use of the three measured inverter voltages and (8.16a) which may be rewritten as

$$\frac{d\hat{\vec{\psi}}_s}{dt} = \underbrace{\vec{u}_s - R_s \vec{i}_s}_{\vec{e}_s} \quad (9.13)$$

in which  $\hat{\vec{\psi}}_s$  represents the estimated stator flux linkage vector. Equation (9.13) shows that this method requires access to the stator voltage vector

$\vec{u}_s$  and requires knowledge of the stator resistance and the current vector  $\vec{i}_s$  as derived by measurement of the stator currents. The *universal* flux linkage vector  $\vec{\psi}_M$  may be found using (9.12) once integration of the *EMF* vector  $\vec{e}_s$  has been undertaken. The observer structure (in space vector form), as determined by (9.13) and (9.12) is given in Fig. 9.15.

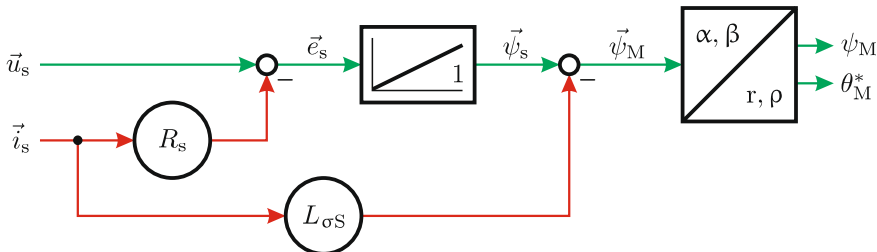


Fig. 9.15 CFO module: DFO with voltage and current transducers

Practical implementation of the DFO observer structure requires access to measured signals on the converter output side which must be linked to the controller module. This may lead to electrical noise problems between these two modules. In addition, an analog or high-frequency integrator must be used to directly process the continuous inverter PWM voltage waveforms. Use of the sampled voltage, synchronized to the PWM modulator, is not feasible given that at the sampling time intervals the zero vector is usually active. The remaining part of the observer may be implemented either in discrete time or via an analog circuit. However, it is important to note that the observer makes use of the parameter  $R_s$  as mentioned above. This parameter is (among others) subject to temperature variations in the motor. This will lead to observer errors which are of particular concern at lower speeds where the converter voltage magnitude approaches the magnitude of the term  $R_s \vec{i}_s$ . This implies that observers of this type may need to estimate the stator resistance variation by way of the measuring or estimating the stator winding temperature. In addition, similar to DFO with stator sensor coils, this method does not function in applications with zero stator frequency.

### 9.2.8 DFO with Current and Shaft Speed Transducers

This current based observer requires access to the measured currents and the measured or estimated shaft speed. The observer structure is based on equation set (8.19) which together with the IRTF module gives the generic observer structure shown in Fig. 9.16.

A complex representation of the observer structure as shown in Fig. 9.16 highlights the presence of the rotor resistance parameter which is subject to large variations as a result of temperature changes in the rotor.

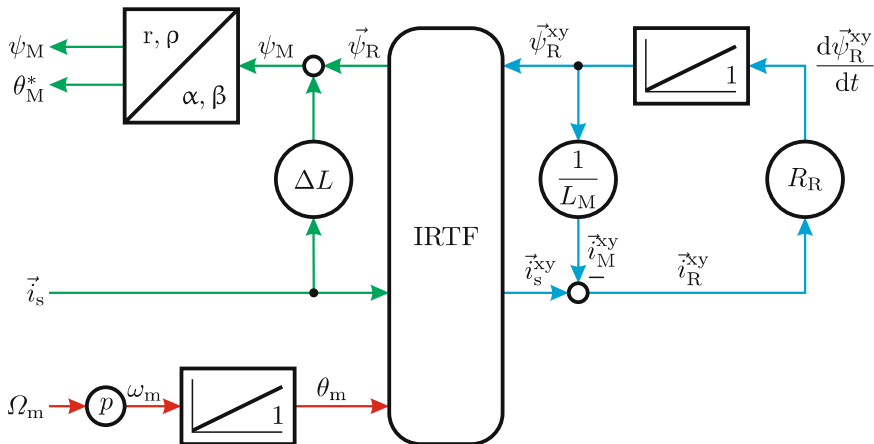


**Fig. 9.16** CFO module: DFO with current and shaft speed transducers

The observer structure is identical to that used on the rotor side of the IRTF rotor flux based generic motor model shown in Fig. 8.15. Consequently, differences between the observer and actual motor rotor resistance  $R_R$ , variations in  $L_M$  due to saturation effects as well as errors between measured and actual shaft speed may affect the estimated *universal* flux linkage vector  $\vec{\psi}_M$ , in particular at low slip frequencies where the integrator gain will be high. The major advantage of this observer is that it avoids the need to measure the converter voltages. Its use is particularly advantageous in the low shaft speed region, high slip area (low stator frequencies), where errors in the shaft speed or rotor resistance will not contribute significantly to an error in the flux linkage estimate.

Computation of the required *universal* flux linkage vector  $\vec{\psi}_M$  may be undertaken with the aid of equation set (8.16) which leads to the following expression

$$\vec{\psi}_M = \vec{\psi}_R + \underbrace{\left( L_{\sigma S}(a = \frac{L_m}{L_r}) - L_{\sigma S}(a) \right)}_{\Delta L} \vec{i}_s \quad (9.14)$$

in which the gain  $\Delta L = (L_{\sigma S}(a = L_m/L_r) - L_{\sigma S}(a))$  is introduced. With the addition of this gain module (see Fig. 9.16) the user is able to select the required transformation value  $a$  which corresponds to the flux linkage vector  $\vec{\psi}_M$  of the observer.

In some cases, the observer in question is used in conjunction with the previous voltage/current based observer. The advantage of this approach is that

at low shaft speeds use can be made of the current based observer, whereas at higher speeds a voltage based observer is used. This approach uses each observer in the speed range for which it is most suited. Care must be taken to ensure a seamless transition from current/shaft speed to voltage/current observer and vice versa.

### 9.3 Operational Drive Boundaries for Rotor Flux Oriented Control

The approach used to visualize the control laws and operating limits imposed by the maximum voltage and current values for the synchronous and DC drives may be readily extended to the field-oriented current-controlled induction machine drive. As with the previous cases a synchronous dq complex plane is used of which the direct axis d is tied to the flux linkage vector  $\vec{\psi}_R$ , given that rotor flux oriented control is considered here. This approach was widely used first due to the simplicity of the controller structure, which is achieved as a result of a natural (simple) decoupling of the direct and quadrature currents (see Fig. 9.10).

#### Steady-State Equations

The machine equation set tied to the direct and quadrature model shown in Fig. 8.24 is reconsidered. The operational drives limitations are derived for quasi-steady-state, which leads to

$$\vec{u}_s^{dq} = R_s \vec{i}_s^{dq} + j \omega_s \vec{\psi}_s^{dq} \quad (9.15a)$$

$$\vec{\psi}_s^{dq} = \vec{\psi}_R + L_{sS} \vec{i}_s^{dq} \quad (9.15b)$$

$$\vec{T}_e = \vec{\psi}_R \times \vec{i}_s^{dq} = \psi_R i_{sq} \quad (9.15c)$$

for the voltage, flux linkage and torque equation respectively. For quasi-steady-state operation, the flux linkage  $\psi_R$  is given as  $\psi_R = L_M i_{sd}$ , which underlines the fact that the direct axis current defines the magnetization in the machine. This is decidedly different when compared to the DC and synchronous machines drives discussed in the previous chapters.

#### General Machine Operation Below and Above Base Speed

In the *base speed range* (which is yet to be defined) the rotor flux linkage is normally held at its rated value henceforth defined as  $\psi_R^{\max}$ , which in turn corresponds to a maximum direct axis current value  $i_{sd}^{\max} = \psi_R^{\max}/L_M$ . Maintaining maximum flux linkage in the machine is beneficial because it gives the user the flexibility to set the torque between zero and maximum value without the need to adjust the flux linkage level  $\psi_R$ , which is governed by the large time constant  $L_M/R_R$  (as can be seen in Fig. 8.24). If the flux linkage is held constant any torque step will only be dictated by the time

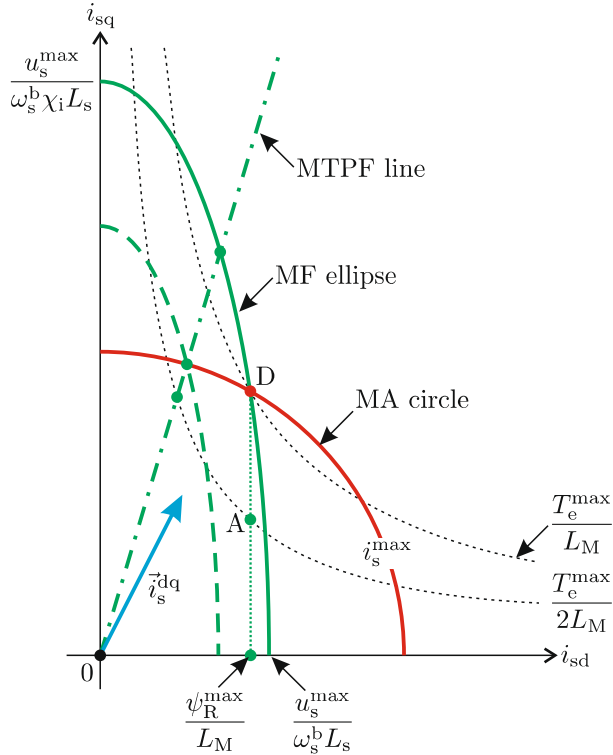


**Fig. 9.17** Operational drive limits for rotor flux oriented induction machine drive

needed to change the quadrature current  $i_{sq}$  (only limited by voltage across  $L_{qs}$ ).

For operation above the base speed the voltage limit is reached. The flux linkage  $\psi_R$  needs to be changed and the *field weakening* region is entered. This allows to extend the operating speed of the drive at the cost of reduced dynamic performance.

### Lines of Constant Torque

It is helpful to rewrite the torque as

$$T_e = L_M i_{sd} i_{sq} \quad (9.16)$$

with  $\psi_R = L_M i_{sd}$ . Contours of constant torque according to (9.16) are given in the operational drive limits diagram for induction machines shown in Fig. 9.17.

### Current Limit (Maximum Ampere, MA)

This diagram also shows the maximum current MA circle with radius  $i_s^{\max}$  introduced earlier. The region within the circle represents the operating region of the drive in terms of the maximum current constraints imposed by the machine, the main supply or by power electronic converters

$$|\vec{i}_s^{dq}| \leq i_s^{\max}. \quad (9.17)$$

### Maximum Rotor Flux Constraint

For the induction machine drive only part of the MA region is accessible given the maximum rotor flux constraint imposed by the machine, which is shown in Fig. 9.17 by way of the vertical line that passes through operating point A and D where  $i_{sd}$  equals its maximum value  $i_{sd}^{\max}$  with

$$i_{sd}^{\max} = \frac{\psi_R^{\max}}{L_M}. \quad (9.18)$$

### Voltage Limit (Maximum Flux Linkage, MF)

Figure 9.17 also shows a set of elliptical contours which are tied to the maximum voltage constraint  $u_s^{\max}$ . The introduction of these maximum flux linkage (MF) contours is based on the use of (9.15a) and the underlying assumption that the dominant term in this expression is formed by the induced voltage. With this assumption in mind, the stator flux linkage variable  $\psi_s^{\max}$  is introduced (as was also done for previous drive topologies), which according to (9.15a) with  $|\vec{u}_s^{dq}| = u_s^{\max}$  and  $\vec{u}_s^{dq} \cong j\omega_s \vec{\psi}_s^{dq}$ , can be written as

$$\psi_s^{\max} \cong \frac{u_s^{\max}}{\omega_s}. \quad (9.19)$$

From an operational perspective the variable  $\psi_s^{\max}$  represents the maximum stator flux linkage value that may be realized by the converter for a given speed  $\omega_s$  and voltage  $u_s^{\max}$ . Use of  $|\vec{\psi}_s^{dq}| = \psi_s^{\max}$  with (9.15b) and equating the real and imaginary components of  $\vec{i}_s^{dq}$  gives

$$i_{sd}^2 + (\chi_i i_{sq})^2 = \left( \frac{\psi_s^{\max}}{L_s} \right)^2 \quad (9.20)$$

where

$$\chi_i = \frac{L_{\sigma S}}{L_s} \quad (9.21)$$

represents the ratio between leakage inductance  $L_{\text{oS}}$  and stator inductance. Observation of (9.20) shows that this expression is indeed an ellipse with its origin at coordinates  $(0, 0)$ . It intersects the direct and quadrature axis at  $\pm u_s^{\max}/\omega_s L_s$  and  $\pm u_s^{\max}/\chi_i \omega_s L_s$  respectively, as may be observed from Fig. 9.17. Note that the value of  $\chi_i$  used in Fig. 9.17 was purposely chosen high for didactic reasons, i.e., to better illustrate the various operating trajectories. The elliptical MF contours will change with frequency  $\omega_s$  and stator voltage (as was the case with previous drive topologies).

### Drive Saturation Point and Base Speed

A base operating point referred to as the *drive saturation point* or *corner point* may be identified. The base speed of the drive corresponds with the ellipse that intersects the maximum current MA circle and maximum rotor flux linkage (MF) lines, i.e., at point D. The base speed may with the aid of (9.20) and (9.19) and  $i_{\text{sd}}^2 + i_{\text{sq}}^2 = (i_s^{\max})^2$  be written as

$$\omega_s^{\text{b}} = \left( \frac{u_s^{\max}}{L_s i_s^{\max}} \right) \frac{1}{\sqrt{\chi_i^2 + \kappa_i^2 (1 - \chi_i^2)}} \quad (9.22)$$

where the variable  $\kappa_i$  is introduced, which is defined as

$$\kappa_i = \frac{\psi_R^{\max}}{L_M i_s^{\max}}. \quad (9.23)$$

### Maximum Torque per Flux Linkage (MTPF) Line

The *maximum torque per flux linkage* MTPF line for this type of machine may be found by considering the torque contours according to (9.16) and the elliptical maximum flux linkage (MF) contours (see (9.20)). For a given torque  $T_e$ , which corresponds to a hyperbola in Fig. 9.17, a operating frequency will occur where the ellipse will no longer intersect said curve but merely touches the  $T_e$  hyperbola in a single point. The direct and quadrature currents for this operation along the MTPF line are represented by the condition

$$i_{\text{sd}} = \frac{u_s^{\max}}{\sqrt{2} \omega_s L_s} \quad (9.24a)$$

$$i_{\text{sq}} = \frac{i_{\text{sd}}}{\chi_i} \quad (9.24b)$$

which may be derived by use of (9.16) and differentiation of the latter with respect to the torque after substitution of (9.20).

Operation along the MTPF line signifies drive operation above the base speed with the highest possible torque level for a given stator flux linkage value. In a practical sense, operation along this line above the base speed is restricted by the need to adhere to the maximum current constraint. This implies that operation along the MTPF line is possible for that part of the trajectory which is within the maximum current MA circle.

### Maximum Torque per Ampere (MTPA) Line

The *maximum torque per ampere* MTPA line as discussed for previous drive topologies is not shown in Fig. 9.17. This line which may be found by use of (9.16) and differentiation of the latter with respect to the torque after substitution of the expression  $i_{sd}^2 + i_{sq}^2 = (i_s^{max})^2$  (which represents the MA circle) represents the control law

$$i_{sd} = 0 \rightarrow \frac{\psi_R^{max}}{L_M} \quad (9.25a)$$

$$i_{sq} = \pm i_{sd} \quad (9.25b)$$

which signifies an operating trajectory where the highest torque is obtained with the lowest stator current value. For induction machines, operation under MTPA conditions is normally not done, given the need to simultaneously vary the flux linkage level  $\psi_R$  and quadrature current, which significantly degrades the dynamic performance of the drive as mentioned earlier. Furthermore, the maximum torque achievable under MTPA conditions is constrained by the maximum allowable direct axis current value  $i_{sd}^{max}$ .

## 9.4 Field Weakening for Rotor Flux Oriented IM Drives

Field weakening for field-oriented induction machine drives is readily achieved by reducing the direct axis current component  $i_{sd}$  and manipulating the quadrature current  $i_{sq}$  according to a chosen control strategy. The current locus and corresponding dq current versus speed characteristics will be examined in this section, which assumes a rotor flux oriented control structure. The current space vector locus as given in Fig. 9.18, shows three specific operating trajectories which exemplify three different operating regions namely base speed range, basic field weakening and maximum torque per flux linkage operation.

**d-Axis Current in Base Speed Range,  $0 \leq \omega_s \leq \omega_s^b$  ( $\psi_R^{max}/L_M \rightarrow A$ )**  
Below the base speed  $\omega_s^b$ , the d-axis current  $i_{sd}$  is set to its rated value, i.e.,

$$i_{sd} = i_{sd}^R = \frac{\psi_R^{max}}{L_M}. \quad (9.26)$$

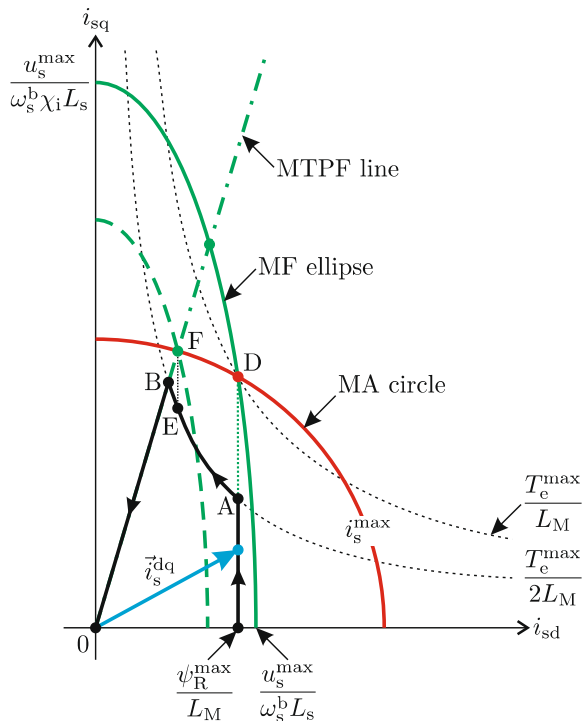


**Fig. 9.18** Current locus diagram: Operational drive limits for rotor flux oriented induction machine drive

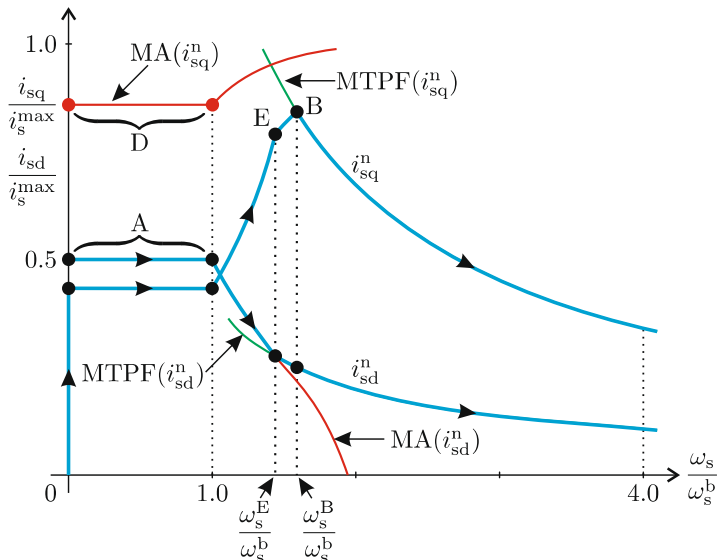


**Fig. 9.19** Current-speed diagram for rotor flux oriented induction machine drive

Note that in point A the torque reaches 50% of its maximum base speed value, which is assumed here as an example.

### d-Axis Current in Basic Field Weakening, $\omega_s^b \leq \omega_s \leq \omega_s^B$ ( $A \rightarrow B$ )

As speed increases, the maximum flux linkage ellipse decreases in size. The base speed  $\omega_s^b$  is reached when the ellipse intersects the MA circle at point D. The available torque then quickly approaches zero if  $i_{sd}$  is kept constant at its rated value and when the speed is increased further. This occurs at speed  $\omega_s^l$  when the MF ellipses intersect with the d-axis at  $i_s = i_{sd} = \psi_R^{\max}/L_M$ . With the aid of (9.20) and (9.23)  $\omega_s^l$  is derived as

$$\omega_s^l = \left( \frac{u_s^{\max}}{L_s i_s^{\max}} \right) \frac{1}{\kappa_i}. \quad (9.27)$$

$\omega_s^l$  is approximately equal to the base speed  $\omega_s^b$ , given that the condition  $\chi_i \ll \kappa_i$  normally holds. Hence, for operation above base speed, field weakening is applied by reducing the direct current  $i_{sd}$ . Strongest field weakening is required where the MA circle intersects the MF ellipse. For the same reason as above,  $i_{sd}$  is used for all torque values at one particular speed. To derive the expression for  $i_{sd}$  in field weakening, the MA expression  $(i_s^{\max})^2 = (i_{sd})^2 + (i_{sq})^2$  is used for  $i_{sq}$  in the MF (9.20). Solving for  $i_{sd}$  leads to the expression

$$i_{sd} = \sqrt{\frac{\left(\frac{\psi_s^{\max}}{L_s}\right)^2 - \chi_i^2 (i_s^{\max})^2}{1 - \chi_i^2}}. \quad (9.28)$$

In normalized form:

$$i_{sd}^n = \sqrt{\frac{\left(i_o^b \frac{\omega_s^b}{\omega_s}\right)^2 - \chi_i^2}{1 - \chi_i^2}} \quad (9.29)$$

with  $i_o^b = u_s^{\max}/\omega_s^b L_s i_s^{\max}$ .

Some simplification of expression (9.29) is possible by taking into account that the condition  $\chi_i \ll 1$  usually holds (which gives an elongated ellipse along the major axis) in which case the above expression may be reduced to

$$i_{sd}^n \simeq \kappa_i \left( \frac{\omega_s^b}{\omega_s} \right). \quad (9.30)$$

### d-Axis Current along MTPF Line, $\omega_s^B \leq \omega_s$ ( $B \rightarrow (0, 0)$ )

The d-axis current  $i_{sd}$  needs to remain greater than the direct current which corresponds to operation along the MTPF line. Therefore, eventually the torque command dependent speed  $\omega_s^B$  (compare Fig. 9.19) is reached. Above this speed, operation occurs along the MTPF line with  $i_{sd}$  being defined by (9.24a). The maximum available torque decreases accordingly.

### **q-Axis Current**

With the analysis undertaken thus far the direct axis current is fully defined. What remains to be defined is the quadrature current versus speed relationship. A constraint is that the dq current stays within the envelope formed by the maximum current circle and MTPF line as may be observed from current locus diagram in Fig. 9.18.

One option is to maintain the user defined torque level beyond the base speed (a control directive also pursued for the synchronous drive) in which case the current is defined as

$$i_q = \frac{T_e}{L_M i_{sd}}, \quad (9.31)$$

where  $i_{sd}$  defined by (9.26) for the base speed range, (9.28) during basic field weakening, and (9.24a) along the MTPF trajectory.

### **Discussion of Trajectories**

In the following, the above derived rules will be briefly discussed on the trajectories in the current locus diagram in Fig. 9.18 and the current-speed diagram in Fig. 9.19.

The first trajectory, from point  $\psi_R^{\max}/L_M \rightarrow A$ , corresponds to a 50% maximum torque step applied when the machine is at standstill. This operation trajectory is, as required, on the rated  $i_{sd}^R$  line and occurs in the basic speed range.

The trajectory A to B lies in the basic field weakening range. The torque is kept constant while the dq current is altered following the voltage limit. Figure 9.18 and Fig. 9.19 show that limited operation under constant torque conditions is feasible in the field weakening mode with the chosen control strategy.

At point B the constant torque can no longer be maintained and decreases while the dq current follows the MTPF trajectory.

This statement is underlined by the tutorial given in Sect. 9.7.5 which examines field weakening according to the control principles set out above. The controller in question is used in conjunction with a current source based, induction machine model operating with rotor flux oriented field control.

### **Alternative Field Weakening Strategy**

An often used alternative field weakening strategy follows the approach taken for the separately excited machine, where the armature current  $i_a$  is held constant for an extended period after the base operating speed has been reached (see Sect. 5.3.2). For the IM drive this condition implies maintaining  $i_{sq}$  constant for operation in excess of  $\omega_s^b$ , in which case

$$i_{sd}^n \simeq \kappa_i \left( \frac{\omega_s^b}{\omega_s} \right) \quad (9.32)$$

according to (9.30) and

$$i_{sq}^n = \text{constant}. \quad (9.33)$$

The current values according to (9.32) and (9.33) are maintained in this so-called constant power mode of operation (akin to operation region B for the DC drive, see Fig. 5.11) provided these variables are within the currents which correspond to the MTPF envelope (see equation set (9.24) and Fig. 9.19).

## 9.5 Interfacing the Field-Oriented Controller with a Current-Controlled Induction Machine

Prior to discussing field-oriented control with a voltage source based machine it is instructive to consider the use of a current based IRTF model. This approach is helpful because it allows the user to examine the interaction between vector control module and induction machine without the need to consider the vagaries of the current controller. The proposed drive concept as given in Fig. 9.20 shows the vector control module as represented by the UFO control module (see Fig. 9.10) and the CFO module. The latter may, as was discussed in the previous sections, use a range of inputs for determining the instantaneous angle  $\theta_M^*$  of the flux linkage vector  $\vec{\psi}_M$  of the machine. For the sake of simplicity an IFO approach has been arbitrarily selected which makes use of the measured rotor angle  $\theta$  of the machine (see Sect. 9.2.4), i.e., use is made of a encoder connected to the motor shaft.

For the representation of the machine the *standard* rotor flux based model as discussed in Sect. 8.3.2.1 is used. However, in this case the model is used with the stator current  $\vec{i}_s$  as an input vector instead of the voltage vector  $\vec{u}_s$ . Observation of equation set (8.19) shows that the corresponding generic model is reduced to the structure given in Fig. 9.20. Note that any of the models given in Chap. 8 could equally have been used to represent the machine. The machine model shown in Fig. 9.20 makes use of a gain module  $\Delta L$ , as introduced earlier (see (9.14)), which is used in conjunction with the current  $\vec{i}_s$  and flux linkage vector  $\vec{\psi}_R$  to generate the flux linkage vector  $\vec{\psi}_M$ . With the introduction of a gain module  $\Delta L$  the user is able to examine the impact of changing the transformation variable  $a$  on the flux linkage vector  $\vec{\psi}_M$  in the machine. More specifically, the amplitude of the flux linkage vector  $\vec{\psi}_M$  should match the flux linkage reference  $\psi_M^*$  for any chosen value of  $a$  within the range  $L_m/L_r \leq a \leq L_s/L_m$ . Furthermore, the instantaneous torque  $T_e$  generated by the machine should match the reference torque  $T_e^*$  used by the UFO controller.

### Tutorial Results

The tutorial given in Sect. 9.7.3 is a direct embodiment of the drive concept shown in Fig. 9.20. The 22 kW delta connected *standard* machine as used earlier in this chapter (see Fig. 9.6) is again used where the flux linkage

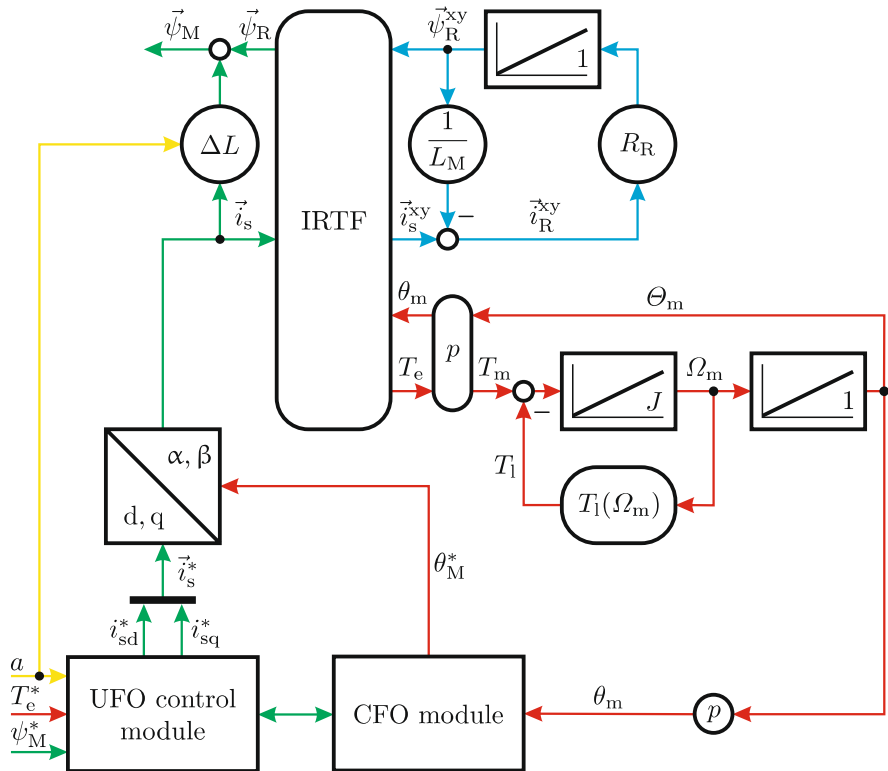


**Fig. 9.20** Field-oriented control with current source induction machine model

reference  $\psi_M^*$  is set to 2.29 Wb. A rated shaft torque step from  $T_e^* = 0 \rightarrow 120$  Nm is applied at  $t = 200$  ms and the torque reference is reversed at  $t = 300$  ms. No external load is connected to the machine. The results given in Fig. 9.21 show the shaft torque, shaft speed and flux linkage  $\psi_M$ , which in this case represents the stator flux linkage given that the variable  $a$  has been set to allow the vector controller to operate under stator flux oriented control.

A comparison with the results given in Fig. 9.21 and those obtained with the classical control approach (see Fig. 9.6) shows the remarkable degree of control that can be achieved using field-oriented control. Note that changing the transformation variable  $a$  will not basically change the results shown, as may be deduced by considering the simulation results given in Sect. 9.7.3. Some minor changes are apparent due to the presence of non-ideal differentiators in the controller. Furthermore, the torque and flux linkage step were moderated through the use of a low pass filter with a time constant of 2 ms and 10 ms respectively. Without these filters unrealistically high currents would appear in the simulation and correspondingly, in the actual machine.

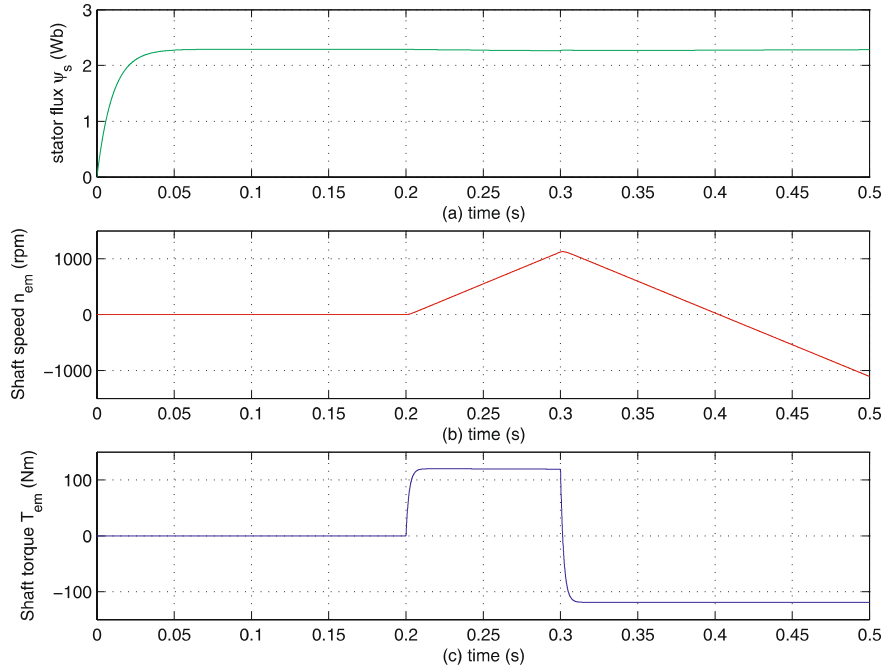


**Fig. 9.21** Delta connected 22 kW machine with UFO based drive controller and shaft encoder

The reader is referred to the tutorial given in Sect. 9.7.3 for further details regarding the simulation model and the opportunity to interactive explore the drive concept presented.

## 9.6 Interfacing the Field-Oriented Controller with a Voltage-Source-Connected Induction Machine

The practical implementation of the current-controlled machine discussed in the previous section requires the use of a voltage source converter. Consequently, a three-phase current control approach as discussed in Sect. 3.2 must be integrated with the drive. In this section, a three-phase model based current controller is used, because these are generally favored in practical drive applications, among others for acoustic noise reasons as was mentioned in Sect. 3.2.2. The generic representation of the current controller in question, as shown in Fig. 3.19 is connected to a generalized load which define the parameters for the discrete model based synchronous current controllers which is tied to the vector  $\vec{\psi}_e$ . For the induction machine drive, the latter vector must be replaced by the flux linkage vector  $\vec{\psi}_M = \psi_M e^{j\theta_M^*}$ , where the

angle  $\theta_M^*$  is generated by the CFO module. Furthermore, the parameters used for the controller need to be redefined, given that the *load* is in this case an induction machine. For the purpose of determining the parameters it is helpful to consider the asynchronous rotor flux oriented direct and quadrature axis symbolic models of the machine shown in Fig. 8.24. For the direct axis current controller calculation of the sampled average voltage reference  $U_d^*(t_k)$  is carried out with the aid of (3.21a), in which the parameters  $R$  and  $L$  must be replaced by the variables  $R_s$  and  $L_{\sigma s}$  given the nature of the *load* in use. A similar approach must be used for the computation of quadrature axis controller sampled average voltage reference  $U_q^*(t_k)$ , where (3.21b) is used, in which case the parameters  $R$  and  $L$  must be replaced by the machine parameters  $R_s$  and  $L_{\sigma s}$ . Furthermore, this expression shows the presence of a disturbance decoupling term  $u_e = \psi_e \omega_e$ , which corresponds to the term  $\psi_M \omega_s$  in an asynchronous drive.

The resultant drive structure as shown in Fig. 9.22 brings together key concepts, such a modulation and current control introduced in earlier chapters of this book.

Readily apparent in Fig. 9.22 is the model based current controller which uses current reference values produced by the *UFO Control module* as discussed in the previous section. The observant reader will note that a disturbance decoupling term  $\psi_M \omega_m$  is shown in the current controller module, whereas in theory the frequency  $\omega_s$  should have been used. In the example given here the shaft speed was deemed to be accessible and it is therefore prudent to utilize this variable, given the need to otherwise obtain an estimate for the slip frequency. This means that the error in the feed forward term needs to be generated by the current controller integrator, which results in a slight loss of dynamic performance. The remaining terms  $\omega_s L_{\sigma s} i_{sd}$  and  $-\omega_s L_{\sigma s} i_{sq}$  are not used in this example, given that their contribution is typically small in comparison with the term  $e_q$ . Also shown in Fig. 9.22 is the generic model of the IRTF based rotor flux based induction machine according to Fig. 8.15. From a simulation perspective the voltage source converter/modulator structure is often replaced by an alternative module which calculates the requires supply vector directly from the average voltage references generated by the current controller. This approach, as outlined in Sect. 3.3.5, reduces the simulation run time and a larger computational step size may be selected.

## Tutorial Results

In the accompanying tutorial given in Sect. 9.7.4 the reader is able to examine in detail an implementation example which involves the 22 kW four pole delta connected machine used in earlier tutorials in this book. Shown in Fig. 9.23 are some of the results obtained with the simulation model given in Sect. 3.3.5. In this instance the UFO controller was set to operate under stator flux oriented control ( $a = L_s/L_m$ ) with a flux linkage reference setting of  $\psi_M = 2.29$  Wb which corresponds to the rated stator flux linkage value of the

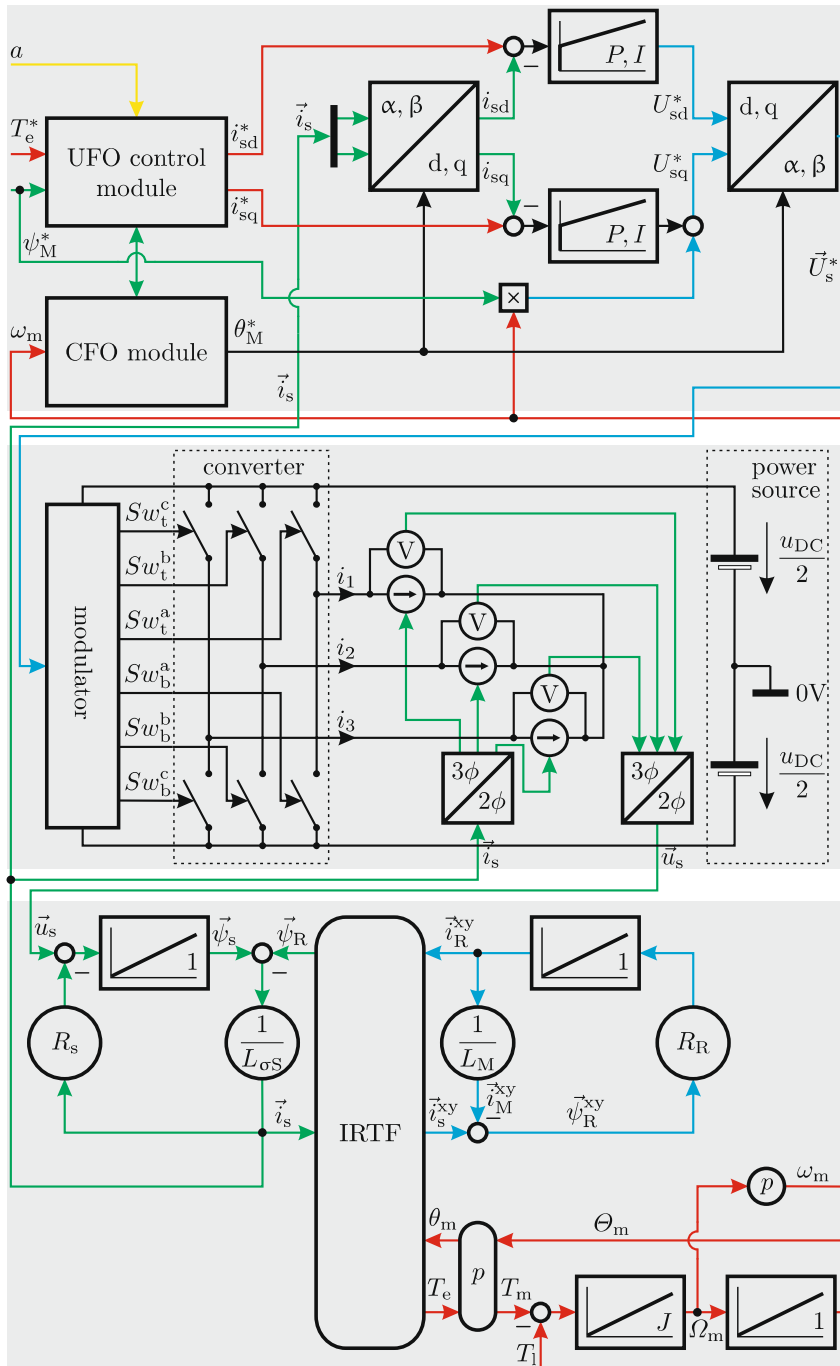


**Fig. 9.22** Field-oriented control with voltage source induction machine model and model based current control

machine in use. A rated torque step was applied at  $t = 3.5$  s and subsequently reversed at  $t = 3.55$  s. The timing of the torque step was purposely delayed to ensure that the stator flux linkage level in the machine was at its steady-state value prior to introducing a quadrature current change. Note that in many applications it is practical to ensure that the machine is kept at its fully magnetized state, when the drive is set to standby. This implies that the drive is able to respond directly if needed. This is particularly relevant in, for example, hoist applications.

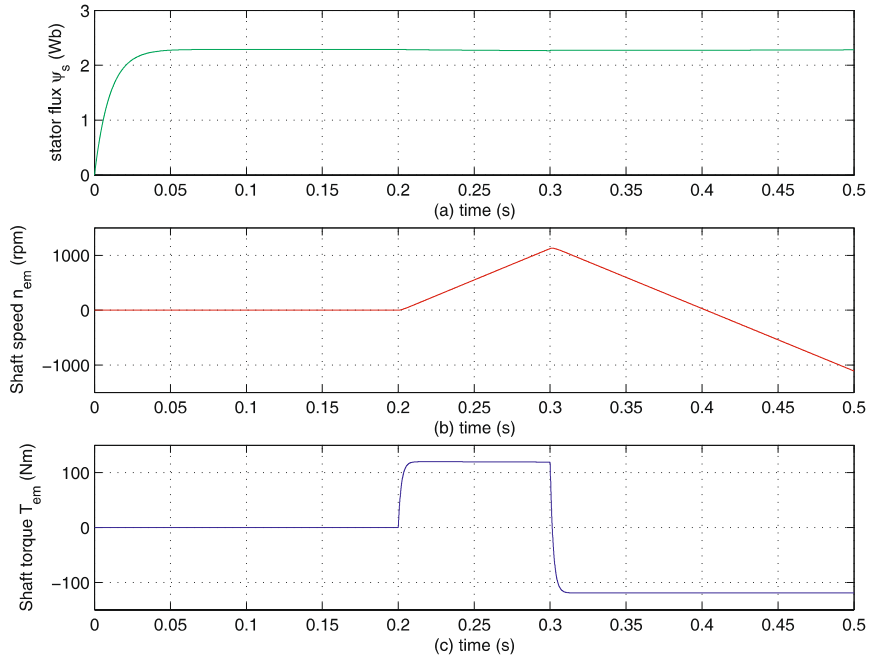


**Fig. 9.23** Delta connected 22 kW machine with UFO based drive controller and shaft tachometer. UFO controller set to stator flux oriented control with  $\psi_M = \psi_s = 2.29$  Wb, rated shaft torque step:  $0 \rightarrow 120$  Nm applied at  $t = 3.5$  s and reversed at  $t = 3.55$  s

The results given in Fig. 9.23 confirm that the stator flux linkage is held constant at its reference value whilst the torque is varied in accordance with the user defined reference torque sequence. Note that a low pass filter with 2 ms time constant has been introduced to moderate the torque reference, and its effect is clearly noticeable in Fig. 9.23(c). More extensive results with the simulation model operating with a rotor flux oriented UFO controller are given in Sect. 3.3.5.

## 9.7 Tutorials

### 9.7.1 Tutorial 1: Simplified V/f Drive

The purpose of this tutorial is to develop a V/f drive model which utilizes the generic controller structure discussed in Sect. 9.1.1. A 22 kW four pole, delta connected induction machine as presented in tutorial Sect. 8.6.7 is to be used in conjunction with a converter. A load module is to be introduced which generates a quadratic torque versus speed characteristic. This module must be configured to ensure that a load torque of 120 Nm is realized at a shaft speed of  $n_m = 1465$  rpm. To simplify the analysis, the PWM converter is replaced by an *Av three-phase modulator*, as discussed in tutorial Sect. 3.3.5 which avoids the need to model the switching behavior of the converter. Inputs to the modulator are the sampled (with  $T_s = 1$  ms) voltages  $U_{s\alpha}^*$ ,  $U_{s\beta}^*$  which are to be provided by the controller. The DC bus voltage for the converter is set to  $u_{DC} = 600$  V. Two UPDOWN modules are to be provided for the variables  $\psi_s^*$  and  $\omega_s^*$  where the latter is to be presented in terms of the four pole synchronous speed in *rpm*.

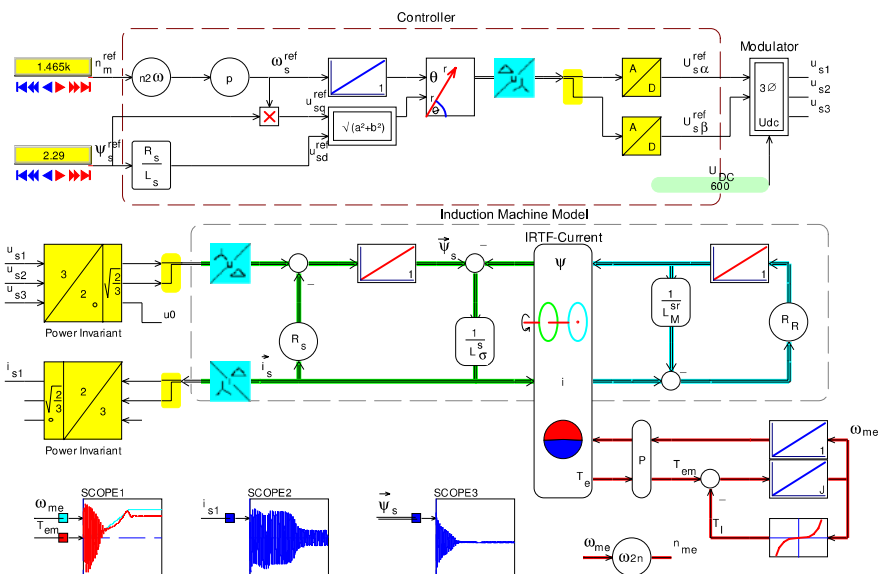


**Fig. 9.24** Model of simplified V/f drive

The simulation model given in Fig. 9.24 shows the rotor flux based model as presented in Fig. 8.46. Parameters for this rotor flux oriented model have been introduced in Table 8.3. The *Av three-phase modulator* consists of a pulse centering unit and non-switching converter module as shown in

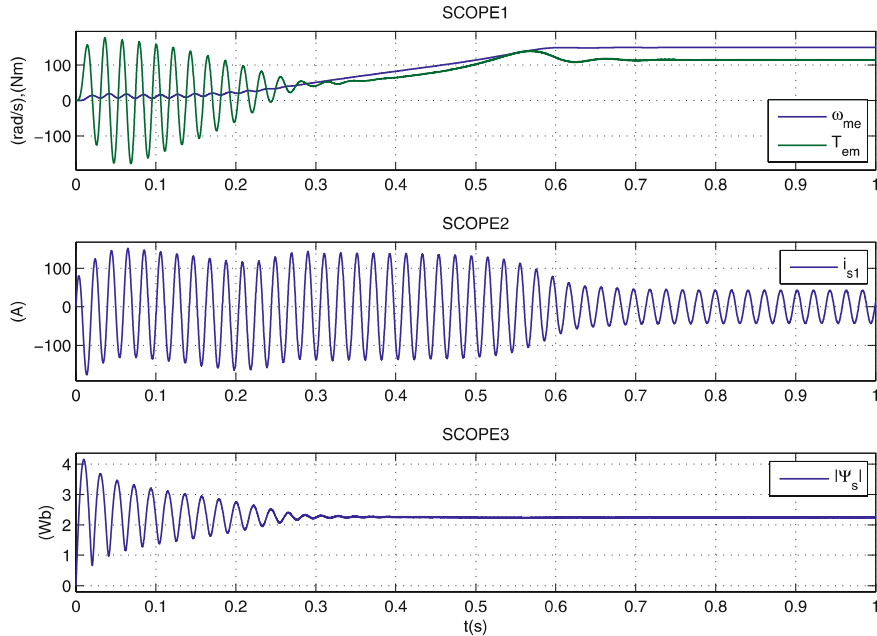


**Fig. 9.25** Simulation results of simplified V/f drive

Fig. 2.28. The latter unit requires access to the DC bus supply value which is set to  $u_{\text{DC}} = 600 \text{ V}$  as indicated above.

The structure of the controller module shown in Fig. 9.24 is consistent with the generic model shown in Fig. 9.2. A gain module with gain  $R_s/L_s$  is used in the controller, of which the parameters may be obtained from Table 8.3 with the understanding that the stator inductance is given as  $L_s = L_{\text{os}} + L_M$ . Note that the parameters given are for a delta connected machine, whereas the voltage inputs for the modulator unit must be expressed for a *star* connected configuration. This requirement is accommodated in the controller by the inclusion of a *delta to star* conversion module which is positioned after the polar to Cartesian conversion unit that generates the voltage vector  $\vec{U}_s^*$ . Inputs to the controller are the stator flux linkage reference value, which is set to the rated value of  $\vec{\psi}_s^* = 2.29 \text{ Wb}$  and the stator flux frequency. The latter is expressed as  $\omega_s^* = 30/\pi p n_s^*$  where  $n_s^*$  represents the four pole ( $p = 2$ ) synchronous speed in *rpm*. Its value has been initially set to the rated speed of the machine. Careful observation of the model shows, among others, that after some large transients, the stator flux linkage level in the machine model is conform to the set reference value. The steady-state shaft speed is however lower than the reference value, which is expected given that the controller sets the synchronous speed of the rotating flux linkage vector and not the actual shaft speed. Hence, the difference between both

readings is the slip frequency which corresponds to the torque generated by the machine.

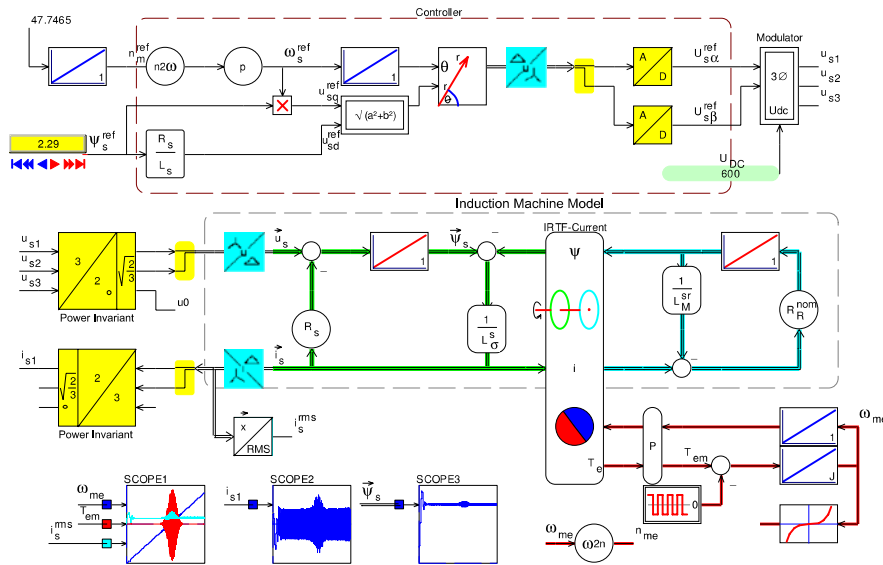


**Fig. 9.26** Simulation of simplified V/f drive for examining instability

The second part of this tutorial considers a modification to the simulation model shown in Fig. 9.24 with the purpose of identifying potential operating regions where instabilities may occur. For this purpose, the load module is replaced with a 4 Hz bipolar, 0.2 Nm square wave oscillator. The introduction of this unit serves to trigger any resonances which may be present over the selected speed range. An integrator is introduced which provides a ramped synchronous speed over the range  $0 \rightarrow 1000$  rpm at a rate of  $\frac{d\omega_s^*}{dt} = 10 \text{ rad/sec}^2$ . For this purpose, set the simulation time to  $T = 20$  s and observe the RMS line current and shaft torque during the frequency sweep. An example of the results obtained with this simulation are shown in Fig. 9.4. Note that the result given was obtained with a lower (than nominal, so the motor is much colder than nominal) rotor resistance value to clearly demonstrate the electro-magnetic resonance phenomenon that can occur in V/f drives. If the simulation is executed with the nominal rotor resistance or with lower stator resistance value, the resonance effect are far less pronounced which underlines the sensitivity of this phenomenon to machine parameters.

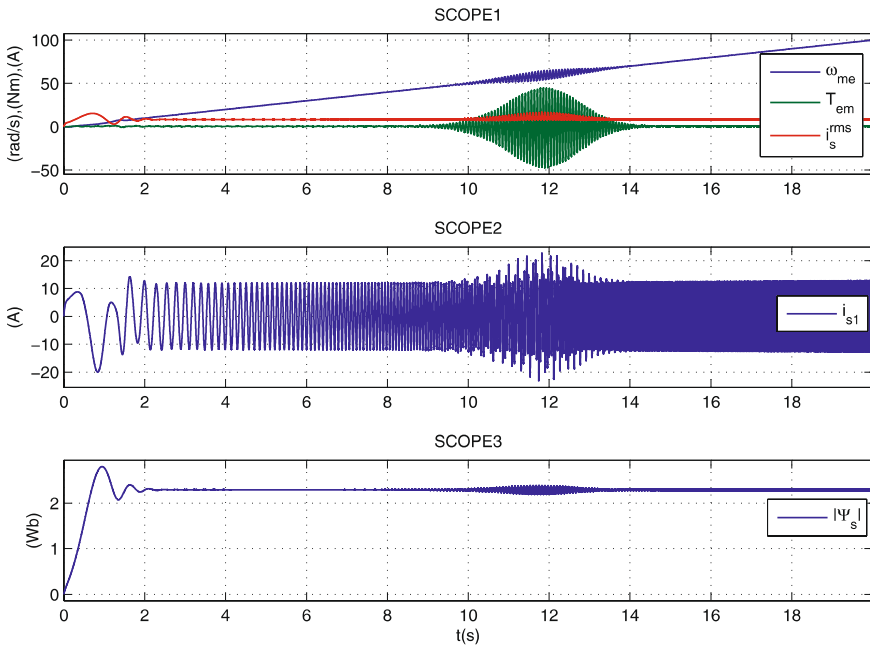


**Fig. 9.27** Simulation results of simplified V/f drive for examining instability

### 9.7.2 Tutorial 2: V/f Drive with Shaft Speed Sensor

This tutorial examines a V/f based drive where use is made of the measured or estimated shaft speed. For this purpose, modify the tutorial discussed in the previous section to accommodate a controller as shown in Fig. 9.5. Inputs to the envisaged control module should be the shaft torque reference  $T_e^*$  and stator flux linkage reference  $\psi_s^*$ . The machine configuration, converter and DC supply configuration remain unchanged when compared to the previous tutorial.

The simulation as given in Fig. 9.28, shows the revised controller structure which is in accordance with the generic model discussed in Sect. 9.1.2. A four pole ( $p = 2$ ) machine is used in this example which implies that the shaft speed and speed reference must be provided with a gain module of  $p$  and  $1/p$  respectively (given the need to use electrical, not shaft based variables in the controller). The controller gain module  $R_s/L_s$  remains unchanged, but the gain  $R_R$  must be calculated. In this context, consideration should be given to the fact that the controller variables have been derived using a stator flux based UFO model (see Sect. 8.3.4.2), which implies that the rotor resistance used in the controller is different to that used in the machine model. Consequently, the controller rotor resistance is found using  $R_R = a^2 R_r$ , where  $R_r$  represent the rotor resistance value of a five parameter

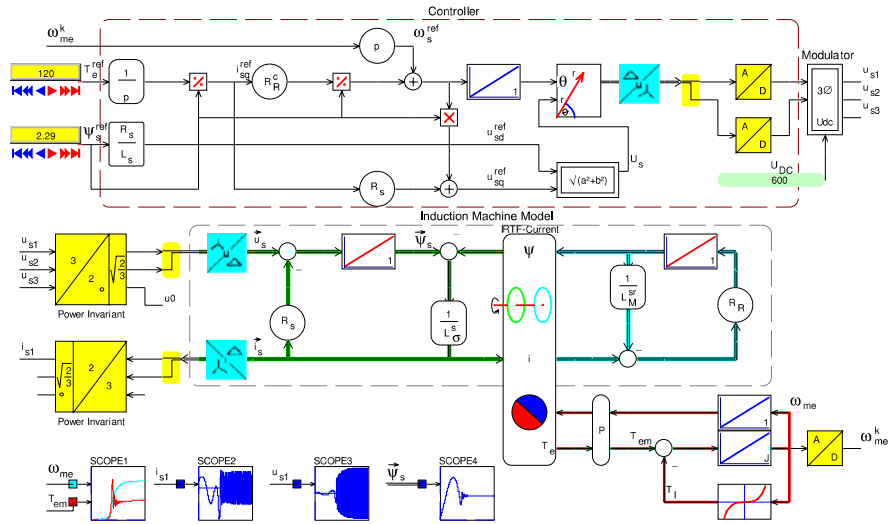


**Fig. 9.28** Simulation of V/f drive with shaft speed sensor

model which for this machine is equal to  $R_r = 0.5377 \Omega$  (see Table 8.2). The transformation variable  $a$  is set to  $a = L_s/L_m$  which for the motor in question gives a rotor resistance value of  $R_R = 0.587 \Omega$  that must be used in the controller.

An example of the results obtained with this simulation model are given in Fig. 9.6, where the shaft torque reference and stator flux linkage reference were taken to be  $T_e^* = 120 \text{ Nm}$  and  $\psi_s^* = 2.29 \text{ Wb}$  respectively. Examination of the results obtained with the model shows that the corresponding steady-state shaft torque and stator flux linkage are equal to  $T_e = 111.0 \text{ Nm}$  and  $\psi_s^* = 2.29 \text{ Wb}$  respectively. The deviation between reference and actual shaft torque is attributed to the approximation used (9.7) to derive the controller slip frequency reference value, which ignores the leakage inductance  $L_{\sigma R}$ . More extensive slip frequency models can however be used, but this is outside the scope of this tutorial.

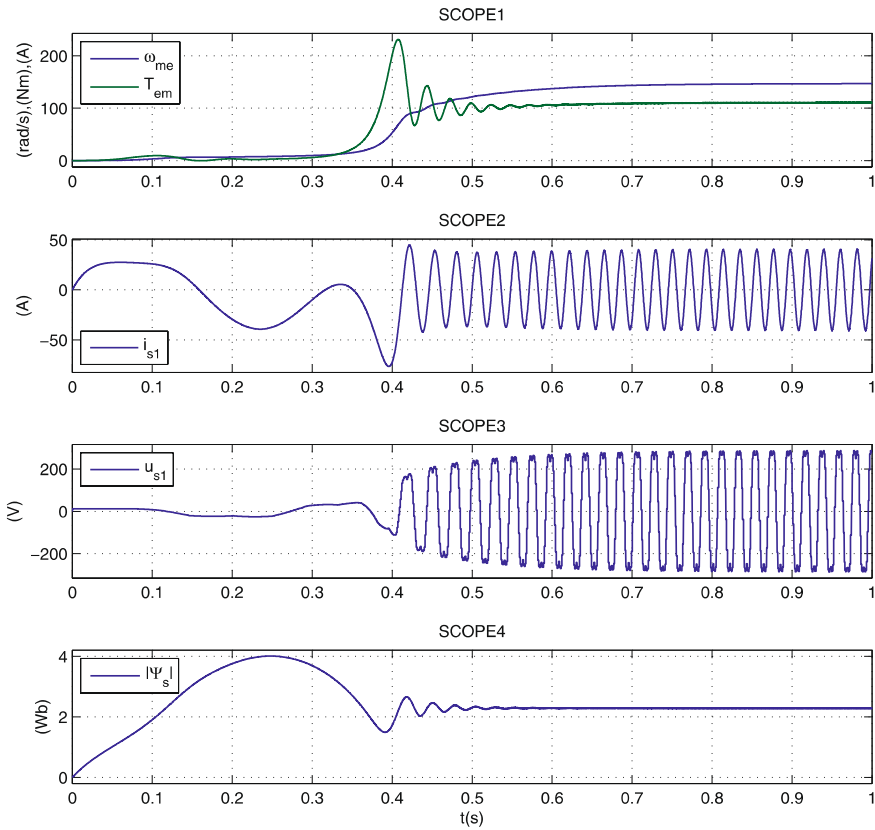


**Fig. 9.29** Simulation results of V/f drive with shaft speed sensor

### 9.7.3 Tutorial 3: Universal Field-Oriented (UFO) Control with a Current Source Based Machine Model and Known Shaft Angle

This tutorial is concerned with a numerical implementation of UFO control where use is made of the *standard* 22 kW four pole machine as characterized by Table 8.3. A simulation model is to be developed of the UFO controller as defined by the generic model given in Fig. 9.10. Input to the UFO controller are the variables  $\psi_M$ , which in this case must be set to  $\psi_M = 2.29 \text{ Wb}$  and electrodynamic torque reference  $T_e^*$  which must be configured to provide a rated shaft torque step from  $T_e^* = 0 \rightarrow 120 \text{ Nm}$  at  $t = 200 \text{ ms}$  and the torque reference must be reversed at  $t = 300 \text{ ms}$ . No external load is to be connected to the machine. A shaft encoder is assumed to be present which provides the electrical shaft angle  $\theta$  and this variable must be used in conjunction with a CFO module as given by Fig. 9.12. Output of the CFO module, which must

be interfaced with the UFO module, is the reference angle  $\theta_M^*$  as required for achieving field-oriented control. A four parameter, IRTF based machine model as given by Fig. 8.15 is to be used. In this case, the stator current  $\vec{i}_s$  is taken to be the input to the model, instead of the voltage vector  $\vec{u}_s$  given that the UFO module generates the reference current vector  $\vec{i}_s^{dq}$  which must be transformed to stationary coordinates by using the reference angle  $\theta_M^*$ . The use of a current source model is helpful because it simplifies the model and provides the ability to visualize the operation of the drive without the complexities of the current controller.

The simulation model as shown in Fig. 9.30 satisfies the requirements for this tutorial. Clearly shown are the UFO and CFO module which generate the required variables  $i_{sd}^c$ ,  $i_{sq}^c$  and  $\theta_M^*$ . Three UPDOWN modules are provided which allow the user to set the peak torque value  $T_e^*$ , flux linkage reference value  $\psi_M^*$  and transformation value  $a$  within the range  $L_m/L_r \leq a \leq L_s/L_m$  (see (8.13)). A first order filter is used to moderate the reference torque and flux linkage values and the time constant for these filters is taken to be 2 ms and 10 ms respectively. Also shown in Fig. 9.30 is the IRTF based machine module, which also includes a gain module  $\Delta L$  as required to generate the flux linkage vector  $\vec{\psi}_M$ . The required torque reference function for this simulation is generated with the aid of the module TEREF1 which contains the first order 2 ms low pass filter discussed above.

A set of scope modules is provided to show the results obtained with this simulation. The data generated via the scope modules is processed via MATLAB and displayed by way of subplots. The results in Fig. 9.32 show the scope output for transformation variable  $a = L_m/L_r$ , i.e., UFO controller set to rotor flux oriented control. Under these conditions the variable  $\psi_M$  shown in SCOPE2 (see Fig. 9.32) represents the variable  $\psi_R$ . A direct current transient during startup is present and this is only partly shown, give that the vertical axis in subplot SCOPE4 has been purposely limited to  $+100, -50$  A to ensure that sufficient detail is available during the critical time frame in which the torque variable is varied. The simulation results for  $a = L_s/L_m$  as given in Fig. 9.33 show the use of the UFO controller with stator flux oriented control. In this case, the variable  $\psi_M$  shown in SCOPE2 (see Fig. 9.33) represents the variable  $\psi_s$ . Note that for both settings the required torque and flux linkage reference values are realized by the UFO controller. Similarly, any intermediate value for the transformation variable  $a$  may be chosen by the user. Note that for stator flux oriented control the slip frequency shows a Dirac type function. This is caused by the fact that a torque step under stator flux oriented control is generated by a near instantaneous displacement of the stator flux linkage vector relative to the rotor flux linkage vector. In practice, however, changes in torque should be slow rate limited (using slow rate limiting controller module), for example to limit mechanical stress or to prevent exciting mechanical eigenfrequencies. Finally, it may be observed for both cases that a change in torque can be done independently of the flux linkage  $\psi_M$ , which is maintained at the required level when torque transients occur.

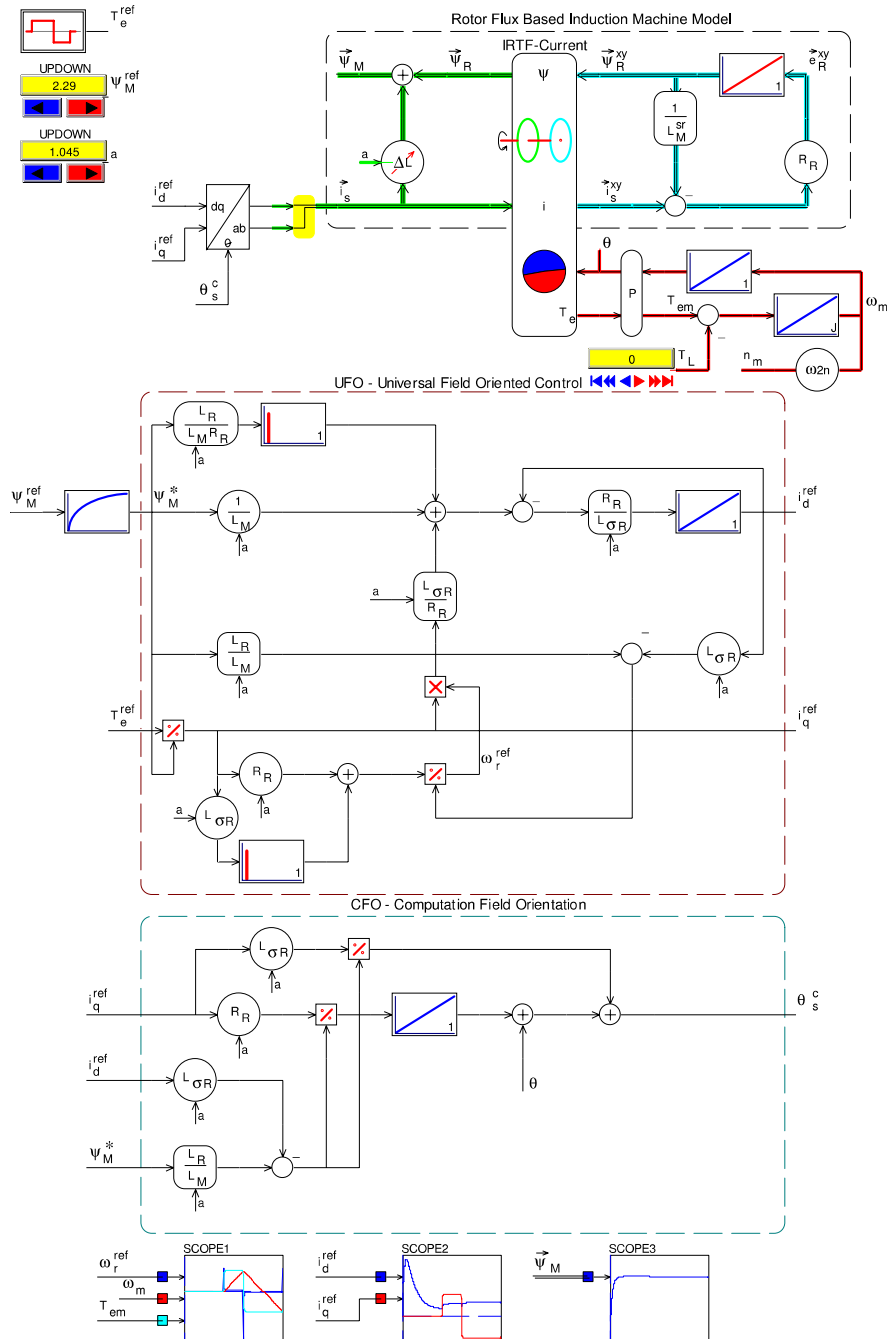
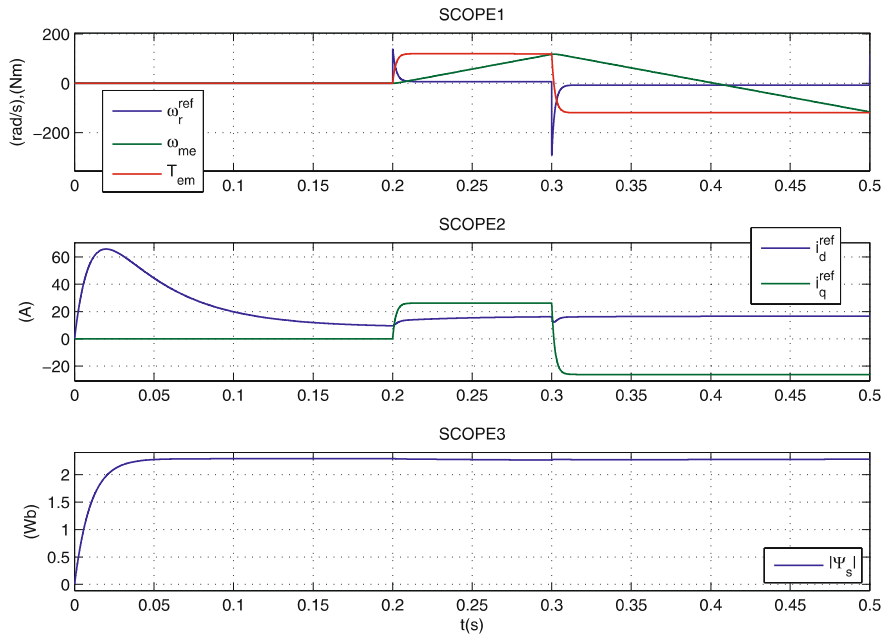
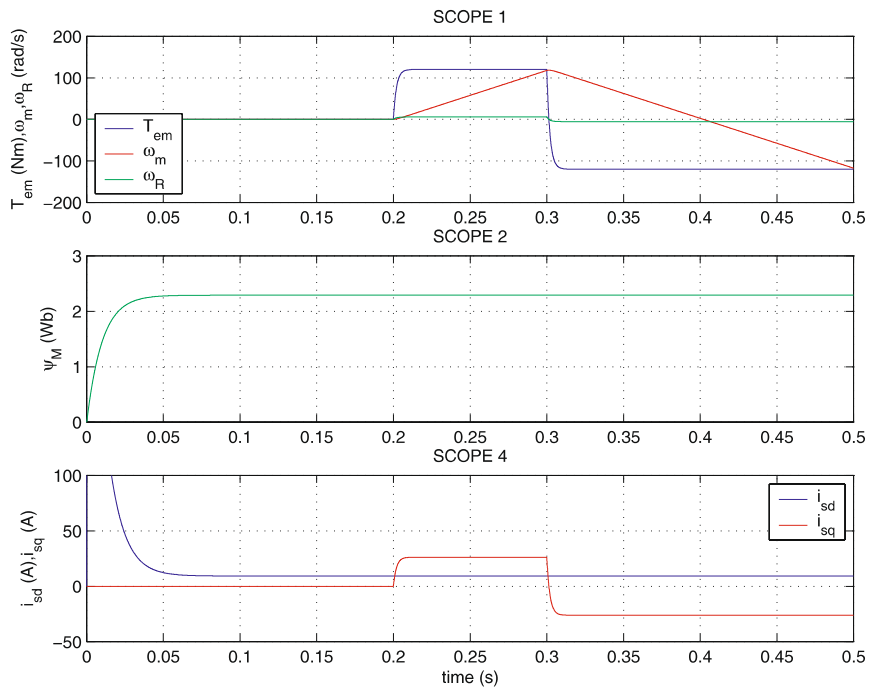


Fig. 9.30 Simulation of UFO controller with current source based machine model



**Fig. 9.31** Simulation results of UFO controller with current source based machine model

When applying step functions to the torque reference, some minor perturbations around the desired value occurs for stator flux oriented control, due to the use of non-ideal differentiators in the UFO controller. In practice, detuning effects, i.e., discrepancies between model and actual machine parameters will cause some coupling between the flux linkage and torque variables. The user is encouraged to detune the UFO parameters to investigate detuning effects [12].



**Fig. 9.32** Simulation results for UFO controller with current source based machine model setting: rotor flux oriented control,  $a = 0.957$

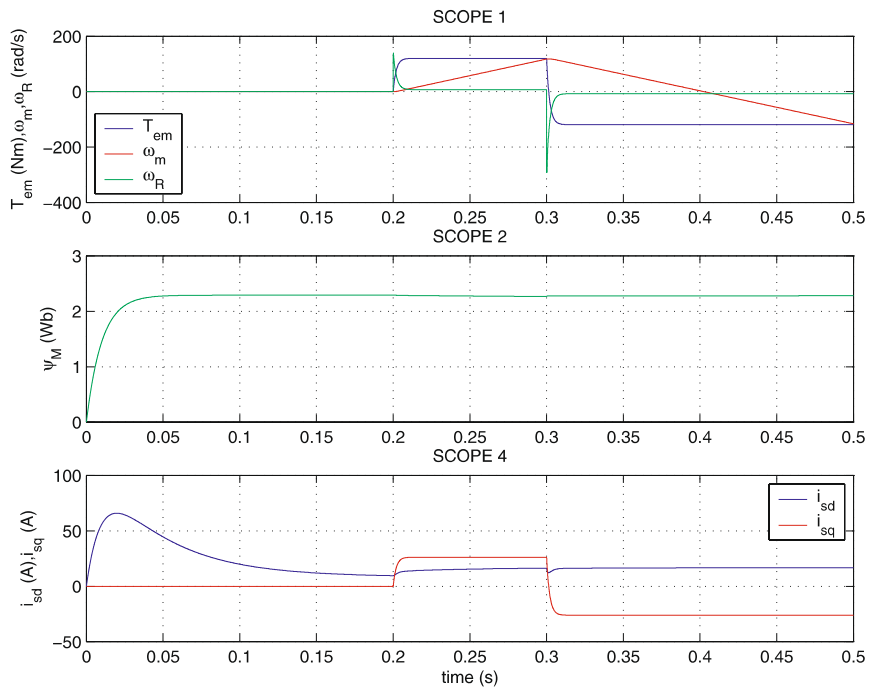


**Fig. 9.33** Simulation results for UFO controller with current source based machine model setting: stator flux oriented control,  $a = 1.045$

### 9.7.4 Tutorial 4: Induction Machine Drive with UFO Controller and Model-Based Current Control

This tutorial examines the operation of a delta connected four pole induction machine operating with a model based current controller and voltage source converter. The proposed concept as discussed in Sect. 9.6 utilizes a four pole *standard* induction machine as used in tutorial 2 (see Sect. 9.7.2). In this exercise, the current commands produced by the UFO module are used as inputs  $i_d^c$  and  $i_q^c$  for the current controller as may be observed from Fig. 9.22. The parameters of the machine are those presented in Table 8.3. A sampling rate of 10 kHz is assumed for the discrete current controllers. For this example the input electromagnetic reference torque is set to  $T_e^* = 60 \text{ Nm}$  at  $t = 350 \text{ ms}$  and this is to be followed by a torque reversal  $T_e^* = 60.0 \rightarrow -60.0 \text{ Nm}$  at  $t = 400 \text{ ms}$ . A first order filter with a time constant of  $\tau = 2 \text{ ms}$  is positioned between the torque reference and synchronous drive controller, in order to limit the torque variations to realistic values. Requesting an instantaneous change in torque is not realistic in any practical drive system, due to limitations imposed by the converter DC bus-voltage to change. Similarly, a first order filter with a time constant of  $\tau = 10 \text{ ms}$  is used to moderate the flux linkage reference value  $\psi_M$  as used for the UFO controller. In this case the UFO controller is provided as a CASPOC module which also houses a CFO module that requires access to the measured shaft speed (as discussed in Sect. 9.2.4). Total simulation run time is to be set to 500 ms while the DC supply is equal to  $u_{\text{DC}} = 600 \text{ V}$ . In this simulation the modulator and converter are not to be implemented at circuit level, i.e., the switching effects should be excluded (as discussed in Sect. 3.3.5) to better visualize the operation of the drive. The first task to be undertaken is to calculate the gains for the two current controllers and in addition identify the disturbance decoupling terms which must be introduced.

Secondly, examine the simulation model of the drive as given in Fig. 9.34 and plot the following results:

- Sampled direct axis reference  $i_{sd}^c$  and *measured* current  $i_{sd}$ .
- Sampled quadrature axis reference  $i_{sq}^c$  and *measured* current  $i_{sq}$ .
- Torque reference  $T_e^*$ , *actual* torque  $T_e$  and mechanical shaft speed  $\omega_m$ .
- Stator flux linkage  $|\vec{\psi}_s|$  and rotor flux linkage  $|\vec{\psi}_R|$  amplitudes.

The computation of the current controller gains and identification of the relevant feed-forward term follows the approach outlined in Sect. 9.6. The two PI controllers shown are of the anti-windup type as discussed in sub-Sect. 3.3.2, which implies that the output limits must be specified. A convenient choice is to set the value to the length of the active converter vector, namely  $\pm\sqrt{2/3}u_{\text{DC}}$  on the grounds that the output voltage vector can never exceed the limits of the hexagon formed by the active converter vectors. The q-axis PI controller is provided with a feed-forward signal  $\omega_m \psi_M$  as discussed in Sect. 9.6. A torque reference module TEREF is shown in Fig. 9.34,

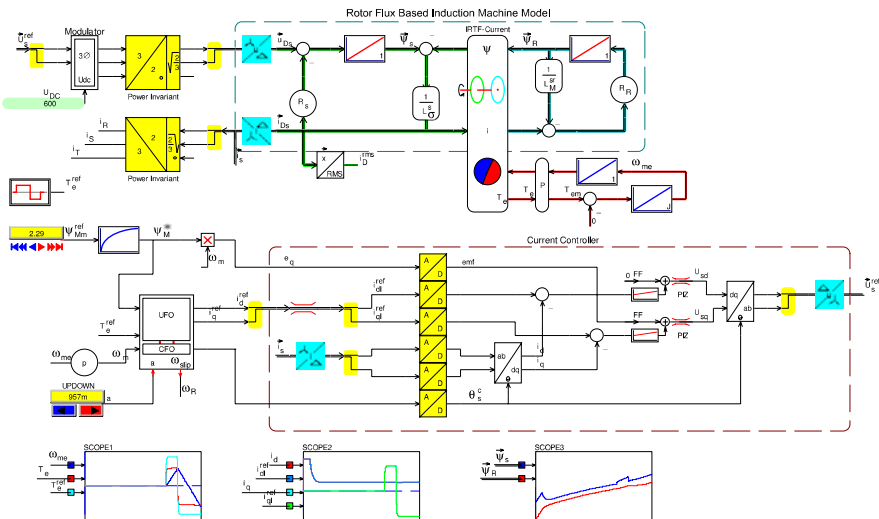


**Fig. 9.34** Simulation of induction machine drive with voltage source converter

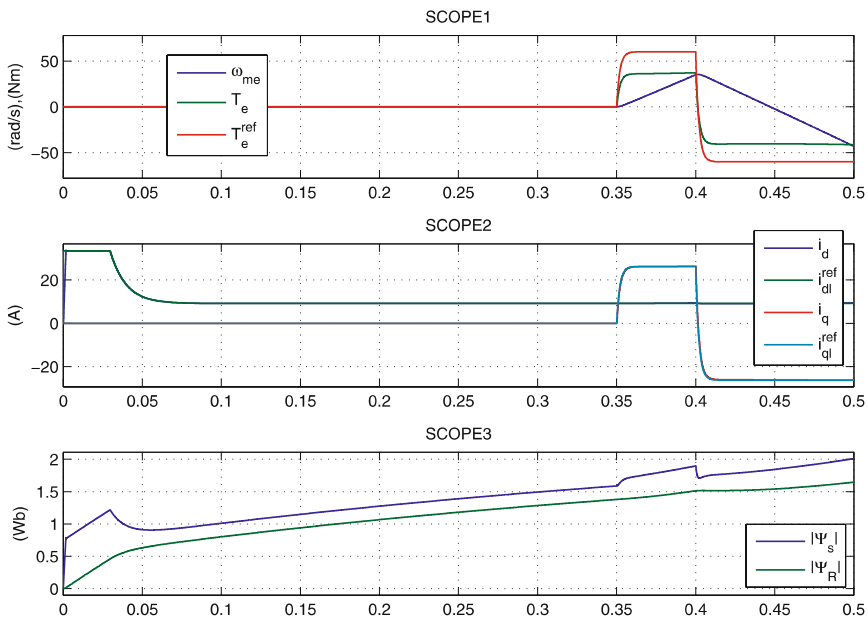


**Fig. 9.35** Simulation results of induction machine drive with voltage source converter

which also contains a 2 ms first order filter used to moderate the torque reference signal supplied to the UFO controller module. Note that a delta connected machine is in use which explains the presence of the star/delta and delta/star space vector modules in the simulation model. These could be avoided, by simply assuming an equivalent star connected machine model (which is achieved by dividing the relevant machine parameters by three). In this case, preference is given to using the delta connected machine, as it is instructive to show how the voltage converter references must be configured to accommodate converter saturation. Four scope modules are given in Fig. 9.34 which show the required variables for this tutorial. These results are given in Fig. 9.36 by way of MATLAB subplots and show operation of the drive under rotor flux oriented control, i.e., UFO controller set to operate with a transformation variable setting of  $a = 0.957$ .

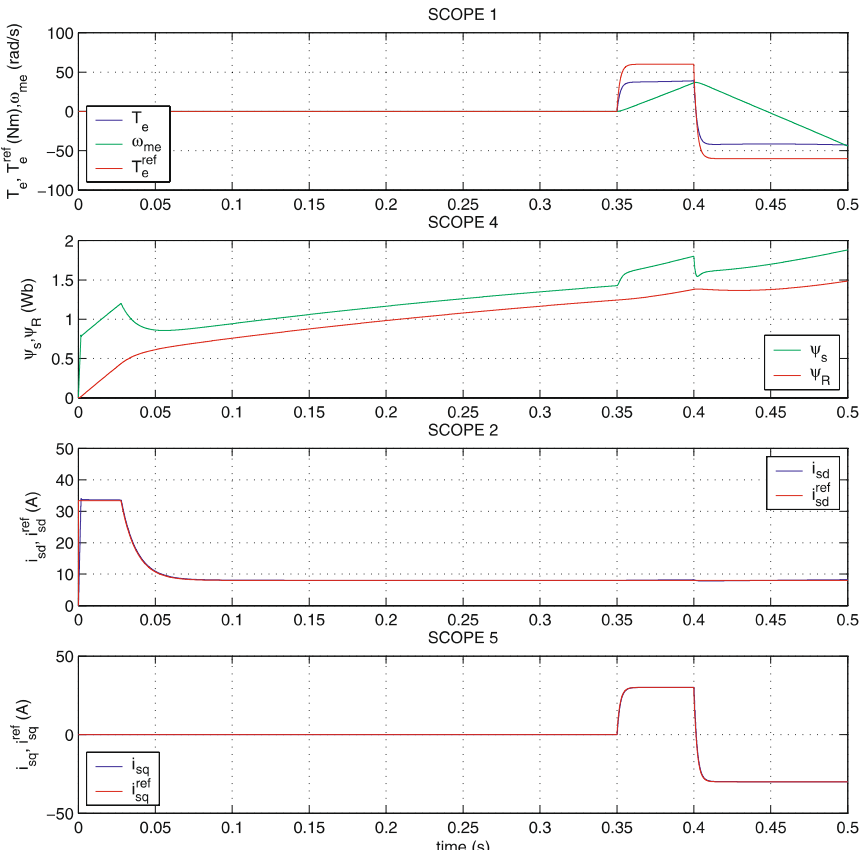


**Fig. 9.36** Simulation result for induction machine drive with voltage source converter and UFO controller, with setting  $a = 0.957$

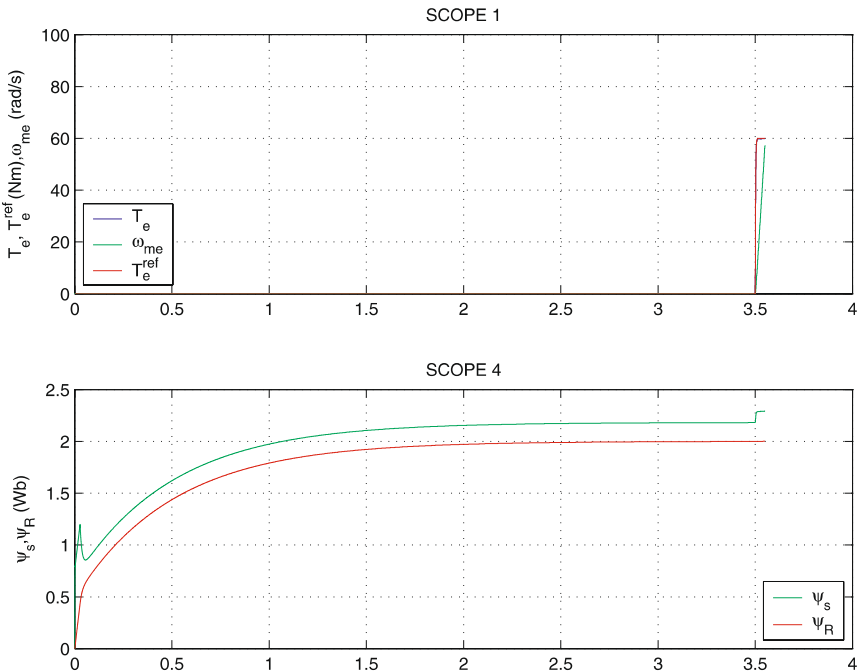


**Fig. 9.37** Simulation result for induction machine drive with voltage source converter and UFO controller, with setting  $a = 0.957$  and extended simulation time

Observation of the results according to Fig. 9.36 shows that the current controller is able to maintain the direct and quadrature currents at the value dictated by the reference values. Note that during the startup sequence the direct axis current reference is purposely held to the maximum 33.4 A rated current value of the machine, which implies that the time required to fully magnetize the machine is increased, as may be observed from the results given in SCOPE4, Fig. 9.36. In this example, a torque step was imposed at  $t = 0.35$  s. At this instance, the machine is not fully magnetized. Consequently, an error will occur between the reference and actual torque as may be observed from the result given in SCOPE1, Fig. 9.36. These results emphasize the need to ensure that the machine magnetization level is held at the reference value during standby operation, in the event that a potential full torque response may be required. If the machine is demagnetized, a substantial delay must be incurred to allow the machine to reach the flux linkage reference, before a torque step can be applied. An example of such operation is given in Fig. 9.37, which was undertaken with the same simulation model. However, in this case a rated torque step was applied at  $t = 3.5$  s. The machine is given first the opportunity to reach its rated rotor flux linkage value of 2.0 Wb prior to the application of a torque step. Under these conditions the actual torque matches the torque reference value, as required. The drive example shown

here was undertaken with a model based current controller. It is left as an exercise for the reader to reconsider this problem with a hysteresis controller as shown in Fig. 3.13.

### **9.7.5 Tutorial 5: Rotor Flux Oriented Induction Machine Drive with UFO Controller and Field Weakening Controller**

This tutorial examines the use of a field weakening controller which operates according to the control principles set out in Sect. 9.4. Said controller is to be used in conjunction with a UFO controller operating under rotor flux oriented control. The direct and quadrature current outputs are to be used directly with a current source rotor flux based induction machine model as discussed in tutorial 3 (see Sect. 9.7.3). For this tutorial, the leakage inductances  $L_{\sigma s}$  and  $L_{\sigma r}$  as defined in Table 8.2 are to be increased to  $L_{\sigma s} = L_{\sigma r} = 25 \text{ mH}$  in order to better visualize operation along the MTPF line of the drive. Note that the gradient of this line is inversely proportional with the parameter  $\chi_i = L_{\sigma s}/L_s$  (see (9.24b)). Consequently, increasing the leakage inductance of the model will decrease the slope of the MTPF line. The rated current for the delta connected remains at  $i_s^{\max} = 33.4 \text{ A}$ , while the maximum supply voltage setting is arbitrarily set to  $u_s^{\max} = 1000 \text{ V}$ . A simulation model is to be developed which makes use of the field weakening controller which must be provided with a torque reference value and electrical stator frequency  $\omega_s$ . Both variables are to be generated using UPDOWN modules, whereby the latter must be shown in terms of the synchronous shaft speed in  $\text{rpm}$ . The UFO model and induction machine model must be provided with a shaft speed input  $\omega_m$ , which can be generated using the UFO model and the user defined variable  $\omega_s$ . In terms of operational requirements, the tutorial is divided in two parts.

The first part deals with operation of the drive under partial and full load conditions, whereby drive operation is to be examined in two phases namely:

- Operation with rated rotor flux linkage reference value of  $\psi_R = 2.0 \text{ Wb}$  whilst the electrical frequency is set to the base speed of the drive. Under these conditions the shaft torque reference is to be varied from  $T_e^* = 30 \rightarrow 130 \text{ Nm}$  in incremental steps of  $20 \text{ Nm}$ .
- Operation with maximum torque setting  $T_e^* = 130 \text{ Nm}$  whilst the synchronous shaft speed is to be varied over the range  $n_s^* = 1672 \rightarrow 3072 \text{ rpm}$  in incremental steps of  $200 \text{ rpm}$ .

The second part of the tutorial is concerned with partial load operation where the torque reference is held at  $T_e^* = 70 \text{ Nm}$ , while the reference flux linkage is set to  $\psi_R = 2.0 \text{ Wb}$ . Under these conditions the synchronous shaft speed is to be varied over the range  $n_s^* = 1672 \rightarrow 3072 \text{ rpm}$  in incremental

steps of 200 rpm. The objective of the tutorial is to plot the trajectory of the synchronous current vector  $\vec{i}_s^{dq}$  in a synchronous IM control diagram together with the MA circle and MF ellipses, which correspond to operation at the base speed and maximum synchronous shaft speed of  $n_s^{\max} = 3072$  rpm respectively. In addition, the user is encouraged to carefully examine the simulation model to ascertain whether or not the operating conditions as prescribed are indeed executed by the controllers.

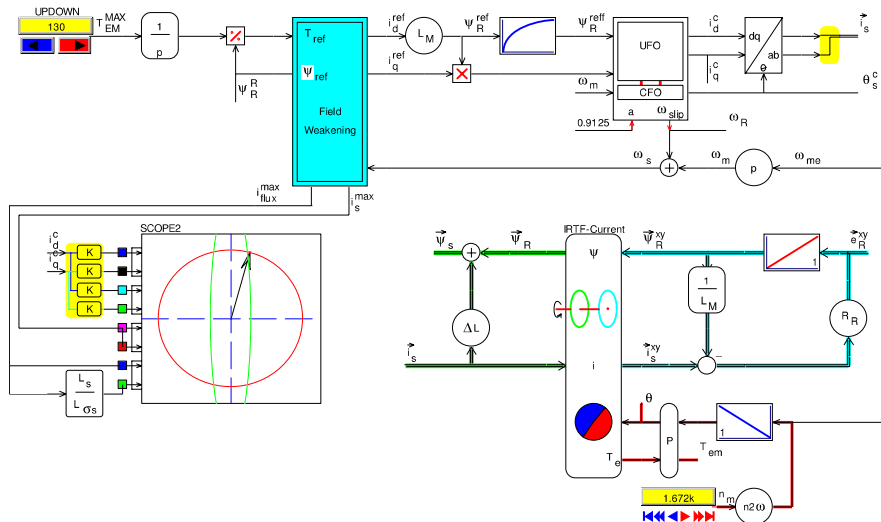


**Fig. 9.38** Simulation of induction machine drive with rotor flux oriented UFO controller and field weakening controller

## Part I

The simulation model, shown in Fig. 9.38, complies with the requirements of this tutorial. Readily identifiable in Fig. 9.38 is the four parameter IRTF model which complies with the generic model shown in Fig. 8.15, where the vector  $\vec{i}_s$  and shaft speed are taken as inputs for the model. Computation of the model parameters  $L_{\sigma s}$ ,  $L_M$  and  $R_R$  is undertaken with the aid of (8.12) and (8.15) and Table 8.2, taking into account the new leakage parameters. The revised four parameter model data of the machine for this tutorial is given in Table 9.1.

The shaft speed  $\omega_m$  for the four-pole machine model is found by making use of the slip frequency  $\omega_{sl}$  value generated by the UFO controller and the electrical frequency  $\omega_s$ , which in turn is obtained via the UPDOWN module that defines the synchronous shaft speed  $n_s^*$ . Inputs to the UFO controller are the electrical shaft speed  $\omega_m$ , rotor flux linkage  $\psi_R^*$  and electrical torque  $T_e^*$ . The latter two are in this case derived from the field weakening module which provides (among others) the direct and quadrature current reference

**Table 9.1** Machine parameters and flux linkage values for the rotor flux oriented model, as used in this tutorial

Parameters		Value
Magnetizing inductance	$L_M$	237.9 mH
Leakage inductance	$L_{\sigma s}$	47.8 mH
Leakage inductance	$L_{\sigma r}$	0 mH
Rotor resistance	$R_R$	0.4477 $\Omega$
Stator resistance	$R_s$	0.5250 $\Omega$
Rated stator flux linkage	$\psi_s^{\text{nom}}$	2.29 Wb
Rated rotor flux linkage	$\psi_R^{\text{nom}}$	2.00 Wb

$i_d^*$  and  $i_q^*$ . Use of these two variables gives  $T_e^* = L_M i_d^* i_q^*$  and  $\psi_R^* = L_M i_d^*$  as required for the UFO controller, which must also be provided with the relevant data given in Table 9.1. In this tutorial rotor flux oriented control is envisaged which implies that the UFO control input  $a$  must be set to  $a = L_m/L_r = 0.9125$ . In addition, the UFO controller must be provided with the five parameter model data as given by Table 8.2, where use must be made of the revised leakage parameters as given at the beginning of this tutorial. The UFO controller used in this tutorial also houses a CFO module which generates the rotor angle  $\theta_M^*$  as required for implementation of indirect rotor flux oriented control, in which use is made of the (known) shaft speed.

A second UPDOWN module is also visible in Fig. 9.38, which provides the shaft torque reference value  $T_e^*$  that is used indirectly by the field weakening module. This module also provide additional data needed to generate the IM synchronous control diagram, which enables the user to examine the MA circle, MF flux linkage ellipse and current space vector  $\vec{i}_s^{dq}$  generated by the UFO controller for a given set of user settings. To accommodate the operational requirements for the first part of the tutorial the base synchronous shaft speed of  $n_s^b = 1672$  rpm must be selected for the appropriate UPDOWN module. Said base speed may be found by making use of (9.22), Table 9.1 and the drive parameters defined for this tutorial. The torque reference was varied over the range:  $T_e^* = 30 \rightarrow 130$  Nm with an incremental step of 20 Nm. The current vector  $\vec{i}_s^{dq}$  generated by the UFO controller was recorded for each torque setting and used to plot the some of the results given in Fig. 9.39. More specifically, the six data points along a vertical axis with  $i_{sd} = 8.04$  A correspond to the operational sequence described above. The last data point in this sequence, which corresponds with a torque setting of  $T_e^* = 130$  Nm, was judiciously chosen to coincide with the base operating point of the drive, which also intersects with the base speed MF ellipse as may be observed from Fig. 9.39. Note that during this first operating sequence, the flux linkage  $\psi_R$  and shaft torque  $T_e$  as found in the machine model, match the chosen the reference values of may be deduced by running the simulation in question.

Also shown in Fig. 9.39 are a set of data points which are located on the MA circle and MTPF line. This set of data points can be found by maintaining the shaft torque reference at the value  $T_e^* = 130$  Nm and varying the

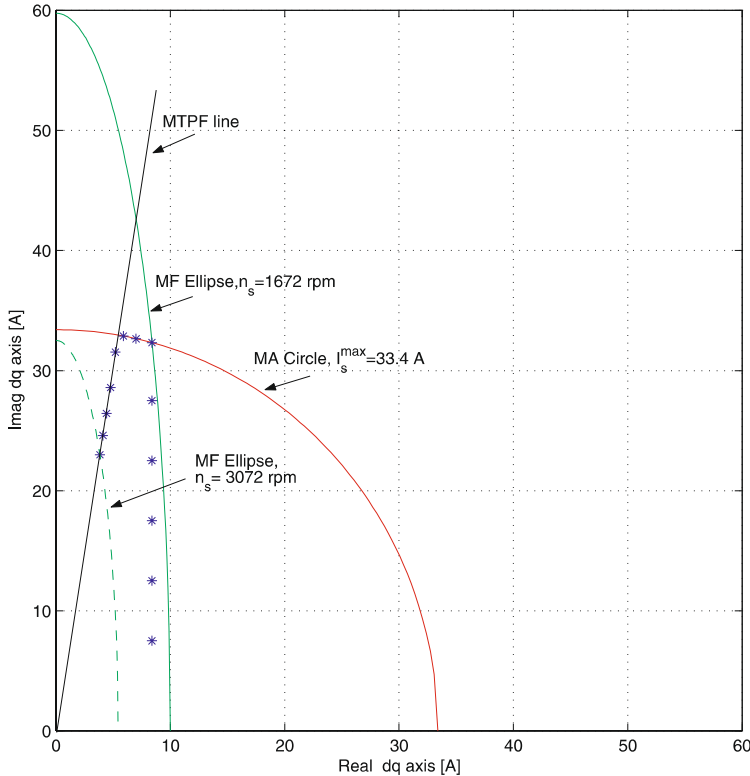


**Fig. 9.39** Simulation results for induction machine drive with rotor flux oriented UFO controller and field weakening controller

synchronous shaft speed over the range  $n_s^* = 1672 \rightarrow 3072$  rpm in incremental steps of 200 rpm as discussed above. During this operating sequence the shaft torque and rotor flux linkage will no longer be equal to the reference values, given that field weakening is active. Note that the supply voltage  $u_s$  is kept within the specified maximum voltage value of the drive, as may be observed by running the simulation with the chosen operating sequence.

## Part II

The second part of the tutorial considers drive operation under partial load conditions, where the torque reference is held at  $T_e^* = 70$  Nm, and reference flux linkage is set to  $\psi_R = 2.0$  Wb. Under these conditions the synchronous shaft speed was varied over the range  $n_s^* = 1672 \rightarrow 3072$  rpm in incremental steps of 200 rpm which leads to a set of data points shown in Fig. 9.40. The set of asterisks represent the endpoint of the vector  $\vec{i}_s^{dq}$  for the chosen operating sequence.

Also shown in Fig. 9.40 are the MA circle and MF ellipses which correspond to a synchronous shaft speed of  $n_s = 1672$  rpm and  $n_s = 3072$  rpm

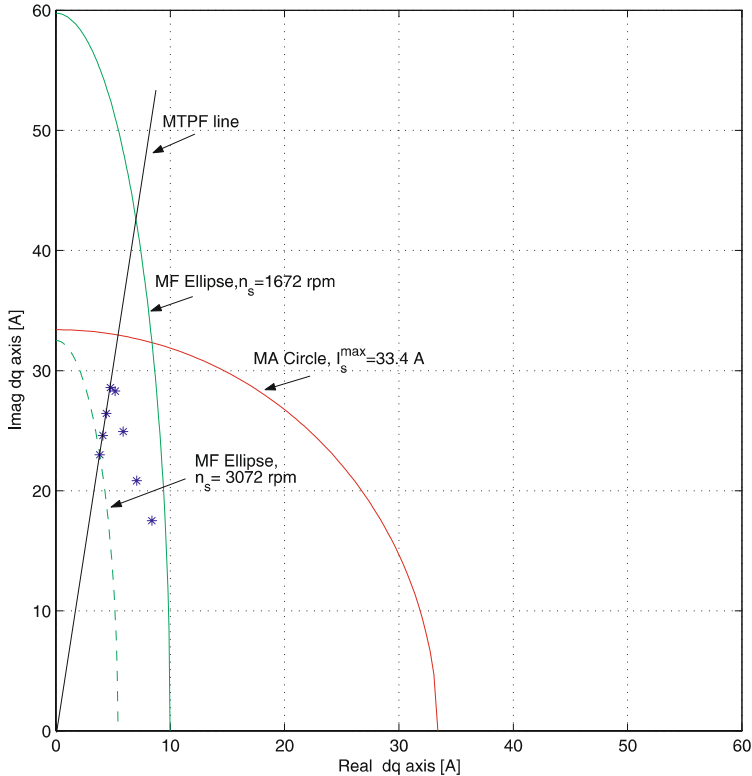


**Fig. 9.40** Simulation results for induction machine drive with rotor flux oriented UFO controller and field weakening controller

respectively. Observation of the results show that the set of data point which are not located on the MTPF line correspond to operation under constant torque conditions as discussed in Sect. 9.3. Observation of the simulation with said operating sequence should confirm that the shaft torque is help at the reference value as required. Once the MTPF line is reached field weakening continues where both flux weakening and the shaft torque reduce as the synchronous speed is increased.

### 9.7.6 Tutorial 6: Experimental Results of an Induction Machine with UFO Controller

To verify the introduced control algorithms for induction machine, the test-bench described in Sect. 1.4 is used. The specifications of the used induction machine are given in Table 9.2. Using the given parameters, a simulation model of the machine and the control is implemented. The control is realized with a universal field orientation, including a field weakening controller, as described in Sect. 9.7.5.

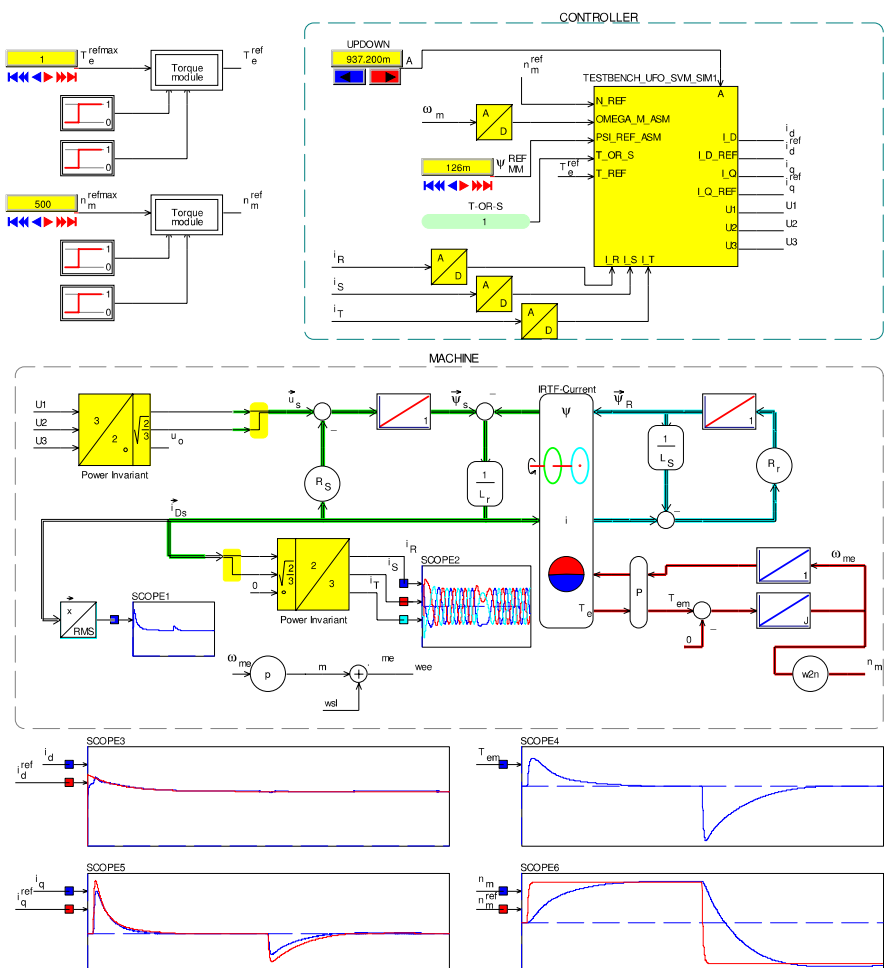


**Fig. 9.41** Simulation of induction machine

**Table 9.2** Specifications of example induction machine

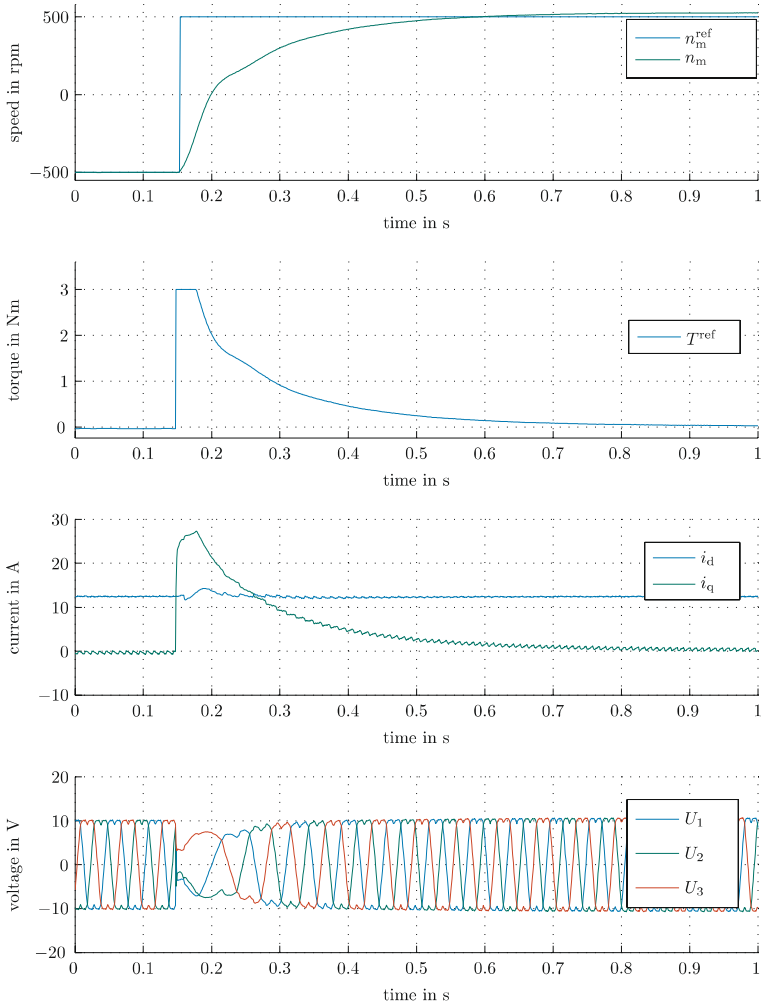
Parameters		Value
Magnetizing inductance	$L_M$	8.09 mH
Stator leakage inductance	$L_{\sigma s}$	0.301 mH
Rotor leakage inductance	$L_{\sigma r}$	0.559 mH
Rotor resistance	$R_R$	0.131 Ω
Stator resistance	$R_s$	0.2 Ω
Rated flux linkage	$\psi_M$	0.126 Wb
Number of polepairs	$p$	2

Figure 9.41 shows the built simulation model of the drive. The controller needs to be provided with the shaft speed  $\omega_m$ , rated flux linkage  $\psi_M$  and the reference torque  $T_e^{\text{ref}}$  or reference speed  $n_m^{\text{ref}}$ , depending on whether torque or speed control is chosen by the variable T-OR-S, as shown in Fig. 9.41. Additionally, the control needs the measured currents  $i_R$ ,  $i_S$  and  $i_T$  as input. As output, the control calculates the reference phase voltages  $U_1$ ,  $U_2$  and  $U_3$ , which are used as inputs for the machine model. The scopes in Fig. 9.41 show the simulated resulting torque and the currents  $i_d$  and  $i_q$  for a speed reversal.

The control is implemented on the test-bench using the C-code export function as explained in Sect. 1.4. The only block exported is the block ‘TESTBENCH\_UFO\_SVM’, shown in Fig. 9.41. Additional to the control necessary for the simulation model, the block includes a pulse centering unit, as described in Fig. 2.10. The centered voltages are then used to calculate the duty cycle for each phase, which is applied to the machine by the converter.

To demonstrate the control, a speed reversal is performed. It shows clearly the function of the speed, torque and current control, for both motoring and generating operation. Figure 9.42 shows a measured speed reversal of the induction machine from  $-500$  rpm to  $500$  rpm. Shown are the reference and measured speed,  $n_m^{\text{ref}}$  and  $n_m$ , the reference torque  $T^{\text{ref}}$ , the measured  $i_d$  and  $i_q$  currents in the rotor reference frame and the phase voltages  $U_1$ ,  $U_2$  and  $U_3$ . It can be seen, that the  $i_q$  current is following the torque command. The  $i_d$  current is almost constant, as the machine is not in field weakening. Regarding the phase voltages, the function of the pulse centering, as explained in Fig. 2.10 can be seen.

With AixScope it is possible to show variables which are in the  $\alpha$ ,  $\beta$ -plane as rotating vectors. Figure 9.43 shows plots of the stator reference voltages  $u_{\alpha,\beta}$  and the currents  $i_{\alpha,\beta}$  in a polar plot, as well as over time. Shown is, as in the example before, a speed reversal from  $-500$  rpm to  $500$  rpm. The black arrow or the line in each figure marks the time, where the reference speed is changed. At the beginning voltage and currents rotate clockwise, corresponding to negative speed. In Fig. 9.43(a) the corresponding voltage and currents are colored blue. After the speed step, the rotation direction changes. The voltage and current curves in the polar plot for  $n > 0$  are colored green, for a better readability.



**Fig. 9.42** Experimental results of speed reversal with induction machine and UFO control

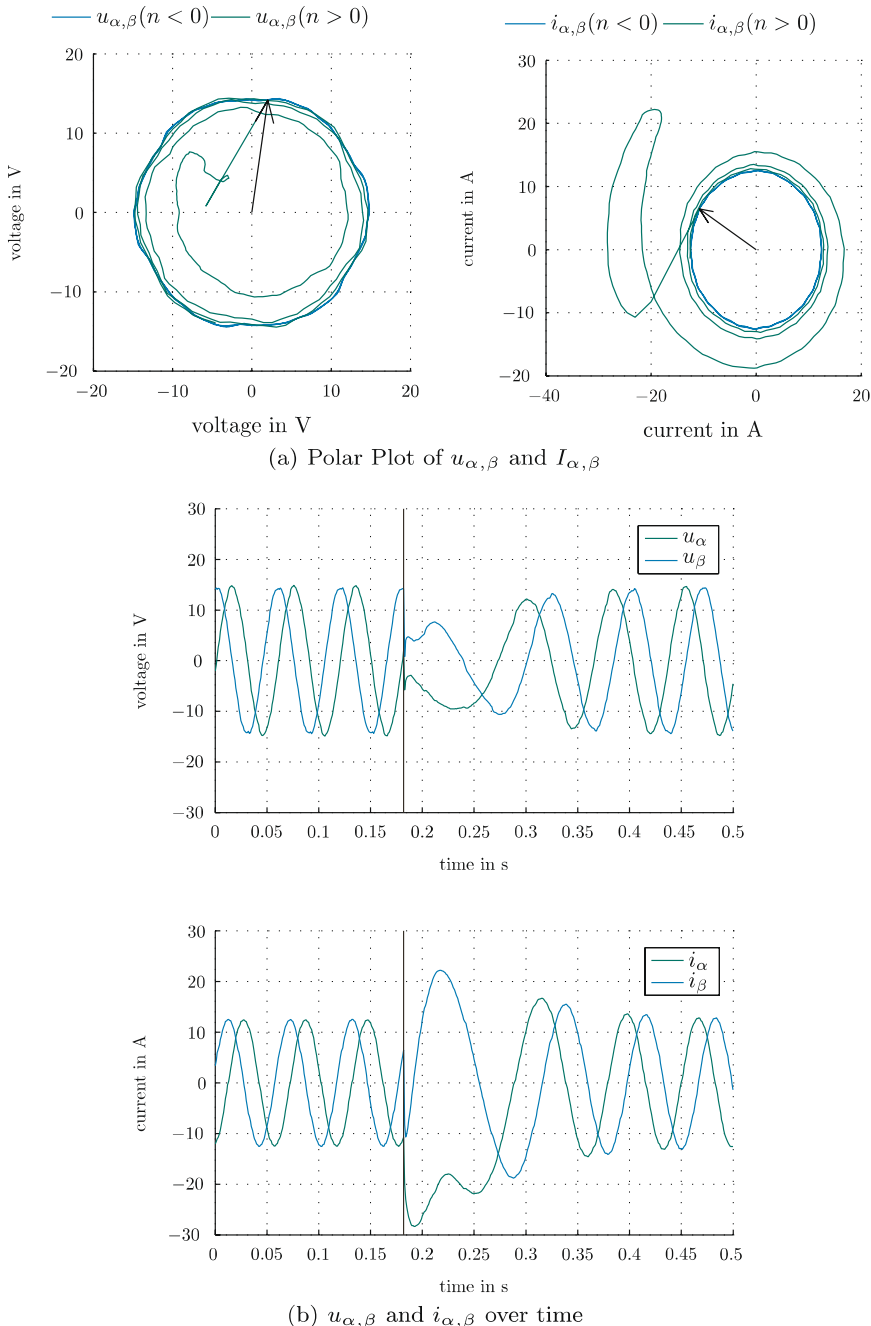


**Fig. 9.43** Experimental results of voltage and current component waveforms in  $\alpha, \beta$ -reference system and as function of time, during a speed reversal

# Chapter 10

## Switched Reluctance Drive Systems

The term *switched reluctance* may to the uninitiated reader convey the notion that the reluctance of the machine is *switched*. In reality the magnetic reluctance of the machine is rotor angle dependent and the term *switched* refers to the electronic commutation of the electrical phases by means of a power electronic converter. Torque production based purely on variation of the magnetic reluctance is well established and the first patent based on this approach stems from 1839 [64]. Despite being one of the oldest known machine concepts, it has not been able to maintain its hierarchical position in comparison to machines which utilize the Lorentz force as a basis for torque production. Since the development of power electronics, there is no readily identifiable single reason for this sequence of events, but it is perhaps useful to consider some of the factors which may well have facilitated this state of affairs.

From a learning perspective, the process of familiarization of, for example, a vector controlled induction machine drive concept, starts from basic modeling principles, leading to a model based control concept. This model-based approach to develop torque controllers (field oriented control) may in turn be followed by a familiarization process that encompasses some form of simulation and practical application. To facilitate this learning process, the reader may acquire an ‘off-the-shelf’ drive concept, with a machine which is well defined in terms of its model and parameters. If we attempt to emulate this learning process for a switched reluctance drive, the process is less well defined simply because this type machine is more difficult to model. Furthermore, the torque production concept of the SR machine is considerably different to the Lorentz force based machine. The latter may for many readers have a degree of familiarity given the fact that the basic principles are often taught at an early stage of education. The learning curve to mastering SR technology is steep and comparatively unfamiliar given the need to understand a machine concept in which non-linear effects, i.e., magnetic saturation, play a key role. The inevitable non-linear modeling techniques required to handle saturation are not standard and machine characteristics are not readily quantified by

few parameters. Today, there are commercial tools available for modeling and designing switched reluctance machines, given the need to optimize the drive with respect to the application.

Notwithstanding the above, SR drive technology is increasingly seen as a cost saving alternative to conventional Lorentz force based machines. One of the key reasons for this is the simple doubly salient machine concept, devoid of permanent magnets, or any form of winding or squirrel cage on the rotor. Consequently, the rotor inertia can be kept low (if needed) and high-speed operation, which is instrumental for realizing high power densities, is not inhibited by the presence of permanent magnets or rotor windings. The latter is also beneficial in terms of improving overall machine efficiency, i.e., no rotor losses due to the absence of rotor windings. However, this perceived advantage is offset by the need for a field which rotates faster than the rotor itself, which increases the magnetic stator losses in the machine. Torque production is not current polarity dependent which provides an additional degree of freedom with respect to the converter topology. In this context, the conventional converter concept (Full-bridge converter) of two series connected switches across the supply may be abandoned in favor of a short circuit proof approach to improve reliability.

Given the above, the reader may well wonder why the SR drive is not universally used today, given its obvious commercial benefits. The answer lies with the pulsed nature of torque production, which is accompanied by large radial mechanical forces, which may contribute to acoustical noise emissions and these may in turn be exacerbated by the type of current control technique used [38]. As with Lorentz force based drives, the use of computer control and low cost DSP's recently provides the opportunity to improve drive performance [14]. For the SR drive the benefits are to reduce torque ripple and eliminating the need for a position sensor by implementing some form of position sensorless control [24]. In the face of equal converter and controller costs the benefits of a very simple rugged machine concept may serve to push SR drive development to greater heights in the future.

The number of SR drive manufacturers is small in comparison with, for example, induction machine drive manufacturers. The manufactures are usually tailored to specific applications. It is instructive to consider applications where the merits of SR drives have warranted their use in comparison to other drive concepts. Its perceived ability to operate at very high speeds has seen its application in the textile processing industry (operating speeds of 100 000 rpm) [5, 46], aerospace industry (150 kW, aircraft turbine starter) [55] and trains (40 kW, high-performance compressors for air conditioning in ICE 3 high-speed trains). Its inherently low cost construction benefit has been used to advantage in hand-held power tools [57], household appliances (mixer/kneading machines, vacuum cleaners with power range 0.5–2 kW), sliding doors and electrical vehicles (traction drives for cars 50 kW range and scooters [34, 56]). Its benefit in terms of robustness, has led to applications

in aerospace other than the one indicated above and in the mining industry (high performance explosion proof drive with a power level of 400 kW).

## 10.1 Basic Machine Concepts

The machine is characterized by discrete stator and rotor poles, which is commonly referred to as a doubly salient structure [39, 6, 44]. Figure 10.1 shows a typical machine configuration. The example three-phase machine ( $N_{ph} = 3$ ) has six stator teeth  $N_s = 6$  and four rotor teeth  $N_r = 4$ , a configuration which is known as a 6/4 structure. The windings are typically positioned around each stator pole, which is why this winding arrangement is referred to as *concentrated* or *short pitched*. From a magnetic perspective, each phase of the 6/4 machine has two *magnetic* poles per phase, i.e., one pole pair ( $p = 1$ ), given that diametrically opposed coils are electrically connected in series or in parallel. For example, phase A is made up of the coils located on teeth A and A'. If this phase is excited, a magnetic flux path is formed by the two stator teeth A–A', the rotor and stator yoke (see Fig. 10.1(b)).

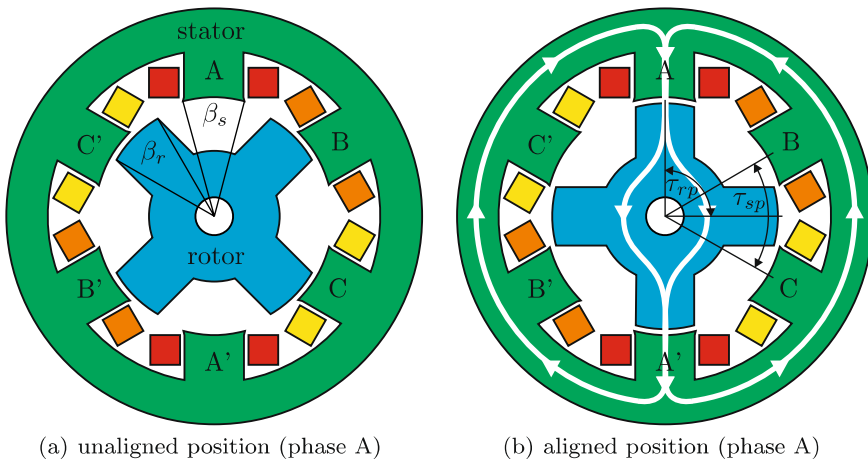


**Fig. 10.1** Radial flux machine examples:  $N_{ph} = 3$ , 6/4 configuration

Observing one phase of Figure 10.1, it can be seen that two equilibrium positions of the rotor exist. The rotor position shown in Fig. 10.1(a) is called the unaligned position with respect to phase A–A'. The rotor angle at this position  $\theta$  is defined as  $\theta^u$ . The position of smallest magnetic reluctance is called the aligned position  $\theta^a$ , as is shown in Fig. 10.1(b). The width of the rotor and stator poles are defined as  $\beta_s$  and  $\beta_r$ . The interpolar arcs of stator and rotor ( $\tau_{sp}$  and  $\tau_{rp}$ ), which represent the angle between two adjacent rotor

or stator teeth, shown in Fig. 10.1(b), are determined by

$$\tau_{sp} = \frac{360^\circ \text{ mech.}}{N_s}, \tau_{rp} = \frac{360^\circ \text{ mech.}}{N_r}. \quad (10.1)$$

### Definition of Electrical Angle

The position of the rotor is directly correlated with the mechanical angle  $\theta_m$ . One period describes one revolution of the rotor. To become independent of the machine configuration it is reasonable to specify the rotor position of switched reluctance machines in electrical degrees. The electrical angle is defined by the periodicity of the machine. For example, in Figure 10.1 the rotor repeats every  $90^\circ$  mechanical ( $\tau_{rp}$ ). Hence, this is defined as one electrical period of  $360^\circ$ . The relationship between electrical and mechanical angle is given in (10.2).

$$\theta_e = N_r \theta_m \quad (10.2)$$

Note that the switched reluctance machine illustrated in Figure 10.1 is *radial flux* oriented, given that the flux which crosses the air-gap is predominantly in the radial direction. Most machines in use are of this type, given the fact that this approach allows the machine to be manufactured by stacked laminations, as used in for example induction and synchronous machines.

### Possible Machine Configurations

The relationship between the number of stator teeth  $N_s$ , magnetic pole pair number  $p$  and number of electrical phases  $N_{ph}$  for switched reluctance machines may be written as

$$N_s = 2pN_{ph}. \quad (10.3)$$

To avoid equilibrium positions in which the SRM cannot provide torque, the number of rotor teeth  $N_r$  must be different from  $N_s$ . Typically,  $N_r$  is calculated using

$$N_r = 2p(N_{ph} - 1), \quad N_r < N_s, \quad \text{for } N_{ph} > 0 \quad (10.4a)$$

$$N_r = 2p(N_{ph} + 1), \quad N_r > N_s, \quad \text{for } N_{ph} > 0 \quad (10.4b)$$

$$N_r = 2p \quad \text{for } N_{ph} = 1. \quad (10.4c)$$

In general, the number of rotor teeth is chosen lower than the number of stator teeth for reasons discussed in the following chapter. Table 10.1 provides some indication of the machine configurations in use.

**Table 10.1** Typical SRM machine configuration

$N_{\text{ph}}$	1		2		3			4		5	
$N_s$	2	4	4	8	6	12	18	8	16	10	20
$N_r$	2	4	2	4	4	8	12	6	12	8	16
$p$	1	2	1	2	1	2	3	1	2	1	2

## 10.2 Operating Principles

The basic operating principles of the switched reluctance machine are discussed on the basis of a single-phase machine. A single-phase model is representative because even in multi-phase SRM machines mutual coupling between electrical phases can be neglected. Consequently, the development of generic models for this single-phase machine are directly applicable to multi-phase concepts.

### 10.2.1 Single-Phase Motor Concept

The machine under consideration is a 2/2 configuration, i.e., two stator and two rotor teeth as shown in Fig. 10.2. In the given example the rotor is displaced by an angle  $\theta_m$  from the stator teeth. An angle dependent current source  $i(\theta_m)$  as shown in Fig. 10.2, is connected to the  $N$ -turn phase winding, which consists of two concentrically wound coils located on each of the two stator teeth.

The inter-pole arc  $\tau_{rp}$  is in this example equal to  $180^\circ \text{ mech}$ . This angle is also equal to one electric period of the two pole rotor.

If the rotor is displaced by an angle  $\theta_m = \tau_{rp}$ , a single torque pulse will result, provided the appropriate phase excitation conditions are met. The number of torque pulses, defined by the variable  $N_{pu}$  is for this machine two. For a multi-phase machine  $N_{pu}$  is given as

$$N_{pu} = N_r N_{\text{ph}} = 2p N_{\text{ph}} (N_{\text{ph}} - 1). \quad (10.5)$$

A mechanical shaft speed of  $\omega_m$  (rad/s) is assumed, which in turn is linked to the fundamental electrical switching frequency  $f_e$  (Hz) of the excitation source. The electrical frequency may be written as

$$f_e = \frac{\omega_m}{\tau_{rp}} = N_r n_m \quad (10.6)$$

where  $n_m$  (rps) represents the shaft speed. Note that the electrical frequency must be equal to the number of torque pulses given the aim of controlling the excitation source in such a manner that the largest possible number of single torque pulses is realized during a rotor displacement interval. Furthermore,

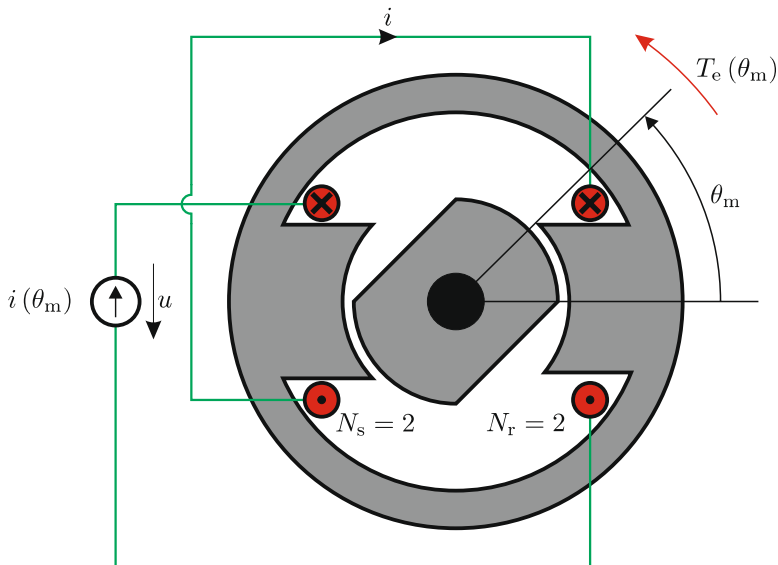


**Fig. 10.2** 2/2 Switched reluctance motor

(10.6) shows that the speed of the stepwise moving magnetic field  $\omega_e = 2\pi f_e$  is higher (by a factor equal to the number of rotor teeth  $N_r$ ) than the shaft speed  $\omega_m$ . The concept of a machine with a rotating magnetic field that is higher than the shaft speed, may be compared in mechanical terms to the planetary gearing. This torque multiplication process, which is referred to as the *vernier* principle in electrical machines, leads to increased switching losses in the converter and core losses in the SR machine, given the need for a higher electrical frequency (see (10.6)). However, the presence of this vernier principle in SR machines is fundamental to its ability to produce a torque that is an average similar, if not higher, than that of an induction machine of the same frame size. In terms of choosing a higher or lower number of rotor teeth with respect to the stator teeth number, it is prudent to chose the latter, given that this leads to comparatively lower core and switching losses.

The terminal voltage equation for this machine is according to Fig. 10.2 and Kirchoff's voltage law of the form

$$u(i, \theta_m) = R i(\theta_m) + \frac{d\psi(i, \theta_m)}{dt} \quad (10.7)$$

where  $R$  represents the phase coil resistance and  $\psi(i, \theta_m)$  the flux linkage depending on current and angle, otherwise referred to as the *magnetization characteristics* of the machine.

### 10.2.2 Torque Production and Energy Conversion Principles

The simplicity of the doubly salient machine structure (see Fig. 10.2) may give the impression that the nature of torque production and energy conversion principles are equally simple. Unfortunately, this is not the case as will become apparent in this section. Initially, the single-phase machine model is examined to ascertain the energy flows that are present between the supply source, magnetic energy in the air-gap and energy supplied to the shaft. In this process, the role of magnetic saturation is duly explored. Iron losses and copper losses will inevitably affect the overall machine performance but do not significantly affect the torque and energy conversion principles. Hence, these are ignored in this analysis. Under these circumstances, the terminal voltage (10.7) reduces to the following form

$$u(i, \theta_m) = \frac{d\psi(i, \theta_m)}{dt}. \quad (10.8)$$

#### Energy Balance Equation

A suitable starting point for this analysis is the overall incremental energy balance equation of the machine. The latter builds on the understanding that the incremental input energy  $dW_{in}(i, \theta_m)$  must be equal to the sum of the incremental magnetic energy in the air-gap  $dW_f(i, \theta_m)$  and incremental energy linked to the shaft  $T_e(i, \theta_m) d\theta_m$ . Consequently, the following energy balance equation (in difference form) holds

$$dW_{in}(i, \theta_m) = dW_f(i, \theta_m) + T_e(i, \theta_m) d\theta_m. \quad (10.9)$$

The incremental input energy  $dW_{in}(i, \theta_m)$  can also be written in terms of the terminal quantities, as shown in equation (10.10), where  $u(i, \theta_m)$  is defined by (10.8). The reader is reminded of the fact that constant shaft speed is assumed, hence the variable time  $t$  may also be expressed in terms of the rotor angle  $t = \theta_m/\omega_m$ . The three key variables for this type of analysis are the flux linkage, current and rotor angle. However, not all three variables may be chosen freely. Hence, it is a matter of selecting two of the three as so-called *independent* variables. For this analysis it is prudent to assign the rotor angle  $\theta_m$  and current  $i$  as independent variables. Under these conditions (10.8) may also be written as shown in equation (10.11).

$$dW_{in}(i, \theta_m) = i(t) u(t) dt \quad (10.10)$$

$$u(i, \theta_m) = \left[ \frac{\partial \psi(i, \theta_m)}{\partial i} \right]_{\theta_m=\text{const}} \frac{di}{dt} + \omega_m \left[ \frac{\partial \psi(i, \theta_m)}{\partial \theta_m} \right]_{i=\text{const}} \quad (10.11)$$

where  $\omega_m = \frac{d\theta_m}{dt}$  represents the shaft speed in rad/s. The partial derivative as shown in (10.12a) represents the flux linkage derivative with respect to the

current and is known as the incremental inductance, while the second term in (10.11) represents the so-called *motional EMF*.

$$l(i, \theta_m) = \left[ \frac{\partial \psi(i, \theta_m)}{\partial i} \right]_{\theta_m=\text{const}} \quad (10.12a)$$

$$u_e(i, \theta_m) = \omega_m \left[ \frac{\partial \psi(i, \theta_m)}{\partial \theta_m} \right]_{i=\text{const}}. \quad (10.12b)$$

In practice, it is useful to introduce a so-called normalized *EMF variable*  $e = u_e(i, \theta_m)/\omega_m$ . Substitution of (10.12) into (10.11) leads to the terminal equation in terms of the chosen independent variables  $i$  and  $\theta_m$ .

$$u(i, \theta_m) = l(i, \theta_m) \underbrace{\frac{di}{dt}}_{u_l} + \underbrace{e(i, \theta_m) \omega_m}_{u_e} \quad (10.13)$$

Equation (10.13) shows that the per phase equivalent circuit of an SR motor can be represented by a series circuit (see Fig. 10.3), which consists of an inductance, a stator winding resistance (which can be easily added to this model) and a voltage source proportional to  $\omega_m$ . The significance of this model representation should not be lost as it shows that the switched reluctance circuit model is similar to that of conventional motors.

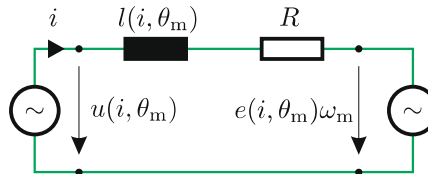


**Fig. 10.3** Single-phase equivalent circuit of a switched reluctance machine

The nature of the energy conversion process is however significantly different given that the flux-linkage/current characteristics are rotor angle dependent and in most cases highly non-linear. In this context the energy conversion process is often referred to as a *parametric* type of energy conversion. Further insight into the energy flow can be obtained by defining the incremental input energy  $dW_{in}$  in terms of the energy linked with the circuit components which leads to

$$dW_{in}(i, \theta_m) = i l(i, \theta_m) di + i e(i, \theta_m) d\theta_m. \quad (10.14)$$

### General Torque Equation

Substitution of (10.14) into (10.9) leads to an expression for the torque  $T_e(i, \theta_m)$  in the event that the incremental field energy component  $dW_f$  present in (10.9) is expressed in terms of its partial derivatives, namely

$$dW_f(i, \theta_m) = \left[ \frac{\partial W_f(i, \theta_m)}{\partial \theta_m} \right]_{i=\text{const}} d\theta_m + \left[ \frac{\partial W_f(i, \theta_m)}{\partial i} \right]_{\theta_m=\text{const}} di. \quad (10.15)$$

Substitution of (10.15) into (10.9) and equating the latter with (10.14) in terms of the derivatives  $di$  and  $d\theta_m$  leads to

$$W_f(i, \theta_m) = \left[ \int_0^i i l(i, \theta_m) di \right]_{\theta_m=\text{const}} \quad (10.16a)$$

$$T_e(i, \theta_m) = i e(i, \theta_m) - \left[ \frac{\partial W_f(i, \theta_m)}{\partial \theta_m} \right]_{i=\text{const}}. \quad (10.16b)$$

Equation (10.16) may also be written in an alternative form by making use of  $l(i, \theta_m) = [\partial \psi(i, \theta_m)/\partial i]_{\theta_m=\text{const}}$ ,  $e(i, \theta_m) = [\partial \psi(i, \theta_m)/\partial \theta_m]_{i=\text{const}}$  which after some manipulation gives

$$W_f(i, \theta_m) = \left[ \int_0^\psi i(\psi, \theta_m) d\psi \right]_{\theta_m=\text{const}} \quad (10.17a)$$

$$T_e(i, \theta_m) = \left[ \frac{\partial}{\partial \theta_m} (i\psi - W_f(i, \theta_m)) \right]_{i=\text{const}}. \quad (10.17b)$$

The term  $(i\psi - W_f(i, \theta_m))$  is known and defined in literature as the *co-energy*  $W'_f$ , which may also be written as

$$W'_f(i, \theta_m) = \left[ \int_0^i \psi(i, \theta_m) di \right]_{\theta_m=\text{const}}. \quad (10.18)$$

Introduction of the term  $W'_f$  in (10.17b) allows the latter to be written as

$$T_e(i, \theta_m) = \left[ \frac{\partial W'_f(i, \theta_m)}{\partial \theta_m} \right]_{i=\text{const}}. \quad (10.19)$$

A further observation of (10.17b) demonstrates that the largest achievable shaft torque level, defined as  $\tilde{T}_e$ , can be realized in case  $W_f \rightarrow 0$ . Under these conditions the torque is given as

$$\tilde{T}_e(i, \theta_m) = \left[ \frac{\partial (i\psi)}{\partial \theta_m} \right]_{i=\text{const}}. \quad (10.20)$$

### Influence of Linear and Non-linear Inductance

The process of designing a machine with a torque output which approaches the theoretical upper limit value  $\tilde{T}_e$  is primarily concerned with the shape of the flux/linkage/current characteristics. This statement is demonstrated with the aid of Fig. 10.4, which shows an incremental rotor angle change of the rotor magnetization curves (under constant current conditions) for the linear and non-linear case.

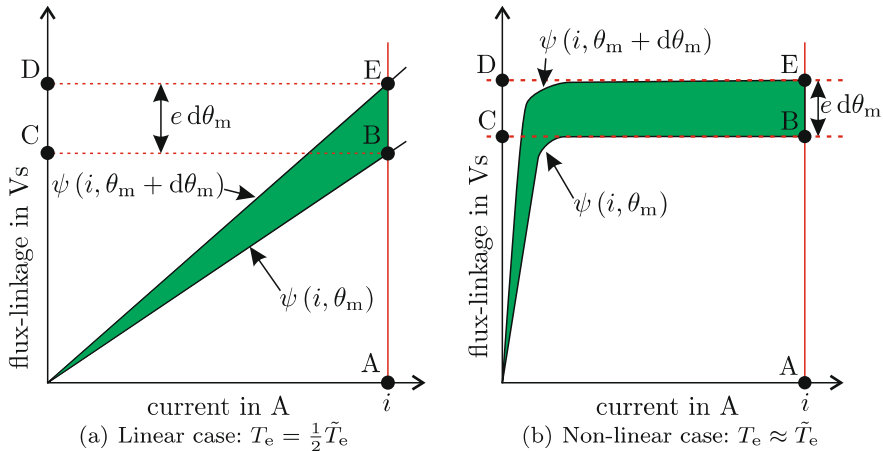


**Fig. 10.4** Magnetization curves for the linear and non-linear case

For the linear case, as shown in Fig. 10.4(a), the output torque is equal to half the maximum value  $\tilde{T}_e$ . The reason for this is that the output energy  $T_e d\theta_m$ , is tied to the incremental co-energy  $dW'_f$ , which corresponds to area 0-B-E-0 in Fig. 10.4(a). Note that in the linear case considered here, the magnetic energy  $W_f$  is equal to the co-energy  $W'_f$ . If we consider the flux-linkage current curve  $\psi(i, \theta_m)$ , then the co-energy and magnetic energy are represented by the areas 0-A-B-0 and 0-B-C-0 respectively. The energy which corresponds to  $\tilde{T}_e d\theta_m$  is given by area B-C-D-E, which is also equal to the energy  $ie d\theta_m$  delivered by the supply source connected to the machine. Under constant current conditions, as assumed here, the energy  $\tilde{T}_e d\theta_m$  represents the total amount of energy supplied to the machine and the area B-C-D-E is double the area 0-B-E-0 linked to the co-energy change.

If the machine is designed with a high magnetic saturation level, as shown (unrealistically high) in Fig. 10.4, it may be observed that the energy and co-energy levels linked to for example the flux-linkage current curve  $\psi(i, \theta_m)$  are very much different. Under these conditions the incremental co-energy as shown by the green area in Fig. 10.4, approaches the maximum output energy level  $\tilde{T}_e d\theta_m$  which corresponds to area B-C-D-E. It is therefore not surprising to learn that switched reluctance machines are usually designed to operate with a substantial level of magnetic saturation. This means that the magnetization curves will be highly non-linear, which in turn has important implications for the simulation models tied to this type of machine.

### Energy Flow of SR Motor

The understanding of the machine is enhanced by considering the energy flows which occur between the supply, load and magnetic energy reservoir  $W_f$  as shown in Fig. 10.5.

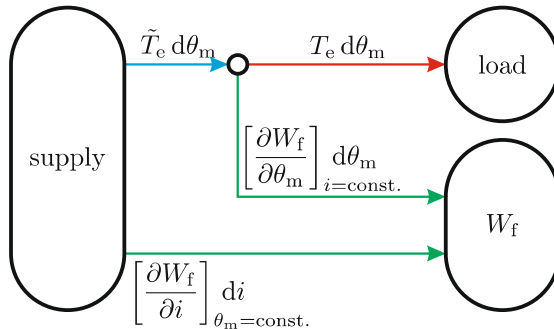


**Fig. 10.5** Energy flow in SR machine

Readily apparent in Fig. 10.5 are the incremental energy flow arrows that are linked with the torque variables  $\tilde{T}_e$  and  $T_e$ . The incremental energy flow arrows tied to the magnetic energy reservoir  $W_f$  can be found by making use of (10.17) and the realization that the current supplied to the machine will be a function of the rotor angle, hence  $i(\theta_m)$ ,  $di = \partial i / \partial \theta_m d\theta_m$ . Given the above, the energy flows tied to  $W_f$  may be written as

$$\left[ \frac{\partial W_f}{\partial i} \right]_{\theta_m=\text{const.}} di = i l(i, \theta_m) \frac{\partial i}{\partial \theta_m} d\theta_m \quad (10.21a)$$

$$\left[ \frac{\partial W_f}{\partial \theta_m} \right]_{i=\text{const.}} d\theta_m = (\tilde{T}_e - T_e) d\theta_m. \quad (10.21b)$$

If we consider the energy flow linked to Fig. 10.4. for the trajectory  $B \rightarrow E$ , we note that the contribution  $[\partial W_i / \partial i]_{\theta_m=\text{const.}} di$  will be zero, given that the current is constant under these conditions. Furthermore, the amount of energy delivered to load and magnetic energy supply will be equal in the linear case. This situation is however drastically changed for the non-linear case, in which most of the energy from the supply is transferred to the load.

#### 10.2.3 Single-Phase Switched Reluctance Machine: A Linear Example

To show the energy flow and torque production principles of a switched reluctance machine, it is helpful at this stage to consider a simple example of

a single-phase switched reluctance motor. In this context, the term *linear* denotes that the machine is not operated in saturation. This leads to the simplification that the inductance only depends on rotor position so that the incremental inductance  $l(i, \theta_e) = L(\theta_e)$ . The flux linkage may therefore be written as

$$\psi = L(\theta_e) i . \quad (10.22)$$

The torque of a linear machine may be found using (10.22) with (10.18) and (10.19) which leads to the following expression

$$T_e(\theta_m) = \frac{1}{2} i^2 \frac{dL(\theta_m)}{d\theta_m}. \quad (10.23)$$

Due to the periodicity of the phase inductance of a switched reluctance machine, it is sufficient to pursue the analysis for one electrical period. Therefore, the rotor position is measured in electrical radians. In (10.23), torque is proportional to the derivative of inductance over the mechanical rotor position. Substituting the mechanical rotor position by its electrical equivalent leads, together with (10.2), to the following expression for the (per phase) torque:

$$T_e(\theta_e) = \frac{1}{2} N_r i^2 \frac{dL(\theta_e)}{d\theta_e}. \quad (10.24)$$

An important observation to be made from (10.23) and (10.24) is the fact that the phase current appears in quadratic form, which implies that its polarity cannot influence the direction in which torque is produced. However, it is possible to produce negative torque by an excitation of the phase in the range of decreasing inductance.

Basically, two main operating modes for the switched reluctance machine can be identified depending on the speed of the machine. In the following, typical phase excitation patterns are examined for an operation at low and high speed.

### Phase Excitation at Low Speed

At low speed, the excitation pattern of one phase can be roughly divided into three steps:

1. Initial magnetization at maximum positive voltage
2. Torque production at constant current
3. Demagnetization at maximum negative voltage

Hence, it is convenient to use a piecewise linear model of the phase inductance, where the slope of the inductance is constant within each of the three ranges.

Figure 10.6 shows in its uppermost diagram the piecewise linear model of one phase inductance. In the range of  $\tau_u/2$  to each side of the unaligned position, the inductance is constant at its unaligned value  $L = L_u$ . In the aligned position, the inductance does also not experience any changes given the rotor is not displaced further than  $\tau_a/2$  to either side. In between, the inductance changes linearly at a constant slope according to  $dL/d\theta_e = \text{const}$ . From (10.24), it becomes obvious that torque can only be produced in the range of changing inductance. As a consequence, one aim during low speed operation is to have the active phase fully excited with the desired current right before the inductance starts to increase, as can be seen in the second graph of Fig. 10.6. This initial excitation can be carried out fast as  $L$  is low and the supply is at maximum dc-link voltage.

Once the current has reached the desired value and the inductance starts to increase, torque is produced according to (10.24). During this time, the phase voltage (blue curve in second diagram of Fig. 10.6) is adjusted to maintain a constant current waveform. Note that the flux linkage increases linearly according to (10.8). At the end of the region of increasing inductance, the phase is turned off (demagnetized) at maximum negative dc-link voltage. Due to the significantly larger inductance in the aligned position, the demagnetization phase takes longer than the magnetization phase.

The resulting torque is shown in the third graph of Fig. 10.6. An important observation to be made in the torque waveform is that no torque is produced in the constant inductance region although the phase is already partially excited. As a result, the produced torque has, in contrast to the current waveform, a rectangular shape.

Although no torque is produced within the regions of constant inductance, which implies that no energy is supplied to the load, magnetic energy is fed into the phase during magnetization. During magnetization, (10.17a) together with (10.22) can be rewritten as

$$W_f(i, \theta_e) = \frac{1}{2} L(\theta_e) i^2. \quad (10.25)$$

The waveform of the magnetic energy can be examined as the blue plot in Fig. 10.7. During magnetization and demagnetization, the magnetic energy changes proportionally to the square of current. In the period of constant current, it rises linearly with the phase inductance. The green curve shows the mechanical energy supplied to the load which is equal to the integral of torque over the rotor position. It should be noted, that the total change of mechanical energy (denoted as  $\Delta W_m$ ) is equal to the change of magnetic energy during the constant current period. The energy flows related to  $W_f$  reservoir can be calculated according to:

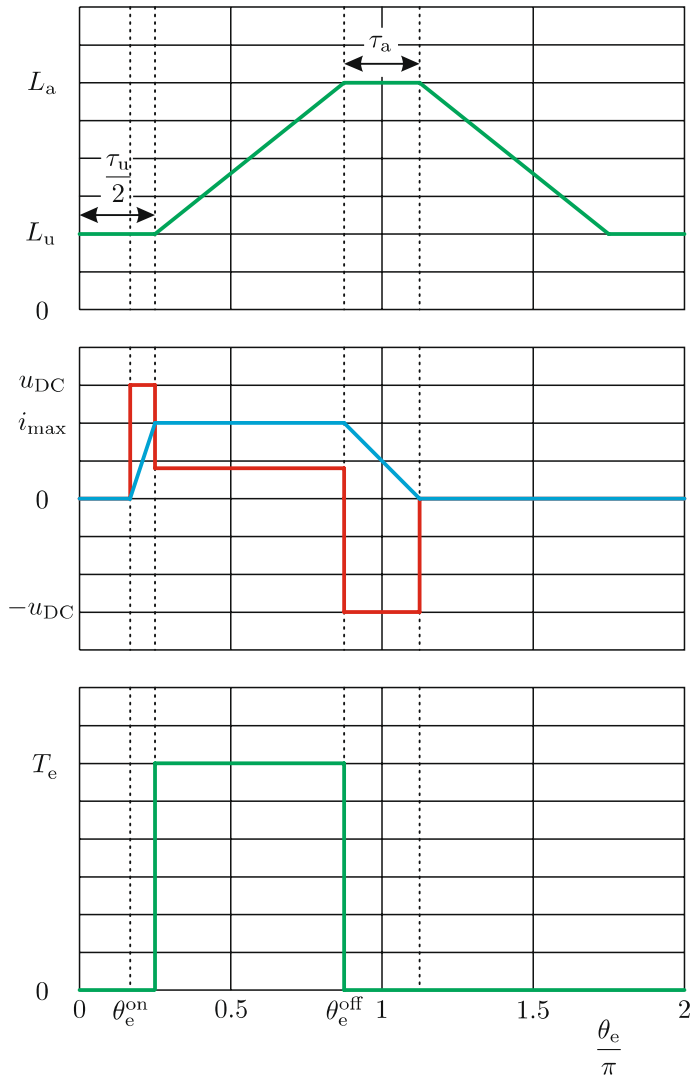


**Fig. 10.6** Piecewise linear inductance, phase voltage (red), current (blue) and resulting phase torque over one electrical period at constant speed

$$\left[ \frac{\partial W_f}{\partial i} \right]_{\theta_e=\text{const}} \frac{di}{d\theta_e} = L(\theta_e) i \frac{di}{d\theta_e} \quad (10.26a)$$

$$\left[ \frac{\partial W_f}{\partial \theta_e} \right]_{i=\text{const}} = \frac{1}{2} i^2 \frac{dL(\theta_e)}{d\theta_e}. \quad (10.26b)$$

The waveforms of both are plotted in Fig. 10.8. Note, that the partial derivative of  $W_f$  over rotor position (green curve) has the same shape as the torque

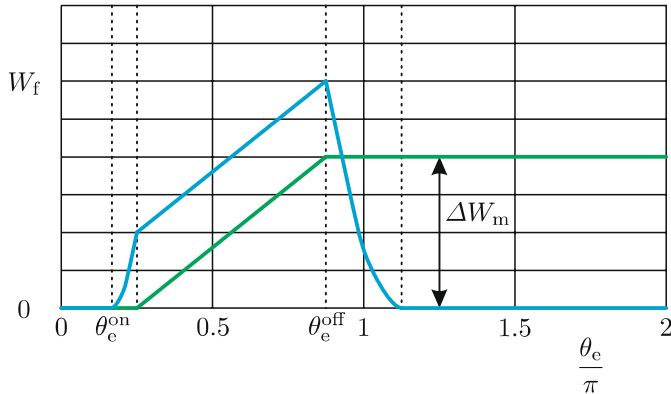


**Fig. 10.7** Magnetic (blue) and mechanical (green) energy over one electrical period

waveform. Another important observation to be made is that the magnetic energy recovered at the end of excitation is substantially larger than the magnetic energy provided by the supply during the magnetization phase.

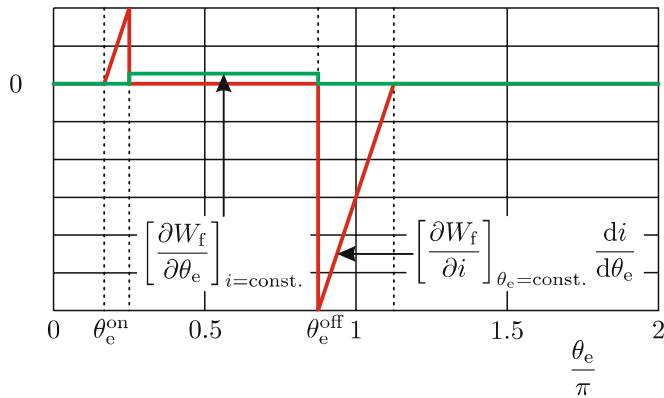


**Fig. 10.8** Energy flows related to  $W_f$  reservoir

For the analysis of switched reluctance drives it is helpful to consider the flux linkage/current locus which appears in the flux linkage/current diagram during an active rotor cycle. The locus which appears with the present choice of current excitation is displayed in Fig. 10.9. The two red trajectories in the diagram correspond to the magnetization (0 to  $\tau_u/2$ ) and demagnetization ( $\pi - \tau_a/2$  to  $\pi + \tau_a/2$ ) processes in the regions of constant inductance. The green leg reflects the constant current region, where the inductance rises linearly. The area, which is surrounded by the entire trajectory is equal to the mechanical energy delivered to the shaft.

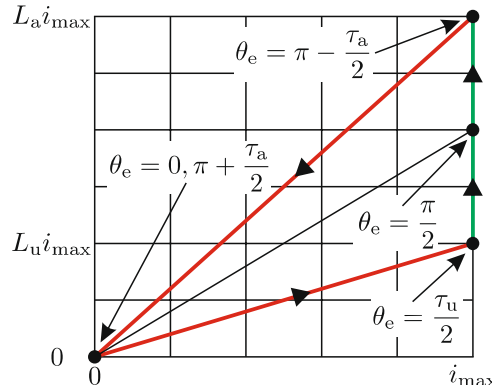


**Fig. 10.9** Half cycle flux linkage current diagram

### Phase Excitation at High Speed (Single Pulse Mode)

At higher speeds, the maximum achievable slope of the stator current over rotor position decreases due to the induced voltage. As a consequence, when a certain speed is exceeded, the nominal phase current cannot be established within the constant inductance range anymore. The same applies for the demagnetization at the end of the active cycle. In general, the time spans of magnetization and demagnetization overlap with the time spans of changing inductance, a condition, which can be avoided at low speed operation.

At high speed, it is hence more instructive to use a continuously differentiable inductance model to describe the mechanisms of energy conversion analytically. Such a model is represented in (10.27) and in the inductance plot of Fig. 10.10 over one electrical period.

$$L(\theta_e) = L_o ((1 + \kappa) + (1 - \kappa) \cos(\theta_e)) \quad (10.27)$$

This inductance profile can be recognized as a harmonic approximation of the piecewise linear model presented at the beginning of this section given that  $2L_o = L_u$  and  $\kappa = L_a/L_u$ . For a machine with two rotor teeth ( $N_r = 2$ ), the given inductance profile repeats twice per mechanical revolution.

In single pulse operation, the positive dc-link voltage (red curve in second plot of Fig. 10.10) is applied for the entire first half of the excitation cycle, so that the flux linkage inside the phase increases linearly according to (10.22). During the second half of the active cycle, the negative dc-link voltage is applied to the phase leading to a linearly decreasing flux linkage. The flux linkage profile during the entire excitation process is mathematically expressed as follows

$$\psi(\theta_e) = \begin{cases} \psi(\theta_e^{\text{on}}) + \frac{u_{\text{DC}}}{\omega_e} (\theta_e - \theta_e^{\text{on}}) & \theta_e^{\text{on}} \leq \theta_e \leq \theta_e^{\text{off}} \\ \psi(\theta_e^{\text{off}}) - \frac{u_{\text{DC}}}{\omega_e} (\theta_e - \theta_e^{\text{off}}) & \theta_e^{\text{off}} < \theta_e. \end{cases} \quad (10.28)$$

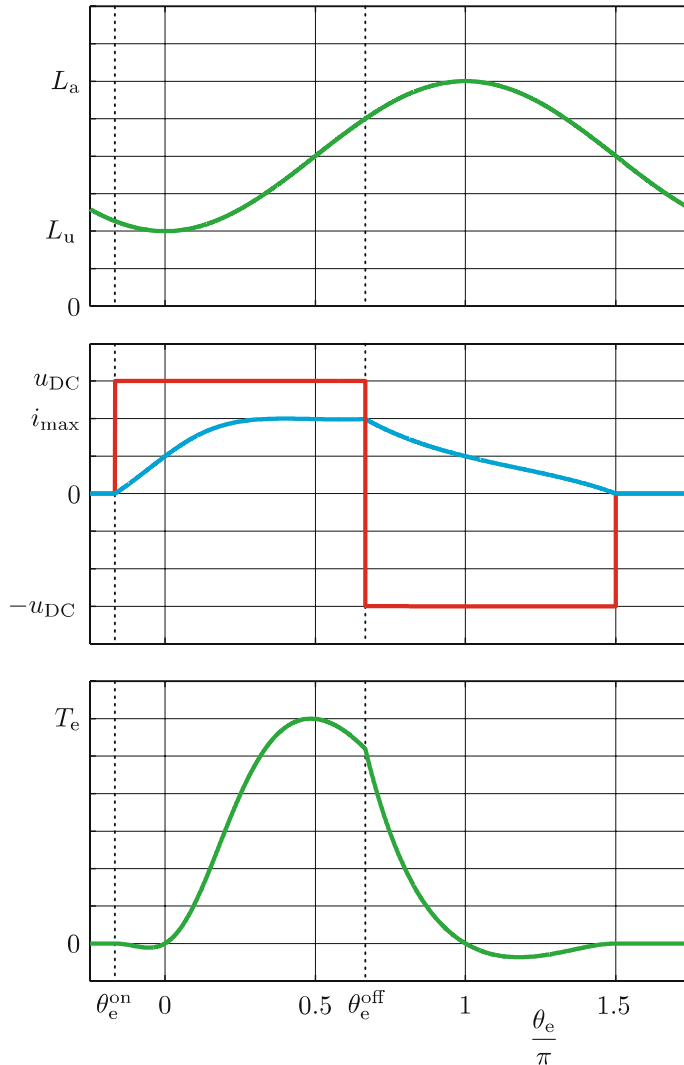


**Fig. 10.10** Sinusoidal inductance, phase voltage (red), current (blue) and resulting phase torque over one electrical period at constant speed

Given a completely demagnetized phase at the beginning of the excitation,  $\psi(\theta_e^{\text{on}}) = 0$ , the current can be calculated using (10.22) with (10.27) and (10.28):

$$i(\theta_e) = \begin{cases} i(\theta_e^{\text{off}}) - \frac{u_{\text{DC}}}{\omega_e L_o} \frac{\theta_e - \theta_e^{\text{on}}}{1 + \kappa + (1 - \kappa) \cos(\theta_e)} & \theta_e^{\text{on}} \leq \theta_e \leq \theta_e^{\text{off}} \\ i(\theta_e^{\text{off}}) & \theta_e^{\text{off}} < \theta_e. \end{cases} \quad (10.29)$$

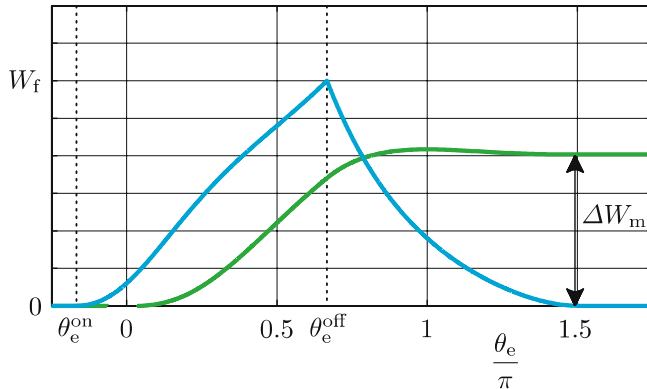


**Fig. 10.11** Magnetic (blue) and mechanical (green) energy over one electrical period

The waveform of the phase current can be observed as the blue curve in the second plot of Fig. 10.10. It should be noted, that the excitation starts in a region, where the slope of the inductance is negative but still rather small. This is usually done to ensure a fully excited phase right before the inductance rises again. However, a small amount of negative torque is produced during this initial magnetization, which can be seen in the third plot of Fig. 10.10.

The torque waveform for the complete active cycle can be calculated by inserting (10.27) and (10.29) into (10.24):

$$T_e(\theta_e) = \frac{1}{2} N_r L_o (\kappa - 1) \sin(\theta_e) i^2(\theta_e) \quad (10.30)$$

and is a function of the choice of the turn-on angle  $\theta_e^{\text{on}}$  and the turn-off angle  $\theta_e^{\text{off}}$ . It becomes obvious that a non-zero average torque can be produced with the chosen excitation profile, although small amounts of negative torque are produced at the beginning and the end of the active cycle.

Figure 10.11 shows the magnetic energy  $W_f$  inside the phase (blue) and the mechanical energy  $W_m$  (green) supplied to the load, which is simply the integral of torque. The magnetic energy is recovered at the end of excitation and does therefore not contribute to torque production. However, this energy exchange causes losses inside a non-ideal drive configuration (ohmic losses inside machine, converter losses due to voltage drops across power switches) and should hence be minimized. A well-suited measure for the relative amount of magnetic energy is the so-called energy conversion factor  $EC$ , which is defined as

$$EC = \frac{\text{energy delivered to the load}}{\text{total energy supplied by the source}}. \quad (10.31)$$

In (10.31), the *total energy supplied by the source* is to be interpreted as the sum of the maximum magnetic energy and the mechanical *energy delivered to the load* after one active cycle.

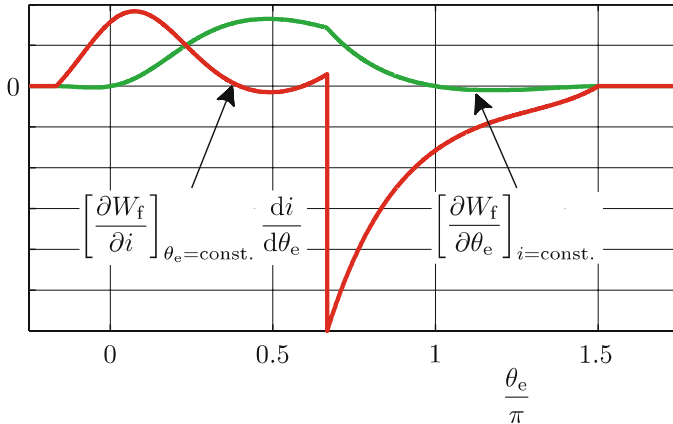


**Fig. 10.12** Energy flows related to  $W_f$  reservoir

Figure 10.12 denotes the energy flows related to the  $W_f$  reservoir according to (10.26a) and (10.26b). The magnetic energy supplied at the start of the interval is lower than the amount recovered at the end. The reason for this is that for the linear case equal amounts of energy are supplied to the load and the magnetic energy reservoir. The amount of energy recovered at the end of the interval is therefore the sum of the magnetic energy supplied at the beginning of the active cycle plus the amount diverted from the node (see Fig. 10.5) to the magnetic reservoir. The sum of these two contributions is the total energy supplied to the motor by the supply, as was mentioned previously.

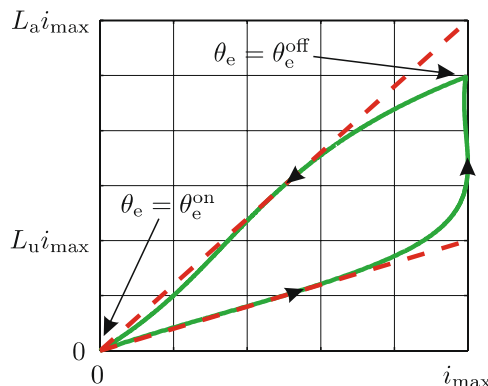


**Fig. 10.13** Half cycle flux linkage current diagram

The flux linkage/current locus for the chosen current waveform is displayed in Fig. 10.13. In contrast to the low-speed case given in Fig. 10.9, the

traces of magnetization and demagnetization cannot be identified as straight lines anymore. Instead, a more smooth transition between magnetization and torque production takes place.

### 10.2.4 Switched Reluctance Modeling Concepts

The development of generic single SR models is readily undertaken with the aid of the theory given in Sect. 10.2.2. Initially, current based models are considered, which assumes that the current as function of the rotor angle is given. In the second part of this chapter voltage based models are discussed which are mostly used because these may be directly coupled to the converter structure, which are typically voltage source converters. The models considered will assume the presence of a phase coil resistance  $R$ .

Current based generic models require access to a current versus angle relationship  $i(\theta_m)$ . The output variables for this model should be the torque  $T_e$  and phase voltage  $u$ . The fundamental modeling component of the SR machine are the magnetization characteristics  $\psi(i, \theta_m)$  which are represented by a single module, with inputs  $i, \theta_m$  and output  $\psi$ . A similar module is also required for the torque, hence its output is the variable  $T_e$ , which is used in conjunction with the mechanical load equation

$$J \frac{d\omega_m}{dt} = T_e(i, \theta_m) - T_l \quad (10.32a)$$

$$\omega_m = \frac{d\theta_m}{dt} \quad (10.32b)$$

where  $J$  and  $T_l$  represent the combined inertia and the load torque of the load and the machine respectively. The so-called static torque/current/angle characteristics are generated with the aid of the magnetization curves, using the theoretical approach given in Sect. 10.2.2. Use of terminal (10.7) and (10.32) leads to the generic model shown in Fig. 10.14.

Also shown in Fig. 10.14 is a module  $T_l(\omega_m)$  which represents a user defined relationship between load torque and shaft speed. The reader is advised to consider the tutorials at the end of this chapter which demonstrate the use of all the generic models presented in this section. In Fig. 10.14, the phase voltage is derived by differentiation of the flux. However, an alternative approach may also be taken by using partial derivatives, as shown in the previous section, where an alternative terminal equation representation (10.13) was developed. The generic model as given in Fig. 10.15 uses the incremental inductance and normalized EMF curves, which are represented by non-linear modules with inputs  $i$  and  $\theta_m$ .

The torque module and generic modules linked with (10.32a) are not shown in Fig. 10.15 given that these are identical to those shown in Fig. 10.14. The

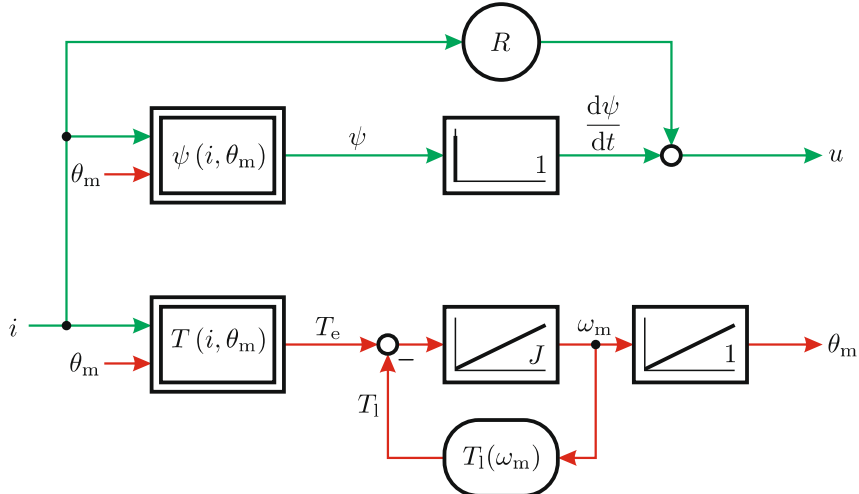


**Fig. 10.14** Model of SRM with current excitation. Magnetization curves are used to generate the  $\psi$  and  $T_e$  tables as function of current and position

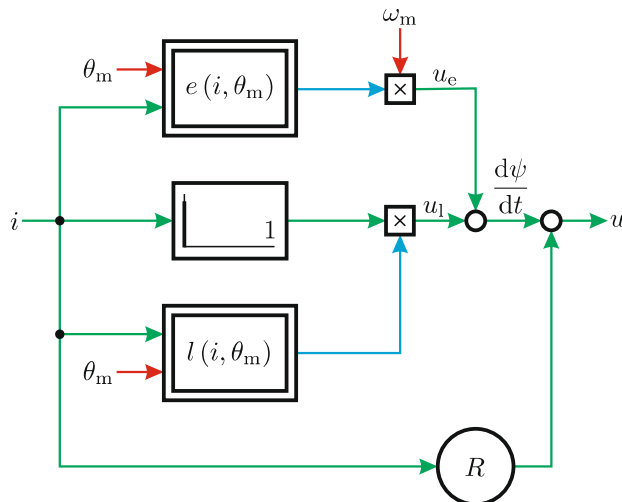


**Fig. 10.15** Current fed model of SRM using incremental inductance and *EMF* curves

advantage of the first model (Fig. 10.14) lies with its simplicity, given that it only requires access to the magnetization and static torque curves. The second model (Fig. 10.15) generates the voltages  $u_e$  and  $u_l$ , which are useful in terms of enhancing the overall understanding of the machine. Furthermore, access to the voltage  $u_e$  is beneficial when considering sensorless SR drive applications. However, the model requires access to the partial derivatives of the magnetization curves. These must in turn be provided as non-linear

modules, with inputs  $i$ ,  $\theta_m$ . Voltage source models are commonly used for simulation purposes because most converter topologies are voltage source converters that control directly the phase voltage. The generic model as given in Fig. 10.16 uses the terminal voltage (10.7), which must be rewritten as an explicit function of the current. The torque module and generic modules linked with (10.32a) are again not shown in the voltage based model, given that these remain unchanged.

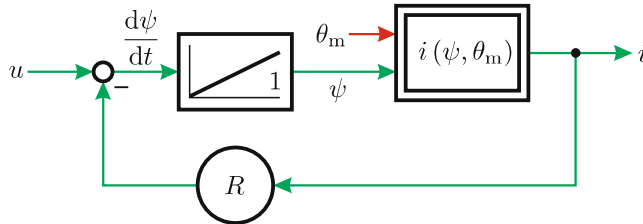


**Fig. 10.16** Voltage fed model of SRM, using inverse magnetization curves

The generic model according to Fig. 10.16 requires access to the *inverse* magnetization curves, which implies that the corresponding non-linear module has as output the current  $i$  and inputs the variables  $\psi$  and  $\theta_m$ . In practice, generation of this function from the magnetization curves  $\psi(i, \theta_m)$  is demanding because it requires an extrapolation process of the latter function. The model in question is the causal counterpart of the model given in Fig. 10.14. The final model in this section is the causal counterpart of the current source model according to Fig. 10.15. This model, as given in Fig. 10.17, requires access to the incremental inductance and *EMF* curves.

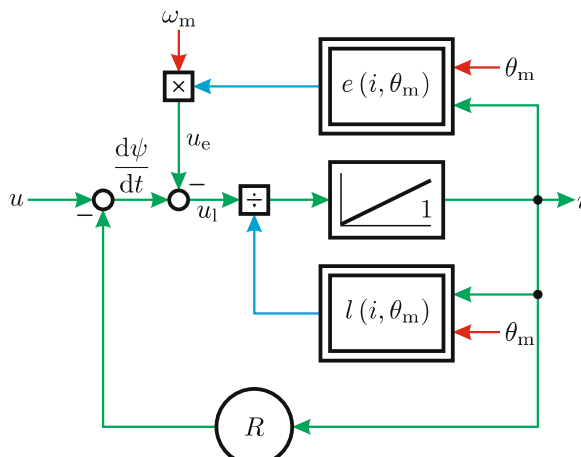


**Fig. 10.17** Voltage fed SR model using incremental inductance and *EMF* curves

### 10.2.5 Representation of the Magnetization Characteristics

Central to the modeling process is the ability to represent the flux linkage depending on current and angle  $\psi(i, \theta_e)$  and their derivatives as defined by (10.12). Due to the periodicity of the flux linkage, the angle will be defined in electrical degrees as described in (10.2). Figure 10.18 shows a typical set of magnetization curves which are represented in two different ways. Those given in Fig. 10.18(a) represent the flux linkage versus current relationship, whereby the rotor angle is held constant. These curves are defined over a current interval  $0 \leq i \leq i_{\max}$ . A parameter set of four rotor angles  $0^\circ < \theta_e^1 < \theta_e^2 < 180^\circ$  is shown, which are defined over the range  $0^\circ \leq \theta_e \leq 180^\circ$ .

As mentioned earlier, the magnetic reluctance of the circuit is at its minimum value for the aligned rotor position, hence magnetic saturation effects are at their highest level, which is reflected in the corresponding flux-linkage current curve  $\psi(i, \theta_e = 180^\circ)$  shown in Fig. 10.18(a).

If on the other hand, the rotor is set to its unaligned position ( $\theta_e = 0^\circ$ ) magnetic saturation effects can be ignored, in which case the flux-linkage  $\psi(i, \theta_e = 0^\circ)$  is a linear function of current, as may be observed from Fig. 10.18(a).

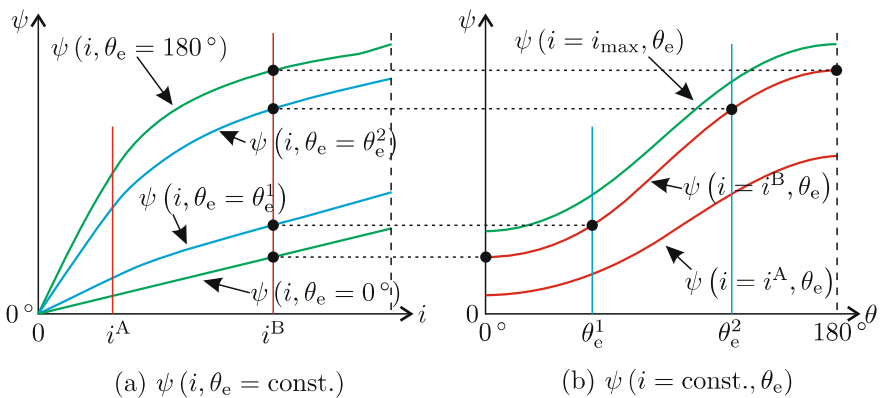


**Fig. 10.18** Typical set of magnetization characteristics

It is also instructive to consider an alternative representation of the magnetization curves as given in Fig. 10.18(b). This set of curves may be derived by using a conformal mapping technique in which, for example, the points  $\psi(i = i^B, \theta_e = \theta_e^{ij})$  with parameter set  $\theta_e^{ij} = 0^\circ, \theta_e^1, \theta_e^2, 180^\circ$  are plotted in a flux linkage versus rotor angle diagram. The set of magnetization curves shown in Fig. 10.18(a) is in fact a subset that can be derived from a comprehensive set of flux linkage versus current curves, as will be discussed in Sect. 10.5.

Note that the flux-linkage/angle characteristics  $\psi(i = \text{const}, \theta_e)$  are periodic functions, which implies that the derivative  $d\psi/d\theta_e$  at the aligned and unaligned rotor position must be zero. A further observation of Fig. 10.18(a) shows that the derivative of these characteristics is precisely the incremental inductance  $l(i, \theta_e)$ , which may in turn be expressed in terms of the variables  $i$  and  $\theta_e$ . The partial derivative of the flux with respect to the rotor angle, with  $i = \text{const}$ , referred to as the normalized *EMF* curves,  $e(i, \theta_e)$  are precisely the derivatives of the flux-linkage/angle characteristics as given in Fig. 10.18(b).

### 10.2.6 Converter and Control Concepts

A commonly used switched reluctance drive configuration shown in Fig. 10.19, utilizes two switches per phase and this topology is referred to as an *asymmetrical half-bridge* converter. The drive has three basic modes of operation, which will be discussed below with the aid of Table 10.2, Fig. 10.19 and Fig. 10.5.

- Mode 1, magnetization state: both switches  $S_b$ ,  $S_t$  are closed, while the diodes  $D_b$ ,  $D_t$  remain non-conducting. The phase voltage  $u$  is equal to the supply voltage  $u_{DC}$  and the supply current  $i_{\text{supply}}$  is equal to the phase current  $i$ . Energy from the supply source is transferred to the load and to the magnetic energy reservoir  $W_f$ .
- Mode 2, free-wheeling state: switch  $S_b$  is closed and  $S_t$  is open. The diode  $D_b$  is conducting and  $D_t$  is non-conducting (or vice versa, i.e., there are two free-wheeling states). The phase voltage  $u$  is equal to zero and the supply current  $i_{\text{supply}}$  is also zero. The supply source is disconnected from the machine, hence energy is transferred from the magnetic energy reservoir to the load.
- Mode 3, de-magnetization state: both switches  $S_b$  and  $S_t$  are open, while the diodes  $D_b$  and  $D_t$  are conducting. The phase voltage  $u$  is equal to  $-u_{DC}$  and the supply current  $i_{\text{supply}}$  is equal to  $-i$ . This mode of operation can only persist for as long as the phase current is greater or equal to zero. Energy from the magnetic reservoir is transferred to the load as well as the supply.

**Table 10.2** Switching states and resulting phase voltage of asymmetrical half-bridge (1: conducting, 0: non-conducting device)

$S_t$	$S_b$	$D_t$	$D_b$	$u$
1	1	0	0	$u_{DC}$
1	0	1	0	0
0	1	0	1	0
0	0	1	1	$-u_{DC}$ for $i > 0$

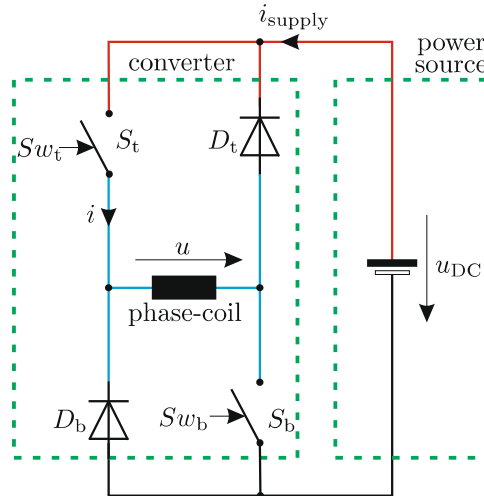


**Fig. 10.19** SR drive with asymmetric half-bridge converter topology

The active modes of operation are governed by a controller module which controls the two switches by way of the logic switch signals  $Sw_t$  and  $Sw_b$ . A logic 1 corresponds to a closed state for the corresponding switch. The inputs to the controller module are the reference  $i^*$  and measured phase currents as well as a logic *phase-active* signal, which is high during the period where the phase should be active. The latter is controlled by a commutator module, to be discussed at a later stage.

An example of a phase control module is given in Fig. 10.20, which utilizes *hysteresis* current control. Basically, the controller aims to keep the measured phase current within the boundaries  $i^* \pm \Delta i/2$ , where  $\Delta i$  represents a user defined current tolerance band. The current controller controls the top converter switch  $S_t$  when the phase-active signal is set to 1. Comparator A is part of the actual hysteresis controller and its output is either 1 or -1, depending on the polarity of the error signal  $\varepsilon$ . The second comparator B is used to convert the bipolar output from the first comparator to a logic signal.

Note that the hysteresis current controller may be replaced by an alternative control concept where the top switch is connected to a PWM generator. In this case, the duty cycle  $\delta$  for the top switch is the control variable, which implies that the average phase voltage during the phase-active period is equal to  $\delta u_{DC}$ . At the end of the phase-active period both switches are opened, in which case the phase voltage is equal to  $u = -u_{DC}$  for the time interval in which the phase current is greater than zero. This type of control has a constant PWM switching frequency, which can be advantageous in terms of acoustic noise. A hysteresis type controller exhibits a variable switching frequency, which yields a decidedly different acoustical signature in comparison with drives that utilize a PWM based control method. The generation of the

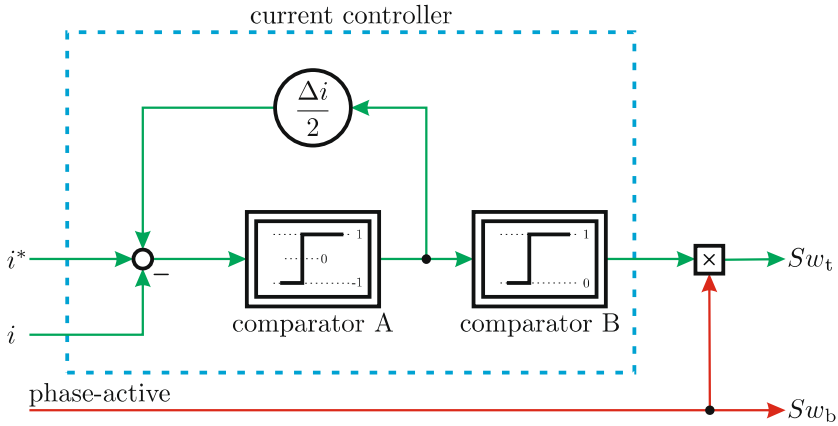


**Fig. 10.20** Phase control module

*phase-active* signal remains to be discussed and this may be done with the aid of Fig. 10.21.

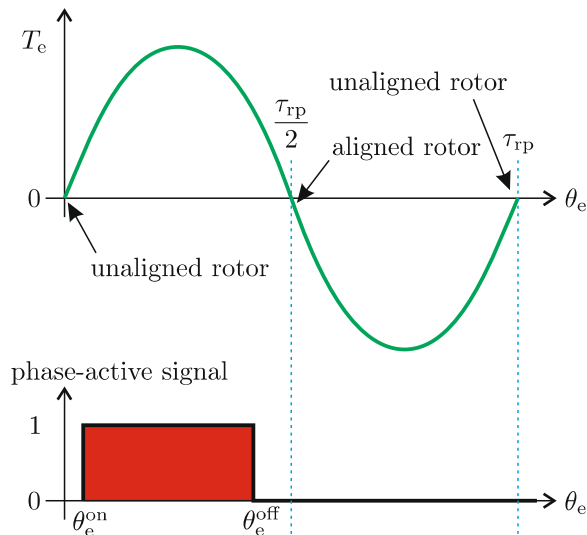


**Fig. 10.21** Definition of *turn-on*  $\theta_e^{on}$  and *turn-off*  $\theta_e^{off}$  angles

This figure shows a typical stator torque versus shaft angle characteristic of a machine without saturation, in which case (10.23) and (10.24) apply. The beginning and end shaft positions of the phase-active signal are defined with respect to the rotor position. In this context, the angles  $\theta_e^{on}$  and  $\theta_e^{off}$  are introduced as may be observed from Fig. 10.21. In this figure, an example

is given which shows that the phase-active signal is set to 1 when the rotor angle  $\theta_e$  is between the *turn-on* and *turn-off* angles ( $\theta_e^{\text{on}} \leq \theta_e \leq \theta_e^{\text{off}}$ ).

If the phase excitation current resembles a square wave phase current, then the *turn-on* and *turn-off* angles should be set to  $0^\circ$  and  $180^\circ$  respectively to maximize the average torque per phase. However, the control angles will need to be adapted with speed in a practical drive to counter the effects of a finite rise and fall time of the current at the beginning and end of the phase-active period, as will become apparent in Sect. 10.4.1.

### 10.2.7 Example of Low and High Speed Drive Operation

The interaction between the converter and machine is very much dependent on the type of converter topology in use, the control methods deployed and the operating speed. Some insight into the behavior of the basic drive by way of typical waveforms for different speeds is given in this subsection. The fact that a single-phase based drive model is used does not affect the operational variable speed drive aspects considered here. The reason for this is that the phases are magnetically and electrically decoupled, hence a single-phase representation is sufficient. At a later stage, a more detailed analysis of drive behavior will be considered. The distinction between *low* and *high* speed operation is defined relative to the *base* operating speed, which is the speed  $\omega_b$  at which the drive is able to operate at its rated current level and rated voltage. A detailed analysis with regards to calculating the base speed, is given in Sect. 10.4.1. An asymmetrical half-bridge converter topology (see Fig. 10.19) is assumed here.

#### Low Speed Operation

For low speed operation, some type of phase current control is required because the induced voltage levels in the machine are low in comparison with the supply voltage  $u_{\text{DC}}$ . In the previous section, hysteresis and PWM type control methods were discussed and these will also be considered here. The key variables (as defined in Fig. 10.14 and Fig. 10.17) as function of time, are the phase voltage  $u$ , induced voltage  $u_e$ , phase current  $i$  and (per phase) torque  $T_e$ . An example of the waveforms which appear in the drive when operating at low speed with a hysteresis type controller is given in Fig. 10.22. These results were obtained with the tutorial given at the end of this chapter (see Sect. 10.6.2).

In this example, the *turn-on* angle is set to zero, hence the phase-active period starts when the rotor is at its unaligned position ( $t = 25 \text{ ms}$ ). The phase-active interval is terminated at  $t = 50 \text{ ms}$ , which corresponds to the aligned rotor position at  $180^\circ$ . The induced voltage waveform  $u_e(t)$ , as shown in Fig. 10.22(a) (amplified by a factor 10), underlines the presence of the un-

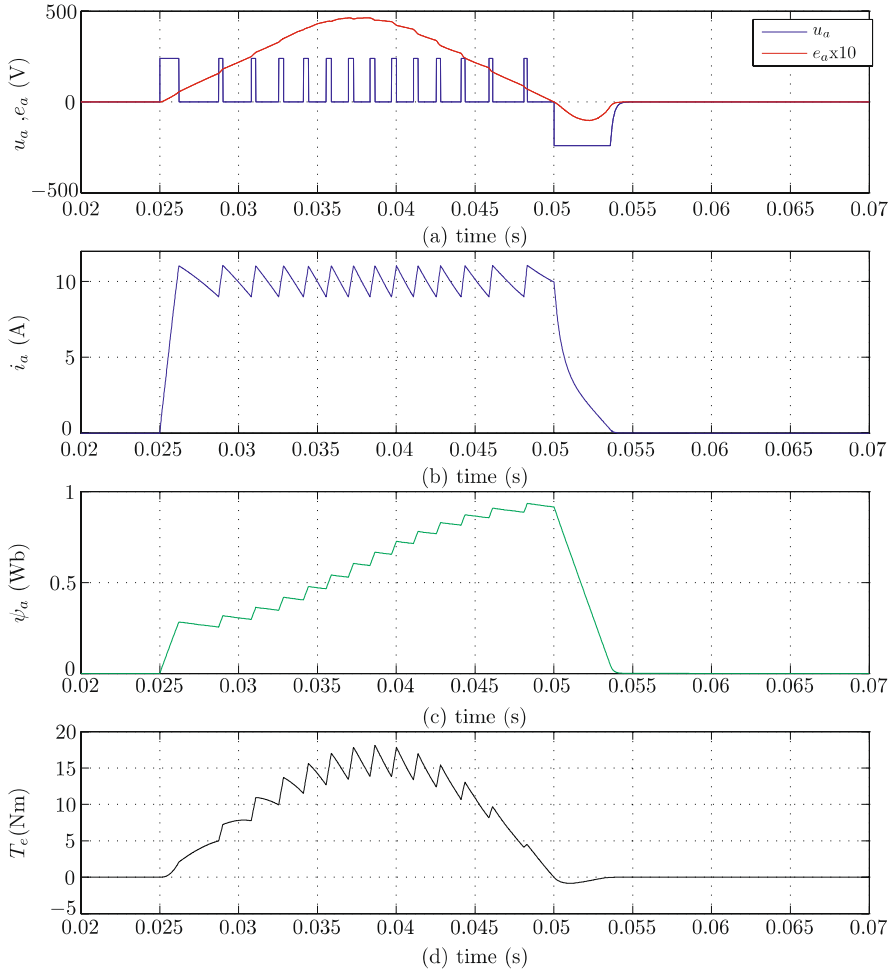


**Fig. 10.22** SR drive with hysteresis controller: low speed operation,  $n_m = 200$  rpm,  $\theta_e^{\text{on}} = 0^\circ$ ,  $\theta_e^{\text{off}} = 180^\circ$

aligned/aligned rotor positions, given that  $u_e$  must then be zero. At the beginning of the phase-active interval both switches of the converter are closed (mode 1 operation), which causes the phase current  $i(t)$  to increase because the phase voltage equals  $u_{\text{DC}}$  as shown in Fig. 10.22(a). A hysteresis controller (see Fig. 10.20) is assumed at present with a reference current of  $i^* = 10$  A and error current value of  $\Delta i = 2$  A, which means that the converter switches to mode 2 (free-wheeling) operation (top switch open) as soon as the instantaneous current reaches  $i^* + \Delta i/2$ . For the remaining part of the phase active cycle, the converter switches between mode 1 and 2 in an effort to maintain the instantaneous current between the  $i^* \pm \Delta i/2$  as may be observed in

Fig. 10.22(b). At the end of the excitation interval, both converter switches are opened (mode 3 converter operation) which causes the current to reduce to zero (demagnetization phase). Also shown in Fig. 10.22 is the corresponding torque  $T_e(t)$  waveform, which in this case has a small negative component caused by the fact that a non-zero phase current is still present after the rotor has passed the aligned position. The remaining waveform to be discussed for this drive configuration is the flux-linkage waveform (Fig. 10.22(c)), which basically represents the integral of the phase voltage, under the assumption that the voltage across the coil resistance is small in comparison with the supply voltage.

The second set of waveforms as given in Fig. 10.23 represent drive operation with the same converter/supply configuration and shaft speed as used to generate Fig. 10.23. However, in this example the hysteresis controller has been replaced by a PWM based controller with a switching frequency of 500 Hz. The latter has been purposely chosen low (factor ten lower than normally in use), to better visualize this operating mode. A duty cycle value of  $\delta = 0.13$  is used, while the control angles were set to  $\theta_e^{\text{on}} = -42^\circ$  and  $\theta_e^{\text{off}} = 138^\circ$ .

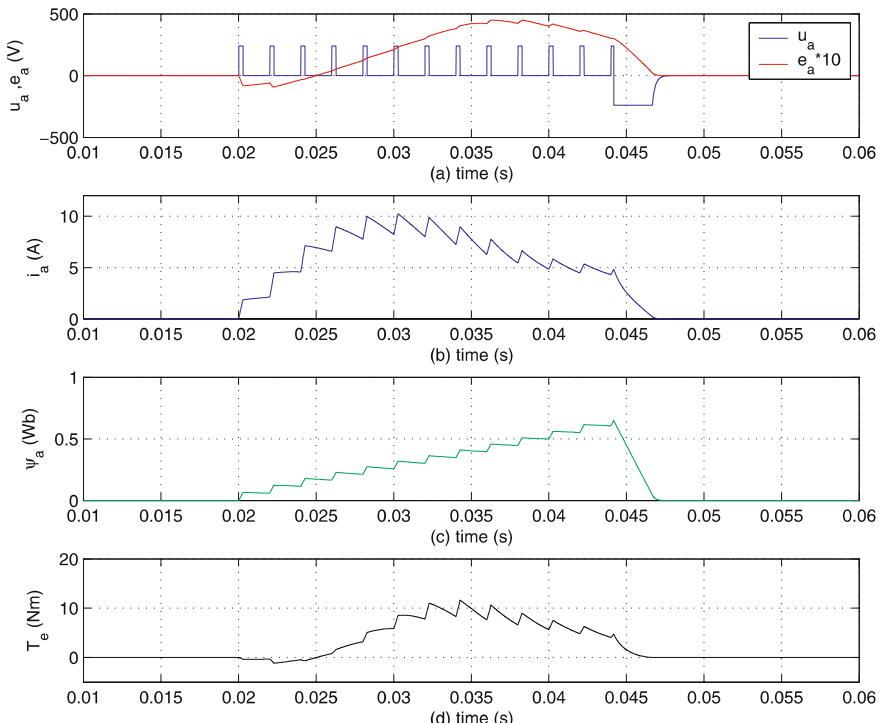


**Fig. 10.23** SR drive with PWM controller: low speed operation,  $n_m = 200$  rpm,  $\theta_e^{\text{on}} = -42^\circ$ ,  $\theta_e^{\text{off}} = 138^\circ$

A comparison between Fig. 10.22 and Fig. 10.23 shows that these two modes of operation are significantly different. The basic difference between the two is that hysteresis type controllers aim to control the current during the phase-active period. This is in contrast to the PWM type controller which controls the average phase voltage (which is equal to  $\delta u_{DC}$ ) during the phase-active interval. The latter is reflected by the nature of the flux-linkage waveform (Fig. 10.23) during the phase-active interval, which must in this case correspond to a linear function, with a gradient that is proportional to the average phase voltage. The phase current waveform follows from the magnetization characteristics with the flux linkage and rotor angle as input variables, together with the chosen control angles. An observation of Fig. 10.23 shows that the induced voltage crosses the time axis at  $t = 25\text{ ms}$  when the rotor is in its unaligned position. Furthermore, the phase-active interval starts before the unaligned position ( $\theta_e^{\text{on}} \leq 0^\circ$ ), which leads to the slightly negative torque after the phase is turned on.

### High Speed Operation

As the shaft speed is increased, the induced voltage increases which reduces the current slope and extends the rise time. Consequently, the average phase voltage during the phase-active interval must be increased. For drives which utilize a hysteresis type controller this occurs *automatically* because the top inverter switch will remain closed if the phase current is unable to reach the reference current value. The duty cycle of the PWM based controller must increase with speed, which inevitably leads to the identical situation, namely that the top switch remains on continuously during the phase excitation interval.

An example of drive operation at a speed higher than the base speed  $\omega_b$  is given in Fig. 10.24. These characteristics resemble those shown for the PWM based current controller (see Fig. 10.23). The notable difference is that the duty cycle for high speed operation is set to unity value. This is directly reflected in the gradient of the flux linkage versus time waveform during the phase-active period, which is now equal (in absolute terms) to that present during the de-magnetization interval. An observation of the induced voltage waveform in Fig. 10.24 confirms that its magnitude is considerably larger than found for low speed operation. The zero cross-over time points at  $t = 2.5\text{ ms}$  and  $t = 5\text{ ms}$  indicate the unaligned and aligned rotor positions respectively. The control angles were set to a value of  $\theta_e^{\text{on}} = -36^\circ$  and  $\theta_e^{\text{off}} = 144^\circ$ .

It is instructive to carefully examine the current as function of the flux linkage for the two examples given in Fig. 10.23 and Fig. 10.24 respectively. If the plot is executed over one electrical period (which in mechanical degrees corresponds to  $\tau_{rp}$ ), as is the case here, a flux-linkage/current locus will result of which the enclosed area is proportional to the average torque produced by the SRM, as was discussed in Sect. 10.2.2 and Sect. 10.2.3. The low and high speed flux-linkage/current trajectories as given in Fig. 10.25, are complemented by the aligned and unaligned flux-linkage/current characteristics.

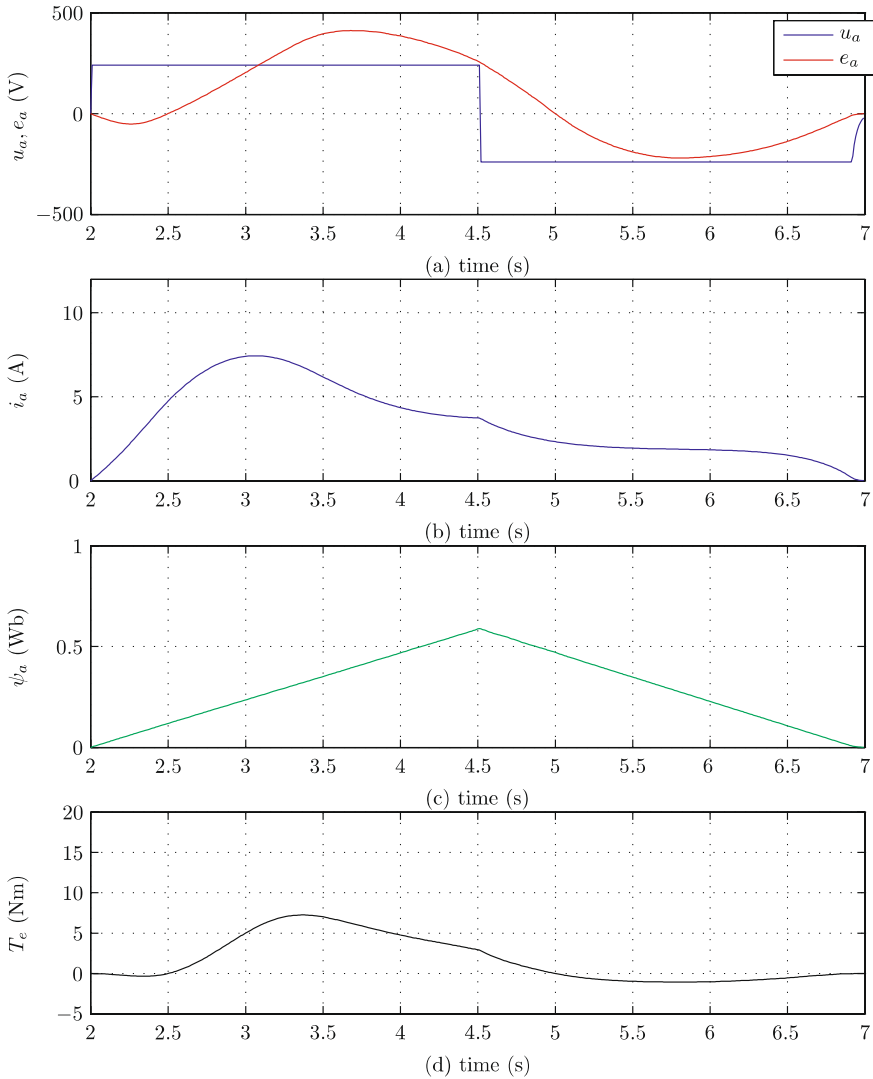
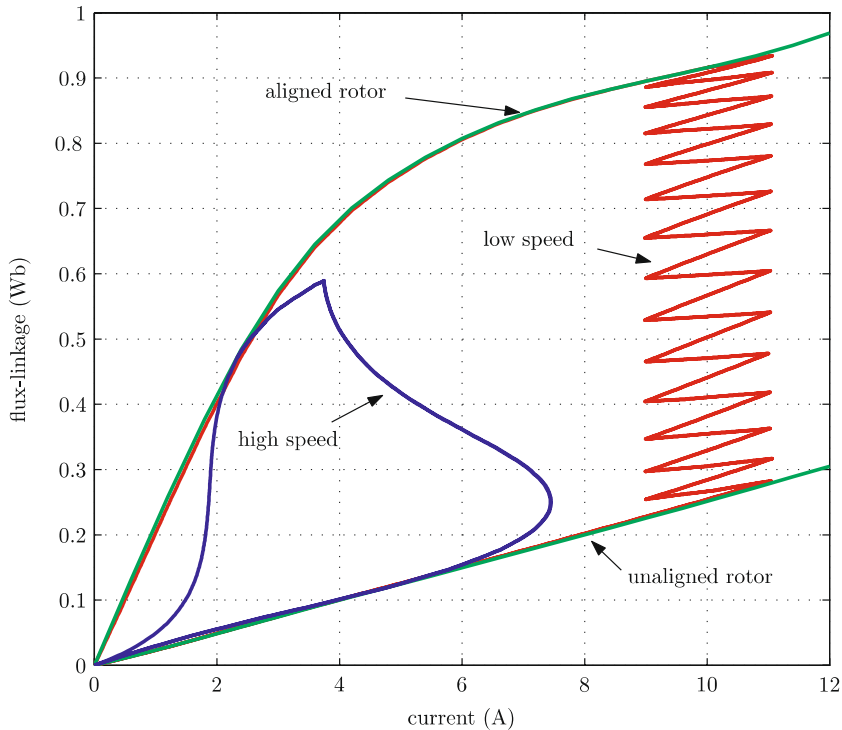


Fig. 10.24 SR drive: high speed operation

An observation of Fig. 10.25 confirms that the low speed flux linkage/current trajectory encompasses the maximum available area, within the available magnetization characteristics for the chosen reference current value. The high speed average torque is substantially lower as may also be deduced from the size of the enclosed surface area generated by the corresponding flux linkage/current locus.



**Fig. 10.25** Typical low and high speed flux-linkage/current trajectories of SRM

### 10.3 Multi-Phase Machines

In the previous section, the single-phase switched reluctance machine was discussed in considerable detail. Such an approach is warranted because the machine phases are electrically and magnetically independent. However, in a practical machine, design criteria, such as maximizing the torque per volume ratio, the need for a self-starting capability and minimizing torque ripple, favor a multi-phase approach. The total shaft torque  $T_e$  of the machine is equal to the instantaneous phase contributions namely

$$T_e = \sum_{ij=1}^{N_{\text{ph}}} T_{eij} \quad (10.33)$$

where  $N_{\text{ph}}$  represents the number of electrical phases and  $T_{eij}$  the instantaneous torque per phase. In the multi-phase machine, the individual torque versus angle waveforms are displaced with respect to each other by a so-called *step angle*  $\tau_{\text{step}}$  defined as

$$\tau_{\text{step}} = \frac{\tau_{\text{rp}}}{N_{\text{ph}}}. \quad (10.34)$$

Figure 10.26 shows the torque per phase waveforms and corresponding phase-active signals for a two and three-phase machine. Also shown in this diagram are the unaligned rotor positions  $\theta_e^u$  for each of the phases. In this example, a square wave current pulse is assumed which corresponds to the length of the phase-active signal. The *turn-on* and *turn-off* angles are set to  $0^\circ$  and  $180^\circ$  respectively. Furthermore, a linear machine model is assumed which implies that the torque per phase is defined by (10.24).

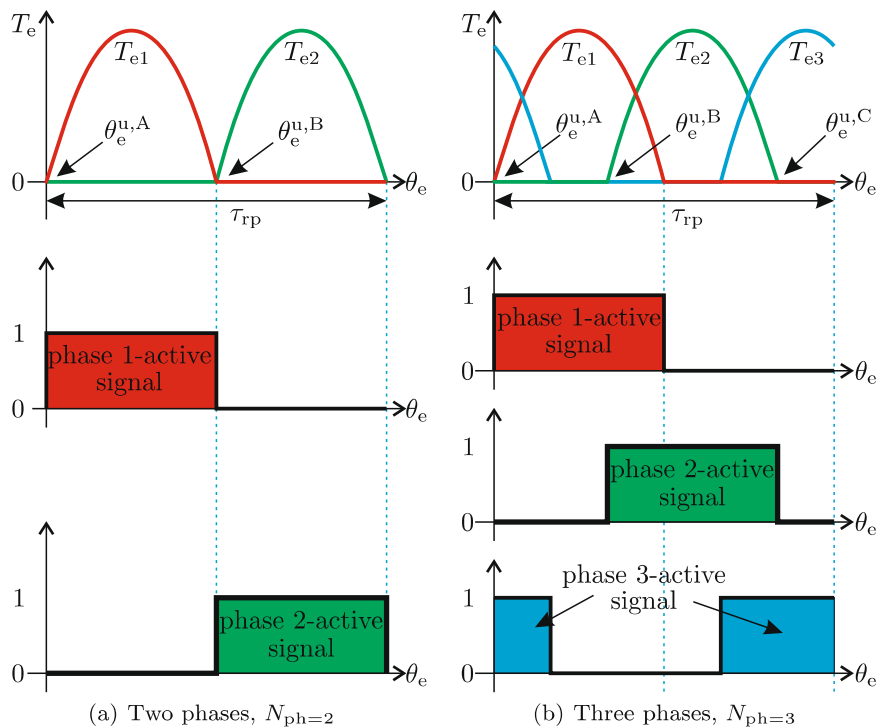


**Fig. 10.26** Multi-phase operation

The self-starting capability, i.e., the ability to produce a non-zero unidirectional torque  $T_e$  (as defined by (10.33)) at any rotor position, is present for the three-phase machine example shown in Fig. 10.26.

### 10.3.1 Converter Concepts

The asymmetric bridge concept as shown in Fig. 10.19 remains the preferred configuration for SR drives, given its simplicity and effectiveness in terms of energy recovery during the demagnetization phase (see Sect. 10.2.6). However, other concepts are in use and two such examples are shown in Fig. 10.27. The dissipative (discharge) based model, shown in Fig. 10.27(a), derives its name from the fact that the de-magnetization energy which is released after the phase is de-activated, is dissipated in an external resistance  $R$ . The duration of this phase may be shortened by inserting a Zener diode (anode connected to the positive supply source) between the external resistance and positive supply terminal. The use of the Zener diode, increases the negative voltage across the phase during the time interval where the switch is opened and the diode  $D$  is conducting, which shortens the de-magnetization interval.

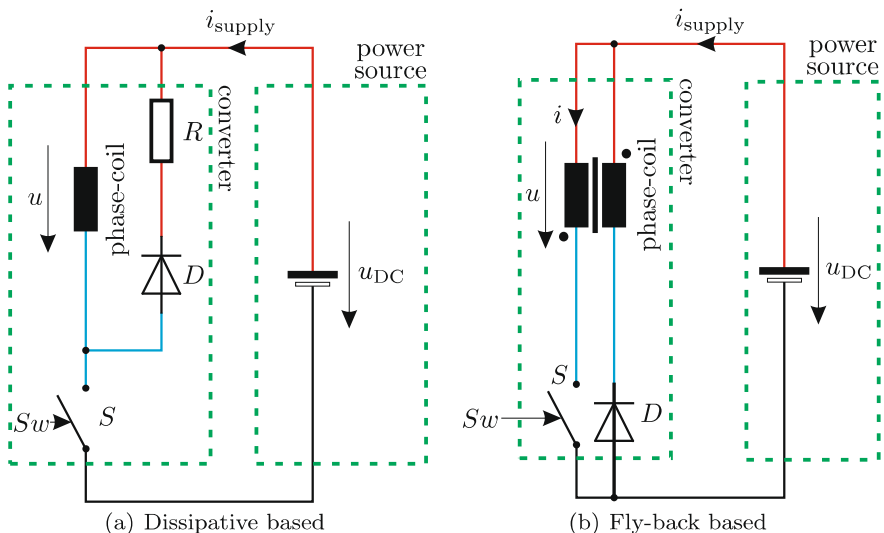


**Fig. 10.27** Single switch per phase converter concepts

The second configuration, as shown in Fig. 10.27(b) requires an additional *fly-back* coil which is bifilar wound with the phase winding. During the de-magnetization interval the energy is returned to the supply, in a manner which is identical to that found in fly-back type converters. The advantage of this converter lies with the use of a single switch per phase. However, the available slot space in the machine which houses the phase must be shared with the fly-back coil. The multi-phase converter provides an opportunity for reducing the overall number of semiconductors. The configuration shown in Fig. 10.28 utilizes a common top switch  $S_t$  for the arbitrarily chosen three-phase machine configuration. The bottom phase switches  $S_b$  are controlled

by their respective phase-active signals (see Fig. 10.26(b)). If a phase-active signal is at a logic level 1 the corresponding selection switch is closed.

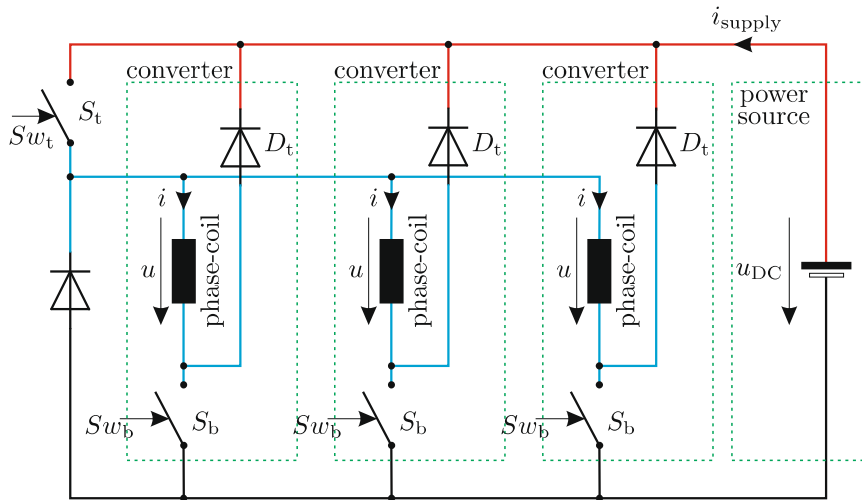


**Fig. 10.28** Three-phase drive concept using a four-switch converter

The top switch may be connected to a PWM modulator, which in effect controls the duty cycle  $\delta$ . The corresponding average voltage on the common phase connection with respect to the zero voltage node of the supply is in this case equal to  $\delta u_{DC}$ . Controlling the duty cycle provides a means of controlling the phase current amplitude for all phases. However, no individual phase current control is possible. Furthermore, the voltage across the average phase during the de-magnetization phase is equal to  $(1 - \delta)u_{DC}$ , which implies that the de-magnetization process will become less effective as the duty cycle is increased. In the extreme case, i.e., with unity duty cycle (switch  $S_t$  closed continuously), the de-magnetization energy cannot be adequately removed, hence the drive becomes inoperative.

Furthermore, a capacitive based energy recovery concept is considered. Drives which utilize this concept make use of one or more capacitors to store the magnetic energy which must be recovered during the de-magnetization interval of each phase. The diode-capacitor combination as shown in Fig. 10.29 is an example of an approach which utilizes this type of energy recovery concept. The diode/capacitor combination may be positioned between the power source and a converter of the type given by, for example, Fig. 10.19 or Fig. 10.28.

The purpose of the diode  $D$  is to ensure that the energy which is normally returned to the supply is now delivered to a relatively small capacitor  $C$ , which is initially charged to the supply voltage  $u_{DC}$ . During the de-magnetization interval the capacitor voltage  $u_C$  will increase by an amount

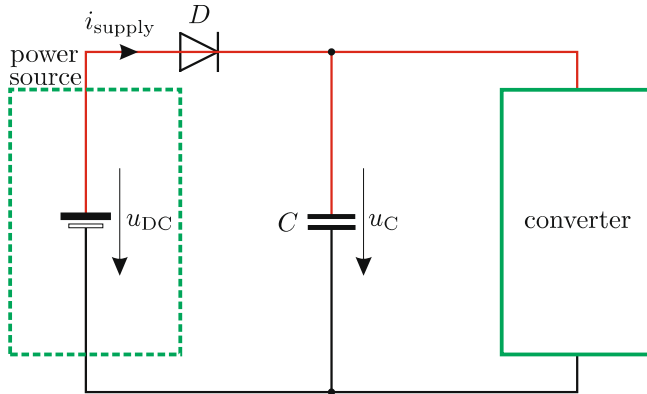


**Fig. 10.29** Capacitive based energy recovery

which is governed by the amount of energy to be stored and capacitor size. This effect can be used to reduce the demagnetizing interval (in motoring mode), when the phase inductance is high. At the start of the phase excitation interval the current rise time will be initially shorter than that achievable without the diode/capacitor combination, which leads to higher torque levels in the drive and a wider speed range [51].

## 10.4 Control of Switched Reluctance Drives

The drive performance of an SR drive cannot be considered without taking into account the converter topology in use, the nature of current control and choice of control angles. It is therefore instructive to provide further insight in terms of how drive performance is affected by these drive variables. In this context, the drive characteristics are initially discussed with the aid of so-called *SR control* diagram's. In the sequel to this section, a modern control strategy known as *Direct Instantaneous Torque Control* (DITC) is considered [33, 32]. The reader is urged to closely examine and run the simulations at the end of this chapter to fully appreciate the concepts discussed in this section.

### 10.4.1 Drive Characteristics and Operating Range

The output power versus shaft speed characteristic of the SR drive is normally used as the main performance indicator. A typical example of such a characteristic is given in Fig. 10.30 for the non-linear SR motor prototype used in this chapter (see Sect. 10.5). An asymmetrical half-bridge converter

topology, as discussed in Sect. 10.2.6, is assumed to be connected to the machine. A DC supply source of magnitude,  $u_{DC} = 240\text{ V}$  is connected to the converter. In terms of current control, two control strategies are considered. The first is hysteresis control, where the hysteresis current band  $\Delta i$  (see Fig. 10.20) is assumed to be infinitely small, which in effect implies that the current ripple associated with this type of control is ignored. The second control strategy adapts the average voltage during the phase-active interval to control the current. A sufficiently high PWM switching frequency, with duty cycle  $\delta$  is assumed with the same objective as above, namely to reduce the current ripple caused by the phase voltage switching functions present during the phase-active cycle. The current reference  $i^*$  value for the controller is taken to be 10.2 A, which is a convenient value as will become apparent shortly.

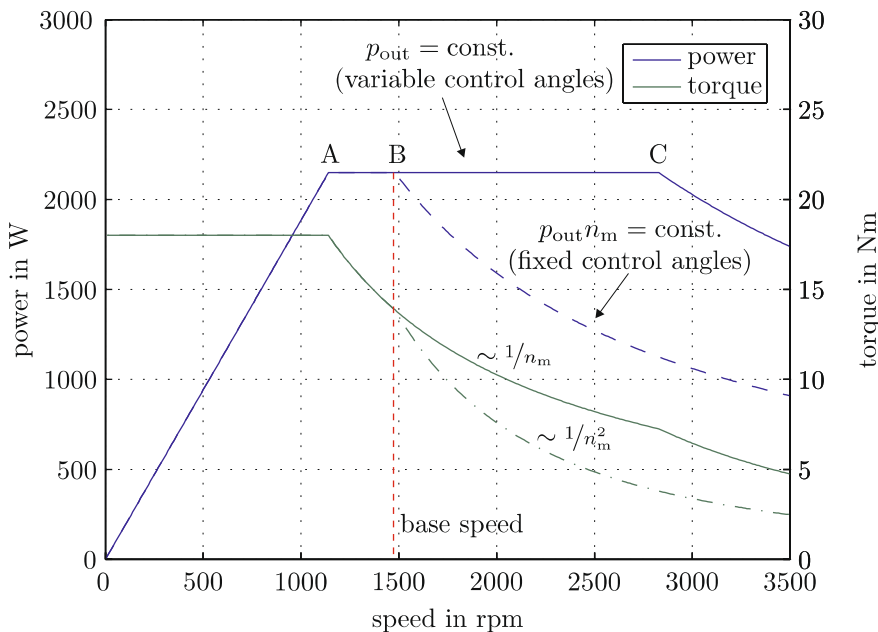


**Fig. 10.30** Operation limits of a switched reluctance machine

The performance characteristic as shown in Fig. 10.30 is represented in a *stylized* form, which implies that variations normally present with non-ideal controllers are not shown. Also the choice of control angles  $\theta_e^{on}$  and  $\theta_e^{off}$  will significantly influence the actual performance curve, which can be understood with the aid of the simulation given in the tutorial section.

An observation of Fig. 10.30 shows that operation is distinctly different for shaft speeds above or below the base operating speed  $n_m^b$ . Its numerical value for the current choice of drive variables is equal to  $n_m^b = 1475\text{ rpm}$  as

will be shown in Sect. 10.4.2. In the operating region 0–A (see Fig. 10.30), constant torque operation is possible, which implies that the ratio of output power to shaft speed is controlled by the average torque produced by the machine. The latter is in turn controlled by the choice of reference current and control angles. The highest current reference value is governed by the thermal limitations of the machine. Typically, phase current densities in the order of  $10 \text{ A/mm}^2$  are permissible without deploying forced cooling techniques in the machine. However, specific design and construction techniques can significantly increase the permissible current density.

As the SR drive operation approaches point A, the output power level reaches its maximum value which in turn defines the maximum supply power requirement for the drive. At point A, the supply source must at least deliver the required output power which is equal to the product of the DC supply voltage and average supply current. In addition, the supply must cover the magnetic core, converter switching and mechanical losses. Operating region A–B (see Fig. 10.30) is a transitional region and the actual power versus speed curve is again strongly influenced by the choice of drive parameters. For operation above the base speed, two distinct modes of operation are found. The first utilizes a fixed set of control angles, which results in a typical output power curve that is approximately inversely proportional to the shaft speed. High-speed operation in this region is referred to as the *natural* performance trajectory, for reasons to be discussed in Sect. 10.4.2. If the control angles are judiciously chosen to maximize the output power for each speed, operation along the trajectory B–C is possible, where the output power level remains approximately constant. However, as speed is increased beyond point C, drive operation reverts to its *natural* mode, i.e., further control angle variation is unwarranted for reasons to be discussed below. Consequently, the operating range of an SR drive can be similar to that of an induction machine.

#### 10.4.2 Drive Operational Aspects

It is apparent that the choice of control angles significantly affects drive performance. To be able to comprehend drive behavior as typified by Fig. 10.30, it is instructive to introduce a so-called *SR control* diagram. Basically, the diagram is a flux linkage versus angle diagram, as shown in Fig. 10.18, in which the flux linkage versus angle locus for drive operation over one period  $\tau_{rp}$  is shown. Prior to discussing the use of this type of control diagram it is instructive to reconsider the flux linkage time derivative  $\frac{d\psi}{dt}$  in terms of its partial derivative with respect to the rotor angle. The latter may be readily undertaken with the aid of (10.7) and partial differentiation of the flux with respect to angle, which gives

$$\frac{\partial\psi}{\partial\theta_m} \simeq \frac{u}{\omega_m} \quad (10.35)$$

where it is assumed that we can ignore the resistance  $R$  in (10.7). Furthermore, a constant shaft speed  $\omega_m = \frac{d\theta_m}{dt}$  is assumed. Equation (10.35) is significant because it defines the gradient of the flux-linkage/angle trajectory within the SR control diagram. During operation in the phase-active interval, the gradient will be equal to  $\delta u_{DC}/\omega_m$  if a PWM controller is used in the low speed region. If a hysteresis type controller is used the gradient will be equal to  $u_e/\omega_m$ , where  $u_e$  represents the induced voltage (see Fig. 10.17). A constant phase current equal to the reference value can be maintained in the phase active interval provided the condition

$$u_e \leq u_{DC} \quad (10.36)$$

is met. If this condition is exceeded the gradient is defined by the term  $u_{DC}/\omega_m$ , which also corresponds to the flux-linkage/angle gradient value that is possible for high speed operation. During the de-magnetization interval, the phase voltage is equal to  $-u_{DC}$  for the asymmetrical bridge topology assumed here, in which case the gradient is defined as  $-u_{DC}/\omega_m$ .

### Control Diagram at Low Speeds

The first SR control diagram to be considered is related to operation in the low speed region of the performance curve (see Fig. 10.30) for the specific case where the control angles  $\theta_e^{on}$  and  $\theta_e^{off}$  are  $0^\circ$  and  $180^\circ$  respectively. Furthermore, a hysteresis type current controller is assumed. The analysis of the drive in its present form is instructive because it provides insight with regard to the need for adapting the control angles, as will become apparent shortly. The SR control diagram, given in Fig. 10.31, shows the flux-linkage/current versus angle curves for the motor prototype described in Sect. 10.5 for a set of discrete current values in the range  $0 \rightarrow 12$  A. The machine in question has six rotor teeth, hence one electrical period is equal to  $\tau_{rp} = 60^\circ$  mech. If we initially ignore the voltage limitations imposed on the current controller, the latter would be able to deliver a rectangular current pulse with a magnitude equal to the reference value  $i^* = 10.2$  A during the phase-active interval. Under these conditions, the flux/angle trajectory in the control diagram would begin at coordinates  $(0^\circ, 0$  Vs) and proceed vertically until the flux-linkage/angle curve  $\psi(i = 10.2$  A,  $\theta_e$ ) is reached. Thereafter, the locus proceeds along this curve until the aligned position, point C, in Fig. 10.31 is reached. At that point of operation, the phase-active interval is terminated and the de-magnetization sequence begins which will in this case result in a trajectory that is along the vertical axis from point C  $\rightarrow (180^\circ, 0)$  in the control diagram. The instantaneous torque follows from the torque versus angle curves, which are given in Fig. 10.45. Operation along the line  $\psi(i = 10.2$  A,  $\theta_e$ ) for  $\theta_e = 0^\circ \rightarrow 180^\circ$  (see Fig. 10.30) is reflected in Fig. 10.45 by considering the cross-sectional view with a constant current of 10.2 A.

Hence, the torque per phase is zero at the unaligned and aligned angles and maximum in the vicinity of  $\theta_e = 90^\circ$ .

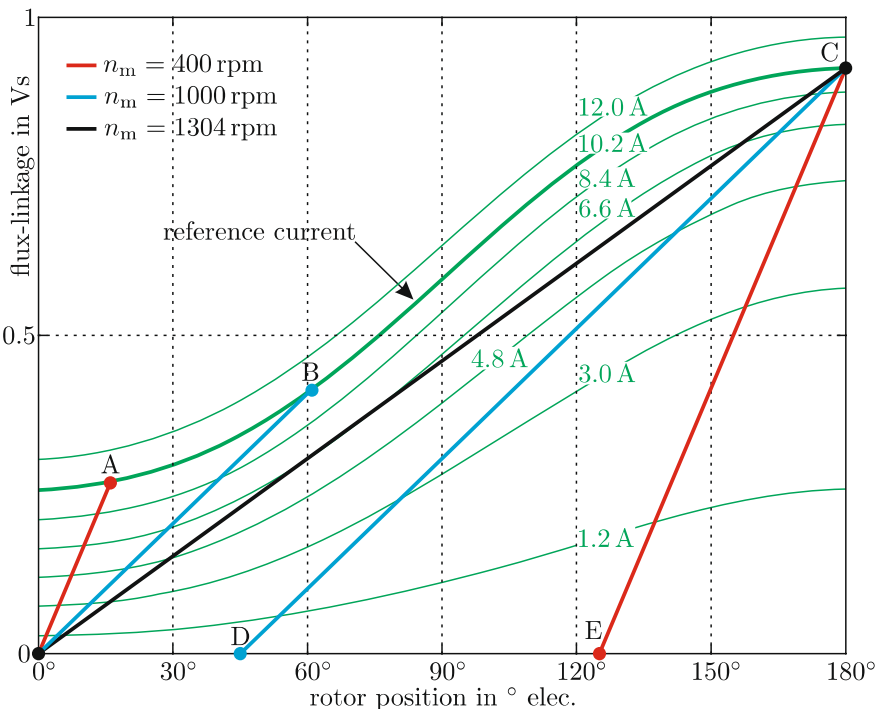


**Fig. 10.31** Drive operation, with hysteresis controller

In reality, the voltage limitations imposed on the current controller must be taken into account as will become apparent in the following example for drive operation at  $n_m = 400 \text{ rpm}$  and given supply voltage value  $u_{DC}$ . At the start of the phase-active interval, the hysteresis controller will switch to the phase voltage  $u = u_{DC}$  until current  $i = i^*$  is reached. In the control diagram, this part of the locus corresponds to a trajectory from coordinate  $(0^\circ, 0 \text{ Vs})$  to point A. The gradient (in absolute terms) of this part of the trajectory is given by (10.35), with  $u = u_{DC} = 240 \text{ V}$  and  $\omega_m = 2\pi 400/60 \text{ Hz}$ . Once point A is reached, the hysteresis controller will maintain the current at its 10.2 A reference value, which leads to an operating trajectory from point A to C along the line  $\psi(i = 10.2 \text{ A}, \theta_e)$ . At point C the de-magnetization sequence starts and the phase voltage is set to  $u = -u_{DC}$ . The gradient of the locus for this part of the trajectory is negative compared to what is shown at the start of the interval. Furthermore, the expectation would be that the locus endpoint would lie behind the aligned rotor position ( $180^\circ$ ). However, the flux-linkage/angle characteristics are symmetrical with respect

to the vertical axis at  $\theta_e = 0^\circ$  and  $\theta_e = 180^\circ$ . Consequently, this part of locus can also be plotted within the boundaries of the control diagram, with the understanding that the instantaneous torque values are taken to be negative. Hence, the line C to E represents the locus which corresponds to the de-magnetization phase of drive operation. Note that this trajectory must be parallel with the line  $(0^\circ, 0 \text{ Vs})$ –A in Fig. 10.31 given that the speed and supply voltage are identical.

### Control Diagram at High Speeds

The process described above is repeated for the higher shaft speed of  $n_m = 1000 \text{ rpm}$  which implies that the constant voltage part of the locus will have a gradient which is factor  $400/1000$  lower with respect to the previous case. Consequently, the first part of the locus starts at coordinate  $(0^\circ, 0 \text{ Vs})$  and proceeds to point B in Fig. 10.31. Hence, the period of constant current operation is shortened given that it extends from point B to C. Similarly, the de-magnetization part of the locus is now represented by the section C–D which implies that a larger (in comparison to the previous case) negative torque component will be present. Note also that the interval D– $(0^\circ, 0 \text{ Vs})$  along the rotor axis represents the interval of the drive cycle  $\tau_{rp}$  in which the phase current, flux and torque are zero. As the speed is increased, the hysteresis controller becomes progressively ineffective in terms of its ability to maintain the phase current at the set reference value. The limit speed  $\omega_m^{\text{limit}}$  as shown in Fig. 10.31 corresponds to the shaft speed at which the interval D– $(0^\circ, 0 \text{ Vs})$  becomes zero and the locus follows trajectory  $(0^\circ, 0 \text{ Vs})$ –C– $(0^\circ, 0 \text{ Vs})$ . In this case the current waveform is identical during the phase-active and non-phase active part of the drive cycle. The torque waveforms are also identical in absolute terms, but positive during trajectory  $(0^\circ, 0 \text{ Vs})$ –C and negative for the period C– $(0^\circ, 0 \text{ Vs})$ . The limiting speed  $\omega_m^{\text{limit}}$ , at which the drive can operate with *turn-on* and *turn-off* angles at  $0^\circ$  and  $180^\circ$  is therefore given as

$$\omega_m^{\text{limit}} = \frac{u_{\text{DC}}}{\psi(i = i^*, \theta_e = 0)} \frac{\tau_{rp}}{2} \quad (10.37)$$

where  $\psi(i = i^*, \theta_e = 180^\circ)$  represent the flux value equal to  $0.92 \text{ Wb}$  at point C. With the given choice of drive variables the limiting speed according to (10.37) is equal to  $n_m^{\text{limit}} = 1304 \text{ rpm}$ . This speed value is below the base speed value of  $n_m = 1304 \text{ rpm}$  (to be calculated shortly), which underlines the need to adapt the control angle values.

### Control Diagram for Advanced Turn-on and Turn-off Angles

The second application of the SR control diagram relates to operation with a hysteresis type current controller for three operating speeds, of which two  $n_m = 400 \text{ rpm}$ ,  $n_m = 1000 \text{ rpm}$  are chosen in the low speed drive area. The third  $n_m^b = 1478 \text{ rpm}$  is at the so-called base operating speed of the drive. In this example, a fixed *turn-on* angle of  $\theta_e^{\text{on}} \approx -40^\circ$  and *turn-off* angle of  $\theta_e^{\text{off}} \approx 140^\circ$  is assumed for reasons to be discussed at a later stage.

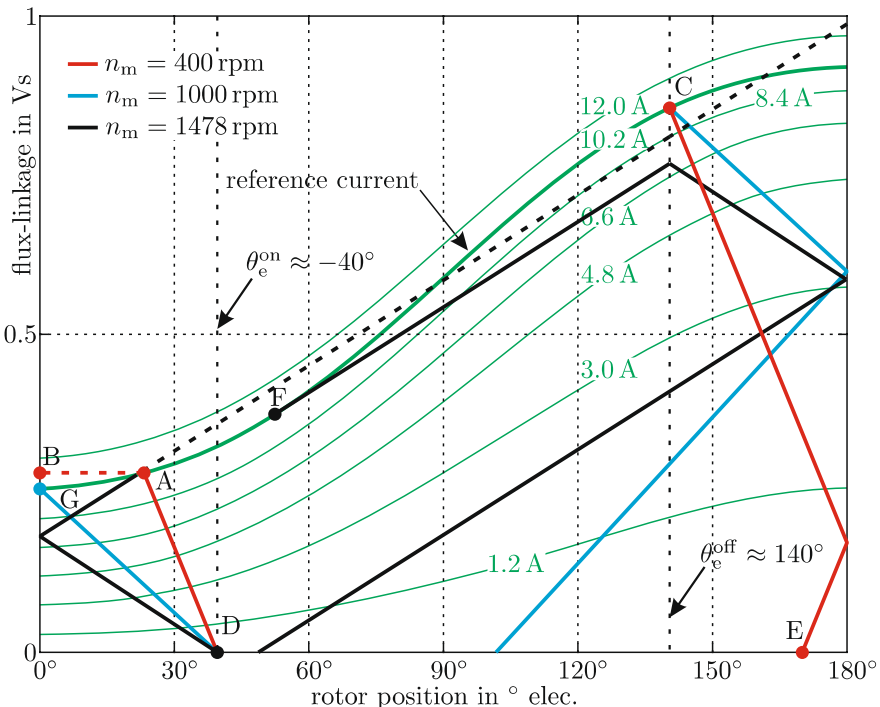


**Fig. 10.32** Drive operation, hysteresis controller

The operating trajectory for the speed  $n_m = 400 \text{ rpm}$  is initiated when the rotor position is equal to  $\theta_e = \theta_e^{\text{on}}$ , which implies that the phase-active interval starts  $40^\circ$  BEFORE the unaligned position. However, as mentioned earlier, the flux-linkage/angle curves are symmetrical with respect to the vertical axis  $\theta_e = 0^\circ$ , hence the first part of the locus may also be plotted with a starting point at  $\theta_e = \theta_e^{\text{u}} - \theta_e^{\text{on}}$  (see Fig. 10.32). The gradient of the locus from D to A is again defined by (10.35). At point A the reference current is reached and the hysteresis controller continues to maintain the current at the 10.2 A reference value. However, the next part of the trajectory is from A to B which is *above* the chosen reference value. The reason for this is that the current controller in its present form only controls the phase voltage using the top switch of the asymmetrical converter (bottom switch is normally closed during the phase-active period). This implies that a flux reduction cannot be initiated by the controller. An alternative chopping technique is to allow the current controller to control both switches during the phase-active interval, in which case the trajectory would be along the reference current line from point A to G. Controlling both switches during the phase-active period increases the switching frequency, which is not beneficial in terms of converter switching losses. The normal approach is to only allow free-wheeling states during this

phase, which is the approach taken in this book. The trajectory which is taken at the beginning of the phase-active interval is therefore D–A–B, where the instantaneous torque will be negative. Once the unaligned position (point B) is reached, the locus will again return to point A and from there onwards along the curve  $\psi(i = i^*, \theta_e)$  until point C is reached which is the end of the phase-active interval, i.e.,  $\theta_e = \theta_e^{\text{off}}$ . During the de-magnetization interval, the locus follows a path which is parallel to the trajectory A–D (shaft speed and supply voltage magnitude remain unchanged) until the aligned rotor position is reached. The trajectory endpoint E is in reality above  $180^\circ$ , but it can also be shown within the control diagram (as is the case here), given the symmetry of the flux-linkage/angle curves to be mirrored with respect to the vertical axis at  $\theta_e = 180^\circ$ . It is however important to realize that the instantaneous torque during the trajectory from the aligned rotor position to point E will be negative.

An increase in speed from  $n_m = 400 \text{ rpm}$  to  $n_m = 1000 \text{ rpm}$  leads to a locus which is similar to that described above. The control angles remain unchanged, but the gradient of the initial part of the trajectory D–G is reduced by a factor  $400/1000$  as may be observed from Fig. 10.32. The fact that the rotor angle for point G coincides with the unaligned rotor position is purely coincidental. The hysteresis current controller maintains the current for the remaining part of the phase-active interval, which leads to trajectory G–C along the curve  $\psi(i = i^*, \theta_e)$ . The de-magnetization trajectory is similar to that described above, but the gradient will be lower (and parallel to locus D–G), as is apparent from Fig. 10.32. For this drive speed, the trajectory reaches the aligned position at a higher flux linkage value (in comparison to the previous case) and then terminates approx. in the vicinity of the coordinates  $(100^\circ, 0 \text{ Vs})$  in the control diagram.

As the operating speed is increased further, a situation will arise where for a substantial part of the phase-active interval current control cannot be maintained because the induced voltage  $u_e$  is greater than the available supply voltage  $u_{DC}$ . The trajectory with shaft speed  $n_m = 1478 \text{ rpm}$  is precisely such an example as may be observed from Fig. 10.32. The control angles remain unchanged, hence the locus starting point is again at coordinates  $(40^\circ, 0 \text{ Vs})$  of the control diagram. During the first part of the phase-active period, the drive is operating under voltage control until the reference current curve is reached at point A. From that point onwards the trajectory is along the curve  $\psi(i = i^*, \theta_e)$  until point F is reached, where the induced voltage becomes equal to the supply voltage  $u_e = u_{DC}$ . From point F onwards the trajectory proceeds along a trajectory with a gradient defined by (10.35). For this particular operating speed, known as the *base speed*  $\omega_m^b$ , the gradient of the trajectory can be represented by a linear function. This linear function is of the form

$$\psi_e = k_\psi \theta_e + \psi_e^o \quad (10.38)$$

for  $0 \leq \theta_e \leq 180^\circ$ . The base speed may then be found by making use of (10.35) and (10.38), which gives

$$\omega_m^b = \frac{u_{DC}}{k_\psi}. \quad (10.39)$$

In the given example,  $k_\psi$  is equal to 1.55 and  $\psi_e^o$  to 0.02. This leads to a base speed of  $n_m^b = 1478$  rpm. When the drive is operating at base speed, the gradient of the locus trajectory (after point F) is equal to the gradient of (10.38) when hysteresis control is no longer possible. However, the *turn-on* angle must be chosen in such a manner, that the flux-linkage  $\psi_e^o$  at  $0^\circ$  is reached. The required *base turn-on* angle at the operating speed which satisfies this condition is given as

$$\theta_e^{on,b} = \frac{\psi_e^{\min}}{k_\psi} \quad (10.40)$$

with  $\psi_e^{\min} = \psi_e(\theta_e = 0^\circ)$ . The choice of *turn-on* angle is such, that the first part of the locus from D to the unaligned angle (with gradient  $u_{DC}/\omega_m^b = k_\psi$ ) intersects the linear function at  $\theta_e = 0^\circ$ . With the current choice of parameters, the *base turn-on* angle is equal to  $\theta_e^{on,b} \approx -40^\circ$ . The remaining control variable to be defined is the *turn-off* angle. Observation of Fig. 10.32 (for the base speed locus) shows that its value must be smaller or equal to  $\theta_e^{off,b} = \theta_e^{on,b} + 180^\circ$  to maintain a non-conduction interval which is greater or equal to zero. As a guideline, the *base turn-off* angle is set to  $140^\circ$ .

### Control Diagram for Pulse Width Modulation with Constant Duty Cycle

The use of pulse width modulation for controlling the average phase voltage during the phase-active interval is considered here with the aid of the SR control diagram given in Fig. 10.33. As with the previous case, three operating speeds are considered, which are precisely those used for the hysteresis controller. For this type of control the (constant) duty cycle  $\delta$  must be a function of speed. The control angles are set to their base values for reasons to be discussed. In terms of identifying a suitable duty cycle it is beneficial to use the linear function as defined by (10.38). This linear function represents the best possible fit to the flux-linkage/angle curve for the chosen reference current  $i^* = 10.2$  A. Consequently, it is prudent to choose the duty-cycle and *turn-on* angle in such a manner that the PWM control trajectory during a substantial part of the phase-active is coincidental with this linear function. This control strategy in effect states that the gradient of the locus should be set equal to the gradient  $k_\psi$  of the linear function  $\psi_e(\theta_e)$  which leads to a duty cycle value of

$$\delta = \frac{k_\psi \omega_m}{u_{DC}}. \quad (10.41)$$

As speed increases, the duty cycle must increase, however the gradient of the trajectory during the phase-active period remains constant as may be observed from Fig. 10.33. The speed at which the duty cycle becomes one, is exactly the base speed as defined by (10.39).

In this case, the trajectory starts at point A and follows the linear function  $\psi_e(\theta_e)$  at the unaligned position. The gradient of this part of the trajectory is maintained at the value  $k_\psi$ . Furthermore, the *turn-on* angle required for the PWM controller is precisely the base value given the fact that the gradient and endpoint of this part of the trajectory are equal to  $k_\psi$  and  $\psi_e^{\min}$  respectively. This means that the *turn-on* angle follows from (10.40). The second part of the trajectory is along the linear function from  $(0^\circ, \psi_e^{\min})$  to point C, at which the rotor angle is equal to the *turn-off* angle value.

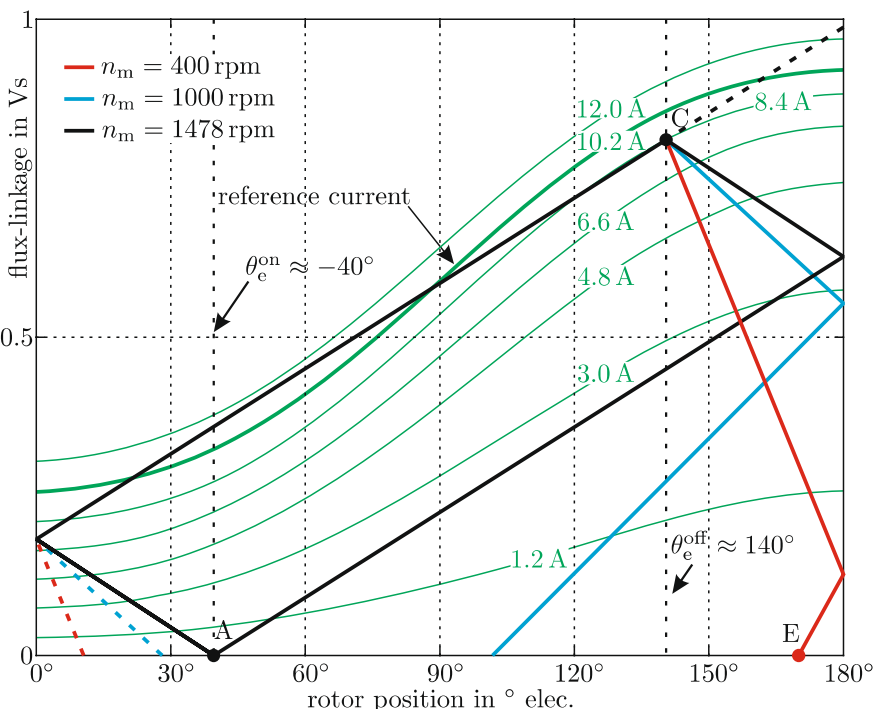


**Fig. 10.33** Drive operation, PWM control

The de-magnetization part of the locus is a function of speed given that the phase voltage during this part of the cycle is set to  $u = -u_{DC}$ . This implies that the gradient of the locus is governed by (10.35) in exactly the same manner as described for the hysteresis type current controller. This is perhaps not surprising given that this mode of operation is the same for both control strategies. Consequently, this part of the locus is identical for both

control strategies, as may be observed by comparing Fig. 10.33 and Fig. 10.32 respectively. Prior to discussing the use of SR control diagram in the high speed drive region, it is instructive to consider a minor change to the PWM control strategy. The standard approach activates the PWM generator at the start of the phase-active period. An alternative would be to compare the measured current with the reference current at the beginning of the active-cycle and switch on the PWM generator once the condition  $i = i^*$  is met. Such a change requires a change to the *turn-on* angle given that the gradient of this first part of the trajectory is then defined by the ratio of the supply voltage and shaft speed. Figure 10.33 (dashed blue and red lines) shows how this control strategy affects the first part of the locus. The positive effect is that the negative torque contribution, which is inherent for this part of the trajectory, is reduced. However, as speed is increased, its effectiveness is reduced.

### High-Speed Operating Range of SR Machine

This section focuses on the high-speed operating range of the drive (see Fig. 10.30). The control strategy with constant control angles is discussed with the aid of the SR control diagram shown in Fig. 10.34. In this example, the operating trajectory for three shaft speeds  $n_m = 1500, 2000 \text{ rpm}$  and  $n_m = 3000 \text{ rpm}$  is shown, with control angles  $\theta_e^{\text{on}} = -36^\circ$  and  $\theta_e^{\text{off}} = 144^\circ$ , which are in the vicinity of the base speed values. At the beginning of the phase-active interval, the trajectory starting point is at coordinates  $(\theta_e^{\text{on}}, 0 \text{ Vs})$  and proceeds to the unaligned position, where the gradient of the trajectory is defined by the ratio of the supply voltage and shaft speed (see (10.35)). The trajectory from the unaligned position to the end of the interval remains unchanged in terms of the absolute gradient value. At the position  $\theta_e^{\text{off}}$ , the end of the phase-active interval is reached which means that the gradient of the locus is reversed (phase voltage switches from  $u_{\text{DC}}$  to  $-u_{\text{DC}}$ ). The de-magnetization trajectory is similar to that shown in the low speed SR control diagrams. However, it is noted that the complete locus will be trapezoidal, because the absolute value of the trajectory gradient before and during the de-magnetization phase remains unchanged. If the *turn-off* angle is decreased, an opening in the trapezoid will appear on the rotor axis, which signifies the presence of a zero conduction interval of operation over the period  $\tau_{\text{rp}}$ . As speed is increased the gradient of the trajectory reduces, as may be observed from Fig. 10.34.

The operating trajectories for the three shaft speed values, as given in Fig. 10.34 may also be shown in a conventional flux linkage versus current diagram as given in Fig. 10.35. The locus for each speed encompasses an area which is directly proportional to the average torque per phase, cycle  $\tau_{\text{rp}}$ . Consequently, an indication of the change in average torque with increasing speed may be found by observing the change of area enclosed by the locus. Observation of Fig. 10.35 shows that doubling the speed (from  $n_m = 1500 \text{ rpm}$  to  $n_m = 3000 \text{ rpm}$ ) leads to an approximate fourfold reduction in the average

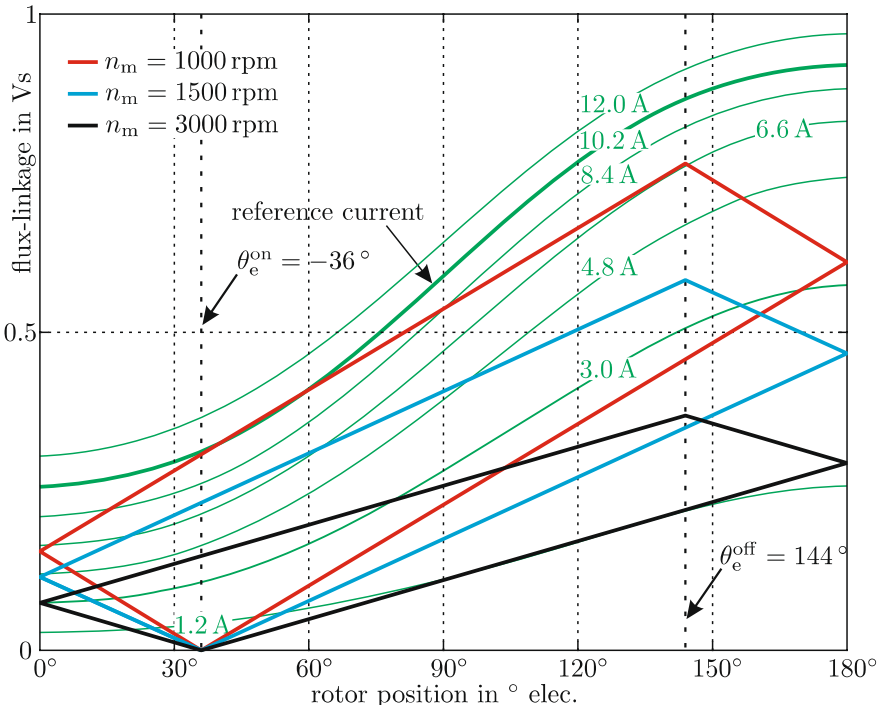


**Fig. 10.34** High speed operation with fixed control angles

torque. Hence, the corresponding output power level is approximately halved, as may also be observed from the *fixed angle* high speed operating trajectory shown in Fig. 10.30.

In the sequel to this section, the SR control diagram is used as a means of determining how the control angles may be varied to maintain an approximately constant output power level in the high-speed operating range, i.e., operation along trajectory B–C in Fig. 10.30. The trajectory for  $n_m = 1500 \text{ rpm}$ , as illustrated in Fig. 10.36, is shown for a set of control variables  $\theta_e^{\text{on}} = -36^\circ$  and  $\theta_e^{\text{off}} = 144^\circ$  which is close to the base speed values given earlier. This is perhaps not surprising given that the trajectory under consideration is only slightly above the base speed  $n_m = 1478 \text{ rpm}$ . In terms of maximizing the average torque, it is important to realize that only the top two trajectories of the trapezoidal locus yield a positive torque contribution. The two positive torque parts of the locus are those which correspond to rotor displacement from the unaligned  $\theta_e^u = 0^\circ$  to the aligned  $\theta_e^a = 180^\circ$  position.

As the shaft speed is increased, the gradient of the locus reduces, as was shown earlier (see Fig. 10.34), which means that the positive torque trajectories of the locus encounter lower currents which in turn leads to a lower average torque. The average torque can be increased if the *turn-on* angle is

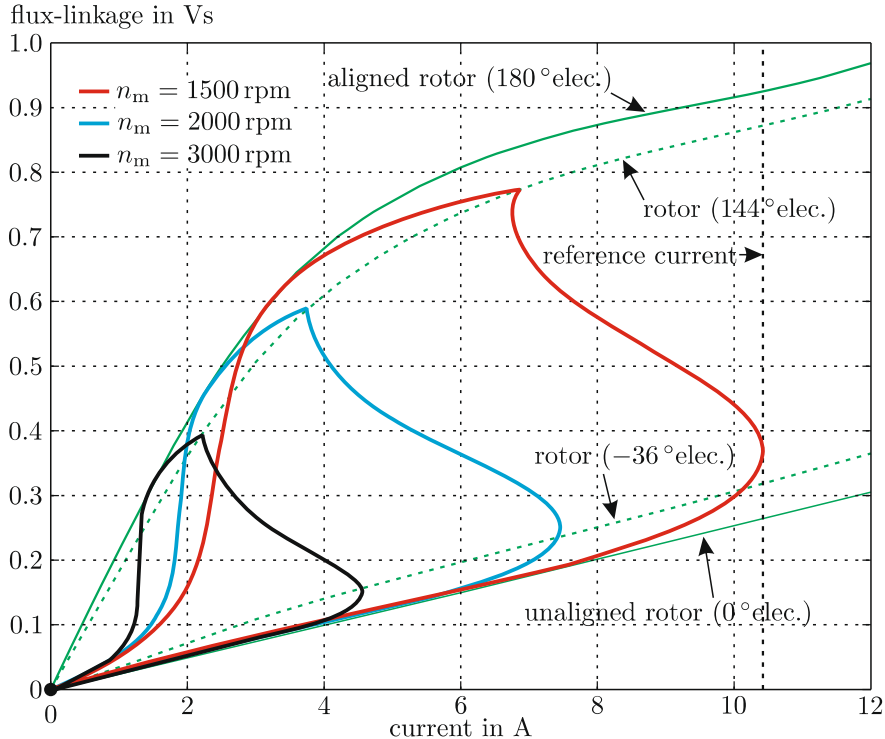


**Fig. 10.35** Flux-linkage/current locus for high speed operation

advanced in such a manner, that the first part of the positive torque producing locus (from the unaligned position to the phase-active *turn-off* angle) coincides for at least one rotor angle with the reference flux-linkage/angle curve with  $i = 10.2$  A. This control strategy as depicted in Fig. 10.36 provides a guideline for a suitable choice of *turn-on* angle.

The *turn-off* angle is chosen to satisfy the equation  $\theta_e^{\text{off}} \leq \theta_e^{\text{on}} + 180^\circ$  at the given speed to avoid an operating mode where the flux linkage is greater than zero for the entire period  $\tau_{\text{rp}}$ .

For the test prototype motor under consideration here, the control angles for the operating speeds  $n_m = 2000, 3000$  were set to  $\theta_e^{\text{on}} = -60^\circ, -108^\circ$  and  $\theta_e^{\text{off}} = 120^\circ, 72^\circ$  respectively. With this choice of *turn-on* and *turn-off* angles, the output power can be maintained at an approximately constant level as shown in Fig. 10.30. As speed is increased even further, the gradient of the locus is also reduced. At a given operating speed, which corresponds to point C in Fig. 10.30, further variation in the control angles become ineffective given that no part of the positive torque producing locus coincides with the flux-linkage/angle curve  $\psi(i = i^*, \theta_e)$ . From this speed onwards the control angles are kept constant in which case the output power decreases in a manner as described previously.

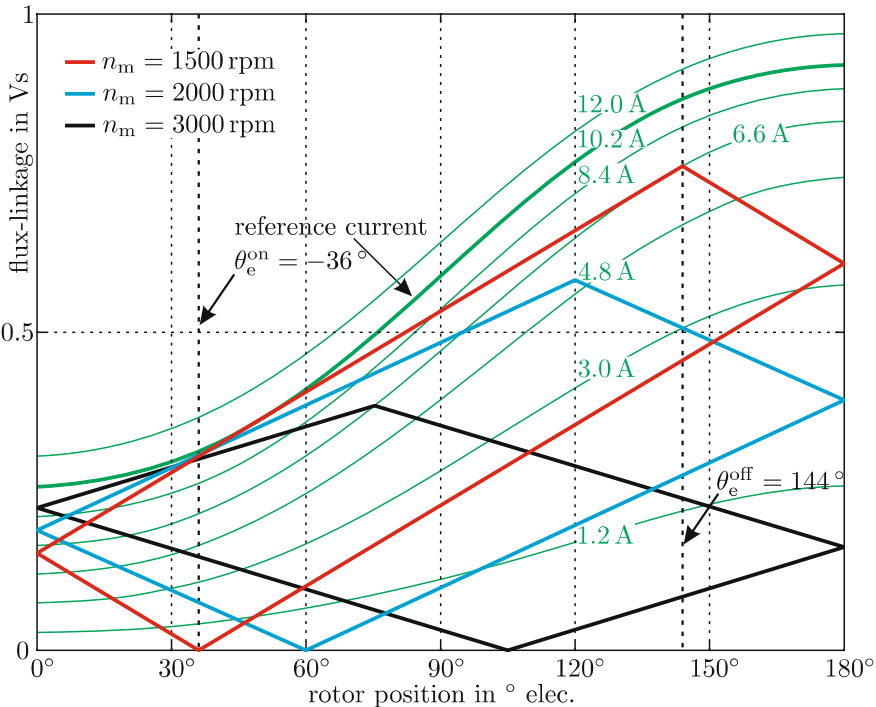


**Fig. 10.36** High speed operation, variable control angles

### 10.4.3 Direct Instantaneous Torque Control (DITC)

In the previous part of this chapter, current and PWM voltage (flux) based control techniques were discussed. The disadvantage of these methods is that the shaft torque of the machine will contain a large torque ripple, as was shown in Fig. 10.26(b) for the linear SR model. In reality, saturation will exacerbate the problem further, which means that mechanical or electronic counter measures are usually taken to realize a smoother torque. A variety of mechanical techniques are available, such as for example, rotor skewing and pole shaping, which unfortunately compromise the overall torque producing capability of the machine. A range of electronic methods are also available which are basically concerned with profiling the phase current or flux-linkage waveform in such a manner as to minimize the torque ripple component present in the shaft torque.

This section considers an alternative approach, referred to as *direct instantaneous torque control* (DITC) [33], which controls the converter switches in such a manner as to ensure that the estimated shaft torque  $\tilde{T}_e$  is held

at approximately (within user specified limits) the reference torque level  $T_e^*$ . The operating principles of DITC will be discussed with the aid of Fig. 10.37, which makes use of the four-phase 8/6 non-linear test machine (see Sect. 10.5).

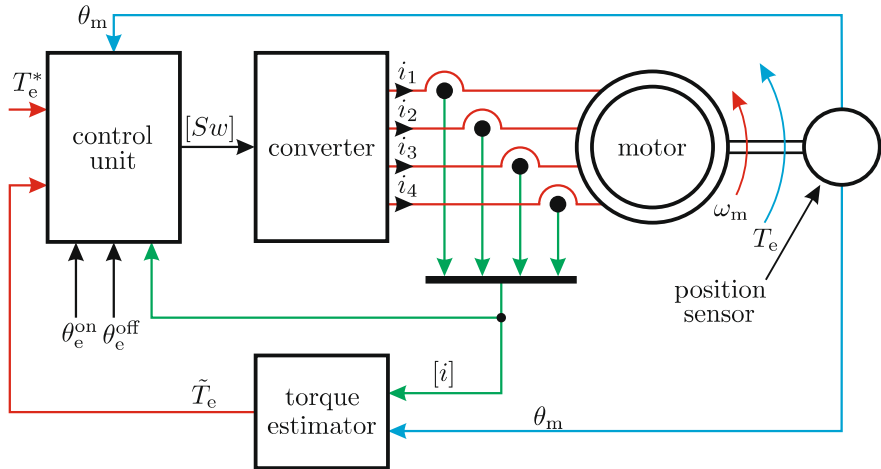


**Fig. 10.37** Basic block diagram of a direct instantaneous torque controlled (DITC) SRM drive

The machine, as illustrated in Fig. 10.37, is connected to a converter module, which may, for example, be formed by four asymmetric half-bridge phase units as shown in Fig. 10.19. The four signal pairs  $Sw_t$  and  $Sw_b$ , which control the top and bottom phase switches respectively are represented by the switch array variable  $[Sw]$ . A control module, as given in Fig. 10.37 generates the required converter switch signals on the basis of the input variables  $T_e^*$  and  $\tilde{T}_e$  and control angles  $\theta_e^{\text{on}}$  and  $\theta_e^{\text{off}}$ . In addition, this module requires access to the shaft angle  $\theta_m$ , which is provided by the position sensor attached to the shaft. Furthermore, the measured phase currents  $i_1, i_2, i_3, i_4$ , as represented by the matrix variable  $[i]$ , are also fed into the control unit.

The torque estimator calculates the instantaneous shaft torque with the aid of the per phase static torque versus current/angle curves of the machine in question in accordance with the approach shown in Fig. 10.14. These torque per phase contributions are then added with the aid of (10.33) which yields the required shaft torque estimate.

In the generic representation of the controller, as given in Fig. 10.38, three torque hysteresis comparators are used, which provide three logic outputs  $S_t^{\text{comp}}$ ,  $S_c^{\text{comp}}$  and  $S_b^{\text{comp}}$  respectively [32]. The switching algorithm for these

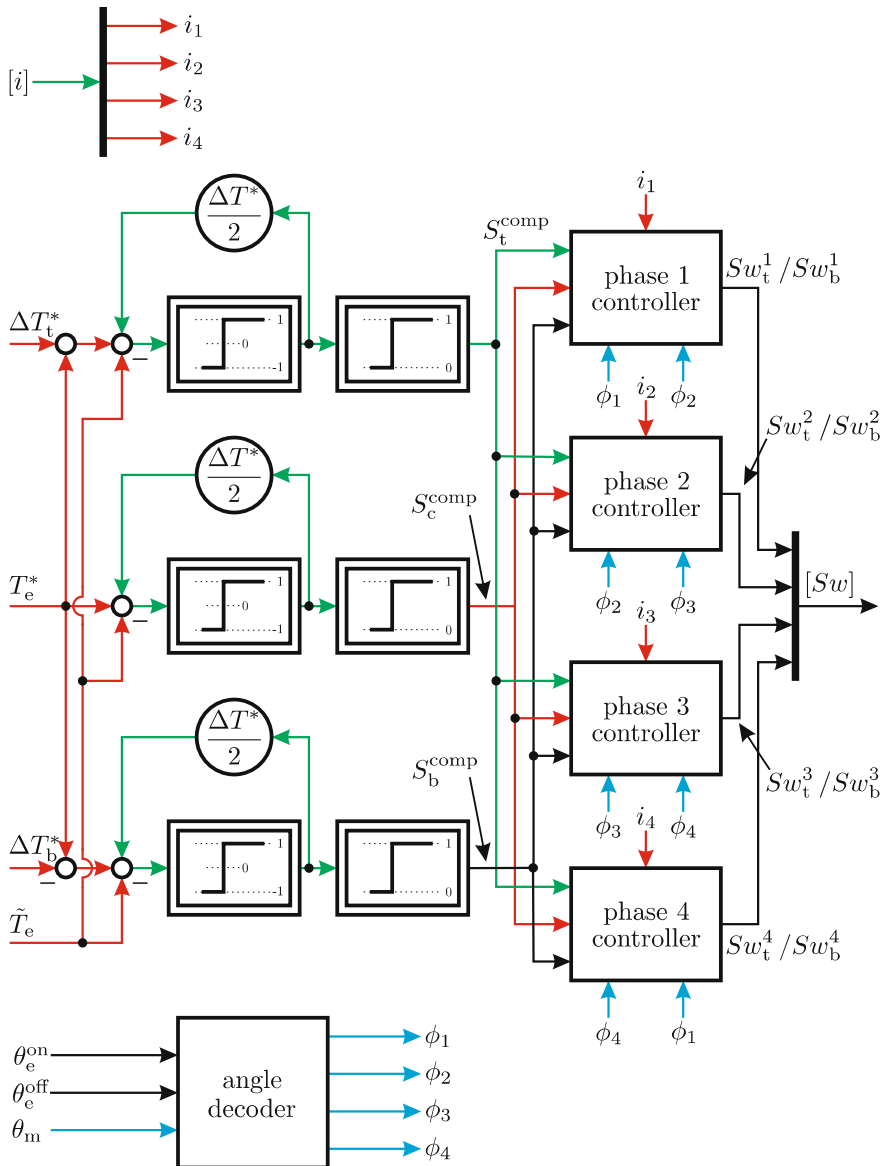


**Fig. 10.38** DITC controller block diagram, showing torque comparators and phase controllers (for a four-phase SRM)

comparators is of the form

$$\text{if } \tilde{T}_e > (T_e^* + \Delta T_t^*) + \frac{\Delta T^*}{2} \text{ comparator output } S_t^{\text{comp}} = 0 \quad (10.42\text{a})$$

$$\text{if } \tilde{T}_e < (T_e^* + \Delta T_t^*) - \frac{\Delta T^*}{2} \text{ comparator output } S_t^{\text{comp}} = 1 \quad (10.42\text{b})$$

$$\text{if } \tilde{T}_e > T_e^* + \frac{\Delta T^*}{2} \text{ comparator output } S_c^{\text{comp}} = 0 \quad (10.42\text{c})$$

$$\text{if } \tilde{T}_e < T_e^* - \frac{\Delta T^*}{2} \text{ comparator output } S_c^{\text{comp}} = 1 \quad (10.42\text{d})$$

$$\text{if } \tilde{T}_e > (T_e^* - \Delta T_b^*) + \frac{\Delta T^*}{2} \text{ comparator output } S_b^{\text{comp}} = 0 \quad (10.42\text{e})$$

$$\text{if } \tilde{T}_e < (T_e^* - \Delta T_b^*) - \frac{\Delta T^*}{2} \text{ comparator output } S_b^{\text{comp}} = 1 \quad (10.42\text{f})$$

where  $\Delta T_t^*$ ,  $\Delta T_b^*$  and  $\Delta T^*$  are user defined values which determine the error band of the torque controller as may be observed from the example shown in Fig. 10.39. In this example, an arbitrary torque versus angle function  $T_e(\theta_e)$  is shown together with the reference torque value  $T_e^*$  and set of incremental reference torque settings  $\Delta T_t^* = \Delta T_b^*$ ,  $\Delta T^*$ . The logic outputs from the three comparators, as shown in Fig. 10.39, is governed by the switching algorithm according to (10.42).

Central to the DITC approach is the way in which the three comparator signals are used by the phase controller modules of Fig. 10.38. The comparator signals  $S_t^{\text{comp}}$ ,  $S_c^{\text{comp}}$ ,  $S_b^{\text{comp}}$  are connected to all the phase controller modules. However, at any one time (or rotor angle) a phase controller module uses either  $S_c^{\text{comp}}$  or a combination of  $S_t^{\text{comp}}$ ,  $S_b^{\text{comp}}$  as inputs. This choice of signals is realized by sub-dividing each phase-active interval into a so-called *incoming phase* (IPI) and *outgoing phase* (OPI) interval as shown in Fig. 10.40. This figure shows an idealized static torque/angle curve for phase 1, together with the phase-active intervals for phases 1 and 2, namely  $\phi_1$ ,  $\phi_2$ . For a four-phase machine  $\tau_{rp} = 60^\circ$  mech. and the phase-active intervals are equal to  $30^\circ$  mech. and displaced by  $15^\circ$  mech., with respect to each other. The incoming phase 1 interval represents the first part of the phase 1 active interval, where there is NO overlap with the next phase  $\phi_2$ . Likewise, the outgoing phase 1 interval is that part of the phase 1 active interval which overlaps with phase 2, as may be observed from Fig. 10.38. For the four-phase machine there will be at any rotor angle an active ICI and OPI interval and these are calculated with the aid of the four phase-active signals which in turn are generated by the angle decoder module. For example, during the ICI phase 2 interval, an OPI interval for phase 1 will be present.

The basic DITC control strategy is based on allocating the primary task of producing the required reference torque value with the incoming phase. The designated outgoing phase is then used to augment the torque production for the duration of the corresponding OPI interval. To implement this control

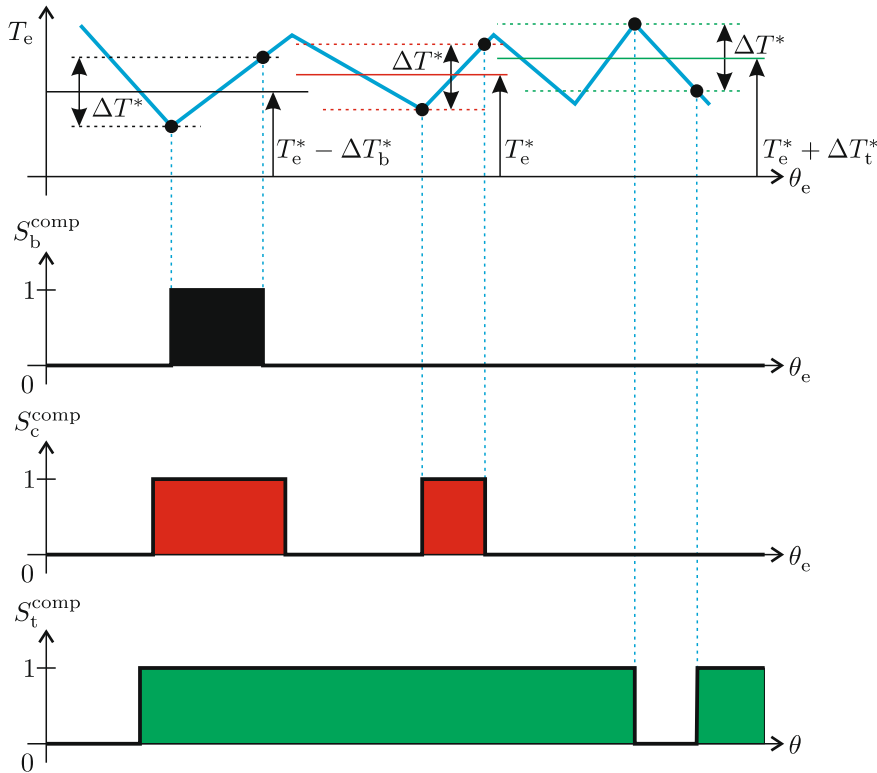


**Fig. 10.39** DITC Comparator signals

**Table 10.3** Phase controller switching algorithm

	Incoming phase	Outgoing phase
$S_{w_t}$	$S_c^{\text{comp}}$	$S_b^{\text{comp}}$
$S_{w_b}$	Phase-active signal	$S_t^{\text{comp}} \times \text{phase-active signal}$

strategy the converter switching signals are directly generated from the three comparator signals according to the algorithm given in Table 10.3.

The algorithm basically states that the top converter switch of the incoming phase is controlled by the comparator with output  $S_c^{\text{comp}}$ . This implies that the incoming phase controller aims to keep the estimated torque between the limits  $T_e^* \pm \Delta T^*/2$ . At the same time, the outgoing controller will make use of the outer comparators with outputs  $S_b^{\text{comp}}$  and  $S_t^{\text{comp}}$  and this controller will activate the top switch if the estimated torque (from the torque observer) falls below the level  $T_e^* - \Delta T_b^* - \Delta T^*/2$ . If the outgoing controller detects an estimated torque in excess of level  $T_e^* + \Delta T_t^* + \Delta T^*/2$ , both switches of the outgoing controller will be opened to de-magnetize that particular phase. Finally, the measured phase current values are also connected to the respec-

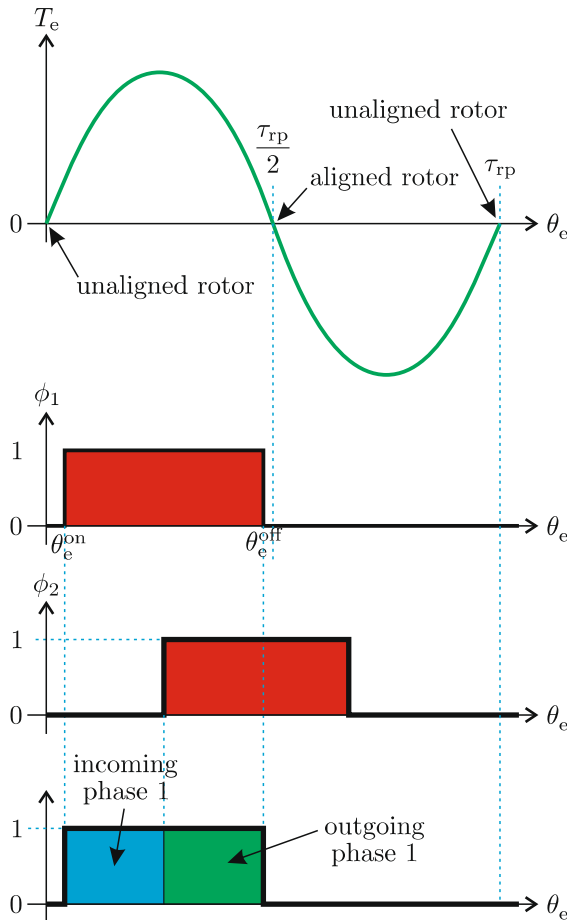


**Fig. 10.40** DITC Control signals

tive phase controller modules. These current signals are used by an internal current hysteresis module which compares the measured current against the specified maximum value. If the latter is met or exceeded, the converter top switch will be modulated irrespective of Table 10.3 to insure that the current cannot exceed the maximum value.

A DITC tutorial is given in the tutorial section at the end of the chapter and an example of the performance, which can be achieved, is given in Fig. 10.41. In this case, the torque reference value is set to  $T_e^* = 10 \text{ Nm}$  and the incremental torque reference value were taken to be  $\Delta T_t^* = \Delta T_b^* = 0.05 \text{ Nm}$ . A 240 V converter supply is assumed with a maximum phase current rating of 11.8 A and the *turn-on* and *turn-off* angles were set to  $\theta_e^{\text{on}} = -30^\circ$  and  $\theta_e^{\text{off}} = 150^\circ$ .

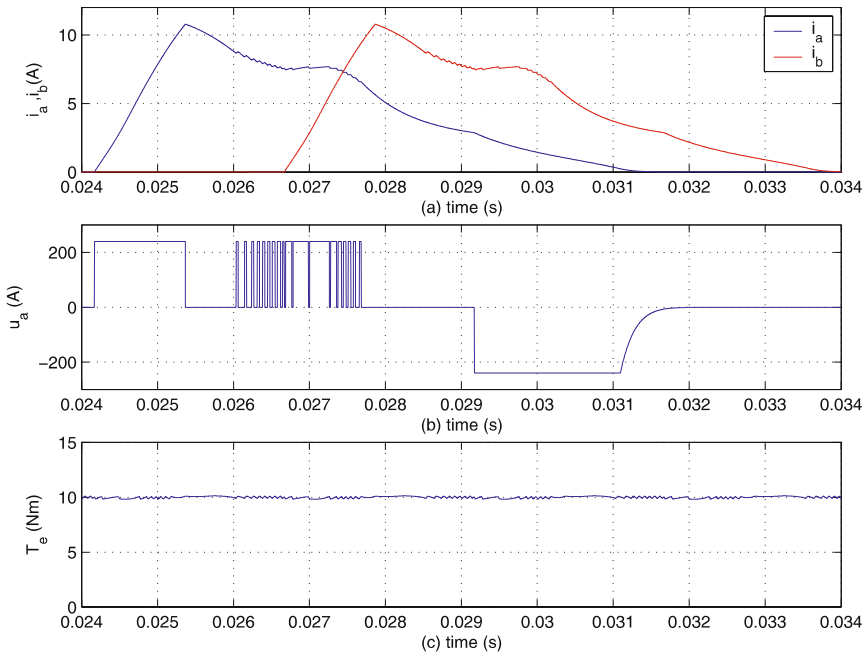


**Fig. 10.41** Waveforms of DITC based SR drive, showing low torque ripple

Shown in Fig. 10.41 are two phase currents, the phase voltage and resultant shaft torque with the 8/6 machine operating at 1000 rpm. It is instructive to compare the DITC based drive with a *standard* hysteresis based drive operating under the same load and speed conditions. The reference current is set to 6.45 A to realize the same average shaft torque as developed in the DITC based drive. The control angles and the supply voltage remain unchanged when compared to the previous case. An observation of the results as given in Fig. 10.42 demonstrates that the current hysteresis based drive has a considerably higher torque ripple component in the shaft torque, when compared to the DITC based drive.

However, the price for this performance lies with the need for a higher dynamic current control range, as may be observed by comparing the phase currents for the two drives. As the shaft torque is increased, the DITC drive peak currents will be limited by the protective current controller, and this in turn will impede the operation of the DITC controller. Furthermore, both controller methods do not operate with constant switching frequencies in the converter, which impedes realization optimized control (to minimize acoustic emissions or to maximize efficiency). Using predictive control principles it is possible to implement DITC with constant switching frequencies. We refer to specialized literature, such as [23, 22].

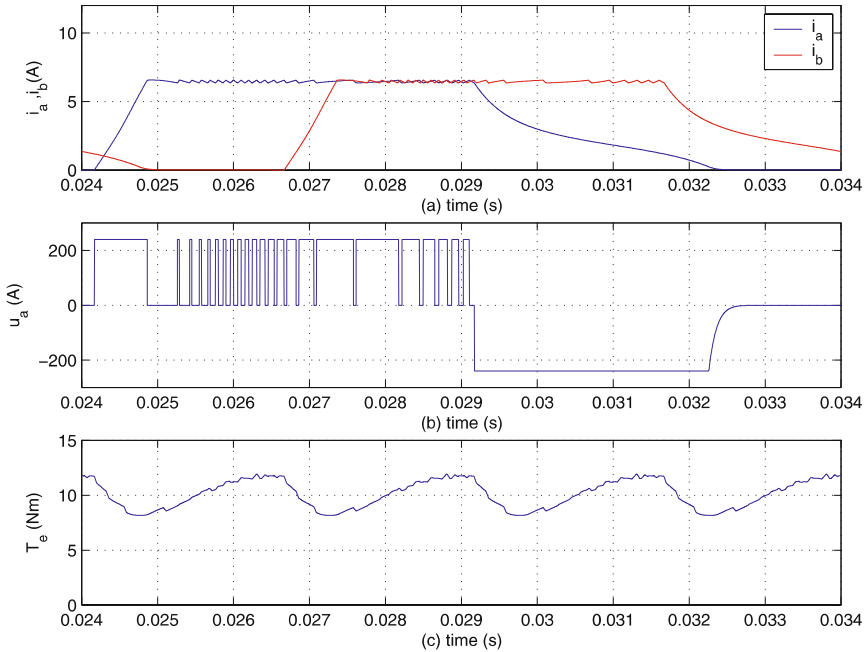
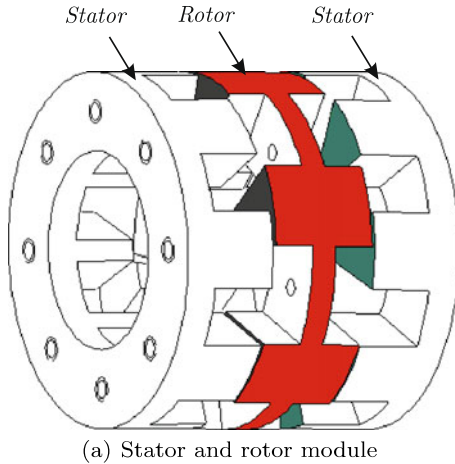


Fig. 10.42 Waveforms of current hysteresis controlled SR drive

## 10.5 Switched Reluctance Demonstration Machine

In various sections of this chapter, including the tutorials, numerical examples are used to demonstrate specific aspects of SR drive behavior. For this purpose, the 8/6 SR axial flux (SRAF) machine [54, 52] as shown in Fig. 10.43 is used. The magnetization characteristics of the machine were derived via a set of *locked rotor* measurements, whereby a phase voltage pulse is applied and the transient current response is measured. Use of (10.7) leads to the representation of the flux-linkage/current curve (for a given rotor angle  $\theta_k$ ) in the form of a set of data points  $\Psi_{ij}(i_{ij}, \theta_k)$ ,  $ij = 1 \dots N_i$ , where  $N_i$  represents the number of measured (or computed) flux-linkage/current data pairs. This measurement process must be repeated for a set  $k = 1 \dots N_\theta$  rotor angles starting from the (in this example) unaligned  $\theta_e = 0^\circ$ ;  $k = 1$  to the aligned  $\theta_e = \theta_{\max}$ ;  $k = N_\theta$  position. Typical values for  $N_\theta$  and  $N_i$  are 11 and 200 respectively and the actual values used are governed by the degree of saturation, i.e., the shape of the magnetization characteristics. Considerable efforts have been undertaken by researchers on the topic of developing a suitable mathematical representation of these characteristics [54] and to automate these measurements [21]. A relatively simple approach to solving this problem is to use a two-dimensional lookup table directly based on a set

of data points  $\Psi_{ij}(i_{ij}, \theta_k)$ ,  $ij = 1 \dots N_i$  derived via measurements [21], finite element analysis or analytical flux path techniques [62]. In the given example, the lookup table is obtained via measurements.



**Fig. 10.43** 8/6 Switched Reluctance Axial Flux (SRAF) example

For some models (see for example Fig. 10.15), derivatives of the magnetization curves are needed. Note also that the torque characteristics can be either measured (lookup tables can be used to represent the data) using locked rotor techniques or derived from the magnetization curves, in which case further processing involving differentiation and integration (see (10.18) and (10.19)) is needed. If further processing of the magnetization curves is required, i.e., to obtain derivatives  $\partial\psi/\partial i$ ,  $\partial\psi/\partial\theta_e$  and torque  $T_e$ , then the use of cubic *B-splines* is particularly effective [53]. The reason for this is that so-called *B-splines* are continuous in terms of the function itself and its derivatives. Furthermore, the latter is readily available, which is beneficial given the need to find derivative functions, as mentioned above.

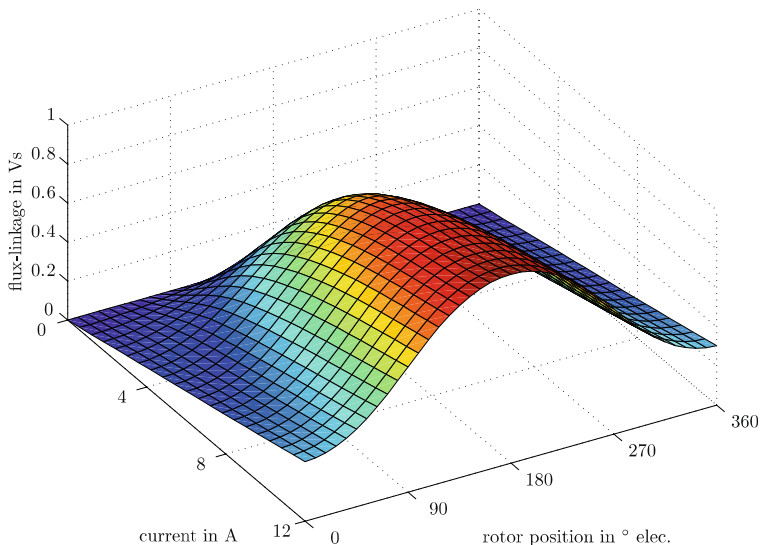
This approach has been used here to represent the characteristics of the machine, in the form of a set of *spline coefficients*. All characteristics in this book are characterized by the magnetization data which is represented in terms of a set of bi-variate splines which in turn are defined by a set of current  $[0 \ i_1^s \ i_2^s \ i_{\max}]$  and angle knots  $[0 \ \theta_1^s \ \theta_2^s \ \theta_{\max}]$  [53] as shown in Fig. 10.18. The values assigned to these knots and the phase resistance value are given in Table 10.4.

Application of the spline curve fitting techniques, as mentioned above, leads to the characteristics shown in Fig. 10.18. A set of spline based routines [53] can be used to generate a bi-variate cubic spline representation of the magnetization curves  $\psi(i, \theta_e)$  (see Fig. 10.44) and *inverse* function

**Table 10.4** SR parameters

Parameters		Value	
Current knot 1	( $i_1^s$ )	3	(A)
Current knot 2	( $i_2^s$ )	5	(A)
Maximum current	( $i_{\max}$ )	12	(A)
Angle knot 1	( $\theta_1^s$ )	10	(° mech.)
Angle knot 2	( $\theta_2^s$ )	20	(° mech.)
Unaligned angle	( $\theta_{\max}$ )	30	(A)
Phase resistance	( $R$ )	1.1	(Ω)

$i(\psi, \theta_e)$ . In addition, the static torque/current/angle curves  $T(i, \theta_e)$  (see Fig. 10.45), incremental inductance curves  $l(i, \theta_e)$  (see Fig. 10.46) and normalized EMF versus current/angle curves:  $e(i, \theta_e)$  (see Fig. 10.47).

**Fig. 10.44** Magnetization curves:  $\psi(i, \theta_e)$

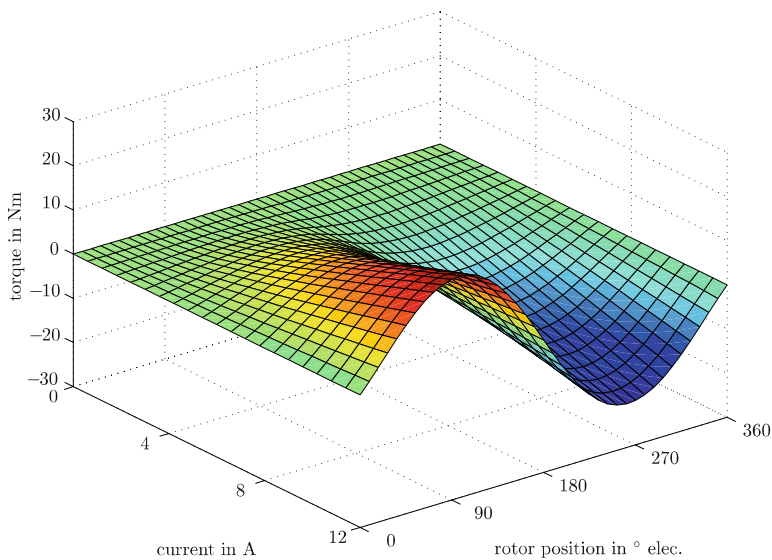


**Fig. 10.45** Torque versus current/angle curves:  $T(i, \theta_e)$

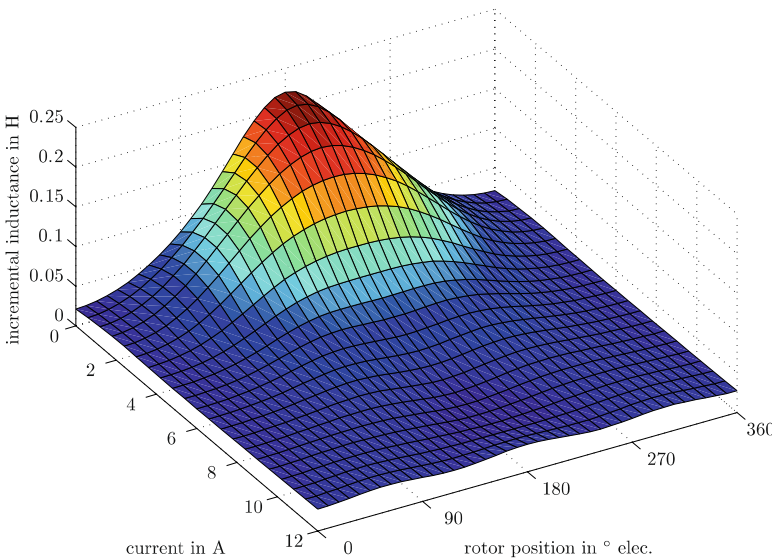


**Fig. 10.46** Incremental inductance versus current/angle curves:  $l(i, \theta_e)$

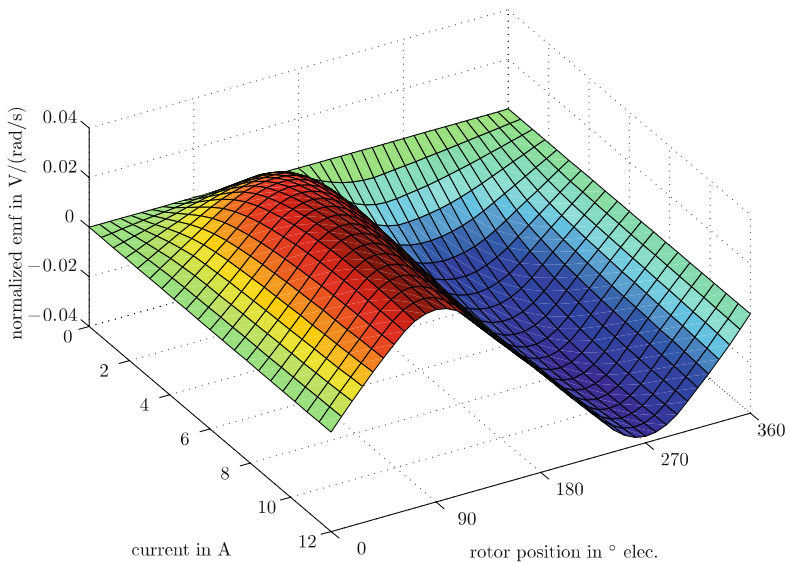


**Fig. 10.47** Normalized *EMF* versus current/angle curves:  $e(i, \theta_e)$

## 10.6 Tutorials

### 10.6.1 Tutorial 1: Analysis of a Linear SR Machine, with Current Excitation

This tutorial considers a simplified SR machine, based in part on the generic models shown in Fig. 10.14 and Fig. 10.15 respectively. A linear 8/6 machine representation is assumed, which is according to the model discussed in Sect. 10.5. In this case a single-phase (phase  $a$ ) is to be connected to a current source, while the shaft speed should be set to a constant value of 1000 rpm. A simulation is to be undertaken which makes use of lookup tables to represent the machine. The aim of the tutorial is to allow the reader to examine the time dependent waveforms which represent the instantaneous torque  $T_e(t)$ , flux linkage  $\psi(t)$ , incremental inductance  $L(t)$ , induced voltage  $u_e$  and input phase current  $i(t)$  of phase  $a$  under constant speed operation. Furthermore, the tutorial should allow the reader to examine the effect of changing the *turn-on*  $\theta_{on}$  and *turn-off*  $\theta_{off}$  control angles (see Fig. 10.21) on these waveforms.

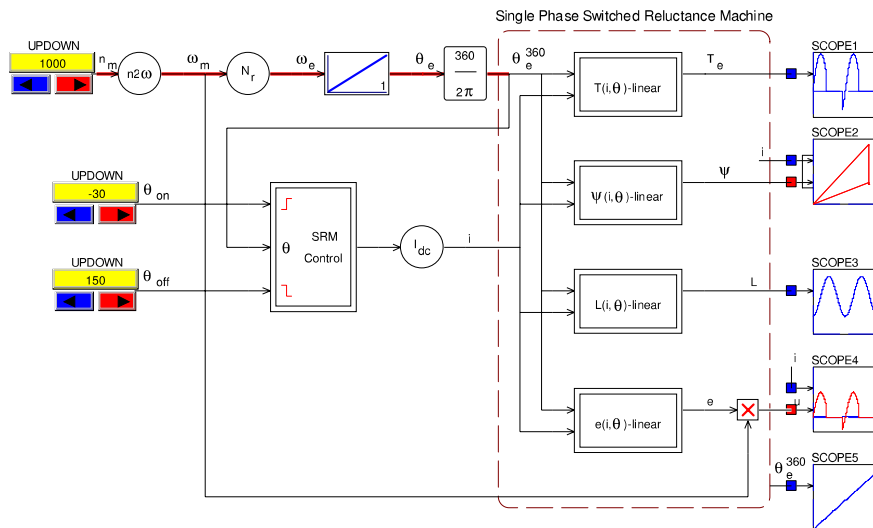


**Fig. 10.48** Simulation tutorial on linear SR model, with current excitation

The simulation model *SR machine*, given in Fig. 10.48, shows the four generic modules which contain the machine characteristics in the form of lookup tables. Inputs to these modules are the phase current  $i$  and rotor phase angle  $\theta$ . The latter variable is a phase related rotor angle, which is derived from the shaft angle  $\theta_m$ . The rotor phase angle  $\theta$  is defined with

respect to the unaligned position of the phase in question. The rotor phase angle variable and the control angles  $\theta_{\text{on}}$  and  $\theta_{\text{off}}$  are used by the *SR controller* module to generate the phase active signal  $S_w$ . The latter is multiplied by a gain factor (6 in this case) in order to derive a signal which represents the ideal phase  $a$  current  $i$  waveform with a magnitude of 6 A.

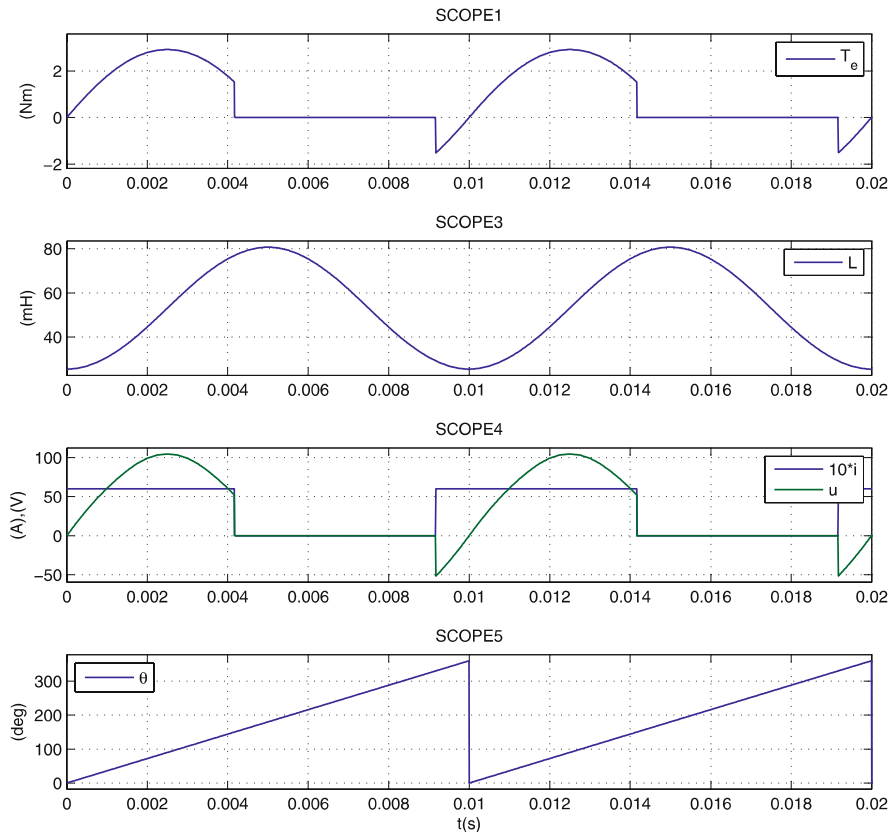


**Fig. 10.49** Simulation results for linear SR model, with current excitation,  $n_m = 1000$  rpm and  $\theta_{\text{on}} = -30^\circ$ ,  $\theta_{\text{off}} = 150^\circ$

The set of MATLAB subplots given in Fig. 10.49 and Fig. 10.50 show the results obtained via the SCOPE modules used in the simulation. In the example the *turn-on* angle is set to  $-30^\circ$ , and the turn-off angle to  $150^\circ$ . This implies that the phase current is set to the value of 6 A,  $-30^\circ$  before the unaligned position (for phase  $a$ ) is reached and switched off when the rotor reaches  $150^\circ$  of the phase in question. If the *turn-on* angle is set to zero, the torque waveform  $T_e$  will be positive only. The flux linkage/current trajectory as shown in Fig. 10.50, should be similar, in terms of shape, to Fig. 10.9.

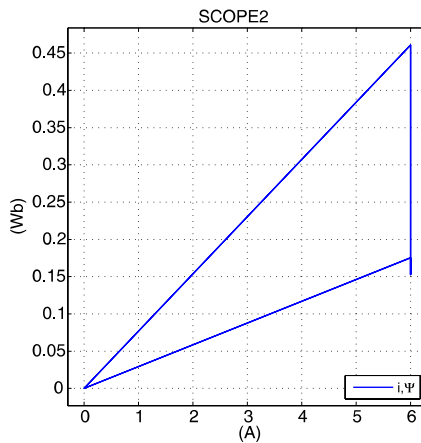


**Fig. 10.50** Simulation results for linear SR model, with current excitation, flux linkage/current diagram with  $n_m = 1000$  rpm and  $\theta_{on} = -30^\circ$ ,  $\theta_{off} = 150^\circ$

The angle values will be different, because the latter figure refers to a 2/2 configuration.

### 10.6.2 Tutorial 2: Non-linear SR Machine, with Voltage Excitation and Hysteresis Current Controller

A single-phase representation of an 8/6 non-linear SR machine is considered, with the characteristics as outlined in Sect. 10.5. The machine in question is to be connected to an asymmetrical half-bridge converter (see Fig. 10.19), which in turn is fed by a DC supply  $u_{DC} = 240\text{ V}$ . Furthermore, a hysteresis type controller as shown in Fig. 10.20 is to be used, with a reference current setting of  $i^* = 10\text{ A}$  and a current error setting of  $\Delta i = 0.4\text{ A}$ . As with the previous case, the rotor shaft is taken to rotate at a constant speed of  $n_m = 1000\text{ rpm}$ . In addition, the control angles should be adjustable to allow the user to examine their effect on the simulation results. A generic model of the machine as shown in Fig. 10.17 is to be used for this tutorial.

The simulation given in Fig. 10.51 shows the generic model representation of the machine, which is connected to the converter. Four modules, i.e.,  $T, \psi, l$  and  $e$ , with input variables  $i$  and  $\theta$  contain the lookup tables required to build the (non-linear) model of the machine, with characteristics as shown in Sect. 10.5. A *circuit* model representation is used for the converter, which in turn is linked with the machine via a *single-phase interface module* which provides the voltage excitation for the machine. The phase current variable is returned to the circuit model via the same *single-phase interface module* placed between the two ideal IGBT based converter switches. The simulation modules used to generate the phase active signal  $Sw$ , remains unchanged with respect to the previous tutorial. An adjustable current reference value set to 10 A is also shown in Fig. 10.51 and this variable, together with the phase current variable  $i$  form the input to the hysteresis controller. The waveforms generated by the simulation are again shown using *scope* modules and subsequently plotted in Fig. 10.52.

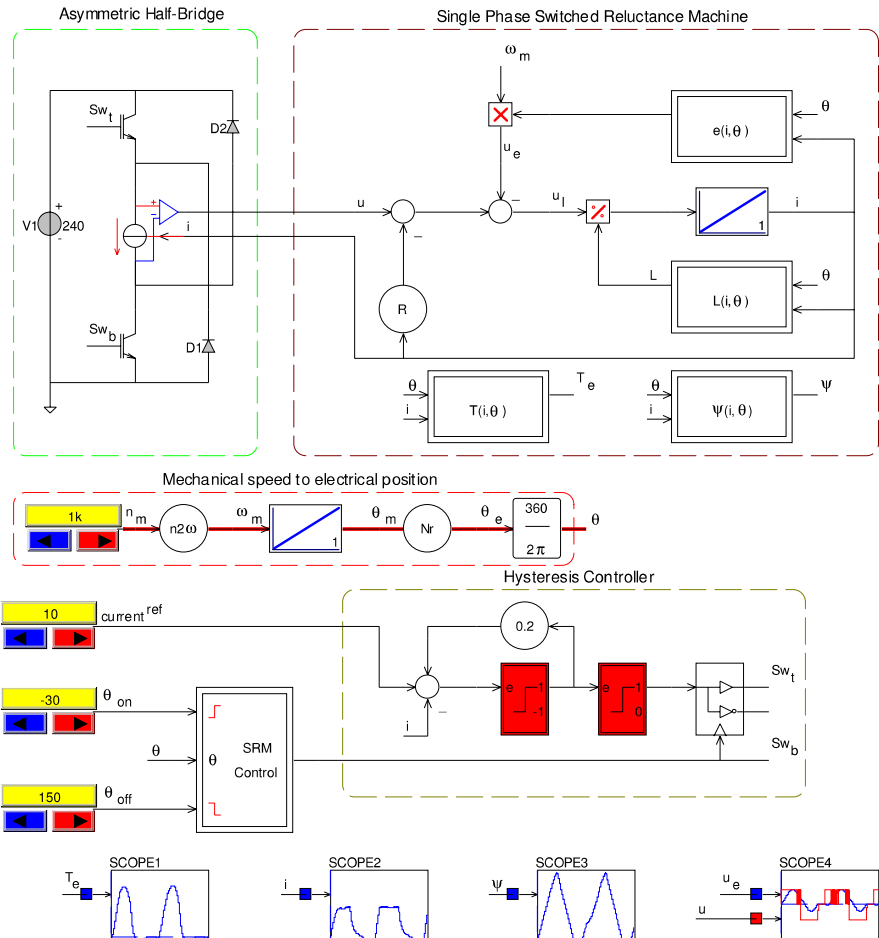


**Fig. 10.51** Simulation tutorial on non-linear SR model, with voltage excitation and hysteresis current controller

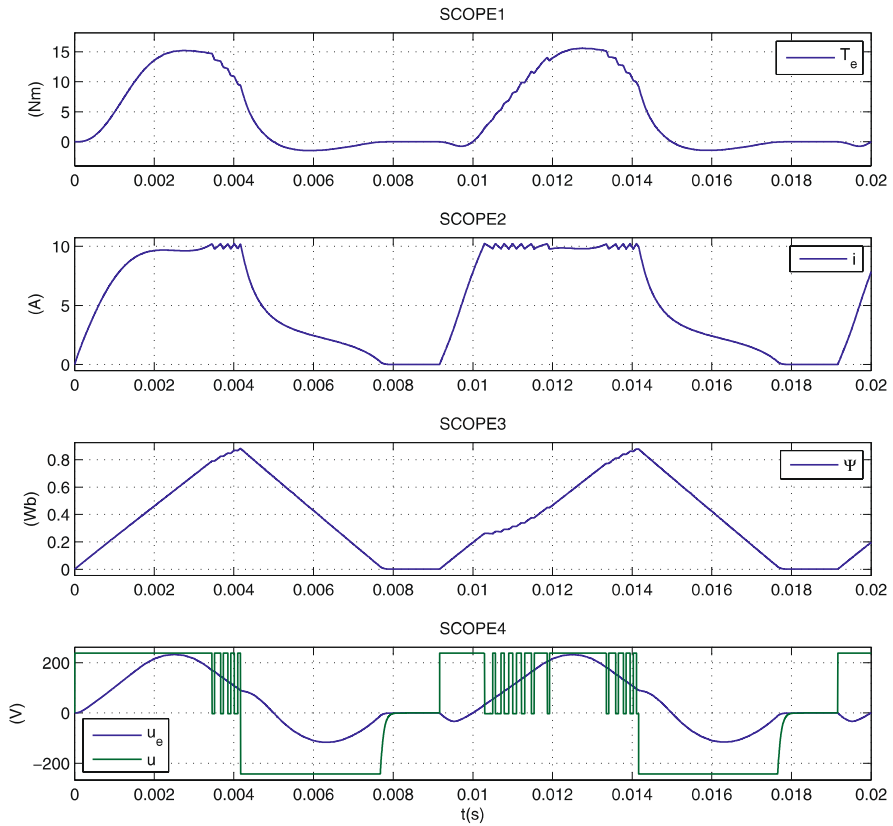


**Fig. 10.52** Simulation results for non-linear SR model, with voltage excitation and hysteresis current controller,  $n_m = 1000$  rpm,  $\theta_{on} = -30^\circ$ ,  $\theta_{off} = 150^\circ$

### 10.6.3 Tutorial 3: Non-linear SR Machine, with Voltage Excitation and PWM Controller

An alternative control approach to the hysteresis current control is a PWM based method as outlined in Sect. 10.2.6. In this case, the average phase voltage during the phase active interval is controlled by varying the duty cycle  $\delta$  of the top switch. The object of this tutorial is to modify the simulation discussed in the previous tutorial by replacing the hysteresis controller with a PWM based controller. The machine model, machine characteristics and drive operating conditions remain unchanged compared to the previous case. An example of the simulation, as given in Fig. 10.53 shows the revised PWM controller with the duty cycle as input variable.

In the simulation, the PWM switching frequency has been purposely set low to  $f_{\text{PWM}} = 2000 \text{ Hz}$  to better visualize the impact on the waveforms with this type of control strategy. Care should be taken by the user to limit the maximum phase current which appears in the simulation to a value below 12 A (maximum current value), by a prudent choice of the duty cycle, otherwise the lookup tables used for the representation of the machine characteristics will yield incorrect results. For the selected shaft speed of  $n_m = 1000 \text{ rpm}$ , a duty cycle value of  $\delta = 0.4$  is used. The output is represented with the same set of scopes used in the previous tutorial. A set of MATLAB based subplots, as given in Fig. 10.54, shows the results obtained with this simulation, with the input conditions specified.

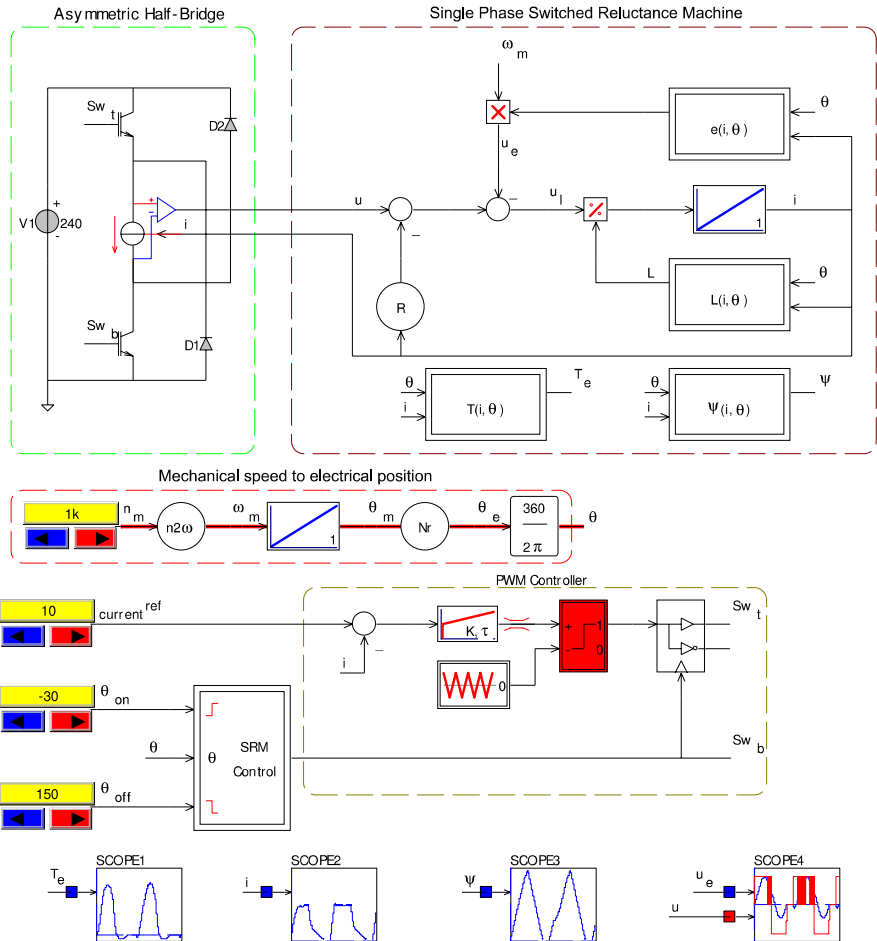


**Fig. 10.53** Simulation tutorial on non-linear SR model, with voltage excitation and PWM controller

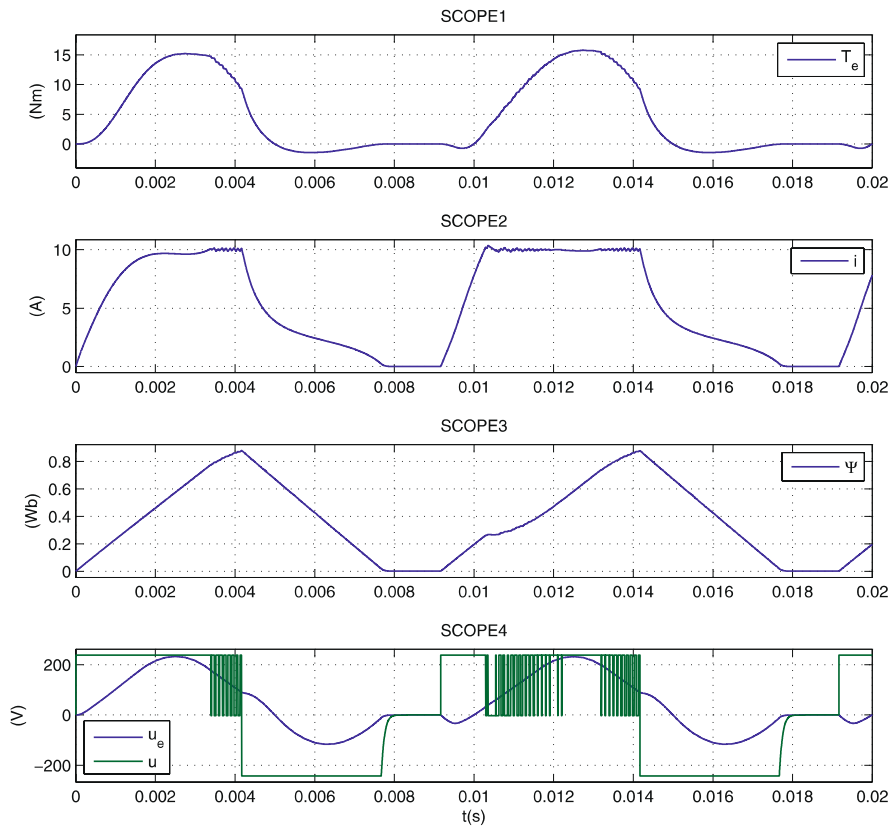


**Fig. 10.54** Simulation results for non-linear SR model, with voltage excitation and PWM controller,  $n_m = 1000$  rpm,  $\theta_{on} = -30^\circ$ ,  $\theta_{off} = 150^\circ$

### 10.6.4 Tutorial 4: Four-Phase Non-linear SR Model, with Voltage Excitation and Hysteresis Control

The tutorial according to Sect. 10.6.2 was concerned with a single-phase representation of an 8/6 SR drive operating with hysteresis type current control. This tutorial considers an extension of this simulation model to encompass all four phases of the drive. Subsequently, the resultant shaft torque may be examined and furthermore the simulation may be extended to accommodate, the combined load/machine inertia, set to  $J = 0.001 \text{ kg m}^2$ . A quadratic load torque speed characteristic is assumed which must be set to provide a load torque of 2 Nm at  $n_m = 3000 \text{ rpm}$ . The simulation should be able to accommodate drive operation under constant and variable speed operation.

An example of a simulation model as given in Fig. 10.55 shows the complete dynamic SR drive structure. Immediately observable are the converter (four phase asymmetric half-bridge converter), a four phase SR machine (each phase is modeled separately) and four control modules, which include the control of the angle and the hysteresis controller, similar to Sect. 10.6.2. The machine module also represents the model discussed in Sect. 10.6.2. The torque outputs of these modules are added, which gives the total machine torque  $T_e$ . The total torque is fed to a mechanical load, to calculate the speed and the position of the rotor. This block uses an integrator block with the gain  $1/J$ , to simulate the inertia of the rotor.

A set of scope modules are used to examine the results which are presented using MATLAB subplots. In this case, two example plots are given. The first set of results, as given in Fig. 10.56, shows machine startup without load. For this example, the current reference setting and control angles were set to  $i^* = 6.45 \text{ A}$  and  $\theta_{\text{on}} = 0^\circ$ ,  $\theta_{\text{off}} = 132^\circ$  respectively. A total simulation time of 60 ms was chosen, which allows the machine to accelerate from zero speed to approximately 3000 rpm.

The second set of results, as given in Fig. 10.57, shows operation under quadratic load, i.e., with a user defined speed, instead of load torque. In this case, the shaft speed quickly settles at about 100 rad/s, while the current reference setting and control angles were set to  $i^* = 6.45 \text{ A}$  and  $\theta_{\text{on}} = 0^\circ$ ,  $\theta_{\text{off}} = 132^\circ$  respectively. Note that operation under constant speed is convenient for optimizing drive performance, for example in terms of selecting the required control angles which yield the highest average torque.

An interesting exercise, left to the reader, is to adapt this simulation model to a drive configuration shown (for a three-phase machine) in Fig. 10.28. In this case, the single top switch operation may be equally well modeled by modulating all four top switches simultaneously (and continuously, i.e., independent of the phase active interval signal), with the aid of a PWM generator as used in the tutorial given in Sect. 10.6.3. Of interest is to consider the impact on the simulation waveforms as a result of varying the duty cycle as well as drive speed.

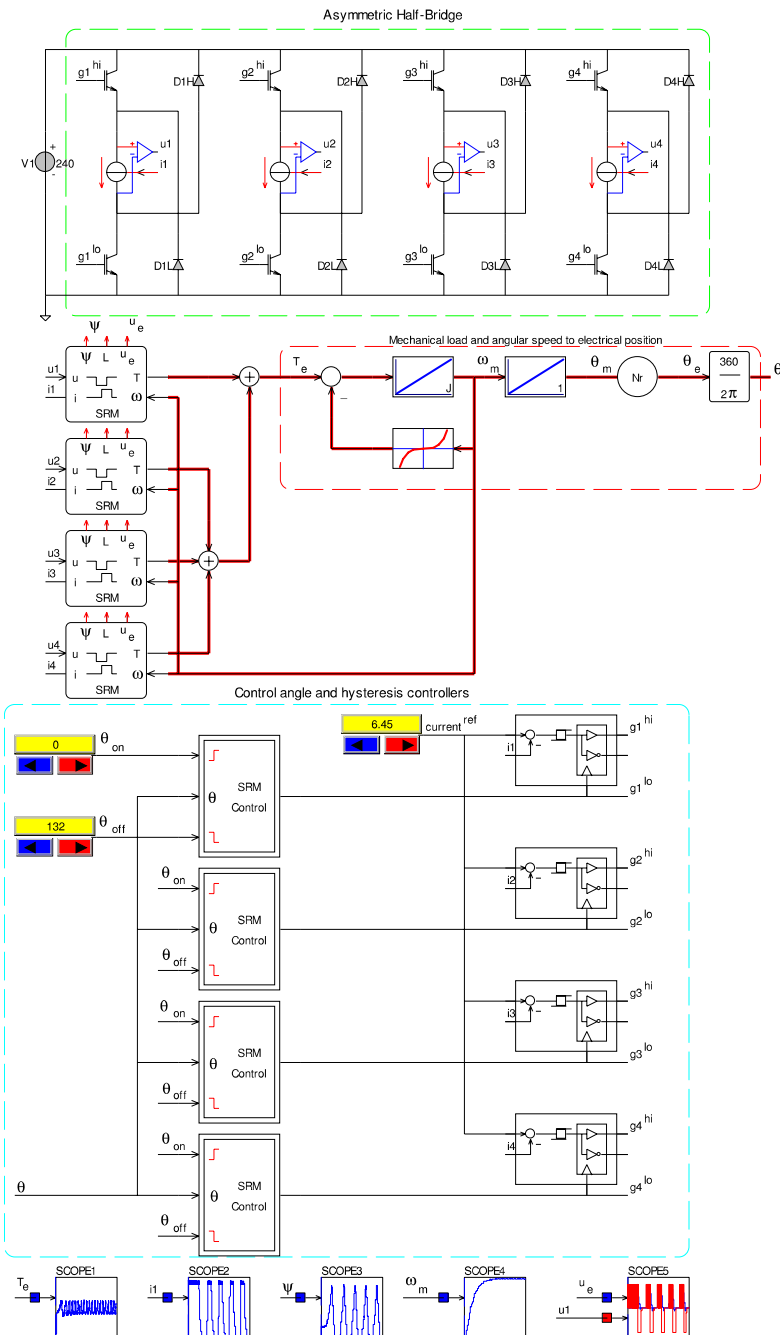


**Fig. 10.55** Simulation tutorial on four-phase non-linear SR model, with voltage excitation and hysteresis control

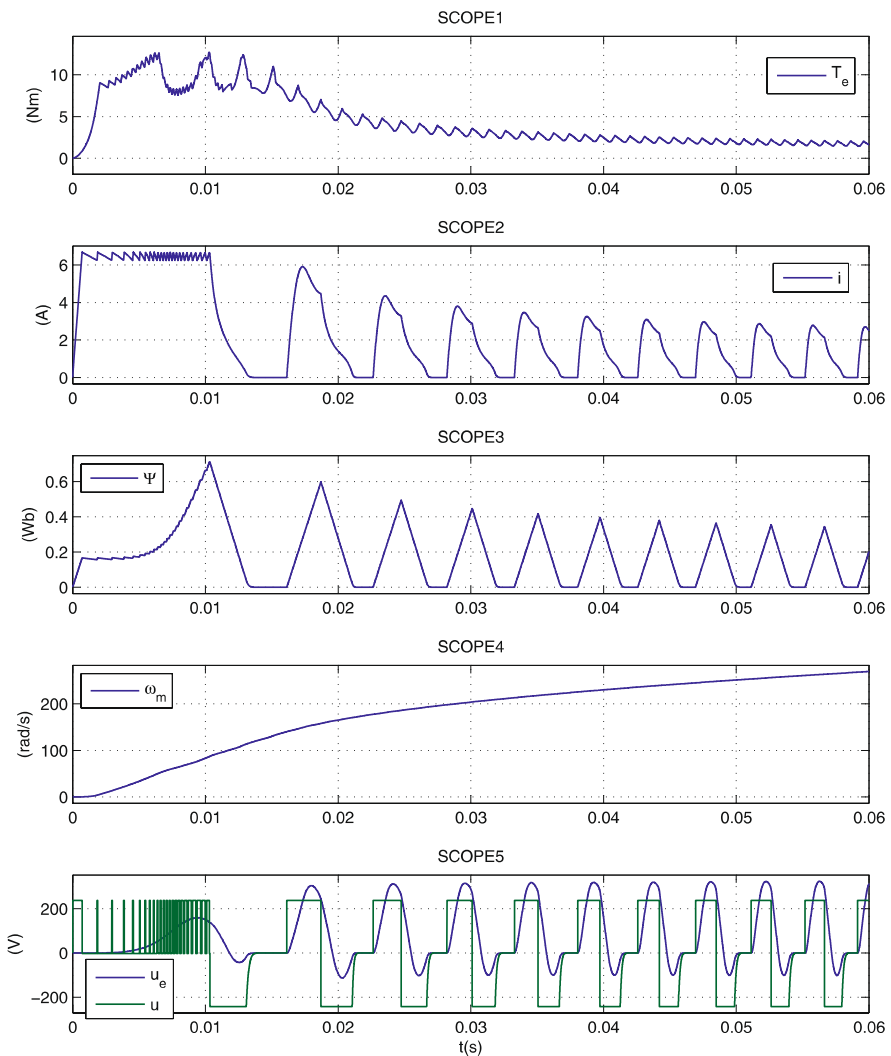


**Fig. 10.56** Simulation results for start-up of non-linear four-phase SR machine, with voltage excitation and hysteresis controller, no-load,  $i^* = 6.45 \text{ A}$ ,  $\theta_{\text{on}} = 0^\circ$ ,  $\theta_{\text{off}} = 132^\circ$

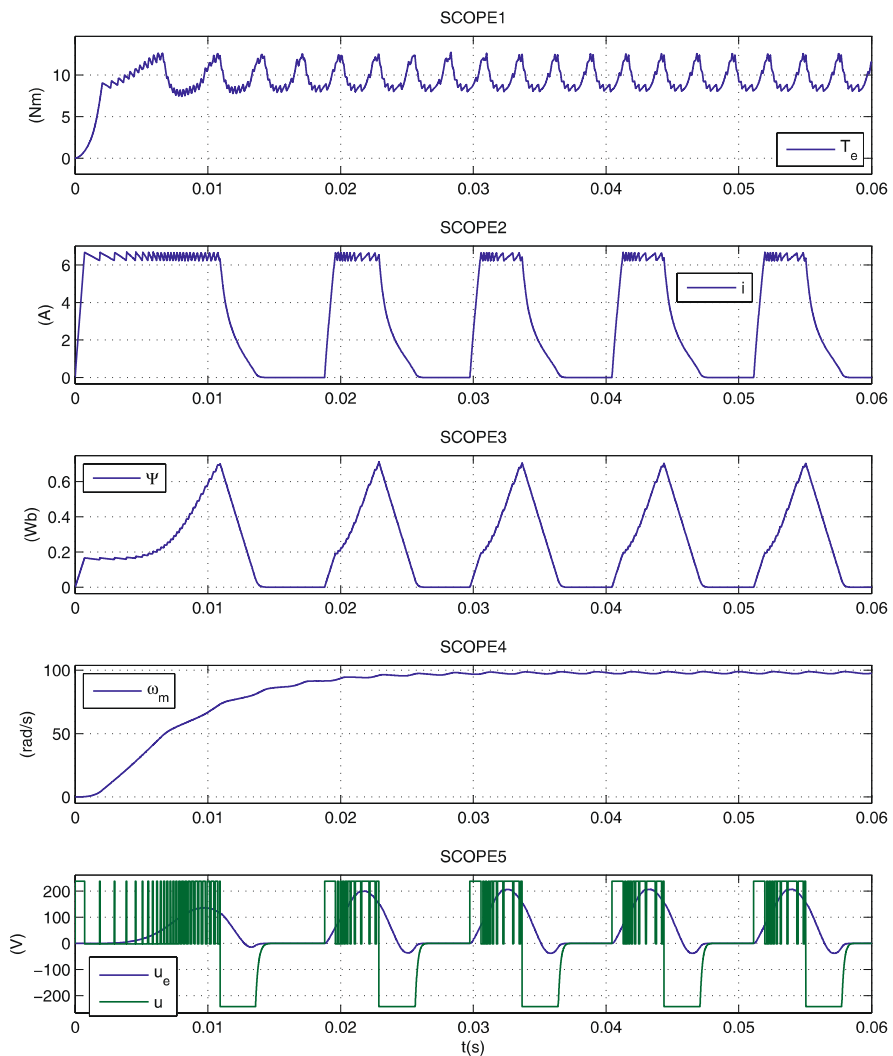


**Fig. 10.57** Simulation results for non-linear four-phase SR model, with voltage excitation and hysteresis controller,  $i^* = 6.45 \text{ A}$ ,  $\theta_{\text{on}} = 0^\circ$ ,  $\theta_{\text{off}} = 132^\circ$ , quadratic load

### 10.6.5 Tutorial 5: Four-Phase Non-linear SR Model, with Voltage Excitation and Direct Instantaneous Torque Control (DITC)

The final tutorial in this chapter considers the use of a DITC type control method for an SR drive as discussed in Sect. 10.4.3. A suitable starting point

for this exercise is the previous tutorial, which deploys a set of hysteresis type current controller together with the phase active signals to manipulate the converter switches. For this tutorial, a DITC type control structure as given in Fig. 10.38 is to be examined. For this purpose, the simulation model according to Fig. 10.55 is to be modified to accommodate a DITC control module which uses the measured torque  $T_e$  (in this case taken directly from the SR machine model), the (user defined) reference torque  $T_e^*$ , the four *measured* phase currents  $i_1, i_2, i_3, i_4$  and four phase active signals  $g_1^{\text{hi},\text{lo}}, g_2^{\text{hi},\text{lo}}, g_3^{\text{hi},\text{lo}}, g_4^{\text{hi},\text{lo}}$ . The simulation model as given in Fig. 10.58 shows a possible implementation of the proposed tutorial. Readily apparent from Fig. 10.58 is the presence of a DITC controller unit with the required inputs. The module itself has a control structure, which is in accordance with the model given in Fig. 10.38. In this simulation the control angles  $\theta_{\text{on}}$  and  $\theta_{\text{off}}$  may be chosen by the user. In industrial DITC SR drive applications lookup tables are used to generate the optimum set of angles at each shaft speed **ref.** Both converter switches of each of the four phases are directly controlled by the DITC module, as may be observed from Fig. 10.58.

In this example the torque reference value is set to  $T_e^* = 10 \text{ Nm}$  and the incremental torque reference value were taken to be  $\Delta T_t^* = \Delta T_b^* = 0.05 \text{ Nm}$ , which are the values used to generate the numerical results shown in Sect. 10.4.3. A set of scopes identical to those used in the previous tutorial are used to evaluate the simulated waveforms, which are presented with the aid of MATLAB subplots. An example of the results, obtained with the DITC controller as given in Fig. 10.59, shows a typical start-up sequence of an SR drive connected to a fan type load, i.e., a load with a quadratic torque/speed characteristic. Both control angles have been purposely set to  $\theta_{\text{on}} = 0^\circ$  and  $\theta_{\text{off}} = 132^\circ$  to facilitate a comparison of results with the previous start up case (see Fig. 10.56). Observation of the results shown in Fig. 10.56 shows that the controller is able to maintain the torque at the reference value below the base speed of the drive, which is 1468 rpm for this drive. As speed increases, the back EMF increases (as may be observed from SCOPE3, trace  $u_e$ ) which implies that the current levels reduce. Operation above the base speed is for both drives (hysteresis and DITC based) identical given that both use the same control angle settings.

The second set of results, illustrated in Fig. 10.60, shows operation under quadratic load, resulting in an almost constant speed. Observation of the results according to Fig. 10.60 shows that the DITC controller is able to maintain a virtually constant shaft torque at the chosen speed. This is markedly different compared to the results obtained with the hysteresis type control under similar drive conditions as may be observed by comparing Fig. 10.60 and Fig. 10.57.

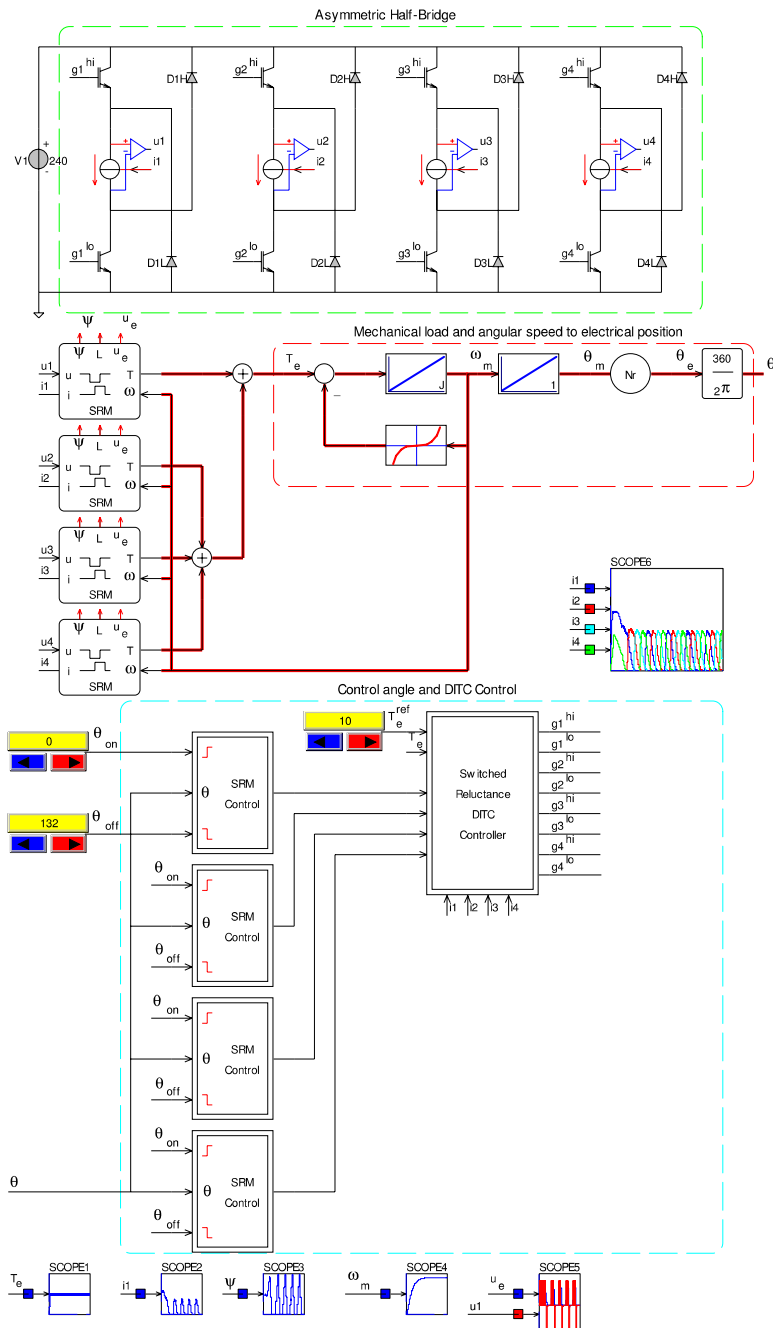


**Fig. 10.58** Simulation tutorial of four-phase non-linear SR model, with voltage excitation and DITC

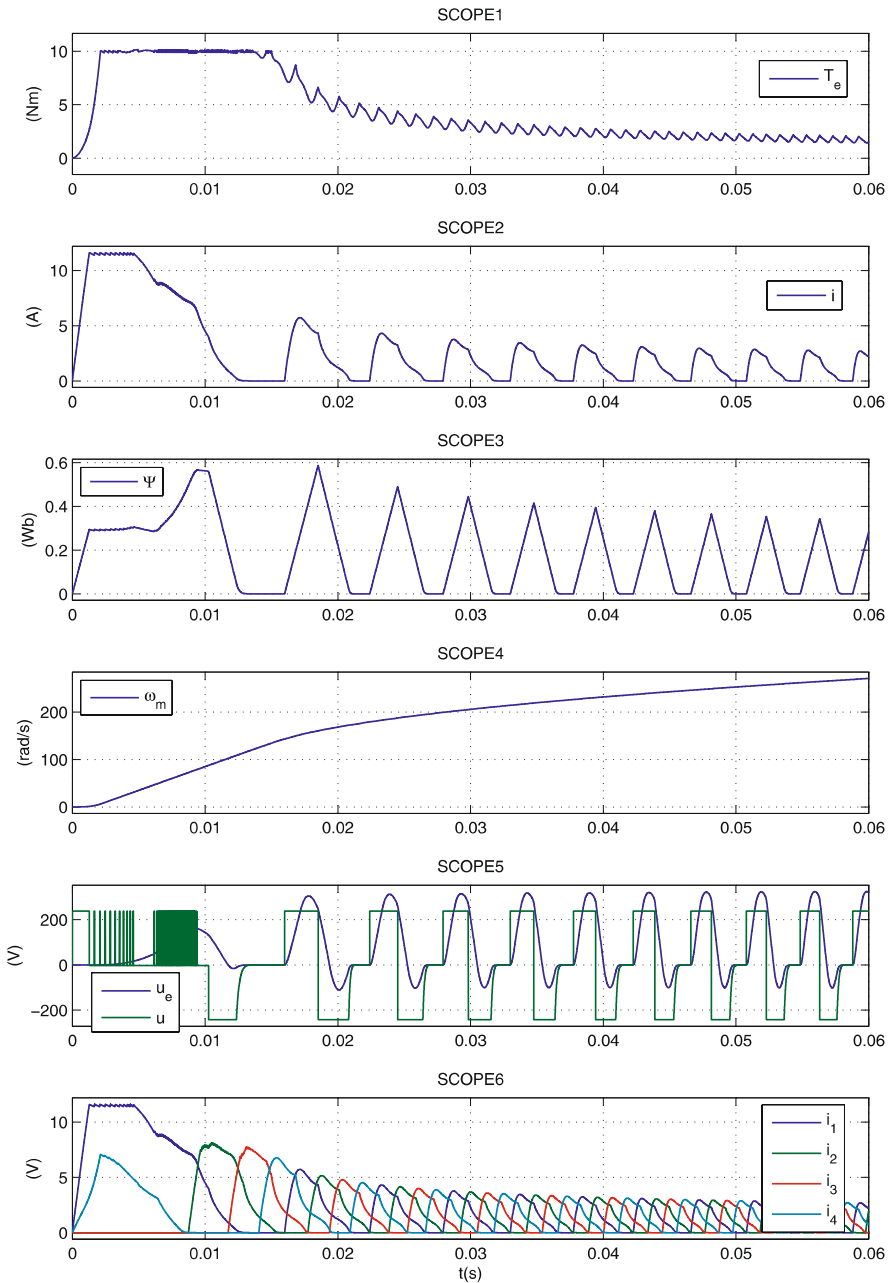


**Fig. 10.59** Simulation results for start-up of non-linear four-phase SR model, with voltage excitation and DITC based controller and no load

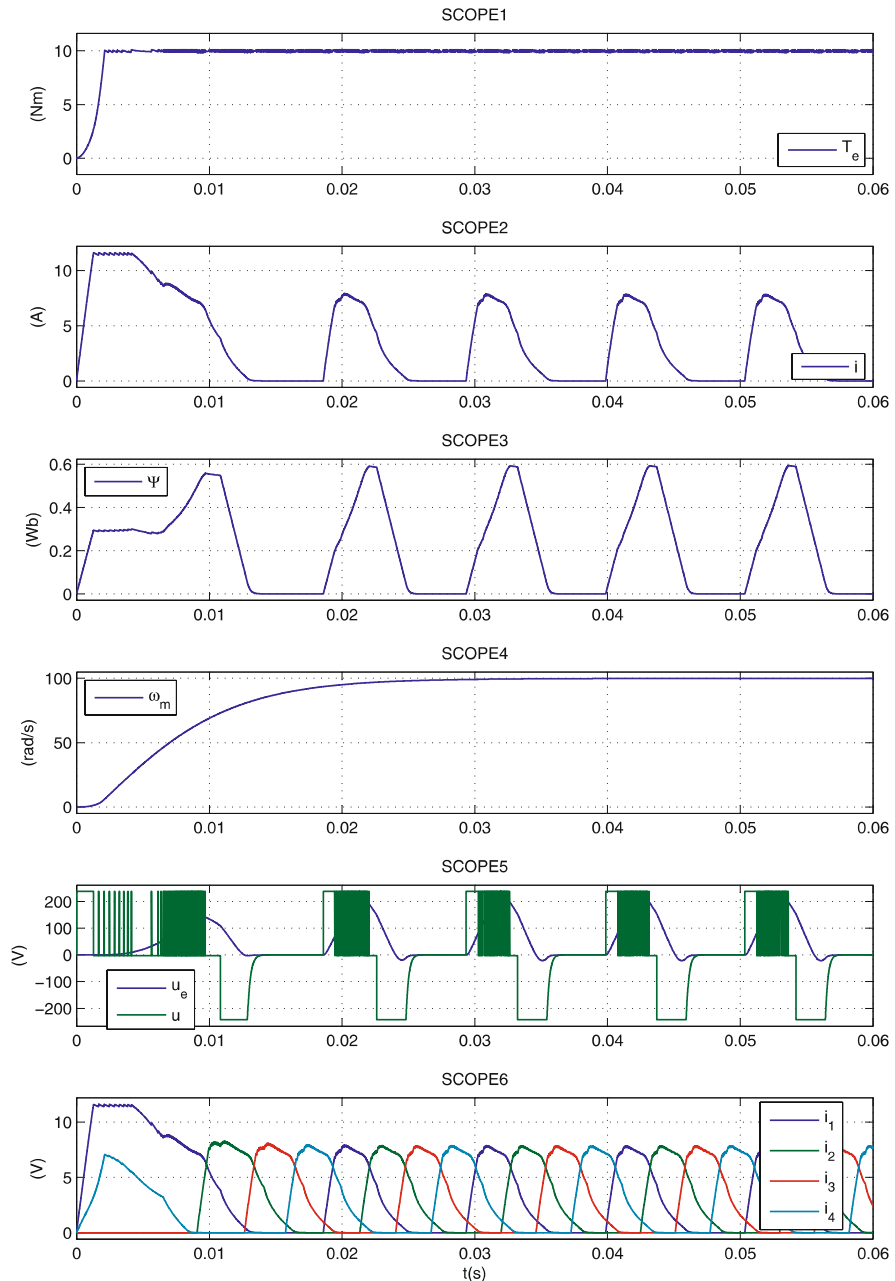


**Fig. 10.60** Simulation results for non-linear four-phase SR model, with voltage excitation and DITC based controller,  $T_e^* = 10.0 \text{ Nm}$ , quadratic load of  $10 \text{ Nm}$  at  $100 \text{ rad/s}$



# References

- [1] AixControl GmbH (2010). <http://www.aixcontrol.de>
- [2] Alakula M, Peterson B, Valis J (1992) Damping of oscillations in induction machines. In: Power Electronics Specialists Conference, 1992. PESC '92 Record., 23rd Annual IEEE, vol 1, pp 133–138. doi:[10.1109/PESC.1992.254702](https://doi.org/10.1109/PESC.1992.254702)
- [3] Alcoa, Inc. (2010). <http://www.alcoa.com>
- [4] Analog Devices, Inc. (2010). <http://www.analog.com/en/embedded-processing-dsp/blackfin/vdsp-bf-sh-ts/processors/product.html>
- [5] Backhaus K, Link L, Reinert J (1995) Investigations on a high-speed switched reluctance drive incorporating amorphous iron. In: European Conference on Power Electronics and Applications, vol 1, pp 1.460–1.464
- [6] Bausch H, Rieke R (1978) Performance of thyristor-fed electric car reluctance machines. In: Proceedings of the International Conference on Electrical Machines, Brussels, Belgium, pp E4/2-1–E4/2-10
- [7] Blaschke F (1972) The principle of field orientation as applied to the new transvector closed-loop control system for rotating-field machines. Siemens Review XXXIX(5):217–219
- [8] Brod DM, Novotny DW (1985) Current control of vsi-pwm inverters. Industry Applications, IEEE Transactions on IA-21(3):562–570. doi:[10.1109/TIA.1985.349711](https://doi.org/10.1109/TIA.1985.349711)
- [9] van der Broeck HW, Skudelny H-C, Stanke GV (1988) Analysis and realization of a pulsewidth modulator based on voltage space vectors. Industry Applications, IEEE Transactions on 24(1):142–150. doi:[10.1109/28.87265](https://doi.org/10.1109/28.87265)
- [10] Carstensen CE, Inderka RB, Netzer Y, De Doncker RW (2002) Implementation of a 75 kw switched reluctance drive for electric vehicles. In: 19th International Electric Vehicle Symposium EVS19
- [11] CEDRAT Group (2010). <http://www.cedrat.com/en/software-solutions/flux.html>
- [12] De Doncker RW (1991) Parameter sensitivity of indirect universal field oriented controllers. In: Power Electronics Specialists Con-

- ference, 1991. PESC '91 Record., 22nd Annual IEEE, pp 605–612. doi:[10.1109/PESC.1991.162737](https://doi.org/10.1109/PESC.1991.162737)
- [13] De Doncker RW (1992) Field-oriented controllers with rotor deep bar compensation circuits [induction machines]. *Industry Applications, IEEE Transactions on* 28(5):1062–1071. doi:[10.1109/28.158830](https://doi.org/10.1109/28.158830)
- [14] De Doncker RW (2003) Twenty years of digital signal processing in power electronics and drives. In: Industrial Electronics Society, 2003. IECON '03. The 29th Annual Conference of the IEEE, vol 1, pp 957–960. doi:[10.1109/IECON.2003.1280112](https://doi.org/10.1109/IECON.2003.1280112)
- [15] De Doncker RW (2006) Modern electrical drives: Design and future trends. In: Proceedings of the International Power Electronics and Motion Control Conference, IPEMC2006, Beijing, China, vol 1, pp 1–8. doi:[10.1109/IPEMC.2006.4777944](https://doi.org/10.1109/IPEMC.2006.4777944)
- [16] De Doncker RW, Novotny DW (1994) The universal field oriented controller. *Industry Applications, IEEE Transactions on* 30(1):92–100. doi:[10.1109/28.273626](https://doi.org/10.1109/28.273626)
- [17] De Doncker RW, Profumo F (1989) The universal field oriented controller applied to tapped stator windings induction motors. In: Power Electronics Specialists Conference, 1989. PESC '89 Record., 20th Annual IEEE, vol 2, pp 1031–1036. doi:[10.1109/PESC.1989.48592](https://doi.org/10.1109/PESC.1989.48592)
- [18] Depenbrock M (1988) Direct self-control (DSC) of inverter fed induction machine. *IEEE Transactions on Power Electronics* 3:4
- [19] Dorf RC, Bishop RH (2007) Modern control systems, 11 edn. Prentice Hall
- [20] Friedland B (2005) Control system design: An introduction to state-space methods. Dover Publications
- [21] Fuengwarodsakul NH, Bauer SE, De Doncker RW (2006) Characteristic measurement system for automotive class switched reluctance machines. *European Power Electronics and Drives (EPE) Journal* 16(3):10 pp. -P.10
- [22] Fuengwarodsakul NH, Bauer SE, Krane J, Dick CP, De Doncker RW (2005) Sensorless direct instantaneous torque control for switched reluctance machines. In: Power Electronics and Applications, 2005 European Conference on, 10 pp. -P.7. doi:[10.1109/EPE.2005.219423](https://doi.org/10.1109/EPE.2005.219423)
- [23] Fuengwarodsakul NH, Menne M, Inderka RB, De Doncker RW (2005) High-dynamic four-quadrant switched reluctance drive based on ditc. *Industry Applications, IEEE Transactions on* 41(5):1232–1242. doi:[10.1109/TIA.2005.853381](https://doi.org/10.1109/TIA.2005.853381)
- [24] Gallegos-Lopez G, Kjaer PC, Miller TJE (1999) High-grade position estimation for srm drives using flux linkage/current correction model. *Industry Applications, IEEE Transactions on* 35(4):859–869, also in Industry Applications Conference, 1998. Thirty-Third IAS Annual Meeting. The 1998 IEEE. doi:[10.1109/28.777195](https://doi.org/10.1109/28.777195)

- [25] Habetler TG, Divan DM (1989) Performance characterization of a new discrete pulse-modulated current regulator. *Industry Applications, IEEE Transactions on* 25(6):1139–1148. doi:[10.1109/28.44257](https://doi.org/10.1109/28.44257)
- [26] Habetler TG, Profumo F, Griva G, Pastorelli M, Bettini A (1998) Stator resistance tuning in a stator-flux field-oriented drive using an instantaneous hybrid flux estimator. *Power Electronics, IEEE Transactions on* 13(1):125–133. doi:[10.1109/63.654966](https://doi.org/10.1109/63.654966)
- [27] Hasse K (1969) Zur Dynamik drehzahlgeregelter Antriebe mit stromrichtergespeisten Asynchron-Kurzschlussläufermaschinen. PhD thesis, TH Darmstadt
- [28] Heyland A (1894) Ein graphisches Verfahren zur Vorausberechnung von Transformatoren und Mehrphasenmotoren. *ETZ* 15(11):561–564
- [29] Heyland A (1906) A graphical treatment of the induction motor. McGraw Publishing Company, New York
- [30] Holtz J (1993) Speed estimation and sensorless control of ac drives. In: *IEEE Industrial Electronics Conference (IECON'1993)*, vol 2, pp 649–654. doi:[10.1109/IECON.1993.339003](https://doi.org/10.1109/IECON.1993.339003)
- [31] Hughes A (2006) Electric motors and drives: Fundamentals, types and applications, 3rd edn. Newnes
- [32] Inderka RB, De Doncker RW (2003) DITC – Direct instantaneous torque control of switched reluctance drives. *Industry Applications, IEEE Transactions on* 39(4):1046–1051, also in *Industry Applications Conference, 2002. Conference Record of the 37th IAS Annual Meeting*. doi:[10.1109/TIA.2003.814578](https://doi.org/10.1109/TIA.2003.814578)
- [33] Inderka RB, De Doncker RW (2003) High-dynamic direct average torque control for switched reluctance drives. *Industry Applications, IEEE Transactions on* 39(4):1040–1045, also in *Industry Applications Conference, 2001. Conference Record of the 2001 IEEE Thirty-Sixth IAS Annual Meeting*. doi:[10.1109/TIA.2003.814579](https://doi.org/10.1109/TIA.2003.814579)
- [34] Inderka RB, Menne M, De Doncker RW (2002) Control of switched reluctance drives for electric vehicle applications. *Industrial Electronics, IEEE Transactions on* 49(1):48–53. doi:[10.1109/41.982247](https://doi.org/10.1109/41.982247)
- [35] Isermann R (2005) Mechatronic systems: Fundamentals, 1st edn. Springer
- [36] Jordan H, Weis M (1969) Asynchronmaschinen. Vieweg, Braunschweig
- [37] Kahlen K, Voss I, Priebe C, De Doncker RW (2004) Torque control of a spherical machine with variable pole pitch. *Power Electronics, IEEE Transactions on* 19(6):1628–1634. doi:[10.1109/TPEL.2004.836623](https://doi.org/10.1109/TPEL.2004.836623)
- [38] Kasper KA, Bosing M, De Doncker RW, Fingerhuth S, Vorlander M (2007) Noise radiation of switched reluctance drives. In: *Power Electronics and Drive Systems, 2007. PEDS '07. 7th International Conference on*, pp 967–973. doi:[10.1109/PEDS.2007.4487821](https://doi.org/10.1109/PEDS.2007.4487821)
- [39] Lawrenson PJ, Stephenson JM, Fulton NN, Blenkinsop PT, Corda J (1980) Variable-speed switched reluctance motors. *Electric Power Applications, IEE Proceedings B* 127(4):253–265. doi:[10.1049/ip-b:19800034](https://doi.org/10.1049/ip-b:19800034)

- [40] Leonhard W (2001) Control of electrical drives, 3nd edn. Springer
- [41] Lipo TA, Krause PC (1969) Stability analysis of a rectifier-inverter induction motor drive. *Power Apparatus and Systems, IEEE Transactions on* PAS-88(1):55–66. doi:[10.1109/TPAS.1969.292338](https://doi.org/10.1109/TPAS.1969.292338)
- [42] Lorenz RD, Novotny DW (1990) Saturation effects in field-oriented induction machines. *Industry Applications, IEEE Transactions on* 26(2):283–289. doi:[10.1109/28.54254](https://doi.org/10.1109/28.54254)
- [43] Malesani L, Tenti P (1990) A novel hysteresis control method for current-controlled voltage-source pwm inverters with constant modulation frequency. *Industry Applications, IEEE Transactions on* 26(1):88–92. doi:[10.1109/28.52678](https://doi.org/10.1109/28.52678)
- [44] Miller TJE (1993) Switched reluctance motors and their control, illustrated edition Oxford University Press, USA
- [45] Mohan N, Undeland TM, Robbins WP (2002) Power electronics: Converters, applications, and design, 3rd edn. Wiley
- [46] Morel L, Fayard H, Vives Fos H, Galindo A, Abba G (2000) Study of ultra high speed switched reluctance motor drive. In: *Industry Applications Conference, 2000. Conference Record of the 2000 IEEE*, vol 1, pp 87–92. doi:[10.1109/IAS.2000.881030](https://doi.org/10.1109/IAS.2000.881030)
- [47] Muller S, Deicke M, De Doncker RW (2002) Doubly fed induction generator systems for wind turbines. *Industry Applications Magazine, IEEE* 8(3):26–33. doi:[10.1109/2943.999610](https://doi.org/10.1109/2943.999610)
- [48] Novotny DW, Lipo TA (1996) Vector control and dynamics of ac drives (monographs in electrical and electronic engineering). Oxford University Press, USA
- [49] Profumo F, Griva G, Pastorelli M, Moreira J, De Doncker RW (1994) Universal field oriented controller based on air gap flux sensing via third harmonic stator voltage. *Industry Applications, IEEE Transactions on* 30(2):448–455. doi:[10.1109/28.287510](https://doi.org/10.1109/28.287510)
- [50] Profumo F, Tenconi A, De Doncker RW (1991) The universal field oriented (ufo) controller applied to wide speed range induction motor drives. In: *Power Electronics Specialists Conference, 1991. PESC '91 Record., 22nd Annual IEEE*, pp 681–686. doi:[10.1109/PESC.1991.162749](https://doi.org/10.1109/PESC.1991.162749)
- [51] Pulle DWJ (1982) Prediction and analysis of variable reluctance stepmotor-drive systems. PhD thesis, University of Leeds, Leeds, UK
- [52] Pulle DWJ (1989) Switched reluctance motor. In: Australian patent AU4005589
- [53] Pulle DWJ (1991) New database for switched reluctance drive simulation. *Electric Power Applications, IEE Proceedings B* 138(6):331–337
- [54] Pulle DWJ (1991) A novel axial flux switched reluctance motor for variable speed drive operations. In: *Australian Conference on Industrial Drives, Townsville*

- [55] Radun AV (1992) High-power density switched reluctance motor drive for aerospace applications. *Industry Applications, IEEE Transactions on* 28(1):113–119. doi:[10.1109/28.120219](https://doi.org/10.1109/28.120219)
- [56] Reinert J, Inderka R, Menne M, De Doncker RW (1998) Optimizing performance in switched reluctance drives. In: *Applied Power Electronics Conference and Exposition, 1998. APEC '98. Conference Proceedings 1998. Thirteenth Annual*, vol 2, pp 765–770. doi:[10.1109/APEC.1998.653984](https://doi.org/10.1109/APEC.1998.653984)
- [57] Reinert J, Schroder S (2002) Power-factor correction for switched reluctance drives. *Industrial Electronics, IEEE Transactions on* 49(1):54–57. doi:[10.1109/41.982248](https://doi.org/10.1109/41.982248)
- [58] Semikron International GmbH (2010). <http://www.semikron.com>
- [59] Siemens AG (2010). <http://support.automation.siemens.com/>
- [60] Simulation Research (2010). <http://www.simulation-research.com/>
- [61] Speed Laboratory (2010). <http://www.speedlab.co.uk/software.html>
- [62] Stephenson JM, Corda J (1979) Computation of torque and current in doubly salient reluctance motors from nonlinear magnetisation data. *IEE Proceedings, Part B* 126:5
- [63] Svensson T (1988) On modulation and control of electronic power converters. Technical Report 186, Chalmers University of Technology, School of Electrical and Computer Engineering
- [64] Taylor WH (1839) Obtaining motive power, 8255
- [65] The MathWorks, Inc. (2010). <http://www.mathworks.com/>
- [66] Toliyat HA, Kliman GB (2004) *Handbook of electric motors*, 2nd edn. CRC Press
- [67] Veltman A (1993) The fish method: interaction between ac-machines and switching power converters. PhD thesis, Delft University
- [68] Veltman A, Pulle DWJ, De Doncker RW (2007) *Fundamentals of electrical drives*. Springer-Verlag
- [69] Walcarius H, Vandenput A, Jordan H, Geysen W (1978) Stability analysis of oscillating induction machines. In: *International Conference on Electrical Machines, 1978, 11–13 September, Brussels, Belgium*
- [70] Xu X, De Doncker RW, Novotny DW (1988) Stator flux orientation control of induction machines in the field weakening region. In: *Industry Applications Society Annual Meeting, 1988. Conference Record of the 1988 IEEE*, vol 1, pp 437–443. doi:[10.1109/IAS.1988.25097](https://doi.org/10.1109/IAS.1988.25097)
- [71] Xu X, De Doncker RW, Novotny DW (1988) A stator flux oriented induction machine drive. In: *Power Electronics Specialists Conference, 1988. PESC '88 Record., 19th Annual IEEE*, vol 2, pp 870–876. doi:[10.1109/PESC.1988.18219](https://doi.org/10.1109/PESC.1988.18219)
- [72] Zener Electric Pty Ltd (2010). <http://www.zener.com.au>



# Abbreviations

ASM	induction machine
CFO	calculation of field orientation
DC	direct current
DCM	DC machine
DFO	direct field orientation
DITC	direct instantaneous torque control
DSP	digital signal processors
FOC	field oriented control
IFO	indirect field orientation
IRTF	ideal rotating transformer
ITF	ideal transformer
MA	maximum ampere
MF	maximum flux
MMF	magneto-motive forces
MTPA	maximum torque per ampere
MTPF	maximum torque per flux
PM	permanent magnet
PMSM	permanent magnet synchronous machine
PWM	pulse width modulation
SM	synchronous machine
SR	switched reluctance
SRAF	SR axial flux
SRM	switched reluctance machine
UFO	universal field-oriented



# List of symbols

$a$	acceleration
$\Theta$	angle in mechanical degrees
$\theta$	angle in electrical degrees
$C$	capacitance
$I$	current
$i$	current
$D$	diode
$e$	back e.m.f.
$E$	energy
$W$	energy
$F$	force
$\psi$	flux linkage
$f$	frequency
$Z$	impedance
$l$	incremental inductance
$L$	inductance
$J$	inertia
$K$	parameter
$k$	factor (e.g. winding factor)
$\kappa$	current ratio (e.g. between short circuit current and maximum current in PM machines)
$\chi$	leakage factor
$m$	mass
$\phi$	magnetic flux
$M$	mass
$N$	number (e.g. Number of segments)
$T$	period
$\text{pf}$	power factor
$P$	power
$p$	power
$p$	pole pair number

$r$	distance
$R$	radius
$r$	radius
$X$	reactance
$R$	resistance
$T$	simulation time
$s$	slip
$\Omega$	angular speed in mechanical degrees
$\omega$	angular speed in electrical degrees
$n$	speed
$S$	switch
$t$	time
$T$	torque
$V$	volume
$v$	velocity
$U$	voltage
$u$	voltage
$n$	winding number
$x$	auxiliary variable
$z$	auxiliary variable
$s$	laplace operator
$c$	damping coefficient
$K_i$	integral gain (e.g. of current controller)
$K_p$	proportional gain (e.g. of current controller)
$m$	modulation ratio
$\nu$	voltage ratio
$s$	displacement vector
$\tau$	time constant
$\kappa$	torsion coefficient
$\zeta$	damping factor
$Sw$	switching signal

# List of indices

$\hat{X}$	amplitude
$X^A$	point in control diagram
$X^{\alpha\beta}$	fix stator coordinates
$X^{av}$	average
$X^B$	point in control diagram
$X^b$	base (e.g. base speed)
$X^{bS}$	base with constant stator flux (e.g. base speed with constant stator flux)
$X^C$	point in control diagram
$X^{comp}$	comparator
$X^c$	control (e.g. reference current for the current controller)
$X^D$	point in control diagram
$X^D$	dead time
$X^{dq}$	field oriented coordinates
$X^E$	point in control diagram
$X^F$	point in control diagram
$X^f$	falling edge
$X^l$	limit (e.g. stator frequency limit)
$X_{limit}$	limit
$X^e$	linear
$X^{max}$	maximum (e.g. maximum current)
$X^{noload}$	no-load (e.g. no-load current)
$X^{nom}$	nominal or rated (e.g. rated stator current)
$X^n$	normalized (e.g. normalized stator current)
$X^\omega$	operating point of DC machine (indicates maximum flux-linkage for a given speed and voltage)
$X^{pn}$	positive-negative (e.g. positive-negative sequence impedance matrix)
$X^*$	reference (e.g. reference current)
$X^{\text{ripple}}$	ripple
$X^r$	rise edge

$X^r$	in rotor flux oriented coordinate system
$X^{sc}$	short circuit (e.g. short circuit current)
$X^{sp}$	speed, single-phase (e.g. single-phase machine impedance matrix)
$X^s$	in stator flux oriented coordinate system
$X^v$	operating point of DC machine (indicates the no-load speed)
$X^{xy}$	rotor-oriented coordinates
$X^0$	point in control diagram
$X_a$	armature quantity (e.g. armature current)
$X_{a1}$	indicates the on-time of the first space vector at SVM
$X_{a2}$	indicates the on-time of the second space vector at SVM
$X_a$	aligned rotor position
$X_\alpha$	real component of quantity in stator coordinates
$X_A$	amplitude
$X_{aux}$	auxiliary (e.g. auxiliary winding of single-phase induction machine)
$X_B$	bandwidth
$X_\beta$	imaginary component of quantity in stator coordinates
$X_b$	bottom
$X_C$	capacity
$X_c$	center
$X_c$	centripetal
$X_o$	characteristic value
$X_{conv}$	converter
$X_c$	correction
$X_i$	counter
$X_{cw}$	compensation winding
$X_d$	real component of quantity in field oriented coordinates
$X_{DC}$	DC (e.g. DC link voltage)
$X_\delta$	delta
$X_e$	indicates an inertia due to translational load
$X_e$	electric (e.g. electrical frequency)
$X_{eq}$	equal
$X_f$	excitation (e.g. excitation flux)
$X_f$	frequency
$X_{hom}$	homopolar (e.g. homopolar inductance)
$X_{in}$	input (e.g. input power)
$X_1$	inductive
$X_i$	integral (e.g. integral component)
$X_{\{101\}}$	switching states for given voltage vector
$X_k$	integer variable used as counter (e.g. time step in discrete system)
$X_1$	line (e.g. line voltage)
$X_1$	load (e.g. load torque)
$X_M$	transformed main quantity
$X_m$	main quantity (e.g. main inductance)
$X_m$	measured

$X_m$	mechanical (e.g. mechanical position)
$X_{\min}$	minimum
$X_-$	negative sequence (indicates a negative rotational direction)
$X_M$	model based quantity
$X_o$	characteristic value (e.g. eigenfrequency)
$X_{\text{off}}$	off
$X_{\text{on}}$	on
$X_{\text{out}}$	output (e.g. output power)
$X_{\text{ph}}$	phase, e.g. number of phases
$X_D$	phase (e.g. phase voltage)
$X_1$	phase 1
$X_a$	phase a
$X_2$	phase 2
$X_b$	phase b
$X_3$	phase 3
$X_c$	phase c
$X_4$	phase 4
$X_d$	phase d
$X_i$	phase index
$X_a$	motoring pinion
$X_r$	generating pinion
$X_+$	positive sequence (indicates a positive rotational direction)
$X_{\pm}$	positive and negative sequence (indicates a positive and negative rotational direction)
$X_p$	power (e.g. power circle)
$X_p$	proportional (e.g. proportional component)
$X_{\text{pu}}$	torque pulses e.g. number of torque pulses
$X_{\text{PWM}}$	pulse-width modulation
$X_q$	imaginary component of quantity in field oriented coordinates
$X_R$	transformed rotor quantity
$X_r$	rotor quantity (e.g. rotor resistance)
$X_{\text{rp}}$	rotor pole
$X_{\text{run}}$	run (e.g. run winding of single-phase induction machine)
$X_s$	sampling (e.g. sampling time)
$X_{\text{seg}}$	segments
$X_{\text{sense}}$	controlled
$X_{\text{sl}}$	slip (e.g. slip frequency)
$X_S$	transformed stator quantity
$X_s$	stator quantity (e.g. stator resistance)
$X_{\text{step}}$	step
$X_{\sigma}$	stray or leakage (e.g. stray or leakage flux)
$X_{\text{supply}}$	supply e.g. supply current
$X_{\bar{s}}$	vector which contains the duty cycles/ switching signals of all phases
$X_t$	tangential

$X_i$	indicates a certain instant in time
$X_t$	top
$X_{\text{total}}$	total
$X_u$	unaligned rotor position
$X_w$	winding
$X_x$	real component of quantity in rotor-oriented coordinates
$X_y$	imaginary component of quantity in rotor-oriented coordinates
$X_0$	zero
$X_{\text{air-gap}}$	air-gap (e.g. air-gap power)
$\underline{\underline{X}}$	phasor
$\vec{X}$	space vector

# Index

## A

amplitude modulation ratio 22  
anti-windup 62  
asymmetrical half-bridge converter 384  
augmented model based control 63  
auxiliary winding 273  
average voltage 21

## B

backward time discretization 63  
Blondel diagram 174, 181

## C

calculation of field orientation (CFO) 313  
capacitor-run machines 273  
co-energy 369  
comparator 22  
concentrated winding 363  
constant power region 145  
control  
    augmented model based control 63  
    current control 55  
    DC machine 131  
    field oriented control 217, 311  
    hysteresis current control 55, 67  
    induction machine 303  
    model based current control 58, 73  
    non-salient synchronous machine 195  
    salient synchronous machine 213  
separately excited DC machine 138  
switched reluctance machine 396  
synchronous machine 193  
    voltage-to-frequency (V/f) 303

controller principles 193  
converter  
    asymmetrical half-bridge 384  
    full-bridge converter 23  
    half-bridge converter 19  
    power converter 6  
    switched reluctance machine 394  
    three-phase converter 28  
corner point 141, 326  
current control 55  
current-controlled synchronous machine 217  
current-speed diagram 202

## D

DC machine 131  
dead time 38  
direct field-oriented control (DFO) 313  
direct instantaneous torque control 409  
drive  
    design 11  
    dynamics 108  
    operational drive boundaries 323  
    technology trends 3  
drive saturation point 141, 326

## E

electrical machine 3  
embedded control 8  
encoderless control 313

## F

field weakening mode 143  
field winding 132

field-oriented control  
 current-controlled synchronous machine 217  
 induction machine 311  
 synchronous machine 193  
 voltage-source connected synchronous machine 219  
 flux linkage 97  
 frequency modulation ratio 22  
 frequency spectrum 81  
 full-bridge converter 23

**G**

gear transmission 113

**H**

half-bridge converter 19  
 Heyland diagram 269  
 hysteresis current control 55, 67

**I**

ideal rotating transformer 99  
 idle mode 19  
 incoming phase interval (IPI) 412  
 indirect field-oriented control (IFO) 313  
 induction machine  
   field-oriented control 311  
 induction machine drives  
   voltage-to-frequency (V/f) 303  
 inertia 100  
 interior permanent magnet machine 175

**K**

Kloss formula 304

**L**

law of inertia 109  
 leakage inductances 247  
 linear motion 109  
 load 151

**M**

maximum output power point 174  
 maximum torque per ampere (MTPA) 199, 213, 327  
 maximum torque per flux linkage (MTPF) 199, 216, 326

model based current control 58, 73  
 motoring 174  
 multi-phase machine 392

**N**

Newton's first law 109  
 Newton's second law 109  
 Newton's third law 112  
 non-salient synchronous machine 165  
   generic model 167  
   rotor-oriented model 169  
   steady-state analysis 171  
   symbolic model 166

**O**

operational drive boundaries 139, 323  
 outgoing phase interval (OPI) 412

**P**

PI controller 61  
   anti-windup 62  
 power converter 6  
 power factor 174  
 pull out (stall) torque 174  
 pull out torque 305  
 pulse width modulation 22

**R**

rack and pinion set of gears 111  
 rotational motion 110  
 rotor 97  
 rotor angle 99  
 rotor flux orientation  
   synchronous machine 194  
 rotor teeth 363  
 rotor-oriented model  
   non-salient synchronous machine 169  
   salient synchronous machine 178  
 run winding 273

**S**

salient synchronous machine 175  
   generic model 177  
   rotor-oriented model 178  
   steady-state analysis 180  
 sampling interval 19  
 sensorless control 313  
 short pitched winding 363  
 single-phase induction machine 273  
 slip 269  
 slip frequency 245, 305

space vector modulation 18, 33  
split-coil machines 273  
squirrel-cage rotor 239  
stator 97  
stator teeth 363  
steady-state analysis  
    non-salient synchronous machine 171  
    salient synchronous machine 180  
    single-phase induction machine 277  
step angle 392  
switched reluctance drive 396  
switched reluctance drives  
    torque 368, 372  
synchronous machine 103, 193  
    control 193  
    field-oriented control 193  
    interior permanent magnet machine 175  
    non-salient 195  
    rotor flux orientation 194  
    salient 175

**T**

three-phase converter 28  
torque 99, 368, 372

triangular 22  
turn-off angle 386  
turn-on angle 386

**U**

universal field-oriented model 258  
universal stationary frame oriented  
    model 257

**V**

vector control module 241  
vernier principle 366  
voltage-source connected synchronous  
    machine  
    field-oriented control 219  
voltage-to-frequency (V/f) control 303

**W**

windup 62

**Z**

zero leakage inductance model 241